ECCM

20

26-30 JUNE

2022

LAUSANNE

SWITZERLAND

Proceedings of the 20th European Conference on Composite Materials

COMPOSITES MEET SUSTAINABILITY

Vol 6 – Life Cycle Assessment

Editors : Anastasios P. Vassilopoulos, Véronique Michaud

Organized by :

EPFL

Under the patronage of :

CCLAB Composite Construction Laboratory

LPAC Laboratory for Processing of Advanced Composites

ESCM EUROPEAN SOCIETY FOR COMPOSITE MATERIALS

ECCM 20
26-30 JUNE 2022
LAUSANNE SWITZERLAND

EPFL CCLAB Composite Construction Laboratory LPAC Laboratory for Processing of Advanced Composites

Proceedings of the 20th European Conference on Composite Materials ECCM20 26-30 June 2022, EPFL Lausanne Switzerland

Edited By :

Prof. Anastasios P. Vassilopoulos, CCLab/EPFL
Prof. Véronique Michaud, LPAC/EPFL

Oragnized by:

Composite Construction Laboratory (CCLab)
Laboratory for Processing of Advanced Composites (LPAC)
Ecole Polytechnique Fédérale de Lausanne (EPFL)

ISBN: 978-2-9701614-0-0
DOI: http://dx.doi.org/10.5075/epfl-298799_978-2-9701614-0-0

Published by :

Composite Construction Laboratory (CCLab)
Ecole Polytechnique Fédérale de Lausanne (EPFL)
BP 2225 (Bâtiment BP), Station 16
1015, Lausanne, Switzerland

https://cclab.epfl.ch

Laboratory for Processing of Advanced Composites (LPAC)
Ecole Polytechnique Fédérale de Lausanne (EPFL)
MXG 139 (Bâtiment MXG), Station 12
1015, Lausanne, Switzerland

https://lpac.epfl.ch

Cover:

Swiss Tech Convention Center
© Edouard Venceslau - CompuWeb SA

Cover Design:

Composite Construction Laboratory (CCLab)
Ecole Polytechnique Fédérale de Lausanne (EPFL)
Lausanne, Switzerland

©2022 ECCM20/The publishers

Disclaimer:

The ECCM20 organizing committee and the Editors of these proceedings assume no responsibility or liability for the content, statements and opinions expressed by the authors in their corresponding publication.

Editorial

This collection gathers all the articles that were submitted and presented at the 20th European Conference on Composite Materials (ECCM20) which took place in Lausanne, Switzerland, June 26-30, 2022.

ECCM20 is the 20th edition of a conference series having its roots back in time, organized each two years by members of the European Society of Composite Materials (ESCM).

The ECCM20 event was organized by the Composite Construction laboratory (CCLab) and the Laboratory for Processing of Advanced Composites (LPAC) of the Ecole Polytechnique Fédérale de Lausanne (EPFL).

The Conference Theme this year was “Composites meet Sustainability”. As a result, even if all topics related to composite processing, properties and applications have been covered, sustainability aspects were highlighted with specific lectures, roundtables and sessions on a range of topics, from bio-based composites to energy efficiency in materials production and use phases, as well as end-of-life scenarios and recycling.

More than 1000 participants shared their recent research results and participated to fruitful discussions during the five conference days, while they contributed more than 850 papers which form the six volumes of the conference proceedings. Each volume gathers contributions on specific topics:

Vol 1 – Materials

Vol 2 – Manufacturing

Vol 3 – Characterization

Vol 4 – Modeling and Prediction

Vol 5 – Applications and Structures

Vol 6 – Life Cycle Assessment

We enjoyed the event; we had the chance to meet each other in person again, shake hands, hold friendly talks and maintain our long-lasting collaborations. We appreciated the high level of the research presented at the conference and the quality of the submissions that are now collected in these six volumes. We hope that everyone interested in the status of the European Composites’ research in 2022 will be fascinated by this publication.

The Conference Chairs

Anastasios P. Vassilopoulos, Véronique Michaud

ECCM 20
26-30 JUNE 2022
LAUSANNE SWITZERLAND

Hosting Organizations

Composite Construction Laboratory (CCLab)
Laboratory for Processing of Advanced Composites (LPAC)
Ecole Polytechnique Fédérale de Lausanne (EPFL)

Venue

Swiss Tech Convention Center (https://www.stcc.ch)

Conference Chairs

Chair : Prof. Anastasios P. Vassilopoulos, EPFL, Switzerland
Co-Chair: Prof Véronique Michaud, EPFL, Switzerland

International Scientific Committee

Prof. Malin Åkermo SE
Dr. Emmanuel Baranger FR
Prof. Christophe Binetruy FR
Prof. Pedro Camanho PT
Prof. Konstantinos Dassios GR
Prof. Brian Falzon UK
Prof. Kristofer Gamstedt SE
Prof. Sotiris Grammatikos NO
Prof. Christian Hochard FR
Prof. Marcin Kozlowski PL
Prof. Stepan Lomov BE
Dr. David May DE
Prof. Stephen Ogin UK
Prof. Gerald Pinter AT
Prof. Silvestre Pinho UK
Prof. Yentl Swolfs BE
Dr. Julie Teuwen NL
Dr. Panayota Tsotra CH
Prof. Wim van Paepegem BE
Prof. Dimitrios Zarouchas NL
Dr. Andrey Aniskevich LV
Prof. Christian Berggreen DK
Dr. Nicolas Boyard FR
Prof. Valter Carvelli IT
Prof. Klaus Drechsler DE
Prof. Bodo Fiedler DE
Dr. Nathalie Godin FR
Prof. Roland Hinterholzl AT
Prof. Ian Kinloch UK
Dr. Thomas Kruse DE
Prof. Theodoros Loutas GR
Prof. Veronique Michaud CH
Prof. Alessandro Pegoretti IT
Prof. Joao Ramoa Correia PT
Prof. Jose Sena-Cruz PT
Prof. Antonio T. Marques PT
Prof. Thanasis Triantafillou GR
Prof. Albert Turon ES
Prof. Anastasios P. Vassilopoulos CH
Prof. Martin Fagerström SE
Dr. Alexandros Antoniou DE
Prof. Lars Berglund SE
Prof. Michal Budzik DK
Prof. Lucas Da Silva PT
Dr. Andreas Endruweit UK
Prof. Mariaenrica Frigione IT
Dr. Larissa Gorbatikh BE
Dr. Martin Hirsekorn FR
Prof. Vassilis Kostopoulos GR
Prof. Jacques Lamon FR
Prof. Staffan Lundstrom SE
Prof. Peter Mitschang DE
Dr. Soraia Pimenta UK
Prof. Paul Robinson UK
Dr. Olesja Starkova LT
Prof. Sofia Teixeira de Freitas NL
Dr. Stavros Tsantzalis GR
Prof. Danny van Hemelrijck BE
Prof. Michele Zappalorto IT
Dr. Miroslav Cerny CZ

Local Organizing Committee

Prof. Anastasios P. Vassilopoulos, EPFL
Prof. Véronique Michaud, EPFL
Angélique Crettenand and Mirjam Kiener, Lausanne Tourisme
And all those who helped, colleagues who reviewed abstracts and chaired sessions, and CCLab and LPAC students and collaborators who worked hard to make this conference a success.

ECCM 20
26-30 JUNE 2022
LAUSANNE SWITZERLAND

Sponsors

SHIMADZU
Excellence in Science

Bristol Composites Institute

JEC GROUP

suprem

Surface Measurement Systems
World Leader in Sorption Science

INSTRON

9T LABS

Anton Paar

DIA-STRON
DELIVERING MEASUREMENT SOLUTIONS

AELER

HRC

ICCM 23
BELFAST 2023
30 JULY – 4 AUGUST

TEIJIN

Functional Composite Materials

materials
an Open Access Journal by MDPI

ELSEVIER

Supporting partners

JEC

CertBond
COST Action CA18120

EsSENce

Switzerland Tourism.

SWISS

SBB CFF FFS

sampe
Switzerland

CU COMPOSITES UNITED | SWITZERLAND

canton de vaud

Lausanne

Contents

A COMPARATIVE STUDY ON THE EFFECT OF HOT/WET AND HOT/DRY AGING ENVIRONMENTS ON THE DEGRADATION OF FILAMENT WINDED COMPOSITES

C. Srivastava[a], *A. Strandlie*[a], *B. Alcock*[b], *and S. A. Grammatikos*[a]

a: Laboratory for Advanced and Sustainable Engineering Materials (ASEMlab), Department of Manufacturing and Civil Engineering, Norwegian University of Science and Technology, Gjøvik 2815, Norway
b: SINTEF Industry, Forskningsveien 1, Oslo 0373, Norway
chaman.srivastava@ntnu.no

Abstract: *Predicting the long-term response of polymer composite materials is a continuous challenge to the composite industry. The service aging of structural composites has different effects on composites' physicochemical behavior manifested as changes in the mechanical properties. This work presents the effects of hot/wet and hot/dry accelerated aging conditions on the interlaminar shear properties of vinyl-ester glass fiber coupons made with filament winding. The test coupons were aged for 224 days, removed and tested after every 28, 56, 112, and 224 days. It was observed that the response of composite coupons is different for the hot/wet and hot/dry aging environments for same duration of aging. This is attributed to the time-temperature-environment coupling during the aging regime. The overall response of the composite behavior is then represented via retention curves and degradation maps that can help correlate the results for both hot/wet and hot/dry aging environment as a function of exposure times and temperatures. The findings of the study thus provide an insight on the dependence of matrix-dominated properties of composite. The results can be taken into account when designing structure made from vinyl-ester glass fiber filament winded composite which foresee aging in hot/wet and hot/dry conditions.*

Keywords: Aging; Filament winded composites; Degradation Maps; Retention Curves

1. Introduction

The service life of composite materials can be approximated using lab-scale accelerated aging methods, where specimens are artificially aged for a defined period and then tested to determine the influence of artificial aging and its correlation with natural weathering. This characterization of the long-term response of the material and its associated structure towards a complex environment presents a continuous challenge to the industries [1]. The understanding behind the aging process is of extreme importance as it can help to prevent catastrophic failure of the structure.

A composite material is composed of reinforcement with a matrix surrounding it. Understanding the aging of structures made of composite materials is complex due to the combined matrix and fiber responses to aging. In this work, a testing regime comprising different aging environments and mechanical tests was formulated to segregate the effects of aging at fiber, matrix, and interface levels. The two most crucial service environments faced by composites are hot/dry and hot/wet conditions. Thermo-oxidation of the matrix, hazing, and formation of microcracks have been reported to severely affect the service life in hot/dry environments [2, 3], whereas hydrolysis, interfacial failure, and selective leaching of the matrix have been reported to degrade

  doi:10.5075/epfl-298799_978-2-9701614-0-0

the composite severely [4]. This paper presents mechanical performance results on vinyl-ester glass fiber filament winded composite coupons subjected to hot/dry and hot/wet environments, for a period of 224 days. The study will focus on matrix degradation through interlaminar shear strength testing.

2. Mechanical testing

Interlaminar shear testing (ILSS) was carried out following the ASTM D2344 test standard using a short beam shear specimen (SBS), where the specimen geometry and the dimensions are shown in Figure *1*. The composite coupon is a bi-layered structure where the top layer is made from unreinforced polyethylene (PE) polymeric layer, which has a thickness of 1.2 mm, and the remainder of the composite coupon is composed of glass fiber reinforced vinyl ester composite produced by filament winding. The fiber volume fraction of the composite was calculated to be 56% using the calcination method [5] and 52% using micro-Computed Tomography (CT-scanning). The glass transition temperature of the unaged vinyl ester matrix is 98-100°C, measured using Differential Scanning Calorimetry (DSC).

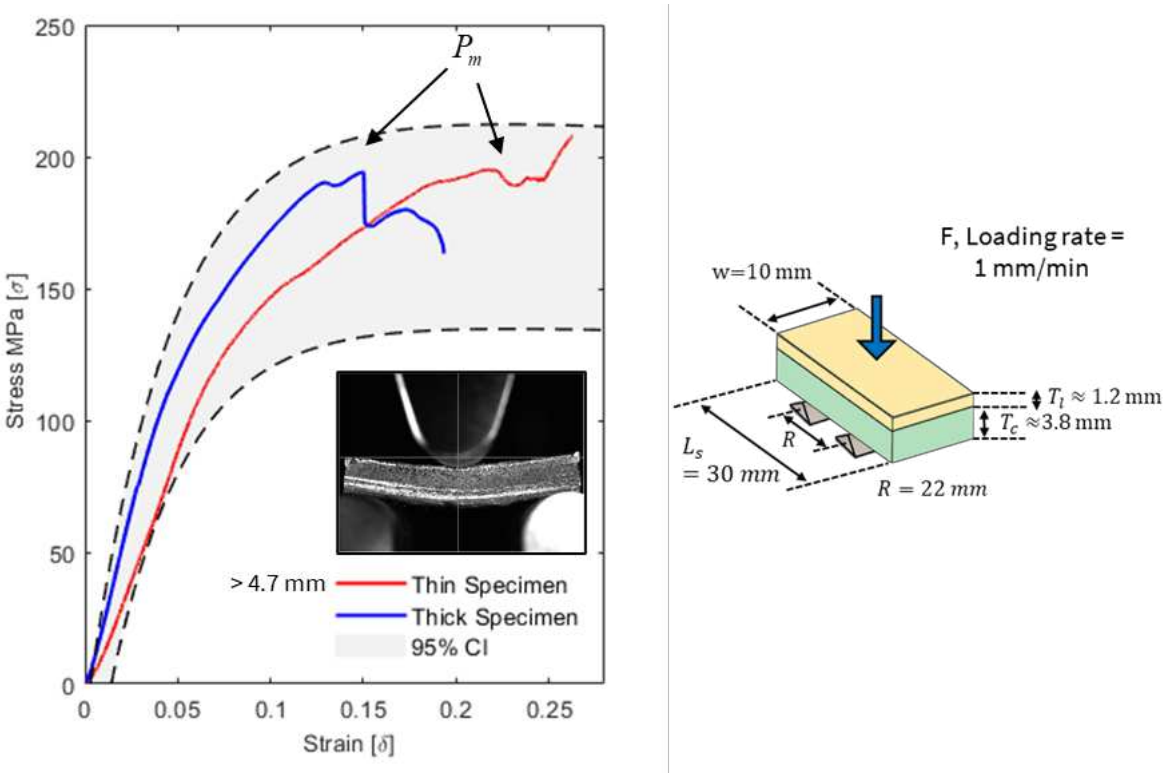

Figure 1: (a) Stress-strain curve for interlaminar shear testing (b) Interlaminar shear strength coupon prepared as per ASTM D2344 standard.

The mechanical tests were performed on the Instron 5966 UTS machine, where the loading pin and support pin diameter is 5 mm. The roller separation is set to 22 mm, 4 times the thickness of the total composite coupon. The loading rate is quasi-static at 1mm/min. A representative stress-strain curve for composite coupons is also presented in Figure *1*. The point of the first load drop in the stress-strain curve is taken to be the P_{max} value, and the interlaminar shear stress is calculated using Equation (*1*).

  doi:10.5075/epfl-298799_978-2-9701614-0-0

$$\tau = \frac{0.75 \times P_{max}}{b \times h} \quad (1)$$

2.1 Hot/Dry Aging

Before aging, the ILSS coupons were dried at 30°C in a vacuum oven for 48 h to remove residual humidity absorbed during storage. After drying, the specimens are removed and allowed to cool overnight in a vacuum desiccator. Termaks laboratory drying oven with fan-controlled airflow was used to create hot/dry conditions where the coupons are aged isothermally at room temperature (23°C), 40°C, 60°C, and 80°C, for a total period of 224 days. The maximum temperature is lower than the glass transition temperature (Tg) of the vinyl-ester matrix of the composite to avoid activating unwanted and unrealistic aging mechanisms above Tg.

2.2 Hot/Wet Aging

Hot/wet aging was conducted in Grant Sub Aqua water baths with a temperature stability of ±0.2°C. Before being placed in heated water baths, the coupons are dried in a vacuum oven at 30°C for 48 h to remove any residual moisture absorbed from the environment during storage. The dried specimens are then placed in water baths at 20°C, 40°C, 60°C, and 80°C. Distilled water is used as a hot/wet aging medium. The maximum temperature is again selected to be below the Tg of the vinyl ester matrix of the composite. The specimens are aged for a total period of 224 days. The specimens are kept in a refrigerator for storage at 4°C and kept to condition overnight before testing.

3. Experimental Results and Discussion

Retention curves and degradation maps are created to study the evolution of interlaminar shear strength as a function of aging time and temperature. The stress vs. the midspan deflection of each composite coupon at each aging interval is plotted to visualize the behavior of composite coupon. From Figure 1, it is observed that the behavior of the composite coupon is linear at the beginning of the mechanical test, but due to the presence of the polyethylene layer, the initial behavior alters after 1-3% strain. The coupon failure is observed as a sharp drop in the stress-strain curve. The point of the first deflection, which drops more than 15%, is considered the maximum load (Pm) for calculating the short beam strength using Equation (1).

Then, interlaminar shear strength retention curves are plotted as a ratio of the interlaminar shear strength at time (t) divided by the interlaminar shear strength of unaged composite coupon. The value 1 is thus chosen as a reference which is also presented as a red dashed line in degradation maps. The absicca represents the test intervals of 0, 28, 56, 112, and 224 days. The average of the retention values at each ageing time and temperature interval and their corresponding standard deviation for 5 specimen replicates under hot/wet aging is tabulated in Table *1*.

Table 1: Interlaminar shear strength retention for composite coupons aged in hot/wet aging environment.

20°C	40°C	60°C	80°C
Ret.	Ret.	Ret.	Ret.

  doi:10.5075/epfl-298799_978-2-9701614-0-0

28	1.186 ± 0.18	1.136 ± 0.19	1.108 ± 0.26	0.954 ± 0.24
56	1.086 ± 0.29	1.057 ± 0.32	1.134 ± 0.10	0.779 ± 0.04
112	1.088 ± 0.13	1.074 ± 0.23	0.885 ± 0.27	0.716 ± 0.13
224	1.095 ± 0.18	0.948 ± 0.45	0.843 ± 0.05	0.651 ± 0.08

Figure *2* (a) and (b) presents the ILSS retention curves and degradation map for hot/wet aging condition. It is observed that for lower temperatures (20°C, 40°C, 60°C) well below the Tg of the vinyl-ester matrix of composite coupons, the coupons exhibit an initial strengthening of ILSS value for 28 days. This strengthening effect can be attributed to additional crosslinking of vinyl ester at lower temperatures, and hence the interlaminar shear strength, which is a matrix-dominated property increases. Similar results have also been reported by Sousa et. al. [6]. A slight strengthening of ILSS which can be masked by an early onset of degradation is observed for 28 days of aging at 80°C. This temperature is close to the glass transition temperature of the vinyl ester matrix and has a higher kinetics of reaction. Thus the degradation of the polymer superimposes the post-curing effect and no appreciable change is observed.

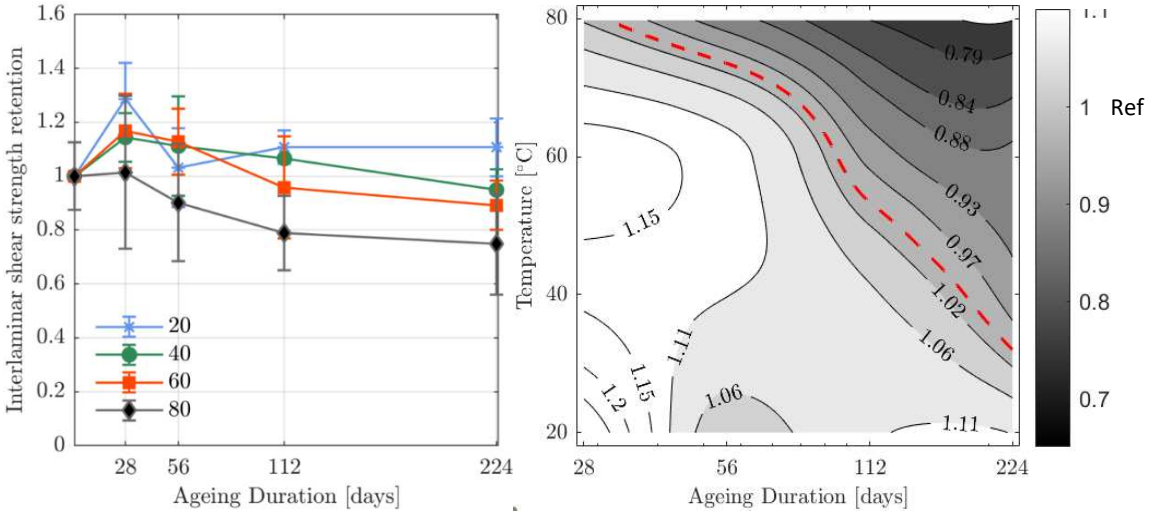

Figure 2: (a) ILSS retention curves (b) degradation map for filament-winded composite coupon aged in hot/wet conditions for 28, 56, 112 and 224 days at 20°C, 40°C, 60°C and 80°C.

For 56, 112, and 224 days, the observed inter-laminar shear strength values starts to fall for temperature ranges of 40°C, 60°C, and 80°C, also reported in [7]. This effect is attributed to the plasticization of the matrix [8, 9] and differential swelling between the fiber and matrix [10] thus leading to an easier fiber/matrix seperation and pull out. Hydrolytic leaching of the silane sizing on the fiber/matrix interface has also been reported to cause eventual degradation within the laminate, which can be visible as swelled up pitted regions on the fiber surface[7, 11]. Interestingly, the competing effect of strengthening and degradation at 20°C leads to a slight increase in the retention values at 224 days. This anomalous behavior can be attributed to possible secondary bonds created between the free radicals of polymer and the hydroxyl molecules at low temperatures as reported also in [12]. At a duration of 224 days, it was observed that the maximum reduction of -3%, -11%, and -23 % was observed for 40°C, 60°C and 80°C at 224 days, respectively.

  doi:10.5075/epfl-298799_978-2-9701614-0-0

Figure *3* (a) and (b) presents the interlaminar shear strength retention curves and degradation map for hot/dry aging over the aging period of 224 days. The general trend for hot/dry aging of filament winded composite varies again for both the aging duration and temperature. The average of the retention values at each ageing time and temperature interval for hot/dry aging and their corresponding standard deviation for 5 specimen replicates is tabulated in Table *2*.

It is observed for 28 days, ILSS retention values for all aging regimes, increases where the maximum strengthening effect is visible for temperatures close to the Tg of the vinyl-ester matrix (60°C and 80°C). This strengthening effect can be again attributed to additional crosslinking of vinyl ester and hence the interlaminar shear strength which is a matrix dominated property increases. The initial strengthening is often due to time-temperature coupling, where higher temperature (but below Tg) and longer exposure duration cause a higher increase in the matrix-dominated properties for vinyl ester-based composites [13]

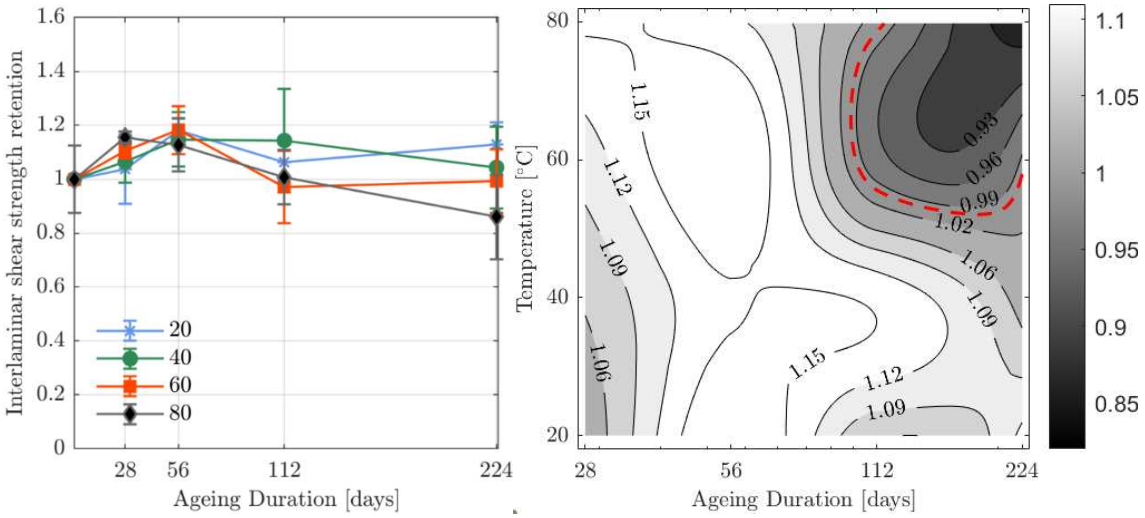

Figure 3: (a) ILSS retention curves (b) degradation map for filament-winded composite coupon aged in hot/dry conditions for 28, 56, 112 and 224 days at 20°C, 40°C, 60°C and 80°C.

For aging duration of 56, 112, and 224 days, the interlaminar shear strength values of the coupons start to fall, but are above the reference unaged value of 1. Hence, no particular degradation is observed at 20°C, 40°C, 60°C for a total ageing duration of 224 days. The onset of degradation in the interlaminar shear strength is observed at a higher aging temperature of 80°C between 112 and 224 days. This degradation zone is visible in the upper right quadrant of the degradation map where the retention values fall sharply below 1 signifying apparent degradation from the unaged interlaminar shear strength values. At a duration of 224 days, it was observed that an increase of +4%, +1%, and +0.2 % was observed for 20°C, 40°C and 60°C respectively, whereas a degradation of -10% was observed at 80°C.

It is also reported that the presence of any micro-cracks [3] during the aging helps to create crevices where the oxygen can percolate and create an oxide layer and thus aids in the oxidation of the whole polymer. However, for filament winded composites, it is observed that due to the presence of fibers in the hoop layer, which is parallel to the surface of the composite, the oxide layer is arrested and hence the diffusion of the oxygen is arrested, which protects the bulk of the coupon to remain unaffected [14]. This barrier towards the diffusion of oxygen can be destroyed close the Tg of the material as the physico-chemical characteristics of the material

  doi:10.5075/epfl-298799_978-2-9701614-0-0

changes and thus allowing more percolation and overall thermo-oxidation of the composite coupon. [15]

Table 2: Interlaminar shear strength retention for composite coupon aged in hot/dry aging environment.

	20°C	40°C	60°C	80°C
	Ret.	Ret.	Ret.	Ret.
28	1.034 ± 0.28	1.025 ± 0.12	1.09 ± 0.02	1.161 ± 0.04
56	1.181 ± 0.05	1.104 ± 0.08	1.172 ± 0.19	1.029± 0.17
112	1.098 ± 0.08	1.258 ± 0.11	1.151 ± 0.23	1.009 ± 0.19
224	1.091 ± 0.11	0.965 ± 0.26	1.058 ± 0.14	0.862 ± 0.35

4. Conclusion

The effects of hot/wet and hot/dry aging of filament winded composites, on interlaminar shear strength are presented in this work. It is observed that the time-temperature-environment coupling plays a critical role in determining the extent of degradation in vinyl-ester glass fiber reinforced composites. It can be concluded that the composite coupons aged in hot/wet aging conditions show a higher degradation of the matrix-dominated properties when compared with hot/dry aging condition for the same duration and temperature aging regimes. The presence of water is shown to accelerate the degradation process as it can initiate secondary degradation mechanisms like hydrolysis and leaching of the matrix which are not present in hot/dry aging environment. The coupons aged in hot/dry aging environment are only prone to degradation through a thermo-oxidative aging which is found to be not aggressive as hot/wet aging and slight degradation was observed at 224 days. This degradation is manifested as reduction of -23% at 80°C in the interlaminar shear strength values in hot/wet aging when compared to -10% at 80°C in hot/dry aging environment. It is also evident from the degradation maps, that the degradation zone size and the onset for the hot/wet aging shifts towards lower temperatures and shorter ageing duration which is not the case in the hot/dry aging. Hence, these findings can be used to make structural application decisions when designing composites structure used in civil engineering applications and made from vinyl-ester glass fiber filament winding.

Acknowledgments

The work reported in this paper is based on activities within the center for research-based innovation, SFI Manufacturing in Norway, and is partially funded by the Research Council of Norway under contract number 237900.

5. References

1. Council, N.R., *Accelerated Aging of Materials and Structures: The Effects of Long-term Elevated-temperature Exposure (Publication NMAB; 479)*. 1996: National Academies Press.
2. de Souza Rios, A., et al., *Effects of accelerated aging on mechanical, thermal and morphological behavior of polyurethane/epoxy/fiberglass composites.* Polymer Testing, 2016. **50**: p. 152-163.
3. Hawileh, R.A., et al., *Temperature effect on the mechanical properties of carbon, glass and carbon–glass FRP laminates.* Construction and Building Materials, 2015. **75**: p. 342-348.
4. Sethi, S. and B.C. Ray, *Environmental effects on fibre reinforced polymeric composites: Evolving reasons and remarks on interfacial strength and stability.* Advances in colloid and interface science, 2015. **217**: p. 43-67.
5. ISO, E., *1172.* Textile-glass-reinforced plastics-Prepregs, moulding compounds and laminates-Determination of the textile-glass and mineral-filler content-Calcination methods (ISO 1172: 1996), 1996.
6. Sousa, J., et al., *Hygrothermal ageing of pultruded GFRP profiles: Comparative study of unsaturated polyester and vinyl ester resin matrices.* Composites Part A: Applied Science and Manufacturing, 2021. **140**: p. 106193.
7. Karbhari, V., *E-glass/vinylester composites in aqueous environments: Effects on short-beam shear strength.* Journal of Composites for Construction, 2004. **8**(2): p. 148-156.
8. Gautier, L., B. Mortaigne, and V. Bellenger, *Interface damage study of hydrothermally aged glass-fibre-reinforced polyester composites.* Composites Science and Technology, 1999. **59**(16): p. 2329-2337.
9. Zhou, J. and J.P. Lucas, *Hygrothermal effects of epoxy resin. Part I: the nature of water in epoxy.* Polymer, 1999. **40**(20): p. 5505-5512.
10. Joliff, Y., et al., *Study of the moisture/stress effects on glass fibre/epoxy composite and the impact of the interphase area.* Composite Structures, 2014. **108**: p. 876-885.
11. Salmon, L., et al., *Hydrolytic degradation of model networks simulating the interfacial layers in silanecoupled epoxy/glass composites.* Composites Science and Technology, 1997. **57**(8): p. 1119-1127.
12. Zhou, J. and J.P. Lucas, *Hygrothermal effects of epoxy resin. Part II: variations of glass transition temperature.* Polymer, 1999. **40**(20): p. 5513-5522.
13. Marouani, S., L. Curtil, and P. Hamelin, *Ageing of carbon/epoxy and carbon/vinylester composites used in the reinforcement and/or the repair of civil engineering structures.* Composites Part B: Engineering, 2012. **43**(4): p. 2020-2030.
14. Gong, J., et al., *A numerical study of thermal degradation of polymers: Surface and in-depth absorption.* Applied Thermal Engineering, 2016. **106**: p. 1366-1379.
15. Pochiraju, K.V., *Modeling thermo-oxidative aging and degradation of composites*, in *Long-term durability of polymeric matrix composites*. 2012, Springer. p. 383-425.

  doi:10.5075/epfl-298799_978-2-9701614-0-0

ASSESSMENT OF THE PROPERTIES OF TWO HIGH-TEMPERATURE THERMOSETTING POLYIMIDES

Valeri, Petkov[a], Patrik, Fernberg[a], Carlos, Solano[b]

a: Department of Engineering Sciences and Mathematics, Luleå tekniska universitet – Valeri.Petkov@LTU.se
b: Nexam Chemical AB

Abstract: *A novel thermosetting polyimide, NEXIMID R300, is introduced and compared with the commercial MHT-R in terms of fracture toughness, thermal properties and ageing behaviour. The new R300 formulation has an altered chemical composition compared to the MHT-R, resulting in a reduced cross-linking density, and was presented as a less susceptible to cracking and a more processable alternative during composite manufacturing with resin transfer moulding. The study uses fracture toughness with single edge notched beam setup, DSC, dilatometry, weight loss measurements and optical microscopy for investigation of the neat resin properties of both material. A slight increase in fracture toughness and a decrease in glass transition temperature for the R300 formulation is observed.*

Keywords: Polyimide; Fracture toughness; Ageing; DSC

1. Introduction

The thermosetting polyimide NEXIMID MHT-R is a high-end polymer resin, particularly suitable for composite manufacturing by resin transfer moulding (RTM), due to the low melt viscosity of the resin prior to cross-linking. MHT-R exhibits a good resistance towards thermal degradation for temperatures up to around 300 ˚C. The presence of oxygen, in addition to the elevated temperature, however, significantly reduces the ability of the polymer to withstand degradation, resulting in thermal oxidation, or thermo-oxidation.[1] The phenomenon has been described by Pochiraju et al.[2]

Previous studies have shown that two of the main factors, affecting the thermal oxidative behaviour of carbon fibre/polyimide composites, are the susceptibility of the polymer towards chemically reacting with oxygen-rich air at elevated temperatures, and matrix cracking.[1-2] The first factor usually results in an oxidation layer with reduced mechanical properties on the exposed surfaces, while the second one creates a direct access for oxygen into the specimen, thus shortening the amount of distance the oxygen has to diffuse through. Cracking can occur due to the presence of residual stresses from manufacturing but can also be enhanced by the locally reduced properties in the oxidized layer.

This study introduces a new polyimide resin formulation, NEXIMID R300, which aims to reduce both matrix cracking and thermal oxidation, and to facilitate RTM processability, by introducing a change in the chemical composition of the original MHT-R matrix. The aim of this work was to investigate and compare the novel NEXIMID R300 to the original MHT-R in terms of fracture toughness, thermal properties (T_g, thermal expansion) and ageing behaviour, for which a series of single-edge notched beam (SENB), differential scanning calorimetry (DSC), dilatometry, weight loss, and light optical microscopy (LOM) experiments were performed. Measuring the

  doi:10.5075/epfl-298799_978-2-9701614-0-0

fracture toughness on bulk specimens of high cross-linking density, RTM-processable, polyimides is a challenging experiment due to the inherent brittleness of these materials, and to the knowledge of the authors, this is one of few studies of this kind.

2. Materials

The original formulation, NEXIMID® MHT-R by Nexam Chemicals AB, contains a 6F-dianhydride (6-FDA) backbone, with a 4-(Phenylethynyl)Phthalic Anhydride (4-PEPA) end-group cross-linker and an ethynyl bis-phthalic anhydride (EBPA) main chain cross-linker. In the new formulation, NEXIMID® R300, all fully aromatic monomers are preserved, except for the in-chain cross-linker EBPA, which accounts for around 5 % of the cross-linking units and is removed in order to reduce the cross-linking density upon curing.

The plates were manufactured by RTM at RISE Sicomp, Sweden. The manufacturing parameters were similar to the previously used settings in [3], including a two-step curing cycle at 320 ˚C (for 30-60 min) and 370 ˚C (for 120-180 min). For the carbon fibre-reinforced frame part of the plates, 370 g/m^2 8-harness satin weave based on Cytec Thornel T650/35 carbon fibres (Sigmatex) were used.

3. Experimental

3.1 Plate manufacturing and specimen preparation

The two PI resin systems were used for manufacturing two separate plates with dimensions 350×350×3 mm^3 by RTM. Manufacturing of neat PI plates is a challenging process, because of shrinkage and void formation during curing. To tackle these issues, the plates were designed to include a carbon fibre preform based on satin weaves as a frame around a centrally located cavity, which was left without fibres. This square section contained a coarse steel wire network that served the purpose of controlling crack initiation and propagation. The neat polymer section with original MHT-R was 160×160 mm^2, and was increased to 240×240 mm^2 with the new R300 polyimide formulation.

Neat cured polymer specimens were cut out from the RTM-manufactured plate with a Dremel cutting device, equipped with a diamond cut-off wheel, and were polished with a sandpaper into the required dimensions for respective test.

3.2 Fracture toughness

Fracture toughness measurements were performed on SENB specimens according to ASTM D5045-14 [4]. Specimen preparation involved creating a shallow notch with a fine saw, while a razor blade mounted in an Instron 3366 tensile testing machine was used to create the sharp initial pre-crack. The specimen dimensions were 26×5.8×3 mm^3. Instron 4411 tensile testing machine with a 500 N load cell and SENB testing setup was used for the experiments, Figure 1. The pre-crack initiation proved very challenging, especially for the MHT-R. Pre-cracks would often spontaneously propagate prematurely through the whole specimen, as soon as it had been initiated by the razor blade, splitting the specimen in half. Due to the brittleness of the material, the notch length recommended in the standard could not be achieved for samples based on the original MHT-R formulation. To ensure that the initial crack was extending through the whole width of the specimen, a Nikon SMZ1270 stereomicroscope was used to investigate the pre-cracks, as shown in Figure 1, before and after test. Another criterion that specimens had to fulfil

to be considered adequate was that their load-extension curves from the SENB tests had to be free from any artefacts, which would suggest e.g. faulty pre-crack geometry or porosity on the path of the crack. Eight correctly pre-cracked R300 specimens were successfully prepared. Four of them resulted in a successful test. For MHT-R, three specimens met the conditions.

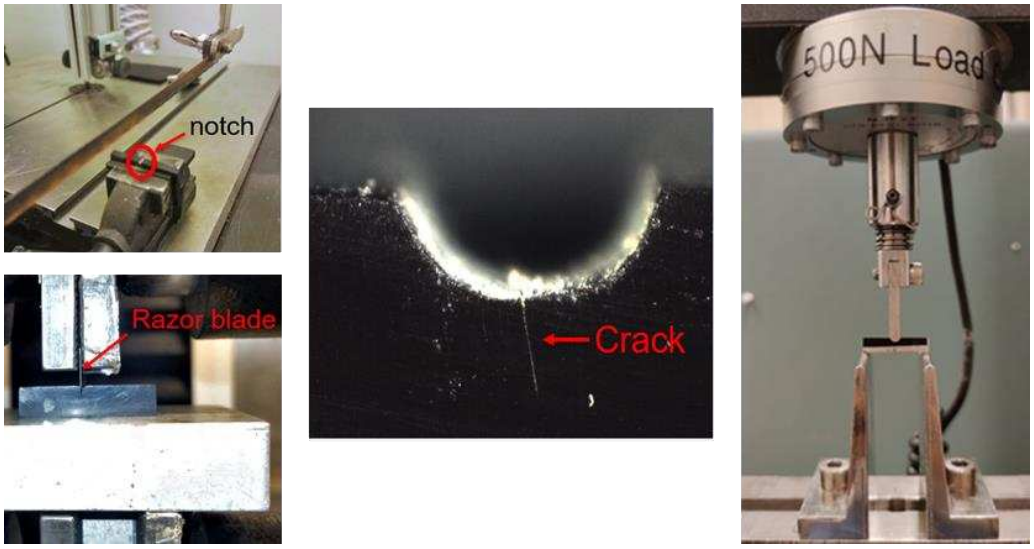

Figure 1: Fracture toughness sample preparation and experiment setup.

3.3 DSC

DSC experiments were performed in a Mettler Toledo DSC 821 to obtain thermal properties such as heat of reaction during curing and glass transition temperature (T_g) for both polymer batches. The uncured polymer powder was dried in an over at 90 ˚C before the DSC experiments. The DSC procedure consisted of three heating steps with cooling down to 25 ˚C between each step: 25–200 ˚C at 10 ˚C/min, 25–500 ˚C at 10 ˚C/min, 25–500 ˚C at 20 ˚C/min.

3.4 Dilatometry and Coefficient of thermal expansion

Netzsch DIL 402 C dilatometer was used for obtaining data for calculating the coefficient of thermal expansion (CTE) of both polymers in their cured state, according to ASTM E831-19 [5]. The experiments were performed under nitrogen environment and consisted of a temperature ramp from 25 ˚C to 450 ˚C with a heating rate of 5 ˚C/min.

3.5 Ageing, weight measurements, LOM

At least five samples from each plate were aged isothermally in a Nabertherm N11/HR furnace at temperature of 288 ˚C for up to 500 hours, in air atmosphere. The dimensions of the samples were approximately 12×6×3 mm^3. The weight was measured at time intervals of 0, 4, 24 72, 168, 336, and 500 hours with a Mettler Toledo AG245 balance with accuracy of 0.01 mg.

The weight loss, *W*, at time, *t*, was calculated according to Eq. (1), where m_0 is the mass before the ageing has been started and *m(t)* is the mass at a specific time.

$$W(t) = \frac{m_0 - m(t)}{m_0} \times 100\ (\%) \quad (1)$$

Additional specimens from both plates were prepared for LOM investigation. The dimensions were 12×6×3 mm^3 and the specimens were aged for 72, 240 and 500 hours in the same

conditions as described previously. The specimens were mounted in epoxy and polished with a 0.06 µm Buehler MasterMet Colloidal Silica polishing suspension. Nikon Eclipse MA200 light optical microscope and Nikon NIS-Elements software were used for observing and measuring the oxidation layer thickness. To detect the oxidation layer, reflected light differential interference contrast (DIC) microscopy was used. The setup includes polarizer/analyser unit (Nikon MA2-PA) and a Nomarski prism (Nikon L-DIC). DIC is a technique that is particularly suitable for looking at specimens, which have differences in height on the surface. For the neat resin specimens, it is expected that the oxidation layer should have different properties than the bulk, resulting in different grinding/polishing rates for the two areas and, thus, differences in the morphology of the surface.

4. Results and discussion

The idea behind the modification of the polyimide resin was to reduce the cross-link density by reducing the internal cross-linking units, thus increasing the toughness of the material and the resistance to cracking when used in composites. Another consequence of the reduced cross-link density could be an increase of thermal oxidative stability of the material, since the PI backbone is generally considered more stable in such conditions than the structure created by the polymerization of the oligomers.

4.1 Fracture toughness

Table 1 compares the fracture toughness of isotropic neat resin specimens for MHT-R and the novel R300 polyimide. The average K_{IC} for R300 (0.87 MPa√m) was slightly higher than for MHT-R (0.78 MPa√m), and can be correlated to the decrease in cross-link density, which was the main motivation behind the new formulation. The material exhibits greater toughness than some epoxy resins, such as the RTM-optimized Hexcel RTM6 (0.62 MPa√m) [6] and Araldite LY 564 (0.68 MPa√m) [7]. Compared to the toughened CYTEC PR520 epoxy resin for RTM, which is generally perceived as a very tough material (2.05 MPa√m [8]), the MHT-R and R300 are still relatively brittle. The studied polyimides have comparable K_{IC} values to other high T_g thermosetting polymers. [9]

Table 1: Fracture toughness data on the two polyimide systems.

	ID-number	K_{IC} [MPa√m]
	MHT-R-1	0.85
	MHT-R-2	0.80
	MHT-R-3	0.70
Average	MHT-R	0.78
	R300-1	0.83
	R300-2	0.83
	R300-3	0.91
	R300-4	0.93
Average	R300	0.87

4.2 DSC

DSC investigations were conducted to obtain information on the thermal properties such as heat of reaction and T_g for the two resins. The DSC results confirmed the initial hypothesis that the new formulation would exhibit lower cross-linking, which was reflected in the lower heat of reaction, and lower T_g of the R300 polyimide, Table 2. There was a noticeable difference in the melting temperatures, $T_{melting}$, which further underlined the differences in the basic form of the two polyimides.

The measured T_gs in the current study were around 405 ˚C for the novel R300 and 432 ˚C for MHT-R, which is in the range of what has been reported earlier for MHT-R.[3] In the same study, it was pointed out that different curing and post-curing cycles can be used to tailor very high T_gs in MHT-R, but such manufacturing procedures might introduce damage into the composite and are not recommended. The curing of the DSC samples in the current study was conducted at temperatures of up to 500 ˚C, during the non-isothermal program. It would be reasonable to expect that the T_g of the materials will be lower in a composite component, which has been produced by the RTM manufacturing schedule for carbon fibre/polyimide composites.

Table 2: DSC and CTE data on the two polyimide systems.

	ID-number	$T_{melting}$ [˚C]	Heat of reaction [J/g]	Cured T_g [˚C]	CTE [µm m^{-1} ˚C^{-1}]
	MHT-R-1	121.5	282.5	437.4	56.8
	MHT-R-2	130.5	271.9	432.2	55.6
	MHT-R-3	119.8	308.3	427.5	55.6
Average	MHT-R	123.9	287.6	432.4	56.0
	R300-1	132.7	257.1	401.1	53.9
	R300-2	132.0	267.8	405.4	54.0
	R300-3	131.0	263.6	408.4	55.7
Average	R300	131.9	262.7	405.0	54.3

4.3 Coefficient of thermal expansion

The CTE, Table 2, is calculated from the linear portion of the dilatometry curves, according to Eq. (2):

$$\alpha = \frac{1}{\Delta T}\frac{\Delta L}{L_0} \quad (2)$$

Where ΔT is the temperature interval, ΔL and L_0 are the elongation and the initial length of the specimen, respectively, giving the CTE, α, in µm m^{-1} ˚C^{-1}. The average values for CTE were 54.3 µm m^{-1} ˚C^{-1} for R300 and 56.0 µm m^{-1} ˚C^{-1} for MHT-R, indicating that there might be a small reduction of CTE in the novel R300. The values are comparable to the CTE of epoxy, which is around 55 µm m^{-1} ˚C^{-1}.

4.4 Weight loss and oxidation layer during ageing

Figure 2 (left) shows the weight loss behaviour of the two polymer systems during ageing at 288 ˚C. The rapid initial desorption, during the first 4 hours of ageing was subtracted from the graphs. During the first days of ageing, the R300 showed a higher weight loss, while MHT-R exhibited an induction period, where no weight loss was detected. The weight loss of the R300 could be due to larger residue entities with slower diffusion rates that were left within the material during manufacturing. Further studies are required to verify this statement, for example using mass spectrometry.

Based on the slope of the curves in Figure 2 (left) at long exposure times (after 72–168 hours), the thermal oxidative stability of R300 appears to be enhanced compared to MHT-R. The lower slope of degradation curve of R300 suggests a lower degradation rate, which supports the hypothesis given in the beginning of the section. However, further studies with e.g. thermal gravimetric analysis equipment should be performed on both materials to obtain more precise data.

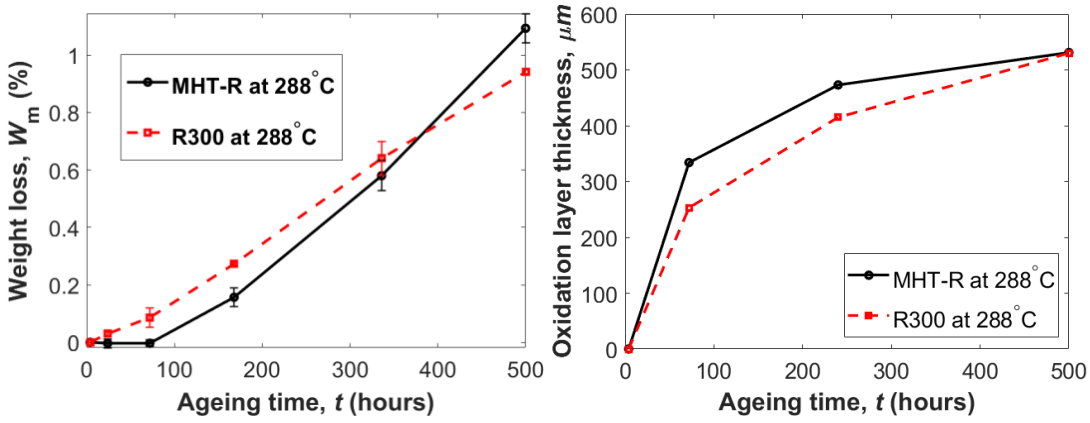

Figure 2: Weight loss (left) and oxidation layer thickness (right) measurements on MHT-R and P300 in air. The rapid, initial desorption stage was removed in the weight loss graph to emphasize on the difference between the two materials with regard to thermal oxidation. The weight loss lines represent the mean of measurements of three specimens. The error bars are the standard deviation.

Oxidation layer was observed in both formulations after ageing. The layer thickness increased with ageing time, Figure 2 (right) and Figure 3. As it was pointed out by Pochiraju *et al.*[2], in some polymer systems, the oxidation layer is difficult to notice with optical microscopy techniques. In the current study, reflected light DIC microscopy was necessary to be able to render the oxidation layer visible. This technique is particularly useful for specimens with slight differences in height. The observed layer was diffuse and a precise measurement of the extent of the oxidation layer was not feasible. Thus, the values of the oxidation layer thickness are approximate.

The oxidation layer thickness is a function of the oxygen diffusion rate and the oxidation reaction rate and changes in both factors can be expected when modifying the chemistry of the resin systems. The degree of cross-linking is one factor that can be expected to alter the diffusion properties of the polymer.[10,11] An increase of diffusion rate, resulting from the lower degree of cross-linking would mean that we should expect the oxidation layer to extend deeper into the

material for the R300, which is not reflected in Figure3. However, the effect might be small enough to be masked by the measurement uncertainty and further measurements with Raman spectrometry and nano-indentation should be performed to verify the results and obtain more quantitatively precise data on the extent of oxidation due to high temperature ageing.

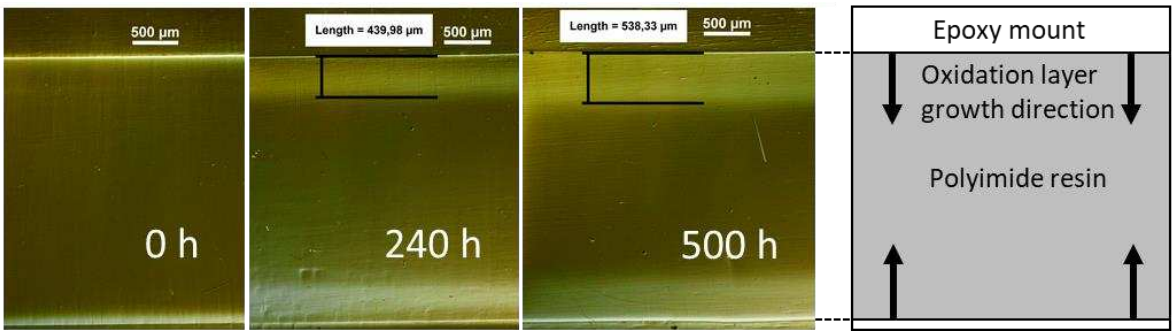

Figure 3: Oxidation layer measurements on MHT-R and P300 in air, done with reflected light DIC microscopy. The microscopy images are on the novel R300 material.

5. Conclusion

The study confirmed the challenge of simultaneously improving the T_g, thermal stability and fracture toughness of the material. The process is not straightforward and includes a certain trade-off between the properties. While a slight increase was noted in the fracture toughness and the rate of weight loss was somewhat lower at ageing times longer than 72 hours, the T_g of the novel R300 was reduced by circa 20 ˚C. Further studies are planned to obtain more conclusive data on both the thermal oxidation kinetics and the oxidation front that forms during ageing.

The measurements in this study, except for the DSC, which was performed on pristine uncured powder, were done on bulk neat polymer specimens. To fully understand the behaviour and the consequences of the implemented changes, further studies on composite material would be required.

Acknowledgements

The authors would like to thank Aurélien Copin and Javier Morell for their work on obtaining the results, Sibin Saseendran for discussions about the DSC measurements and Nexam Chemical for providing matrix material.

6. References

1. Petkov VI, Joffe R, Fernberg P. Thermal oxidative aging of satin weave and thin-ply polyimide composites. Polymer Composites 2022; 1.
2. Schoeppner G, Tandon G, Pochiraju K. Predicting Thermooxidative Degradation and Performance of High-Temperature Polymer Matrix Composites, Chapter 9 in *Multiscale Modeling and Simulation of Composite Materials and Structures*. Springer US, New York. 2008.
3. Fernberg P, Gong G, Mannberg P, Tsampas S. Development of novel high Tg polyimide-based composites. Part I: RTM processing properties. Journal of Composite Materials 2018; 52(2).

4. ASTM D5045-14 – Standard Test Methods for Plane-Strain Fracture Toughness and Strain Energy Release Rate of Plastic Materials.
5. ASTM E831-19 – Standard Test Method for Linear Thermal Expansion of Solid Materials by Thermomechanical Analysis.
6. Zotti A, Elmahdy A, Zuppolini S, Borriello A, Verleysen P, Zarrelli M. Aromatic Hyperbranched Polyester/RTM6 Epoxy Resin for EXTREME Dynamic Loading Aeronautical Applications. Nanomaterials 2020; 10(2):188.
7. Domun N, Hadavinia H, Zhang T, Liaghat G, Vahid S, Spacie C, Paton KR, Sainsbury T. Improving the fracture toughness properties of epoxy using graphene nanoplatelets at low filler content. Nanocomposites 2017; 3:3, 85-96.
8. Li Y, Huang K, Yu H, Hao L, Guo L. Experimentally validated phase-field fracture modeling of epoxy resins. Composite Structures 2022; 279.
9. Dutruch L, Pascal T, Durand V, Senneron M, Sillion B. Toughening of a High-performance Bis-nadimide Thermoset by Blending with High-Glass Transition Temperature Linear Polyimides. Polymers for Advanced Technologies 1997; 8: 8-16.
10. Robert CCR, Buri PA, Peppas NA. Effect of degree of crosslinking on water transport in polymer microparticles. Journal of Applied Polymer Science 1985; 30: 301-306.
11. Krongauz VV. Diffusion in polymers dependence on crosslink density. Journal of Thermal Analysis and Calorimetry 2010; 102**,** 435–445.

METHODOLOGY FOR TRANSVERSE CRACKING SIMULATION IN 90 PLIES OF COMPOSITE LAMINATE UNDER FATIGUE LOADING

Vivek Richards Pakkam Gabriel[a], Mohamed Sahbi Loukil[b], Patrik Fernberg[a], Janis Varna[a,c]

a: Department of Engineering Sciences and Mathematics, Luleå University of Technology, SE-97187 Luleå, Sweden – vivek.pakkam@ltu.se
b: Department of Management and Engineering, Linköping University, SE-58183 Linköping, Sweden.
c: Laboratory of Experimental Mechanics of Materials, Riga Technical University, Riga, Latvia

Abstract: *Methodology for crack density evolution simulation in tension-tension fatigue and parameter determination in a model that relies on failure stress distribution (Weibull) in the 90 ply is presented. Cyclic loading is performed at one stress level to obtain detailed crack density dependence on the number of cycles. In addition, one data point (crack density at specified number of cycles) is necessary at a different stress level. Non-interactive crack density region is used to determine Weibull parameters. Then, crack density in a whole crack density range and for arbitrary stress level is predicted using the obtained Weibull parameters, the Monte Carlo method for failure stress distribution and a novel model for stress distribution between cracks. The predictions are in good agreement with test results.*

Keywords: Transverse cracking; Weibull failure stress distribution; Fatigue loading; Monte-Carlo simulations.

1. Introduction

Damage in composite laminate subjected to tensile loading, starts with intralaminar or transverse cracks in off-axis layers with respect to $0°$ layer. With increasing the loading, the number of transverse cracks increases. These cracks lead to significant degradation of thermo-elastic constants of the laminate **[1,2,3]** and eventually to final failure of the laminate. In this study, the transverse cracks are analyzed and characterized as crack density ρ in a ply, which is the number of cracks per unit length. The transverse crack covers the whole thickness of the ply as in **fig 1(a)**, creating a crack plane which is perpendicular to the laminate middle-plane (x-z plane in **fig 1(c)**) and runs parallel to fiber direction in the ply, forming well-defined tunnels as shown in **fig 1(b)**.

The growth of each transverse crack is usually defined in two stages a) initiation and b) propagation. The initiation of the crack starts with fiber/matrix debonding [**4,5**], then matrix cracking between fibers takes place [**6,7**] followed by coalescing of these small defects into a critical size in thickness direction. In case of quasi-static loading the crack propagates along the fiber direction, creating a tunnel, once the critical value of the strain energy release rate (ERR) (called also "fracture toughness") is reached. In cyclic loading the Paris law, relating crack growth rate to ERR changes during a single cycle when loading changes from min to max, is often assumed as governing.

Also, the ERR for through-the-thickness crack propagation is limited by the ply thickness t_k. Thicker the ply, larger the ERR. In quasi-static loading, the dependence on ply thickness of the stress required for propagation is well known from [**8**]. In cyclic loading, cracks in thick plies at the same stress have much higher propagation rate and almost instantly form tunnel as soon as a sufficiently large flaw is created in the initiation stage.

  doi:10.5075/epfl-298799_978-2-9701614-0-0

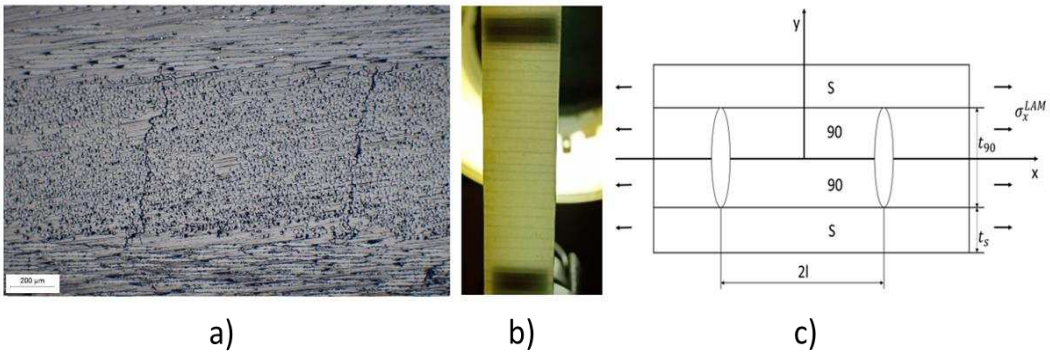

Figure 1. a) Micrograph of two through-the-thickness transverse cracks in 90-ply; b) Tunneling cracks (surface view of GF/EP [0/90]s specimen); c) Schematic showing of the repeating unit between two cracks in [S/90]s laminate (S- support lay-up which for cross-ply is 0-ply, t_{90} – thickness of the 90-ply and t_s – thickness of support lay-up)

In the relatively thick laminate that is used here, optical surface observations showed that majority of cracks were tunneling through the width of the specimen and hence the additional number of cycles required for propagation is much smaller than for the initiation of a crack. Therefore, in the specimens used here, the number of cycles to create a tunneling crack is almost the same as the number of cycles required to initiate a crack at a sufficiently large stress concentration. The number of cycles for initiation in a given position depends on local fiber and flaw distribution (stress concentration) and can be described as statistical failure resistance distribution.

Using this approach, a fatigue model was developed and presented in **[9,10]**, where Weibull distribution assigned with Monte Carlo method and stress distribution model between cracks are employed to predict the crack density under fatigue loading. The Weibull scale parameter was assumed to degrade monotonically with increase in number of cycles, describing the effect by introduced fatigue parameter. The shape parameter in the fatigue model was assumed to be the same as in quasi-static loading. Results in **[10]** suggest that the shape parameter in fatigue may be different. In this paper, this possibility is investigated, validating new methodology to determine the Weibull shape parameter and to find the degradation rate of the scale parameter. Fatigue test at one stress level is used to gather detailed data on crack density development with the number of cycles. Then, fatigue test for a pre-determined number of cycles is performed at different stress level, counting the number of cracks after the test. All crack density data for parameter determination have to be within the non-interactive crack density region.

2. Materials and experiment description

From **[10],** using vacuum bag and hot press, glass fiber epoxy laminate with layup [0/90]s was made of UD prepreg. Elastic constants, experimentally obtained from unidirectional (UD) laminates, are in table 1. Laminate resulted in average thickness $h = 1.5mm$. The difference between coefficients of thermal expansion in transverse and longitudinal direction is $\Delta\alpha = 2.389e^{-5}\ 1/℃$ and $\Delta T = -95℃$ represents the difference between room and manufacturing temperature. Specimens were made with dimensions $200\ \text{mm x}\ 16\ \text{mm}$ and edge-polished to minimize free edge effect. The gauge length between tab region was 100mm and strain was measured by extensometer in 50mm in the middle of gauge length.

Tension-tension fatigue tests were performed using INSTRON E10000, with stress ratio R=0.1, frequency 6 Hz. Fatigue tests were performed using three thermo-mechanical stress levels in the 90 ply and they are 70.27 MPa, 61.1 MPa and 52 MPa. Thermal stress in the 90 ply was

  doi:10.5075/epfl-298799_978-2-9701614-0-0

15.24 MPa. The crack density versus number of fatigue cycle were obtained at these chosen stress levels.

Table 1: Elastic constants from UD plate

E_1 (GPa)	E_2 (GPa)	ν_{12}	G_{12} (GPa)	ν_{23}	G_{23} (GPa)	ΔT $^{\circ}C$	t_{90} (mm)
37.86	9.28	0.28	4.77	0.42	3.27	-95	0.75

3. Intralaminar cracking in tension-tension fatigue.

3.1 Weibull failure stress distribution

The non-uniform distribution of fibers (fiber clustering), is the reason behind the distribution in local stress concentrations. We claim that it leads to distribution of transverse failure stress along the transverse direction of the 90 layer and this distribution can be described by Weibull distribution. Considering the ply as consisting of small elements, the Weibull failure stress distribution is the probability of failure P_f of the elements for an element length equal to t_{90} when the thermo-mechanical stress is changing from 0 to σ_T. The Weibull distribution (1) is defined by two parameters, shape parameter m and scale parameter σ_{0ref} in case of quasi-static loading.

$$P_f = \frac{M_f}{M_0} = 1 - exp\left(-\left(\frac{\sigma_T}{\sigma_{0ref}}\right)^m\right) \quad (1)$$

where M_f is the number of failed elements and M_0 is the total number of elements. P_f can be expressed as crack density ρ over maximum crack density ρ_{max} when all elements are failed.

3.2 Assumptions regarding failure stress degradation in cyclic (fatigue) loading

As in **[9]** it is assumed that the Weibull shape parameter m reflects the non-uniformity of fiber distribution in the layer and, hence, it has the same value in quasi-static and in cyclic tests. In the suggested scenario, similarly as in **[9,10],** the transverse failure stress in a given position is degrading during cyclic loading and the Weibull failure stress distribution is changing. This overall reduction of the resistance of the ply to transverse failure during cyclic loading can be interpreted as a monotonous decrease of the scale parameter $\sigma_0 = f\left(\sigma_T^{fat}, N\right)$, where σ_T^{fat} is the stress amplitude in the cycle. A power function represents one of the simplest relationships

$$\sigma_0 = A \cdot N^{-\alpha}\left(\frac{\sigma_T^{fat}}{B}\right)^{-\gamma}, \qquad \gamma \geq 0 \qquad \alpha \geq 0 \quad N \gg 1 \quad (2)$$

Parameters *A*, α, γ and *B* are unknown material constants. Using (2) in (1) we obtain

$$P_f = 1 - exp\left[-N^{\alpha \cdot m}\left[\left(\frac{\sigma_T^{fat}}{B}\right)^{\gamma}\frac{\sigma_T^{fat}}{A}\right]^m\right] \quad (3)$$

Without losing generality, we can introduce new unknown parameters and rewrite (3) as

$$\frac{\rho}{\rho_{max}} = 1 - exp\left[-N^n\left(\frac{\sigma_T^{fat}}{\sigma^*}\right)^{m(1+\gamma)}\right] \quad (4)$$

According to (4) the shape parameter in fatigue, $m^* = m(1+\gamma)$ may be larger than in quasi-static loading. Analysis in [**9**] for non-crimp fiber composites showed that parameter $\gamma \ll 1$ and therefore $m^* = m$ from quasi-static test. However, results in [**10**] for GF/EP prepreg tape laminates showed that $\gamma \neq 0$ for the used material. The new methodology on determining the shape m^* and scale σ^* parameter is introduced in section 4.2.

  doi:10.5075/epfl-298799_978-2-9701614-0-0

Parameter n in (4) is defined using data at non-interactive crack density where stress σ_T^{fat} in an arbitrary position between two cracks is almost as the thermo-mechanical stress obtained with the Classical Laminate Theory (CLT), $\sigma_T^{fat} \approx \sigma_{T0}^{fat}$, and (4) can be written as

$$\frac{\rho}{\rho_{max}} = 1 - exp\left[-N^n \left(\frac{\sigma_{T0}^{fat}}{\sigma^*}\right)^{m^*}\right] \quad (5)$$

In log-log axis the relationship (5) is linear with respect to number of cycles,

$$\ln\left(-\ln\left(1-\frac{\rho}{\rho_{max}}\right)\right) = n\ln N + m^* \ln\frac{\sigma_{T0}^{fat}}{\sigma^*} \quad (6)$$

4. Weibull parameter determination

4.1 Fatigue n-parameter

As discussed in section 1&3, the fatigue test at one stress level is performed and the data points selected within $0.05 < P_f < 0.3$, that belongs to the non-interactive crack density region, are used for Weibull parameter determination. The fatigue test was performed at 61.1 MPa thermo-mechanical stress in the 90-layer and the data points for Weibull analysis were selected between 0.07 cr/mm < ρ < 0.36 cr/mm. **Fig 2**, shows the Weibull parameter determination. From the underlined linear fitting expression in the **fig 2,** which is in form of (6), the fatigue n-parameter is 0.72.

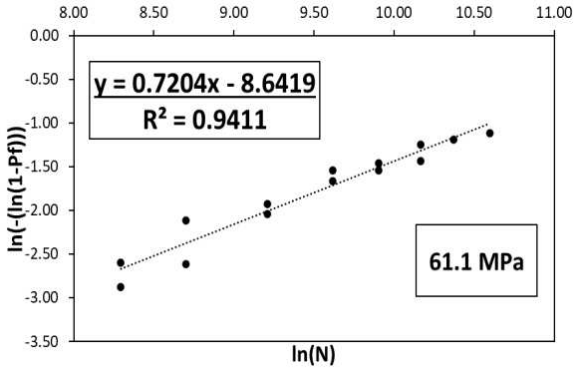

Fig 2. Linear regression curve of the fatigue test performed at stress 61.1 MPa. Linear fit equation of data points selected within $0.05<P_f<0.3$ is underlined in black

4.2 Shape parameter m^* and Scale parameter σ^*

Since the presented approach on determining the shape m^* and scale σ^* parameter does not involve static tests, one more fatigue test at a different stress level for a pre-determined number of cycles has to be performed. In this methodology, fatigue parameter n, shape parameter m^* and scale parameter σ^* are same for fatigue tests at all stress levels. The second cyclic test was at stress level 70.27 MPa in the 90-layer and 1250 cycles were performed. The test result was $\rho = 0.25$ cr/mm. Substituting these values in (6) we obtain

$$\ln\left(-\ln\left(1-\frac{0.25}{\rho_{max}}\right)\right) = 0.72\ln(1250) + m^* \ln\frac{70.27}{\sigma^*} \quad (7)$$

where $\rho_{max} = 1.33\ cr/mm$. From eq (7)

$$m^* \ln\frac{70.27}{\sigma^*} = -6.71 \quad (8)$$

From the test at 61.1 MPa represented by equation shown in fig. 2

$$m^* \ln\left(\frac{61.1}{\sigma^*}\right) = -8.64 \quad (9)$$

Dividing (8) with (9) we obtain $\sigma^* = 113.57\ MPa$.

Then, we use (8) to calculate m^*, then $m^* = 13.94$. Analyzing transverse cracking in quasi-static test, see [10], the obtained value of shape parameter was $m = 11.123$. Hence, $\gamma = 0.25$.

The Weibull parameters from [10] and Weibull parameters obtained in this work are summarized in table 2.

Table 2: Weibull parameters obtained in [10] and presented work

Test method	Features	Fatigue parameter n	Shape parameter m^*	Scale parameter σ^* (MPa)	γ
[10]	Detailed fatigue test at 61.1 MPa and static test	0.72	11.123	132.88	0
Presented work	Detailed fatigue test at 61.1 MPa and one data point at 70.27 MPa	0.72	13.94	113.57	0.25

5. Crack density simulation

First, we present the crack density prediction using Weibull failure stress distribution or as called here P_f-approach when the stress between two crack is assumed to be equal to the CLT stress of the undamaged laminate ($\sigma_T^{fat} = \sigma_{T0}^{fat}$) and Eq. (5) is used. This assumption is valid for the non-interactive crack density region. As shown, in the **fig 3,** the prediction using P_f-approach, gives good results only in the non-interactive crack density region. It is expected because, it is the region which was used to determine the Weibull parameters. However, it overestimates the crack density in the interactive crack density region, where stress between cracks is lower than the CLT stress as the cracks get closer.

Monte Carlo simulations

Monte Carlo simulation methodology is described in [10] and results are shown in **fig.3**. In **fig 3(a-c)**, Monte Carlo simulations expose the experimentally observed effect of interaction at high crack density but results are not in good agreement with the test results.

The Monte Carlo simulated crack density in **fig 3(d-f)** using Weibull parameters obtained in this paper agree good with the test results both in non-interactive and interactive crack density region.

Thus, performing detailed crack density analysis at one stress level (61.1 MPa) in the cyclic test and in addition obtaining one data point at a different (higher) stress level (70.27 MPa) is a better

  doi:10.5075/epfl-298799_978-2-9701614-0-0

option. The number of cycles and microscopy observations required to establish parameters are reduced at the same time as agreement between model and experiments are improved.

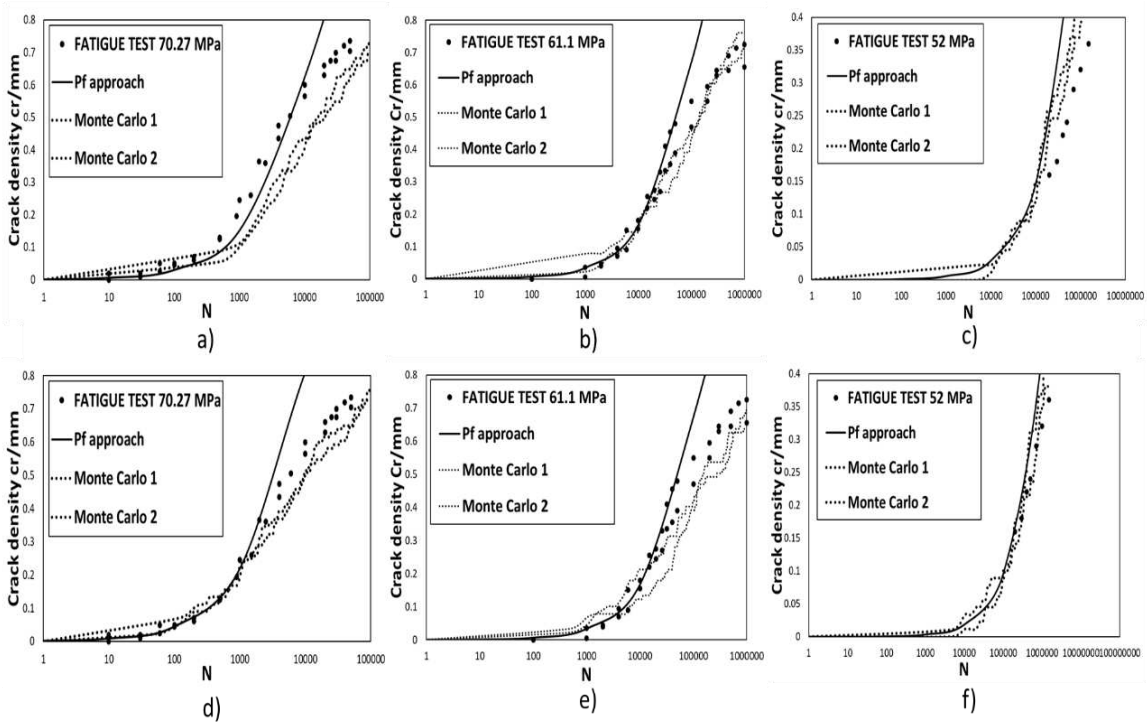

Fig 3. Crack density vs Number of fatigue cycles. Black dots are test data, solid black line is P_f-approach, and dotted black line is Monte Carlo simulated results, where, (a-c) based on Weibull parameters from [1], (d-f) based on Weibull parameters from the presented work.

6. Conclusion

Efficient methodology to determine parameters for transverse cracking simulation in fatigue test is explained.

Detailed analysis of crack density evolution with the number of cycles in tension-tension fatigue test at one stress level is required. In addition, one more data point is obtained in another cyclic test with a different pre-determined stress. Data in the non-interactive crack density region are used to find parameters in modified Weibull failure stress distribution that is used to describe statistical variation of failure properties. Monte Carlo simulations are performed using the determined parameters, calculating the stress distribution in all positions between cracks, comparing with failure stress in this position and predicting cracking in the whole crack density region. The failure stress distribution degrades with the number of cycles according to power law with experimentally found parameters describing the scale parameter reduction.

Acknowledgements

This work has been performed within the Swedish Aeronautical Research Program (NFFP7), project 2019- 02777.

  doi:10.5075/epfl-298799_978-2-9701614-0-0

7. References

1. Parvizi A, Bailey JE. On multiple transverse cracking in glass fibre epoxy cross-ply laminates, Journal of Materials Science, 1978, V13(10): 2131-2136.
2. Varna J. Modeling Mechanical Performance of Damaged Laminates, Journal of Composite Materials, 2013, V47(20-21): 2443-2474.
3. Kashtalyan M, Soutis C. Stiffness and fracture analysis of laminated composites with off-axis ply matrix cracking, Composites: Part A, 2007, V38: 1262-1269.
4. París F, Cano JC, and Varna J. The fiber-matrix interface crack—a numerical analysis using boundary elements, Int. J. Fract., 1996, 82(1): 11-29.
5. Zhuang L, Pupurs A, Varna J, Talreja R, Ayadi Z. Effects of inter-Fiber spacing on fiber-matrix debond crack growth in unidirectional composites under transverse loading, Composites Part A, 2018, 109: 463-471.
6. Zhuang L, Talreja R and Varna J. Transverse crack formation in unidirectional composites by linking of fibre/matrix debond cracks, Composites Part A, 2018, 107: 294-303.
7. Herráez M, Mora D, Naya F, Lopes CD, González C, LLorca J. Transverse cracking of cross-ply laminates: A computational micromechanics perspective, Composites Science and Technology, 2015, 110: 196-204.
8. Dvorak GJ, Laws N. Analysis of progressive matrix cracking in composite laminates II. First ply failure, J. of Composite Materials, 1987, 21: 309-329.
9. Ben Kahla H, Ayadi Z, Edgren F, Pupurs A, Varna J. Statistical model for initiation governed intralaminar cracking in composite laminates during tensile quasi-static and cyclic tests, International Journal of Fatigue, 2018, 116: 1-12.
10. Pakkam Gabriel VR, Loukil MS, Varna J. Intralaminar cracking during cyclic loading in laminates with distributed failure stress in 90-plies, International Journal of Fatigue, 2022, *Accepted*.

  doi:10.5075/epfl-298799_978-2-9701614-0-0

TRANSVERSE CRACKING CHARACTERIZATION AND PREDICTION IN HEAT TREATED POLYMER COMPOSITES UNDER QUASI-STATIC TENSILE LOADING AT ELEVATED TEMPERATURE

Vivek Richards Pakkam Gabriel[a], Patrik Fernberg[a], Spyros Tsampas[b], Janis Varna[a,c]

[a]Department of Engineering Sciences and Mathematics, Luleå University of Technology, SE-97187 Luleå, Sweden. – patrik.fernberg@ltu.se
[b]Huntsman Advanced Materials Gmbh, 4052 Basel, Switzerland.
[c]Laboratory of Experimental Mechanics of Materials, Riga Technical University, Riga, Latvia.

Abstract: *Transverse cracking in high temperature polymer cross-ply composite laminate was experimentally studied. In the tests, pristine as well as heat treated cross-ply laminate specimens were subjected to quasi-static tensile loading at room temperature and 150℃. Microscopy studies revealed that manufacturing induced transverse cracks were present in 90° layer of pristine cross-ply laminates. An increase in number of transverse cracks were observed after the heat treatment. Transverse crack density (number of cracks/unit length) growth upon applied thermo-mechanical transverse stress in 90° layer was analyzed using 3-parameter Weibull failure stress distribution. The Weibull location parameter, in efforts to address the influence of temperature and heat treatment of crack density growth, is modified based on empirical data. The predicted results were in good agreement with the test results.*

Keywords: Transverse cracks, Quasi-static tensile test, Heat treatment, Elevated temperature, Three-parameter Weibull distribution, Location parameter.

1. Introduction

High temperature polymer composites (HTPC) have potential to be used in numerous applications. One such is in aero-engine parts operating in temperature range of 150°-200℃. At these temperatures, damage initiation and growth under mechanical loading in composite laminates are critical and it is necessary to analyze and accurately predict the damage accumulation. Damage accumulation described here is the increase in number of transverse cracks in off-axis plies with respect to the main loading direction. This growth in number of transverse cracks also causes the degradation of the thermo-elastic constants of the composite laminate [1,2]. The analysis and prediction of transverse cracking in prepreg laminates were already well explained by the authors in [3]. Based on the crack development stages explained in [3], certain stress level required for crack initiation at a position in damaged layer (or 90° layer here) is the failure initiation stress at that position. Also, failure initiation stress is the failure stress at a position that governs the creation of a fully grown crack in a thick 90° layer. The objective of this work is to analyze and compare transverse cracking in pristine and heat treated HTPC subjected to quasi-static tensile loading at room temperature and 150℃. Based on the analysis of the crack density evolution, using Weibull failure stress distribution, a predictive model for transverse crack density is developed.

2. Experimental methodology

2.1 Material description

  doi:10.5075/epfl-298799_978-2-9701614-0-0

An RTM-manufactured cross ply laminate [0/90$_2$]s based on unidirectional (UD) fabric, consisting of carbon fibers held together by a sparsely woven structure made up from warp and weft yarns, and a temperature resistant polymer is used in the study. The average thickness of the laminate was 1.09 mm with an average volume fraction of fibers V_f (obtained from image analysis) of 52%. Experimentally determined elastic ply-constants, obtained from UD laminates are given in table 1 along with data on temperature difference between room and manufacturing temperature, ΔT , 90° layer thickness $t_{90,}$ and the difference between transverse and longitudinal coefficient of thermal expansion $\Delta\alpha$**.** $\Delta\alpha$ was estimated based on elastic ply-properties and literature data on constituent expansion properties.

Table 1: Material properties used in classical laminate theory analysis

E_1 (GPa)	E_2 (GPa)	ν_{12}	ΔT (°C)	t_{90} (mm)	$\Delta\alpha$ (1/°C)
120	9.31	0.32	-239	0.73	$3.55e^{-5}$

Specimens' edges from cross ply laminate were grinded and polished prior to testing. This was done to minimize the free edge effect and facilitate observation of the progressive development of edge damage in 90° layer during mechanical and thermal loading. A selected number of specimens were subjected to a conditioning **heat treatment (HT)** in ambient air and pressure at 150℃ for 500 and 1000 hours respectively.

2.2 Step-wise quasi-static loading

Quasi-static tensile tests were performed at a controlled displacement rate of 2mm/min using an Instron ElectroPuls™ E10000 testing machine equipped with 10KN load cell and a thermal chamber Instron 3119-605 with temperature capacity -100℃ to 250℃. Tests were performed at two temperatures: room temperature (RT) and 150℃ (elevated temperature, ET), on specimens of average width 13 mm. A gauge length (distance between the grips) of 100 mm was maintained throughout the tests.

In each step at **RT**, the specimen was loaded to pre-determined strain level to introduce damage in 90° layer and then unloaded. Before and after each step, specimens were subjected to low strain of 0.15%, during which the axial modulus corresponding to each damage state was determined. Stiffness was determined from unloading ramp within strain interval of 0.12%-0.05%. In next loading step, the pre-determined strain level was higher.

At **elevated temperature (ET)**, the damage inducing loading steps with increasing strain level were performed within the environmental chamber. The practical procedure for ET testing involved mounting the specimen at RT and maintaining the specimen at a constant preload of 2N. While at the constant preload, the specimen was heated to ET at a rate of 5℃/mm and maintained for 15 min to reach temperature equilibrium. Then the mechanical loading-unloading step to desired strain level to introduce damage was performed. After that, the specimen was left to cool-down inside the chamber. Once at RT, the stiffness of the pre-strained material was determined using same method as previously described for RT tests.

After each stiffness measurement, both specimen edges were inspected using optical microscope to determine damage development in 90° layer. This is done either by removing the

  doi:10.5075/epfl-298799_978-2-9701614-0-0

specimen from testing machine or using Struers RepliSet. The step-wise procedure was repeated until final failure both for RT and ET tested specimens.

3. Damage development in 90° layer

3.1 Manufacturing induced cracks

Edge observations showed that after manufacturing the fiber bundle meso-structure of the UD-fabric, although highly compacted, remained intact in the composite with impregnated bundles surrounded by resin rich regions. Warp and weft yarns from the weave are observed in the vicinity or within the resin rich regions. In addition to that, the pristine 90° layer had also several through-the-thickness transverse cracks (or called as manufacturing induced cracks here) like in **fig 1a** that were passing through whole width of the specimen. These cracks are formed as a consequence of thermal residual stress buildup in 90° layer during the cooling down from manufacturing temperature to the room temperature ($\Delta T = -239℃$). Using classical Laminate Theory (CLT) and the data in **table 1**, the thermal residual stress at RT in a 90° layer is estimated to be 66 MPa. It was observed that almost all the manufacturing induced cracks pass through or originate from warp yarns in the 90° layer. Also, several debonds between warp yarn fibers and matrix were observed. As observed during subsequent mechanical tests, these regions serve as crack initiation points for the new through-the-thickness cracks upon additional thermal or mechanical loading.

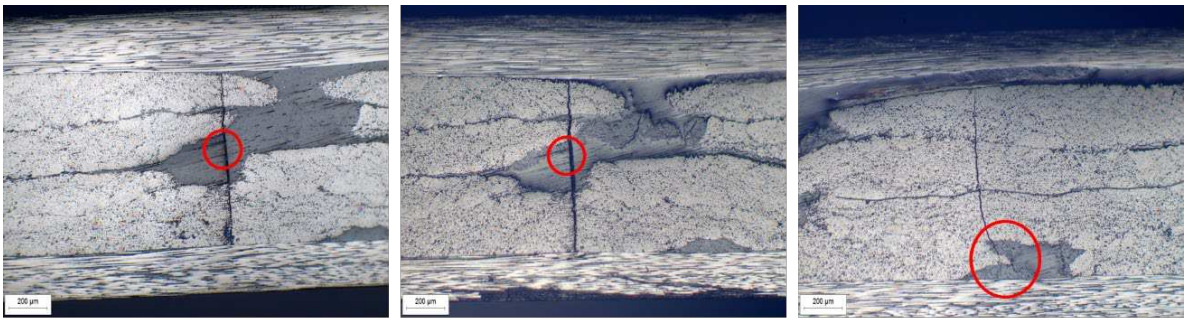

a) b) c)

Figure 1.a) Transverse crack from manufacturing; b) Same transverse crack after 1000 hours of HT; c) Crack observed after HT; Vicinity to warp yarns are marked in red circles

3.2 Cracks after heat treatment (HT)

Initial edge crack densities of as-manufactured pristine specimens and specimens subjected to the HT are presented in **fig 2a.** Transverse cracks were observed to grow in number after HT at 150℃ for both 500 hours and 1000 hours. However, the crack density hardly increased between 500 hours to 1000 hours of HT. There are three possible reasons for the increase in number of cracks after HT. One is that formation of new cracks is due to thermal cycling effect (samples were removed 7 times from oven for weight measurements during the first 500 hours exposure but only 2 times between 500 and 1000 hours), the second is degradation of the material due to long-term temperature exposure during HT. Finally, new cracks could be formed due to the rapid cool down from HT temperature. Regardless of origin, new cracks formed after HT were predominantly found developing through or in the vicinity of the warp yarns as in **fig 1c**. Another observation is that HT appears to lead to wider opening of the manufacturing induced cracks as

  doi:10.5075/epfl-298799_978-2-9701614-0-0

shown in **fig 1b**. A possible explanation is that this could be due to hygroscopic matrix shrinkage occurring as a consequence of diffusion driven drying during long term HT. Such shrinkage would also generate stress in 90° layer and could have also contributed to the increase in number of cracks. Therefore, thermal cycling, material degradation, rapid cool down effects together with developed shrinkage stress could have possibly resulted in the increased crack density in pristine specimens after HT.

To investigate the possible effect of hygro-shrinkage and thermal cycling in crack density growth, a specimen was subjected to HT for 500 hours at 150℃ without taking out of oven. It was found that only one new crack formed after the HT exposure. Thus, the thermal cycling or the rapid cool down is the most likely cause for the increase in transverse cracks after HT. The effect of hygroscopic stresses is small in comparison and can be neglected in first order approximations. More experiments are required to verify the stress state after HT methodology described above to have a solid understanding.

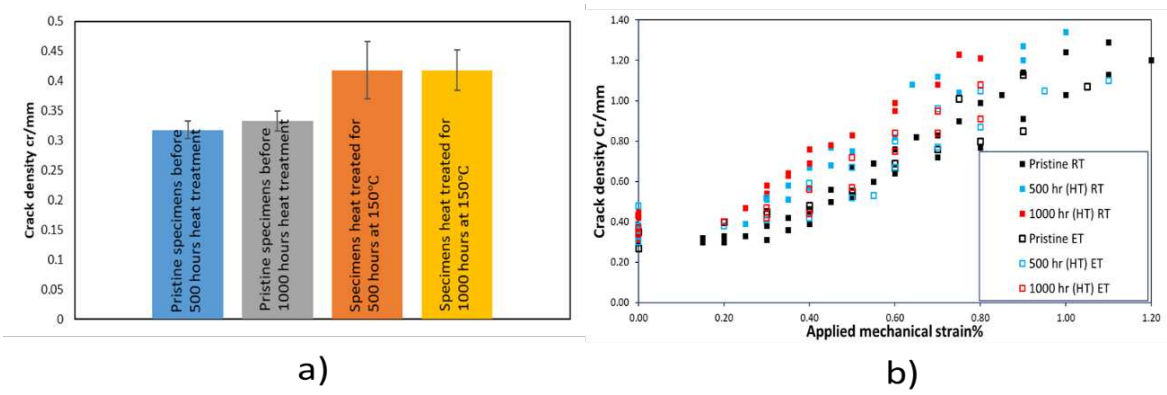

Figure 2. a) Initial crack density in pristine specimens and after heat treatment; b) Experimental edge crack density vs applied mechanical strain at RT and ET; HT refers to heat treated specimens.

3.3 Cracks from quasi-static testing

Upon quasi-static loading at both RT and ET, the number of through-the-thickness transverse cracks observed on the specimen edge increased. The tendency to have the edge cracks initiated in regions containing warp yarns continued but was less pronounced as the level of mechanical loading increased. With increasing thermo-mechanical load, the number of edge cracks initiated in high V_f within bundle regions, increased. A general observation is that the opening of the cracks developed during quasi-static loading were smaller compared to the opening of the manufacturing induced cracks. Edge crack density versus applied mechanical strain, is presented in **fig 2b.** When comparing crack density growth in pristine specimens tested as-received at RT (black filled squares) and ET (black open squares), no difference is observed. On the contrary, heat treated specimens tested at RT (red and blue filled squares), had crack density higher than the pristine specimens tested at RT. A majority of this difference is explained by the difference in initial damage state before and after HT exposure discussed in previous section. At ET, heat treated specimens (red and blue open squares) tested had crack density growth slightly higher than in pristine specimens at ET. However, the difference between the crack density growth of pristine and heat treated specimens tested at ET is not significant. Onset of local delamination

  doi:10.5075/epfl-298799_978-2-9701614-0-0

was observed at lower strain levels around 0.3% and continued to grow upon loading in all test conditions.

CLT was used to determine the thermo-mechanical transverse stress in 90° layer at various temperatures and at various mechanical load. Though the transverse stress in 90° layer determined using CLT is representative at low crack density where the neighboring cracks are far apart, it is used for the whole crack density region. Thermo-mechanical transverse stress in 90° layer versus crack density is shown in **fig 3a**. With this representation of the experimental results, one can see that transverse cracking appear at lower stress levels during loading at elevated temperatures (the residual thermal stress at ET is 30.38 MPa) and that there is a tendency that thermal exposure (HT) decreases the resistance towards transverse cracks at RT and ET. In heat treated specimens, the thermo-mechanical transverse stress values were estimated by assuming the thermal transverse stress in 90° layer is same as in pristine specimens at respective test temperatures. As discussed in previous section, it has to be investigated in detail on the increase in crack density, the transverse stress and also the transverse cracking resistance in 90° layer after HT. However, an empirical model capable to capture the observed behavior is presented in section 4.

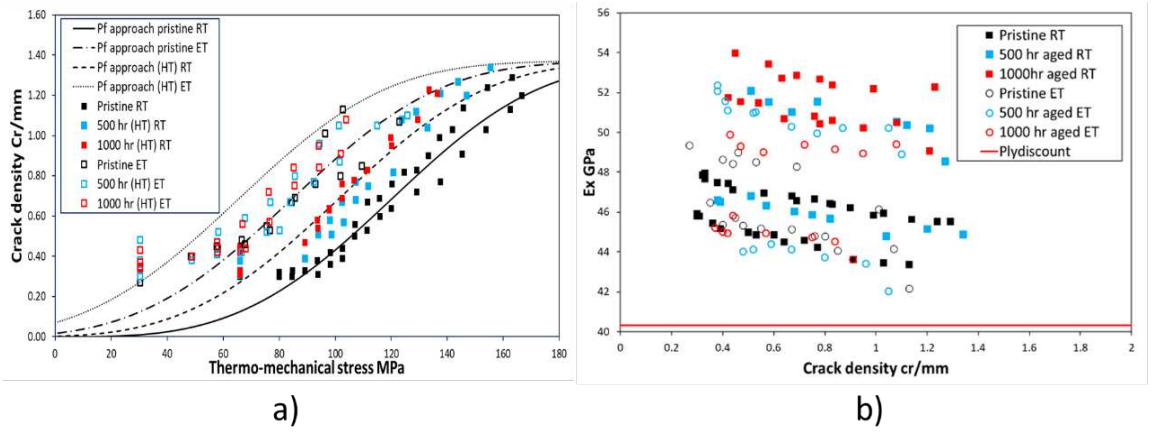

Figure 3. Experimental test results showing a) edge crack density vs thermo-mechanical transverse stress in 90° layer; In legend, black lines (P_f approach) are the probability of failure based prediction results for different test conditions of both pristine and heat treated specimens. b) Axial modulus (Ex) degradation with respect to crack density.

3.4 Axial modulus degradation

Axial modulus degradation versus the crack density is presented in **fig 3b**, with the value obtained from ply discount model indicated with a red line. Very consistent results are obtained for each individual specimen showing small but steady decrease of modulus with increasing crack density. The variation in initial axial modulus between specimens is, however, significant. This is due to local variations in fiber volume fraction in the 0° plies of different specimens caused by irregular deformation of the UD weave during laminate manufacturing. This affects the fiber bundle density (number of bundles per unit length) distribution in the 0° layer of the laminate. Eventually that leads to the different fiber volume fraction and different axial modulus for each specimen. In other words, the used specimen width is smaller than the RVE of this rather non-uniform material. Unfortunately, wider specimens could not be used due to load limitations of available testing machines.

  doi:10.5075/epfl-298799_978-2-9701614-0-0

4. Weibull failure stress distribution

The distribution of the failure stress in 90° layer is from; 1) the random fiber distributions within the fiber bundles causing fiber clustering and stress concentration regions; 2) distribution of the warp yarns between bundles acting as weak regions. This leads to different failure resistance in different positions in the 90° layer.

Considering the distribution of failure stress along the transverse direction of the layer as a chain of weak and strong links (small elements), the weakest link (such as element with warp yarns) fails first at lower thermo-mechanical load. Then the less weak links (such as fiber clusters and/or an element with warp yarn) fail upon continuous loading. The distribution of failure stress can be described by 3-parameter Weibull failure stress distribution, a distribution that provides the means to predict the probability of failure P_f of elements with element length equal to t_{90} when the thermo-mechanical stress increases from 0 to σ_T. Mathematically it is described by the shape parameter m, scale parameter σ_{0ref} and location parameter σ_{cond}. Also, an assumption here is that shape and scale parameter remain constant and do not depend on temperature or conditioning. It is equivalent to assuming that the distribution of the failure stress does not depend on the test temperature nor HT condition.

The probability of failure of elements described by a 3-parameter Weibull distribution and it is given by

$$P_f = 1 - exp\left(-\left(\frac{\sigma_T - \sigma_{cond}}{\sigma_{0ref}}\right)^m\right). \quad (1)$$

In the case of multiple transverse cracking in 90° layer of cross-ply laminates, P_f can also be established experimentally from data as crack density ρ over maximum crack density ρ_{max}. ρ_{max} is the condition when the number of cracks in 90° layer is saturated and does not change upon continuous quasi-static loading. It has been observed in [4] that the cracking pattern (characteristic damage states CDS) is often related to the 90° layer thickness, that is at maximum crack density, the spacing between cracks are approximately equal to the thickness of 90° layer, $\rho_{max} = \frac{1}{t_{90}}$. Then (1) becomes,

$$\frac{\rho}{\rho_{max}} = 1 - exp\left(-\left(\frac{\sigma_T - \sigma_{cond}}{\sigma_{0ref}}\right)^m\right). \quad (2)$$

It is supposed that the location parameter σ_{cond} incorporates the effects of heat treatment and test temperature on material behavior. Whereas σ_{0ref} defines data shift in log-log axis commonly used for Weibull parameters determination, the location parameter defines shift in axis of transverse thermo-mechanical stress. The intention is predicting transverse cracking in non-ambient conditions using Weibull parameters determined from static tests performed at reference temperature in pristine state of the composite. This reference temperature happens to coincide with the Room Temperature (RT) here. Therefore, for the calculations in this work, the location parameter is formulated with respect to material state at RT directly after manufacturing ($\sigma_{cond} = 0$ at RT in a pristine state).

In first approximation the location parameter is considered as a sum of effect of heat treatment and the effect of test temperature on material behavior,

  doi:10.5075/epfl-298799_978-2-9701614-0-0

$$\sigma_{cond} = \sigma_{cond\_HT} + \sigma_{cond\_Temperature}. \quad (3)$$

The location parameter contribution $\sigma_{cond\_Temperature}$, corresponding to the test temperature is assumed proportional to temperature change,

$$\sigma_{cond\_Temperature} = K \cdot \Delta T, \quad (4)$$

where $\Delta T = T_{test} - T_{RT}$ (difference between test and reference (room) temperature), K is an empirical constant based on material behavior with respect to temperature.

To account for material changes due to heat treatment and/or thermal cycling, an empirical parameter x has been introduced, $x = 1$ for pristine specimens and $0 < x < 1$ for heat treated specimens. In first approximation the location parameter σ_{cond_HT} is a linear function of x, so

$$\sigma_{cond\_HT} = (1 - x) \cdot M. \quad (5)$$

Substituting (4) and (5) in (3) for combined effect of HT and test temperature gives

$$\sigma_{cond} = K(\Delta T) + M(1 - x). \quad (6)$$

Analysis of test data for the studied composite showed that good agreement with data can be obtained using $M = \sigma_{T\,@RT}^{CLT}$ and $K = \frac{\sigma_{T\,@RT}^{CLT}}{T_{manuf} - T_{RT}}$, $\sigma_{T\,@RT}^{CLT}$ is the thermal stress in 90° layer at RT calculated using CLT.

As in [3], assuming that at low crack density $\sigma_T \approx \sigma_T^{CLT}$, (2) can be written in log-log axes as

$$\ln\left(-\left(\ln(1 - \frac{\rho}{\rho_{max}})\right)\right) = m \ln(\sigma_T^{CLT} - \sigma_{cond}) - m \ln \sigma_{0ref}. \quad (7)$$

Using (7), the Weibull parameters were determined from the experimental crack density ρ and applied thermo-mechanical transverse stress data for pristine specimens tested at RT. In [3], the data points for fitting with (7) were selected within non-interactive crack density region ($0.05 < P_f < 0.3$). However, specimens tested in this work, had average manufacturing induced crack density of 0.32 cr/mm ($P_f = 0.23$). As a compromise between theoretical requirement and available practical options, data points corresponding to $0.28 < P_f < 0.50$ were included in the analysis and the parameters $\boldsymbol{m = 3.30}$ and $\boldsymbol{\sigma_{0ref} = 134.30\ MPa}$ were obtained.

Crack density prediction

Using the determined Weibull parameters in (1), the transverse failure probability and corresponding crack density development was predicted for pristine specimens ($x = 1$) and finding $x = 0.71$ as a good fit for heat treated specimens. It was assumed that $\boldsymbol{\sigma_T = \sigma_T^{CLT}}$, that is the stress in elements between a pair of existing crack is equal to stress in the undamaged laminate (which is acceptable at non-interactive crack density region) and the crack density is predicted for the whole crack density region. The predicted crack density versus thermo-mechanical transverse stress in 90° layer for pristine specimens tested at RT and ET and heat treated specimens tested at RT are in good agreement with the test results in whole crack density region, shown in **fig 3a**. The predictions for heat treated specimens at ET were slightly larger than the test results. The results obtained suggest that the UD fabric reinforced HTPC used in this work has rapid crack density growth even at interactive crack density region, which could

  doi:10.5075/epfl-298799_978-2-9701614-0-0

be due to the severe effect of failure stress distribution from fiber clustering and warp yarns, which are acting as the weak regions. The work presented here also suggests that detailed analysis of temperature and time of the heat treatment as well as the effect of thermal cycling between the heat treatment steps is necessary.

5. Conclusion

UD fabric with sparsely woven warp and weft yarns and high temperature polymer were used to manufacture different HTPC laminates in RTM. Upon observing the 90° layer of manufactured laminates, the bundle structures of the fabric retained their shape with yarns located between the bundles and resin rich region. The influence of warp yarns, test temperature and heat treatment in transverse crack density growth in the 90° layer of cross-ply laminate were analyzed. It was found that warp yarns acted as a weak region in the 90° layer and found to influence the cracks of as-received manufactured laminate, after HT stage and crack density growth at early stages of applied load to a great extent. A 3-parameter Weibull distribution was successfully used to predict transverse crack density growth upon applied thermo-mechanical transverse stress in the 90° layer. Weibull shape and scale parameter were assumed to be constant for test conditions and the location parameter was claimed to depend on the test temperature and HT conditions. Though predicted results were in good agreement with test results, it was suggested to perform in detailed analysis on heat treatment effects, also thermal cycling effect in the crack density growth.

Acknowledgements

This work has been performed within the Swedish Aeronautical Research Program (NFFP7), project 2019- 02777.

6. References

1. París F, Cano J, Varna J, “The fiber-matrix interface crack – a numerical analysis using boundary elements”, International Journal of Fracture 1990, 82(1): 11-29.
2. Parvizi A, Bailey JE, “On multiple transverse cracking in glass fiber epoxy cross-ply laminates”, Journal of Material Science 1978, 13(10): 2131-2136.
3. Vivek Richards Pakkam Gabriel, MS Loukil, J Varna, Analysis of intralaminar cracking in 90-plies of GF/EP laminates with distributed ply strength, J. of Composite Materials 2021; 0(0): 1-18.
4. Reifsnider KL and R Jamison, Fracture of fatigue-loaded composite laminates, International Journal of Fatigue 1982; 4(4): 187-197.

  doi:10.5075/epfl-298799_978-2-9701614-0-0

LASER STRIPPING OF THERMALLY AGED EPOXY COATINGS FOR AERONAUTICAL APPLICATIONS

Selen, Ünaldı[a], Elif , Atay[a], Matthieu, Gervais[a], Laurent, Berthe[a] and Emmanuel, Richaud[a]

a: PIMM, UMR8006 ENSAM, CNRS, CNAM, 151 bd de l'Hôpital, 75013 Paris, France
selen.unaldi@ensam.eu

Abstract: *During the time spent in the air, the external parts of the aircraft suffer an extensive damage. With temperatures ranging from -55 to 120 °C in the air, thermal ageing leads to mechanical failure. The focused work is with samples based on aluminum-coated-epoxy and corresponding created pure epoxy films. During the various stages of the analysis, the chemical and physical characteristics of the epoxy network are highlighted. Finally, a complete analysis of an initial material states, physico-chemical characterization and laser shock tests coupled for laser paint stripping and laser adhesion tests.*

Keywords: epoxy; aircraft coatings; thermal ageing; adhesion test

1. Introduction

For aeronautical applications, laser paint stripping technique has been very popular since 1980s [1,2]. The main objective of laser paint stripping is to remove each layer of external aircraft coatings to create selective stripping. In literature, most of the work for the laser paint stripping is based on the ablation phenomena from the painted side of specimens [3]. However, both previously and in the scope of this paper, we created an epoxy stripping and test epoxy adhesion from the substrate side of specimens with the shock wave propagation due to laser shock [4,5].

The external coated part of aircrafts are not composed of a simple mixture that can be found in any artwork or personal use applications. There are different layers that contribute to the final appearance of the external parts of aircraft. One of the component is the epoxy resin made by polymerizing monomers with hardener. This thermosetting material is irreversibly cross-linked, insoluble and difficult or impossible to deform even at high temperatures [6,7].

The stripping process was already studied for virgin (unaged) coatings but the effect of ageing on the stripping process is a grey zone. Aluminum plates (AA 2024 - T3) coated with cross-linked epoxy and the reference epoxy network films have been investigated. The chemical and physical characteristics of the epoxy network are analyzed by Fourier Transform InfraRed (FTIR) spectroscopy, especially after ageing of these networks. The work has conducted at high temperatures (120 °C) to further examine the behavior of the material under extreme conditions. After the samples have been aged, the laser shock impacts have been applied on specimens. These experiments were carried out on the aluminum side to avoid creating epoxy ablation. The power density used is a modifiable parameter that allows determining the epoxy removal point within the material if it occurs, i.e. the threshold where the epoxy layer was totally detached from the aluminum plate. Eventually, laser adhesion tests and laser stripping processes are coupled with physico-chemical analysis.

  doi:10.5075/epfl-298799_978-2-9701614-0-0

2. Materials & Methods

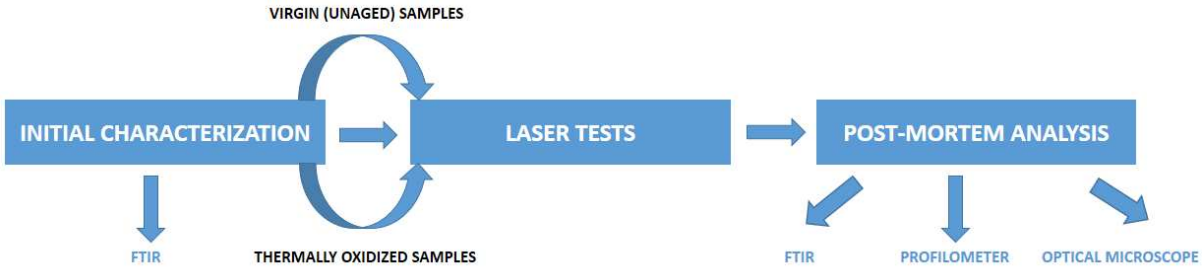

Figure 1. Followed Methodology.

2.1 Materials

The epoxy resin used is made of diglycidyl ether bisphenol A (DGEBA). The monomer used is mainly bisphenol A diglycidyl ether or more commonly known as DGEBA which has epoxy functions necessary for the formation of the resin. As for the hardener, diamines or anhydrides are mainly used as hardeners [9,10]. In this work, the used material as a base material is AA 2024-T3. It's known that 2XXX alloys used when the damage tolerance is the main concern. T3 subset represents the further modification of the properties (strength,hardness) [11]. Before any paint application, surface treatment might be applied for corrosion protection and promote paint adhesion on substrates [12]. For the presented work, Chromic Acid Anodization (CAA) is applied onto already manufactured specimens by industrial collaborators. For the epoxy resin film produced, the ratios used are listed in Table 1. These datas are also provided by the manufacturer and the choice of quantities is calculated according to the need (thickness of the film, approximately about 20 µm or less (i.e) conditions under which the epoxy can be considered as homogeneously degraded.

Table 1: Ratio of components used for the epoxy film.

Component	Supplier Ratio	Mass Introduced (mg)
Base	3.5	1400
Activator	1	400
Reducer	1	400

For the presented work, AA 2024 - T3 + Epoxy and prepared epoxy film are used (see Figure 1).

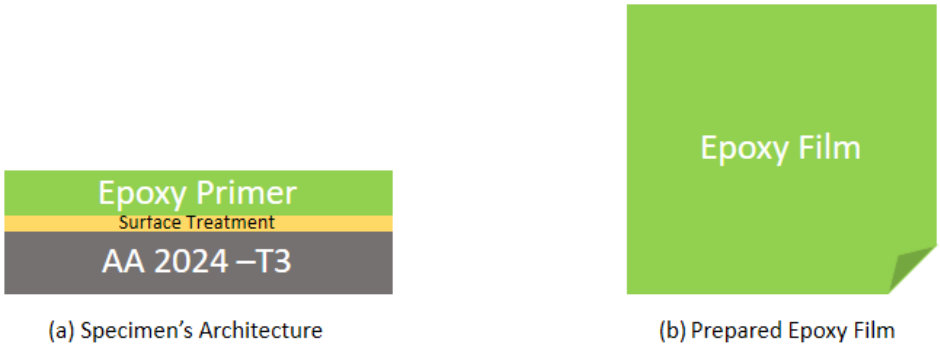

Figure 2. AA 2024-T3+Epoxy & Prepared Epoxy Film.

2.2 Methods

2.2.1 Fourier Transform Infrared Spectroscopy (FTIR)

FTIR (Fourier Transform InfraRed) spectra is collected in ATR (Attenuated Total Reflectance) mode using a Frontier 100 apparatus (Perkin Elmer) equipped with a diamond crystal and driven by the spectrum software for coated plates. 16 scans are collected from 650 to 4000 cm^{-1} with a 2 cm^{-1} minimal resolution. Then, the crystal in which the sample is in contact with allows an attenuated total reflectance (ATR). A signal is then detected on a detector which, by Fourier transform, converts it into a spectrum [13]. For the prepared epoxy films, analyses have been conducted by transmission mode.

2.2.2 Laser

Laser operations are carried out at PIMM, Hephaistos facility. The laser is a Gaïa HP from THALES which is a Nd:Yag laser. It generates at a wavelength of 532 nm with a pulse duration of 7 ns. The laser contains two beams, each with an energy of 7 Joules, i.e. 14 J in total [4]. Mono pulse laser beam applied from the AA 2024 T3 part of the specimens with a water confinement to make laser adhesion tests and laser paint stripping determination on aged and non-aged samples.

2.2.3 Profilometer

The profilometer is an instrument used to determine the surface profile of a sample. With the help of a fine diamond tip, the device comes into contact with the surface to be analysed and makes it possible to obtain the differences in depth present on a space reference. The device used during the work is a Dektak 150. The adjustment is made via a software program that traces the depth reached according to the length covered by the tip on the sample. The used device is a Dektak 15.

2.2.4 Optical Microscope

In order to characterize material properties such as surface analysis both before and after laser application or thickness investigation from the cross-section cut (cut-off machine Discotom-6 is used), optical microscopy is used. The used optical microscopy is ZEISS Axio Imager 2.

2.2.5 Thermal Ageing

In order to simulate the natural exposure conditions of the external parts of the aircraft, ageing can be considered. To do this, samples of AA 2024 + Epoxy are inserted into ventilated ovens heated at 120 °C. Small plates are placed on a support to analyze the chemical evolution and for laser shock tests. In parallel, parts of the previously developed epoxy films are also aged by placing them in Teflon adhesive tapes.

Samples	Conditions	Duration (Days)
Epoxy Film	120°	21
AA 2024 + Epoxy	120°	21

Table 2. Thermal ageing conditions for Epoxy Film and AA 2024 - T3 + Epoxy.

3. Results & Discussion

3.1 Chemical Characterization - FTIR

During the ageing stages, several absorption spectras are obtained. These will be analyzed in detail and will allow us to determine the structural changes in the epoxy network that take place. When epoxy resin networks undergo a temperature increase, the major changes observed are the formation of carbonyl and amide products. The adhesives lose their mechanical properties and their shear strength decreases.

Figure 3. Aged and Non-aged samples.

The FTIR analyses therefore start at t=0, they will serve as a reference for detecting possible changes and are continued until oxidation has taken place on the plates and films. This phenomenon can also be observed by the naked eye with the change in colour as the epoxy turns increasingly brown as can be seen in Figure 3.

After analysis of the spectra, the significant changes observed are those around the bands at 1720 cm^{-1}, 1650 cm^{-1} and those between 1200 and 1000 cm^{-1}. These are the characteristic of carbonyl, amide and amine functions respectively. The consumption of OH (around 3000-3600 cm^{-1}) testimony of the destruction of the hydroxypropylether group and the appearance of various species (carbonyls, amides) in the 1600-1800 cm^{-1} region, coming at least in part from hydroxypropylether groups [8].

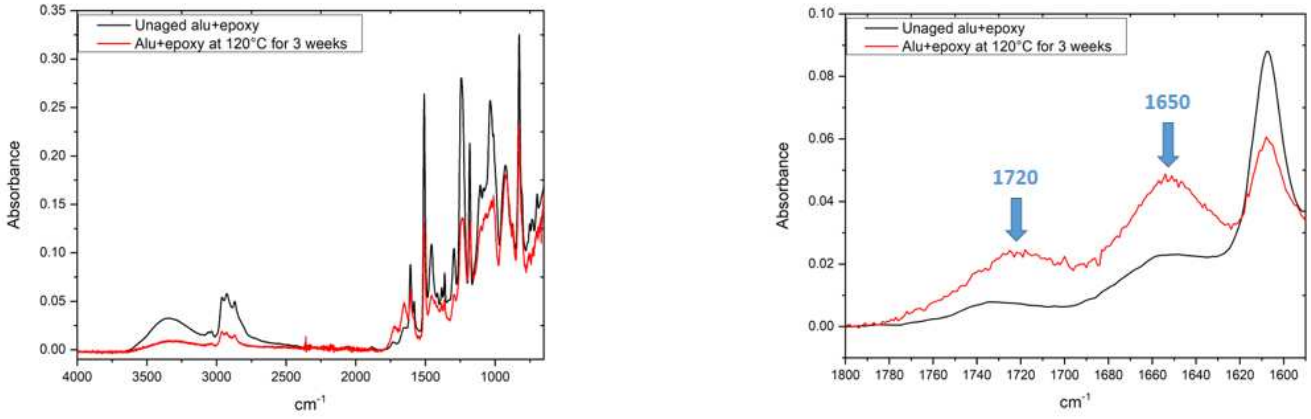

(a) FTIR Analysis for AA 2024 + Epoxy

(b) Close up to FTIR Analysis for AA 2024 + Epoxy

Figure 4. FTIR Analysis for AA 2024-T3+Epoxy.

3.2 Laser Adhesion Tests and Post-Mortem Analysis

After removal from the oven, the AA 2024+Epoxy samples were used for laser shooting. The unaged plate was the first to be tested as a reference. Indeed, to better visualize the evolution of the adhesion level between the epoxy layer and the aluminum, it is necessary to rely on a reference and keep it for the other experiments. In order to have as few factors as possible influencing the level of stripping and adhesion, all samples had a 43 µm thick epoxy layer for the thermal ageing experiments.

All samples were tested to see the effect of thermal ageing and adhesion level changes. In the beginning, threshold determination (the lowest value that complete epoxy stripping occurred) was made for each type of samples as function of power density. Figure 6 shows the different responses of the plates as a function of the applied power density. Images of each shots were analyzed using an optical microscope to have a more clear view and also to calculate the diameter of the stripped spot created by the shot. For the case of the unaged plate, the exfoliation condition was not present and there was a direct threshold followed by a complete stripping afterwards. On the contrary, for the aged plate, an exfoliation state was present before the threshold. By increasing the power density, a complete stripping follows [4].

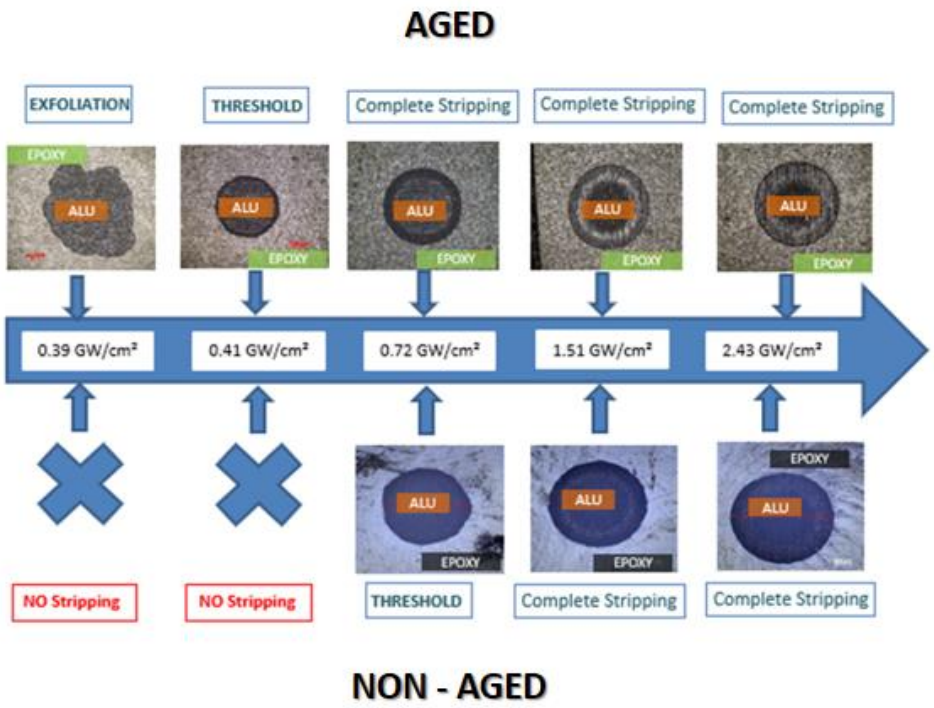

Figure 5. Comparison of Applied Laser Impacts on Aged (120°C for 3 weeks) and Non aged Samples.

Even though, the obtained trend for power density vs diameter is similar for both aged and unaged samples, stripped diameter via laser is bigger for aged samples than unaged ones regardless of the applied power density (see Figure 6) especially within the range of 0.75 GW/cm^2 to 2.5 GW/cm^2.

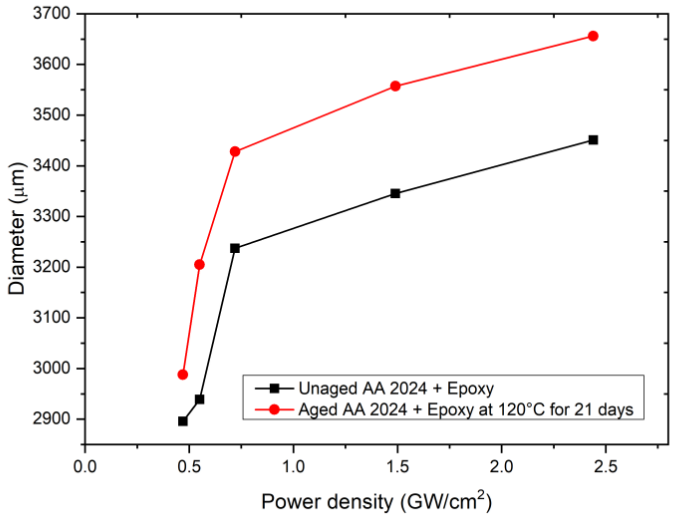

Figure 6. Comparison of Stripped Diameters on Aged (120°C for 3 weeks) and Non aged Samples.

4. Conclusion

The presented work covers the combination of chemical analysis for the paints which are used for aircrafts' exterior parts and laser adhesion tests. The main analysis was made on the question of how paints age under natural conditions of use. To address this, epoxy plates were introduced into the ageing protocol. The plates were aged at temperature of 120°C. First, chemical analysis was performed using absorption spectra (FTIR). Secondly, laser shoots were applied from the aluminum face of the samples.

Chemical changes were observed to the thermal oxidation of the epoxy network constituting the coating. This chemical degradation results in chain scissions, disappearance of hydroxyl isopropyl ether groups and mass loss [9]. Those phenomena finally result results in a bigger stripping diameter. Therefore, different thresholds were obtained with the laser shots, the higher the ageing the easier it was to strip the paint. This provides a basis for further experiments and understanding what happens at the layer level.

5. References

1. Jinsong, L. and Kintak, L. Multifunctional polymer nano composites. CRC Press, 6000 Broken Sound Parkway175 NW.

2. Kozol, J. An Environmentally Safe and Effective Paint Removal Process for Aircraft. JOM 2001, 53 , 20–21, doi:doi.org/10.1007/s11837-001-0172-y.

3. Jasim, H.A. and Demir, A.G. and Previtali, B. and Taha, Z.A. Process development and monitoring in stripping of a highly transparent polymeric paint with ns-pulsed fiber laser. Optics and Laser Technology 2017, doi:doi.org/10.1016/j.optlastec.2017.01.031.181.

4. Unaldi, S. and Papadopoulos, K. and Rondepierre, A. and Rouchausse, Y. and Karanika, A. and Deliane, F. and Tserpes, K. and Floros, G. and Richaud, E. and Berthe, L. Towards selective laser paint stripping using shock waves produced by laser-plasma interaction for aeronautical applications on AA 2024 based substrates. Optics and Laser Technology 2021, doi:doi.org/10.1016/j.optlastec.2021.1070953.

5. Tserpes, K. and Papadopoulos,K. and Unaldi,S. and Berthe, L. Development of a Numerical Model to Simulate Laser-Shock Paint Stripping on Aluminum Substrates. Aerospace 2021.

6. Auvergne, R. and Caillol, S. and Ghislain, D. and Boutevin, B. and Pascault, J.P. Biobased Thermosetting Epoxy: Present and Future. Chemical Reviews 2013, American Chemical Society, doi:doi.org/10.1021/cr3001274.

7. Pascault, J. and Sautereau, H. and Verdu, J. and Williams, R.J.J. Thermosetting Polymers. Marcel Dekker: New York, NY, USA 2002, ISBN 0824706706, doi:doi.org/10.1021/cr3001274.

8. Delozanne, J. and Desgardin, L. and Coulaud, M and Cuvillier, N and Richaud, E. Failure of epoxies bonded assemblies: comparison of thermal and humid ageing. Journal of Adhesion 2018.

9. Ernault, E. and Richaud, E. and Fayolle, B. Origin of epoxies embrittlement during oxidative ageing. Polymer Testing, 63, 2017, doi: https://doi.org/10.1016/j.polymertesting.2017.09.004.

10. Allen,R., O. and Sanderson,P. Characterization of epoxy glues with ftir Applied Spectroscopy Reviews.

11. R. Rioja and J. Liu. “The evolution of Al-Li base products for aerospace and space applications”. In: Metallurgical and Materials Transactions 43A.3325-3337 (2012)

12. G. Bierwagen. “Next Generation of Aircraft Coating Systems”. In: Journal of Coatings Technology 73 (2001), pp. 45–52. doi: 10.1007/BF02730030. url: https://doi.org/10.1007/BF02730030.

13. Griffiths,P. and Hasseth,J.A. Fourier transform infrared spectrometry. Wiley Blackwell 2007.

14. Devanne,T. Vieillissement radiochimique d’un réseau époxyde. 2003.

HYGRO-THERMAL EFFECTS ON THE TRANSLAMINAR FRACTURE TOUGHNESS OF COMPOSITE LAMINATES

Ganapathi A. Sengodan[a,b], Shengkai Li[a], Giuliano Allegri[a], Stephen R. Hallett[a]

a: Bristol Composites Institute, University of Bristol, United Kingdom –
gana.ammasaisengodan@bristol.ac.uk
b: School of Science, Engineering & Environment, University of Salford, United Kingdom.

Abstract: *The translaminar fracture toughness of wet (fully saturated) and dry (as manufactured) IM7/8552 laminates was measured using compact tension tests. Cross-ply ($[90/0]_{8S}$) and quasi-isotropic ($[90/45/0/-45]_{4S}$) laminates were tested at three different temperatures, namely 23 °C, 40 °C and 90 °C. The translaminar fracture toughness decreases non-linearly with the temperature for the dry laminates. However, for the wet laminates, the translaminar fracture toughness increases. The room-temperature tested wet cross-ply laminates exhibited a lower fracture toughness than the dry laminates. However, the initiation fracture toughness of the wet quasi-isotropic laminates is higher than for the dry laminates at all the test temperatures. The fractographic analysis of the failed specimens revealed that the hot-wet conditions promote additional fibre pull-out, which increases the fracture energy. The degradation of the epoxy matrix in the wet multi-directional laminates affected the progressive failure mechanism, and either increased or decreased the overall fracture energy depending on the lay-up sequence.*

Keywords: Translaminar; composites; fracture toughness; hygro-thermal; fibre pull-out.

1. Introduction

Laminated composite materials are ideal candidates for structural applications due to their weight-saving potential. The failure mechanisms of such heterogeneous materials are complex because of the progressive and interactive nature of different damage mechanisms, such as matrix cracking, delamination, fibre/matrix debonding and fibre failure. The interaction of multiple failure modes is evident in multi-directional laminates [1]. This represents a significant challenge for the understanding of the overall process of damage development. In in-service operating conditions, the failure modes tend to become more complex, since mechanical loading is complemented by the temperature and moisture. Polymer-based matrices are more sensitive to moisture and temperature degradation than the reinforcing fibres, especially if the latter are carbon. For example, Figure 1 (a) compares the matrix dominated strength properties of IM7/8552 laminates tested at room temperature dry (RTD, i.e., Dry@23 °C) and elevated temperature wet (ETW, i.e., Wet@ 121 °C) conditions. The strengths of the ETW specimens were lower than for the RTD specimens, and similar trends were observed for the stiffness [2].

The fibre-dominated strength properties of different laminates are compared in Figure 1(b). The longitudinal tensile is lower for ETW unidirectional ($[0]_6$) and unnotched $[\pm45/0/\pm45/90/\pm45_2]_S$ laminates when compared to that of RTD laminates. Surprisingly, the unnotched $[45/0/-45/90]_{2S}$ quasi-isotropic (QI) laminates showed an increase in the strength in ETW conditions when compared to RTD conditions. This is likely because the residual stress relaxation under hot-wet

  doi:10.5075/epfl-298799_978-2-9701614-0-0

conditions positively influences the stress transfer mechanism for such QI lay-ups, overcoming the effect of the degradation of matrix-dominated properties.

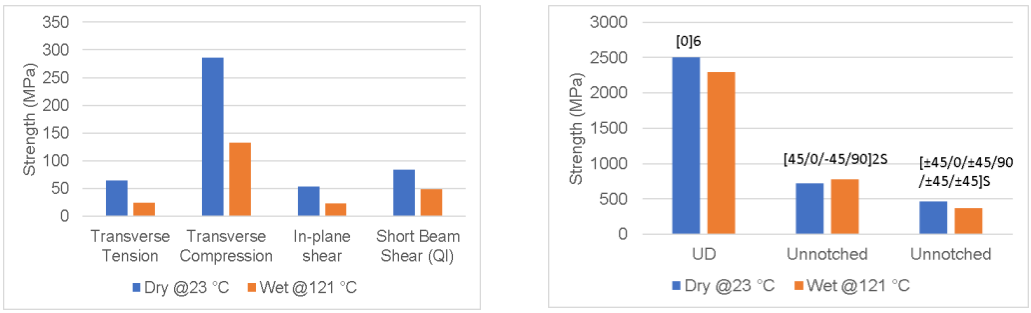

(a) (b)

Figure 1. Comparison of (a) matrix dominated strengths, (b) longitudinal tensile strengths of room temperature dry and hot-wet IM7/8552 laminates [2]

The longitudinal tensile failure of composite laminates is typically controlled by the fracture toughness associated with the tensile fibre (i.e., translaminar) failure. Progressive failure mechanisms such as fibre breakage, fibre-matrix debonding, and fibre pull-out generally contribute to the total dissipated energy in the translaminar failure of laminates [3-5]. Temperature and moisture considerably affect the translaminar fracture behaviour of the composite laminates by degrading the mechanical performance of the bulk matrix, of the matrix/fibre interface, and the inter-laminar strength and toughness. Furthermore, moisture uptake and matrix swelling alter the inter-ply and intra-ply stress distribution. Therefore, these environmental effects are typically detrimental to the performance of composites structures [6]. However, the longitudinal strength properties at ETW conditions can be improved by carefully selecting material combinations, as well as lay-up configurations [2, 7].

Even though thermoset matrices are prone to environmental degradation, the longitudinal failure of the composite structures primarily depends on the fracture toughness associated with the tensile fibre failure. A better understanding of the failure mechanism of laminates made up of different material combinations and layup configurations tested at varying in-service conditions will help to improve the life-cycle and in-service performance of composite structures. In the past, significant research works dedicated to the translaminar fracture toughness measurement of the laminated composites [8-13]. Compact tension (CT) tests of cross-ply laminates were used to obtain the translaminar fracture toughness as a material property [12]. Xu et al. [14, 15] investigated the size and stacking sequence effects on the translaminar fracture toughness of quasi-isotropic laminates using over-height compact tension tests. Bullegas et al. [16] used a bio-inspired pattern of micro-cuts to improve the translaminar fracture toughness of thin-ply composites. Most of the toughness tests were conducted on dry (as manufactured) specimens at room temperature conditions. Marin et al.[6] investigated the translaminar fracture toughness of cross-ply laminates (T800S/M21) at hygrothermal conditions. Fractographic analyses of double edge notched tensile test specimens revealed some important failure mechanisms occurring in hot-wet laminates. The key conclusion is that the fracture toughness of hot-wet specimens is enhanced by the increased fibre pull-out lengths and the larger size of associated fracture process zones.

In this work, the translaminar fracture behaviour of cross-ply and quasi-isotropic laminates are investigated for dry and wet laminates at three different test temperatures. The longitudinal

  doi:10.5075/epfl-298799_978-2-9701614-0-0

initiation fracture toughness of unidirectional plies is obtained from cross-ply CT specimens. The overall fracture energy of the QI laminates is calculated by accounting for different failure mechanisms. The progressive failure mechanisms following crack initiation are investigated using fractographic analysis via scanning electron microscope (SEM) and photographic images. A comprehensive explanation for the increase in the initiation fracture energy in hot-wet conditions is detailed in this paper.

2. Material and hygro-thermal conditioning

Cross-ply ($[90/0]_{8S}$) and quasi-isotropic ($[90/45/0/-45]_{4S}$) laminates were manufactured employing IM7/8552 unidirectional prepreg, using an autoclave as per the prepreg manufacturer's recommended cure cycle. The average thickness of the cured plies was 0.125 mm. The test specimens of the required size were cut from the panels using carbide coated endmill cutters, as shown in Figure 1(a). Loading pinholes of 9.6 mm diameter were cut using carbide coated drill bits. A pre-crack of 30 mm length from the longest edge of the specimen was made by using a 4 mm end mill cutter. The pre-crack was further extended to 10 mm using a saw machine with ~0.4 mm thick diamond cutting disc.

The “wet” specimens were hygrothermal conditioned in a humidity chamber at 70 °C and ~85% relative humidity. The cross-ply and QI specimens were left in the humidity chamber, and the weight gain of a representative coupon was recorded at different time intervals, as shown in Figure 1(b). The wet specimens were considered fully saturated when the averages of three consecutive weight measurements differed by less than 0.2%.

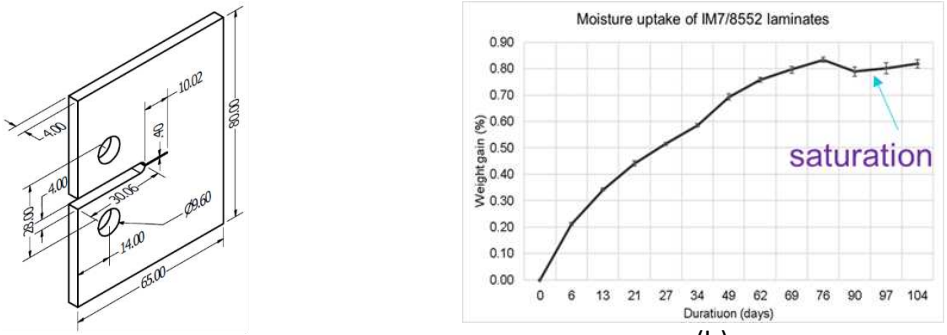

(a) (b)

Figure 2. (a) Dimensions (in mm) of the compact tension test specimens cut from the IM7/8552 cross-ply and QI laminates (b) Moisture uptake of a representative IM7/8552 compact tension test specimen at 70 °C and 85% relative humidity (RH)

3. Experiment and data reduction

The compact tension tests were conducted at three different temperature conditions, namely 23 °C, 40 °C and 90 °C for the dry and wet specimens. The elevated temperatures values were selected based on the following rationale: (a) the maximum operating temperature for an off-shore wind turbine blade is ~ 38 °C; and (b) the maximum temperature experienced by aircraft components is ~90 °C. A Shimadzu universal testing machine with a suitable test fixture was used for the compact tension tests, as shown in Figure 4(a). A thermal chamber was used for the elevated temperature tests, as shown in Figure 4(b). A thermocouple was used to measure the specimen surface temperatures. The specimens were loaded at a rate of 1 mm/min. The

extension of the pre-crack was monitored using a video gauge set-up. Figure 4(c) shows the snapshot of a video gauge image.

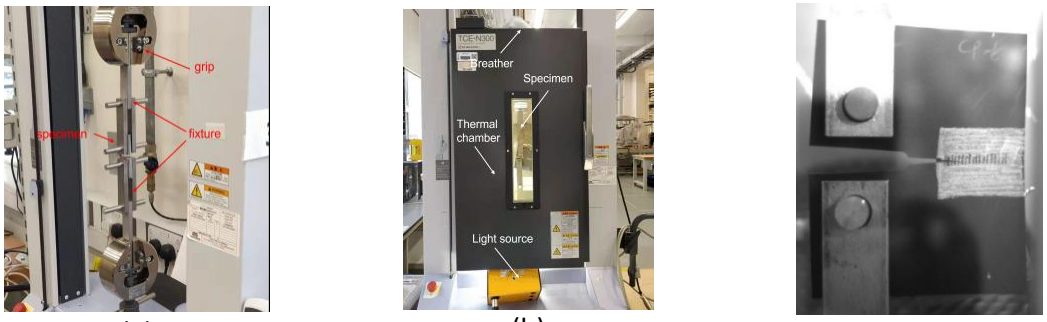

(a) (b) (C)

Figure 3. (a) Loading fixture, (b) Thermal chamber, and (c) video gauge image of a loaded specimen, of the compact tension tests.

The critical fracture energy of a compact tension specimen is calculated by using [10]

$$G_c = \frac{P_c^2}{2t}\frac{\partial C}{\partial a} \tag{1}$$

where, C and a are the compliance and crack extension of the specimen. P_c is the critical load and t is the total thickness of the compact-tension specimen. In this work, the modified compliance calibration (MCC) method was used to calculate the critical initiation fracture energy of the specimens [17]. The initiation fracture energy of the 0° plies is calculated from the total fracture energy of cross-ply laminates by using

$$G_{0Cini}(a) = \frac{-P_c^2}{2t^0}\frac{\alpha(\beta+\alpha a)^{-\left(1+\frac{1}{\chi}\right)}}{\chi} \tag{2}$$

where t^0 is the overall thickness of the 0° plies, and the constants α, β, and χ are obtained from the best fit of the compliance versus crack extension curve. Similarly, the initiation fracture energy values for the QI laminates are calculated as [17]

$$G_{Cini}(a) = \frac{-P_c^2}{2t}\frac{\alpha(\beta+\alpha a)^{-(1+1/\chi)}}{\chi} \tag{3}$$

where, t is the total thickness of the QI laminate.

4. Results & discussion

The load-displacement curves of four tests chosen from the total test cases are compared in Figure 5. The wet cross-ply specimens tested at 90 °Care stiffer than the dry specimens tested at room temperature. However, the peak failure load of the dry laminate is higher than the wet cross-ply laminates, and the damage is more progressive. The load-displacement curve of the hot-wet cross-ply specimens is slightly non-linear just before the peak failure load. On the other hand, the wet QI specimens tested at 90 °C exhibit higher stiffness and peak failure loads than the dry laminates tested at room temperature. The damage appears more progressive in the room-temperature tested dry QI specimens compared to the the hot-wet specimens.

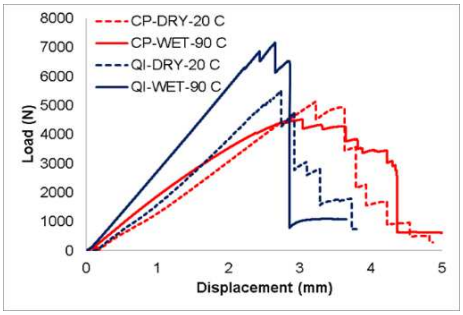

Figure 4. Load-displacement curves of the selected test cases for the cross-ply and quasi-isotropic laminates.

Figure 6(a). shows the initiation fracture energy of 0° plies obtained from the translaminar failure of cross-ply (CP) laminates. As expected, the fracture energy of dry specimens decreases non-linearly with the increase in test temperature. Interestingly, the fracture energy of fully saturated (wet) coupons increases with the temperature. This is because the fibre/matrix interface of the wet specimens becomes weaker and promotes the fibre pull-out in the laminates. The fibre pull-out length and the fracture process zone of the wet laminates increase with temperature, and this results in a higher energy dissipation. Fractographic analysis of the failure surfaces revealed that the wet specimens had more pulled out fibres than the dry specimens.

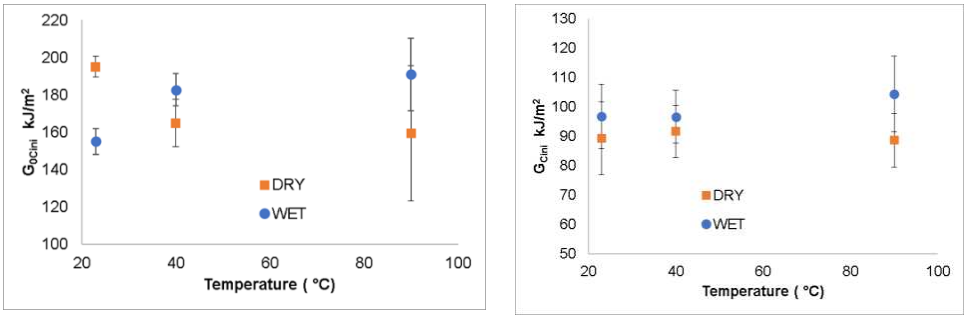

Figure 5. Initiation fracture energy of the (a) 0° plies obtained from the translaminar failure of [90/0]8S cross-ply laminates and (b) [90/45/0/-45]4S Quasi-Isotropic laminates.

Figure 6(b) compares the initiation energy of dry and wet quasi-isotropic laminates. The initiation energy of the dry coupons slightly increases (~2%) as the temperature increase from 23 °C to 40 °C. This effect becomes less pronounced at 90 °C (~1%). It can be concluded that the initiation facture energy of the dry QI laminates is not significantly affected by the increase in temperature. The fracture energy of the wet QI specimens is higher than the dry specimens due to the weak fibre/matrix interface and increased fibre pull-outs. The initiation fracture toughness of the elevated temperature (90 °C) wet QI specimens is ~17% higher than the room temperature (23 °C) dry specimens.

5. Fractography

Preliminary investigations suggested that the increase in fracture energy of the wet specimens is due to the fibre pull-out of the 0° plies. Nevertheless, it is critical to examine the fracture surface of the failed laminates due to the progressive nature of the failure. Therefore, the failure morphology at the crack initiation region was investigated in detail. Figure 7 compares the fracture surfaces of the dry and wet cross-ply specimens tested at 23 °C, 40 °C and 90 °C.

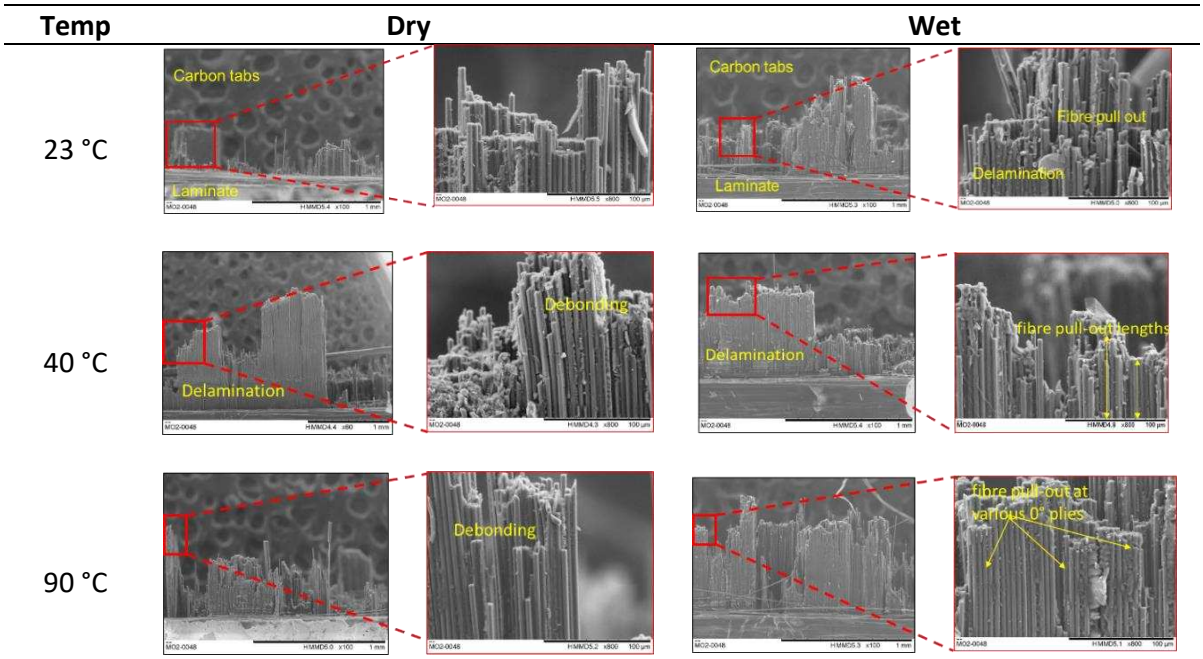

Figure 6. Fractographic comparison of the dry and wet cross-ply laminates tested at three different temperatures

At 23 °C, dry specimens show minimal delamination of 0° plies from the 90° plies and a clean longitudinal fibre breakage normal to the pre-crack direction. Therefore, the debonding of fibre from the matrix is insignificant. The wet specimens exhibit higher delamination between the 0° and 90° plies than the dry specimens, due to the degradation of matrix properties at ply interfaces. The fibre/matrix interfaces of the wet laminates are clearly weakened, and extensive debonding is observed. This debonding affects the stress transfer of the fibre/matrix interface and leads to lower dissipation energy than in the dry specimens, as shown in Figure 6(a).

At 40 °C, dry specimens show larger delamination of 0° plies from the 90° plies when compared to RTD specimens. The increase in temperature weakens the fibre/matrix interface and leads to increased debonding and less fracture resistance than in the RTD specimens. The amount of delamination in wet laminates is similar to that observed in the dry specimens. However, the fibre/matrix debonding length is reduced due to the residual stress relaxation of the wet interface, and this contributes to the overall energy dissipation. The fibre pull-out lengths of the wet specimens are larger than in the dry specimens. Therefore, wet laminates exhibit a larger overall fracture energy than the dry specimens at 40 °C, as shown in Figure 6(a).

At 90 °C, dry specimens show more extensive delamination than the RTD specimens, but less than the dry specimens tested at 40 °C. The matrix strength degrades with the increase in temperature, and an increased debonding length is noticed in the specimens. The debonding of the fibre/matrix interface is more prominent than the delamination of the 0/90 interfaces. Therefore, the overall fracture toughness of the dry specimen tested at 90 °C is less than for the dry specimens tested at lower temperatures. The breadth of delamination in hot-wet specimens are shorter than the wet specimens tested at lower temperatures. However, this shorter delamination patterns appears across the plies and in several plies. This failure behaviour is controlled by pull-out of fibre bundles. The debonding between the fibre and matrix is less than in the other specimens due to the relaxation of residual stresses occurring in hot-wet conditions.

The transfer of load between the fibre and matrix is higher enough to promote the fibre pull-out lengths. The delamination of plies, fibre/matrix debonding, and the increased fibre bundle pull-out lengths all contribute to the overall fracture energy dissipation of the specimens. Thus, the fracture toughness of wet specimens increases with temperature, as shown in Figure 6(a).

The fractographic analyses of QI dry specimens tested at 23 °C (i.e., RTD) and wet specimens tested at 90 °C (i.e., hot-wet or ETW) are presented and compared in Figure 8. The RTD specimens show a clean longitudinal fibre breakage normal to the pre-crack direction, followed by the delamination of off-axis plies. The fracture energy is mostly dissipated via the longitudinal fibre breakage. The hot-wet specimens show a more pronounced broom-like structures of the 0° fibres than in the RTD specimens. The residual stress relaxation of the wet fibre/matrix interface promotes the fibre pull-out. The delamination of the off-axis plies and the longitudinal fibre breakage compete, and it difficult to establish which one occurs first. Furthermore, the size of the plastic zone at the crack tip in the hot-wet specimens is larger than in the RTD specimens, and this increases the failure strength of the specimens. Thus, the initiation fracture toughness of the wet QI specimens is higher than for the dry QI specimens, as shown in Figure 6(b).

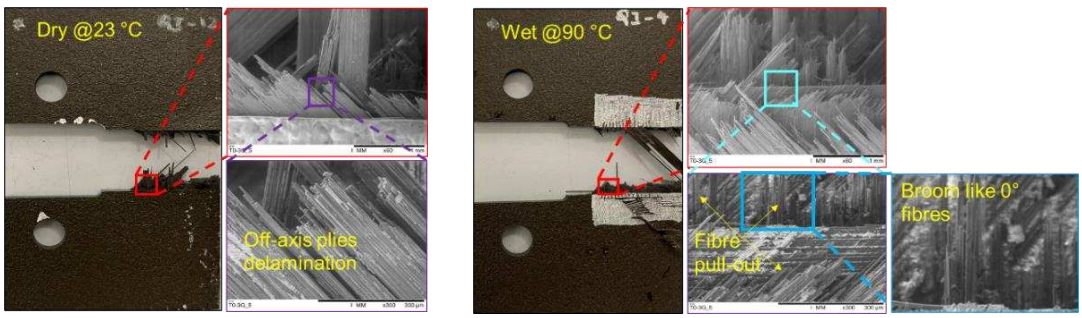

Figure 7. Fractographic analysis of (a) Dry tested at 20 °C and (b) Wet testes at 90 °C quasi-isotropic laminates.

6. Summary

The matrix dominated properties of the carbon/epoxy laminates are affected by hot-wet service conditions. The longitudinal properties of unidirectional laminates also drop in hot-wet environments. However, multi-directional laminates may offer improved fracture properties in hot-wet conditions, depending on the lay-up sequence of the plies. Different progressive failure mechanisms such as matrix failure, fibre/matrix debonding, delamination of the off-axis and 0° plies, fibre pull-out, fibre breakage, friction between the pulled-out fibres and the matrix all contribute to the overall fracture toughness of specimens tested in hot-wet conditions. Therefore, properly chosen lay-up configurations offer improved longitudinal strength, stiffness, and toughness properties at elevated temperatures and moisture saturation conditions. For example, the initiation fracture toughness of wet QI coupons tested at elevated temperature (90 °C) is ~17% higher than for dry specimens characterized at room-temperature (23 °C). The composites laminate design process and the underlying material selection can therefore be enhanced by accounting for the effect of in-service conditions on the mechanical performance.

Acknowledgements

The authors would like to acknowledge Supergen Offshore Renewable Energy Hub, UK for their support of this research through the Supergen Early Career Research Fund.

7. References

1. Nixon-Pearson OJ, Hallett SR, Withers PJ, Rouse J. Damage development in open-hole composite specimens in fatigue. Part 1: Experimental investigation. Composite Structures 2013; 106:882-889.
2. Marlett K, Ng Y, Tomblin J. Hexcel 8552 IM7 unidirectional prepreg 190 gsm & 35%RC qualification material property data report, in National Center for Advanced Materials Performance. 2011. Wichita State University: Wichita, KS.
3. Coats TW, Harris CE. A progressive damage methodology for residual strength predictions of notched composite panels. Journal of Composite Materials 1998; 33(23).
4. Li X, Hallett SR, Wisnom MR. Numerical investigation of progressive damage and the effect of layup in overheight compact tension tests. Composites Part A: Applied Science and Manufacturing 2012; 43(11):2137-2150.
5. Teixeira RF, Pinho ST, Robinson P. Translaminar fracture toughness of CFRP: from the toughness of individual plies to the toughness of the laminates, in 15th European Conference on Composite Materials. 2012: Venice, Italy.
6. Marín L., Gonzalez EV, Maimi P, Trias D, Camanho PP. Hygrothermal effects on the translaminar fracture toughness of cross-ply carbon/epoxy laminates: Failure mechanisms. Composites Science and Technology 2016; 122:130-139.
7. Sengodan GA, Allegri G, Hallett SR. Simulation of progressive failure in laminated composites under variable environmental conditions. Materials & Design 2020; 196.
8. Pinho ST, Robinson P, Iannucci L. Fracture toughness of the tensile and compressive fibre failure modes in laminated composites. Composites Science and Technology 2006; 66(13):2069-2079.
9. Catalanotti G, Camanho PP, Xavier J, Davila CG, Marques AT. Measurement of resistance curves in the longitudinal failure of composites using digital image correlation. Composites Science and Technology 2010; 70(13): 1986-1993.
10. Laffan MJ, Pinho ST, Robinson P, Iannucci L. Measurement of the in-situ ply fracture toughness associated with mode I fibre tensile failure in FRP. Part I: Data reduction. Composites Science and Technology 2010; 70(4):606-613.
11. Zobeiry, N. Extracting the strain-softening response of composites using full-field displacment measurement, in the faculty of Graduate studies (Civil Engineering). 2010. The University of Bristish Columbia, Vancouver.
12. Camanho PP, Catalanotti G. On the relation between the mode I fracture toughness of a composite laminate and that of a 0° ply: Analytical model and experimental validation. Engineering Fracture Mechanics 2011; 78(13):2535-2546.
13. Gutkin R, Laffan ML, Pinho ST, Robinson P, Curtis PT. Modelling the R-curve effect and its specimen-dependence. International Journal of Solids and Structures 2011; 48(11-12):1767-1777.
14. Xu X, Wisnom MR, Hallett SR, Zobeiry N, Leslie S, Poursartip A, Vaziri, R. Stacking sequence effects in oevr-height compact tension tests of quasi-isotropic laminates, in the 19th international conference on composite materials. 2013.
15. Xu X, Wisnom MR, Mahadik Y, Hallett SR. Scaling of fracture response in Over-height Compact Tension tests. Composites Part A: Applied Science and Manufacturing 2015; 69:40-48.
16. Bullegas G, Pinho ST, Pimenta S. Engineering the translaminar fracture behaviour of thin-ply composites. Composites Science and Technology 2016; 131: 110-122.
17. Dávila CG, Rose CA, Camanho PP. A procedure for superposing linear cohesive laws to represent multiple damage mechanisms in the fracture of composites. International Journal of Fracture 2009; 158(2): 211-223.

RECOVERY AND REUSE OF CARBON FIBRE AND ACRYLIC RESIN FROM THERMOPLASTIC COMPOSITES USED IN MARINE APPLICATION

Haithem, BEL HAJ FREJ[a], Romain, LÉGER[a], Didier, PERRIN[b], Patrick, IENNY[a], Pierre, GÉRARD[c], Jean-François, DEVAUX[d]

a: LMGC, IMT Mines Ales, University of Montpellier, CNRS, Ales, France
haithem.bel-haj-frej@mines-ales.fr
b: Polymers Composites and Hybrids (PCH), IMT Mines Ales, Ales, France
c: Arkema France, Groupement de Recherches de Lacq, 64170 Lacq, France
d: Arkema France, CRRA, rue Henri Moissan, 69491 Pierre Bénite, France

Abstract: *This study examines the feasibility of recovering and reusing the reinforcement and matrix of a carbon fibre reinforced thermoplastic composite. A proof of concept based on pyrolysis allowed the depolymerisation of the acrylic matrix (Elium©) and the recovery of clean carbon fibres and the matrix monomer. Subsequently, distillation was used to purify the monomer from impurities and to synthesise a recycled Elium© resin. The morphological and compositional differences at the fibre scale led to the assumption that the sizing was removed during the depolymerisation process and that only small traces of the polymer are still present on the fibre surface. New composites based on virgin and recycled matrix with recovered carbon fibre were manufactured by resin infusion. Although in-plane mechanical properties remained almost unchanged, the interlaminar shear strength results showed an improved fibre-matrix interface bonding. Dynamic mechanical analysis confirmed the good quality of the recovered carbon fibres and the similar properties of the virgin and repolymerised resin.*

Keywords: Carbon fibre; Recycling; Thermoplastic composite; Mechanical properties; Marine application

1. Introduction

Fibre reinforced thermosets and thermoplastic resins are increasingly used to replace conventional materials in a number of industrial, transport and sporting applications. One of the biggest challenges posed by fibre-reinforced composites, in particular in marine application, is their recycling (1). Environmental legislation is becoming more and more restrictive and end-of-life solutions for leisure boats waste are limited. The environmental impact of these materials disposed in landfills or drowned in seawater is accelerating the urgency to reach more industrial scale solutions to the recycling of composite. The use of thermoplastic composites allows the recovery of raw materials from end-of-life parts, which could have a substantial environmental and economic benefit. The newly developed reactive methacrylate thermoplastic matrix Elium© presents an alternative to thermoset resins currently used in composites for marine structures (2). It can be processed at room temperature with processing techniques typical of thermosets, like resin infusion. This thermoplastic resin reinforced by carbon fibres presents good mechanical and durability properties, compared to a carbon fibre reinforced vinylester composite (3). The recycling of the carbon fibre reinforced thermoplastic resin was investigated by pyrolysis process developed by Arkema. The high temperature associated to a pressurised inert atmosphere allows the recovery and the reuse of both the carbon fibre and the thermoplastic resin by depolymerisation. This method allows the reuse of the recovered fibres

  doi:10.5075/epfl-298799_978-2-9701614-0-0

either with virgin resin to form a semi-recycled composite or with recycled resin to form a totally recycled composite. In this study, the efficiency of this method is studied by analysing the residual rate of the polymer into the recovered fibres. The surface quality and diameter change of recycled fibre was investigated using scanning electron microscopy. Further tests consisting in the comparison of the mechanical properties of the initial composite and the totally and semi-recycled composites were carried out.

2. Materials and methods

2.1 Materials

The material considered in this study is a carbon fibre reinforced acrylic matrix laminate composite. The Elium© 188-O resin was kindly provided by ARKEMA and the reinforcement was a Cbx600 24 K T620 biaxial stitched carbon fabric from Sicomin. It is a 2 plies (±45°) non-Crimp balanced biaxial carbon fibre fabric with an areal weight of approximately 640.5 g/m². Elium© 188-O resin is a polymer solution of methyl methacrylate (MMA) monomer (>80 %) and acrylic copolymers, with a viscosity of 100 cPs and activated by a benzoyl peroxide (BPO) initiator from AkzoNobel. The glass transition temperature of the polymerised polymer is approximately 109 °C. The compatibility of the fabric, according to the manufacturer, is for general use as epoxy, polyester and vinylester. Therefore, there is no specific sizing for acrylic resin. Composite laminates of 4 plies ($[0/90/0/90]_s$) of CF fabric of 450 × 420 mm² were produced by Vacuum Assisted Resin Infusion (VARI) method at room temperature. During curing, an exothermic reaction took place, characterised by a temperature peak. After demoulding, no particular post-curing was performed on the infused plates, which were conditioned at 23 °C and 50% RH. The average thickness of the 4-ply infused laminate is about 2.5 mm. Density measurements on at least three samples of 35 × 12 × 2.5 mm^3 were performed using a Micromeritics gas pycnometer (model AccuPyc 1330) with helium gas in order to calculate the apparent volume fraction of the constituents according to ASTM D317-15. The volume fraction of the voids was deduced from the volume fraction of the fibres and the matrix.

2.2. Methods

2.2.1. Recycling method

Around 30 rounded discs having a diameter ranging from 135 mm to 142 mm (Figure 1.a) were machined from composite laminates using a water jet-cutting machine and were stacked into a 4.5L reactor at Arkema CRRA research center (Figure 1.b). Two sets of around 1500 g of composites were depolymerised under pressurised nitrogen atmosphere and a temperature range from 350 to 450 °C. The condensed vapours were gradually recovered in a liquid receiver flask as the depolymerisation continues. The recovered monomer liquid is then stabilised using hydroquinone as a polymerisation inhibitor. Once the reactor has cooled down to room temperature, the recovered carbon fibre reinforcement was collected from the reactor (Figure 1.c). The experimental results of the two depolymerisations, in terms of recovered fibre weight and raw MMA monomer, are shown in the table below.

Table 1 : Depolymerisation process results

Run	Introduced composite weight [g]	Reclaimed carbon fibre weight [g]	Reclaimed crude MMA weight [g]	Solid residue fraction [% vs initial composite weight]	Liquid residue fraction [% vs initial composite weight]	Material balance [%]
1	1577	1137	394	72.1	25.0	97.1
2	1634	1177	428	72.1	26.2	98.2
Total	3211	2314	822	72.1	25.6	97.7

Initial length and orientations of initial fibres were not modified during pyrolysis process. In addition, it was found that the fraction of solid residues in the top of the reactor was slightly higher than in the central region (72.0% versus 70.8%, respectively), which is likely due to the temperature gradient in the reactor due to heat transfer. The reclaimed crude liquid monomer had yellow-orange colour (Figure 1.d). In fact, during the degradation process, a number of small radicals were formed via disproportionation, and they cannot be depolymerised efficiently thus giving rise to the generation of by-products. In order to analyse reclaimed monomer purity and to identify by-products, analysis of the reclaimed crude liquid of present study was performed by gas chromatography with flame ionization detection. Quantification of MMA content in crude MMA using an internal standard was found to be 77% and 72% for respectively for first and second depolymerisation tests. Main identified by-products are methyl isobutyrate, ethyl acrylate, methyl acrylate, methacrylic acid and methanol. Many heavier compounds were detected, but have not been identified (4). Crude monomer solution from both depolymerisation trials were distilled (Figure 1.e). From 703 g of crude MMA at 75% purity, 385 g of MMA with 99.5% GC purity was recovered and formulated by ARKEMA (GRL, France) to finally obtain around 500 g of recycled Elium© 188-O resin (Figure 1.f) which will be denoted rElium.

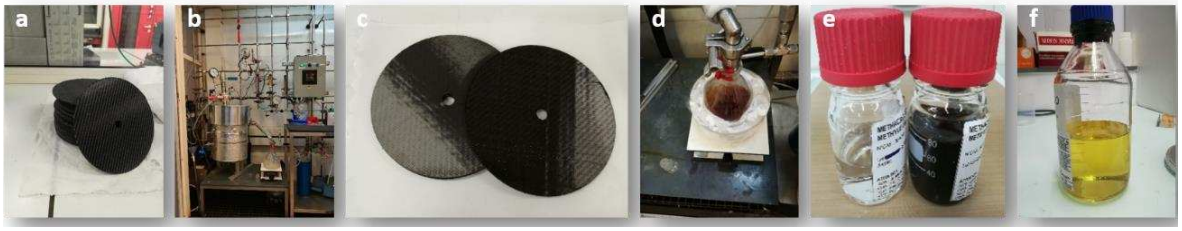

Figure 1 : a) CFRP discs, b) Pyrolysis reactor, c) recovered CF, d) recovered crude monomer solution, e) distilled MMA monomer (transparent) and by-products (dark), f) repolymerised resin

2.2.2. Analysis methods

Several techniques were used at both fibre and composite scale in order to investigate the differences between virgin and recovered constituents. Scanning electron microscopy (FEI Quanta 200 FEG) and Thermogravimetric Analysis (Setaram SETSYS Model) were used in order to identify the effect of depolymerisation method at fibre scale. An MTS Criterion C45.105

tensile machine equipped with a 100 kN load cell was used to measure in-plane tensile properties of virgin (vCF/vElium), semi recycled (rCF/vElium) and totally recycled (rCF/rElium) composites. In addition, a Zwick-Roell testing machine (model Z010/TH, 1 mm/minute on load cell of 10 kN and an accuracy of 0.1 N) was used to monitor the quality of fibre/matrix bonding by mean of failure resistance calculations and failure modes identification related to the short-beam test according to ASTM D2344 / D2344 M standard. Finally, Dynamic Mechanical Analysis were conducted in Double Cantilever mode according to ASTM D5418–15 standard on a METRAVIB DMA50 machine (5 Hz frequency, 10 µm dynamic strain amplitude, temperature range from 40 to 160 °C, heating rate of 3 °C/min). The storage modulus, loss modulus and loss factor data were directly collected from testing machine and glass transition temperature were reported from tan delta curve peak.

3. Results

3.1 Analysis at fibre scale

SEM observations on fibre surface showed a smooth surface of virgin fibres compared to recycled fibres where a residual polymer layer was observed as shown in Figure 2.b. This residual polymer is a local phenomenon as it is not coating the whole fibre surface. Figure 2.c and Figure 2.d present an example of fibre diameter calculations. Measurements performed on around 30 different vCF and rCF showed a similar distribution but a difference in mean diameter of around 600 nm as shown in Table 2.

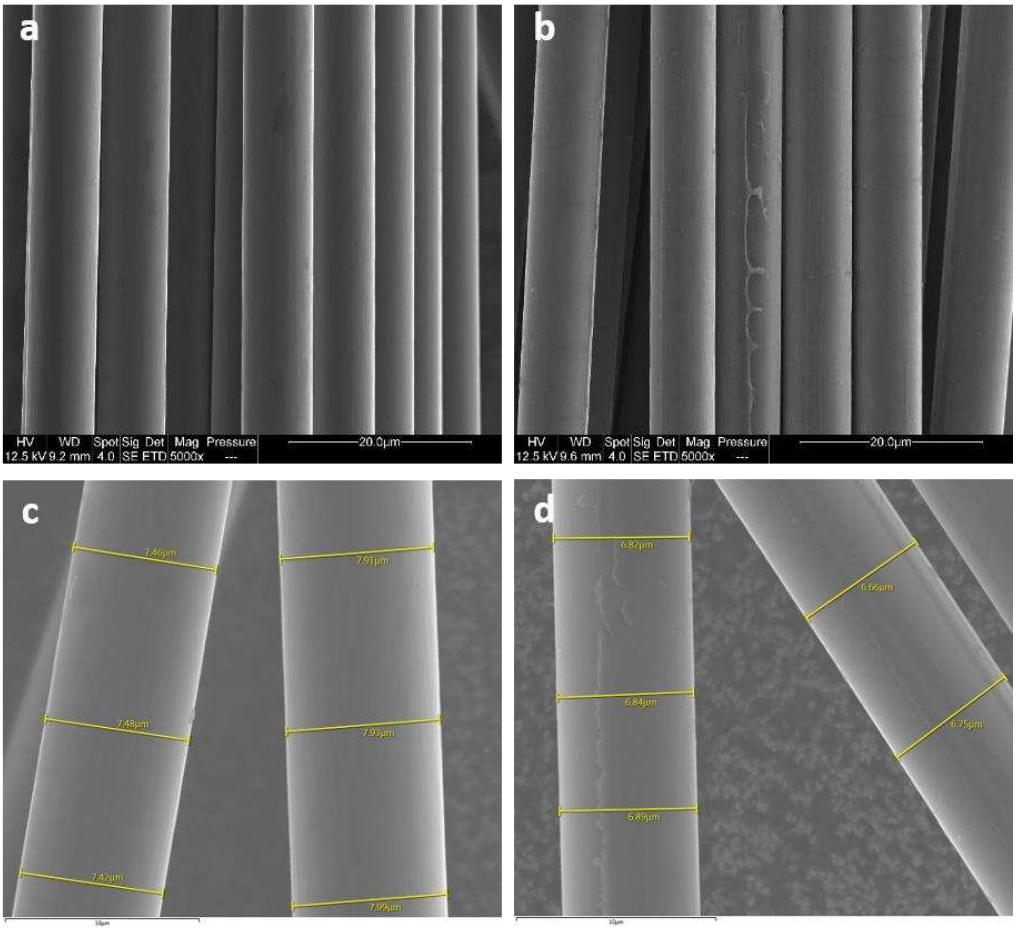

Figure 2: SEM images of virgin (a and c) and recovered (b and d) carbon fibre

  doi:10.5075/epfl-298799_978-2-9701614-0-0

Table 2: rCF and vCF diameter measurements

Fibre	vCF	rCF
Diameter [µm]	7.48 (0.23)	6.90 (0.29)

Thermogravimetric analysis on virgin and recovered fibres showed a major difference in the 220~400 °C temperature range as virgin fibres have lost around 1% of their initial weight as shown in Figure 3.a. This weight change may be related to the fact that, when depolymerised, carbon fibres have lost the polymer-based sizing layer already present on fibre surface. The derivative TG curves (Figure 3.b) showed a pic of depolymerisation at around 345 °C. In addition, an acceleration of weight loss rate can be observed starting from around 620 °C indicating the damage of fibres.

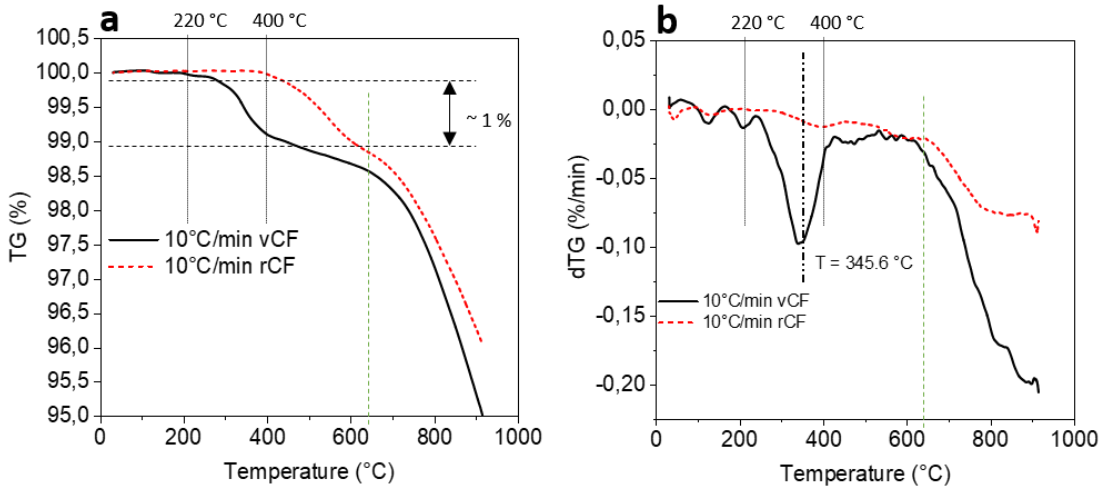

Figure 3 : Thermogravimetric analysis (TG) and derivative thermogravimetric analysis (dTG) of vCF and rCF at 10°C/min under nitrogen atmosphere

3.2. Analysis at composite scale

To assess the mechanical properties of semi- and fully recycled composites in comparison to virgin material, composite plates were manufactured by VARI method like reference material using rCF and rElium resin.

Table 3: Calculated constituent volume fractions of virgin, semi- and fully recycled composite laminates.

Properties	Fibre volume fraction v_f [%]	Matrix volume fraction v_m [%]	Void volume fraction v_v [%]	Fibre weight fraction [%]	Fibre areal weight [g/m²]	Density [g/cm³]
vCF/vElium	61.9 (0.53)	36.6 (0.51)	1.5 (0.02)	70.9 (0.39)	640.5 (2.66)	1.53
rCF/vElium	54.8 (1.1)	43.6 (1.27)	1.6 (0.16)	66.4 (1.14)	631.4 (4.89)	1.49
rCF/rElium	55.4 (1.12)	42.9 (1.9)	1.7 (0.77)	67.1 (0.38)	628.2 (1.08)	1.50

After optimisation of the infusion method for round shaped fabric, the fibre volume fraction of semi-and fully recycled composites was measured and compared to virgin composites. Results are presented in Table 3 and standard deviations are given between parentheses. It can be noted that laminates with rCF presents higher matrix volume fractions compared to reference material. Subsequently, the difference can be observed on fibre volume fraction, which decreased from around 62% to 55%. This difference is mainly related to the total degradation of PET stitching fibre after depolymerisation, which led to more free volume between carbon fibre tows.

Mechanical tensile tests performed on 125×12.5×2.5 mm^3 samples from virgin, semi-recycled and fully recycled composites in longitudinal direction (at 0/90°) showed a similar elastic and brittle behaviour. In addition, regarding tensile modulus and ultimate stress and strain, the decrease is statistically slight and within the standard deviation range (Figure 4). As load direction and fibre direction are superimposed, the results are known to be fibre-dependant. Therefore, an evidence can be obtained about the good quality of rCF by pyrolysis method.

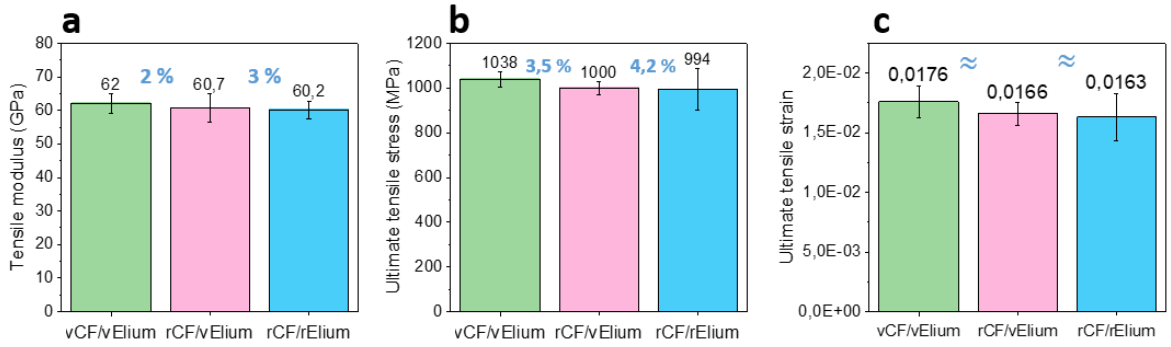

Figure 4 : Tensile elastic modulus (a), ultimate tensile stress (b) and strain (c) obtained by longitudinal tensile tests on virgin, semi-recycled and fully recycled composites

Furthermore, short beam bending tests performed on 5 mm thick samples showed significant differences in interlaminar shear strength between virgin and recycled composites as can be seen in Figure 5.

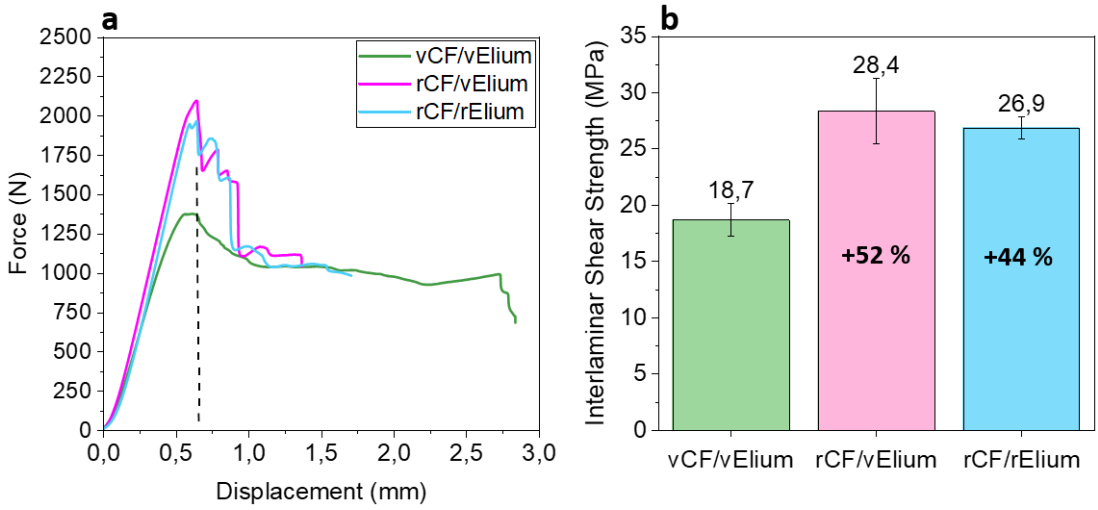

Figure 5: a) Load-displacement curves and b) Interlaminar shear strength of virgin, semi-recycled and fully recycled composites

However, load displacement curves of virgin fibres reinforced composites show a continuous drop after reaching the maximum force that may be related to a plastic deformation and an initially limited fibre/matrix bonding. On the other hand, semi- and fully recycled composites have undergone an interlaminar failure with sharp and instantaneous drop in force-displacement curve. These differences are directly reflected in the calculation of the interlaminar shear strength as they present values 50% higher than virgin material (Figure 5.b)

The glass transition temperature of virgin and recycled Elium© resin was measured from the loss factor (tan δ) peak and results are presented in Figure 6.a. A slight difference of around 3.5 °C can be noticed between virgin and recycled neat Elium© resins. These findings lead to admit the hypothesis of the good properties of recovered Elium© resin as no significant difference was recorded compared to virgin resin. Concerning the composites, a significant difference of around 10 °C is found between virgin and rCF based composites as illustrated in Figure 6.b. Furthermore, it was observed that the virgin material showed a higher damping peak and a 10°C shift in the onset of the tan δ peak. As the loss factor is defined by the ratio of the loss modulus to the storage modulus, a higher peak corresponds to greater molecular mobility through temperature effect. As the same virgin Elium© resin was used for both the reference and the semi-recycled composite (rCF/vElium), the difference may therefore be due to different polymerisation conditions in the absence of sizing of the polymer to the fibre surface resulting in a better fibre/matrix bond. These differences in loss factor curves confirm previous results on the drop of ILSS of virgin composites. In fact, in the absence of a good fibre/matrix bonding, the matrix exhibits a plastic deformation that explains the continuous drop in force-displacement curves related to ILSS tests.

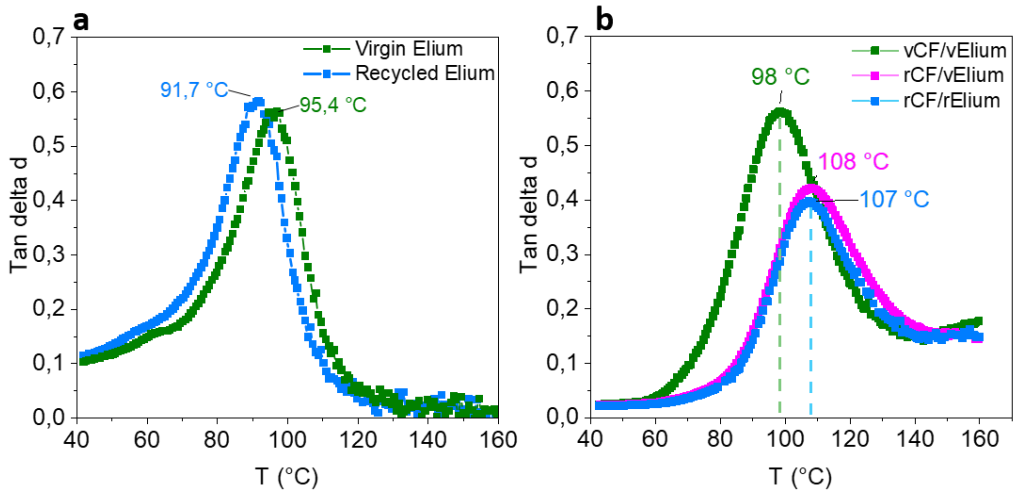

Figure 6 : DMA tan delta curves as a function of temperature of a) virgin vs recycled Elium© resin and b) virgin vs semi- and fully recycled composites

4. Conclusions

This study was carried out with the aim of developing an initial proof-of-concept of the recyclability of a carbon fibre reinforced Elium© composite using the pyrolysis method. The resin-infused composite was depolymerized at a temperature range of 350-450 ◦C. The solid residue from the pyrolysis method containing carbon fibres was about 72%, while the condensed gas fraction was about 26%, from which a purified monomer solution was used to

formulate the recycled Elium© matrix. TGA on the recycled fibres showed degradation of the sizing, which was approximately 300 nm thick. The recovered carbon fibres with the recycled matrix were used to remanufacture good quality semi- and fully recycled composites by resin infusion with a fibre volume fraction of about 55%. The mechanical tensile properties were sufficiently conserved compared to the reference material. The same trend was found by dynamic mechanical analysis, with clear similarities between the virgin and recycled Elium© resin. Interlaminar shear analysis showed significantly higher interfacial strength than the reference material. This is the first time that this approach is proposed for a complete valorisation of good quality recovered carbon fibre and Elium© monomer from a reference material used in marine environment.

Acknowledgements

Authors would like to acknowledge the financial support from Occitanie region in France and REV inside, France as project partner.

5. References

1. Oliveux G, Dandy LO, Leeke GA. Current status of recycling of fibre reinforced polymers: Review of technologies, reuse and resulting properties. Prog Mater Sci. 2015;72:61–99.

2. Bel Haj Frej H, Léger R, Perrin D, Ienny P. A Novel Thermoplastic Composite for Marine Applications: Comparison of the Effects of Aging on Mechanical Properties and Diffusion Mechanisms. Appl Compos Mater [Internet]. 2021 Aug 16;28(4):899–922. Available from: https://link.springer.com/10.1007/s10443-021-09903-0

3. Davies P, Le Gac P-Y, Le Gall M. Influence of Sea Water Aging on the Mechanical Behaviour of Acrylic Matrix Composites. Appl Compos Mater. 2017 Feb 26;24(1):97–111.

4. Bel Haj Frej H, Léger R, Perrin D, Ienny P, Gérard P, Devaux J-F. Recovery and reuse of carbon fibre and acrylic resin from thermoplastic composites used in marine application. Resour Conserv Recycl. 2021;173(December 2020):105705.

NEW WAYS TO RECYCLE COMPOSITES AND BIOCOMPOSITES FROM WINDBLADES AND AIRPLANES (EROS AND ELIOT PROJECT)

Nora Lardiés-Miazza[a], Andrés Luengo[a], Rajesh Mehta[b]

a: AIMPLAS – nlardies@aimplas.es
b: TNO

Abstract: *The results of two ongoing projects related to the recycling of composites and biocomposites are presented. The first one is the ELIOT project which studies until pilot plant level the best end-of-life (EoL) route for biocomposites and the second one is the project EROS, in this project residues from the wind blades (made of glass fiber and polyester resin) and from the aeronautic sector (made of carbon fiber and epoxy resin) are recycled by pyrolysis and solvolysis techniques to obtain powder glass and glycols for the ceramic sector and carbon fiber for the transport sector. Both projects are being coordinated by AIMPLAS (Plastics Technology Centre), ELIOT is a European project in collaboration with the Dutch TNO research center and EROS is a national project with the collaboration of the ITC (Institute of ceramic technology) research center and Spanish companies (Fritta, Keraben, Reciclalia and Sofitec).*

Keywords: Recycling; composites; biocomposites; pyrolysis; solvolysis

1. ELIOT PROJECT

1.1. Introduction

Bio-FRP (fibre-reinforced polymers) that use natural fibres as reinforcement and resins from renewable sources (see Figure 1) are being increasingly used in sectors like aviation, building & construction, sports, home equipment, as they are a key technology to reduce environmental impact thanks to their favourable combination of mechanical properties and low weight (reducing fuel consumption and CO_2 emissions into the atmosphere). However, the widespread use of FRP and bio-FRP has led to waste management difficulties since the polymer matrices are usually thermosetting resins which have a cross-linked molecular structure that pose a challenge to conventional recycling technologies [1]. In fact, despite all the advantages of these biocomposites, no efficient solutions have been found for End-of-Life (EoL) management when they become waste and this is more pronounced in the case of biocomposites, a new material, which, unlike conventional composites, does not contain carbon fibres with a high market value.

The search for new solutions for recovering biocomposites is the goal of the ELIOT project, which reviews current composite recycling technologies to analyse the most feasible alternatives with respect to environmental, economic, resource and technical performance. Next, the most promising candidates are being adapted to the characteristics of biocomposites and tested to scale in the laboratory. Finally, the project is expected to demonstrate technical feasibility at pre-industrial scale, thus full-scale demonstration will be provided for 2 EoL methods for 2 target biocomposites, respectively, including their technical validation at pre-industrial scale and their validation in terms of life-cycle sustainability. These EoL methods will be ready to be further scaled up in industrial environments.

  doi:10.5075/epfl-298799_978-2-9701614-0-0

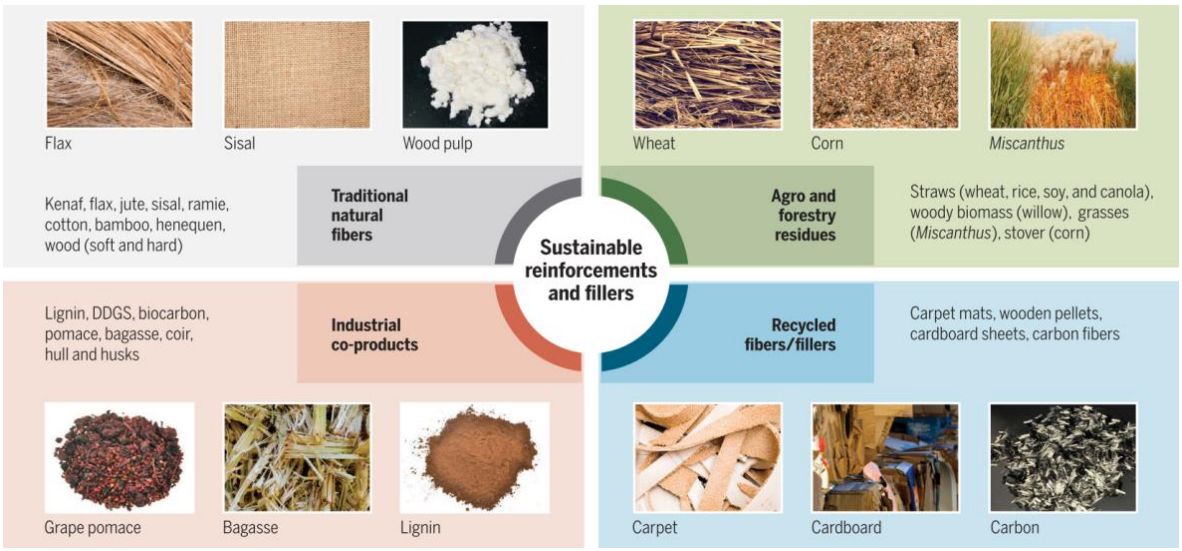

Figure 1. Sustainable reinforcements and fillers that can be used in biocomposites composition [2]

The ELIOT Project is coordinated by AIMPLAS (Plastics Technology Centre) and the project is performed in collaboration with the Dutch research organisation TNO. It has received funding from the European Union's Horizon 2020 research and innovation programme within the framework of the Clean Sky Joint Technology Initiative under grant agreement number 886416.

1.2. Results and discussion

The ELIOT project, which started 01/07/2020 and it will end on 01/03/2023, aims to finally demonstrate 2 EoL methods for 2 target biocomposites. Within the frame of ELIOT project, a deep study has been done regarding the EoL technologies available nowadays in literature and industry for composites and biocomposites (state of the art). Afterwards, the selection of the best EoL technologies have been done following a MCDA (multi-criteria decision analysis) methodology which ranks the EoL technologies.

The conclusions of the state of the art show the key difference between composites and biocomposites recycling technologies: the higher level of maturity for composites. For biocomposites, almost all recycling technologies are either at lab scale or early pilot scale, see Figure 2 as it summarises the TRL of each EoL option for biocomposites. Regarding the circularity potential, where TRL and the quality of products recovered are involved, four technologies seem to have more circularity potential than the others for biocomposites, those are Solvolysis, Dissolution, Mechanical recycling and Pyrolysis.

  doi:10.5075/epfl-298799_978-2-9701614-0-0

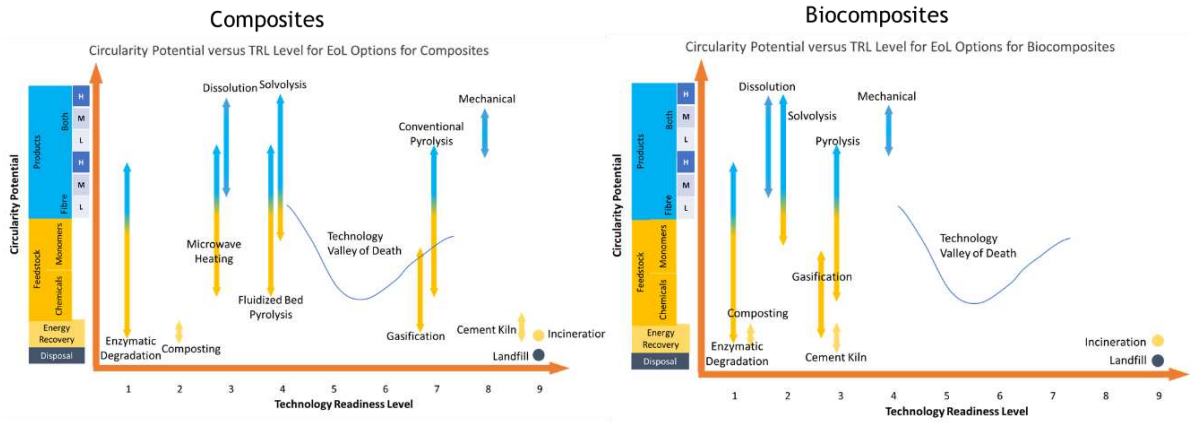

Figure 2. Circularity potential versus TRL level for EoL Options for composites and biocomposites

To enables the project members to select the three/four most optimal EoL methods, the MCDA methodology and tool was built, this tool uses four main aspects or performance categories, agreed with the stakeholders as being most relevant for sustainable EoL technology development:

1. Technical performance
2. Economic performance
3. Resource performance
4. Environmental performance

Once the MCDA tool was clear, each EoL technology was scored for 2 already selected types of bio composites (basalt fibre with bioepoxy resin and flax fibre with bioepoxy resin). The result of the overall scores of the MCDA analysis are summarised in Figure 3 and Figure 4. On average, the basalt fibre-based composites are better than those of the flax-based ones as in thermal processes the flax fibres will be lost due to (partial) incineration, and this lowers the performance. The technical and resource performance tend to have the highest scores for both types of composites.

Composite	EoL technology	Cement kiln	Dissolution	Energy recovery (MSWi)	Enzymatic degradation	Gasification	Mechanical recycling	Pyrolysis, classic	Pyrolysis, fluidised bed	Pyrolysis, microwave	Solvolysis	Average
Basalt twill weave - bio-epoxy	Technical	2.5	2.1	2.3	1.6	2.4	2.3	2.2	1.8	1.6	2.2	2.1
	Economic	1.2	2.2	0.9	0.9	1.3	0.7	1.6	1.5	1.7	1.9	1.4
	Resource	1.6	3	1.6	2.2	2.3	2.8	2.4	2.6	2.6	2.6	2.4
	Environmental	1.5	2.7	1.7	2	2	2.3	2	2	2.1	2.4	2.1
	Overall	**1.7**	**2.5**	**1.6**	**1.7**	**2**	**2**	**2.1**	**2**	**2**	**2.3**	**2.0**
Flax tape - bio-epoxy	Technical	2.1	2.2	2.3	1.3	2.1	2.3	2	1.3	1.1	2.2	1.9
	Economic	1.2	2.2	0.9	1	0.9	0.7	1.3	1.5	1.2	1.9	1.3
	Resource	1.6	3	1.6	2.2	1.3	2.8	1.4	1.5	1.5	2.4	1.9
	Environmental	1.5	2.7	1.7	2	1.6	2.3	1.4	1.4	1.4	2.3	1.8
	Overall	**1.6**	**2.5**	1.6	**1.6**	**1.5**	**2**	**1.5**	**1.4**	**1.3**	**2.2**	**1.7**

Figure 3. MCDA results per aspect and the overall score for the biocomposites selected per end-of-life technology. A greener colour indicates a higher score. Overall scores with an orange border have a ten percent above average score

The economic performance tends to show the lowest scores. The best overall performance is seen for the following top four combinations:

1. Dissolution of basalt twill weave and bio-epoxy (score 2.5)
2. Dissolution of flax tape and bio-epoxy (2.5)
3. Solvolysis of basalt twill weave and bio-epoxy (2.3)
4. Solvolysis of flax tape and bio-epoxy (2.2)

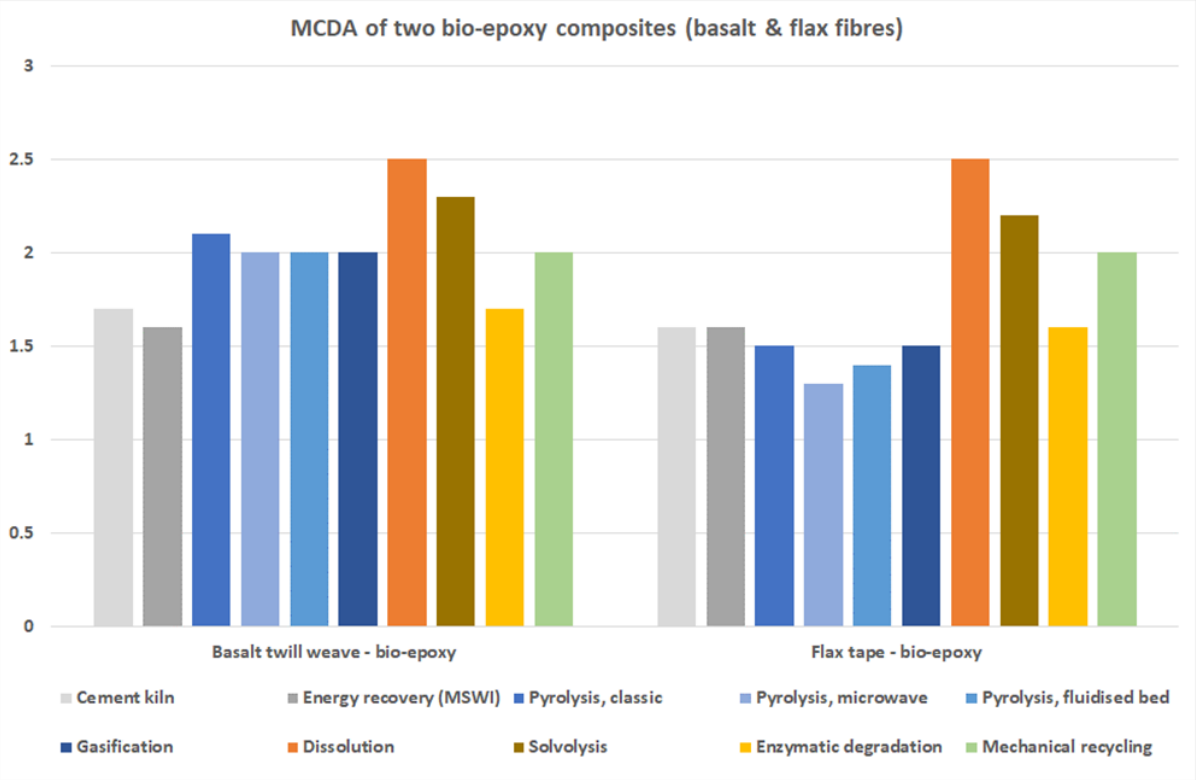

Figure 4. MCDA overall results for composites made of basalt twill weave and bio-epoxy and flax tape and bio-epoxy per EoL technology

For the flax-based composite the thermal processes like pyrolysis and gasification have a lesser performance than energy recovery in the cement kiln and municipal waste incinerator (MSWI). In case of the basalt fibres these thermal processes score better as the basalt fibre can be retrieved. Mechanical recycling has an intermediate performance.

The following table shows the best results of the two types of fibres separately with the aim of selecting the best EoL techniques:

Table 1. MCDA results of the best EoL technologies for the two selected bio-PRFs

Basalt/bioepoxy	Flax/bioepoxy
1. Dissolution (2,5)	1. Dissolution (2,5)
2. Solvolysis (2,3)	2. Solvolysis (2,2)
3. Classic pyrolysis (2,1)	3. Mechanical recycling (2)
4. Mechanical recycling (2)	4. Cement klint and enzymatic degradation (1,6)
	5. Classic pyrolysis (1,5)

1.3. Conclusions

The initial objective of the ELIOT project was to select the 3 or 4 best EoL technologies to be tested at laboratory scale. Based on the results of the MCDA and the information obtained from the project review, the following recycling technologies were selected:

1. Dissolution
2. Solvolysis
3. Mechanical recycling
4. Conventional pyrolysis

At the time of writing this paper, the four selected recycling technologies are being tested at laboratory level, together with LCA (Life Cycle Assessment) data collection, for the following bio-PRFs:

- ✓ Flax fibre with bioepoxy matrix.
- ✓ Basalt fibre with polyfurfuryl alcohol matrix (PFA)
- ✓ Carbon fibre with bioepoxy matrix

Laboratory testing will be completed in May 2022, and the next step will be to select the two best technologies to be tested at pilot plant level together with full techno-economic analysis and LCA.

2. EROS PROJECT

2.1. Introduction

The EROS Project is focused on the recycling of composites from the aeronautic and the wind energy sector. The residues coming from these sources are made of an epoxy resin reinforced with carbon fibers when they come from the aeronautic sector, while the wind blades residues are mainly composed of an unsaturated polyester resin reinforced with glass fibers. The project proposes a combination of pyrolysis and solvolysis of these residues with the aim of obtaining carbon fibers for its reintroduction in the aircraft sector replacing virgin carbon fibers, and glass fibers for its utilization in the ceramic sector to replace feldspars, employed as flux. Additionally, the solvolysis products of the glass fiber reinforced polymers (GFRP), are thought to replace solvents in the production of inks for the ceramic sector.

2.2. Description of work

Two approaches have been developed for the depolymerization of the unsaturated resin. The recycling by pyrolysis has been subjected in a 5L batch reactor, without the employ of catalysts. In collaboration with the industrial partner Reciclalia, different temperatures and reaction times ranging from 450ºC to 550ºC and 30 to 60 min respectively were tested. Once completed the pyrolysis reaction, the recovered fibers were coated by a layer of char, a byproduct obtained from the decomposition of the polymer. To remove this char and obtain clean fibers, they were submitted to an additional step of oxidation, trying different times and temperatures, ranging from 450ºC to 600ºC and 30 to 60 min respectively (Table 2). The total organic content of the

glass fibers measured for the best conditions was 0.058% in mass, pointing out the efficient removal of the char over these fibers. In the case of the carbon fibers, a thermogravimetric analysis showed a 95% removal of the residual organic matter over the fibers.

Table 2. Summary of tested conditions and best results

Material	Pyrolysis	Oxidation	Estimated yield	Residual organic matter
GFRP	450-550ºC	450-550ºC	**91%**	0.058%
CFRP	500-600ºC	500-600ºC	**80%**	5%

The recovered fibers were analyzed by Scanning Electron Microscopy to determine their morphology and integrity. Concerning the glass fibers (Figure 5), it was found that the oxidation at low temperatures could not remove completely the organic residue over the fibers while the oxidation at high temperatures started to damage them. Although the mechanical properties and thus the integrity of the glass fibers was not an essential factor for the final application, it was concluded that the oxidation at 550ºC was good enough for cleaning the fibers without damaging them.

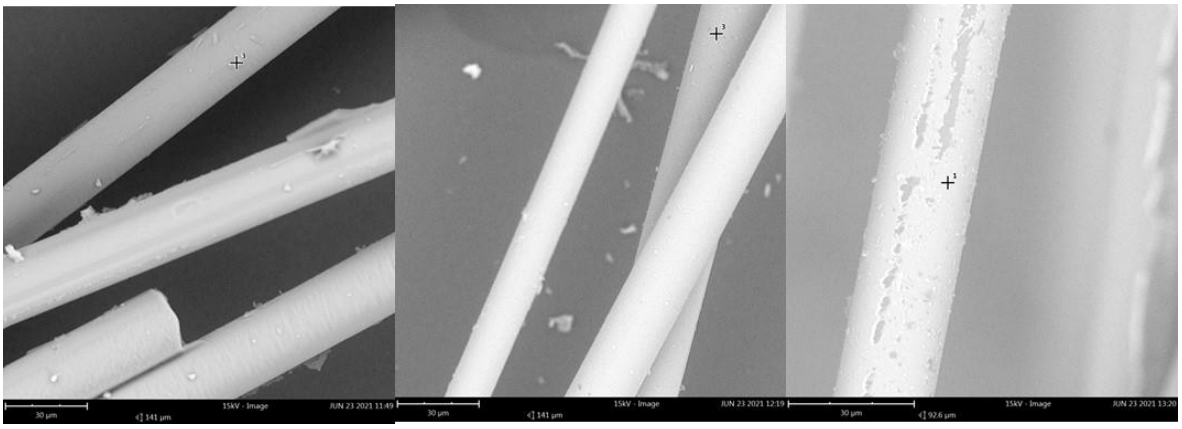

Figure 5. SEM images of the glass fibers after oxidation at 500ºC (left), 550ºC (centre), 600ºC (right).

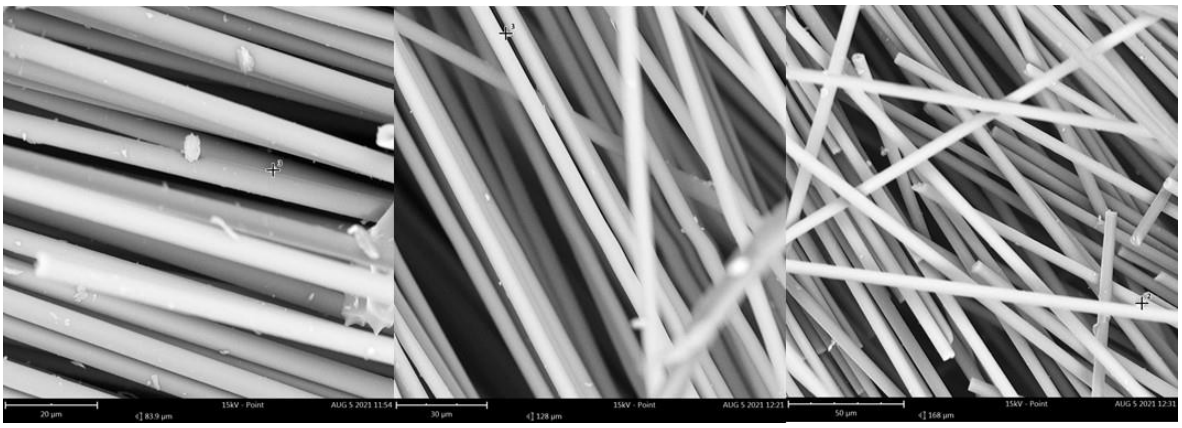

Figure 6. SEM images of the carbon fibers after oxidation at 450ºC (left), 500ºC (centre), 550ºC (right).

In the case of the carbon fibers (Figure 6), SEM analysis showed that oxidation at 500ºC and 550ºC produced similar results, therefore the lower temperature was selected to design the less energy demanding process with the maximum conservation of the mechanical properties of the fibers.

The second approach for the recovery of clean fibers from the starting composites consisted of the depolymerization of the unsaturated resins by solvolysis. A wide range of sub and supercritical conditions were employed, observing the best results with a glycolysis step of long reaction times and high temperatures for the GFRP, while in the case of the CFRP, the conditions implied an alcoholysis reaction under supercritical conditions. (Table 3).

Table 3. Best results observed in solvolysis tests

Material	Reagents	Conditions	Estimated yield
GFRP	HAc/$AlCl_3$[3]	Subcritical conditions	**60%**
GFRP	$Zn(OAc)_2$, EG	Subcritical conditions	**27%**
GFRP	PEG200, NaOH	Subcritical conditions	**67%**
GFRP	HAc/H_2O_2[4]	Subcritical conditions	**44%**
GFRP	EtOH, KOH	Subcritical conditions	**33%**
GFRP	Acetone/H_2O, KOH	Supercritical conditions	**40%**
GFRP	1) EG, 2) H_2O, 1-propanol, KOH[5]	Supercritical conditions	**71%**
GFRP	EG	Subcritical conditions	**80%**
CFRP	HAc/H_2O_2[4]	Subcritical conditions	**64%**
CFRP	PEG200, NaOH[6]	Subcritical conditions	**64%**
CFRP	PEG200, H_2O, NaOH	Subcritical conditions	**28%**
CFRP	1) HAc, 2) $KMnO_4$	Subcritical conditions	**28%**
CFRP	H_2O/Acetone[7]	Supercritical conditions	**62%**
CFRP	Phenol, KOH, H_2O	Supercritical conditions	**66%**
CFRP	1-propanol, KOH[8]	Supercritical conditions	**88%**

2.3. Conclusions

Two methods of chemical recycling have been evaluated for the recovery of the fibers contained in the composites. Pyrolysis has shown to be an effective method yielding very clean fibers after an oxidation step, while solvolysis was only successful under the use of long reaction times or supercritical conditions. Preliminary analysis by SEM and TGA show very similar properties of the recovered fibers by both methods, while the final comparison will be achieved by the manufacture of the proposed demonstrators.

References

1 Pickering SJ. Recycling technologies for thermoset composite materials-current status. Compos Part A Appl Sci Manuf. 2006;37(8):1206-1215.

2 Mohanty AK, Vivekanandhan S, Pin JM, Misra M. Composites from renewable and sustainable resources: Challenges and innovations. Science (80-). 2018;362(6414):536-542.

3 Wang Y, Cui X, Yang Q, Deng T, Wang Y, Yang Y, Jia S, Qin Z, Hou X. Chemical recycling of unsaturated polyester resin and its composites via selective cleavage of the ester bond. Green Chemistry 2015; 17, 4527-4532.

4 Das M, Chacko R, Varughese S. An Efficient Method of Recycling of CFRP Waste Using Peracetic Acid. ACS Sustainable Chemistry & Engineering 2018; 6: 1564-1571.

5 Mattsson C, André A, Juntikka M, Tränkle T, Sott R. Chemical recycling of End-of-Life wind turbine blades by solvolysis/HTL. IOP Conference Series: Materials Science and Engineering 2020; 942: 012013.

6 Yang P, Zhou Q, Yuan X-X, van Kasteren J M N, Wang Y-Z. Highly efficient solvolysis of epoxy resin using poly(ethylene glycol)/NaOH systems. Polymer Degradation and Stability 2012; 97:1101-1106.

7 Keith M J, Oliveux G, Leeke G A. Optimisation of solvolysis for recycling carbon fibre reinforced composites. 17th European Conference on Composite Materials.

8 Piñero-Hernanz R, García-Serna J, Dodds C, Hyde J, Poliakoff M, Cocero M J, Kingman S, Pickering S, Lester E. The Journal of Supercritical Fluids 2008; 46: 83-92.

THE USED SURGICAL MASKS: FROM WASTE TO RESOURCE

Sithiprumnea Dul, Luca Fambri, Alessandro Pegoretti

University of Trento, Department of Industrial Engineering and INSTM Research Unit, Via Sommarive 9, 38123 Trento, Italy – luca.fambri@unitn.it

Abstract: *The general focus of research is the development of recycling protocols for disposable surgical masks into new raw materials for different possible applications. Separation of various constituent materials was performed by manual procedure or by water floating. The potentially targeted end applications are thin film and glass fibre composites. Polypropylene thin-films with a thickness of 100 micron were produced by compounding the face mask polymer with different content of a virgin PP, in the range 20-80 wt%. Face mask polypropylene (FM-PP) composites containing glass fibre of 15 wt% and 30 wt% were also prepared, evidencing an improvement of stiffness and strength, furtherly increased in presence of coupling agent.*

Keywords: Recycling; surgical face mask; Covid pandemic; polypropylene.

1. Introduction

Due to the Covid 19 pandemic, personal protective equipment such as face masks has become mandatory for all citizens in many places worldwide. Disposable surgical masks are mainly composed of a non-woven polypropylene (PP) filtering medium, and their widespread global use, in the long run, will cause a massive environmental impact, documented from many researchers [1-3]. Recycling plastic materials is becoming increasingly important because of the amount of plastic waste accumulating in the planet's oceans and soils and of the growing global production and demand for plastic materials, especially polyethylene (PE) and polypropylene (PP) [4]. In particular, PP is the more widely used polyolefin with a total amount close to about 10 Mt (a share of about 20%). The global adoption of disposable surgical masks as protective equipment against COVID-19 created another large source of PP waste, with potential formation and release of microplastics in both terrestrial marine ecosystems [5-7]. Various approaches have been studied in order to evaluate the post-user applications of plastic face mask (FM), such as mechanical recycling [8], thermo-chemical valorization [9] or concrete addition [10-11].

This work aims at establishing a practical approach to recycle plastic waste from surgical masks, with a specific focus on PP. Constituent materials of disposable face mask were identified through morphological, chemical, physical, and thermal analyses. In particular, a thermo-mechanical recycling protocol consisting of melt compounding and compression moulding was adopted and selected for composite preparation.

2. Experimental. Materials, processing and characterization.

2.1 Face Mask

Common plastic Face Masks were selected from Medical Device Branch of Zhangzhou Easepal Industrial Co (code D30014AB00-EU-R). Various batches produced in November 2020 were

  doi:10.5075/epfl-298799_978-2-9701614-0-0

studied. The weight of a single mask was 3.17 ± 0.02 g, as average of ten specimens. Masks were separated in various constituent in order to identify the materials and their relative percentage. The results are shown in Figure 1 and summarized in Table 1.

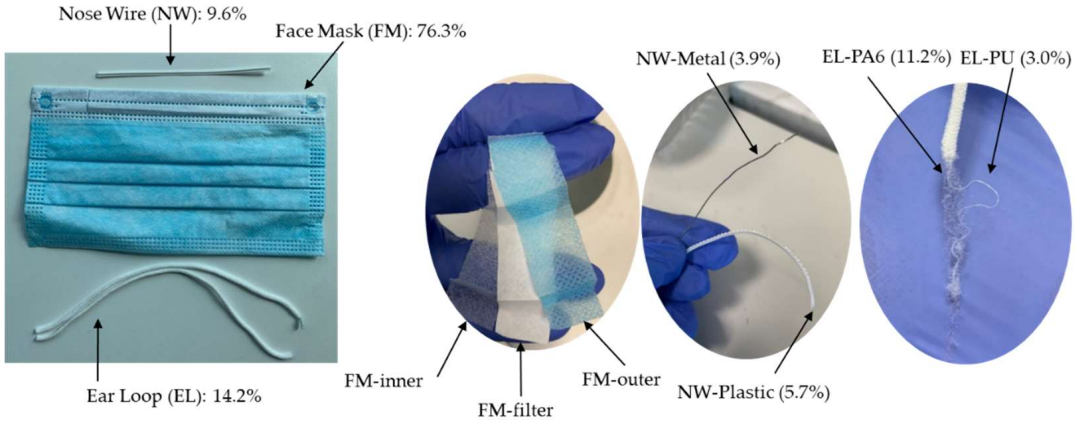

Figure 1. Separation of the main components of Face Mask.

The main component of the Face Mask is constituted by three polypropylene woven non woven layers; a couple of elastomeric ear loop (EL) and a rigid nose wire (NW). Polymeric materials were identified by FTIR and DSC analysis. Density results were also obtained.

Table 1: Analysis of constituents. Code, material, percentage and density.

Component	ID code	Material	composition [%]	density [g/cm^3]
Face Mask	FM	Polypropylene	76.3	0.879 ± 0.011
Ear Loop	EL-PA	Polyamide 6	11.2	1.110 ± 0.009
Ear Loop	EL-PU	Polyurethane	3.0	---
Nose Wire	NW-M	Metal	3.9	7.60 ± 0.30
Nose Wire	NW-P	Plastic	5.7	1.288 ± 0.012

2.2 Characterization

Fourier transform infrared (FTIR) spectra were recorded by a Spectrum One spectrometer (Perkin Elmer ATR-FTIR) in a wavenumber range from 4000 to 650 cm-1.

Morphology of particles and fracture surface of materials and composites was studied by using a Carl Zeiss AG Supra 40 field emission scanning electron microscope (FESEM).

Differential Scanning Calorimetry (DSC). Differential scanning calorimetry tests were performed by a Mettler DSC 30 calorimeter on samples with a mass of about 10 mg. A thermal cycle of heating–cooling–heating in the range -50-250 °C at a rate of ± 10 °C/min under a nitrogen flow of 100 mL/min was selected. Melting temperature of PP and PA6 were registered.

Density measurements of nanoparticles were carried out by gas pycnometry technique on a Micromeritics® Accupyc 1330 helium pycnometer (Norcross USA), at a temperature of 23.0°C, using a testing chamber of 10 cm^3 and performing at least 99 measurements.

The melt flow index (MFI) measurements were carried out according to ASTM D 1238 standard (procedure A), through a Kayeness Co. model 4003DE capillary rheometer, at a temperature of 230 °C under an applied load of 2.16 kg on samples with a mass of about 3 g (pre-heat and compaction time of about 5 min).

Uniaxial tensile tests were performed at room temperature on ISO 527 type 1BA specimens by using an Instron® 5969 universal testing machine (Norwood, MA, USA), equipped with a 1 kN load cell. Test specimens were die-cut from compression moulded plates (gauge length of 30 mm; width of 5 mm; thickness of 2.0 mm). Elastic modulus was determined at a crosshead speed of 0.25 mm/min with the secant method between strain levels of 0.05% and 0.25% according to ISO 527 standard and by using an electrical extensometer Instron® Model 2620-601 (Norwood, MA, USA) with a gauge length of 12.5 mm for strain monitoring. Yield stress, stress at break and strain at break, were evaluated at a crosshead speed of 1 mm/min without an extensometer.

2.3 Separation methods

In order to remove the metallic nose wire, face masks constituent materials were separated by floating in water separation methods. The face mask were grinded by a Piovan grinder Model RN 166, then soaked into the water with magnetic stirring for 20 min and then stabilized for 1 hour. Due to the low density of polypropylene, the main polymeric component of the face mask could be drained on the surface of the water. The wet materials were dried in the oven at a temperature of 90 °C for 40 hours until the mass of materials remained constants for the last 8 hours. For comparison recycled PP was also prepared after manual separation

2.2 Material processing

Melt compounding (MC). Face masks were melted compounded by a Thermo-Haake Polylab Rheomix counter-rotating internal mixer at 200 °C and 230 °C, rotor speed 60 rpm for 10 min. The batches of about 50 g were processed for each composition of both manual and water separation.

Compression Molding (CM). Dried pieces were compression moulded using a Carver Laboratory press (Carver, Inc., Wabash, IN, USA) at 200 °C for 10 min under a load of 10 tons. Square plates (100 × 100 × 2 mm) were produced.

3. Results and discussion

3.1 Comparison of properties of recycled PP

The properties of recycled PP obtained from grinded face masks and separated by manual procedure and by floating water procedure were compared. Some minor remaining contaminations of other polymers (PA6 and PU) were found after water separation, as documented in Table 2, and they directly affected the melt flow, mechanical properties and density. A summary of morphological and mechanical results is also shown in Figure 2.

Table 2: Comparative properties of face masks after manual (M) or water (WS) separation and melt compounding (MC) at different temperature.

Sample	Melt Flow [g/10min]	Tensile Modulus [MPa]	Stress at break [MPa]	Elongation at break [%]	Density [g/cm^3]
M_MC200	54 ± 7	1550 ± 63	20.2 ± 1.3	4.9 ± 0.9	0.905 ± 0.002
M_MC230	78 ± 10	1565 ± 50	18.6 ± 1.2	3.6 ± 0.4	0.907 ± 0.003
WS_MC200	22 ± 1	1490 ± 82	13.0 ± 1.0	2.6 ± 0.4	0.930 ± 0.007
WS_MC230	44 ± 1	1554 ± 67	18.3 ± 0.4	5.4 ± 0.4	0.944 ± 0.001

Figure 2. Polypropylene from recycled face mask by manual (left) and water separation (right)

3.2 Blending of recycled Face Mask PP and virgin PP.

Polypropylene from recycled face mask after water separation was melt compounded with virgin polypropylene (trade name: Atofina PPH 7089) by a Thermo-Haake Polylab Rheomix counter-rotating internal mixer at 230 °C, rotor speed 60 rpm for 10 min. The batches of about 50 g were processed for each composition, and the resulting materials were compression moulded using a Carver Laboratory press (Carver, Inc., Wabash, IN, USA) at 200 °C for 10 min under a load of 10 tons. Square plates (100 × 100 × 2 mm) and thin film (200 × 200 × 0.1-0.15 mm) were produced and compared. The higher the content of recycled PP, the lower the yield stress and the lower the deformation at break,

3.3 Glass Fiber Composite Page numbers and footnotes

Face mask PP was melt compounded with glass fiber (trade name: 248AF Chopped Strands) from Owens Corning by using a Thermo-Haake Polylab Rheomix counter-rotating internal mixer at 230 °C, rotor speed 60 rpm for 10 min. Coupling agent PPgMA (trade name: Compoline CO/PP H60) provided by Auser Polimeri was also used at different content in the range 2-10 wt.% for the preparation of GF composite. The resulting materials were compression moulded at 200 °C

for 10 min under a load of 10 tons by using a Carver Laboratory press (Carver, Inc., Wabash, IN, USA) for the production of square sheets (120 × 120 × 1.0 mm) of FM/GF composites.

Table 3: Tensile properties of glass fiber reinforced polypropylene at different content of PPgMA.

Sample	Tensile Modulus [MPa]	Stress at break [MPa]	Elongation at break [%]
PP	1512 ± 64	32.7 ± 0.6	19.0 ± 1.9
PP-GF15	2513 ± 257	34.5 ± 3.7	3.7 ± 0.5
PP-PPgMA2-GF15	2614 ± 260	41.5 ± 4.1	4.3 ± 0.3
PP-PPgMA5-GF15	2314 ± 176	41.2 ± 2.7	4.7 ± 0.5
PP-PPgMA10-GF15	2759 ± 242	45.6 ± 4.1	4.8 ± 0.4
PP-GF30	3471 ± 204	27.4 ± 3.2	1.7 ± 0.3
PP-PPgMA2-GF30	2913 ± 64	31.3 ± 6.6	1.8 ± 0.3
PP-PPgMA5-GF30	3594 ± 489	42.2 ± 6.1	2.4 ± 0.4
PP-PPgMA10-GF30	3534 ± 664	29.8 ± 1.7	2.0 ± 0.2

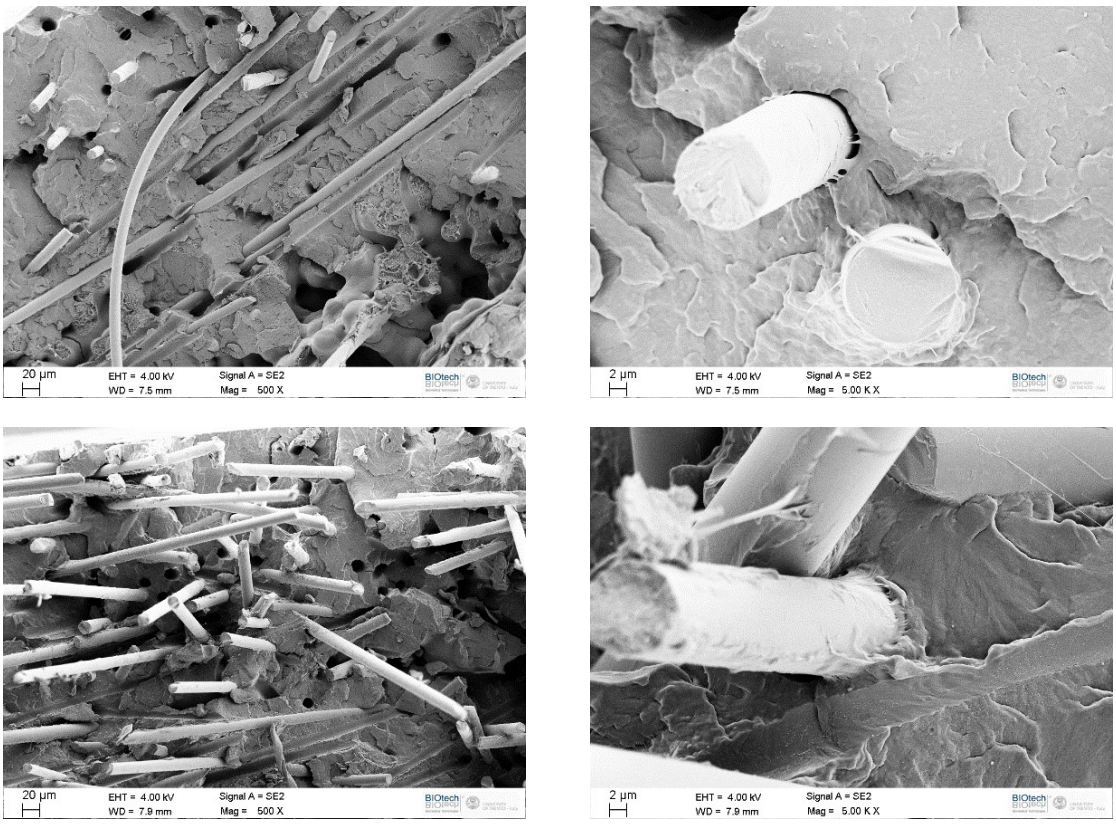

Figure 3. SEM micrographs at different magnifications (500x left; 5000x right) of fracture surface of PP-PPgMA2-GF15 (top) and PP-PPgMA5-GF30 (bottom).

Conclusions

The general focus of research was the development of recycling protocols for disposable surgical masks into new raw materials for different possible applications. Film and glass fiber reinforced composite were successfully produced from recycled PP derived from grinded masks and water separation. In this work, the validation of recycling approaches was performed using only new disposable face masks due to biological hazards in handling used masks that were not professionally disinfected. In practice, the collection of masks after use and their disinfection will be implemented by municipalities. Future developed processes will have to ensure compatibility with potential alteration of materials during their use and disinfection process, and to confirm the post-user recycling and reprocessing for both film and composites production.

Acknowledgements

The authors thank the University of Trento for funding this research through the *REMASK* project.

4. References

1. Sangkham, Face mask and medical waste disposal during the novel COVID-19 pandemic in Asia. Case Stud. Chem. Environ. Eng. 2020; 2: 100052.
2. Torres FG, De-la-Torre GE. Face mask waste generation and management during the COVID-19 pandemic: An overview and the Peruvian case. Science of the Total Environment 2021; 786: 147628.
3. Tesfaldet YT, Ndeh NT. Assessing face masks in the environment by means of the DPSIR framework. Science of the Total Environment 2022; 814: 152859.
4. Plastics – the facts 2020, Plastics Europe. 2020.
5. Aragaw TA, Surgical face masks as a potential source for microplastic pollution in the COVID-19 scenario. Mar. Pollut. Bull. 2020; 159: 111517.
6. Saliu F, Veronelli M, Raguso C, Barana D, Galli P, Lasagni M. The release process of microfibers: from surgical face masks into the marine environment. Environmental Advances 2021; 4: 100042.
7. Uheida A, Mejía HG, Abdel-Rehim M, Hamd W, Dutta J. Visible light photocatalytic degradation of polypropylene microplastics in a continuous water flow system. Journal of Hazardous Materials 2021; 406: 124299.
8. Battegazzore D, Cravero, F, Frache, A. Is it possible to mechanical recycle the materials of the disposable filtering masks? Polymers 2020; 12(11): 2726.
9. Jung S, Lee S, Dou X, Kwon EE. Valorization of disposable COVID-19 mask through the thermo-chemical process. Chemical Engineering Journal 2021; 405: 126658.
10. Kilmartin-Lynch S, Saberian M, Li J, Roychand R, Zhang G. Preliminary evaluation of the feasibility of using polypropylene fibres from COVID-19 single-use face masks to improve the mechanical properties of concrete. Journal of Cleaner Production 2021; 296: 126460.
11. Koniorczyk M, Bednarska D, Masek A, Cichosz S. Performance of concrete containing recycled masks used for personal protection during coronavirus pandemic. Construction and Building Materials 2022; 324: 126712.

DYNAMIC MECHANICAL ANALYSIS OF POLYAMIDE 11 (PA11), POLYAMIDE 12 (PA12) AND THEIR RECYCLED LONG CARBON FIBER COMPOSITES

José Antonio, Butenegro[a], Yentl, Swolfs[b], Jan, Ivens[b], Miguel Ángel, Martínez[a], Juana, Abenojar[a,c]

a: Materials Science and Engineering and Chemical Engineering Department, IAAB, Universidad Carlos III Madrid, 28911 Leganés, Spain – jbuteneg@ing.uc3m.es
b: Department of Materials engineering, KU Leuven, 3001 Leuven, Belgium
c: Mechanical Engineering Department, ICAI, Universidad Pontificia Comillas, 28015 Madrid, Spain

Abstract: *The increasing use of carbon fiber and epoxy resin composite materials means an increase in the amount of waste. The main objectives of this research project are to study the manufacturing and characterization by dynamic mechanical analysis (DMA) of recycled long carbon fiber composites with two thermoplastic matrices, polyamide 11 (PA11) and polyamide 12 (PA12) and to compare those composites with the polymers. The results reveal that in the case of PA11 composites, the glass transition temperature (T_g) is unmodified, while in the case of PA12 composites, the T_g is decreased, in both cases compared with the polymers. For both composites, the storage modulus is strictly decreasing just right before the T_g. The results obtained illustrate the viability of the recycling and re-use route to prevent the deterioration of the carbon fibers and, furthermore, the reduction of the environmental impact, because of the use of a thermoplastic matrix.*

Keywords: Recycled carbon fibers; Thermoplastic matrices; Carbon fiber reinforced thermoplastic polymers; Thermal Analysis; Dynamic Mechanical Analysis

1. Introduction

The demand for carbon fiber reinforced polymer (CFRP) composite materials as high-performance, lightweight materials has swiftly increased over the past decade driven by many industries such as aerospace, automotive, defense, wind turbines, construction, marine or leisure [1–5]. The soaring increase in the demand of CFRP is especially due to their high specific strength, high specific stiffness, high fatigue resistance and durability, good corrosion resistance, and low density. Nonetheless, one of the most critical disadvantages of fiber reinforced polymer (FRP) composite materials is the difficulty of recycling these materials. While FRP recycling is not motivated strictly by economic reasons, the objectives of obtaining recycled fibers lie in minimizing the high volume of FRP waste that is expected to exist in the coming years [6].

The need of recycling these materials is aligned with the objectives of circular economy, in order to make manufacturing and recycling processes more efficient while minimizing the waste of CFRP composites at their end-of-life. Strategies for minimizing the environmental impact of composite materials tackle different key points, among which the development of new materials using recycled carbon fibers, natural fibers or bio-based polymers can be highlighted [7]. On the matrix side, thermoplastic matrices are also employed, as opposed to the thermosetting

  doi:10.5075/epfl-298799_978-2-9701614-0-0

matrices that have been commonly used up to now, especially polyester, epoxy and acrylic resins. A trade-off is present in terms of properties, since thermosetting polymer matrices typically have better mechanical properties and exhibit better fiber-matrix adhesion compared to thermoplastic matrices.

Regarding the selection of thermoplastic matrices, two Z-type polyamides, polyamide 11 (PA11) and polyamide 12 (PA12), were chosen. Although PA6 and PA66 account for almost 90% of the polyamide market, PA11 and PA12 also have a significant market share. PA12 is an oil-based thermoplastic polyamide, with outstanding mechanical properties, including tensile strength, impact and fatigue resistance, resistance to aromatic hydrocarbons and low coefficient of friction close to those of PA6 and PA66 [8]. On the other hand, PA11 is a bio-based polyamide obtained from castor oil, a renewable source, thus resulting in a reduced carbon footprint compared to PA12 [9]. Apart from being bio-based, PA11 is experiencing a sharp increase in demand due to several features, including low moisture absorption, high impact and fatigue resistance, and chemical and aging resistance [10]. In addition, both PA11 and PA12 have a relatively low melting temperature (around 40-50 °C below PA 6 and 90-100 °C below PA66), which reduces energy consumption and makes it possible to manufacture composites using natural fibers [11, 12].

A cost-effective solution to reduce environmental impact is the mechanical recycling of carbon fibers, which avoids using the chemicals required for chemical recycling or reduces the high energy inputs required for both chemical and thermal recycling. Furthermore, problems related to the emission of pollutant gases or having to deal with solvents disposal are prevented. Thus, mechanical recycling makes it possible to obtain carbon fibers or composite in the shape of small sticks of different lengths. To preserve the mechanical properties of carbon fibers, the objective is to obtain long fibers, defined as those that retain properties similar to the properties of continuous fibers [13].

The present research project studies the dynamic-mechanical characterization of two polyamides used as matrix in two thermoplastic matrix composites reinforced with mechanically recycled long carbon fibers, as well as the composites manufactured with those polyamides.

2. Materials and methods

2.1. Materials

Pultruded carbon fiber plates used for structural strengthening (Sika CarboDur E 812, Sika, Switzerland) were used, after mechanical recycling, as reinforcement. The plates of 80 mm width and 1.2 mm thickness were mechanically cut and reduced to sticks of 40 mm length and variable width, typically between 1-1.5 mm of maximum transversal dimension. The composite has a fiber volume content higher than 70%, a tensile strength of 2.2 MPa, a tensile modulus of elasticity of 180 GPa and an elongation at break of 1.22 % (mean values given in longitudinal direction of fibers).

Commercial thermoplastic polyamide pellets of polyamide 11 (PA11) and polyamide 12 (PA12) were provided by Arkema (Madrid, Spain).

2.2. Manufacturing of samples

  doi:10.5075/epfl-298799_978-2-9701614-0-0

Polyamide sheets were prepared by means of a hot plate press machine (Fontijne Presses TPB374, Barendrecht, The Netherlands). Polyamide sheets of 280 x 280 x 1.2 (dimensions in mm) were prepared by placing PA pellets inside a steel mold of inner dimensions 280 x 280 (dimensions in mm). The thermal cycle reaches a maximum temperature of 200 °C and a maximum force of 45 kN. The manufacturing process is shown in **Figure 1**.

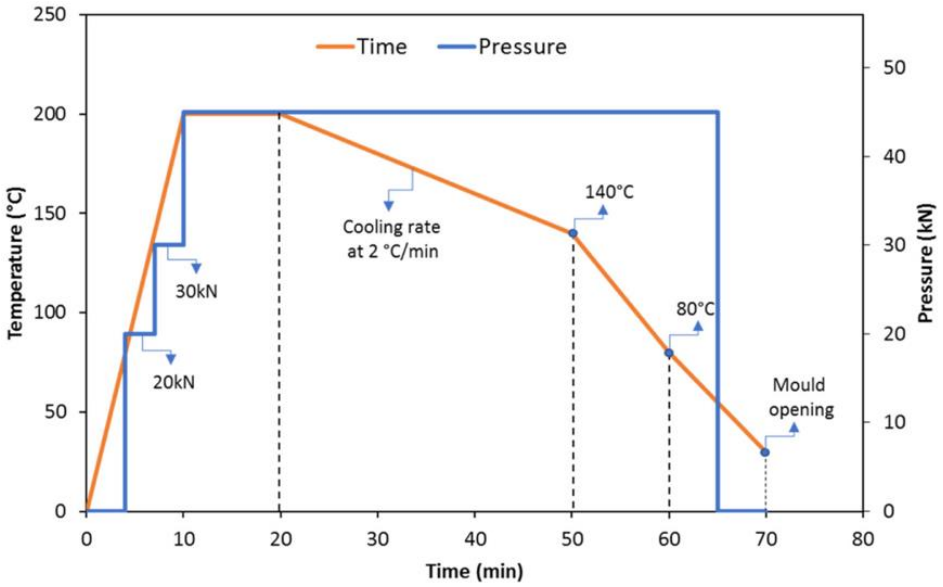

Figure 1. Hot press cycle for the manufacturing of PA and composite samples [14]

After the preparation of the polyamide sheets, a given quantity of composite sticks was placed on each of them, targeting a one-dimensional orientation of the sticks, after which the composite was pressed again, emulating the manufacture of a prepreg.

Depending on the polyamide used as matrix, the thickness of the composites varies between 1.2 and 1.5 mm. Samples for testing were then cut to the desired shape by waterjet.

2.3. Dynamic Mechanical Analysis

Dynamic mechanical analysis (DMA) was carried on a Q800 (TA Instruments, USA) equipment using a dual cantilever setup, with a distance between fixed clamps of 35 mm, and a movable clamp in the center, as showed in **Figure 2**. The procedure for testing followed the standard ASTM D4065 [15] for polymers and ASTM D7028 [16] for composites. In general, but especially regarding composites, and for the sake of better reliability in statistical terms, five specimens were tested for both polymers and composites, more than the two tests indicated in the section 6.1 of the standard ASTM D7028. Likewise, the heating rate was 3 °C/min, lower than that indicated by the said standard in the section 6.3. The standard itself indicates in the *Note 1* the disadvantages of employing a heating rate of 5 °C/min, in the form of lower precision, as well as it advises against reducing this heating rate to lower values, such as 1 °C/min, in which case the precision is higher, but eventually causes specimen drying, therefore inducing significant biases, altering the results.

  doi:10.5075/epfl-298799_978-2-9701614-0-0

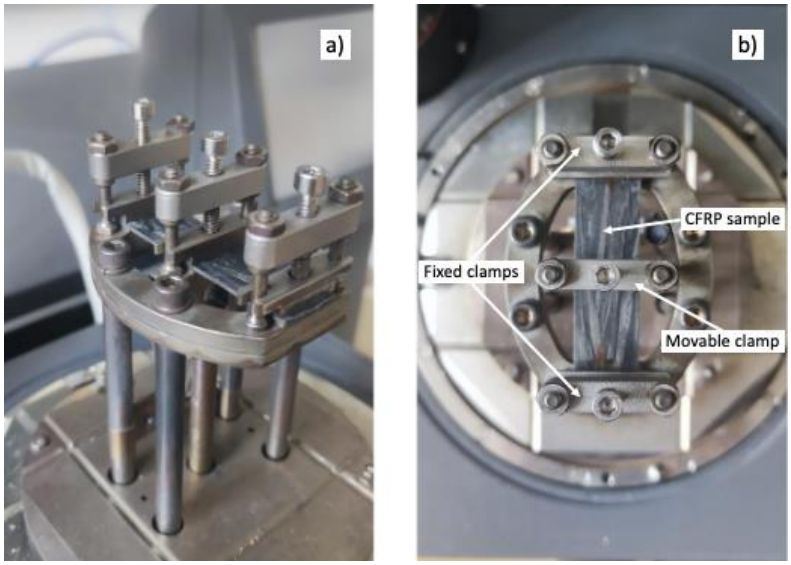

Figure 2. Specimen mounted in the DMA dual cantilever setup. The specimen is a composite made of PA11 and recycled CFRP. **a)** Oblique view, **b)** Upper view

The edges of the samples cut by waterjet were sanded with sandpaper. For polymers, their final dimensions were 50 mm length and 15 mm of width, with a varying thickness of 0.75 ± 0.10 mm. For composites, the same values of 50 x 15 (in mm) were selected as length and width, respectively, with a varying thickness of 1.3 ± 0.15 mm, depending on the polyamide. As stated before, five samples were tested for each polyamide and for each composite. The samples were tested at constant frequency of 1 Hz and at constant amplitude of 40 μm by means of temperature sweeps, equilibrating first at -40 °C, employing liquid nitrogen (N_2) for cooling, and then increasing temperature at a heating rate of 3 °C/min, up to 10 °C below the melting point.

To guarantee statistical reliability, a Grubbs Test was applied with a 95% confidence level to every configuration.

3. Results and discussion

3.1. DMA of polymers

The loss factor, or damping factor, tan (δ), which is the ratio of the loss modulus, E'', to the storage modulus, E', is a measure of damping. The real and imaginary parts of the complex modulus, E*, are the storage and loss moduli, respectively. The loss modulus, denoted by the product of the storage modulus E' and the loss factor, tan (δ), is a figure of merit often used to characterize the damping qualities of materials [17].

Figure 3 shows the loss factor, or damping factor, tan (δ), for both polymers, prepared under the conditions described before. The glass transition temperature, or T_g, can be obtained either by interpreting the plots of the storage modulus, E', the loss modulus, E", or the loss factor, tan (δ), obtaining slightly different values depending on the measure used. In this case, the loss factor is used to obtain the T_g of both polymers. Furthermore, the maximum value in the loss factor is 25% higher in the case of PA11, compared to PA12, indicating the energy absorbed in the peak corresponding to the T_g is higher compared to the energy lost. The last increasing trend

  doi:10.5075/epfl-298799_978-2-9701614-0-0

towards the end of both plots indicate the proximity of the melting point, T_m, as expected. The low peak value corresponding to the T_m could be due to the fact that the amorphous part of these polyamides is quite small.

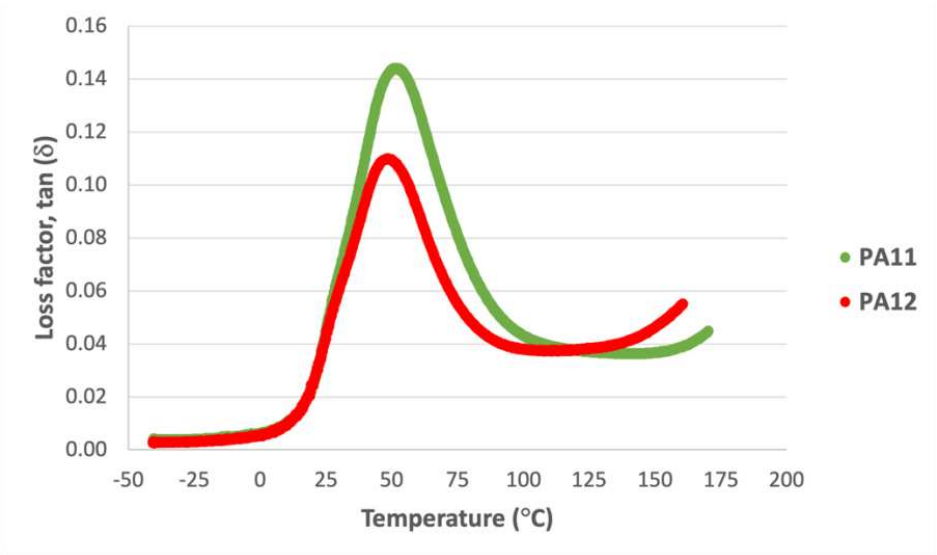

Figure 3. Loss factor as a function of temperature for PA11 polymer (in green) and PA12 polymer (in red)

Bahrami et al. [14] recently characterized both PA11 and PA12 manufactured by hot pressing by means of differential scanning calorimetry (DSC) to examine their thermal properties. The results found in this paper are compared against those obtained by Bahrami et al., since the manufacturing conditions of both papers is identical. Said results are shown in **Table 1**.

Table 1. Glass transition temperature calculated from dynamic mechanical analysis as opposed to calculated by differential scanning calorimetry

Research	Equipment	Heating rate (°C/min)	Glass transition temperature, T_g (°C)	
			PA11	PA12
Actual	DMA	3	51.0 ± 1.7	47.2 ± 1.7
Bahrami et al. [14]	DSC	20	44.5	42.8

As can be expected, the glass transition temperature obtained by DMA is significantly higher than that obtained by DSC, due to the different nature of the experiment and the calculation method. The standard ASTM D7028 [16], employed for testing composites by DMA, states that heat transfer limitations are more significant in DMA than in other thermal analysis techniques, such as DSC or thermomechanical analysis (TMA).

3.2. DMA of recycled composites

The recycled composite samples were manufactured with the CFRP sticks on top of the polyamide sheets during the second pressing cycle. Thus, we can assume there is a higher concentration of sticks in one of the sides of the sample. While the accumulated stress on one

side could compromise the behaviour of a sheet, the samples for DMA are small enough to avoid the problematic derived from this issue.

Error! Reference source not found. exhibits the storage modulus and the loss factor against temperature for the composites. The legend indicates the polyamide used as a matrix in each case.

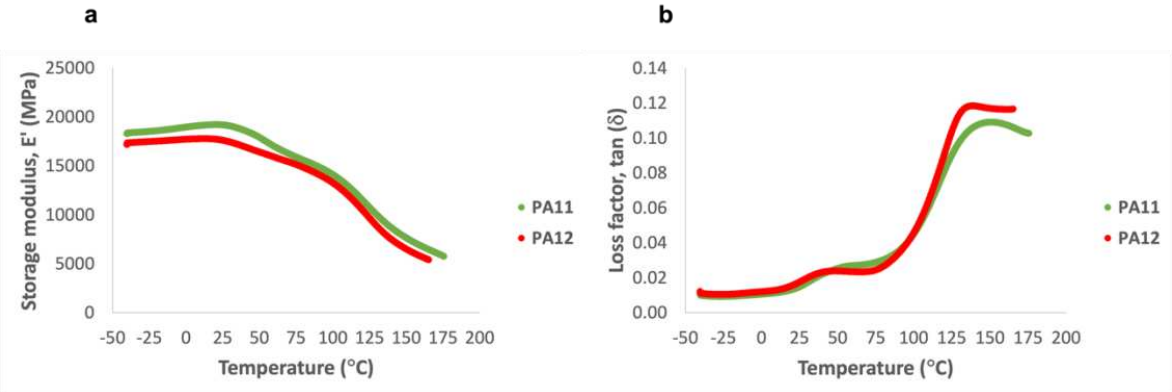

Figure 4. Storage modulus and loss factor as a function of temperature for PA11 composites (in green) and PA12 composites (in red). **a)** Storage modulus, E'. **b)** Loss factor, tan (δ)

As can be seen in figure **a** of **Figure 4**, the storage modulus values are very similar in both polyamides, although PA11 has in general a higher value at low temperature and also at high temperature. At the peak that marks the maximum of the graph, the storage modulus values are 8% higher in the case of composites made with PA11 as matrix. Despite the aforementioned, in **Figure 4b**, PA11 presents a lower loss factor, or damping factor, at high temperature. However, the results obtained show variations of up to 20% due to the inherent inhomogeneity of the material, due to deviations from the one-dimensionality hypothesis, as well as fluctuations in the fiber volume content between samples.

Considering the local maximum located around 50 °C in **Figure 4b**, it is possible to calculate the T_g of both polyamides working as matrix, in order to establish a comparison with the polymers. In the case of the PA11 composites, considering the loss factor as a criterion according to ASTM D7028, the T_g is 57.66 $\pm$ 3.91 °C, while for PA12 the T_g is 47.83 $\pm$ 2.55 °C [16]. This shows that in the manufacture of composites using polyamides as matrix and CFRP sticks as reinforcement, the T_g of PA11 is modified, with a rise of between 6-7 °C, while the T_g of PA12 is not modified. The higher variability in the results for T_g obtained by DMA of composites compared to polymers is due to the intrinsic heterogeneity of these materials, as indicated above.

4. Conclusions

The key aspect of this project and its motivation are strictly related to sustainability. With an increasing volume of CFRP used in various industries, there is a critical need to find effective solutions for the recycling and reuse of carbon fibers and composite materials at their end-of-life. On the other hand, employing green polymers, such as PA11, as a matrix is the other side of the same coin, achieving even more sustainable solutions. In this project, we studied the dynamic-mechanical characterization of two polyamides used as matrix in two thermoplastic

  doi:10.5075/epfl-298799_978-2-9701614-0-0

matrix composites reinforced with mechanically recycled long carbon fibers, as well as the composites manufactured with those polyamides. The following conclusions can be drawn:

- The process of obtention of long fibers and manufacture of polymers and composites has been validated and optimized, in view of the results obtained.
- PA11 polymer shows a higher value for the loss factor at temperatures around its glass transition temperature, or T_g, compared to the PA12 polymer.
- The storage modulus is 8% higher in the case of PA11 composites, compared to the PA12 composites, at temperatures close to the T_g.
- The T_g is increased by 6-7 °C in the case of the PA11 composites, while it remains unaltered in the case of the PA12 composites.
- The fluctuations in the values of storage modulus, loss modulus, loss factor or in the calculation of the T_g by the loss factor criterion are due to the intrinsic inhomogeneity of the recycled composite materials manufactured, in terms of deviations from the one-dimensionality hypothesis, as well as variations in the fiber volume content between samples.

Acknowledgements

This work was carried out with financial support from the University Carlos III Madrid and Álvaro Alonso Barba Institute of Chemistry and Materials Technology (IAAB). The authors also gratefully acknowledge the help of those in KU Leuven Materials Engineering Department (MTM) who kindly contributed to the development of this project, especially to D. Winant for the assistance with the measuring devices.

5. References

1. Galvez P, Quesada A, Martinez MA, Abenojar J, Boada MJL, Diaz V. Study of the behaviour of adhesive joints of steel with CFRP for its application in bus structures. Compos Part B Eng 2017; 129:41–6.
2. Xiong Z, Wei W, Liu F, Cui C, Li L, Zou R, et al. Bond behaviour of recycled aggregate concrete with basalt fibre-reinforced polymer bars. Compos Struct 2021; 256:113078.
3. Akbar A, Liew KM. Assessing recycling potential of carbon fiber reinforced plastic waste in production of eco-efficient cement-based materials. J Clean Prod 2020; 274:123001.
4. Galvez P, Lopez de Armentia S, Abenojar J, Martinez MA. Effect of moisture and temperature on thermal and mechanical properties of structural polyurethane adhesive joints. Compos Struct 2020; 247:112443.
5. Rubino F, Nisticò A, Tucci F, Carlone P. Marine application of fiber reinforced composites: A review. J Mar Sci Eng 2020; 8(1).
6. Mishnaevsky L. Sustainable end-of-life management of wind turbine blades: Overview of current and coming solutions. Materials (Basel) 2021; 14(5):1–26.
7. Bahrami M, Abenojar J, Martínez MÁ. Recent progress in hybrid biocomposites: Mechanical properties, water absorption, and flame retardancy. Materials (Basel) 2020; 13(22):1–46.
8. Salazar A, Rico A, Rodríguez J, Segurado Escudero J, Seltzer R, Martin De La Escalera

  doi:10.5075/epfl-298799_978-2-9701614-0-0

Cutillas F. Monotonic loading and fatigue response of a bio-based polyamide PA11 and a petrol-based polyamide PA12 manufactured by selective laser sintering. Eur Polym J 2014; 59:36–45.

9. Park M, Hong S, Lee S, Kim N, Shin J, Kim Y. Effects of Hard Segment Length on the Mechanical Properties of Poly(PA11-co-DA) Periodic Copolymers. ACS Sustain Chem Eng 2022; 10(14):4538–50.
10. Feldmann M, Bledzki AK. Bio-based polyamides reinforced with cellulosic fibres - Processing and properties. Compos Sci Technol 2014; 100:113–20.
11. Hine PJ, Bonner MJ, Ward IM, Swolfs Y, Verpoest I. The influence of the hybridisation configuration on the mechanical properties of hybrid self reinforced polyamide 12/carbon fibre composites. Compos Part A Appl Sci Manuf 2017; 95:141–51.
12. Swolfs Y, Gorbatikh L, Verpoest I. Fibre hybridisation in polymer composites: A review. Compos Part A Appl Sci Manuf 2014; 67:181–200.
13. Butenegro JA, Bahrami M, Abenojar J, Martínez MÁ. Recent progress in carbon fiber reinforced polymers recycling: A review of recycling methods and reuse of carbon fibers. Materials (Basel) 2021; 14(21):6401.
14. Bahrami M, Abenojar J, Martínez MA. Comparative characterization of hot-pressed polyamide 11 and 12: Mechanical, thermal and durability properties. Polymers (Basel) 2021; 13(20):1–21.
15. ASTM D4065. Standard Practice for Plastics: Dynamic Mechanical Properties: Determination and Report of Procedures. 2008.
16. ASTM D7028. Standard Test Method for Glass Transition Temperature (DMA Tg) of Polymer Matrix Composites by Dynamic Mechanical Analysis (DMA). 2012.
17. Woigk W, Masania K, Gantenbein S, Poloni E, Studart AR. Damping behaviour of hierarchical natural fibre composites. In: ECCM18 -18th European Conference on Composite Materials 2017. p. 24–8.

  doi:10.5075/epfl-298799_978-2-9701614-0-0

PERFORMANCE OF RECYCLED GLASS FIBERS FROM COMPOSITE PARTS BY DIFFERENT TREATMENTS

Zainab Al-Maqdasi[a], Richard Sott[b], Cecilia Mattsson[b], Alann André[b], Roberts Joffe[a]

a: Luleå University of Technology, 97187 Luleå, Sweden – Roberts.Joffe@ltu.se
b: RISE Research Institutes of Sweden, 431 22 Mölndal, Sweden

Abstract: *In this work, glass fibers have been retrieved from decommissioned composite parts by three different methods. Namely, (i) pyrolysis, (ii) a novel solvolysis and (iii) a combination of solvolysis followed by pyrolysis. The techniques allowed successful recovering of sufficiently long fiber bundles (> 30 mm) that enabled separating single fibers for manual handling and testing. Single fiber tensile tests were performed to evaluate the efficiency of different recovery methods to preserve properties in comparison to the virgin fibers. The mechanical test results revealed that the stiffness of the recovered fibers has not been affected by the treatments. On the other hand, around 45% of the fiber's strength was retained after the solvolysis process which is a comparable value to that found in literature.*

Keywords: Glass fiber; recovery; solvolysis; pyrolysis; mechanical properties

1. Introduction

Wind turbine blades and leisure boats are examples for large lightweight structures mainly made of glass fibers reinforced polymer composites (GFRP). In the strive for sustainability and circular economy, recycling materials from decommissioned blades or boats and giving them a new life seems to be an effective solution to build sustainable industries and circular business models. Currently, GFRPs are regarded as unrecyclable within reasonable cost to price compromise, and those structures are foreseen to soon impose a severe environmental problem that needs immediate attention. Available recycling techniques for GFRP have their limitations in terms of recovered fiber length, mechanical properties, and scalability.

Krauklis et al. [1] have recently performed a comprehensive review on the topic of recycling fiber reinforced polymer composites where they highlight the currently available techniques and their technological readiness level. Apart from incineration and landfill disposal which is foreseen to increasingly being banned in the EU countries following Germany [2,3], mechanical, thermal and chemical recycling are the alternative processes for recycling with different efficiencies depending on the selected parameters and type of composites to be recycled.

There is today limited information about fiber strength being recovered from same GFRP materials by different processes. Only some results are available in literature reporting on the mechanical properties of individual recycled fibers by specific techniques [4–6]. Instead, the approach followed is to assess macroscopic properties of composites made of the recycled fibers [7–9] compared to those made of virgin fibers. Moreover, surface of fibers is typically modified after the recovery to enhance the bonding with matrix which is otherwise degraded by the loss

  doi:10.5075/epfl-298799_978-2-9701614-0-0

of fiber sizing during treatment [9]. This results in some ambiguity on the actual properties of the fibers after the specific treatment.

Solvolysis is the last added recycling method for GFRPs, and it is known that high temperature water (i.e., subcritical and supercritical) reduces the properties of recycled glass fibers. Therefore, water in solvolysis needs to be substituted with organic solvents. During the optimization of this solvolysis process several solvent systems have been tested in small scale on waste glass fiber composites from wind turbine blades and leisure boats (unpublished results and [10]). The aim was to find a simple and green solvent system that could be applied on both unsaturated polyester (UPE) and epoxy composite waste.

This paper will discuss the findings regarding the mechanical properties of recycled glass fibers from UPE leisure boat waste by solvolysis with propylene glycol (350 C, <180 bar, 16 h). Since very few studies have compared different recycling methods using the same composite material, a comparison with pyrolysis (600°C, inert atmosphere, 15 min) and with pyrolysis of solvolyzed fibers was done. The strength of recovered glass fibers was analyzed with 'single fiber tensile test' and the fiber surface was studied with optical microscope. The data generated in this study is an important contribution for further understanding regarding how various technologies affect the mechanical properties of recovered GF

2. Experimental

2.1 Materials

Composite of GF/UPE recovered from leisure boats are used in this work. The glass fibers used in the original component are biaxial 45°/45° E-glass fabric from AHLSTROM. Virgin glass fibers from the same supplier were investigated as reference (Figure 1a)) to assess quality of the surface and the performance of the treated fibers.

2.2 Methods

2.2.1. Recovery of Fibers

The fiber recovery is done on ~0.25 g composite pieces cut from the original parts (Figure 1 b)) that could be fit inside the reactors (Figure 1c)). The conditions for treatment presented here are identified based on results from previous work [10]. Pyrolysis: composites were pyrolyzed at 600°C for 15 min under inert environment using nitrogen gas flowing at 0.5 l/min. Solvolysis: Pieces of composites were solvolyzed in a high-pressure vessel of stainless steel having an inner diameter of 10 mm and a volume capacity of 7 mL connected to a safety pressure valve operates at up to 180 bars. The temperature of 350°C was applied for 16 hours with addition of 5 mL of liquid (propylene glycol). After the experiment, the vessels were cooled in water to room temperature and the solvate was rinsed with water and acetone followed by separating the solid material by filtration. Part of the solvolyzed material was then followed by pyrolysis with the same parameters to achieve cleaner surface. In the following, fibers treated by solvolysis are denoted as "Solvo" and those by pyrolysis are named "Pyro" and the fibers going through both treatments are referred to as "Solvo+Pyro". Virgin fibers are used for comparison as a reference material and is denoted by "VF".

  doi:10.5075/epfl-298799_978-2-9701614-0-0

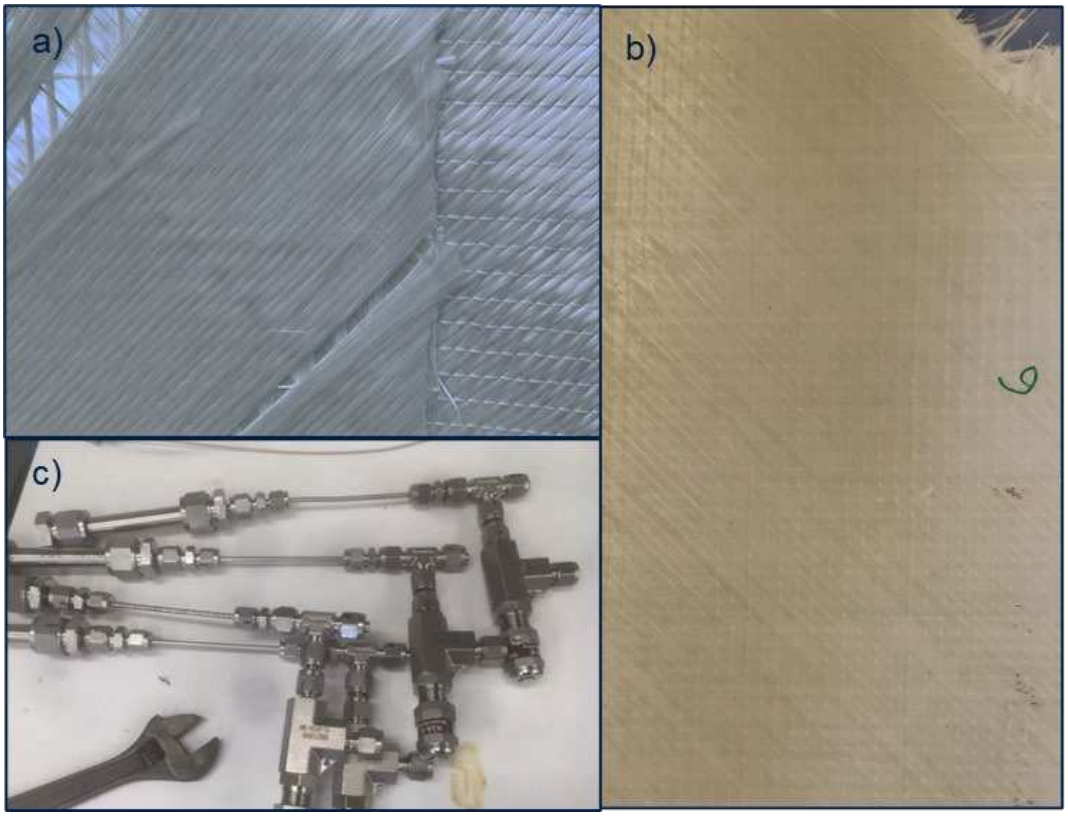

Figure 1. a) reference virgin GF mat used in manufacturing the original part. Note that the stitches were removed from the top layer to free the fibers for handling; b) the composite part to be treated; c) the pressure vessels/reactors used in the treatment.

2.2.2. Single fiber tensile test

The single filaments of ~40 mm in length were separated from the bundle manually with clean tweezers and mounted carefully on a paper frame with the aid of a super glue drop at each end of the frame. Diameters of the fibers were measured at 9 points along the fiber length as shown in Figure 2 using light optical microscope (Nikon). The average of these 9 measurements was used for the calculation of the cross-sectional area. Tensile testing was performed following ASTM D 3379 [11] on an Instron 4411 equipped with 5 N loadcell and pneumatic grips. The fibers were mounted with the paper frame for easy handling. Then, the paper was cut, and the fiber was loaded with a displacement rate of 2mm/min (corresponding to 10%/min). Since it is not possible to mount an extensometer on the sample for strain measurement, relative displacement of the grips was used instead to calculate strain. However, due to the final length of fibers being tested, the strain calculated from the displacement is overestimated due to the machine compliance. Consequently, the apparent stiffness is underestimated, and it should be corrected by measuring the compliance on different lengths of VF and calculating the stiffness (E) using eq. (1).

$$E = \frac{L}{C_{true}\, A} \tag{1}$$

where C_{true} is the difference between the measured compliance of fibers and the compliance of the machine (compliance of machine was found to be 0.532 mm/N), and A is the cross-sectional area of the fiber.

  doi:10.5075/epfl-298799_978-2-9701614-0-0

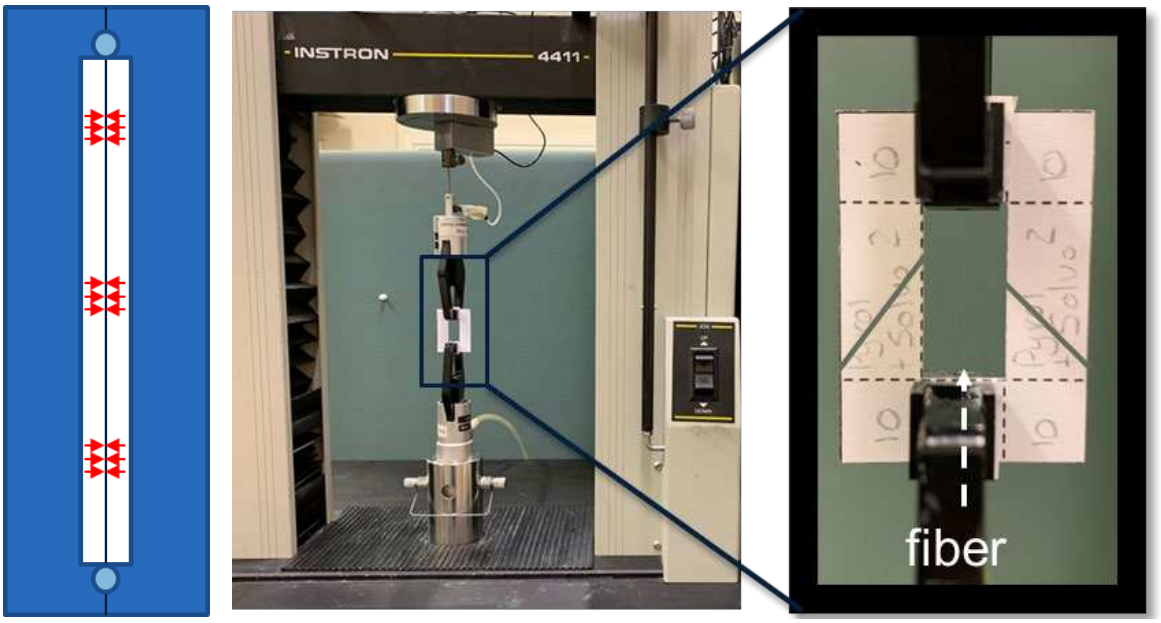

Figure 2. Schematics of the fiber mounted in the center of the paper frame (cutout length 20 mm) showing an example of the diameter measurement points. Right, an image of the fiber mounted on the machine for testing.

3. Results and Discussions

3.1 Optical Microscopy

Optical microscopy was used for initial assessment of quality of recovered fibers by observing the surface of fibers with aim to detect any polymer residues. At this stage it is not possible to assess whether the treatment has completely released the fibers from the binding organic material, but the possibility to separate single fibers from the bundle implies that the fibers were relatively free of polymer to be handled. For larger pieces, of the composites longer time might be required to degrade the resin and release the fibers [10]. However, it has to be mentioned that result of observation of the fiber surface may depend on the location of the fibers selected for examination. Indeed, fibers extracted from the outermost positions in the bundle are more exposed to the treatment conditions and may look cleaner with less traces of matrix. Figure 3 shows the surface of the fibers of different treatments under the microscope compared to that of the VF. The surface of VF is relatively smooth with presence of some marks due to handling and manufacturing imperfections. On the other hand, micrographs of the surface of treated fibers show traces of particles of material, which is likely to be residual matrix that has not been completely removed. The 'Pyro' sample shows the largest amount of residues on the surface. The surface of the 'Solvo' sample looks more severely degraded than others with defects that look like pits on the surface. Both temperature and treatment time affect the quality of the surface and the final mechanical properties of the fibers. For the work in [7], pyrolysis at 500 °C did not remove all the organic material and fibers were still bonded together until oxidation for 30 minutes was performed to separate them and obtain cleaner fibers.

  doi:10.5075/epfl-298799_978-2-9701614-0-0

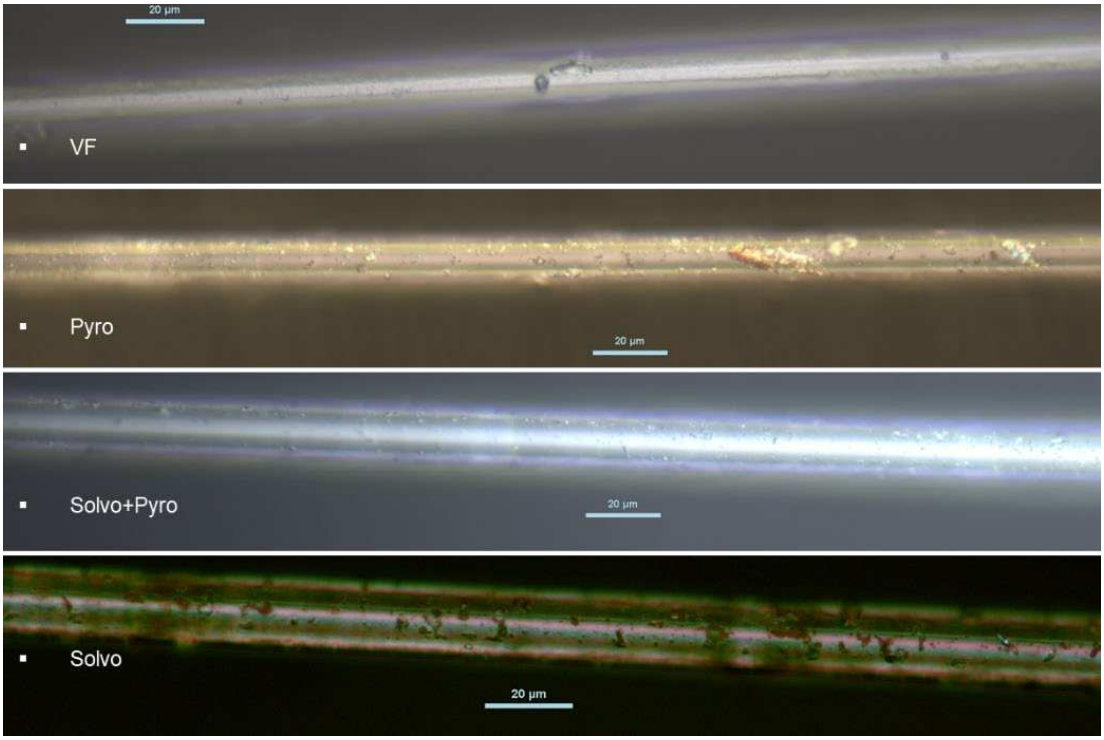

Figure 3. Light optical micrographs for the surface of the VF and the fibers from different treatments.

The effect of the treatment is also visible on the statistical measurements of the diameter of fibers. Variation is initially inherent from the variations of commercial virgin fibers, but the different treatments resulted in larger variations of the diameter as can be seen from values in Table 1. It is difficult to handle the fragile fibers (glass fibers in general but even more fragile are those after the treatment) as they tend to break before succeeding to mount them on the paper frames for investigations. This causes that only the strongest fibers being handled successfully reach the test and lead the results to skew towards the higher values. This could also be seen in the statistics of diameter presented in Table 1. The fibers which have been treated by the solvolysis showed a minimum diameter measurement as small as 10 µm at some points, but still the fibers treated by the combination of the two methods showed the highest average diameters. This may be an indication that the weakest (thinnest) fibers failed to be picked up for the investigations and the strongest (thickest) ones are the ones being tested (probably the ones with more resin on the surface). This also explains why the surface of the fibers under the microscope looks similar for the different treatments. The remaining organic residue on the surface of the fibers act as protection to the fibers forming some kind of micro-composites.

Table 1. Statistics for the measurements of fibers diameter

	Avg (µm)	STD (-)	Min (µm)	Max (µm)	Min (µm)	Max (µm)
			Based on average measurements		Based on all individual measurements	
VF	15.66	0.46	14.37	16.01	13.71	16.51
Pyro	14.77	2.02	11.88	19.34	11.20	20.50
Solvo+Pyro	15.49	1.45	13.6	17.42	13.20	17.74
Solvo	14.69	1.29	12.4	17.31	10.65	17.98

  doi:10.5075/epfl-298799_978-2-9701614-0-0

3.2 Tensile Properties

The tensile properties of the fibers recovered by different treatments compared to those of VF are presented in Figure 4. Representative stress-strain curves are shown in Figure 4a) while values normalized to the VF are presented in Figure 4b). The results show that there is no degrading effect of the different treatments on the tensile modulus. This is in accordance with previous studies where modulus was not affected by the different processing parameters for fiber recovery [4]. Despite the scatter in the result, the average values are within the same range of the average value of VF (86 ± 7 GPa). On the other hand, the strain at break and strength are drastically affected by all treatments. The strain at break has been reduced from 3% for VF to around 1.5% for the 'Solvo' sample and even lower for the other treatments. The 'Solvo' samples show the maximum retention of the strength (44% of VF, strength of VF was 2.4 ± 0.2 GPa) followed by samples of the combined treatments with around 35% strength retention. Numerical values of the properties are presented in Table 2. The 'Pyro' sample exhibited the largest degradation of up to 75%. The fibers of the combined treatments (Solvo+Pyro) might be the weakest but due to the same reason mentioned above - the ones surviving to the test are the strongest fibers. That is also the reason for the largest average diameter as only fibers with enough resin or least intact surfaces are surviving the handling.

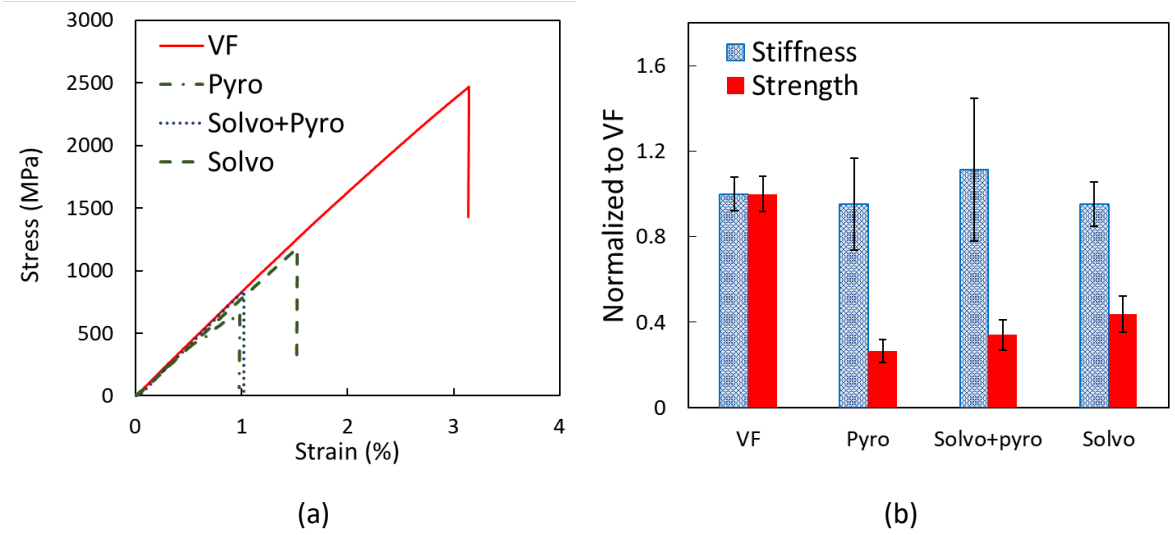

Figure 4. Tensile properties of the treated fibers: a) representative stress-strain curves; b) mean values normalized to the properties of VF

Table 2. Values of tensile properties for virgin GF and fibers recovered by different techniques

	VF	Pyro	Solvo+Pyro	Solvo
Strength (GPa) ± std	2.48 ± 0.21	0.66 ± 0.13	0.85 ± 0.18	1.09 ± 0.21
Modulus (GPa) ± std	86.43 ± 6.90	82.29 ± 18.48	96.17 ± 28.82	82.33 ± 9.05
Strain at break (%) ± std	2.90 ± 0.39	0.83 ± 0.22	0.95 ± 0.33	1.32 0.23

4. Conclusions

The glass fiber bundles of length sufficient for the tensile testing were recovered from decommissioned composite parts by pyrolysis, solvolysis and a combination of these methods (solvolysis followed by pyrolysis). As it was possible to separate single filaments from bundles, it seems that the recovery procedures were able to eliminate the polymer matrix from composite specimens. However, some small residues of polymer still remained on the surface of fibers recovered by pyrolysis, while solvolysis seem to introduce defects on the fiber surface. From the optical microscopy results it may be concluded that the combination of pyrolysis and solvolysis is most effective method to get rid of the polymer matrix, yet preserve fiber surface intact. Nevertheless, the optical microscopy results did not correlate with the data from mechanical characterization as the highest residual tensile strength was found for solvolysis recovered fibers, which looked most damaged on the surface. The lowest strength showed fibers after the pyrolysis treatment with combined recovery method being in between solvolysis and pyrolysis. In general the reduction of strength for fibers recovered by all methods is rather significant and ranged between 56% and 73%. On the other hand, the stiffness is almost unaffected by the recovery procedures. It may be stated that these fibers can be used in the structural applications where the main design parameter is stiffness.

This study showed that there may be good potential for the recovery of glass fibers in terms of mechanical performance however, the possibility to scale up these treatments and economical (as well as environmental) feasibility still needs to be explored.

Acknowledgements

The authors would like to acknowledge the financial support from the Swedish Innovation agency “Vinnova” through the funded project ReComp – Circular streams from glass fibre composite (Ref. No. 2018-04132). The Authors also appreciate the help received from PhD student at Luleå University of Technology, Marina A. Corvo, with the preparation of the single fibre specimens for the tensile tests.

5. References

1. Krauklis AE, Karl CW, Gagani AI, Jørgensen JK. Composite material recycling technology—state-of-the-art and sustainable development for the 2020s. J Compos Sci. 2021;5(1).

2. WindEurope. Wind industry calls for Europe-wide ban on landfilling turbine blades | WindEurope [Internet]. [cited 2022 Apr 1]. Available from: https://windeurope.org/newsroom/press-releases/wind-industry-calls-for-europe-wide-ban-on-landfilling-turbine-blades/

3. Vattenfall. Vattenfall commits to landfill ban and to recycle all wind turbine blades by 2030 - Vattenfall [Internet]. 2021 [cited 2022 Apr 1]. Available from: https://group.vattenfall.com/press-and-media/pressreleases/2021/vattenfall-commits-to-landfill-ban-and-to-recycle-all-wind-turbine-blades-by-2030

4. Kao CC, Ghita OR, Hallam KR, Heard PJ, Evans KE. Mechanical studies of single glass fibres recycled from hydrolysis process using sub-critical water. Compos Part A Appl Sci Manuf. 2012;43(3).

  doi:10.5075/epfl-298799_978-2-9701614-0-0

5. Oliveux G, Bailleul JL, Salle ELG La. Chemical recycling of glass fibre reinforced composites using subcritical water. Compos Part A Appl Sci Manuf. 2012;43(11).

6. Cunliffe AM, Jones N, Williams PT. Pyrolysis of composite plastic waste. Environ Technol. 2003 May 1;24(5):653–63.

7. Onwudili JA, Miskolczi N, Nagy T, Lipóczi G. Recovery of glass fibre and carbon fibres from reinforced thermosets by batch pyrolysis and investigation of fibre re-using as reinforcement in LDPE matrix. Compos Part B Eng. 2016 Apr 15;91:154–61.

8. Rahimizadeh A, Kalman J, Henri R, Fayazbakhsh K, Lessard L. Recycled glass fiber composites from wind turbine waste for 3D printing feedstock: Effects of fiber content and interface on mechanical performance. 2019;12(23).

9. Nagel U, Yang L, Kao CC, Thomason JL. Effects of Thermal Recycling Temperatures on the Reinforcement Potential of Glass Fibers. Polym Compos. 2018;39(4).

10. Mattsson C, André A, Juntikka M, Tr nkle T, Sott R. Chemical recycling of End-of-Life wind turbine blades by solvolysis/HTL. In: IOP Conference Series: Materials Science and Engineering. 2020.

11. American Society of Testing and Materials. ASTM D 3379-75 Standard Test Method for Tensile Strength and Young's Modulus for High Modulus Single Filament Materials. Vol. 75, ASTM International. 1989.

  doi:10.5075/epfl-298799_978-2-9701614-0-0

ECO-CLIP: DEVELOPMENT OF NOVEL RECYCLED MATERIAL FROM CF/ LMPAEK FACTORY WASTE.

C Martín-Pérez [a], D.J Rodriguez-Del Rosario [a], N González-Castro [a], R Travieso-Puente [a] and E Rodríguez-Senín [a].

a: Advanced Materials, AIMEN Technology Centre, Calle Relva 27A, 36410, O Porriño, Spain
E-mail: celia.martin@aimen.es

Abstract: *This paper reports the most important ECO-CLIP project's development, in this sense, a novel recycling route for cCF/LMPAEK scraps was developed by shredding and compounding with unreinforced LMPAEK. A mechanical recycling route was selected to fully take advantage of the matrix and the reinforcement for subsequently manufacturing structural pieces for the aircraft industry by Injection Molding and FGF. Mechanical and thermal properties and geometrical accuracy were measured for both technologies.*

Keywords: LMPAEK; Recycling; Injection Molding; Additive Manufacture; Aerospace.

1. Introduction

The introduction of composites in aerospace contributes to the continuous evolution of this sector that is constantly looking for lighter materials with good performance. Thermoset composites (TSCs) are starting to replace metal parts, and nowadays there is an increasing interest in thermoplastic composites (TPCs) due to a new era of ecological concern since TPCs can be recycled.

Reinforced fiber TPCs are on the rise, and it can be anticipated that the use of these materials will increase by 200 to 300 percent in the coming decade. Airbus has pioneered the use of TPCs, nowadays represented by A350 XWB with carbon fiber reinforced thermoplastic (CFRTP) in primary structure parts. Moreover, waste management has become crucial in the European Union. This management must start at the production stage through the reuse of waste, and new recycling techniques must be developed to meet European concerns (1).

The recycling routes for recent TPCs are not determined yet and there is a concern about end-of-life parts. In general terms, carbon fiber composites are thermally and chemically treated to recover the fiber by the elimination of the polymer matrix. This represents an environmental and economic issue due to chemical harmful products utilized and the elimination of high-performance matrixes that can be recycled.

Within the possibilities, mechanical recycling seems to be optimal from a technical and economical point of view for this type of product since it does provide a second life to carbon fiber and matrix even though fibers suffer fiber length reduction. This type of recycling is an ecologically responsible alternative since no chemical solvents are used, and CO_2 or NO_x emissions are significantly lower.

ECO-CLIP project is based on a combination of innovation activities oriented to achieve lighter structural parts from TPCs factory waste for the next generation of aviation fuselage demonstrator, which is undertaken as part of Clean Sky 2. ECO-CLIP addresses the development of thermoplastic short fibers reinforced low-melting PAEK (sCFLMPAEK) using recycled

  doi:10.5075/epfl-298799_978-2-9701614-0-0

continuous carbon fiber reinforced low-melting PAEK (cCFLMPAEK) from factory waste by mechanical recycling for the manufacturing of structural parts such as frame clips and system brackets to be installed in the Next Generation Multi-Functional Fuselage Demonstrator (MFFD), undertaken as part of Clean Sky 2, Large Passenger Aircraft – Platform 2. The different demonstrators manufactured during the project are listed in Figure 1.

Figure 1: ECO-CLIP project demonstrators.

2. Materials and methods

Different scrap materials, supplied by Fokker, Stelia, and Toray were used for the development of the project. These materials are presented in different formats and are made from cCFLMPAEK tape: off-spec tape, laminates, or trimming from larger pieces. For the development of the project, a selection of the available materials was done, and pieces with contaminations such as kapton tape, fiberglass, vacuum bags, etc. were discarded. LMPAEK unreinforced powder, supplied by Victrex (AETM 250PWD), was used for melt state extrusion compounding.

2.1 Material development

The material was developed by shredding the starting materials using two different cutting mills: UNTHA RS40 mill and B 08.10 from Wanner. Subsequently, sieving was carried out using 0.3- and 3.35-mm mesh sieves from Filtra. A twin-screw extruder (HAKE Rheomix) was used for the compounding of recycled material and LMPAEK powder.

2.2 Injection molding

Victory 40 (ENGEL) injection molding machine was used to produce test specimens. Parameterization was carried out to obtain the best results. A 150x40x4mm mold was used to produce rectangular test specimens which were subsequently machined according to the mechanical tests to be performed.

2.3 3D printing

For the 3D printing process (3DP) , an adapted destock printer was developed with a pellet extrusion printhead according to FGF technology (Fused Granulated Fabrication). A thermal chamber was also installed to control the temperature during the high-performance materials printing process. Parameterization was carried out to obtain the best results.

2.4 Differential Scanning Calorimetry

Material thermal properties were analyzed by Differential Scanning Spectroscopy (DSC). The experiments were carried out in a DSC Q2000 (TA Instruments). DSC tests were performed with

N_2 as the purge gas. The heating cycle starts at r.t to 360 °C at 10 °C/min. After the first heating cycle, the temperature is held at 360 °C for 15 min to erase the thermal history, then cooled to r.t at 10 °C/min, finally, the second heating from r.t to 360 °C at 10 °C/min. Crystallinity was determined by equation 1 (2).

$$\chi = \frac{\Delta H_m}{(1-W)130} \times 100\% \quad (1)$$

Where ΔH_m, is the melting enthalpy as the integral area of the endothermic peak and W is the fiber percentage (0.4). 130 J/g is the melting enthalpy of a 100% crystalline PEEK sample (2).

2.5 Mechanical tests

Tensile and compression tests were performed to characterize the samples using a 5 kN capacity standard tensile/compression machine (Shimazdu®). Tensile properties were evaluated according to ISO 527. Compression tests were carried out according to ISO 604. At least five repeated specimens were tested, and the data were averaged.

2.6 Geometry measurements

For the dimensional validation of the demonstrators, different measurements were carried out with a HANDYSCAN3D_Black handheld laser scanner, with a precision of 0.025mm. The resulting CAD was then compared to the theoretical one to evaluate the production accuracy

3. Material development

The development of the material was carried out at a pilot plan scale, for this, several types of laminates, tapes, and cut-offs were used to study how the origin of the material affects the overall process and check its versatility. After selection, the shredding was carried out with the help of a laboratory cutting mill. Afterward, sieving was carried out to separate 3 portions.

Figure 2 shows the 3 different portions that were separated. A first portion (F1) that represents a 5wt% with particle sizes between 0 and 2 mm will be used for FGF, and a second portion (F2) that represents a 82wt% with lengths between 0 mm and 18 mm will be used for the for IM. Finally, a third portion (F3) is obtained representing 10wt% of the initial material with a size greater than 20 mm. This portion was reprocessed by shredding to increase the efficiency of the cycle, increasing F1 by 56wt%, F2 by 6wt%, and decreasing F3 by 89wt%. This means that only 3.55% is not recovered. This could be further optimized by successive shredding.

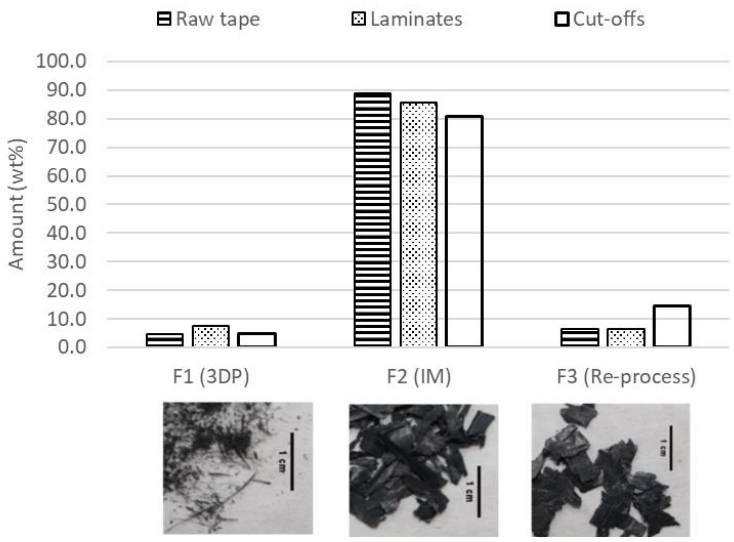

Figure 2. Input material sieving distribution after shredding.

Fraction F2 from the different factory waste sources was fed into the extruder directly. It was found that fiber length, thermal properties, and carbon fiber percentage were similar for all the materials after processing, so all of them can be treated as a whole. To assess optimal processing conditions torque values were evaluated.

Rheology studies, fiber length distribution, and specific heat capacity for rPAEKCF (recycled low-melting PAEK short carbon fiber reinforced material) mixtures with 40, 50, 60, and 66wt% CF were performed to supply information for injection simulations. Due to the filling difficulties encountered for larger pieces such as bracket 2a during the injection process when using loads higher than 40wt%CF, it was decided to manufacture clips and brackets with rPAEK40CF mixture.

When analyzing the thermal properties of the mixtures, it can be found that crystallinity tends to increase directly with the fiber percentage (from 26 to 31%), this could be due to the ability of fibers to act as crystallization nuclei. When carbon fiber percentage is higher than 60wt%, the number of fibers and the space occupied by them exceeds this capacity, and the crystallinity grade starts decreasing (27%).

A scale-up of the rPAEK40CF manufacturing process was carried out after simulations. For this purpose, UNTHA cutting mills were used to perform a first size reduction. After this first step, a second shredding was done with the above-mentioned mill to facilitate the material feeding during extrusion.
Different trials with (F2 material only) and without (F1, F2, and F3 together) the sieving process were done to ensure final properties. It was found that as carbon fiber percentage increases mean fiber length decrease. This could be due to the reduction of matrix space for the fibers to move. Furthermore, when increasing carbon fiber percentage, fiber-fiber breakage is potentiated. Also, extruder shear rates were found as critical parameters in the fiber length reduction, causing a fiber length homogenization during extrusion to approx. 200 µm mean values.

Thermal and rheological properties remain similar in both conditions (with and without sieving), allowing to avoid the sieving process. Therefore, the material was directly manufactured by compounding under optimal conditions previously established in laboratory trials.

Six different types of brackets and one clip (as shown in Figure 1) were manufactured by IM with the resulting material. As a proof of concept, an FGF (Fused Granulated Fabrication) printer was specifically built in the frame of the project and one type of bracket (Bracket 2b) was manufactured.
The use of FGF technology allows using the same material as the one used for IM. Both processes were parametrized for this novel material to ensure the highest quality of the parts.

4. Results and analysis

4.1 Thermal properties

The DSC thermograms for the first heating ramp are shown in Figure 3, all tests were carried out in standard specimens. In the first heating cycle, FGF samples present a cold crystallization transition before melting. Interestingly, the unreinforced LMPAEK melting curve presents two melting peaks for the presence of different crystalline structures that were already reported in the literature (2). To determine melting enthalpy, the total area under the melting signals is used for calculations.

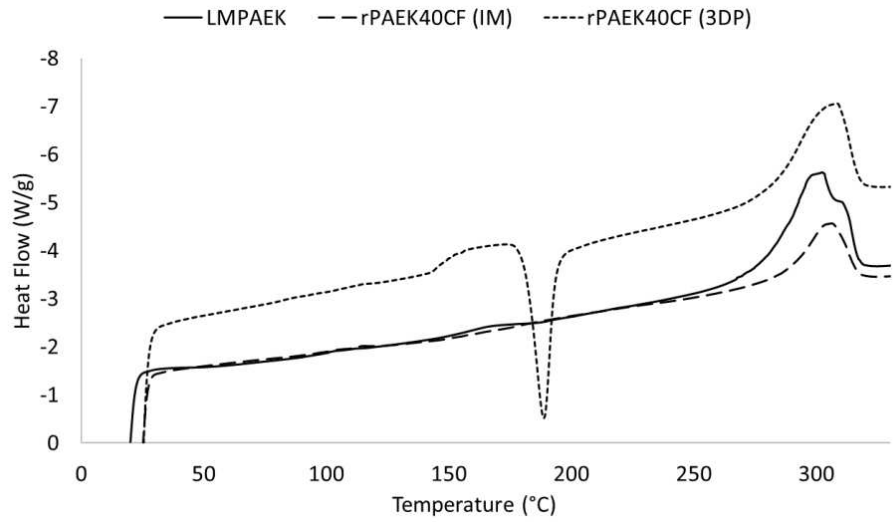

Figure 3. DSC, first heating cycle for LMPAEK powder (LMPAEK), rPAEK40CF (IM) and rPAEK40CF (3DP). Exo down.

The resulting crystallinity degree of the samples is, as expected, higher for IM at 26% than does for FGF at 7%, this is due to the cooling rate that the material suffers after processing. IM samples remain in the mold at 190°C, but FGF samples cool down in an 80°C chamber, both cooling from a processing temperature of 320°C. This difference leads to this cold crystallization event that decreases the total crystallinity.

As mentioned above, the two melting peaks are not recorded when carbon fiber is present in the matrix, also a higher crystallinity is documented. This can be due to transcrystalline growth around the fiber. This event will promote crystal growth and the two different crystalline structures will no longer be able to form.

4.2 Mechanical properties

As can be seen in Figure 4, the mechanical properties, as measured in standard specimens, increase when adding fiber to LMPAEK. Tensile strength increases by 50% when adding carbon fiber for both technologies, and compression by 8% for IM.

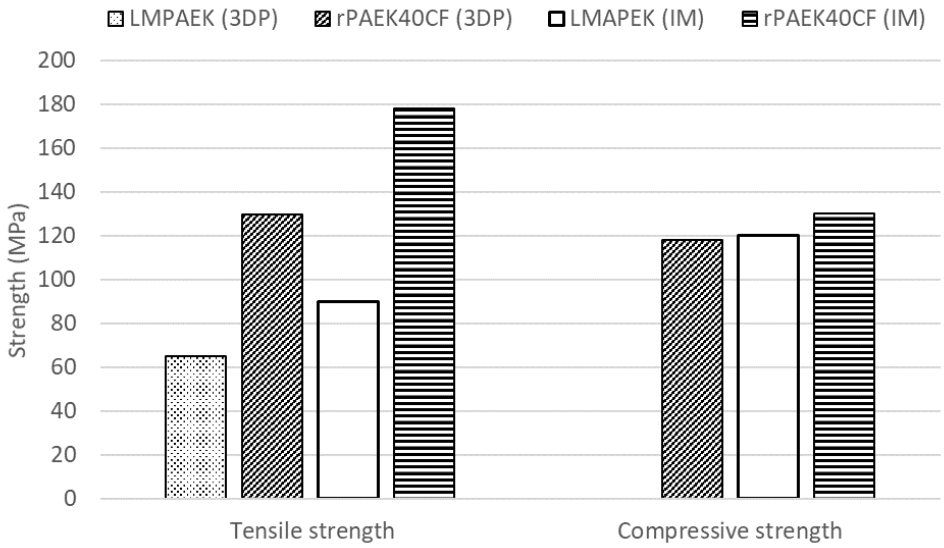

Figure 4: Mechanical properties (tensile and compressive results) for rPAEK40CF and LMPAEK samples manufactured by IM and FGF.

Due to the layer-by-layer production, FGF samples register lower mechanical properties than their analogous process by IM. 37% lower in the case of tensile strength and 10% in compressive strength. This is mainly due to the absence of layer-layer bonding strength and the discontinuity of the final part.

4.3 Geometrical stability

It was found that FGF brackets were more geometrical accurate. This is since the printer can ensure lower tolerances in small parts, which means that for example, a drill hole does not have to be done after processing which usually occurs IM. Also, FGF enables the material to cool layer by layer, this decreases the percentage of total shrinkage and gives the final part a more accurate geometry.

Figure 5 demonstrates how the parts fit the selected tolerance (+/- 2mm) in both cases although FGF parts can achieve better geometry precision. It can also be seen how the surface roughness in FGF is higher than that achieved by injection molding. Depending on the final use of the piece this may involve sanding after production.

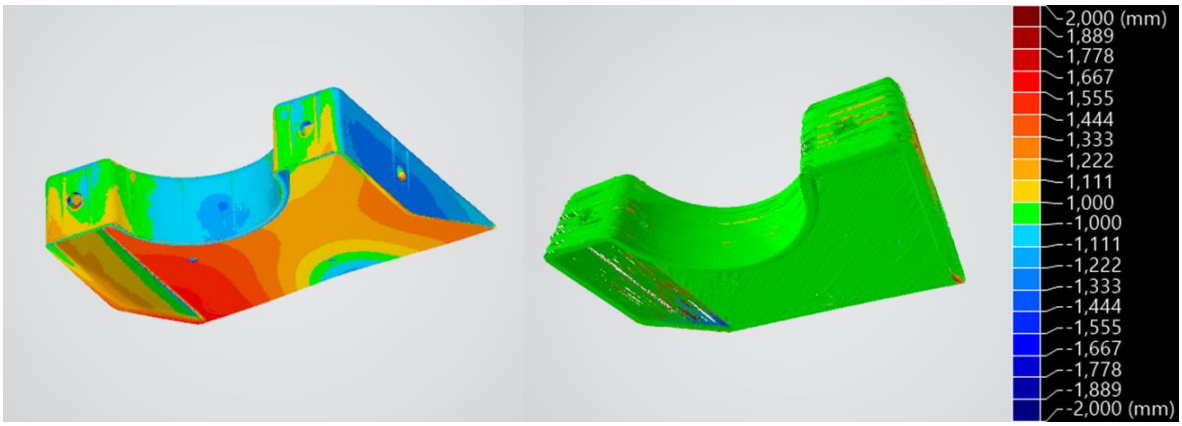

Figure 5: Laser measurements for bracket2b. IM on the left and FGF on the right.

On the other hand, in the injected part, symmetrical deviations are observed in the parts of the plane (mark in red) this is due to the ejector's position in the mold. This means that the pieces were not totally cooled when demolding.

5. Conclusions

During the Project, a novel recycling route was set for cCFLMPAEK leading to a recycled sCFLMPAEK. Mechanical recycling was carried out giving the industry an alternative to conventional recycling processes.

Different mixtures were obtained with different carbon fiber percentages content to study how this parameter affects the processing, thermal, rheological, and physical properties. It was observed that:

- The most influential parameter on fiber size was the shear rate of the extruder, achieving materials with 200 µm fiber regardless of the starting fiber size.
- Crystallinity was observed to increase with fiber percentage due to transcrystallinity with the limit of increase being 60wt%CF.
- Two melting peaks were observed for the unreinforced LMPAEK which disappear when the fiber is added to the unreinforced matrix.
- The optimum material was determined to be rPAEK40CF based on injection filling simulation studies.

A processing comparison between IM and FGF was performed. The mechanical properties achieved by both techniques were studied as well as their thermal properties and geometrical stability observing:

- Higher crystallinity for IM (26%) than for FGF (7%) due to the rapid cooling undergone during the FGF process.
- Tensile strength increases by 50% when adding carbon fiber for both technologies, and compression by 8% for IM.
- FGF samples register lower mechanical properties than their analogous process by IM. 37% lower in the case of tensile strength and 10% in compressive strength. This may be due to both crystallinity and layer-by-layer construction in FGF.

  doi:10.5075/epfl-298799_978-2-9701614-0-0

- It was observed that the FGF parts conformed more geometrically to the theoretical model than those produced by IM since they suffer the less shrinkage due to their layer-by-layer construction.

Furthermore, in-depth studies on the different mixtures and the limits of both technologies regarding the carbon percentage will be made. LCA and LCC to ensure the process's economic and ecological sustainability are ongoing.

Acknowledgments

This project has received funding from the Clean Sky 2 Joint Undertaking (JU) under grant agreement No 886810. The JU receives support from the European Union's Horizon 2020 research and innovation program and the Clean Sky 2 JU members other than the Union.

6. References

1. Krauklis AE, Karl CW, Gagani AI, Jørgensen JK. Composite material recycling technology—state-of-the-art and sustainable development for the 2020s. J Compos Sci.; 5(1):28
2. Jérémie Audoit, Lisa Rivière, Jany Dandurand, Antoine Lonjon, Eric Dantras, et al.. Thermal, mechanical and dielectric behaviour of poly(aryl ether ketone) with low melting temperature. Journal of Thermal Analysis and Calorimetry, Springer Verlag, 2019, 135 (4), pp.2147-2157. ⟨10.1007/s10973-018-7292-x⟩. ⟨hal-02067744⟩

FROM SAIL TO STRUCTURE
END-OF-LIFE SAILS AS A FEEDSTOCK FOR CIRCULAR MANUFACTURING

Marcelle Hecker[a], Marco Longana[a], Ole Thomsen[a], Ian Hamerton[a]

a: Bristol Composites Institute, University of Bristol,
Queen's Building, University Walk, Bristol, BS8 1TR, United Kingdom
yo18950@bristol.ac.uk

Abstract: *The yachting industry currently does not have a waste-management plan for end-of-life (EOL) sailcloth. The most advanced sails produced by the world's largest sailmaker, North Sails, are flexible carbon fibre reinforced polymer (CFRP) composites, and the aim of this project is to reclaim the highest-value components from North Sails' "3Di" range of sails, i.e. the carbon fibres, via two gasification-type processes. One process was conducted in a controlled air atmosphere (carried out by ELG Carbon Fibre (prior to 2022)), and the other in a controlled superheated steam (SHS) atmosphere, while undergoing pressure-swing cycles (carried out by Longworth). The successfully reclaimed carbon fibres were subsequently remanufactured into aligned discontinuous fibre reinforced composites (ADFRCs), using the High-Performance Discontinuous Fibre (HiPerDiF) manufacturing technology, invented at the University of Bristol, to lay out a possible waste-management route for EOL 3Di sails.*

Keywords: EOL composite; reclaimed carbon fibre; aligned discontinuous short fibres; HiPerDiF; sustainable composites

1. Introduction

The recycling of CFRP composites is divided into two distinct steps, the reclamation of the constituents (fibres and matrix) and the remanufacturing of composite products using the recovered materials.

To date, many reclamation techniques have been explored for CFRP composites using thermosetting matrices. Various mechanical (grinding, crushing), thermal (pyrolysis, gasification in various atmospheres), and chemical (solvolysis) methods have been investigated and their results are collated in a number of reviews published over the last two decades [1-4]. While mechanical reclamation techniques process the composite as a whole, the recovered product can only find use as low-value filler or particle reinforcement [1]. However, the thermal and chemical techniques degrade the thermoset polymer matrix, enabling the recovery of the fibres. The primary focus is the reclamation of carbon fibres with properties as close to the virgin carbon fibre (vCF) as possible, to make the remanufacture of high-value composites possible.

The first part of this research aims to investigate whether the carbon fibre content of a 3Di sail, which is a complex composite made up of several polymer fibres and resins, can be recovered *via* two thermal reclamation methods which have been proven successful for the more common epoxy-based CFRP composites; gasification in air (the most common industrial method to recover carbon fibre), and gasification in superheated steam (a highly mature process).

Owing to the reclamation processing techniques, the reclaimed carbon fibres (rCFs) are typically fluffy, short, and randomly orientated, and are therefore most commonly manufactured into

randomly oriented fibre-reinforced composites, such as non-woven mats, which can be compression moulded, or compounded into pellets for injection moulding [2, 4]. Alternatively, randomly oriented fibres can be aligned before being impregnated with resin. Aligning the reclaimed carbon fibres before composite production is of particular interest due to higher fibre volume fractions (V_f) and thus the higher mechanical performances that can be achieved [5].

The second part of this research aims to show the possibility of manufacturing high-value composite coupons by realigning the rCF from the 3Di sail, using the University of Bristol's HiPerDiF manufacturing method. The latter has previously been used to produce tape-type prepreg material with a fibre alignment in the range of ±3° for 65–67% of the 3 mm long fibres used, resulting in some of the best structural results reported in literature from a short fibre alignment technique using water as the carrier fluid [5].

Details of both reclamation processes, mechanical and chemical properties of recovered carbon fibres, the HiPerDiF manufacturing process, and mechanical properties of remanufactured composite coupons are presented here.

2. Materials and methods

2.1 EOL composite

The EOL North Sails 3Di sail being recycled in this work (supplied by North Sails) are made up of carbon fibres, polyester fibres, ultra-high molecular weight polyethylene (UHMWPE) fibres, polyester resin, and polyester-based polyurethane resin; the exact composition is proprietary and cannot be disclosed. The virgin carbon fibres (GRAFIL 34-700, Mitsubishi Rayon Carbon Fibre and Composite, Inc., USA) used in the manufacture of the 3Di sail were used as the reference material (supplied by Future Fibres).

2.2 Reclamation process

The carbon fibre content of the 3Di sail was reclaimed by two companies operating in the UK. The DEECOM process, operated by Longworth, is a gasification-type process in SHS atmosphere, where CFRP composite waste is loaded into a pressure vessel, SHS is introduced and pressure-swing cycles are carried out for the duration of the operation. The legacy ELG process, operated by ELG Carbon Fibre (before 2022), is a gasification-type process in air atmosphere, where CFRP composite waste is placed on a conveyor belt and passed through a heated chamber.

Processing conditions trialled were based on earlier thermogravimetric analysis (TGA) of the sailcloth (not included in this paper), as shown in Table 1.

2.3 Fibre surface morphology

The surface morphology of the vCFs and rCFs were examined under a scanning electron microscope (SEM) (Hitachi TM3030Plus, Hitachi Ltd., Japan). Randomly selected fibres were placed on electrically conductive carbon tape, and an accelerating voltage of 15kV was used.

2.4 Mechanical properties

Single fibre tensile tests (SFTT) were performed on more than 25 individual fibres from each reclamation scenario and the baseline vCFs, to investigate the tensile properties of each fibre-type. Single fibres were mounted on plastic tabs, adhered with DYMAX 3099 adhesive, and cured under a UV source. The fibre diameters were measured under a Zeiss microscope (Zeiss Axio

Imager M2, Carl Zeiss AG, Germany). Three measurements were taken for each fibre, such that the cross-sectional area of each fibre could be calculated individually. Tensile testing was conducted at room temperature, with a 20 N load cell and at an extension rate of 0.033 mm/s, using a Dia-Stron Lex820 extensometer (Dia-Stron Limited, UK).

Table 1: Processing conditions for reclamation trials.

Reclamation trial ID	Processing conditions
DEECOM T3	Atmosphere: SHS. 450°C for 8 hours. Steam process pressure: 345 kPa. Steam blowdown pressure: 427 kPa.
DEECOM T4	Atmosphere: SHS. 500°C for 8 hours. Steam process pressure: 345 kPa. Steam blowdown pressure: 427 kPa.
ELG T1	Atmosphere: air. 450°C for 1 hour.
ELG T2	Atmosphere: air. 480°C for 1 hour.
ELG T3	Atmosphere: air. 500°C for 1 hour.

2.5 HiPerDiF 2.5 manufacturing method

The HiPerDiF manufacturing method was used to realign the short fibres and produce a tape-type prepreg material, as is shown in the schematic in Figure 1.

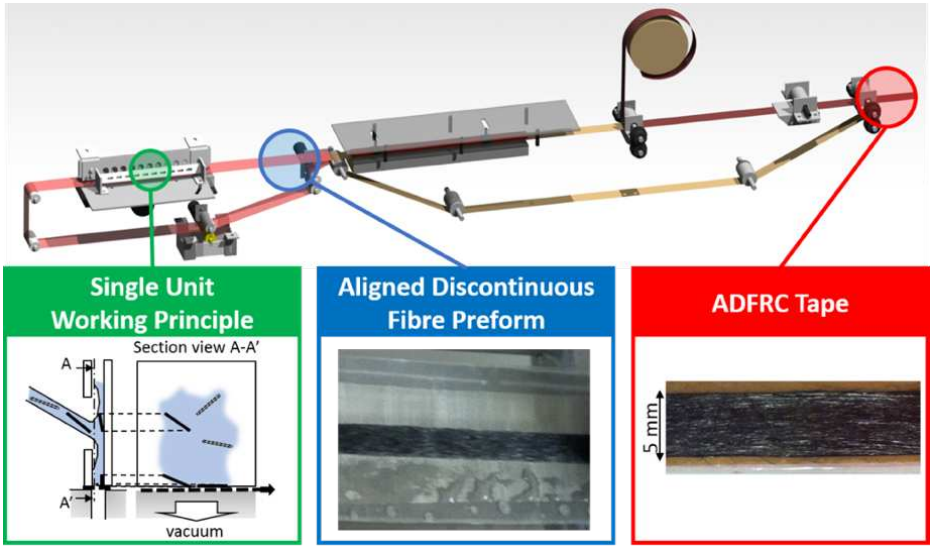

Figure 1: HiPerDiF 2.5 machine. Image reproduced directly from [6].

The HiPerDiF system is a water-based manufacturing method in which short fibres are dispersed and mixed in several tanks of water to create a low concentration suspension of fibres in water. This suspension is accelerated through a series of nozzles, which are directed at the orientation head (green box in Figure 1). The orientation head is made up of a series of parallel plates spaced 0.3 mm apart, such that when the fibres hit the plates, the change in momentum causes the fibres to change their direction transversely to the water jet direction and fall on the moving perforated belt beneath the head, aligning parallel to the belt [5]. The water is removed from the moving fibres by vacuum suction and partially recycled. The aligned discontinuous fibre preform (blue box in Figure 1) continues to travel along the conveyor belt, passing under infrared

radiation to dry completely, before being collected for the resin impregnation phase (red box in Figure 1) to produce the prepreg tape (in this work the automated resin impregnation phase was not operating and instead this was done by hand, as explained below).

2.6 Materials for remanufacture

Owing to the construction of the 3Di sail, which consists of multiple layers of carbon fibre prepreg tapes in many different orientations, it was decided to cut the sail material into 2 mm wide strips before reclamation, to ensure that rCFs would range between 2-10 mm. For the vCF a length of 3 mm was chosen, to stay consistent with previous research done on the HiPerDiF 2.5 machine using carbon fibre. A bio-based epoxy resin film (SHD composites - DF439) was used for manufacture.

2.7 Sample preparation

The HiPerDiF method was used to produce dry fibre preforms with the three fibre-types: DEECOM T5 (a new reclamation run, operated following DEECOM T3 conditions), ELG T1, and vCF. Each preform was then sandwiched between two layers of resin film to create a single ply of prepreg tape, which was consolidated by passing through a hot press at 60°C, causing the resin to partially impregnate the dry fibres.

To produce each composite coupon, four prepreg plies were stacked inside a semi-closed mould in a unidirectional lay-up. The composite was cured by vacuum bag moulding in an autoclave at 6 bar and 120°C, for 120 minutes. After cure, specimens of a nominal thickness of 0.3 mm (Figure 2) were released from the mould and cotton-epoxy composite end-tabs attached with epoxy adhesive (Araldite 2014-2). 7 x vCF, 7 x DEECOM T5, and 7 x ELG T1 coupons were tested.

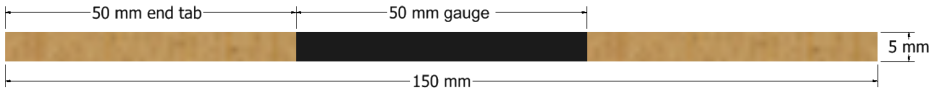

Figure 2: Specimen prepared for tensile testing.

2.8 Mechanical properties

Tensile testing was performed on a servo-electric tensile test machine (Shimadzu, Japan), following the ASTM D3039 standard. The specimens were loaded at a constant cross-head displacement speed of 1 mm/min. The load was recorded with a 10 kN load cell and the strain was measured by tracking white spots drawn on each specimen with a video extensometer.

2.9 Micro-structural analysis

To investigate the internal micro-structure of the coupons, the specimens were sectioned and potted in epoxy resin (Prime20LV, Gurit, UK), before being sanded and polished to expose the cross section for optical microscopy (Zeiss Axio Imager M2, Carl Zeiss AG, Germany). The fracture surfaces of several specimens were imaged with a scanning electron microscope (SEM) (Hitachi TM3030Plus, Hitachi, Ltd., Tokyo, Japan) at an accelerating voltage of 15kV.

2.10 Fibre length measurement

To measure the average fibre length used in each coupon-type, a section of dry fibre preform was re-dispersed in a beaker of water, by stirring and ultrasonication for around 30 seconds. The

dispersed fibres were then gravity filtered and allowed to dry. A sample of the dry fibres was scanned in a high-resolution scanner (Epson Expression 11000XL, Epson, Tokyo) and 1600+ fibre length measurements were made in the image processing software, ImageJ, for each fibre-type.

3. Results and discussion

3.1 Fibre surface morphology

Figure 3 shows representative SEM images of the vCFs and rCFs. The rCFs have more striations when compared to the vCFs (Figure 3A), indicating that the fibre sizing has likely been removed from the fibre surfaces in reclamation trials. The fibres reclaimed in the ELG process were generally clean from resin (Figure 3B, C). Processing conditions for trial 1 (Figure 3B) and trial 2 did not induce any visible damage to the fibres, however the trial 3 processing conditions (500°C for 1 hour) are clearly too harsh and begin oxidising the fibres themselves (pitting evident in Figure 3C).

The DEECOM process efficiently degraded the resin matrix under both trial conditions, however, in both trials residual particles covered many of the outer layer fibres (as can be seen in Figure 3D, E). The majority of the residue appears to only be lightly bonded or attached to the fibres, as many particles readily fell off the fibres during sampling. This was likely the same residue that was found to have adhered to the sample bags, rather than being undegraded resin. This suggestion is supported by the fact that the fibres from inner layers (Figure 3F) of the waste material appear much cleaner than the outer layer fibres, despite these fibres having less exposure to the degrading SHS atmosphere.

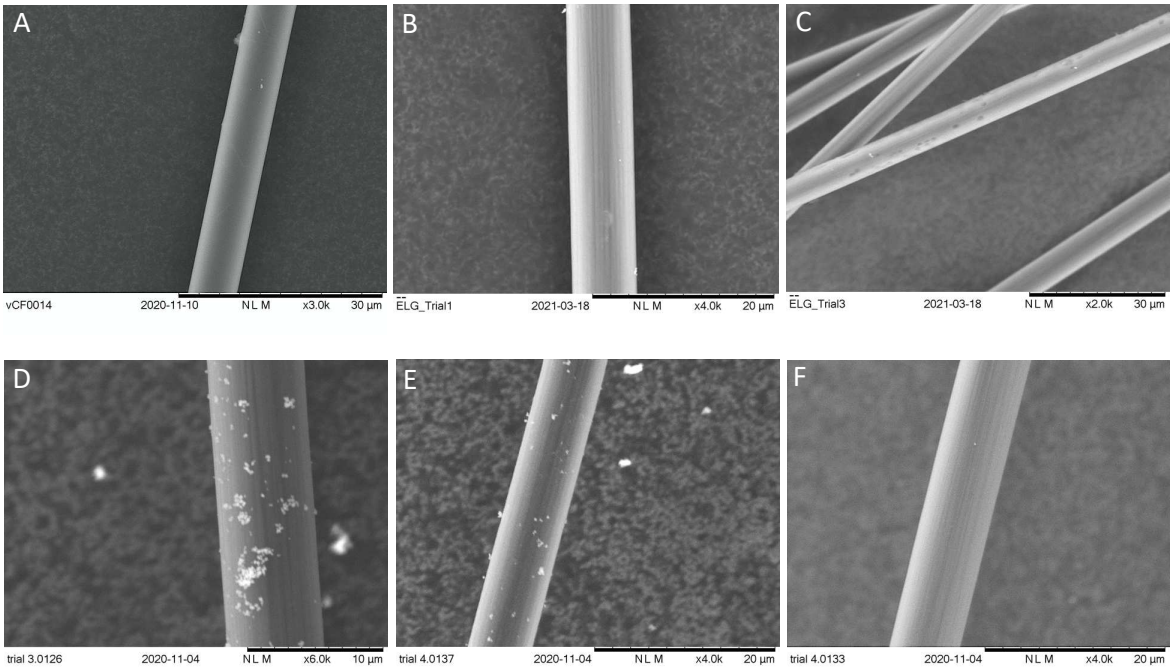

Figure 3: SEM images of A) vCF. B) ELG T1 rCF. C) ELG T3 rCF. D) DEECOM T3 rCF – from outer layer. E) DEECOM T4 rCF – from outer layer. F) DEECOM T4 rCF – from inner layer.

3.2 Single fibre tensile properties

As seen in Figure 4, single fibre tensile testing showed that the reclamation under SHS atmosphere at 450°C (DEECOM T3) had the lowest impact on the residual strength and stiffness

of the fibres. DEECOM T3 rCFs retained over 94% strength, 97% strain, and 97% of their modulus, when compared to vCFs. The higher temperature reclamation, DEECOM T4 trial, caused a significant reduction in rCF tensile strength and strain ($p < 0.05$), however the modulus remained unchanged when compared to vCF ($p > 0.05$).

For the legacy ELG reclamation process, increasing the processing temperature from 450°C to 500°C, similarly had no statistically significant effect on the modulus of the rCFs, when compared to vCF ($p > 0.05$). However, across all three trials a reduction in rCF strength and strain of around 50 – 60 % was observed, when compared to vCF. Trial 1 fibres have a significantly higher strength than trial 2 fibres (no significant difference to trial 3) and a significantly higher breaking strain than both trial 2 and 3 fibres ($p < 0.05$). There is no statistically significant difference in breaking stress, strain, and modulus between trial 2 and 3 fibres ($p > 0.05$).

In literature, higher retained tensile strengths have been reported for the legacy ELG process [7]. However, while there may be room for optimising these results, for the purposes of showing a complete recycling pathway, the processing conditions of DEECOM T3 and ELG T1 were used to reclaim fibres for manufacturing and testing of composite coupons.

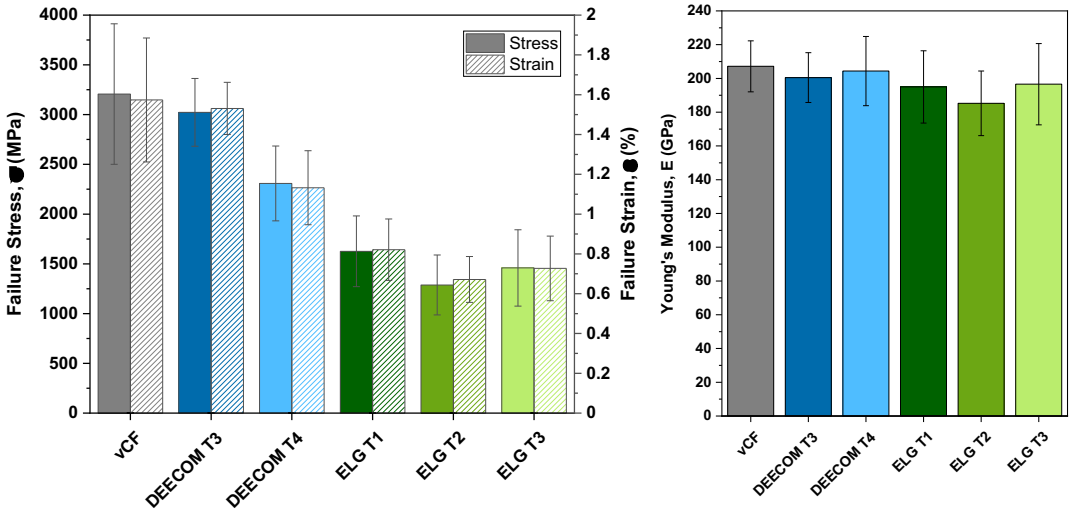

Figure 4: SFTT results expressed as the mean ± SD. A) Failure stress and failure strain. B) Young's modulus. Statistical comparisons were performed using two-tailed Student's t-test. Differences with p < 0.05 are considered significant.

3.3 Coupon tensile properties

All specimens showed linear-elastic tensile behaviour and brittle failure. From the tensile tests, the failure strength, failure strain, and Young's modulus of the coupons were determined. The mean values and standard deviations are collated in Table 2.

Table 2: Experimental tensile test results expressed as the mean ± SD.

Coupon properties		vCF	DEECOM T5	ELG T1
Fibre V_f *(1 SD)*	[%]	24 (*± 5)*	25 (*± 2)*	28 (*± 1)*
Failure stress (*1 SD)*	[MPa]	499 (*± 78)*	300 (*± 26)*	225 (*± 13)*
Failure strain *(1 SD)*	[%]	1.2 (*± 0.1)*	0.87 (*± 0.05)*	0.7 (*± 0.05)*
Young's modulus *(1 SD)*	[GPa]	40 (*± 4)*	35 (*± 2)*	34 (*± 2)*

The large reduction in properties between vCF coupons and the rCF coupons indicates that, as was seen in Figure 3, the reclamation likely removed the sizing from the fibres, which has influenced the fibre-matrix interfacial adhesion. Furthermore, manufacturing defects can significantly reduce mechanical properties, as discussed further below.

3.3 Coupon micro-structure

From Figure 5A to C, it is evident that the manufacturing process did not achieve the high degree of fibre alignment that was desired. Furthermore, large voids were also observed in some coupons (Figure 5B). The extensive fibre misalignment can be linked to the fibre lengths and the HiPerDiF machine set-up, as explained below.

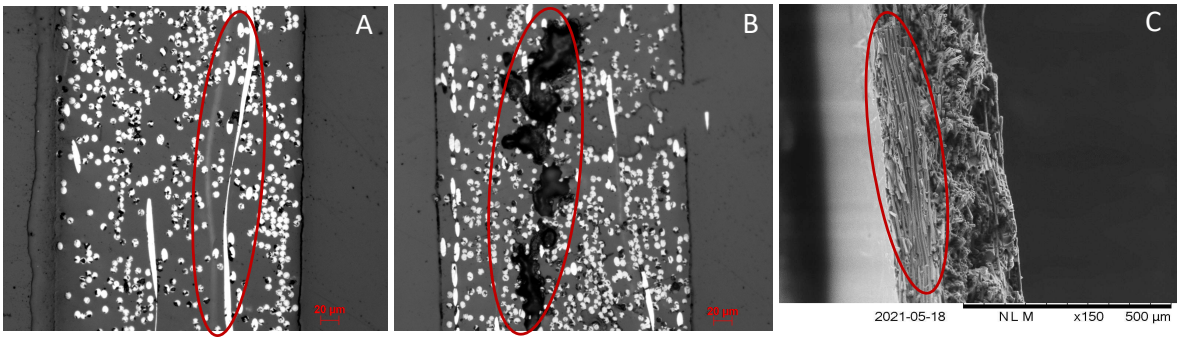

Figure 5: A) Microscope image of cross-section of vCF coupon - misaligned fibres. B) Microscope image of cross-section of DEECOM T5 coupon - voids. C) SEM image of ELG T1 coupon fracture surface – misaligned fibres.

3.4 Fibre length distribution

The fibre length distributions of the three fibre-types are shown in Figure 6.

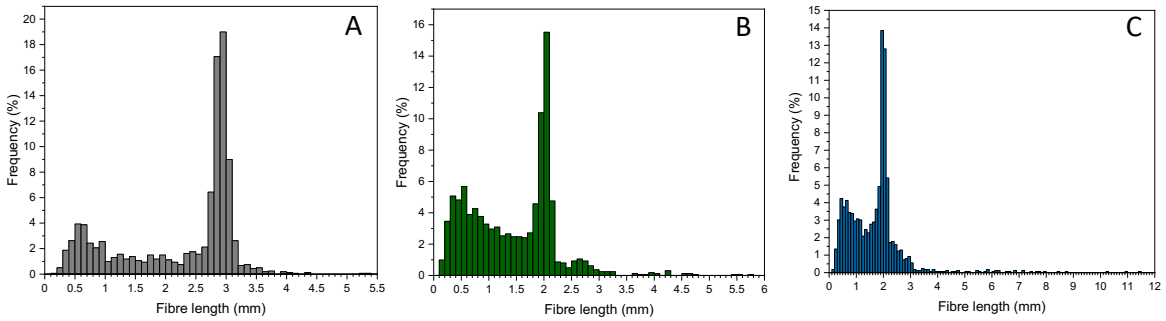

Figure 6: Fibre length measurements. A) vCF fibre lengths. B) ELG T1 fibre lengths. C) DEECOM T5 fibre lengths.

Owing to the cutting method used on the EOL material prior to reclamation, the rCF samples contained longer fibres than the vCF samples, (see Figure 6C). During prepreg tape manufacture it was observed that long fibres were initiating flocculation in the water tanks. The fibre flocks, inherently misaligned, were then pumped through the system and were integrated in the dry fibre preform. There were also many fibres shorter than the desired 2 or 3mm. Around 20% of the vCFs, 26% of the DEECOM T5 rCFs, and 35% of the ELG T1 rCFs were shorter than 1 mm. These short fibres can more easily misalign in-between the parallel plates of the orientation head (spaced 0.3 mm apart), and thus likely contributed to the fibre-misalignment seen in all specimens [8].

From these results, it is clear that the fibre length distribution needs to be narrowed, bounded at the lower end by the minimum fibre length which can be aligned by the HiPerDiF set-up and at the upper end by the maximum fibre length which can be sustained in suspension without initiating flocculation. As flocculation is related to the overcrowding of fibres in the suspension, the fibre concentration can also be altered to shift the upper bound/the maximum fibre length.

4. Conclusions and future work

This work shows the feasibility of recycling EOL 3Di sails, by reclaiming carbon fibres using two different gasification-type reclamation technologies and remanufacturing composite coupons using the HiPerDiF manufacturing technology. Early characterisation work has shown manufacturing defects such as voids and many misaligned fibres, indicating that both the pre-reclamation EOL waste-chopping and the coupon manufacturing method require refinement.

Future manufacturing trials will be repeated with longer fibres of a narrower fibre length distribution, dispersed at lower concentration. The alignment achieved in these trials will be quantified in order to evaluate the changes made to the manufacturing method.

Acknowledgements

This work was funded under the UK Engineering and Physical Science Research Council (EPSRC) Centre for Doctoral Training in Advanced Composites for Innovation and Science (EP/L016028/1) and North Sails. We would like to thank North Sails, Future Fibres, and the National Composites Centre for supplying materials, and Longworth and ELG Carbon Fibre for carrying out reclamation trials.

5. References

1. Pickering SJ. Recycling technologies for thermoset composite materials-current status. *Compos Part A Appl Sci Manuf.* 2006;37(8):1206–15.
2. Pimenta S, Pinho ST. Recycling carbon fibre reinforced polymers for structural applications: Technology review and market outlook. *Waste Manag*. 2011;31(2):378–92. Available from: http://dx.doi.org/10.1016/j.wasman.2010.09.019
3. Oliveux G, Dandy LO, Leeke GA. Current status of recycling of fibre reinforced polymers: Review of technologies, reuse and resulting properties. *Prog Mater Sci*. 2015;72:61–99.
4. Pakdel E, Kashi S, Varley R, Wang X. Recent progress in recycling carbon fibre reinforced composites and dry carbon fibre wastes. *Resour Conserv Recycl*. 2021;166(November 2020):105340. Available from: https://doi.org/10.1016/j.resconrec.2020.105340
5. Yu H, Potter KD, Wisnom MR. A novel manufacturing method for aligned discontinuous fibre composites (High Performance-Discontinuous Fibre method). *Compos Part A Appl Sci Manuf*. 2014;65:175–85.
6. Longana ML, Yu H, Lee J, Pozegic TR, Huntley S, Rendall T, Potter KD, Hamerton I. Quasi-isotropic and pseudo-ductile highly aligned discontinuous fibre composites manufactured with the HiPerDiF technology. *Materials*. 2019;12(11).
7. Pimenta S, Pinho ST. The effect of recycling on the mechanical response of carbon fibres and their composites. *Compos Struct*. 2012;94(12):3669–84.
8. Huntley S, Rendall T, Longana M, Pozegic T, Lee J, Potter K, Hamerton I. Modelling of the HiPerDiF method for manufacturing recycled composites using smoothed particle hydrodynamics. *ICCM Int Conf Compos Mater*. 2019;2019-August.

COMPOSITE PYROLYSIS OIL: A SOURCE OF INDUSTRIALLY RELEVANT CHEMICAL FEEDSTOCK MOLECULES?

Jonathan Meegan[1], Claude Billaud[2], Ann-Christine Johansson[3], Jonas Persson[3], Mirva Niinipuu[3], Tommy Öman[4]*

[1]Solvay Materials, Abenbury Way, Wrexham LL139UZ, UK; jonathan.meegan@solvay.com

[2] Solvay Materials, 87 Av. des Frères Perret, 69190 Saint-Fons, France

[3] Division Bioeconomy and Health, Biorefinery and Economy, RISE Energy Technology Center AB, SE-941 28 Piteå, Sweden

[4] Division Material and production, Polymer, fiber and composite, RISE SICOMP AB, Box 271, SE-94333 Öjebyn, Sweden

Abstract: *Pyrolysis is emerging as a leading technology to enable the recycling of the carbon fiber component of composite materials and the related circular economies that might develop from its reuse. To date, typical pyrolysis operations divert the vapours and gases of the pyrolysed composite to abatement units and recycle the heat generated back into the pyrolysis furnace to reduce the overall energy burden of the process. This report demonstrates that the vapour phase originating from pyrolysed commercial epoxy resin composites contains up to 30 wt% of amines and phenols, and that those molecules are accessible by selecting the temperature of the pyrolysis reaction and trapping the vapour phase as an oil. The molecules recovered from the oil could be used as potential feedstocks for the chemical industry and enhance the circular economy associated with composite materials.*

Keywords: Pyrolysis; composite; circular economy; recycling; upgrading

1. Introduction

The ability to recycle reinforced composite materials has become a topic of growing interest and priority for the composites industry in recent years. This is due to increased use of the materials in aerospace, automotive, wind energy and recreational applications as a result of their high stiffness to weight ratio.

In combination with societal pressure to ensure that industries, markets and materials reduce their environmental footprints, and supply chain pressure to minimise waste, efforts are underway in the composites industry to understand and demonstrate the most appropriate, lowest environmentally impacting [1] way of managing the waste products created during both the manufacturing and the end-of-life phase of reinforced composite materials. The ultimate goal of these efforts is for the composites industry to be able to demonstrate that it can play a viable role within a true circular economy for chemical products [2].

Recent advances in areas such as 'Vitrimer' chemistry [3] offer an indication that inherently recyclable thermoset chemistries may be just over the commercial horizon, but the current challenge in enabling any circular economy for composite materials, is until recently the design philosophy has been one of ultimate permanency in the application environment. This permanency is a key driver in the application, or use phase of a composite material as they are often used as longer service lifetime alternative, or direct substitute for incumbent metallic

  doi:10.5075/epfl-298799_978-2-9701614-0-0

solutions with service lifetimes in the order of 10 to 15 years. Furthermore, composite materials have evolved over the last 30 years from simple combinations of non-modified matrices and glass or carbon fiber reinforcement to become a complex material formulation of resin matrix, filler particles, toughening additives, polymeric and non-polymeric interlaminar modifiers, and highly engineered reinforcement phases and optional stitching materials which can create difficulties relating to the management of materials in chemical or solvent based recycling processes [4].

Pyrolysis is a known and attractive option for recycling mixed plastic waste materials [5] [6]. A ranking of the various recycling technologies and a fit to a Technology Readiness Level (TRL) vs. an attractiveness ranking and cost of investment to achieve an economically viable scale has been proposed [7] with the conclusion that pyrolysis offers the best balance of TRL, energy balance and recovery of useful mass from composite materials [1].

Composite material has been demonstrated to be compatible with the pyrolysis process, with a range of glass or carbon fiber composites being shown to be recyclable [8] [9], and the gas yield of pyrolysed polyester, phenolic and epoxy composite matrices evidenced to contain a number of short chain alkane or alkene materials; the ratio of each component in the gas phase was shown to be dependent on the pyrolysis temperature used.

The aim of this work was to use a novel pyrolysis approach in which pyrolysis vapour originating from non toughened (CYCOM®890) and toughened (CYCOM®977-2) carbon fiber reinforced composite was condensed to form an oil phase. The oil phase was then compositionally analysed to determine if it it could be used as a source of industrially relevant molecules.

2. Materials and Method

2.1 Composites

Two commercialised, high volume aerospace composite materials, CYCOM® 890 and CYCOM® 977-2, were selected by Solvay. CYCOM® 890 is a non-toughened thermosetting epoxy chemistry, processed using liquid processing methods, whereas CYCOM® 977-2 is an autoclave cured polyether sulfone toughened thermosetting epoxy chemistry.

The preparation method, fiber volume fractions of the composite and the atomic composition of each resin phase are shown in Table 1 below.

Table 1: Composite samples used in this study and the theoretical resin composition

Resin	Fiber	Preparation method	Fiber volume fraction (%)	Theoretical resin composition (wt%)					
				C	H	N	O	S	Cl
CYCOM® 890	T300 3k Plain Weave	Infusion	53	68.1	7.25	6.76	9.27	0	8.58
CYCOM® 977-2	STS40 UD	Autoclave	63	60.6	15.5	3.51	16.9	3.47	0.01

  doi:10.5075/epfl-298799_978-2-9701614-0-0

2.2 Pyrolysis

Pyrolysis operations were performed on the laboratory scale system as described in Figure 1. The equipment comprises of a batch pyrolysis reactor, an oil recovering system and gas analysis. In the reactor the composite material is pyrolysed in an inert atmosphere to form pyrolysis vapour, solid product and non-condensable gas. In the oil recovering system the pyrolysis vapours are condensed to an oil and collected in two vessels and finally the composition of the non-condensable gas is analysed using Gas Chromatography (GC).

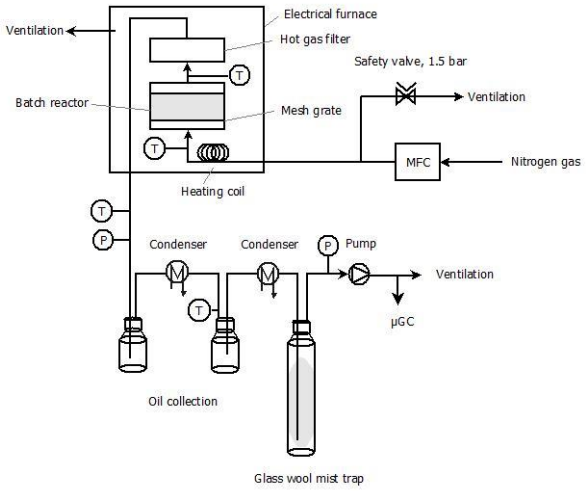

Figure 1. Schematic drawing of laboratory batch pyrolysis system.

In a typical pyrolysis experiment, approximately 500 g of 4 mm thick composite laminate cut into 2.5 x 2.5 cm² square coupons were placed in the pyrolysis reactor positioned in an electrical furnace. The furnace was heated at 5 °C/min to an internal gas temperature of 500 °C and inerted by a flow of nitrogen of 3.0 L/min. The residence time of the hot pyrolysis vapors varied during the pyrolysis depending on the rate of degradation but was estimated to be less than 1 minute. The residual solid product remained in the reactor while the pyrolysis vapours were continuously condensed and collected using indirectly condensers filled with cooling liquid maintained at -15 °C. and monitored by two thermocouples were mounted on the oil condensing bottles. The residual pyrolysis aerosols were collected in a glass wool mist trap. Gas composition was monitored using a Varian 490 micro gas chromatograph equipped with two thermal conductivity detectors (TCD) and checked for CO, CO_2, H_2, N_2, O_2, CH_4. The pyrolysis operation was ended when no pyrolysis gas was detected by the online gas chromatograph, typically after approximately 120 minutes at 500 °C. The furnace was switched off and allowed to cool to room temperature under a low nitrogen flow (0.5 L/min) before being dismantled and the collected oils recovered from the bottle traps. By weighing the composite material, the oil and the solid product and by calculating the weight of the pyrolysis gas components it was possible to make mass balances and determine the product yields.

  doi:10.5075/epfl-298799_978-2-9701614-0-0

2.4 Analytical methods

2.4.1 Composite samples

Thermogravimetric analyses (TGA) on composite samples were performed using a TA Instruments Q500 instrument operating under an air or N_2 atmosphere. Samples were ramped at 5 °C/min to 1000 °C or subjected to an isothermal hold for 2 h at 50 °C increments from 50 °C to 1000 °C.

Analytical pyrolysis, pyro-GC-MS/FID, analysis was performed on powdered composite samples using a Shimadzu QP2010 gas chromatograph coupled to a mass spectrometer (MS) and flame ionization detector (FID) using an Y connector. Initially the column (Restek RTX-1701) temperature was 35°C (held for 6 min) followed by ramping the temperature by 3 °C/min to 75 °C then ramping was changed to 10 °C/min to reach the final temperature of 270 °C (held for 10 min). The MS mode was EI at 70 eV, the temperature was 240°C and the scan was 29-500 m/z.

A powdered composite sample was placed in a stainless-steel pyrolysis cup (PY1-EC80F, Frontier Laboratories Ltd.) which was attached to a multi-shot pyrolyzer (EGA/PY-3030D Frontier Laboratories Ltd.). The sample was kept at 200 °C for 1 h while the MS and FID data was acquired. The sample was then moved from the heating zone while running a blank sample and ramping the temperature to the next temperature. The same procedure was repeated at 260 °C, 320 °C, 380 °C, 440 °C and 500 °C. The compounds were identified by comparing their mass spectra profiles to those in the NIST 2014 library (National Institute of Standards and Technology, US). Semi-quantitative analysis of detected chemicals was done by dividing the individual peak area from the FID-spectra with the total detected FID area. To emphasize the results from the analytical pyrolysis the pyrolysis products were grouped into following categories: Hydrocarbons, Chlorinated amines, Phenols, Amines, Heterocyclic, Sulphur containing compounds, Other oxygenated compounds, and Unidentified.

2.4.2 Pyrolysis products

For the GC-MS/FID analysis of oil samples, the samples were diluted in ethanol (1:10), and the instrumental parameters for the GC-MS/FID analysis were the same as described in section 2.4.1.

SEM analysis of fibers was performed on a Hitachi TM3030 plus instrument.

Thermogravimetric analyses (TGA) on pyrolysed fibers were performed using a TA Instruments Q500 instrument operating under an air or N_2 atmosphere. Samples were ramped at 5°C/min to 1000 °C under an air atmosphere.

Liquid Chromatography – Mass spectrometry (LC/MS) was performed using Agilent UPLC 1290 instrument (LC) with a Poroshell 120-EC-C18, 50 x 2.1 mm 1.9 µm column, and an Agilent MSD 6125C (MS) detector.

3. Results and discussion

3.1 Analytical evaluation of composite samples

The thermal decomposition and the pyrolysis products of the two composite materials were evaluated using TGA (Figure 2) and analytical pyrolysis. Non toughened CYCOM® 890 resin is

  doi:10.5075/epfl-298799_978-2-9701614-0-0

shown to display a much more rapid mass loss than CYCOM® 977-2 which shows greater persistence at higher temperatures, presumably due to the thermoplastic toughening agent increasing the char yield of the sample [10].

Table 2. Calculated residual resin content on fiber after ramped TGA to 500°C

Resin phase	Calculated composite resin fraction (wt%)	TGA determined mass loss (wt%)	Residue remaining on fiber (Composite resin fraction – TGA mass loss) (wt%)
CYCOM® 890	37	30	6
CYCOM® 977-2	28	19	9

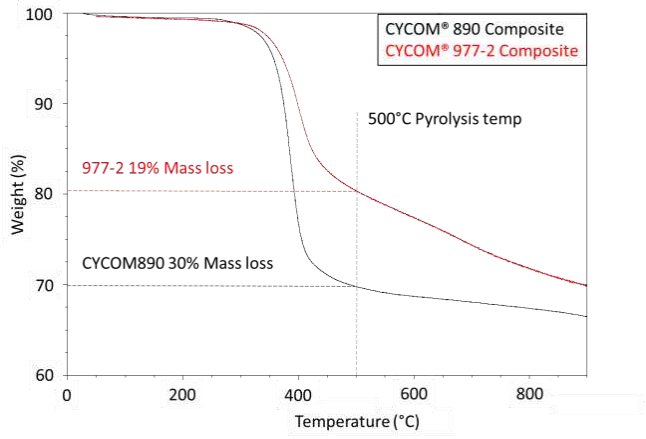

Figure 2. Ramped TGA analyses of composite materials performed in a N_2 atmosphere at a 5 °C/min ramp rate.

Comparative TGA analysis in air or N_2 of the composite samples using a 50 °C, 60 minutes dwell, stepwise isothermal profile is shown in Figure 3. Through comparison of the experiments on similar samples performed in an oxidizing atmosphere (air) and an inert atmosphere (N_2) it can be seen that the cumulative mass loss profile occurs over two temperature regions, <500°C and >500 °C. The carbon fiber component of the composite is prone to oxidative degradation at high temperatures, and as such the common mass loss in the region >500 °C is attributed to the degradation of the carbon fiber material [10]. The mass loss events in the region <500 °C for each sample, are attributed to unique, chemistry dependent degradations of the resin phase. For this reason 500 °C was used as the dwell temperature for the pyrolysis experiments.

Pyro-GC-MS/FID analysis at isothermal temperatures between 200 °C and 500 °C (Figure 4) showed that the pyrolysis products of the degraded resin phases were reflecting of the elemental composition of each composite material (Table 1); with the more oxygen rich CYCOM®977-2 sample evolving a higher wt% of phenolic species that the nitrogen rich CYCOM®890 sample. It is important to note that pyrolysis products from both the composite materials also contained a significant amount of material which could not be confidently matched to known mass spectrum fragmentation patterns using library matching, this material was labelled as unidentified in Figure 4.

  doi:10.5075/epfl-298799_978-2-9701614-0-0

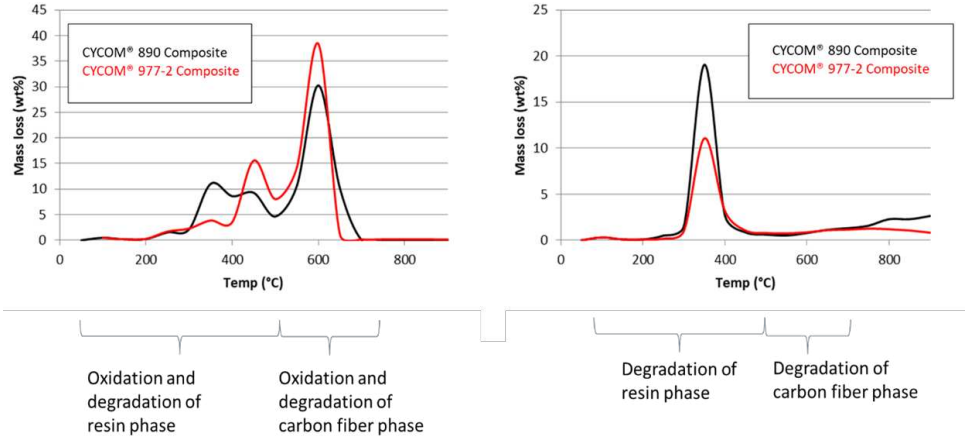

Figure 3. Results of stepped isothermal TGA of composite samples in air (left) and nitrogen (right) atmospheres.

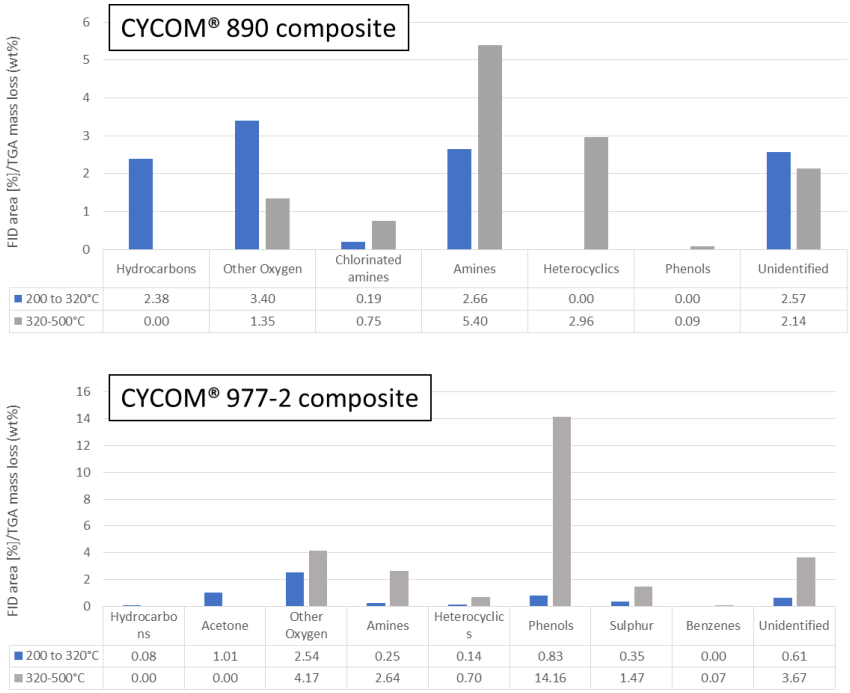

Figure 4. Composition of pyrolysis products from stepwise pyrolysis of composites expressed as relative amount of pyrolysis product groups from FID detector normalised with mass loss from TGA.

3.2 Batch pyrolysis of composite materials

The products from the pyrolysis of the composite materials are a solid product (mostly fibers but also some coke produced from the polymers during the pyrolysis), a liquid (one aqueous fraction and one oily fraction) and non-condensable gas.

The total recovered mass from the pyrolysis experiments were relatively good at 95-97 wt% of the original charge. The resin matrix in the composite was mainly converted to a oily liquid fraction, 20.4 wt% versus 10.3 wt % for CYCOM® 890 and CYCOM® 977-2, respectively, but also some aqueous liquid fraction and non-condensable gas, mainly composed of methane, carbon oxides and hydrogen. It is clear that the chemistry of the resin phase had a strong influence over

the efficiency of the mass of the oil fraction and non-condensable gas recovered from the process, with the mass balance of CYCOM® 890 resulted in significantly more oil fraction and less water fraction than CYCOM® 977-2.

3.2.1 Characterization of recovered fibers

TGA analysis of the pyrolyzed fiber recovered from the reactor agreed with SEM analysis (Figure 5), and indicated that the obtained fibers were contaminated with a residue, which could be removed by combustion treatment in air [11] to deliver a fiber surface which was shown to be as visibly clean as a commercially sourced pyrolysed fiber sample.

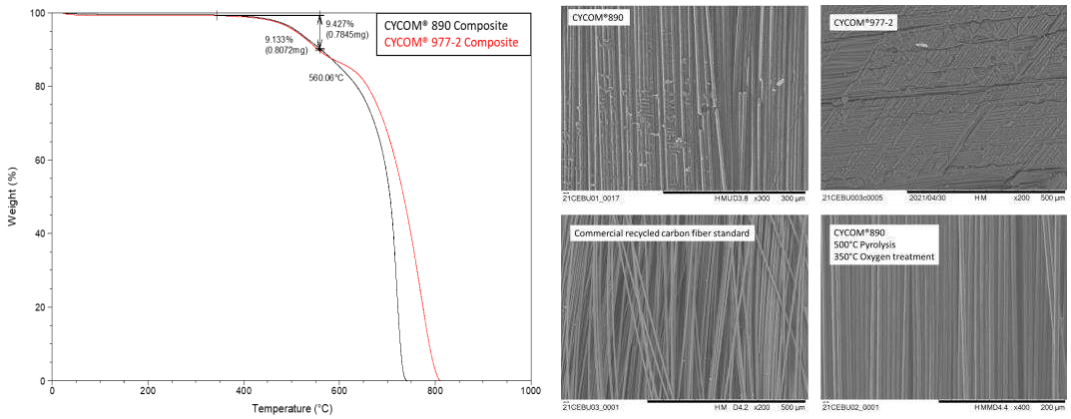

Figure 5. TGA in air of recovered fiber fractions showing mass change due to coke residue on the fiber (left) and SEM images of recovered fibers (right).

3.2.2 Characterization of pyrolysis liquids

GC-MS/FID was used to analyse the composition of the pyrolysis liquids (Figure 6). In keeping with the data reported for the analytical pyrolysis analysis in the earlier experiments (Figure 4) The CYCOM® 890 composite returned an amine rich oil phase and the CYCOM® 977-2 composite returned an oil phase rich in phenolic functionalities.

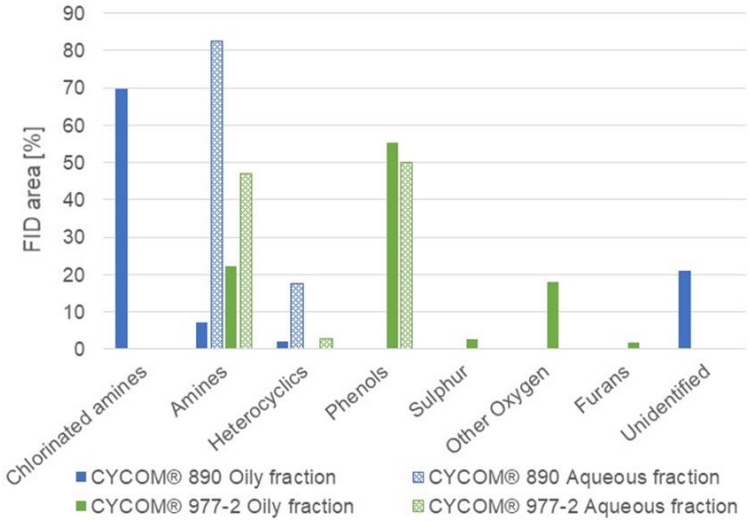

Figure 6. Gas chromatograph analysis of the pyrolysis liquids. The composition is expressed as relative amount of pyrolysis product groups from the FID detector.

  doi:10.5075/epfl-298799_978-2-9701614-0-0

4. Conclusions

The principle of using mixed composite waste as a feedstock for a selective pyrolysis process to produce aniline, and phenol based molecules has been demonstrated. This concept, in combination with optional segregation of composite waste by resin type could lead to the utilisation of the resin phase in composite materials as a feedstock for building block chemicals by the chemical industry.

5. Acknowledgments

This work was in part funded by the European Regional Development Program (ERDF) SMART Cymru 2014-2020 East Wales: Feasibility of reclaiming propylene from carbon fiber composite waste.

6. References

[1] Krauklis AE, Karl CW, Gagani AI, Jorgensen JK, Composite Material Recycling Technology—State-of-the-Art and Sustainable Development for the 2020s, Journal of Composites Science, vol. 5, no. 28, 2021.

[2] Ellen MacArthur Foundation, Universal circular economy policy goals, Ellen MacArthur Foundation, 2021.

[3] Yue L, Guo H, Kennedy A, Patel A, Gong X, Ju T, Gray T, Manas-Zloczower I, Vitrimerization: Cnverting Thermoset Polymers into Vitrimers, ACS Macro Letters, vol. 9, no. 6, pp. 836-842, 2020.

[4] Pickering SJ, Recycling technologies for thermoset composite materials -current status, Composites Part A: applied science and manufacturing, vol. 37, pp. 1206-1215, 2006.

[5] Jeswani H, Kruger C, Russ M, Horlacher M, Antony FL, Hann S, Azapagic A, Life cycle environmental impacts of chemical recycling via pyrolysis ofmixed plastic waste in comparison with mechanical recycling andenergy recovery, Science of the Total Environment, vol. 768, p. 144483, 2021.

[6] Klaimy S, Lamonier J-F, Casetta M, Heymans S, Duquesne S,Recycling of plastic waste using flash pyrolysis – Effect of mixture composition, Polymer Degradation and Stability, vol. 187, p. 109540, 2021.

[7] Balaji A.B, Rudd C, Xiaoling L, Recycled Carbon Fibes in Automobiles: Towards Circular Economy, Materials Circular Economy, vol. 4, 2020.

[8] Cunliffe AM, Jones N, Williams PT, Pyrolysis of Composite Plastic Waste, Enivronmental Technology, vol. 24, pp. 653-663, 2002.

[9] Torres A, De Marco I, Caballero BM, Laresgoiti MF, Legarreta JA, Cabrero MA, González A, Chomón MJ, Gondra K, Recyling by pyrolysis of thermoset composites: characteristics of the liquid and gaseous fuels obtianed, Fuel, vol. 79, pp. 897-902, 2000.

[10] Tranchard P, Duquesne S, Samyn F, Estébe B, Bourbigot S, Kinetic analysis of the thermal decomposition of a carbon fibre-reinforced epoxy resin laminate, Journal of Analytical and Applied Pyrolysis, vol. 126, pp. 14-21, 2017.

[11] Irisawa T, Aratake R, Hanai M, Sugimoto Y, Tanabe Y, Elucidation of damage factors to recycled carbon fibers recovered from CFRPs by pyrolysis for finding optimal recovery conditions, Composites Part B, vol. 218, p. 108939, 2021.

  doi:10.5075/epfl-298799_978-2-9701614-0-0

DEVELOPMENT OF RECYCLED THERMOPLASTIC COMPOSITES TECHNOLOGY FOR AEROSPACE IN A REAL-WORLD ENVIRONMENT

Johan Meuzelaar[a], Ilse ten Bruggencate[b], Thomas de Bruijn[a], Ferrie van Hattum[b]

a: GKN Fokker Aerostructures B.V., the Netherlands (johan.meuzelaar@fokker.com)
b: TPAC / Saxion, University of Applied Sciences Enschede, the Netherlands

Abstract: *Usage of composite materials reduces aircraft structural weight and thereby fuel consumption and emissions. Thermoplastic composites not only feature excellent mechanical properties, but also the opportunity for re-cycling.*

This paper presents the further development of the so-called Low-Shear Mixing process; a low-energy, low-cost technique to re-use fiber-reinforced thermoplastics by transforming waste in compression-molded products. Previous fundamental research has already shown the potential in terms of processability, cost, CO_2 and weight reduction.

Current follow-up research focusses on feasibility of this technology in a real-world operational aircraft environment, progressing towards series production. For that, the recycled material's strength was tested under extreme in-service environmental conditions, impact-resistance has been verified and lightning strike protection was explored. Finally, demonstrators have been developed to be test-flown on an experimental rotorcraft.

Keywords: Recycling; Thermoplastic Composites; Aerospace; Sustainability

1. Introduction

It is the ambition of GKN to be the most sustainable partner for any aerospace OEM. To achieve that, GKN is actively involved in development of technologies for new aircraft and propulsion concepts, which will enable emission-free flight in the near future. One of these new technologies exploited to the full by GKN is thermoplastic composite with its high mechanical performance (leading to lower structural weight) and unique short-cycle processes like press-forming (reduces energy consumption per production cycle) and welding (eliminating fasteners, thus weight and cost). Apart from these readily used advantages, there is another clear benefit of thermoplastics over more traditional thermoset composites: the opportunity to easily re-use fiber and matrix (i.e. the total composite). To turn this recycling opportunity into a reality, GKN has been collaborating with the TPAC of Saxion for many years in a variety of development programs.

The ThermoPlastic composite Application Center (TPAC) focuses on the application of thermoplastic composites and related technologies by developing proofs of concepts for industry. One of the research areas of TPAC is the recycling of thermoplastic composites. Together with partners, including GKN Fokker Aerostructures, TPAC has recently finished the TPC-Cycle project [1]. In this project a recycling route for Thermoplastic Composite (TPC) materials was developed, with the focus on finding the optimum process and process settings to cost-effectively recycle TPC waste to obtain the highest performance possible. This project

  doi:10.5075/epfl-298799_978-2-9701614-0-0

resulted in a fully recycled rotorcraft access panel from carbon/polyphenylenesulfide (C/PPS) Toray TC1100 [2]. For TPAC the research goal would be to further develop and industrialize the developed recycling route, for varies industries including aerospace, automotive, etcetera.

2. Technology Description

Different recycling approaches are possible for TPC waste material. With thermal or chemical recycling the biggest disadvantage is that often the resin is discarded in these processes (consuming energy and creating more waste) and only the fibers are reclaimed. With mechanical recycling, as used here, both the fibers and matrix can be reused.

TPAC developed a new recycling route (rTPC) within the TPC-Cycle project, Figure 1, which recycles both the thermoplastic matrix and the fibers (i.e. full material). In this process, the post-industrial material, continuous carbon fiber-reinforced polyphenylenesulfide waste, is first collected (A). To keep the waste stream traceable, ideally the rTPC process would be placed close to the production site of the original parts that produce the waste stream. Hereby the traceability will be high, and the material transport will be kept to a minimum resulting in a lean process.

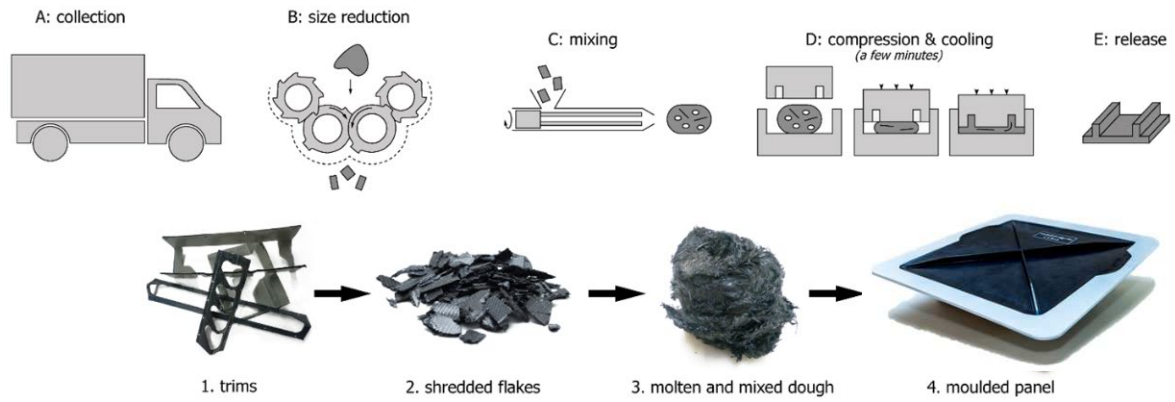

Figure 1. rTPC Recycling Process [3]

After collection, the trims and offcuts of a consolidated C/PPS laminate are reduced in size by means of an Untha S20 shredder without a screen. This shredding step (B) is repeated five times, to ensure the desired fiber length of 15 to 20 mm [4]. The shredded composite is diluted with PPS pellets (Celanese Forton 0214), the same matrix as the C/PPS laminates. This dilution is done to achieve a lower fiber volume content (Vf) of 20%, promoting flow in the mold cavity. The material is dried in a convection oven for a minimum of 2 hours at 120 °C.

Next, the dried material is fed into the hopper of a low-shear mixer (C). This machine heats and mixes the material, without reducing the fiber length, to ensure a long fiber output. The mold is mounted in an Engel insert IN130-500V, and kept at a temperature of 160 ± 10 °C. After the low-shear mixing cycle is completed, the material charge is quickly transferred to the mold, and compressed (D). After 3 minutes, the part is released from the mold (E). With this process, it is possible to manufacture complex geometries net-shape, all with a cycle time of minutes; thereby creating a fast and economic route for the production of recycled parts.

The resulting material has a low fiber volume fraction compared to continuous fibers and features a non-layered form of discontinuous fiber bundles, see Figure 2 for a typical cross-

section. Since also relatively large scatter in mechanical properties is expected [4], the foreseen applications are merely non-structural parts.

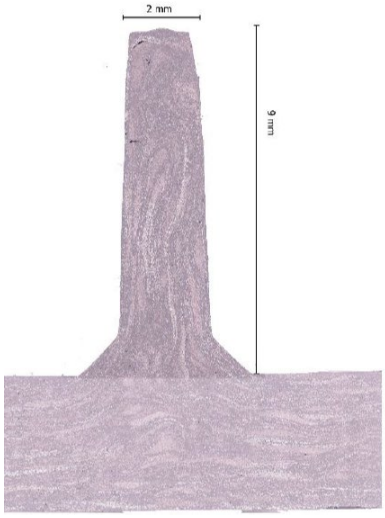

Figure 2. Cross-section of Stiffened Panel showing Fiber Distribution

3. Coupon Testing

To enable design of future applications, the strength values of the rTPC material needs to be established, including the effect of the most severe in-service environmental conditions (temperature, moisture). From previous screening tests, it is known that tensile strength is lower than compression strength for this rTPC material, which would be quite unusual for any continuous fiber-reinforced composite, but is understandable for a discontinuous fiber composite with a high matrix content. Hence, further testing focused on the critical tensile strength in this research.

Because the failure mode is highly influenced (if not dominated) by the matrix or fiber-matrix interface, the critical environmental condition is at elevated temperature. Typically, the strength of composites at elevated temperatures is reduced further by the absorption of moisture. Therefore, the tensile tests are executed at 80 ^{o}C (commonly the maximum in-service temperature to be considered for most aerospace structures) after being saturated in a climate chamber at 70 ^{o}C/85% RH.

The test standard selected is ASTM D5677, [5] for the determination of Open Hole Tensile strength (OHT, i.e. the tensile strength in the presence of a hole – commonly used to cover stress concentrations at holes/fasteners, but also defects), which is commonly used to determine the allowable design value for a continuous fiber reinforced laminate. Batch-to-batch variability and process variance is taken into account by producing test samples from four plates, made out of four different 'blends' of material (unique combinations of two different laminate and two different matrix batches). Negative effect of the expected large scatter is accounted for by testing 40 specimen in total; a larger number of samples than recommended in the ASTM and [6] is chosen to statistically compensate for the expected large variability in properties.

When testing, not all samples failed at the hole, see Figure 3. This has been observed more often when testing discontinuous fiber-reinforced plastics [7] and can be considered as an indication that internal weaknesses of the material are more critical than the stress raiser of a hole. Except

for the lowest test results (failure away from the hole), obtained individual failure load levels were independent of the failure modes/locations. Independent of the failure mode, brittle failures occurred for all samples ('sudden death').

Figure 3. Tensile Test Open Hole (left) and Global Tension Failures (mid and right)

As expected, test results showed large scatter (Coefficient of Variation was 26.0%), but no batch-to-batch variation was observed. Since a Normal distribution was present, the rather severe statistical knockdown by the large scatter was partly compensated and STAT17 analysis [6] resulted in a reasonable B-basis strength allowable (significantly higher as modern 3D-printed polymers [8] for instance). This OHT strength data can be utilized in the design of useful, safe applications in rTPC technology, Figure 4 depicts the statistical evaluation of the test results.

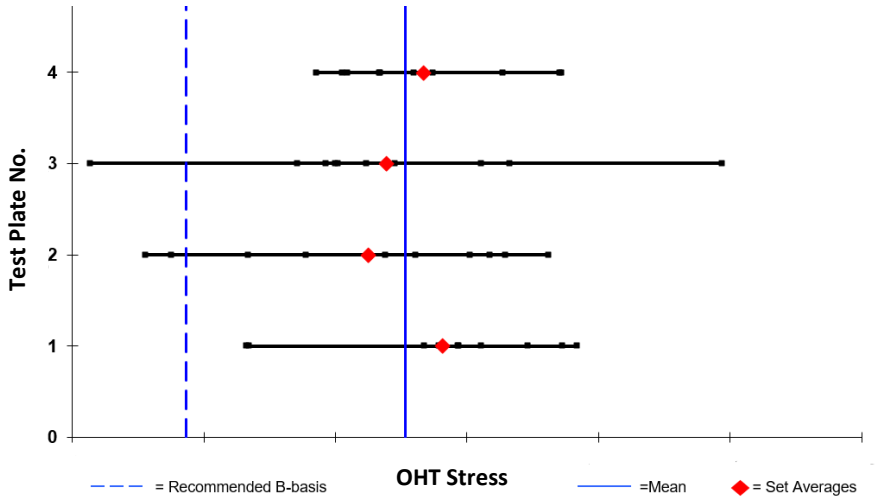

Figure 4. STAT17 Evaluation of the Tensile Test Data

4. Impact Sensitivity Trials

Continuous fiber-reinforced composites are known to be sensitive to impact, where damages small in visual appearance can lead to significant reductions in (compressive) strength. Therefore, composites used in aerospace structural applications are tested and designed for

impact strength as a part of their certification philosophy. Although the foreseen applications of the rTPC technology are non-structural parts and therefore strictly speaking do not have to be damage tolerant (as they are non-load carrying and their failure is not catastrophic by definition), impact sensitivity has been studied as complete loss of these parts could result in subsequent damage when the non-structural part would be lost from the aircraft. Moreover, it is economically undesirable to have parts damaged too easily.

Aim of testing is to investigate the structural damage of the product when subjected to a Barely Visible Impact (BVID), which is defined as the damage caused by the energy needed to produce a 1.0 mm (unrelaxed) dent *or* the damage caused by the cut-off energy, which is here set at 35 J (legacy value) – whatever comes first. The 1.0 mm unrelaxed dent is a traditional value in aerospace, which is believed to result in a relaxed dent of 0.3 mm, the 'classic' limit for visual detectability. 35 J is the energy level associated with a typical tool drop on aircraft and therefore the maximum energy to be accounted for BVID.

The chosen test article is a stiffened panel similar to a typical application with known reference data (geometry, loading) from the previous work in the TPC-Cycle project (ref. [4]), see Figure 5 for the geometrical definition of the test panel and impact locations A-H.

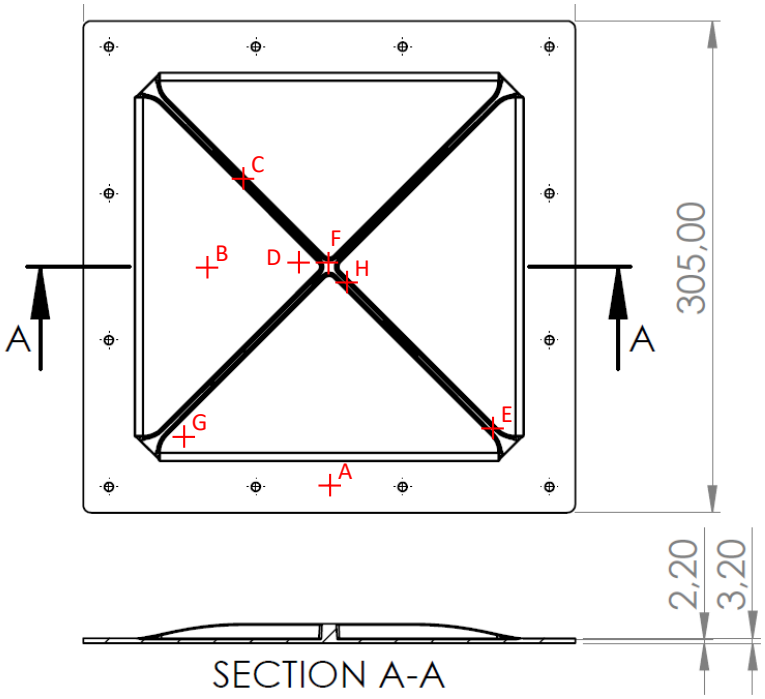

Figure 5. Test Article for Impact Testing incl. Target Locations (dimensions in mm)

4.1 Impact Testing

A typical procedure to create realistic and reproducible impact damage is the so-called Drop Weight method according ASTM D7136 [9], where a steel weight with a hemispherical tip of 12.7 mm diameter is used in a tower with guiding rail to create low-velocity impacts (≤ 15 m/s) using gravity. Panels were bolted on the edges of the (stiff) test support at locations representative for a real application, see Figure 6.

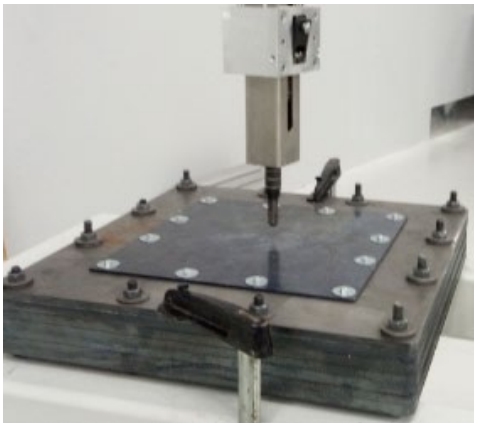

Figure 6. Impacting Set-up

Multiple panels have been impacted at various locations (at the edge, just next to the stiffeners, panel center and quadrant centers, etc. see Figure 5) with increasing energy levels to find the most critical locations and worst damages (large damage with poor visibility from topside of panel). Critical damages found were just next to and right at the stiffener crossing in the center (locations H and F), where impacts up to 10 and 20 J respectively could not create a 1.0 mm BVID dent (but cracking of the stiffener on the backside, see Figure 7). However, increasing the energy by just 2.5-5 J resulted in clearly visible cracks thru the whole panel (i.e. resulting in a *Clearly* Visible Impact Damage, which was much more than the intent).

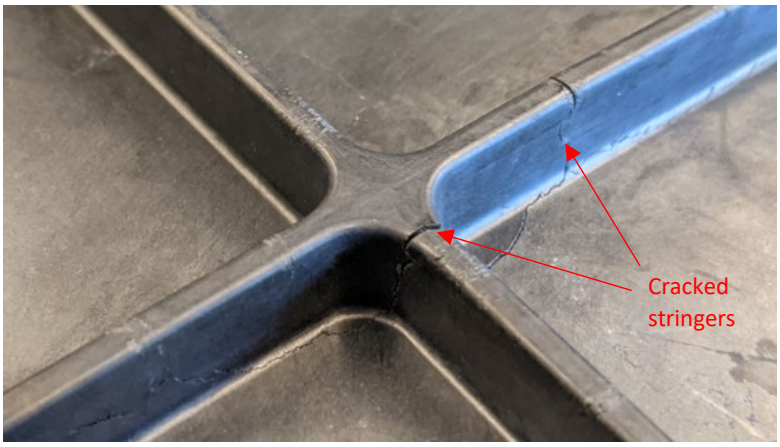

Figure 7. Typical Post-impact Damage at H (backside of panel, 10 J off-center impact)

Non-destructive inspection by means of Phased-Array on a subset of the panels gave no indications of any additional damage other than the visual damage, which is in line with expectations (the non-layered morphology does not create large-scale delaminations as often observed on continuous fiber-reinforced composites).

4.2 Residual Strength Verification

Since it was impractical to find the exact energy level that created a 1.0 mm visible dent, it was decided to impact multiple (new) panels at a single location, one with an energy just below BVID and one with a more energy leading to a damage well beyond BVID. This has been performed for both critical damage locations.

With three of these panels, it was possible to perform a residual strength test on a dedicated set-up simulating the aerodynamic loading by means of air pressure, see Figure 8 (note that the damaged stiffeners are intentionally loaded in tension). For the fourth panel (center impact >> BVID), the damage was too large to seal off during the tests. An undamaged panel has been added as a reference.

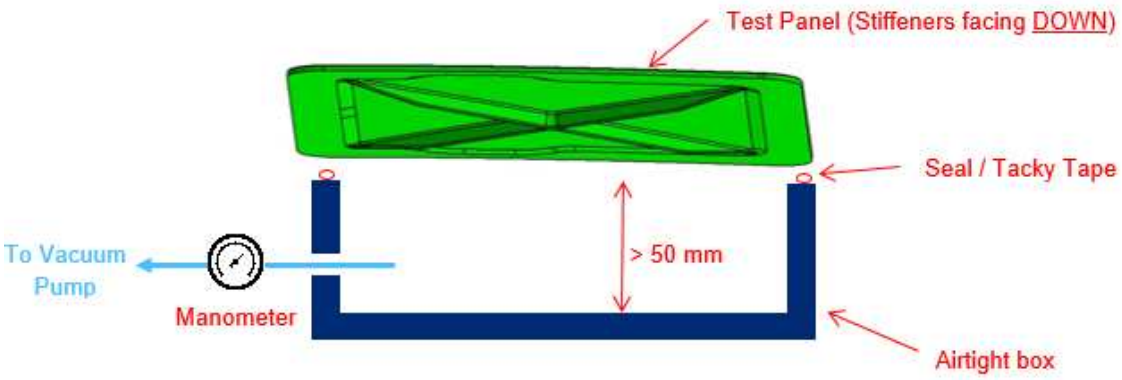

Figure 8. Test Set-up for Residual Strength Test

All panels, including the panel having a damage beyond Barely Visible Impact Damage, were successfully tested up to a 0.9 bar pressure difference, which is well beyond the typical Ultimate Load for these kind of applications (as is required for aircraft certification according [10]) – thereby proving a safe design of the rTPC panels with impact damage. After loads relief, no growth of any of the impact damages was observed.

5. Screening of Lightning Strike Resistance

At the majority of the foreseen rTPC applications, the parts are located in areas of the aircraft that are exposed to lightning threats during flight. Therefore, the parts themselves and any underlying (electric) systems will have to be protected to the direct and indirect effects of lightning. The most common method to protect composite parts is to add an external conductive (metallic) layer that will reduce the mechanical and thermal damage caused by lightning arc attachment on the part and also will create a Faraday's cage to protect any underlying system against electromagnetic effects. It has been investigated if it is possible to integrate such a Lightning Strike Protection (LSP) layer into the rTPC manufacturing process and, if so, how effective it is against lightning direct attachment.

5.1 Manufacturing of LSP Layers

A variety of legacy and novel LSP materials were included in the manufacturing trials: various densities of copper and bronze mesh, expanded & perforated foils have been included in the molding process of standard flat panels to investigate formability and potential effect on final consolidated part quality. Evaluation criteria were final LSP quality (deformations, tears), molded composite quality (homogeneity, presence of any pinholes etc.) and minimum part thickness for complete mold filling. Success rate varied per LSP type (meshes proved very vulnerable), but acceptable part qualities were obtained for most samples featuring foil. The formability results were successfully repeated on strongly curved parts, where only (acceptable) folding and edge effects were observed, see Figure 9 for typical results.

Figure 9. Typical Results for Integrated LSP Foils on Flat and Contoured Parts

5.2 Lightning Strike Testing

After the manufacturing trials, all suitable flat panels (LSP and panel thickness combinations) were selected for arc entry testing. To get realistic results, a typical maximum in-service paint thickness layer of 250 µm was applied to all panels (as the dielectric paint reduces the effectivity of LSP materials [11]). High current testing according test standard ED105A, [12] was used to simulate lightning attachments according standardized threats Zone 1A and 2A on the various rTPC panels, see Figure 10 for the test set-up used.

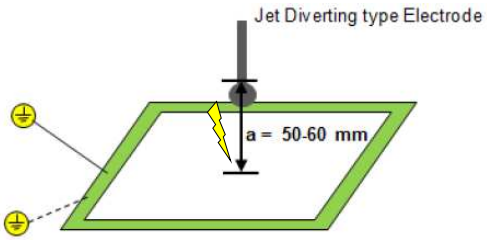

Figure 10. Test Set-up for Lightning Tests

Testing was successful for most of the LSP materials: Zone 2A strikes could be sustained with external damage only (“no puncture”) for all panel thicknesses, but the most severe Zone 1A strikes (applicable only for the aircraft extremities like nose, wing & tail tips) would need a minimum panel thickness of 3mm and/or reinforcement ribs to prevent puncture.

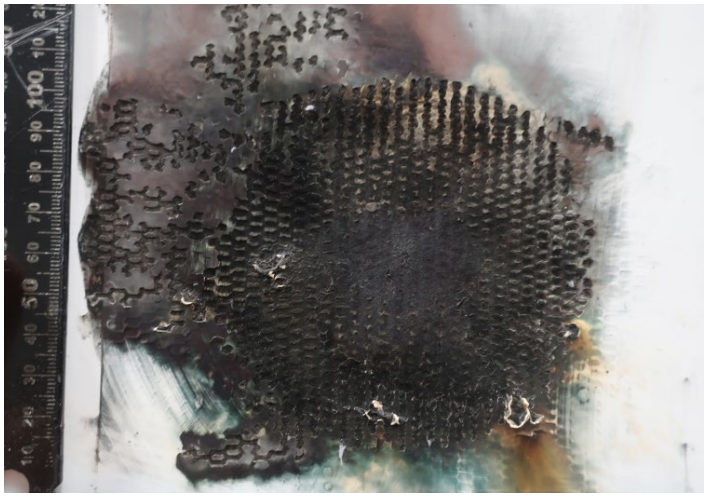

Figure 11. Typical Zone 2A Lightning Damage (photo by Element Materials Technology)

This testing confirms that integrated LSP foils can sufficiently protect aircraft systems/wiring underneath rTPC panels/fairings from direct lightning attachments according to Zone 2A (applicable to the majority of the foreseen applications) and, with some reinforcements, also to the most extreme Zone 1A threats.

6. Demonstrators for Next Generator Civil Tilt Rotor

Last but not least, this research program was also intended to widen the design envelope of the rTPC technology by developing and manufacturing of more complex, contoured parts than the existing near-flat, stiffened panels from the TPC-Cycle project. In the framework of Clean Sky 2 project LIFTT, GKN Fokker Aerostructures develops a new empennage for Leonardo's Next Generation Civil Tilt Rotor (NGCTR) Technology Demonstrator, see Figure 12. Apart from other thermoplastic developments, this Empennage features eight identical (two-piece) small aerodynamic fairings with strongly curved shape which were an ideal candidate for the rTPC technology (continuous fiber-reinforced composites would face large drape-ability issues).

Figure 12. Leonardo's NGCTR Technology Demonstrator with rTPC Fairing (modified from [13])

After several design iterations, Finite Element Method structural analyses (using the OHT allowables from this research program) and design for manufacturing evaluations, a final shape for the fairings was selected. After tool design, the parts have successfully been manufactured at the TPAC laboratory of Saxion. Quality of resulting parts was good (filling, geometry, appearance), which proves the capability of this rTPC process for more complex (non-structural) parts as well thereby expanding the potential application area. The rTPC demonstrator parts are planned to fly in 2023.

7. Conclusions & Recommendations

The additional testing carried out in this research with respect to strength, impact resistance and lightning protection proves the feasibility of the low-shear mixing recycling technology for thermoplastic composites for (non-structural) aerospace application under realistic in-service conditions (including temperature/moisture and damage tolerance aspects). Based on the executed testing, a set of complex-shaped fairings has been successfully developed and manufactured for flying on an experimental rotorcraft, thereby further expanding the design envelope and in-service experience with the rTPC technology.

Next steps would be the industrialization and full qualification of the process, which would enable to re-use the manufacturing leftovers of large, structural thermoplastic components to create panels & fairings for the same application, creating a more closed-loop of manufacturing waste and improving Buy-to-Fly ratio of the utilized thermoplastic material.

  doi:10.5075/epfl-298799_978-2-9701614-0-0

Future research is needed to also enable other thermoplastic matrix composites with a higher melt temperature and viscosity, such as PEKK and PAEK. Moreover, the applicability of rTPC technology for end-of-life products is to be investigated, where traceability, material impurity and ageing aspects would be the major challenges for new applications in aerospace. These efforts are necessary however to lead to a more circular manufacturing concept for (thermoplastic) composites in aviation.

8. Acknowledgements

The testing and manufacturing part of this project was partly financed by Tech For Future (TFF), through the project grant TFF 1916; the design and development of the fairings was co- funded by the European Union through Clean Sky 2. The authors would like to thank in particular the GKN Fokker Aerostructures colleagues of the Global Technology Center and the paint shop in Hoogeveen for their help with the test(samples). Moreover, we would like to express our gratitude to 3M for the various LSP materials received for trials and DTC for the collection of waste material.

9. References

1. https://www.thermoplasticcomposites.nl/research-areas/recycling/project-tpc-cycle/. March 2022.
2. De Bruijn TA, Vincent GA, Meuzelaar J, Nunes JP, van Hattum FWJ. Design, Manufacturing & Testing of a Rotorcraft Access Panel Door from Recycled Carbon Fiber Reinforced Polyphenylenesulfide. SAMPE Journal. 2020.
3. Vincent GA. Recycling of Thermoplastic Composite Laminates – The role of processing. TPRC / University of Twente. 2019.
4. De Bruijn TA. Recycling of Continuous Fibre Reinforced Thermoplastic Composites. Universidade do Minho / Escola de Engenharia. 2020.
5. ASTM D5766/D5766M-11. Standard Test Method for Open-Hole Tensile Strength of Polymer Matrix Composite Laminates. American Society of Automotive Engineers. 2011.
6. Composites Material Handbook 17G. Volume 1 - Polymer Matrix Composites Guidelines for Characterization of Structural Materials. CMH17, Wichita State University. 2012.
7. Salviato M, Ko S, Yang J, Tuttle M. Certification of Discontinuous Composite Material Forms for Aircraft Structures. JAMS 2017 Technical Review.
8. NCP-RP-2018-007. Stratasys Certified ULTEM™ 9085 Fortus 900mc Additively Manufactures Polymer Material Qualification Statistical Analysis Report. NIAR Wichita State University. 2019.
9. ASTM D7136/D7136M-07. Standard Test Method for Measuring the Damage Resistance of a Fiber-Reinforced Polymer Matrix Composite to a Drop-Weight Impact Event impact. American Society of Automotive Engineers. 2007.
10. AMC20-29. Composite Aircraft Structure. European Union Aviation Safety Agency. 2010.
11. Chemartin L, Lalande P, Peyrou B, Chazottes A, Elias PQ, Delalondre C, Cheron BG, Lago F. Direct Effects of Lightning on Aircraft Structure: Analysis of Thermal, Electrical and Mechanical Constraints. Aerospace Lab Journal, Issue 5. December 2012.
12. ED-105A. Aircraft Lightning Test Methods. Eurocae. 2013.
13. https://www.clean-aviation.eu/media/results-stories/the-only-way-is-up-nextgenctr-takes-shape . March 2022.

EFFECT OF SHREDDING PARAMETERS ON THE FORMATION OF AIRBORNE FIBER DUST DURING MECHANICAL RECYCLING OF FIBER-REINFORCED THERMOPLASTICS

Lisa, Tölle [a], Matthias, Hopp [a]

a: University of Paderborn, Kunststofftechnik Paderborn, Warburgerstraße 100, 33098 Paderborn, Germany, lisa.toelle@ktp.uni-paderborn.de

Abstract: *Thermoplastic fiber-reinforced composites can be sustainably recycled in a mechanical recycling process, but during the shredding of the fiber-reinforced scrap, the fibers can break into alveolar fiber fragments which can be potentially toxic. This research aims to investigate the effect of the shredding parameters rotational speed, screen size and feedstock size on the formation of airborne, alveolar fiber fragments. Therefore, polypropylene and polyamide-6 with glass fiber fabric reinforcement and a polycarbonate with carbon fiber fabric reinforcement are shredded in a single screw shredder. The respirable fiber dust was collected and the particles in micrometer and nanometer scale were counted and analyzed. Results show that brittle materials tend to create smaller fiber fragments than tougher materials. A higher rotational speed and a smaller screen size generally lead to a higher particle concentration and to a higher respirable fiber mass for all investigated materials.*

Keywords: airborne fiber dust; mechanical recycling; shredding; fiber-reinforced thermoplastics

1. Introduction

Fiber-reinforced plastics are mainly used to enhance the sustainability of a product or an application. Therefore, it is necessary to find sustainable recycling processes at the end of their life. The mechanical recycling process represents a sustainable recycling method for thermoplastics as they can be further processed into a recyclate via shredding, extrusion or compounding and granulation [1–3]. Size reduction by shredding the fiber-reinforced material with single- or multi-screw shredder or cutting mills is a necessary first processing step. One challenge in the shredding of fiber-reinforced plastics is the fiber dust formation. As a consequence of the mechanical loads during cutting or shearing, the fibers can break into small fiber fragments which can be alveolar (aerodynamic diameter of 4.25 ± 1.5 µm [5]) and thus potentially toxic [4]. When the fibers break into fragments with WHO-fiber dimensions (length > 5 µm, diameter < 3 µm, length: diameter > 3:1 [6]), they could also cause carcinogenic reactions in the lungs [7].

It is the aim of this research to gain know-how about the parameters that are responsible for the fiber dust formation during shredding. So far research on shredding focusses on maximizing the throughput or minimizing the energy demand but has not investigated the effect of shredding parameters on the fiber dust formation yet. The cutting velocity, for example, affects the energy demand during shredding and it was found, that the cutting energy was minimized for a rotational speed of 10 m/s [8, 9]. Because of the time-dependent visco-elastic behavior of thermoplastics, the matrix material embrittles with increasing cutting velocity [8, 9]. A brittle

  doi:10.5075/epfl-298799_978-2-9701614-0-0

breaking behavior leads to a fast and uncontrolled crack propagation which needs little energy [10]. Another well described effect is the screen size. A reduction in screen size leads to a significant increase in energy demand, due to the longer cutting time until the material is small enough to leave the cutting chamber [11]. This means that the material needs to undergo more cutting steps and more impact events before the particles are small enough to pass through the screen. Parameters like the gap width, the number of cutting blades or the wedge angle of the blades are also known to affect the cutting performance [9] in terms of energy demand, but these researches do not describe the influence on the formation of airborne and respirable fiber dust.

2. Materials and Methods

2.1 Materials

Three different thermoplastic organic sheets, provided by Bond Laminates GmbH (Lanxess), were used in these investigations. A polypropylene reinforced with glass fiber fabric (PP-GF) (trade name: Tepex® dynalite 104-RG600(x)/47 %), a polyamide-6 with glass fiber fabric (PA6-GF) (trade name: Tepex® dynalite 102-RG600(x)/47 %) as well as a polyamide-66 with carbon fiber fabric (PA66-CF) (trade name: Tepex® dynalite 201-C200(x)/50 %) were chosen. The organic sheets were pre-cut into plates with 250 x 250 mm or 50 x 50 mm size.

2.2 Shredding Process and Fiber Analysis

The single screw shredder WSC 250-400 of Weima Maschinenbau GmbH was used for the investigations. The rotational speed was varied from 60 to 120 rpm and the screen size was varied between 10 mm and 20 mm. In order to ensure a constant throughput, 1 kg pre-cut organic sheets were added every 120 sec.

Table 1 : The table summarizes the shredding parameters that are combined with each other in the investigations. The pictograms and the arrows symbolize the respective shredding parameters in the following diagrams.

Material	Rotational Speed	Screen Size	Feedstock Size
PP-GF PA6-GF PC-CF	60 rpm ↓ 120 rpm ↑	10 mm ↓ 20 mm ↑	50 x 50 mm ↓ 250 x 250 mm ↑

A Scanning Mobility Particle Sizer (SMPS, Modell 3080, TSI Inc.) counted and measured particles in nanometer scale (9 - 414 nm) whereas an Aerodynamic Particle Sizer (APS, Modell 3321, TSI Inc.) counted and measured particles in micrometer scale (0.5-20 µm). The inhalable fiber fraction (E-dust) was collected on a cellulose nitrate filter by using a VC25-sampling device (former, Ströhlein GmbH). The filter was weighed before and after the shredding process and the fiber mass was standardized by dividing the collected fiber mass through the feedstock mass and the filtered air. In figure 1 the position of the measurement devices and the shredder is depicted.

  doi:10.5075/epfl-298799_978-2-9701614-0-0

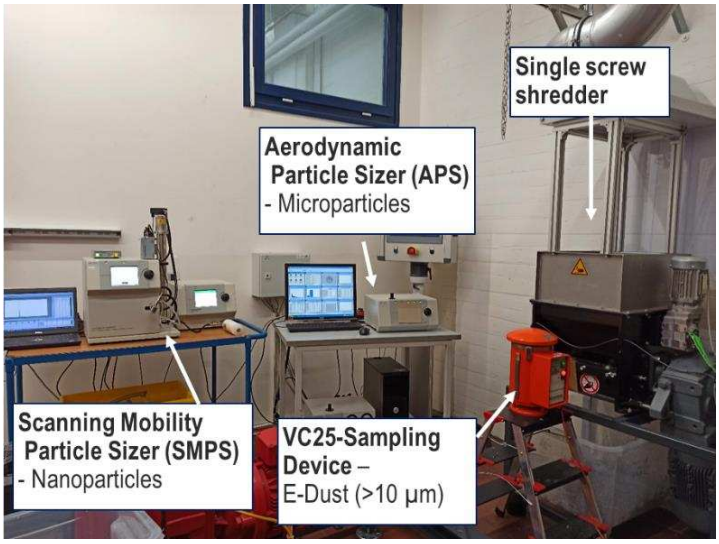

Figure 1: Position of the APS, SMPS, the single screw shredder and VC25-sampling device

3. Results and Discussion

Shredding the three different materials in the single screw shredder by varying the shredding parameter rotational speed, screen size and feedstock size lead to the particle concentration in nanometer scale (9 - 414 nm) shown in figure 2 and to the particle concentration in micrometer scale (0.5-20 µm) in figure 3. The collected fiber mass is depicted in figure 4. All parameter combinations were tested with the PP-GF organic sheets whereas the investigations with the PA6-GF and the PC-CF were restricted to limited parameter combination. For this reason, the diagrams do not show data for every parameter combination and every material.

3.1 Impact of the Breaking Mechanisms of the Material:

In all three figures the impact of the breaking behavior of the material gets obvious. The PP-GF organic sheets do not release as many respirable fibers during cutting as the PA6-GF organic sheets. The concentrations at micrometer scale or of the fiber mass are more than ten times higher for the PA6-GF organic sheets. The reason is the more brittle breaking behavior of the PA6 compared to the PP. The brittle breaking leads to uncontrolled crack propagation through the material and thus also to an uncontrolled breaking of the fibers which results in a high amount of airborne glass fiber dust. It is the same reason for the high amount of fiber dust released by shredding the PC-CF organic sheets. Carbon fibers and the polycarbonate matrix are very brittle and thus lead to brittle material fracture with a high amount respirable fiber dust. This impact of the material specific breaking behavior on the airborne fiber dust amount can be observed in all three diagrams.

3.2 Impact of Screen Size:

For the PP-GF and the PC-CF organic sheets, investigations on the effect of the screen size have been conducted. For the PP-GF organic sheets, a reduction of the screen size from 20 mm to 10 mm leads to an increase of the particle concentration at low rotational speed. Especially at nanometer scale the particle concentration is twice as high as compared to the bigger screen size (see figure 2). In the case of a higher rotational speed, the nanoparticle concentration is

  doi:10.5075/epfl-298799_978-2-9701614-0-0

lowered compared to bigger screen size. This can be seen in the nanoparticle concentration as well as in micrometer scale (see also figure 3).

A smaller screen size reduces the maximal particle size of the ground material and also extends the duration of the material in the cutting chamber. The material needs to be cut more often until it can leave the cutting chamber [11]. Moreover, with increasing number of cutting impact, the possibility of uncontrolled breaking of the fibers increases. Therefore, it was expected, that a reduction of screen size leads to an increase in small, airborne fiber dust. For the PP-GF at higher rotational speed, this can not be seen in the nano- and micrometer scale particle concentration. A reason is the electrostatic charge of the small particles. Due to the high rotational speed and the higher number of cutting steps, the friction is enhanced and thus small particles are electrostatically charged, agglomerate and stick at the wall of the cutting chamber.

At high rotational speed, the PC-CF was also shredded with a smaller screen size. In the nanometer scale the particle concentration increases about 57.5 % by reducing the screen size. Whereas in micrometer scale, a reduction of the particle concentration is observed. As the standard deviation of the concentrations are high, a comparison of the concentrations is difficult.

A reason for the high standard deviations figure 2 and figure 3 is the high concentration of airborne fibers with a high length-diameter ratio. During shredding of the PC-CF organic sheets, the release of airborne fibers was especially high, so that the fibers partly block the inlet of the APS or the SMPS from time to time. As a result the concentrations vary between the different measurements and lead to the high standard deviations.

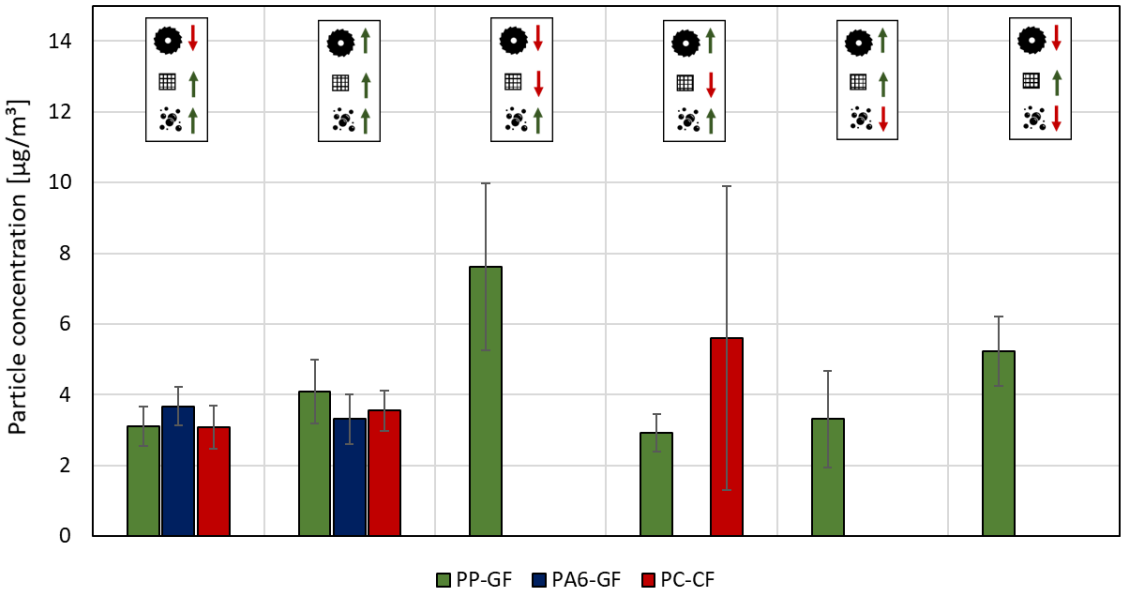

Figure 2 : Measured nanoparticle concentrations while shredding three different organic sheets. The pictograms visualize the different shredding parameters.

Figure 4 depicts the collected airborne, respirable fiber mass, which contains E-dust but also particles in micro- and nanometer scale. In this figure a reduction of the screen size leads to an increase of the collected fiber mass, independent of the rotational speed or the shredded

  doi:10.5075/epfl-298799_978-2-9701614-0-0

material. This supports the afore mentioned explanation that a reduction of screen size leads to a higher amount of respirable fiber dust.

In order to prevent the formation of respirable fiber dust, the screen size should be chosen as large as possible.

3.3 Impact of Feedstock Size:

The feedstock size could be varied for the PP-GF organic sheets only. A reduction of the feedstock size does not lead to a significant reduction of the particle concentration, neither in nanometer scale nor in micrometer scale. The smaller pieces are harder to cut for the shredder because they can move easily in the cutting chamber. Therefore, no favorable effect of the smaller feedstock size can be observed. In figure 4 a high fiber mass was collected on the filter for the smaller feedstock size. This is contrary to the results of the APS and SMPS, but can be explained by the existence of some big particles of the fiber-matrix that could be found on the filter and are responsible for the high weighed mass. The big particles on the filter are a result of the enhanced movement in the cutting chamber of the smaller pieces.

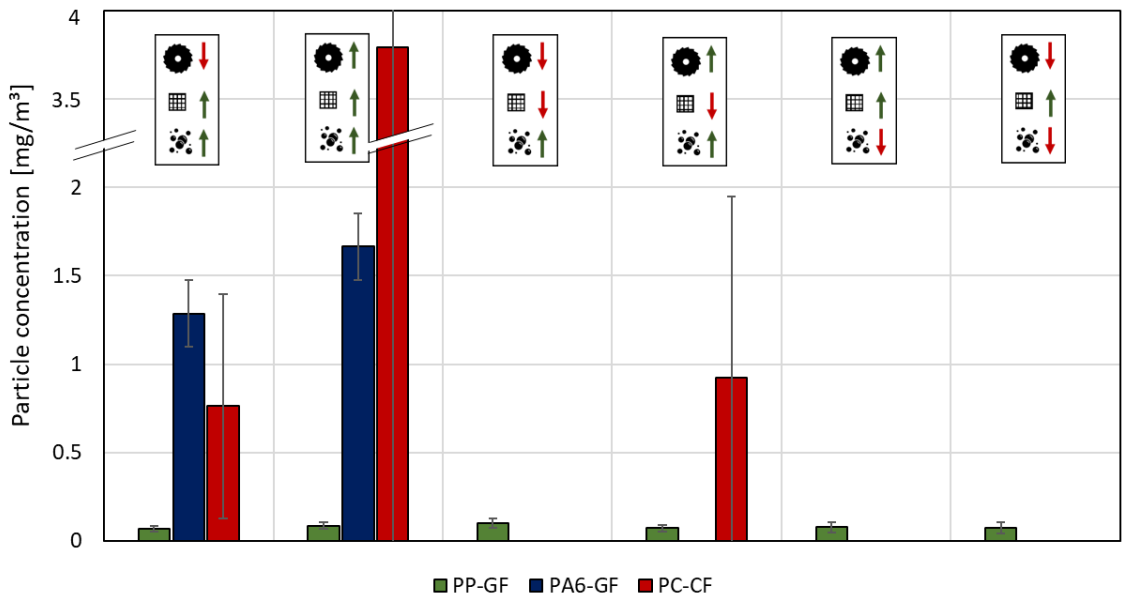

Figure 3: Measured particle concentrations in micrometer scale while shredding the three different organic sheets. The pictograms visualize the different shredding parameters.

3.4 Impact of Rotational Speed:

An increased rotational speed leads to a rising particle concentration for all three materials. Whereas the increase is not significant in nanometer scale, there is a big increase in fiber concentration in micrometer scale. The PP-GF organic sheets show little variation in micrometer scale. As described before, at smaller screen size or smaller feedstock size the nanoparticles get electrostatically charged and thus agglomerate and get too big to be analyzed by the SMPS (see figure 2). Therefore, the increasing particle concentration at higher rotational speed cannot be observed for those parameter combinations. But the effect of the high rotational speed is obvious for the PA6-GF and the PC-CF organic sheets (see figure 3). Furthermore, the airborne collected fiber mass increases with higher rotational speed for all materials and parameter

  doi:10.5075/epfl-298799_978-2-9701614-0-0

combinations (see figure 4). Here, the increase is obvious also for the PP-GF samples shredded at smaller screen size or with smaller feedstock size. For the PC-CF shredded with small screen size and high rotational speed, a very high fiber mass was collected. The high rotational speed leads to a more brittle breaking behavior in the material and thus to the increased fiber dust formation. In the case of the PC-CF organic sheets, the effects of the small screen size and the high rotational speed together with the brittle material breaking behavior lead to the high amount of fiber mass. The collected fiber mass even exceeded the workplace limit of 1.25 mg/m³ for granular, bio persistent dust [12].

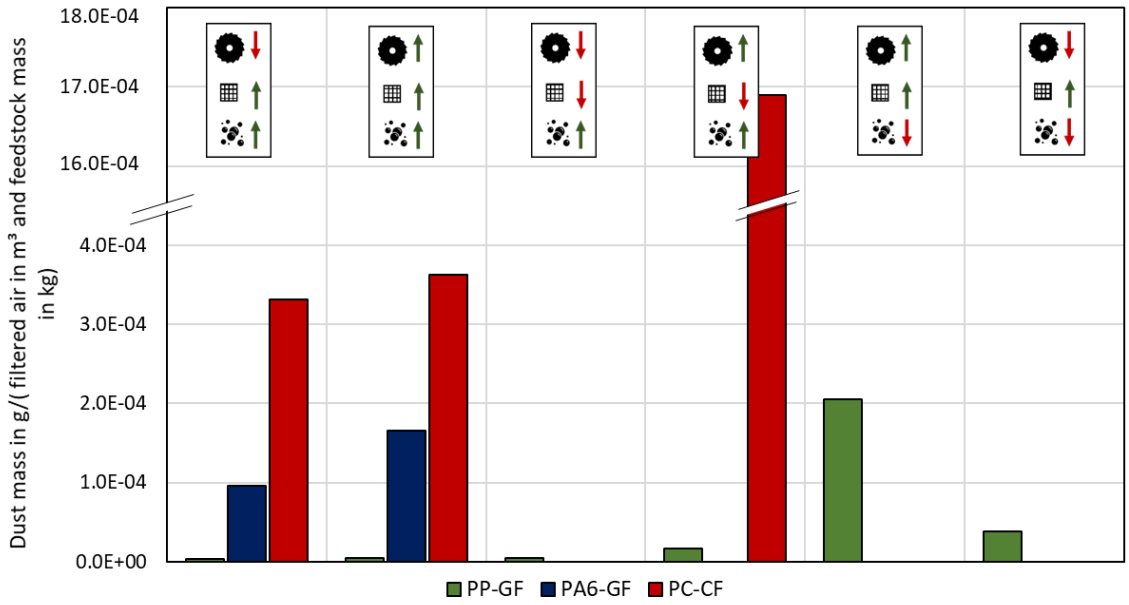

Figure 4: Weighed fiber mass, collected during shredding of the three different organic sheets. The fiber mass is standardized by dividing the collected fiber mass through the filtered air and the feedstock mass.

4. Conclusion

In these investigations it has been shown that respirable fiber dust is formed by shredding organic sheets with a single screw shredder. A higher particle concentration and respirable fiber mass was measured by shredding more brittle materials and at higher rotational speed as well as with a smaller screen size. Even though these investigations give just a small insight in the topic of potentially toxic fiber dust formation, it was shown that especially for carbon fibers the released fiber mass exceeds the workplace limit of 1.25 mg/m³ for granular, bio persistent dust. Therefore, the rotational speed should be reduced and the screen size should be chosen as big as possible in order to reduce the release of respirable fiber dust. Especially during shredding of carbon fiber-reinforced organic sheet, personal safety equipment should be worn.

  doi:10.5075/epfl-298799_978-2-9701614-0-0

Acknowledgements

We would like to thank the German Federation of Industrial Research Associations ”Otto von Guericke” e.V. (AiF) for the financial support of the research project, which is funded by the Federal Ministry for Economic Affairs and Climate Action (BMWK). We would also like to thank the companies of the project committee and the project partner, the “Institut für Prävention und Arbeitsmedizin” (IPA), for their excellent cooperation.

References

1. Bernasconi A, Rossin D, Armanni C. Analysis of the effect of mechanical recycling upon tensile strength of a short glass fibre reinforced polyamide 6,6. Engineering Fracture Mechanics. 2007; 74:627–41.
2. Howarth J, Mareddy SS, Mativenga PT. Energy intensity and environmental analysis of mechanical recycling of carbon fibre composite. Journal of Cleaner Production. 2014; 81:46–50.
3. Wood K. Carbon fiber reclamation: Going commercial. High-Performance Composites. 2010; 3:1–2.
4. Mattenklott M, van Gelder R. Carbonfaser und carbonfaserverstärkte Kunststoffe (CFK): Teil 1: Charakterisierung, Exposition, Bewertung und Schutzmaßnahmen. Gefahrstoffe Reinhaltung der Luft. 2019; 9:317–22.
5. DIN Deutsches Institut für Normung e.V. Festlegung der Teilchengrößenverteilung zur Messung luftgetragener Partikel: DIN EN 481. 1993.
6. WHO. Determination of airborne fibre number concentrations: A recommended method, by phase constrast optical microscopy (membrane filter method). Geneva; 1997.
7. Westphal GA, Monsé C, Walter D, Brüning T, Bünger J. Gefährdungsanalyse für Carbonfaser-verstärkte Kunststoffe: PICMA-Test weist auf sehr geringe Entzündungswirkungen hin. IPA Journal. 2019; 1:10–4.
8. Schönert K, Schubert G. Zerkleinerungstechnik für nicht-spröde Abfälle und Schrotte. Aufbereitungs Technik. 2002; 9:6–23.
9. Woldt D. Zerkleinerung nicht-spröder Stoffe in Rotorscheren und -reißern [Dissertation]: Technische Universität Bergakademie Freiberg; 2004.
10. Bauer W, Wüstenberg D. Bruchverhalten von Polypropylen bei dynamischer Schneid- und Scherbeanspruchung in Schneidmühlen. Mat.-wiss. u. Werkstofftech. 2001; 32:601–6.
11. Shuaib NA, Mativenga PT. Energy demand in mechanical recycling of glass fibre reinforced thermoset plastic composites. Journal of Cleaner Production. 2016; 120:198–206.
12. BAuA Bundesanstalt für Arbeitsschutz und Arbeitsmedizin. Technische Regeln für Gefahrstoffe - Arbeitsplatzgrenzwerte: TRGS 900; 2006.

  doi:10.5075/epfl-298799_978-2-9701614-0-0

A COMPOSITE APPROACH TO MECHANICALLY UPCYCLE POST-CONSUMER MIXED ENGINEERING PLASTICS

Kanjanawadee, Singkronart[a], Siti Ros, Shamsuddin[a], Koon-Yang, Lee[a,b]

a: Department of Aeronautics, Imperial College London, Exhibition Road, London, UK, SW7 2AZ
b: The Institute for Molecular Science and Engineering, Imperial College London, Exhibition Road, London, UK, SW7 2AZ

Abstract: *Owing to the heterogeneous composition of the engineering plastics and ineffective sorting at the end-of-life of these plastics, the post-consumer engineering plastics are destined to incineration or landfill sites as mixed engineering plastic wastes (MEPs). In this work, MEPs were upcycled by reinforcing them with three different types of short fibres, particularly short carbon fibres (CF), short glass fibres (GF) and wood flour (WF), herein composite approach. The results showed that incorporating these reinforcements improved the tensile modulus and strength. With a higher weight fraction of the reinforcements, higher stiffness and strength of MEP composite were accomplished.*

Keywords: Life cycle assessment; Mechanical recycling; Post-consumer engineering plastic waste; Upcycling

1. Introduction

The demand of engineering plastics in electronic equipment and automotive application in European countries has increased in the last decade; in 2019, it rose to 8.01 million tons, an 11.2% increase by weight from 2015. The increasing demand for these plastics subsequently increases plastic wastes in the system [1,2]. The arising weight of these plastic wastes at the End-of-Life Vehicles (ELVs) and Waste Electrical and Electronic Equipment (WEEE) accumulate to 250-360 kt and 110 kt, respectively, in 2020 in the UK [3]. European countries and the UK have put an effort to manage the corresponding wastes by employing the WEEE Directive 2002/96/EC and the ELV Directive 2000/53/EC. These regulations set the target of 85% of the material recycling rate of ELV materials by 2015 [3,4], while the WEEE wastes should be recycled between 50% - 80% for most product categories [5]. These regulations push large-scale shredding plants to extract some rigid plastics for the onward recycling process [3].

Recycling plastics has several routes. One of them is mechanical recycling which is a straight-forward, technologically-available, and economically-friendly process. Mechanical recycling is generally performed on a contaminant-free single-plastic stream [6]. However, engineering plastic wastes (MEPs) in WEEE and ELVs have a complex composition —generally composed of Acrylonitrile Butadiene Styrene (ABS), Polystyrene (PS), Polypropylene (PP), Polyethylene (PE), Polycarbonate (PC), etc.— with overlapping density and conductivity, leading to a challenge in the sorting process. Hence these engineering plastics ended up in the mixed-plastic stream where 70% by weight of these plastics went to landfill sites and incineration in 2017 in France [7]. Furthermore, mixing different types of polymers and additives from different sources possesses poor performance compared to their virgin counterparts, associated with chemical structures, processing temperature, and degradation profile which decreases the technical and

  doi:10.5075/epfl-298799_978-2-9701614-0-0

economic value of these mixed polymers. The place in the existing market for these plastics often involves downcycling, less attractive or less demanding applications [4,6,8].

To expand the available markets for MEPs, the strength and stiffness properties of these materials must be enhanced by adding reinforcement or other chemical additives. Compatibilizers, one of the most popular chemical additives, are generally made of copolymers where one segment is compatible with one phase, while another segment compatible with another phase. This mechanism lowers the interfacial tension and minimizes dispersed droplet size, which enhances the phase adhesion and ultimately improves the mechanical properties [6,8-13]. Various compatibilizers have been explored for a different binary blend of MEP composition, for instance; PP/ABS polymer blend [8,9] or PS/PP polymer blend [10,11] or ABS/PS polymer blend [12,13]. Despite the improvement in mechanical properties of compatibilized immiscible polymer blends, the usage of compatibilizers is restricted to certain compositions and types of polymer blends [6,9]. This is true for the mixed plastic waste system which is composed of unknown/unpredictable weight fraction of heterogeneous blends does not have a universal compatibilizer to enhance their properties.

Reinforcements, on the other hand, can improve the mechanical properties and add value to the heterogeneous systems beyond the virgin polymer performance. This is due to the load transfer capability of the composite materials that the stress is proportionally dispersed and carried by individual component. Fibres, having higher strength and stiffness than matrix, can relatively carry a high proportion of the external applied load [14]. There are some studies utilizing this composite concept by reinforcing carbon fibres or glass fibres to the polymer blend to improve the mechanical properties [15-20]. Due to their high strength-to-weight ratio, especially carbon fibres, flexural modulus and strength of recycled-PP/PET binary blend increases 65% and 27%, respectively, after 5%wt short carbon fibre loading [15]. Short glass fibre has a similar trend where 5%wt reinforcement increases the tensile strength of PA6/HDPE binary blend matrix by 20% [18]. With the concern of the environmental burden of non-biodegradable reinforcement, renewable natural reinforcement was also examined, particularly wood flour [21,22]. Wood flour was incorporated into PP/recycled-PET matrix as a reinforcing filler, where the flexural modulus increases 27% after reinforcing 30%wt wood flour to the matrix [21]. While this composite approach has been successfully upgraded the mechanical properties of the binary polymer blend, this composite approach has never been applied to multi-component polymer blends.

Therefore, reinforcement was utilized in this work to tackle with highly heterogenous engineering plastic wastes. This approach aims to provide a sustainable alternative solution by diverting the MEPs away from the landfill and increasing the market value of these wastes which, essentially, reducing petroleum reliance. To mechanically upcycle MEPs with the composite approach, short carbon fibre (CF), short glass fibre (GF) and wood flour (WF) were incorporated to MEPs in various weight fraction to create upcycled MEP/CF composites, MEP/GF composites and MEP/WF composites, respectively. These composites were, then, investigated for their tensile properties.

2. Experimental

2.1 Materials

  doi:10.5075/epfl-298799_978-2-9701614-0-0

Mixed engineering plastic waste granules (MEPs) were supplied from Axion Ltd., (Manchester, UK) which are composed of 50-40 wt.-% ABS, 40-30 wt.-% PS, 15-10 wt.-% PP, 3 wt.-% Rubber, 2 wt.-% PE and 2 wt.-% of others. Chopped carbon fibres (CF) (Carbiso CT IM56D, length = 6 mm) were purchased from ELG Carbon Fibre Ltd. (Coseley, UK). Chopped glass fibres (GF) (562A, length = 6 mm) were purchased from Jushi group co., Ltd (Zhejiang, China). Wood flour (WF) (EPC200, 180 mesh) was purchased from Eden products Ltd., (Middlewich, UK).

2.2 Fabrication of MEPs, MEP/CF composites, MEP/GF composites and MEP/WF composites

Mixed engineering plastic wastes (MEPs) and reinforced MEPs (2.5, 5, 10, 20 and 40 wt.-% of each reinforcement) were compounded by using a co-rotating twin-screw extruder (Eurolab XL, ThermoFischer Scientific, Karlsruhe, Germany). The screws have a length-to-diameter ratio of 25 with a diameter of 16 mm. The processing temperature and speed were set at 210 °C with 30 rpm from a feeding zone through a circular die. Prior the extrusion process, the reinforcements were manually mixed with the MEPs in a batch of 500 g by using a spatula at the different weight fraction. The wood flour was oven dried at 80 °C for 120 minutes before this manual mixing process. The compounded materials were then pelletised into 3 mm granules by using Haake VariCut (ThermosFischer Scientific, Karlsruhe, Germany) and fed into the Haake Minijet Pro injection moulder (Thermofischer Scientific, Karlsruhe, Germany). The injection barrel and mould temperature were set at 210°C and 40°C, respectively, with 10 s of 650 bar for injection pressure and 60 s of 650 bar for packing pressure. The dog-bone mould (65 mm overall length, 10 mm gauge length, 3 mm thickness) mould were used.

2.3 Tensile testing of MEPs, MEP/CF composites, MEP/GF composites and MEP/WF composites

The tensile testing of MEPs, MEP/CF, MEP/ GF and MEP/WF composite were performed according to ASTM D638-14. Tensile testing was performed by using a universal testing machine (Instron 5960, High Wycombe, UK) equipped with a 10 kN load cell with a cross head speed of 1 mm min^{-1}, equivalent to a strain rate of 0.1% s^{-1}. Dog-bone specimens were stamped with white dots in the gauge length prior testing which were tracked the deformation by an optical strain camera (iMetrum Ltd., Bristol, UK). Tensile test was performed at room temperature (20 °C). Average results of seven test specimens are reported for each sample.

2.4 Scanning electron microscopy (SEM)

The SEM micrographs were conducted using scanning electron microscope (S-3700N, Hitachi High-Technologies Corporation, Tokyo, Japan) with an accelerating voltage of 12kV. Prior the investigation, the specimen was cryofractured and fixed onto aluminum stubs using carbon tabs and Au coated (Agar Auto Sputter coater, Agar Scientific Ltd., UK) at a coating current of 40mA for 20s.

3. Results and discussion

Tensile properties of MEPs, MEP/CF composites, MEP/GF composites and MEP/WF composites

The tensile properties of the mixed engineering plastic waste and its composites are indicated in Table 1. The MEPs exhibited brittle behavior due to the heterogenous sea-island morphology from compounding immiscible polymers together [23] as shown in Figure 1. After incorporating

  doi:10.5075/epfl-298799_978-2-9701614-0-0

reinforcements, the tensile modulus and strength of MEPs were enhanced. Increase in weight fraction of the reinforcements, tensile modulus increased correspondingly. With 10 wt.-% of wood flour reinforcement, the tensile modulus increased 40% compared with unreinforced MEPs. Increasing wood flour content to 40 wt.-%, tensile modulus increased 2.2 folds. This is due to the increased weight fraction of stiff components into a weak matrix [14]. This trend was also appeared in short glass fibre reinforced MEP composite and short carbon fibre reinforced MEP composite where the highest fibre weight fraction accomplishes the highest improvement in tensile modulus. MEP/GF and MEP/CF composites have a sharper rise in tensile modulus than MEP/WF composites. After incorporating 40 wt.-% of short glass fibre to MEPs, tensile modulus rose 3.55 folds, while MEP/CF 40%wt accomplished the highest modulus of 22.05 GPa which is 7.3 folds compared to MEPs. It is reasoned that the high mechanical properties of glass fibre and carbon fibre provided a higher improvement in tensile modulus to MEPs than wood flour [14]. Expectedly, the stiffness component such as short carbon fibres accomplished the highest improvement.

The increment trend of tensile strength is similar to tensile modulus where the higher fibre loading accomplishes the higher tensile strength. In the case of short glass fibre and short carbon fibre composites, the tensile strength increased responding to the fibre content. Whereas MEP/CF 10%wt possessed tensile strength at 46.73 MPa which is a 47% improvement, with higher fibre loading of MEP/CF 40%wt, tensile strength increased 82% compared to MEPs. Short glass fibre composites showed a similar incremental pattern, but with a lower tensile strength than MEP/CF composites. Short glass fibre composites possessed the highest improvement at 40 wt.-% reinforcement at 51.1 MPa which is a 60% improvement from MEPs. This is due to the lower mechanical properties of glass fibre compared to carbon fibre [14]. Furthermore, with the same fibre loading of 40 wt.-%, wood flour composite possessed the lowest tensile strength compared to other reinforcement types. The maximum tensile strength of wood flour composites was accomplished at 40 MPa which is a 26% increase after 40 wt.-% reinforcement, while other weight fractions of wood flour secured the tensile strength at ~30 MPa. This is due to the hydrophilic surface of cellulose [21,22] and the significant short initial length of wood flour ranging from 50-500 µm acting as a filler rather than reinforcement [14].

With the successive increases in tensile modulus and tensile strength, strain at break decreased corresponding to the weight fraction of the reinforcements. The strain at break of MEPs, MEP/WF composites, MEP/GF composites and MEP/CF composites are presented in Table 1. The strain at break decreased by 59%, 68% and 72% compared to MEPs, after cooperating 40 wt.-% of wood flour, glass fibre and carbon fibre, respectively. This is due to the higher amount of brittle component in the composite and the limited plastic deformation of MEPs [14].

Table 1. Tensile strength, modulus and strain at break of MEPs, MEP/WF composites, MEP/GF composites and MEP/CF composites

Materials	Tensile modulus [GPa]	Tensile strength [MPa]	Strain at break [%]
MEPs	3.01 (0.22)	31.84 (3.04)	1.4 (0.19)
MEP/WF reinforced			
2.5% wt	3.56 (0.22)	28.92 (2.96)	0.94 (0.14)
5% wt	3.60 (0.22)	29.45 (2.95)	0.87 (0.12)
10% wt	4.22 (0.23)	28.51 (1.48)	0.69 (0.07)

20% wt	6.22 (0.50)	32.99 (1.59)	0.62 (0.07)
40% wt	6.68 (0.60)	39.99 (2.92)	0.55 (0.11)
MEP/GF reinforced			
2.5% wt	3.72 (0.33)	31.19 (1.47)	1.25 (0.19)
5% wt	4.26 (0.34)	34.87 (1.23)	1.03 (0.20)
10% wt	5.16 (0.36)	40.13 (2.95)	0.88 (0.13)
20% wt	8.08 (0.57)	45.37 (1.98)	0.64 (0.12)
40% wt	10.69 (1.27)	51.10 (3.37)	0.44 (0.03)
MEP/CF reinforced			
2.5% wt	4.85 (0.78)	35.01 (2.92)	0.89 (0.20)
5% wt	8.93 (0.52)	42.88 (6.42)	0.59 (0.10)
10% wt	17.04 (1.28)	46.73 (4.16)	0.52 (0.11)
20% wt	18.63 (1.02)	53.25 (7.38)	0.50 (0.11)
40% wt	22.05 (3.02)	57.87 (6.35)	0.39 (0.02)

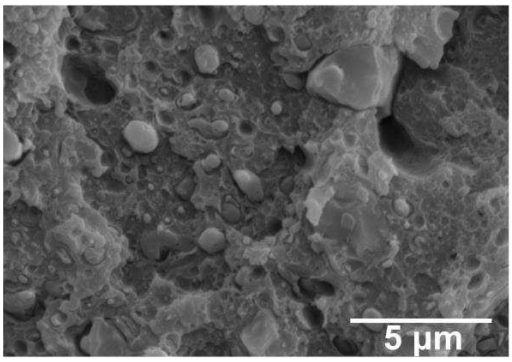

Figure 1. A SEM image of compounded mixed engineering plastic wastes (MEPs)

4. Conclusions

In this work, the mechanical properties of MEPs were enhanced by adding CFs, GFs and WFs. MEPs have a poor tensile modulus and strength of 3.01 GPa and 31.84 MPa, respectively. The incorporation of 20 wt.-% of WF increased tensile modulus and strength to 6.22 GPa and 33 MPa, respectively. The higher tensile modulus and strength were accomplished by adding higher fibre content to 40 wt.-% which possesses a tensile modulus of 6.68 GPa and tensile strength of 40 MPa. In both GF and CF composite, 40 wt.-% reinforcement incorporation provided the highest improvement compared to other weight fraction. Together with the high mechanical properties of GF and CF, the tensile modulus and strength of 40%wt GF/MEP rose to 10.7 GPa and 51 MPa, respectively, where the highest improvement was accomplished by reinforcing 40%wt of carbon fibre to MEP achieving tensile modulus and strength of 22 GPa and 57.87 MPa, respectively.

Acknowledgements

The authors would like to thank the Royal Thai government scholarship for funding Kanjanawadee Singkronart.

  doi:10.5075/epfl-298799_978-2-9701614-0-0

5. References

1. PlascticsEurope. Plastics-the Facts 2016 An analysis of European plastics production, demand and waste data [Internet]. Brussels; 2016 [cited 2022 Feb 7]. Available from: https://plasticseurope.org/knowledge-hub/plastics-the-facts-2016/
2. PlascticsEurope. Plastics-the Facts 2020 An analysis of European plastics production, demand and waste data [Internet]. Brussels; 2020 [cited 2022 Feb 7]. Available from: https://plasticseurope.org/knowledge-hub/plastics-the-facts-2020/
3. British Plastic Federation. BPF Recycling Roadmap [Internet]. 2021 Jan [cited 2022 Feb 7]. Available from: https://www.bpf.co.uk/roadmap.aspx
4. European Commission. Evaluation of Directive (EC) 2000/53 of 18 September 2000 on end-of-life vehicles [Internet]. Brussel; 2021 [cited 2022 Feb 3]. Available from: https://eur-lex.europa.eu/legal-content/EN/TXT/?uri=CELEX%3A52021SC0060
5. Bates M, Griffiths G, Harding A, Hawkes A, Holloway L, Keal L, et al. Waste Electrical and Electronic Equipment (WEEE) Regulations: Individual Producer Responsibility (IPR) in a UK context. IPR Working Group [Internet]. 2012 Jul [cited 2022 Feb 3]. Available from: https://www.gov.uk/government/publications/waste-electrical-and-electronic-equipment-weee-regulations-individual-producer-responsibility-ipr-in-a-uk-context
6. Ghosh A. Performance modifying techniques for recycled thermoplastics. Vol. 175, Resources, Conservation and Recycling. Elsevier B.V.; 2021.
7. Développement Durable D, Monier V, Benhallam R, Maccario F, Basciano R. Annual report the End-of-Life Vehicle observatory-2017 data-120pages. 2019.
8. Brostow W, Holjevac Grguric T, Olea-Mejia O, Rek V, Unni J. Polypropylene + Polystyrene Blends with a Compatibilizer. Part I. Morphology and Thermophysical Properties
9. Bonda S, Mohanty S, Nayak SK. Influence of compatibilizer on mechanical, morphological and rheological properties of PP/ABS blends. Iranian Polymer Journal (English Edition). 2014 Jun 1;23(6):415–25.
10. Aziz AA, Akil HM, Jamaludin SMS, Ramli NAM. The effect of multiple compatibilizers on the impact properties of polypropylene/polystyrene (PP/PS) blend. Polymer - Plastics Technology and Engineering. 2011 May;50(8):768–75.
11. Feng J, Yuan Q, Sun X, Yang F, Cui K, Li W, et al. Improving the properties of ABS by blending with PP and using PP-g-PS as a compatibilizer. Polymer-Plastics Technology and Materials. 2021;60(7):798–806.
12. Vazquez Y v., Barbosa SE. Recycling of mixed plastic waste from electrical and electronic equipment. Added value by compatibilization. Waste Management. 2016 Jul 1;53:196–203.
13. Chen B, Evans JRG. Mechanical properties of polymer-blend nanocomposites with organoclays: Polystyrene/ABS and high impact polystyrene/ABS. Journal of Polymer Science, Part B: Polymer Physics. 2011 Mar 15;49(6):443–54.
14. Hull D, Clyne TW. An Introduction to Composite Materials [Internet]. Cambridge University Press; 1996 [cited 2022 Feb 7]. Available from: https://www.cambridge.org/core/product/identifier/9781139170130/type/book
15. Saifullah ABM, Inampudi VVK, Nikzad M, Sbarski I, Hussain M. Evaluation of Mechanical and Thermal Performance of Polyethylene Terephthalate Recycled Ribbon and Carbon-Reinforced Compatibilized Polypropylene. Polymer Engineering and Science. 2020 Mar 1;60(3):575–80.

  doi:10.5075/epfl-298799_978-2-9701614-0-0

16. Allawi AN, Shuaib NA, Omar NWY, Azmi AI. Mechanical properties and environmental assessment of recycled carbon fibre reinforced polypropylene and acrylonitrile butadiene styrene products. In: IOP Materials Science and Engineering. IOP Publishing Ltd; 2020.
17. Li J, Zhang YF. The tensile properties of short carbon fiber reinforced ABS and ABS/PA6 composites. Journal of Reinforced Plastics and Composites. 2010 Jun;29(11):1727–33.
18. Palabiyik M, Bahadur S. Tribological studies of polyamide 6 and high-density polyethylene blends filled with PTFE and copper oxide and reinforced with short glass fibers. Vol. 253, Wear. 2002.
19. Dobrovszky K. Upcycling of polymer waste from automotive industry. Periodica Polytechnica Mechanical Engineering. 2011;55(2):73–7.
20. Lingesh BV, Rudresh BM, Ravikumar BN. Effect of Short Glass Fibers on Mechanical Properties of Polyamide66 and Polypropylene (PA66/PP) Thermoplastic Blend Composites. Procedia Materials Science. 2014;5:1231–40.
21. Dairi B, Djidjelli H, Boukerrou A, Migneault S, Koubaa A. Morphological, mechanical, and physical properties of composites made with wood flour-reinforced polypropylene/recycled poly(ethylene terephthalate) blends. Polymer Composites. 2017 Aug 1;38(8):1749–55.
22. Maou S, Meghezzi A, Grohens Y, Meftah Y, Kervoelen A, Magueresse A. Effect of various chemical modifications of date palm fibers (DPFs) on the thermo-physical properties of polyvinyl chloride (PVC)–high-density polyethylene (HDPE) composites. Industrial Crops and Products. 2021 Nov 1;171.
23. Bartczak Z, Galeski A. Mechanical Properties of Polymer Blends. In: Utracki LA, Wilkie CA, editors. Polym. Blends Handb., Dordrecht: Springer Netherlands; 2014, p. 1203–97. https://doi.org/10.1007/978-94-007-6064-6_13.

NOVEL METHOD FOR UNPOLYMERIZED PREPREG RECYCLING USING SUPERCRITICAL CO_2 EXTRACTION

Sophie Martin[a], Henry-Pierre Guriec[a], Sandy Moisan[a]
a: Nantes Université, IRT Jules Verne, 44000 Nantes, France – sandy.moisan@irt-jules-verne.fr

Abstract: *For the first time, supercritical CO_2 extraction, already an industrial process, was used to remove some components from uncured prepreg. This innovative approach allows to produce a new type of secondary raw material useful for thermoplastic (TP) or thermoset (TS) composite applications without any damage on the fibres and remove the stacking behaviour of the prepreg. IMA/M21E (UD) from Hexcel uncured prepreg, available in large quantity in aeronautic industry was chosen as model. Firstly, uncured prepreg is cut at desired length. Then supercritical CO_2 extraction is performed under 40°C and 29 MPa in a semi-continuous equipment for ten hours to remove partially bisphenol A, F and aminophenol. Recycled carbon fibres (rCF) still embedded inside prepreg components (32wt% of matrix) ready to be used are so recovered. Depending on the cutting size at the beginning, several application examples are presented.*

Keywords: recycling; uncured prepregs; supercritical CO_2 extraction

1. Introduction

Prepreg-based production wastes from cut-off or out-of-date are an issue in aerospace industry. Today, they are currently landfilled or incinerated [1]. Several options for their reuse were developed at demonstrator level for sporting and recreation equipment, non-critical aerospace and automotive structures are obtained [2] . For such options, uncured thermosetting prepreg wastes must be kept at low temperature, until they are cut in chips form and moulded. The second option consists on recycling the material to recover the carbon fibre (CF) as it is done for cured materials. Several well-known ways can lead to this objective: the mechanical recycling, the thermal recycling, which include pyrolysis, and the chemical recycling [3] [4]. For instance, hydrolysis of epoxy matrix to recover the CF can be done with water as solvent at sub- or supercritical state, i.e. near or above the critical point of water, at high temperature and pressure (380°C and 220 bar), to avoid the use of organic solvents. Supercritical fluids are interesting media for chemical reaction as they have properties intermediate between liquid and gas: low viscosities, high transport properties, high diffusivities; their solvent power is dependant also of the pressure [5]. Water in particular can support ionic, polar non-ionic or free-radical reactions, so that it is said to be an adjustable solvent [6], and it is inexpensive, recyclable, and non-toxic, compatible with the principles of “green chemistry” [7]. Hydrolysis of composites based on CF and epoxy resin with sub-critical water has been performed by Aymonier et al. [8] allowing to obtain fibres with good mechanical properties. But this process is conducted under highly corrosive conditions, is energy-intensive and still at lab-scale or pilot-scale [9].

The first breakthrough of our approach is to use industrial scale process for making the recycling. Supercritical CO_2 (sc-CO_2) extraction is one famous process used at industrial scale for extraction of caffeine from coffee, neutralization of cork for wine storage, textile dying, degreasing… Indeed, the sc-CO_2 point is very low (31°C, 74 bar), compared to supercritical water. Due to its chemical structure, sc-CO_2 is a bad solvent, but very selective [10], and can be simply removed by evaporation. For our concern, we explore this solvent to extract the bisphenol components from the epoxy matrix well-known to be soluble under sc-CO_2 conditions. Extraction of epoxy

  doi:10.5075/epfl-298799_978-2-9701614-0-0

resin with sc-CO_2 was already studied for cleaning purpose of metallic parts: Y. Medina-Gonzalez worked on solubilization and removal epoxy components from metallic part [11]. The optimal operating conditions were 45°C and 145 bars. Another study relates the interactions between CO_2 and epoxides by combining FTIR with quantum chemistry calculations; it shows that the Lewis acid-base interactions occurs between epoxides and CO_2 and are mainly governed by the partial charge on the oxygen atom of the epoxides. The solubility of model epoxy molecules were determined in the range of 40 to 100°C until 200 bar using specific FTIR equipment [12]. Another study related the solvation effect of CO_2 and its effect on the curing temperature of model epoxy resin [13]. It seems that CO_2 get a plasticization of epoxy resin but doesn't change the reactional mechanism. In addition, pressure seems not having any significant effect. Finally, an article relates that pressure of CO_2 accelerates the polymerization reaction [14].The conclusion is that sc-CO_2 can diffuse easily inside uncured prepreg and could help the polymerization reaction. Regarding these studies, a counterbalance must be found between favouring the solubilization versus polymerization limitation. The temperature must be as low as possible to avoid the polymerization reaction and a potential reaction with CO_2. But it should be high enough to get high density to favour solubilization. It depends on the formulation of the epoxy resin, and in all studies, the considered material is model pure epoxy. In an industrial material, uncured epoxy is composed of more than 2 components, and in this study, it is known that aminophenol and bisphenol A are part of the composition of the epoxy matrix, and they are soluble (at 40% and 50%) in sc-CO_2 [15] [16] . The use of sc-CO_2 could lead to a partial extraction of the polymer matrix, and the remove of some constituents of the formulation would block the polymerization reaction.

The second breakthrough is to not clean as much as possible the CF to allow a more easily processability. It could also help to improve the interaction with the matrix for the reuse. But tacky aspect of uncured prepreg must be removed also to get a more easily processability.

This study presents how an already industrial process, sc-CO_2 extraction, can be used to remove bisphenol A and aminophenol from a real epoxy resin from uncured prepregs. The rCF thus recovered can be reincorporated in thermoplastic (TP) and thermoset (TS) processes like thermocompression and contact moulding.

2. Materials and methods

2.1. Materials

The material for this study is IMA/M21E prepreg used by Airbus for its A350 program. It is made of unidirectional continuous high tensile strength CF IMA-12K, pre-impregnated with Hexply® M21E thermosetting epoxy. It has a resin content of 34% by weight and a fibre weight of 268 g/m^2. Prepreg is stored with its paper protection under -18°C. Two width are cut with a Zund equipment: 6 mm and 10 cm. 6 mm is chosen as a standard size for compound incorporation (done in Repair3D by Centexbel but not showed here).

Regarding the formulation of M21E resin, no public information is found contrary to M21 [17] [18].M21 formulation is described as follow: three types of epoxy (bisphenol F, aminophenol, amine), one hardener (amino sulfone) and blended with two thermoplastic polymers (PES and PA6/12) (*Table 1)*. We assume that M21E formulation is close to M21's one with more than 30% in wt TP content (E= enriched) to improve impact strength or toughness of composites. That

  doi:10.5075/epfl-298799_978-2-9701614-0-0

gives some indication regarding prepreg's nature, which is important to understand the next extraction process. Nevertheless, no quantitative study is completed.

Table 1: Components of the M21 epoxy formulation [17] [18]

Types/Names			Weight % content
Resin	Diglycidyl ether bisphenol F	DGEBF	15-20 wt%
	Triglycidyl meta aminophenol	TGMAP	20-30 wt%
	Para-glycidyl amine	PGAm	5-15 wt%
Hardener	4-4'-diaminodiphenyl sulfone	DDS	15-20 wt%
Thermoplastic blend	Polyethersulfone	PES	10-20 wt%
	Polyamide 6/12	PA 6 /12	3-10 wt% ratio 80%/20%

2.2. Supercritical CO_2 extraction

The operating conditions are defined regarding the balance between solubility and polymerization, to run the process at 40°C with an extraction pressure of 290 bars [15]. The extraction occurs in a semi-continuous pilot scale reactor (Figure 1). CO_2, stored in a liquid state, is compressed and pre-heated to get the desired properties. Then, it passes through a reactor full of prepreg (4L) with 10kg/h flow rate. Molecules extracted from prepreg are collected via the separator. CO_2 is then condensate and restart again the loop. CO_2 is recycled at 95% (5% are lost during the extraction). The reaction is stopped when 100kg/kg of CO_2 ratio is obtained (general rule for extraction). After the extraction, rCF are recovered free of solvent and "dry" (not tacky anymore).

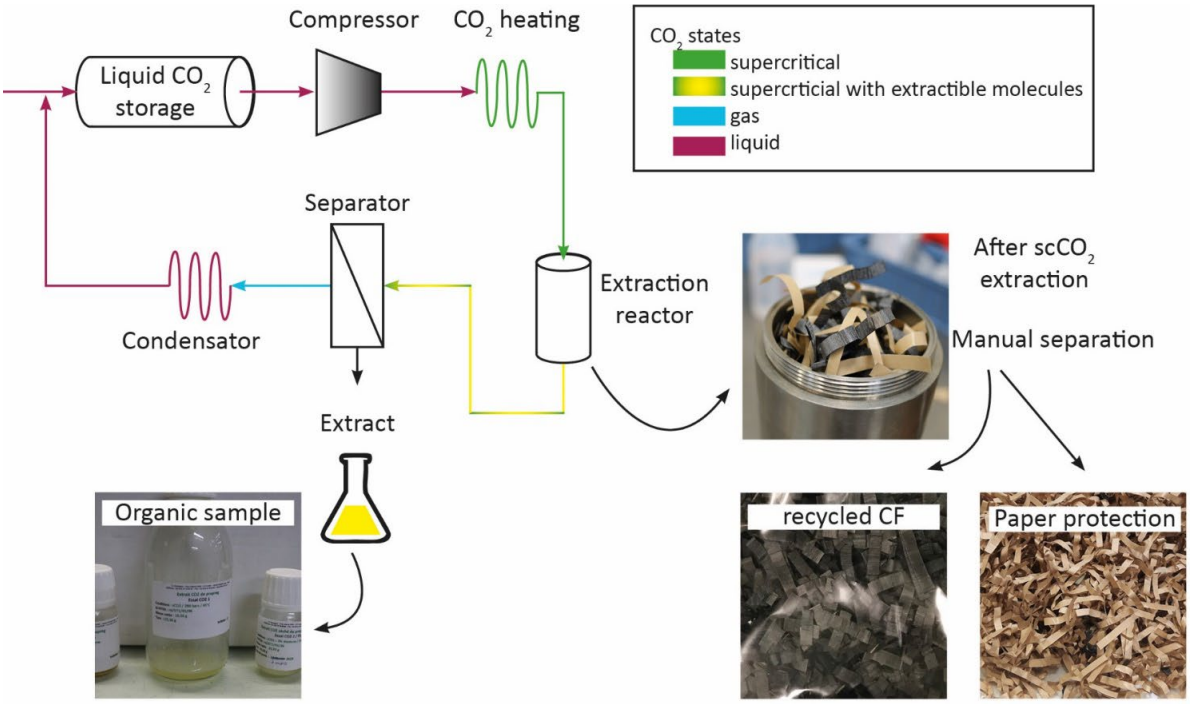

Figure 1: Schema of the extraction using sc-CO_2

2.3. Reuse of rCF with TS or TP processes

Thermocompression was tested with the consolidation of 6 mm rCF with polyamide PA6 film at 280°C during 15 minutes under 10kN of pressure with a 50T Pinette PEI press, to observe interface between CF and matrix. PA6 was chosen because it is a part of prepreg (Table 1).

To assess the rCF reuse with epoxy matrix (Araldite® LY 50-52), plates are done by contact moulding with pump down. The resin is first mixed with the hardener (Araldur®) with a proportion of 100g of resin for 38g of hardener, and then left to rest 10 minutes under vacuum to remove gas and avoiding bubbles formation. Fibres are placed in a vessel and mixed manually with the good amount of resin. A 250x250 mm marble, which contain the mixture, is placed under vacuum in an oven at 60°C during 6h. After curing, plate is demoulded and post-cured at 100°C during 4h.

To check the interest of our rCF, comparison with (i) pristine CF (pCF) 6 mm FT300-3k, (ii) fresh uncured prepreg (U-PREG), (iii) cured prepreg (C-PREG) is done (Table 2).

Table 2: pristine carbon fibres (pCF), b) sc-CO_2 rCF (rCF), c) uncured prepreg (U-Preg) and d) cured prepreg (C-Preg)

pCF	rCF	U-Preg	C-Preg
FT300-3k	IMA+org. Materials	IMA-M21E	IMA-M21E
Dry fibre	After scCO_2 extraction	Fresh	Cured (vacuum/180°C/2h)
			

For each type of fibre, the amount of resin was calculated to obtain a fibre volume fraction of 25%, considering the presence of epoxy inside the prepregs fibres (rCF, U-Preg and C-Preg), estimated to 34% wt of resin in the whole materials. The quantity of matrix for the plate with pCF is so more important than for the other types of fibres, to obtain the same fibre volume fraction for each plate and being able to compare them. The four 250x250mm plate are done simultaneously.

2.4. Characterization

Observations on prepregs and micro cuts are made with an optical stereographic microscope Olympus, with magnification from 6.3 to 57. Analysis of CF and extracted organic molecules are performed by FTIR spectrometer Perking Elmer Spectrum One, in reflexion directly on samples. The resolution is cm-1 and the results are compared with database Sadtler Spectral® and BIO RAD®. Gas Chromatography/Mass spectrometer (GC/MS) is used to analyse the organic extract. GC is a Perkin Elmer Clarus 600 apparatus, coupled with a MS Perkin Elmer Clarus 600C; products are identified with NIST 2008® database. Samples are prepared by dissolving 0.2g of organic extract in 10 ml of dichloromethane. 1µL is used for GC/MS liquid injection. The morphology is determined by SEM using a Philips Quanta Inspect microscope with W filament 25 kV equipped with Edax Genesis.

  doi:10.5075/epfl-298799_978-2-9701614-0-0

3. Results and analysis

The extractions are conducted seven times varying the volume reactor (2/4L) and the width. The process is well reproducible (Trials 4 to 7 -Table 2) for the 4L and 6 mm rCF, with a yield of 8% in weight (considering the matrix weight and not the prepreg weight). It is quite low but enough for stopping the polymerization reaction, as the samples after extraction have totally lost their tackiness behaviour at ambient temperature. This is one of the biggest advantages of our innovative process to easily store and process such type if rCF.
Better yields are obtained for 6mm samples compared to 10 cm (Table 3) even if the loading for 10 cm is more important.

Table 3: Trials performed for sc-CO_2 extraction at 40°C and 290 bar

Trials	Reactor	Load g	Granulometry	Yield%
1	2 L	140	10 cm	2.4
2	2 L	300	6 mm	5.9
3	2 L	583	10 cm	4.3
4	4 L	870	6 mm	8.4
5	4 L	889	6 mm	8.0
6	4 L	887	6 mm	8.0
7	4 L	885	6 mm	8.0

Table 4: Peaks from FTIR comparison between organic mix after extraction and bisphenol F diglycidyl ether (Ruetapox)

Molecule	Characteristic peaks also present on FTIR spectra of organic mix (cm^{-1})								
Ruetapox 0158	3002	2922	1610	1582	1509	1451	1345	1297	1241

Table 5: peaks from GC/MS diagram of organic mix recovered after scCO_2 extraction from prepreg

Retention time (min)	29.56	30.6	31.66	32.66
Molecule	Aminophenol	Bisphenol F	Bisphenol F	Bisphenol A

Regarding the organic molecules analysis, only a qualitative analysis can be done with FTIR and GC/MS. Bisphenol F diglycidyl ether DGEBF (Ruetapox) were detected by FTIR analysis. GC/MS diagram shows that the organic mix is mainly composed of bisphenol F, bisphenol A and Aminophenol (TGMAP) (Tables 4 and 5). It means that, regarding the Table 1, sc-CO_2 is able to extract two components from M21E (DGEBF and TGMAP). The limited number of molecules is a great advantage for a potential valorisation contrary to classical solvolysis were minimum of 10 components (phenol aniline, quinolone, ketone derivatives) are detected [8]. Nevertheless, the extraction efficiency is only 8% in weight considering the matrix weight; sc-CO_2 is not able to extract 100% of its soluble molecules due to its bad solvent properties as already mentioned.

Regarding the rCF analysis, by comparing the images before and after scCO_2 extraction (Figure 3), CF are still embedded inside a matrix as expected. Some particles are observed on the rCF surface after extraction.

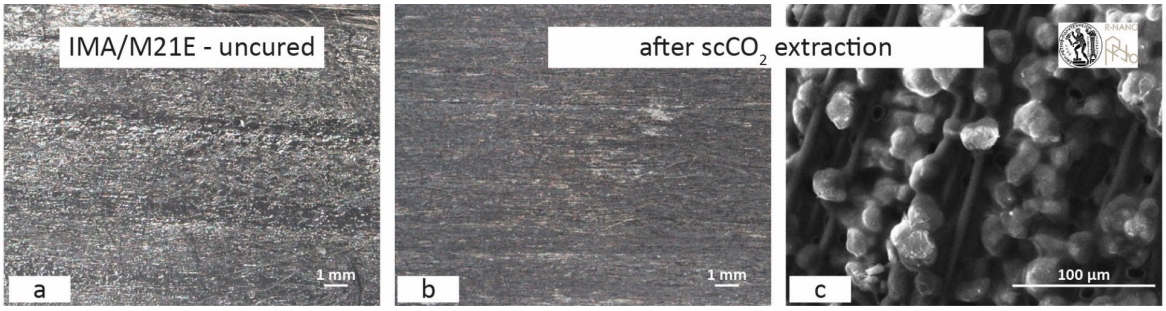

Figure 2: Optical Images of uncured prepreg before and after $scCO_2$ extraction (a and b); SEM image of rCF after $scCO_2$ extraction (c)

FTIR analysis shows that these nodules are PA6 and PES thermoplastics. This could be a limitation for the reincorporation: the matrix must be compatible with the remanent molecules. But it is also an advantage in terms of processability: the rCF are not volatile, which is one issue when rCF are totally clean. Further investigation needs to be done to analyse the remanent epoxy, not detected by FTIR spectroscopy.
Another advantage is that rCF are ready to be used due the nature of CO_2. And the conditions are so low in terms of temperature that we assume that rCF conserved their mechanical properties.

Regarding the reincorporation in PA6 film by thermocompression, fibres distribution within the matrix is not homogeneous as showed by optical microscopy image (Figure 4a). However, interaction between CF and PA6 seems to be good regarding the SEM images (Figure 4 b and c).

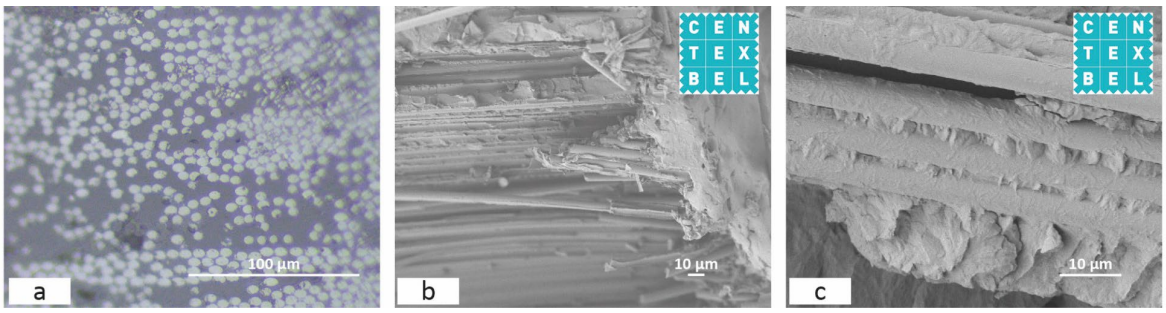

Figure 3: a) SEM and b) optical microscopy images of rCF impregnated with PA6 film

Some further investigation needs to be done to determine the link between TP and remanent epoxy components still present after sc-CO_2 extraction.

Regarding the reincorporation in TS via contact moulding, pCF shows the best repartition in the epoxy. This is due to its flexible behaviour. It is also the case for rCF (Figure 5). Nevertheless, al lot of porosity is observed, meaning that the process must be optimized before discussing the wettability behaviour between fibre and epoxy. But the proof of concept is done for reincorporation into epoxy resin. And the untacky behaviour is a huge advantage in terms of processability as already mentioned. For C-Preg, the main issue was for cutting the cured prepreg.

  doi:10.5075/epfl-298799_978-2-9701614-0-0

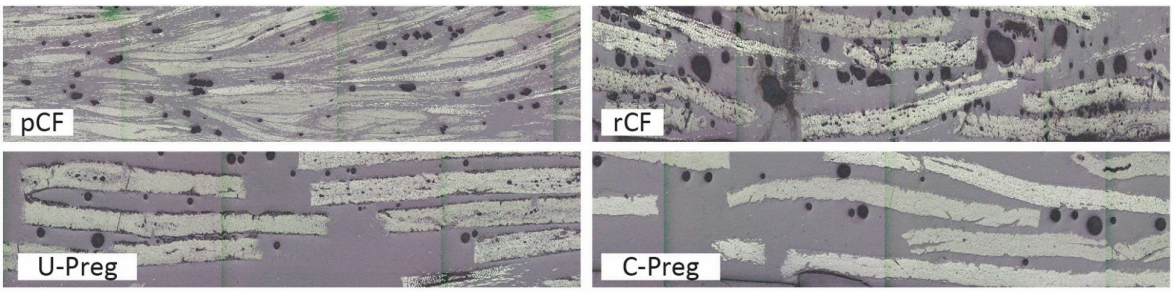

Figure 4: Micrometric cuts of a) pCF, b) rCF, c) U-PREG and d) C-PREG plates

4. Conclusions & perspectives

The use of supercritical CO_2, well-known as environmentally benign was chosen for partial extraction of the epoxy matrix of uncured epoxy prepregs, which constitute an important part of aeronautical industry wastes. Aminophenol and bisphenol A and F were partially extracted, leading to the freezing of the epoxy's polymerization. The resulting rCF was successfully included in a TP (with PA6) and TS (epoxy) processes. Further development needs to be done to measure the mechanical behaviour of the new composite.

The sustainability assessment of this process is presented in another article of this conference; it proves the benefit of this approach environmentally and costly speaking [19].

In another study, rCF are also functionalized after sc-CO_2 extraction with magnetic nanoparticles in supercritical media to bring induction heating properties, useful for repairing thermoplastic/carbon fibre composite [20].

Acknowledgements

The Repair3D project has received funding from the European Union's Horizon 2020 research and innovation programme under grant agreement N° 814588.We acknowledge the National Technical University of Athens (NTUA) and Centexbel (Belgium) for the SEM characterizations.

5. References

1. Nilakantan G, Nutt S. Reuse and upcycling of aerospace. Reinforced Plastics 2015; 59(1): 44-51.
2. Nilakantan G, Nutt S. Reuse and upcycling of thermoset prepreg scrap: Case study with out-of-autoclave carbon fibre/epoxy prepreg. Journal of Composite Materials 2018; 53(3): 341–360.
3. Sukanto H, Raharjo WW, Ariawan D and Triyono J. Carbon fibres recovery from CFRP recycling process and their usage: A review. IOP Conf. Series: Materials Science and Engineering 2021.
4. Oliveux G, Dandy LO,Leeke GA. Current status of recycling of fibre reinforced polymers: Review of technologies, reuse and resulting properties. Progress in Materials Science 2015; 72: 61-99.
5. Wu BC, Klein MT, Sandler SI. Solvent effects on reactions in supercritical fluids. Ind Eng Chem Res. 1991; 30: 822-828.

  doi:10.5075/epfl-298799_978-2-9701614-0-0

6. Oliveux G, Bailleul JL, Le Gal La Salle E, Lefèvre N, Recycling of glass fibre reinforced composites using subcritical hydrolysis: reaction mechanisms and kinetics, influence of the chemical structure of the resin. Polym Degrad Stab. 2013; 98: 785-800.
7. Anastas P, Eghbali N. Green chemistry: principles and practice. Chemical Society reviews 2009; 39(1): 301-312.
8. Henry L, Schneller A, Doerfler J, Mueller WM, Aymonier C, Horn S, Semi-continuous flow recycling method for carbon fibre reinforced thermoset polymers by near- and supercritical solvolysis Polym. Degrad. Stab. 2016; 133; 264–274.
9. PARCCA project. https://irt-jules-verne.fr/en/projets/advanced-carbon-fibre-composite-recycling-processes/
10. Eastoe J, Peach J. Supercritical carbon dioxide: a solvent like no other. Beilstein J Org Chem. 2014; 10: 1878–1895.
11. Medina-Gonzalez Y. Étude des phénomènes de solubilisation de pre-polymères de résine epoxy dans les esters d'acide gras comme biosolvants 2006.
12. Foltran S, Cloutet E, Cramail H, Tassaing T. In situ FTIR investigation of the solubility and swelling of model epoxides in supercritical CO_2. The Journal of Supercritical Fluids 2012; 63: 52-58.
13. Hu DD, Lyu JX, Liu T, Lang MD, Zhao L. Solvation effect of CO_2 on accelerating the curing reaction process of epoxy resin. Chemical Engineering and Processing 2018; 127: 159-167.
14. Lyu J, Hu D, Liu T, Zhao L. Non-isothermal kinetics of epoxy resin curing reaction under compressed CO_2. J Therm Anal Calorim. 2018; 131: 1499–1507.
15. Mouloungui Z, Medina-Gonzalez Y, Thiebaud-Roux S, De-Caro P, Hernandez-Ochoa L. The role of co-additive on epoxy resin pre-polymers solubilization in supercritical CO_2. The Journal of Supercritical Fluids 2006; 38(1): 13-17.
16. Martín Á, Rodríguez-Rojo S, de Pablo L, José Cocero M. Solubility of Bisphenol A in Supercritical Carbon Dioxide. J. Chem. Eng. Data. 2011; 56(10): 3910–3913.
17. Tranchard P, Duquesne S, Samyn F, Estèbe B, Bourbigot S. Kinetic analysis of the thermal decomposition of a carbon fibre-reinforced epoxy resin laminate. Journal of Analytical and Applied Pyrolysis 2017; 126: 14-21.
18. Paris C, Etude et modélisation de la polymérisation dynamique de composites à matrice thermodurcissables, PhD study, 2011.
19. Gkika A, Petrakli F, Vlysidis A, Karagiannis P, Moisan S, Koumoulos E, Life Cycle Assessment and Life Cycle Costing on recycled post-industrial composite waste, ECCM 2022.
20. Moisan S, Guriec HP, Martin S, Gkika A, Koumoulos E, Kainourgios P, Charitidis C, Innovative process for uncured carbon fibers prepreg recycling and functionalization with magnetic nanoparticles using supercritical fluid chemistry, ISGC 2022.

  doi:10.5075/epfl-298799_978-2-9701614-0-0

NEW TRENDS IN PLASTICS AND THERMOPLASTIC COMPOSITES UPCYCLING: THERMOPRIME® & THERMOSAIC® TECHNOLOGIES

F. Ruch[a], C. Callens[a]

[a] : Cetim Grand Est ; 21, rue de Chemnitz, Mulhouse, 68068, France - frederic.ruch@cetimgrandest.fr

Abstract: *In a general context of scarce accessible material and energy resources, Cetim Grand Est developed two eco-processes for the recovery of composite and plastic waste to help reduce the environmental footprint of materials and support companies in their technological and ecological changes.*

Recycling thermoplastic composite materials with an "upcycling" approach is a way to contribute to the grow of the global thermoplastic composite market. As a lot of waste is generated during the production process of panels and preforms, finding solutions for recycling it with more added value is a real concern.

In the coming years, this work will make it possible to respond to the regulatory challenges that companies will have to face in order to optimize the use of energy and the resources available to them.

Keywords: *Thermoplastic composite ; Recycling ; Upcycling ; Thermosaic® ; ThermoPRIME®*

1. Introduction

Nowadays, the global production of composites and plastics currently amounts to 11 and 367 million tons a year, respectively [1,2]. These materials, which were developed on a large scale in the last century and have now become unavoidable, are struggling to find technically and economically viable recovery routes. What might once have appeared as a minor inconvenience is now becoming a threat to industrial activity. Indeed, the predicted scarcity of non-renewable material and energy resources [3] is leading to tighter regulations, gradually forcing the composites and plastics industries to reduce their environmental footprint. Even though the objective is the same for all, the historical context is significantly different.

The composites industry, which is not highly automated and mainly targets niche markets, produces high-value-added and long-lasting goods, made from a long or continuous fibre reinforcement (glass) and a thermosetting resin (unsaturated polyester) in nearly 90% of cases [4]. While production waste remains more or less stable from year to year despite an overall increase in production, end-of-life waste is increasing sharply as the first generations of products designed 20, 30 or 40 years earlier (boat hulls, wind turbine blades, cladding panels, etc.) come to the end of their life cycle. The sharp increase in waste deposits is not necessarily a problem in itself. However, given the infusible nature of the resin, landfill remains the only option in

  doi:10.5075/epfl-298799_978-2-9701614-0-0

in itself. However, given the infusible nature of the resin, landfill remains the only option in nearly 90% of cases [4]. This percentage has not decreased for many years, despite numerous R&D efforts in this area. Technical solutions exist, but none of them convincingly overcomes the barrier of economic viability (with the exception of composites containing carbon fibre, but they represent only à few percent of the market) [5].

This situation is no longer acceptable today. The composites industry needs to find an alternative to the thermosetting resins historically used. It is currently undergoing a transformation by innovating in the field of materials, on the one hand (for example Arkema's Elium® resins [6]), and in materials and processes, on the other hand, by moving closer to plastics processing. In both cases, the idea is to use thermoplastic resins, which have a higher recycling potential than thermosetting resins. However, these materials will only be massively adopted once their recyclability has been proven on an industrial scale.

The highly automated plastics industry, which is mainly aimed at mass markets, produces low-value-added and short-lived goods from thermoplastic resins. This short lifespan generates very high waste volumes every year [7]. A material recycling channel does exist, but for the moment it only manages to capture a small part of the waste stream (around 10% worldwide) [8]. Thus, on a global scale, since the 1950s, nearly 80% of waste is dispersed in nature or landfilled [9]. As before, this situation is no longer acceptable at present. The plastics industry must increase the recycling rate of its resins through the use of applications with a higher added value, by approaching the composites industry in particular.

2. What prospects for plastics and composites recycling?

2.1 Two technologies with the same production line…

This mutual understanding between two formerly compartmentalised industries offers new waste recovery prospects. In this respect, Cetim Grand Est developed two eco-technologies that meet the upcycling expectations for two kinds of materials [10].

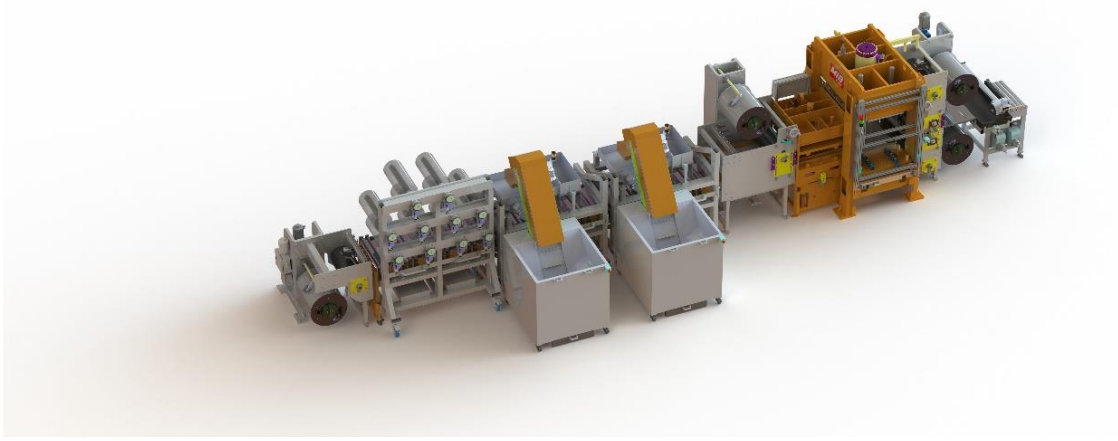

Figure 1. Thermosaïc® and ThermoPRIME® process line

Using a step-by-step thermomechanical process, this innovative process (Figure 1) allows the continuous production – from waste – of recycled semi-finished products in the form of large-scale thermoplastic composite panels. The pre-industrial production line, designed in a flexible, cost-effective and versatile way, and with an "upcycling" approach, allows the recovery of various thermoplastic waste into ranges of recycled composite semi-finished products with high added value and an optimised and competitive cost/performance ratio.

Starting from the same production line, but with two different feed systems, the Thermosaïc® and ThermoPRIME® (Thermo Plastic Recycling for Innovative Material and Ecodesign) eco-technologies were developed to fully exploit the recycling potential of composite and thermoplastics materials.

2.2 Thermoplastic composite wastes: Thermosaïc® technology

Starting from a deposit of production waste (and then end-of-life products), this technology consists in shredding the material in order to maximize its economic potential for recovery. The Thermosaïc® technology (Figure 2) retains the intrinsic value of the initial composite material, continuously moulding these shreds by thermocompression into panels. Compared to recycling into short fibre compounds, Thermosaïc® panels have significantly better mechanical properties and a high formability potential.

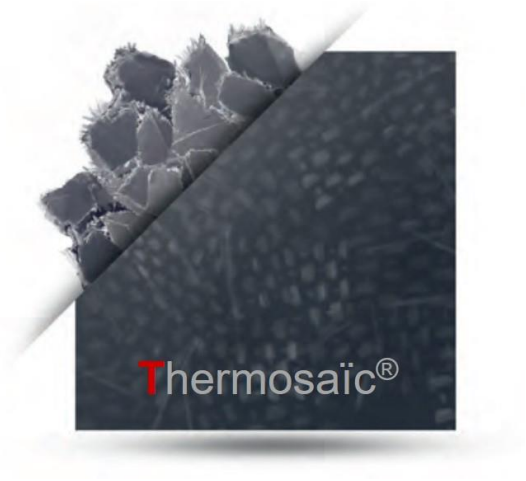

Figure 2. Thermosaïc® recycled composite

2.3 Thermoplastic wastes: ThermoPRIME® technology

Starting from a recycled plastic material with low added value, formulated to the specific needs of the application (controlled quality), ThermoPRIME® (Figure 3) consists in associating this polymer with continuous or long fibre reinforcements to produce continuous laminates with high durability and economic recovery potential.

  doi:10.5075/epfl-298799_978-2-9701614-0-0

Figure 3. ThermoPRIME® recycled thermoplastic

2.4 Industrial applications

Thermoplastic composite waste recycling has already been the subject of various studies, in particular with Porcher Industries, the aim being to find ways of recovering materials such as PPS/glass with a high added value (Figure 4).

Figure 4. Porcher PPS/GF Thermosaïc® panel

Generally speaking, the aeronautical industry shows interest in any technology capable of recycling various production waste (up to 40% waste) resulting from stamping or thermocompression operations.

With the same logic of economic optimization and reducing the environmental footprint of materials, an eco-designed laptop case demonstrator (Figure 5) made of recycled and/or bio-sourced materials is currently being developed for the fashion and luxury sector (CARATS) of the Carnot institutes.

  doi:10.5075/epfl-298799_978-2-9701614-0-0

Figure 5. Example of a laptop including thermostamped foils produced from ThermoPRIME® technology

Similarly, another development can be cited. In collaboration with the company EMI SAS [11], a recycled variant of an electric skateboard brand-named Okmos [12], has been developed, demonstrating that semi-finished products made from thermoplastic wastes can find sustainable and value-added outlets.

Figure 6. Example of an electric skateboard, based on a Thermosaïc® stamped panel overmoulded with thermoplastic resin

  doi:10.5075/epfl-298799_978-2-9701614-0-0

3. Conclusion

These examples show the interest of manufacturers and academics in major subjects that meet strong societal expectations. This flexible and agile technology makes it possible to recycle all types of thermoplastics (from PP to PEEK) and reinforcements (glass, carbon, flax, etc.). It is mature enough to support industrial needs through feasibility studies, proofs of concept, specific formulations, pilot production, etc.

Acknowledgements

This article was firstly edited in 2020, with the following title: “New trends in composites and plastics recycling” (JEC Composites Magazine ; n°136 ; p.36-37). This updated version is proposed with courtesy of JEC Composites Magazine.

Cetim Grand Est would sincerely acknowledge Carnot MICA Institute, for participating to laptop and electric skateboard developments.

4. References

1. “Overview of the global composites market” ; 2017 ; JEC Group ; ISBN 978-2-9526276-7-2

2. https://www.statista.com/statistics/282732/global-production-of-plastics-since-1950/

3. “Indicateurs d’épuisement des ressources en analyse de cycle de vie” ; Charlotte Petiot, François Witte, Yannick Le Guern ; (Rapport de recherche) 2012-02 ; SCORE LCA. 2014. hal-02269178

4. “Recyclage des composites“ ; Patricia Krawczak ; Techniques de l’ingénieur ; ref. AM5895 V1

5. https://carbonfiberresource.com/production-capacities/

6. https://www.arkema.com/global/en/products/product-finder/product-range/incubator/elium_resins/

7. “Production, use, and fate of all plastics ever made” ; R. Geyer, J.R. Jambeck, K.L. Law ; 2017 ; Science Advances, 3(7)

8. https://www.lemonde.fr/planete/article/2022/03/02/pollution-plastique-l-onu-fait-un-pas-de-plus-vers-un-texte-juridiquement-contraignant_6115875_3244.html

9. https://www.lemonde.fr/pollution/article/2017/07/19/depuis-1950-l-homme-a-fabrique-8-3-milliards-de-tonnes-de-plastiques_5162660_1652666.html

10. https://youtu.be/Ga-Pm9KJ6ms

11. https://www.emi-wissler.com/en

12. https://www.okmos.fr/

HIGH PERFORMANCE MULTI-FUNCTIONAL COMPOSITE STRUCTURES WITH INKJET PRINTED EMBEDDED CIRCUITS

Bruno, Giuntoli[a], Rajasundar, Chandran[b], Gioele, Balestra[b], Joël, Cugnoni[a]

a: School of Management and Engineering Vaud, HES-SO, Switzerland (Yverdon-les-Bains, Switzerland) – joel.cugnoni@heig-vd.ch
b: iPrint Institute, HEIA-FR, HES-SO University of Applied Sciences and Arts Western Switzerland

Abstract: *Electronic is essential in functional structural components. Whether it is for power supply, data communication or structural sensing & reliability, these signals need to be connected from the source to the component's terminals. State of the art solutions use standard wiring and thermoplastic flexible PCB (printed circuit boards) presenting three main disadvantages: the increase of overall weight, structural weakening due to matrix incompatibility and the inherent dimensional and geometrical constraints. The Multi-Functional-Composite Ply (MFCP) concept tackles the state-of-the-art inconveniences of electronics systems in composite structures with an embedded structural and multi-functional composite ply integrated into a laminate. Electrically conductive circuits are inkjet printed on a thin-ply substrate prior to the integration into a CFRP structure before curing. This flexible substrate has the capability to carry power, analogic and digital signals and forms an integral part of the laminate in terms of its mechanical response.*

Keywords: Multi-Functional Structures; Smart materials; IoT; inkjet printing; conductive flexible substrates

1. Introduction

The integration of electronics in virtually any manufactured component is a reality in today's world. From an aerospace component to a household appliance, any of these elements use an electric circuit to provide power, acquire or transmit data to sensors, and communicating to onboard computers. To provide thin (>100µm), compact and reliable electronic connections, the industry state of the art in high end electronics uses flexible PCBs [1, 2]. These thermoplastic substrates (i.e. PET, PC) are the established solution to be used on exposed surfaces or internal cavities, usually adhered with relatively heavy adhesives. Thin-ply composites provide excellent mechanical properties [3, 4, 5] and open the design space allowing to integrate more individual plies into a pre-defined thickness than standard thick (>100µm) composite plies. In this work, a thin-ply inkjet-printed composite substrate is tested in unnotched tension (UNT), three-point bending (TPB) and interlaminar fracture toughness (DCB) to evaluate the mechanical and electrical limitations of the inkjet-printed Multi-Functional Composite Ply. A demonstrator of a smart wingfoil handle is also presented, integrating the mechanical and electrical capabilities of the MFCP using analogic and digital circuits embedded in the structure to acquire gyroscopic, atmospheric, and structural sensing data.

  doi:10.5075/epfl-298799_978-2-9701614-0-0

2. Materials and methods

2.1 Substrates preparation

To ensure the electrical insulation of the MFCP, a thin-ply GFRP substrate is used to adhere the inkjet printed conductive layers. This prepreg layer is cured on a standard curing cycle. The 50µm nominal thickness substrate is composed by a 25gsm non-oriented fiberglass mat with epoxy prepreg. The curing process is needed to provide a stable surface prior to the conductive ink-jet printing process.

2.2 Specimen design

Three series of specimens were designed for the UNT, TPB and DCB testing. All tests were supported and bonded to pre-cured GFRP 3mm plates using Gurit SA80 high toughness prepreg adhesive. The electrical design of each testing had the purpose of evaluating the relation between the mechanically exposed stressed and the electrical behavior of the MFCP conductive traces. For these tests, a glass fibre (GFRP) composite was chosen used as a model substrate to maximize the achievable strain without risks of premature failure.

2.3 Unnotched Tensile Testing (UNT) specimens

The tensile testing consisted in a 3mm support GFRP plate of 25mm by 250mm as a standard ASTM D3039 where the MFCP was bonded using Gurit SA80 under vacuum. For deformation monitoring and correlation, all samples had a strain gauge on the opposite side of the MFCP as seen on Figure 1. The inkjet-printed conductive traces were monitored for resistance variation and continuity with a four-point resistivity measuring method.

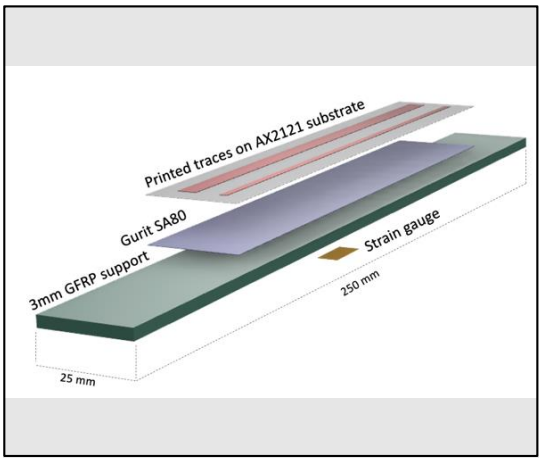

Figure 1 - Exploded CAD view of UNT specimen

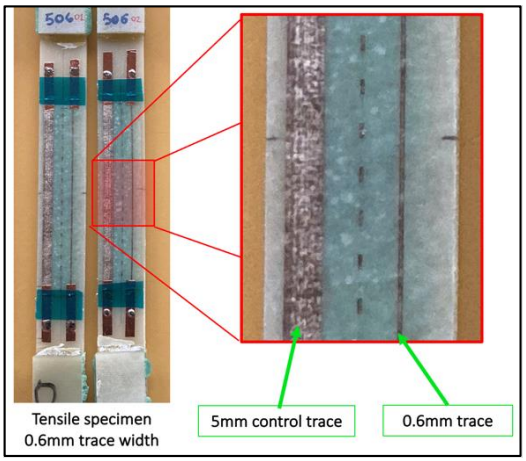

Figure 2 - UNT 506 specimen close up

Five sample patterns with width variations were designed and manufactured, with two traces on each one. The left-hand side is the reference trace and the right-hand side varies its width from 0.4mm to 5.0mm. The “UNT 506” specimen and a traces close-up can be seen on Figure 2. All specimens were inkjet printed with a two-pass process using a commercial silver nanoparticle-based Metalon® ink to increase electrical conductivity, as referenced on Table 1.

  doi:10.5075/epfl-298799_978-2-9701614-0-0

Table 1 - UNT specimens, traces and inkjet printing passes

ID number	Ref. Trace width (rL)	Variable trace width (rR)	Number of passes
504	5 mm	0.4 mm	2
506	5 mm	0.6 mm	2
510	5 mm	1.0 mm	2
520	5 mm	2.0 mm	2
550	5 mm	5.0 mm	2

2.4 Three-point bending testing (TPB)

Analog to the UNT test, the TPB testing has a pair of traces to monitor the variation of the resistance under the loading and unloading phases as shown on Figure 3. On the other hand, the placement of the strain gauge on the TPB is as close as possible to the inkjet printed traces on the tension side to capture the strain and resistance variations as linearly as possible. For this test, 5mm parallel traces pairs were printed to acquire two resistance values for the same specimen. This resistance variation (ΔΩ/Ω) is evaluated on a pseudo static and short cycle fatigue test schedule using a Shimadzu 20kNX tabletop universal machine.

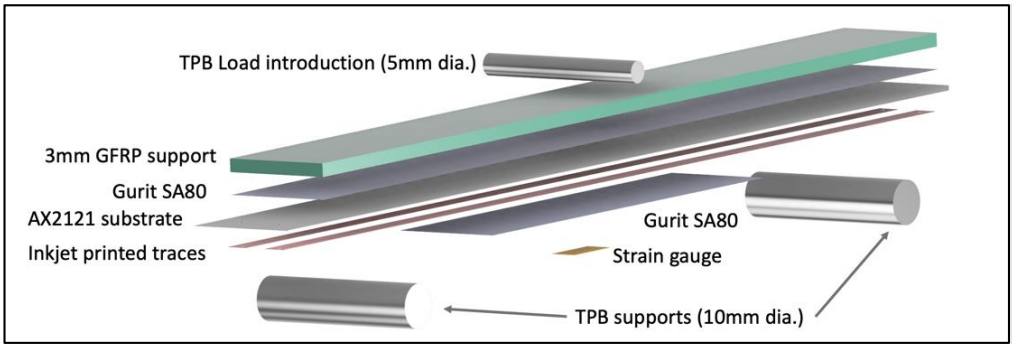

Figure 3 – Three-point bending specimen exploded view

2.5 Inter-laminar Toughness (DCB) on "Zebra" specimen

The Zebra DCB test aimed to evaluate the inter-laminar strength impact of traces width and spacing on a MFCP. Four patterns with 30mm cycle length section and one third printed area is evaluated as seen on Figure 4. A reference "raw" sample without any print or exposure was also prepared and tested on the same manner.

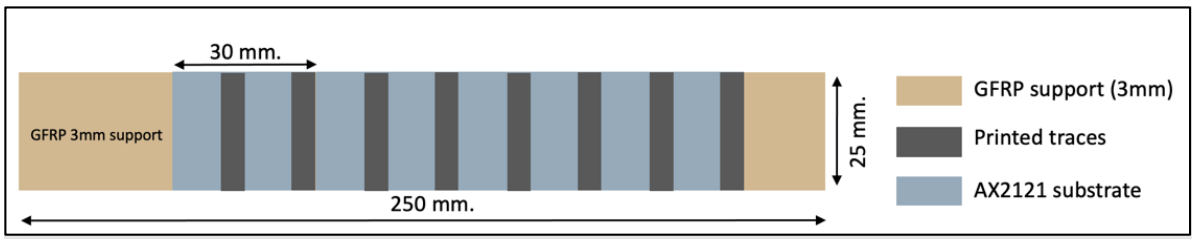

Figure 4 – Top view of general Zebra DCB specimen

  doi:10.5075/epfl-298799_978-2-9701614-0-0

The traces widths of 1.0, 2.0, 2.5 and 5.0mm were evaluated as shown on Figure 5. The MFCP specimen were integrated to a DCB testing setup, following ASTMD5528 standard with a pre-crack length of 50mm using non-perforated ETFE film. All interlayers were bonded with Gurit SA80 pre-preg adhesive and cured under full vacuum.

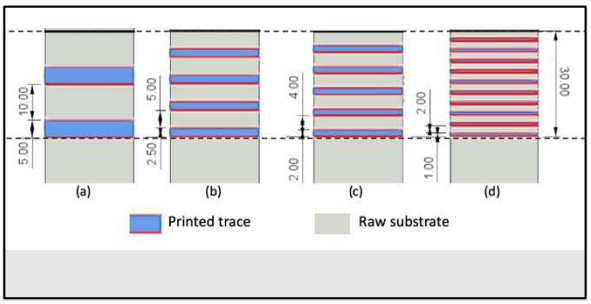

Figure 5 -Zebra specimen 30mm length patterns

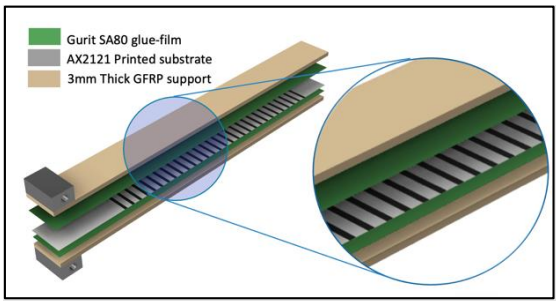

Figure 6 – DCB Zebra specimen assembly

2.6 Inkjet printing of MFCP

A twin trace pattern as seen in Figure 1,Figure 2, Figure 3 as well as the Zebra patterns seen on Figure 5 were printed over the 25 mm x 250 mm composite substrates. The conductive ink used was a water-based silver nanoparticle ink Metalon® from Novacentrix. A custom-built printer platform fitted with a piezo-based DOD Ricoh inkjet print head and an Adphos near infrared lamp (9.3 kW air cooled module) for the curing was used. Several printing trials were performed with different print resolutions and curing conditions. The most favorable conditions for print quality and conductivity were optimized for multi-pass 1200 dpi print resolutions leading to surface resistances on an average less than 0.2 Ohms per square.

3. Results and discussion

3.1 UNT Results

The pseudo static tensile tests were conducted until 0.8% strain on all samples. The results seen on Figure 7 show a direct resistance measurement in Ω (Ohms) vs Strain (%) for both the Left-hand side reference traces (5mm) and the variable width traces on the Right-hand side presented on Table 1.

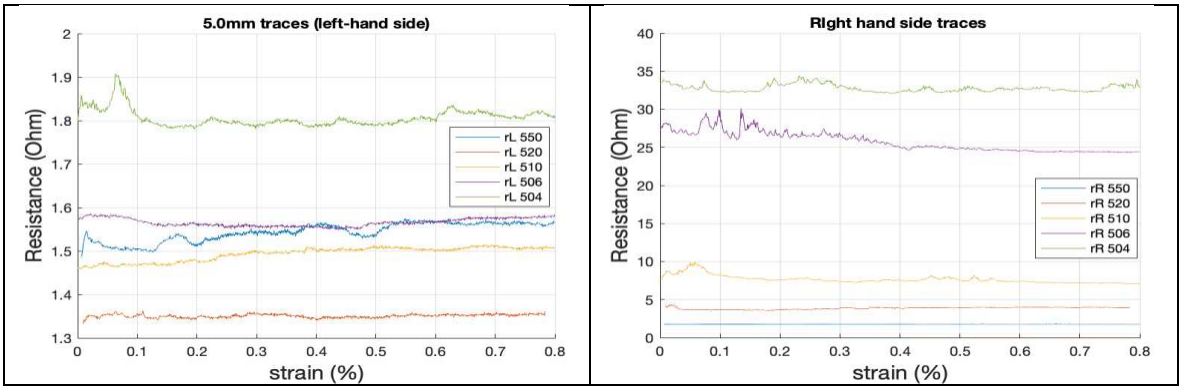

Figure 7 – Resistance (Ω) vs. strain (%) on UNT tensile tests

The left-hand side traces at 5mm width present little variation between the specimens, for inkjet-printed conductive traces (<0.5Ω). On the right-hand side, the narrower traces show higher resistance values and present higher “noisy” peaks, specially at lower strain values.

The signal presents considerable variations no systematic tendency of resistance increase. Several phenomena could explain these variations. First, it is important to note that the electric conduction in such printed traces is carried out by local bonds between partially sintered nanoparticles. Thus, during the first cycle, a preconditioning effect can happen in which weak bonds can break but also particles contacts can rearrange with strain. Moreover, creating a perfect bonding between the measurement probes and the traces is difficult due to their very sensitive nature (a few nm thickness), and thus small contact resistance variations could also affect the readings. Nevertheless, the main finding is that, even though not suitable yet for sensing, the printed traces remain reliable for data transfer or low current power supply under a high strain of 0.8% which is usually beyond the onset of damage of typical CFRP composite laminates.

3.2 Three Point Bending results

The cyclic testing results gave a new perspective to the use of the MFCP. While the main objective being the evaluation of the Metalon inkjet-printed traces capabilities for design allowances at 0.5% strain, the plotting results of the 500 cycles Strain (%) vs ΔΩ/Ω (%) observed on Figure 8 presented a linear relation between them. While not perfectly equivalent due to the inkjet printing process variations, the 0.175 Ω/cm and 0.21 Ω/cm static measured resistances of the parallel traces could be potentially used as an embedded strain measurement component.

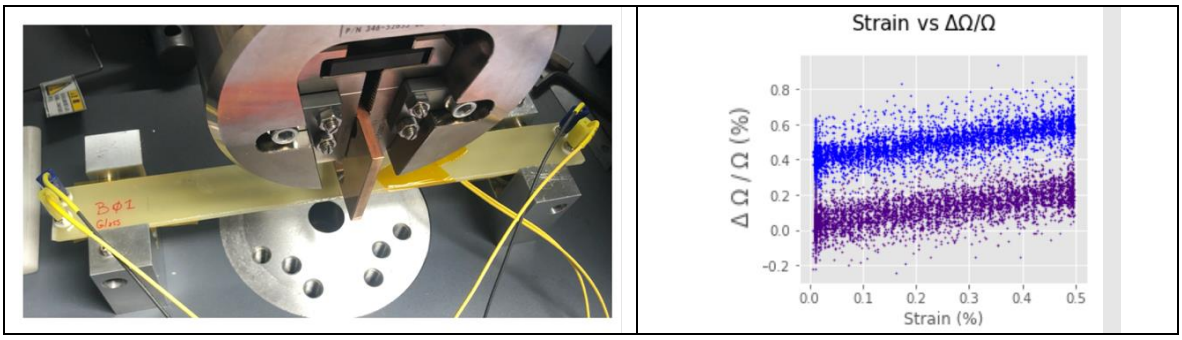

Figure 8 - TPB test and cyclic results

The plots on Figure 9 show the stability of the Multi-Functional Composite Ply on a 1000 cycles pseudo-fatigue testing schedule. The average variation of +/- 0.17% on both specimen shows the stability of the resistive performance.

The TPB test cycle shows a much more stable relative resistance variation results than the UNT results on section 3.1. Subsequent tests not shown on this work lead to evaluations at 0.8% strain, providing equivalent results, without a damage to the MFCP.

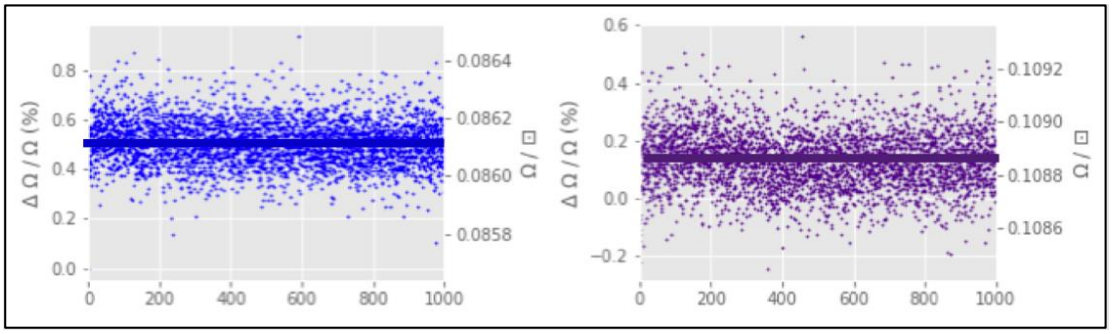

Figure 9 - Resistance variation vs cycles @ 0.5% strain

3.3 Zebra DCB testing results

The results of this non-conventional DCB test were surprisingly below expectations. The Load vs. Crack opening (displacement) plot on Figure 10 presents less but more abrupt sawtooth peaks on the 5mm traces specimen (black) than on the 1mm width traces specimens (green). This result could be explained by the higher number of sections on the smaller width traces specimen and extrapolates to the other two intermediate traces width specimen (2.0mm and 2.5mm). With a one third of the total surface made of weak printed traces, a 33% critical ERR reduction is expected when compared to the blue non-printed raw specimen. The critical ERR results observed on Figure 11 show a reduction of ≈ 55% in all patterns, with a small advantage on the 1.0mm traces.

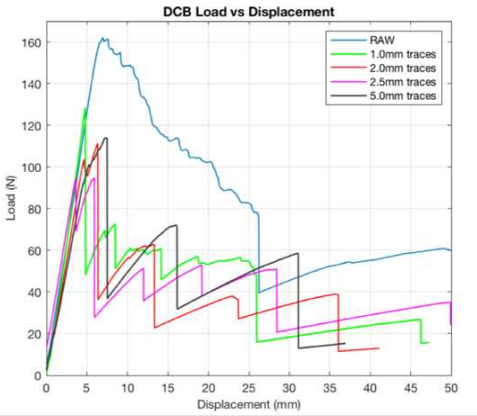

Figure 10 - DCB Load-Displacement on Zebra specimen

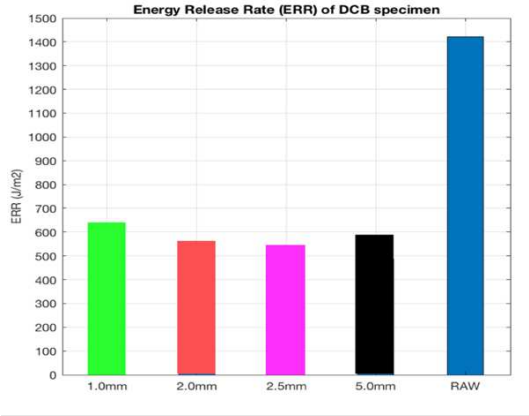

Figure 11 - ERR on Zebra specimen samples

A hypothesis on the large ERR drop phenomena is the fact that the inkjet-printed substrates are cured with a NIR (Near Infra-Red) light. This exposure of a fraction of a second to the IR light could be the cause of the matrix deterioration and its mechanical properties. Nevertheless, even with an extreme 33% of printed surface, the level of mode I interlaminar toughness of the MFCP remains sufficiently high compared to values observed in CFRP laminates and thus can be used in many applications without creating a weak point in terms of delamination.

4. Integration and demonstrator

4.1 Objectives

The objective to this demonstrator was the integration of the multiple capabilities of the MFCP. Using a sport support, such as the wingfoil is the perfect benchmark test as it combines the complexity of a reduced geometrical design space, and the challenge of a lightweight solution. The chosen wingfoil wing for the prototype is a Duotone Slick being the only wing in the market with a CFRP tubular handle. The goal of the prototype was the integration of the Multi-Functional Composite Plies into the thin-ply CFRP prepreg 26mm diameter tubular structure.

4.2 Electronics block diagram & interconnectivity

The MFCP electrical interconnection seen on Figure 12 consists in three main elements; The data acquisition unit embedded into the handle, managed by an ESP32 microcontroller with wireless and I2C capabilities; a Raspberry Pi Zero used as a server for wireless data acquisition and clients connectivity and one or multiple clients (i.e. cellphone) to read the live data or access the log.

  doi:10.5075/epfl-298799_978-2-9701614-0-0

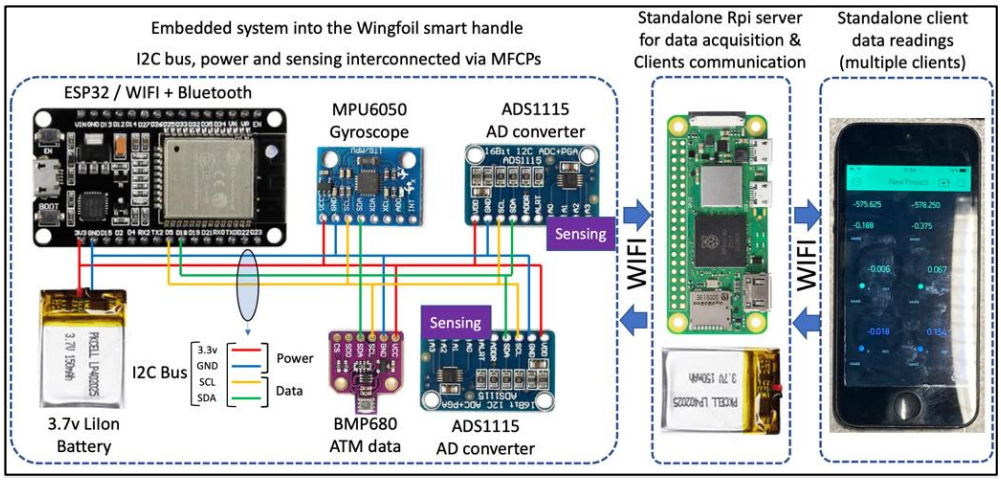

Figure 12 - Block diagram of demonstrator

The manufacturing of the thin-ply prepreg CFRP tube with MFCPs was done with a ply-by-ply method with intermediate debulks using a CNC machined female mold and cured at 7Bar. The I2C bus, composed by 4 conductors is placed in the internal face of the tube and interconnects all sensors reliably as seen on Figure 13.

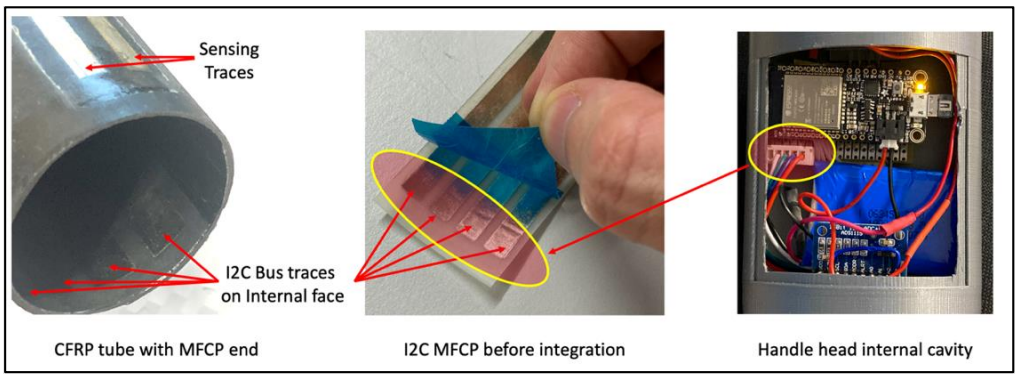

Figure 13 - I2C bus and Sensing traces

The final integration with the wingfoil wing and smart handle with MFCP handle can be seen on Figure 14 where the sensing traces are exposed to the tension side of the tube loading. While the systems are up and reliable, both electrically and mechanically, in land testing is ongoing on the prototype.

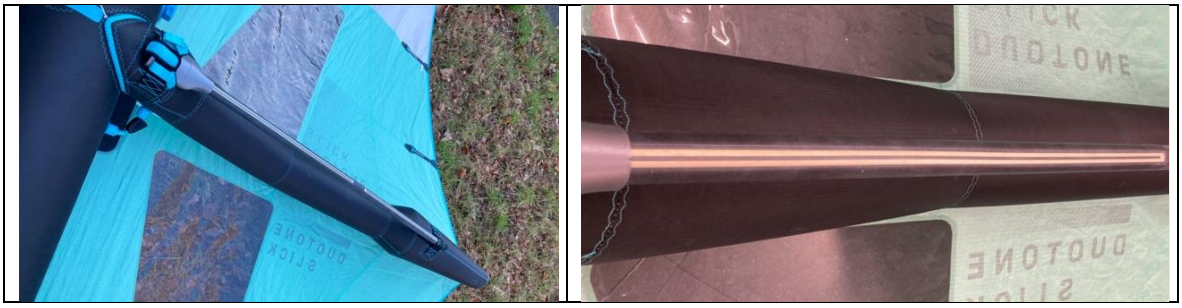

Figure 14 - Final installation of the Smart Handle into the Duotone Slign Wing

  doi:10.5075/epfl-298799_978-2-9701614-0-0

This prototype has proven the feasibility and reliability of the MFCP integration into a compact thin-ply and fully functional CFRP principal structure. Both mechanically and electrically, this prove of concept shows the potentials of the technology.

5. Conclusions

This work presents a solution to functionalize composite structures by embedding a thin-ply multifunctional ply (MFCP) into composite structure typically made of CFRP epoxy composite prepregs. A key challenge is to ensure that the embedded MFCP does not introduce a weakness in the composite laminate and can provide reliable electric functions up to the onset of damage of the laminate. The results from the tests shown in this work demonstrate that the developed MFCP provide stable electric functions for data transmission and low power electronics up to 0.8% strain in both static and low cycle fatigue while maintaining a mode I interlaminar toughness higher or equal to most CFRP laminates. Being very thin, the MFCP ply can be easily conformed and integrated in the prepreg stacking sequence of parts with relatively high curvature. Specific solutions have also been developed to integrate and connect the MFCP printed traces (through the thickness via, interface with surface mount components) which opens a large spectrum of potential applications, from consumer products and sports to the aerospace and defense industry. Since the series of tests presented in this work, different inkjet printing techniques, parameters and settings have been adapted to optimize the electrical stability and mechanical performance of the printed traces.

Acknowledgements

HEIG-VD and HEFR thank the EcoSwissMade program of HES-SO for supporting this work.

References

1. Wetzel ED. "Reducing weight: multifunctional composites integrates power, communications and structure". AMPTIAC Quarterly 2004;8(4):91-5
2. A. Duarte et al., "Multifunctional Materials Systems: A state-of-the-art review". Composite Structures, Vol. 151, paper number, pp 3-35, September 2016.
3. R. Amacher, J. Cugnoni, J. Botsis, L. Sorensen, W. Smith, C. Dransfeld. Thin ply composites: experimental characterization and modeling of size-effects. Composites Science and Technology, 101,121-132, 2014
4. R. Teixeira, S. Pinho, P. Robinson. Thickness-dependence of the translaminar fracture toughness: Experimental study using thin-ply composites. Composites Part A. 90, 2016.
5. R. Amacher et al., Toward aerospace grade thin-ply composites, Proceedings of 17th European Conference on Composite Materials (ECCM17), Munich, Germany, June 2016
6. M. Jalalvand, G. Czél, M. R. Wisnom. Damage analysis of pseudo-ductile thin-ply UD hybrid composites - A new analytical method. Composites: Part A, 69, 83-93, 2015

  doi:10.5075/epfl-298799_978-2-9701614-0-0

VALIDATING SIMULATED RESIDUAL STRAINS DUE TO THERMOFORMING USING FBGS

Michael, Paulitsch[a], Maximilian Pollak[a], Christoph Zanghellini[a], Johannes Jungbauer[a], Franz Maier[a], Roland Hinterhölzl[a]

a: Research Group of Lightweight Design and Composite Materials, University of Applied Sciences Upper Austria, Stelzhamerstraße 23, 4600 Wels, Austria – Michael.Paulitsch@fh-wels.at

Abstract: *Accurately determining process induced residual strains in carbon fiber reinforced plastic (CFRP) and CFRP-metal hybrids is vital for understanding the behavior of manufactured components and to validate simulations of process induced deformations. The required local strain measurements for this task can be obtained with Fiber Bragg Gratings (FBGs), embedded between CFRP layers. The required strain and temperature calibrations is carried out in a tensile testing machine. FBGs were used to monitor the manufacturing process of CFRP and hybrid plates in a thermoforming station until demolding. Good agreement in terms of strain results and visibility of major effects such as crystallization behavior between measurement data and process simulation results has been achieved.*

Keywords: FRP-metal hybrid; FBG; Process simulation; Thermoforming; Residual stresses

1. Introduction

FBGs are fiber optical sensors using a Bragg grating, i.e., a periodical modulation of the refractive index in the core of the fiber. Changes in the state (temperature, strain, pressure) of the embedding material result in a deformation of the grating and cause a modulation of the wavelength of the reflected light. FBGs have been used for process monitoring and structural health monitoring in various CFRP components [1–3] and have also been applied in Fiber Metal Laminates (FMLs) [4]. They are placed between layers and measure the local strain the direction of the FBG, to validate cool- down- and warpage- simulations by comparing the measured strain to the predicted strain in the simulation.

2. Materials

For this study, carbon fiber reinforced plastic (CFRP) and CFRP-metal hybrid plates with a length of 200mm, width of 100mm and a total thickness of 4 mm were manufactured. The constituents were UD carbon fiber reinforced PA6 (SIGRAPREG®TP C U157-0/NF-T340/46%) and 2 mm 1.4301 stainless steel or EN AW-1050A aluminum (Al) sheets. For hybrid components, an approximately 25µm thick layer of the adhesion promoter Vestamelt Hylink (Evonik) was deposited onto the sandblasted metal surfaces. The investigated layups are summarized in *Table 1*.

Table 1 Layups of investigated CFRP and hybrid plates

$0_2/90_2/0$	TC, FBG	$0/90_2/0_4/90_2/0_2/90_2/0_2$
0_5	TC, FBG	$0_7/90_8$
Metal/0_2	TC, FBG	0_8
Metal/0_2	TC, FBG	$90_2/0_2/90_2/0_2$

  doi:10.5075/epfl-298799_978-2-9701614-0-0

FBGs with standard gratings and Thermocouples Type K (TC) for strain and temperature measurement respectively were placed centrally in the indicated layers. Their positions in the layup were chosen to avoid the neutral axis and determined by a preliminary simulation with Esacomp (Altair). In the hybrid laminate, the cable of the TC was put in the layer adjacent to the FBG, however, the sensor tip was pushed through in the layer to measure in the immediate vicinity of the FBG. The position of the FBG in the layup after processing was confirmed by investigating cross-sectional cuts. For the analysis, FBGs and an interrogator of the company Miopas were used.

3. FBG strain and temperature calibration

In order to carry out quantitative measurements, FBGs have to be calibrated for strain, temperature and pressure. The aim was to identify a sensor signal at corresponding temperatures and strains respectively, to calibrate one influence at a time. As recommended by the manufacturer, the calibration was carried out with the sensor embedded in the host material used in the actual experiments, to account for the shear deformation of the coating, and moisture and bounding conditions of the sensor to the host material [5]. Strain and temperature calibration were carried out using a tensile test machine (Zwick, 20kN) with a climate chamber on a 4mm thick UD CFPA6 specimen ($[0_5/FBG/0_{15}]$). Data was analyzed using Matlab scripts. No measurable effect on the embedded FBG was evident when applying the maximal pressure on the specimen in the thermoforming press. Therefore, no pressure calibration was carried out.

Based on [4,5], it was assumed that FBGs from the same series have the same sensitivity but could have a different strain-free wavelength λ_0, at which the FBG is experiencing zero strain. Instead of the measured wavelength (λ) or a normalized wavelength $\frac{\lambda-\lambda_0}{\lambda_0}$, a change of wavelength $\Delta\lambda = (\lambda - \lambda_0)$ was used for the calibration to compensate for potential influences of varying values for λ_0 in different sensors.

3.1 FBG strain calibration

For the strain calibration, strains of 0.14% were applied at 50° and 100°C and held for 5 minutes, exceeding the minimal recommended strain value of 0.1% in VDI/VDE2660. Preliminary tests confirmed a linear relationship between the change in wavelength $\lambda - \lambda_0$ and strain ε (eq. 1):

$$\lambda - \lambda_0 = k\varepsilon + d \qquad (1)$$

where k and d are fitting parameter. To evaluate the measured data, the strain-free wavelength λ_0 was set at 215°C. At this temperature the material solidified sufficiently to ensure slip-free bonding of the sensor while the sensor can still be considered strain-free, i.e., establishing a zero-strain baseline. Parameters k and d were determined by a least square regression. The slope k is divided by λ_0 to make it comparable with normalized measurements, amounts to 0.7875, representing good agreement with the correlation of 0.78 between wavelength and strain found in the literature. [1]

3.2 FBG temperature calibration

The test plate was heated to 20, 50, 100, 150 and 200°C and held for 3 min to realize plateaus in the temperature profile. Temperature was measured with a TC embedded in the plate. During temperature calibration, the specimen was clamped on the upper edge and free to expand otherwise.

There are two temperature related influences on the detected wavelength of the FBG: Firstly, the thermal strain due to expansion of the host material $(\lambda - \lambda_0)_{\alpha(T)}$, which is the desired parameter to be measured during the manufacturing process. Secondly, the change of the refractive index of the FBG i.e., the thermo-optical effect $(\lambda - \lambda_0)_T$, which needs to be both calibrated and compensated for, from the total change in wavelength. The measured shift in wavelength $(\lambda - \lambda_0)_{tot}$ is the sum of those influences.

The thermal strain of the host material can be calculated using the (temperature dependent) coefficient of thermal expansion (CTE(T)) of the host material, which was measured in fiber direction from 30 to 190°C via thermo-mechanical analysis (TMA) and approximated by a polynomial fit. Outside of the measurement interval, the CTE was assumed to be constant. The calculated thermal strain can be converted into a shift in wavelength $(\lambda - \lambda_0)_{\alpha(T)}$ using Eq. (1).

Subtracting the shift of wavelength due to thermal expansion or contraction $(\lambda - \lambda_0)_{\alpha(T)}$ from the total wavelength shift $(\lambda - \lambda_0)_{tot}$ results in the temperature sensitivity or thermo-optical effect of the FBG $[\lambda - \lambda_0]_T$:

$$(\lambda - \lambda_0)_T = (\lambda - \lambda_0)_{tot} - (\lambda - \lambda_0)_{\alpha(T)} \quad (2)$$

A quadratic model was fitted to eliminate the thermo-optical effect:

$$(\lambda - \lambda_0)_T = p_1 * T^2 + p_2 * T + p_3 \quad (3)$$

For temperature measurements, TCs were used instead of FBGs because of the significantly lower costs and reusability. A comparison between temperature measurement of TC and FBG confirms a neglectable difference in measurement accuracy resulting in a neglectable difference in the measured strain (*Figure 1*).

Therefore, the strain is calculated from the measured temperature and wavelength as Eq. (4):

$$\varepsilon(\lambda, T) = \frac{(\lambda - \lambda_0)_{measured} - p_1 * T^2 + p_2 * T + p_3}{k} \quad (4)$$

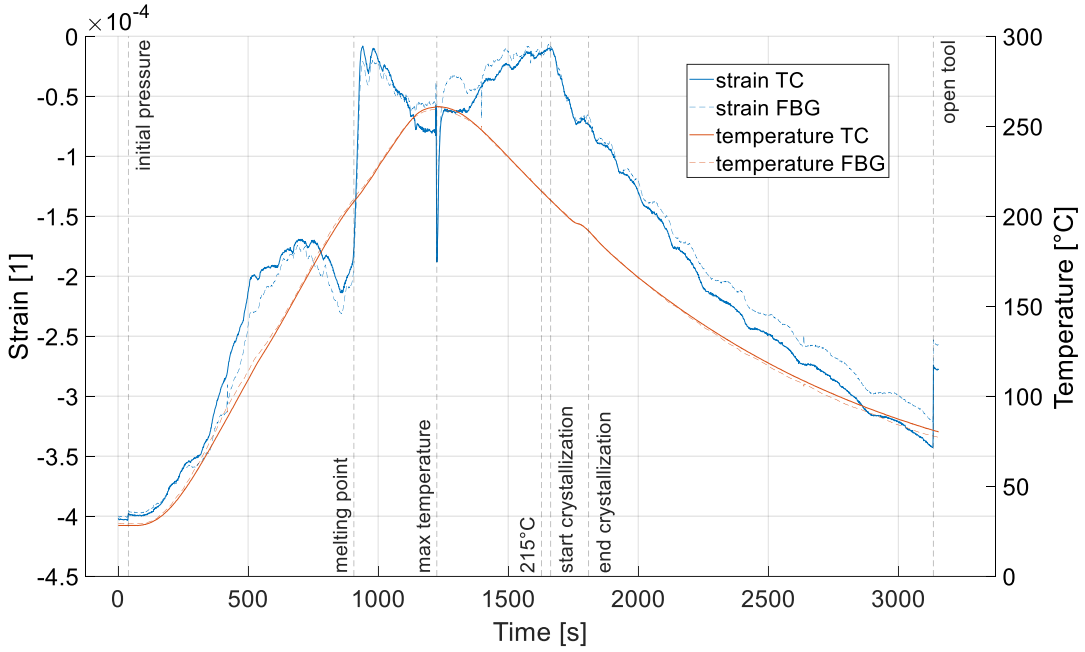

Figure 1. Comparison of strain results based on temperature measurements via TC and FBG

4. Sample manufacturing

The plates were manufactured in a thermoforming press. CFRP plates comprised 20 unbonded 0.2 mm thick prepreg layers. Hybrid plates comprised 10 unbonded prepreg layers and a 2mm thick metal sheet, coated with the adhesion promoter Vestamelt. A small silicon hose at the exit point of the FBG from the laminate prevents breakage of the glass fiber. The layup was heated to 260°, followed by a 2 min hold for temperature homogenization and the application of 100kN pressing force. Maintaining the pressure, the cool down to 80°C is accelerated by active ventilation, followed by demolding and subsequent cooling at ambient temperature.

5. Results and Comparison with process simulation:

The recorded FBG strain and TC temperature are shown in *Figure 2,* and several key events (initial pressure, melting point, max temperature, etc.) in the manufacturing process are indicated. The measured signal contains a superposition of crystallization shrinkage and cooling shrinkage. Crystallization initiates at 200°C and is mainly completed at 185°C, visible as steeper slope in shrinkage strain, followed by a transition to constant shrinkage due to cooling. Based on the exothermic nature of the crystallization process, the temperature curve during crystallization shows a steeper increase in compressive strain. The measurement is stopped shortly after demolding. The next recorded data point is at room temperature, causing the apparent step as the cool down process from demold temperature to room temperature is not depicted.

The effect of temperature on the measured strain in the FBG depends on the current state of the laminate, i.e., in a solid state the CTE of the laminate must be considered, while in the molten state only the CTE of the fiber affects the FBG via friction. Because of these different embedding conditions of the FBG in molten and solid state and material consolidation (unbonded layers prior to heating) the strain results of the measurement can only be evaluated quantitatively

  doi:10.5075/epfl-298799_978-2-9701614-0-0

after a reliable connection of the sensor to the laminate is established, i.e., after 215°C at cooling. Experiments with the same layup led to the same qualitative result but an offset in strain, indicating a stable process and measurement system.

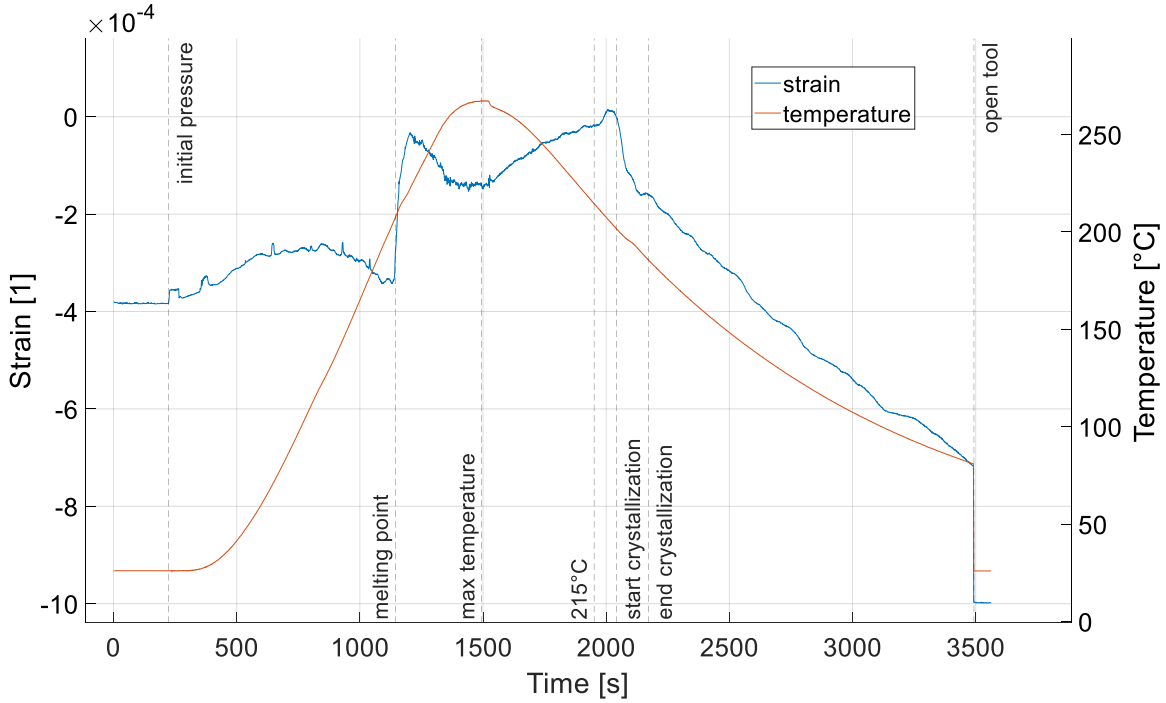

Figure 2. Measured strain (blue) and temperature (orange) from the FBG during the manufacturing of [Steel/0₂/90₂/0₂/90₂/0₂] with key steps being highlighted

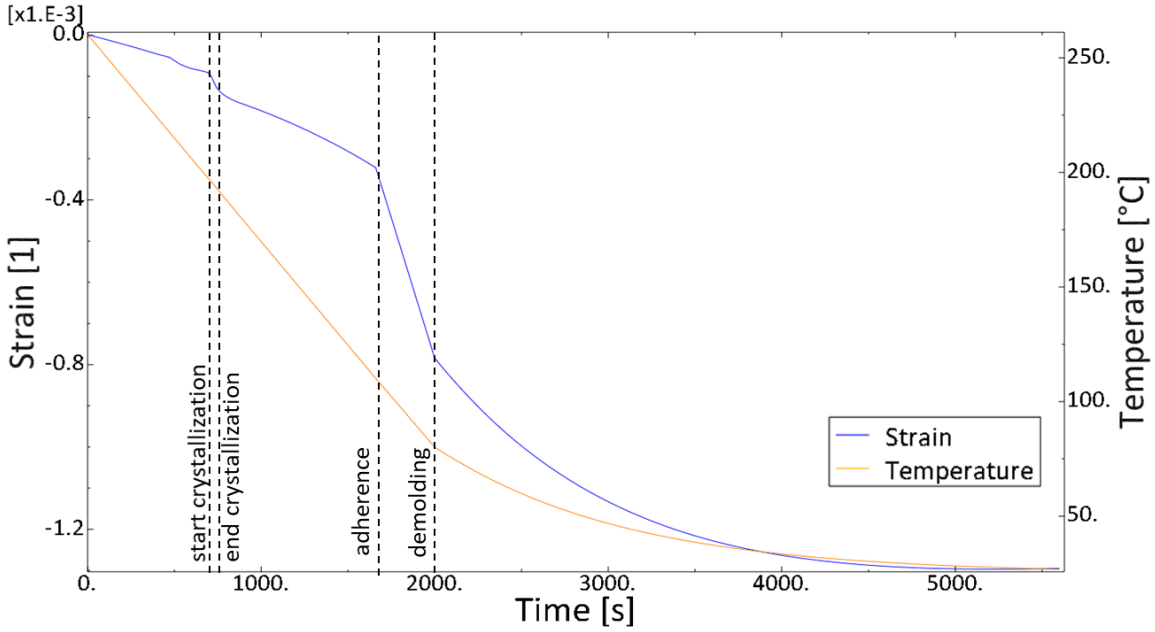

Figure 3. Resulting strain (blue) and temperature (orange) of the cool down and warpage simulation of [Steel/0₂/90₂/0₂/90₂/0₂] layup

Results of the measurements were compared with cool down and warpage simulation results of the respective layer the FBG was put in (*Figure 3*, *Table 2*). These simulations were implemented in Abaqus using the COMPRO (Convergent) plug-in and model the cool-down behavior from 260°C to 20°C based on a constant cooling rate of 5.5°C/min. Material characterization was performed according to [6]. *Figure 3* depicts the entire simulated cooling process, showing the crystallization at roughly 750s and the demolding at 2000s. The sharp decrease after 1660s stems from reaching 110°C which is the chosen adherence temperature of constituents. This behavior is not shown in the experiment and is attributed to modelling the adherence behavior in the simulation. It is modelled with a discrete step at 110°C but the experiment suggests a continuous transition from sliding to bonding. However, the additional modelling effort was outside the scope of this study. In contrast to the measurement in *Figure 2*, cooling after demolding is included in *Figure 3*. Strain measurement results are in good agreement with the simulated strain.

*Table 2: Measurement and simulation results for residual strains after cool down and demolding (3500s in Figure 2, 5600s in Figure 3). The * indicates that only of valid specimen was tested for this configuration.*

	Material Combination	Measurement Strain [10^{-3}]	Simulation Strain [10^{-3}]
CFRP	$[0_2/90_2/0_2/90_2/0_2]s$	-0.56	-0.55
		-0.49	-0.55
	$[0_{12}/90_8]$*	-0.59	-0.37
CFRP-metal hybrid	$[Al/0_{10}]$	-0.68	-0.95
		-0.67	-0.95
	$[Al/0_2/90_2/0_2/90_2/0_2]$	-1.22	-1.3
		-1.17	-1.3
	$[Steel/0_{10}]$	-0.47	-0.85
		-0.47	-0.85
	$[Steel/0_2/90_2/0_2/90_2/0_2]$	-1.00	-1.1
		-1.27	-1.1

The measurement strains depend strongly on the CTE of CFPA6 in fiber direction. A relatively large deviation in the specimen tested with TMA has been found. Using those individual results from TMA, an increase in strain of $1.5 \cdot 10^{-4}$ compared to the results in *Table 2*, representing a 12% to 30% deviation, can occur. Therefore, a larger sample size with precisely aligned specimen, to account for the dependency on the fiber orientation, must still be realized to improve the data. A potential explanation for variability is assumed to be fiber orientations deviating from 0°, therefore samples will be investigated prior to testing.

The extent of the thermo-optical effect is different for each sensor, therefore an exact result would require the calibration of each sensor. The deviation from the exact result is approximately $2 \cdot 10^{-5}$, so one order of magnitude smaller than the result and therefore neglectable. This effect is also responsible for λ_0 not being at 0 strain in *Figure 2*.

The definition of temperature at which residual strains start to build up, i.e. the stress free temperature can be chosen differently. [7,8] argue that the stress free temperature is found near peak crystallization temperature and before that potential stress build up can be relaxed via molecular chain movement. The difference amounts to about $2 \cdot 10^{-5}$ and was determined to be neglectable.

6. Conclusion

A process monitoring method for residual strain in CFRP and CFRP-metal hybrids was established with FBGs. In order to interpret the measurement data quantitatively, strain and temperature calibrations were carried out on a UD-CFRP plate. In the in-situ strain monitoring during the manufacturing process of CFRP-metal hybrid plates several key events such as crystallization are recorded. Measurement data is in good agreement with simulations of the crystallization kinetics and the residual strains in the manufactured part.

Acknowledgements

We gratefully acknowledge the financial support of the Upper Austrian Government under the FTI-structural-funding program in the scope of the project ‘Erforschung von Methoden für die Mobilität der Zukunft’, project number “Wi-2018-466449/18-WieM”.

7. References:

1. Dobb H, Webb DJ, Kalli K, Argyros A, Large MCJ, van Eijkelenborg MA, et al. Continuous wave ultraviolet light-induced fiber Bragg gratings in few- and single-mode microstructured polymer optical fibers. Opt Lett [Internet]. 2003;161(8):417–82.
2. Lee B. Review of the present status of optical fiber sensors. Opt Fiber Technol. 2003;9(2):57–79.
3. Friebele EJ, Askins CG, Bosse AB, Kersey AD, Patrick HJ, Pogue WR, et al. Optical fiber sensors for spacecraft applications. Smart Mater Struct. 1999;8(6):813–38.
4. Prussak R, Stefaniak D, Hühne C, Sinapius M. Evaluation of residual stress development in FRP-metal hybrids using fiber Bragg grating sensors. Prod Eng [Internet]. 2018;12(2):259–67. Available from: http://dx.doi.org/10.1007/s11740-018-0793-4
5. Gmbh M. User Manual MIOPAS Interrogator SPK-155. 2020;
6. Gordnian K. Crystallization and Thermo-Viscoelastic Modelling of Polymer Composites. University of British Columbia; 2017.
7. Nairn JA, Zoller P. Matrix solidification and the resulting residual thermal stresses in composites. J Mater Sci. 1985;20(1):355–67.
8. Jeronimidis G, Parkyn AT. Residual Stresses in Carbon Fibre-Thermoplastic Matrix Laminates. J Compos Mater. 1988;22(5):401–15.

  doi:10.5075/epfl-298799_978-2-9701614-0-0

ADVANCED MULTIFIELD MODELS FOR WAVES PROPAGATION ANALYSIS IN METALLIC PANELS

Jamal, Najd[a,b], Enrico, Zappino[a], Erasmo, Carrera[a], Walid, Harizi[b], Zoheir, Aboura[b]

a: Mul2 Group, Department of Mechanical and Aerospace Engineering, Politecnico di Torino, Torino, Italy (jamal.najd@polito.it)
b: Université de Technologie de Compiègne, Roberval, Compiègne Cedex, France

Abstract: *Active health monitoring of structures throughout their life cycle is a privilege in the different industrial domains. However, it is essential to the domains where the structures are made of composite materials due to the complex damage mechanisms involved compared to metals* [1] *and due to the absence of an accurate numerical model that permits the prediction of their failure. In this work, the assessment of a multifield layer-wise finite element dynamic plate model (MUL2) based on the Carrera Unified Formulation (CUF) is conducted, on an isotropic aluminum material strip, in order to verify the validity of the model and to finely tune the parameters needed to accurately model wave propagation in the future in laminated material of orthotropic nature. The convergence of the plate model was studied under different modeling parameters, including mesh density, to-the-thickness kinematic model, plate element type and the number of timesteps.*

Keywords: Wave propagation; Lamb waves; Plate model; Carrera Unified Formulation (CUF)

1. Introduction

Composite structures have by nature a complex damage mechanism. This requires the use of different measures to monitor the health of structures made by these materials. The use of various non-destructive testing (NDT) approaches has been studied for the past several decades so that the health of the structure can be determined without affecting its integrity. This is where the application of elastic guided waves propagation in structures excelled for the inspection of structures. Out of these waves, we can mention and focus on Lamb waves that propagate in elastic solid plates with free boundaries. These waves have a displacement direction that is both parallel and perpendicular to the midplane of the plate. Lamb waves have two unique modes of propagation found in isotropic plates, known as symmetric (S) and antisymmetric (A) modes. They are characterized of being the dispersive kind, and the number and nature of modes propagating in a plate depends on the excitation frequency imposed [2]. It can be noticed that for the lower values of frequency-thickness, the excited modes are the fundamental S_0 and A_0 modes exclusively. Among these modes, it is desired to choose the excitation frequency-thickness so that the dispersion effect is relatively low. This can be done by plotting the solution equations of the Lamb wave propagation, named dispersion curves and checking the domain where the velocities are almost constant. As the propagation of these waves is fairly simple in isotropic materials, the taken example under which convergence was studied involves an isotropic aluminum strip. This is also due to the validity of a benchmark with all the properties needed to model wave propagation.

  doi:10.5075/epfl-298799_978-2-9701614-0-0

2. Refined Numerical FE Model

The numerical FE model utilized is the MUL2 model, which is based on the Carrera Unified Formulation. In this model, the mechanical 3D displacement vector u (x, y, z) can be split into two terms. The first term, along the xy plane, which has to do with the FEM 2D mesh, and a second term, along the thickness z, that deals with the kinematics of the used model.

$$u(x, y, z) = u_\tau(x, y).F_\tau(z)$$

In commercial FEM programs, it is possible to tune the first terms by deliberately reducing mesh size, increasing the mesh density, or by changing the type of the shell element used. However, it is not possible to tune the second item which deals with the plate kinematics. This means that no matter how much the refined mesh may be, the solutions available can not deliver highly accurate results compared to a 3D model. Using a higher order expansion to-the-thickness allows for the modeling of 3D problems using plate models. This higher order expansion can either be in the form of an equivalent single layer (ESL) referred to as TE, where the whole plate thickness is considered as one layer and Taylor Expansion polynomials are used to the specified order; or it can be a Layer-wise expansion (LW) referred to as LE, where Lagrange Polynomials (linear B2, quadratic B3, or cubic B4) are used in each layer.

In TE for the nth order (TE*n*), the second term $F_\tau(z)$ is written in the terms of z^n where n is the order of the expansion. Taking the third order as an example, the general displacement is given as:

$$U = 1.U_0 + z.U_1 + z^2\,U_2 + z^3\,U_3$$

Where U_i are the unknowns of the problem and U representing the displacement vector {u,v,w}

For LE on the other hand, and taking the linear B2 element as an example, the displacement vector U can be written in terms of linear Lagrange polynomials F_1 and F_2 as:

$$U = F_1U_1 + F_2U_2$$

Where U_1 and U_2 are the actual displacements at the top and the bottom of the plate element, and the polynomials F_1 and F_2 are given by:

$$F_1 = \frac{1+\zeta}{2} \quad and \quad F_2 = \frac{1-\zeta}{2}$$

Where -1< ζ < 1. On the top, ζ =1, F_1 = 1 and F_2 =0. On the bottom, ζ =-1, F_1 = 0 and F_2 =1

It can be referred to [3,4] for more information about the Taylor and in refined plate models.

3. Benchmark problem

In this work, the propagation of both fundamental modes was studied using a dynamic numerical analysis which composes of an assessment of the problem regarding the different numerical parameters. In order to efficiently compare the different variations, it is important to specify a guideline to compute the propagation of the ultrasonic waves. The used setup was the one mentioned in [2]. The wave propagation was studied in a thin plate of a 2 mm thickness, a width of 10mm and a length of 500mm. A set of boundary conditions was applied at the boundaries along the width limiting the displacement in the X-axis and ensuring the

  doi:10.5075/epfl-298799_978-2-9701614-0-0

unidirectional propagation of the wave along the y direction. A left boundary condition was applied at the plane y=0 as proposed by the benchmark reference mentioned above. The shape of the excitation force imposed is shown in Eq. (1). The two forces are applied perpendicularly and of equal magnitude through time. However, the direction of the forces might differ. Opposite forces produce symmetric waves whereas if both forces have the same direction, antisymmetric waves are generated. In this paper, the applied forces are of opposite direction leading to fundamental symmetric wave generation (S_0). The shape of the load is shown in Eq. (1),

$$F(t) = \tilde{F} sin\omega t \sin^2\left(\frac{\omega t}{2n}\right) \quad (1)$$

where $\omega = 2\pi f$ represents the proper pulsation with the central frequency f and n represents the number of cycles within the signal. The central frequency was chosen so that there would be only a single mode of excitation present, such that $f.d < 1.5\ MHzmm$ according to the dispersion curves in Figure 1 of a 2mm thick aluminum plate of mechanical characteristics found in Table 1.

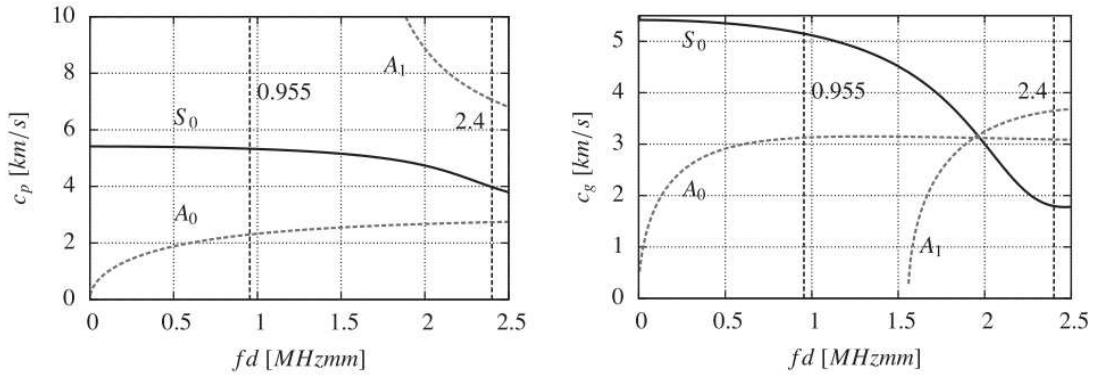

(a) Phase velocities *(b) group velocities*

Figure 1. Dispersion curves of 2mm aluminum plate showing (a) phase and (b) group velocities of the antisymmetric modes (A_i) 'dashed' and the symmetric modes (S_i) 'continuous' [2]

For this reason, the excitation frequency was chosen to be $f = 477.5\ kHz$ with $n = 32$. To study the convergence behavior, two points were chosen (A and B) located on the top of the plate and on the midplane. The position of these points along the y-axis is respectively l_A and l_B(Figure 2)

Table 1 . Material data for aluminium

Youngs modulus (E)	Poisson's ration (ν)	Mass density (ρ)	Longitudinal speed (c_y)	Transversal speed (c_x)
$7 \times 10^{10} \frac{N}{m^2}$	0.33	$2700 \frac{kg}{m^3}$	$6197 \frac{m}{s}$	$3121 \frac{m}{s}$

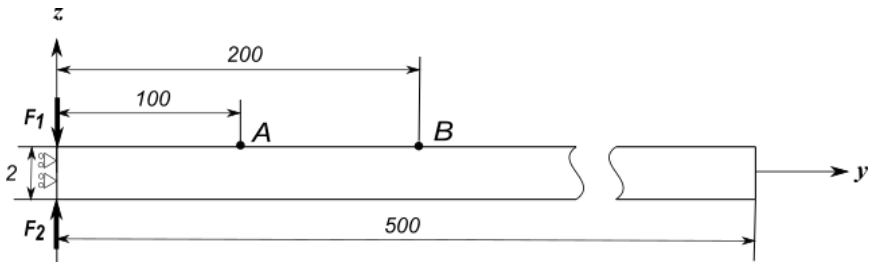

Figure 2. Benchmark of a 2mm aluminum plate showing the distances and the applied forces

4. Evaluation Methodology

The quality of the numerical tool was determined by numerically computing the time-of-flight (TOF) of the propagating Lamb wave packet between points A and B in Figure 3, and comparing this time to an analytical time, computed here by assuming a wave velocity similar to that of the analytical group velocity from the dispersion curves, according to the mode being excited (Table 2). In order to estimate the time at each point, the envelope of the propagating wave had to be generated from the u_z displacement using the Hilbert transform Eq. (2 & 3).

$$H_{A,B}\big(u(t)\big) = \frac{1}{\pi}\int_{-\infty}^{\infty} u_{A.B}(\tau)\ .\ \frac{1}{t-\tau}\ d\tau \tag{2}$$

$$e_{A,B} = \sqrt{H_{A,B}\big(u(t)\big)^2 + u_{A.B}(t)^2} \tag{3}$$

Table 2. Phase and group velocities obtained from dispersion curves [4]

$c_{p_{S0}} \cong 5316\frac{m}{s}$	$c_{p_{A0}} \cong 2298\frac{m}{s}$
$c_{g_{S0}} \cong 5130\frac{m}{s}$	$c_{g_{A0}} \cong 3126\frac{m}{s}$

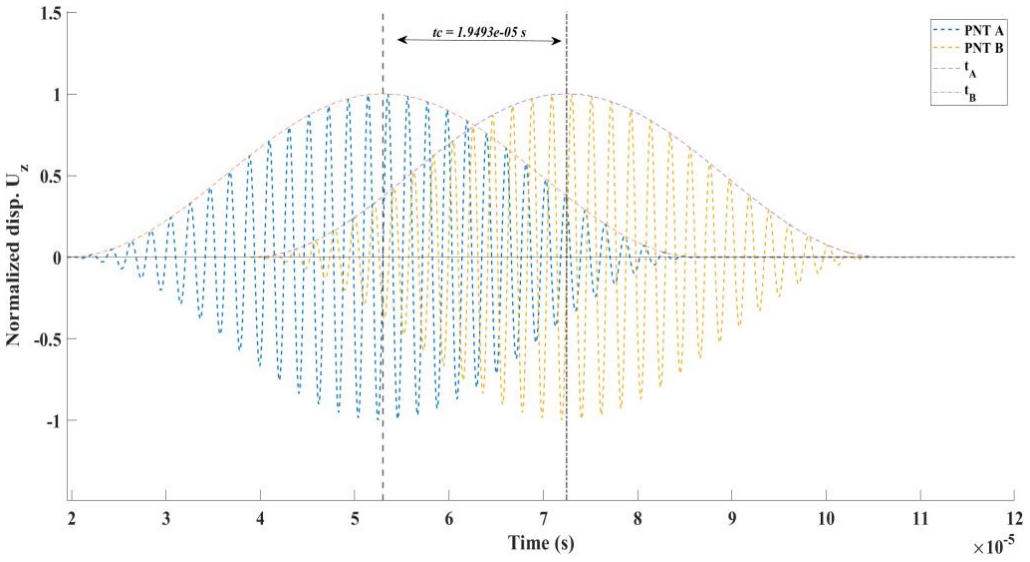

Figure 3. Normalized analytical displacement U_z at points A and B with $t_{c_{ana}}$

The centroid representing the time of each envelope was obtained Eq. (4). This was done using MATLAB commands and coding. The difference of the computed time between point B and A denoted by t_c. Eq. (5) is the time needed for the wave to travel from point A to B.

$$t_{A,B} = \frac{\int_0^{t_{end}} e_{A,B}(t).t\ dt}{\int_0^{t_{end}} e_{A,B}(t)} \tag{4}$$

$$t_c = t_B - t_A \tag{5}$$

And the calculated relative error is the percentage difference between the analytical and the numerical TOF of points A and B, it is calculated as it is seen in Eq. (6)

$$Error\ (\%) = \frac{t_{c_{ana}} - t_{c_{num}}}{t_{c_{ana}}} \times 100 \tag{6}$$

5. Assessment Results and Discussion

5.1 Plate element type

The type of the plate elements used was varied between three. The linear element type consisting of 4 nodes, the quadratic type consisting of 9 nodes per element and the cubic type consisting of 16 nodes per element. These elements are denoted by Q4, Q9 and Q16 respectively. Only one element was imposed to the width and the mesh density to the direction of propagation of the wave was altered between 100 to 2000 elements, 4000 for Q4 elements to show convergence. The results in Figure 4 show the convergence of the error with respect to the degrees of freedom according to the number of elements used in each of the three plate element types. Note that this was done for a fixed to-the-thickness Taylor expansion of the third order TE3 and with 2000 timesteps between 0 and 120 µs. It can be clearly shown that the higher order elements (Q9 and Q16) converge faster, for a lower mesh density, than the lower order. But these elements already have higher DOF for each element. The low mesh density leads to a stiff structure which explains the high error at the beginning of the curves.

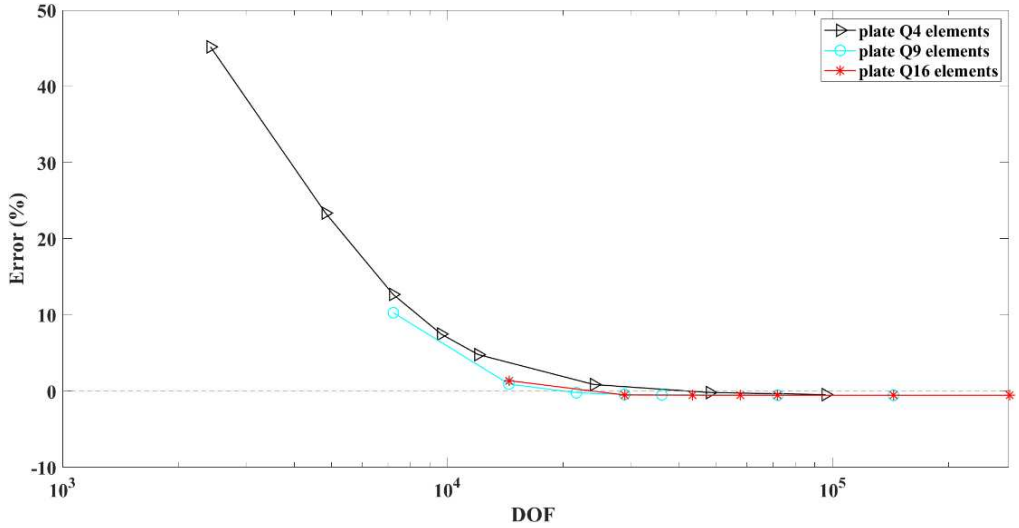

Figure 4. Convergence of different plate element types according to the degrees of freedom

5.2 Model kinematics

The convergence of the problem with different model Kinematics, or to-the-thickness expansion, was also studied in this paper. The Kinematics range between Taylor 1 to 4th expansion, and Lagrange expansion of linear, quadratic and cubic elements denoted by B2, B3 and B4 respectively, where 2B4 means two cubic elements of expansion. These models were compared with one another under the same plate element type, using the same timestep mentioned above (2000 timesteps between 0 and 120 µs) but under different mesh density to the thickness. The classical plate theories such as classical lamination theory and first order shear deformation theories fail to capture wave propagation through the structure. The results shown in Figure 5 show clearly the convergence of the out of plane expansions to different values. Noting that the linear expansion of both Taylor and the one Lagrange element to-the thickness have exactly the same results with the same DOF. The same goes for TE2 and LE B3, and to TE3 and LE B4. The advantage of using Lagrange expansion lies in the ability to impose boundary conditions on the top and bottom nodes of the plate separately. Also using many elements to the thickness for layered structures, i.e. composites, to accurately depict their behavior.

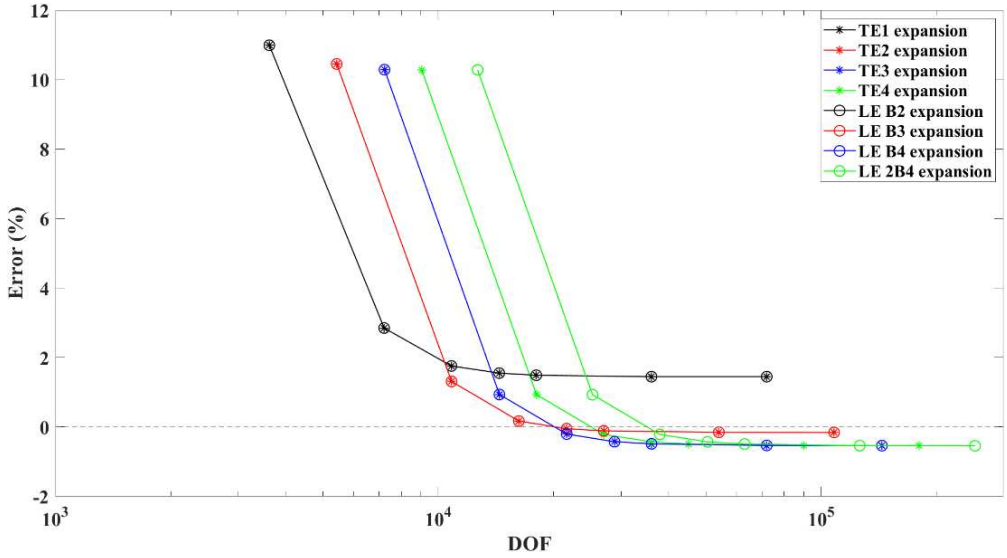

Figure 5. Convergence analysis of the different out of plane expansions according to the degrees of freedom

It is also clearly shown in Figure 6, where the results were plotted with respect to the mesh number along the thickness. It is true that the convergence value of the higher order expansion has a higher error in these results, but this is mainly due to the choice of the timestep as the next results will bring to light.

5.3 Time step analysis

As mentioned above, the effect of the timestep number within the modeling time ranging from 0 to 120 µs was studied for only one case. The chosen case was a structure having Q9 elements and with TE3 (or LE B4) expansion as these produce the same results for a one layered structure. The reason behind choosing this order of expansion lies in the fact that the higher order expansions used in the comparison (TE4 and LE 2B4) converged to the same values as that of this expansion but for a higher computational cost, see Figure 5. The number of timesteps chosen was 500, 1000, 2000 and 4000. The analysis was done for different mesh densities as earlier.

  doi:10.5075/epfl-298799_978-2-9701614-0-0

The results of Figure 7 show the clear relation between minimizing the time step (using more steps) to the convergence towards the analytical value. The lower the timestep is, the more accurate the value of convergence, for the same model kinematics. This is due to the higher accuracy of the imposed variable load at lower timesteps and due to the higher accuracy during the integration of the produced displacement curve under higher value of timesteps.

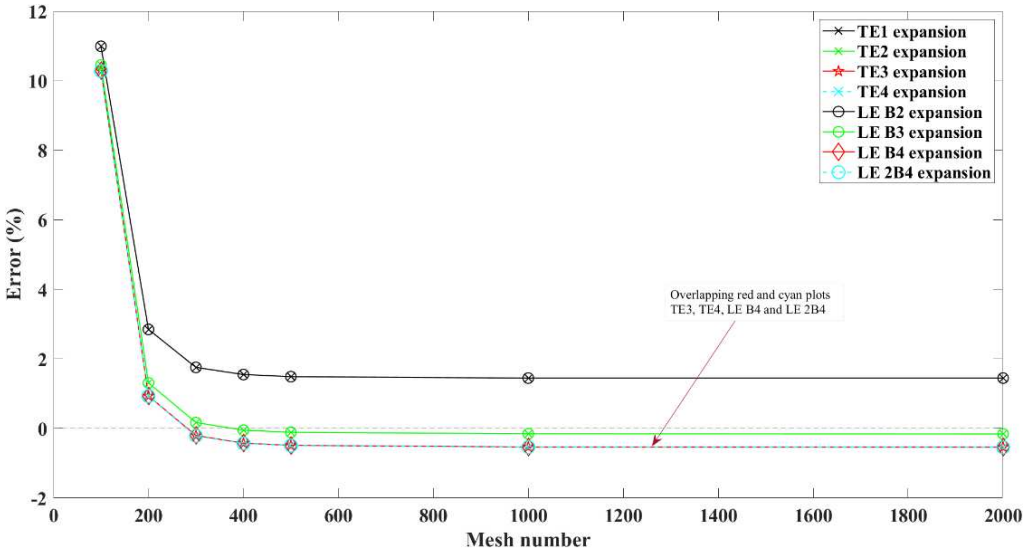

Figure 6. Convergence analysis of the different out of plane expansions w.r.t mesh number

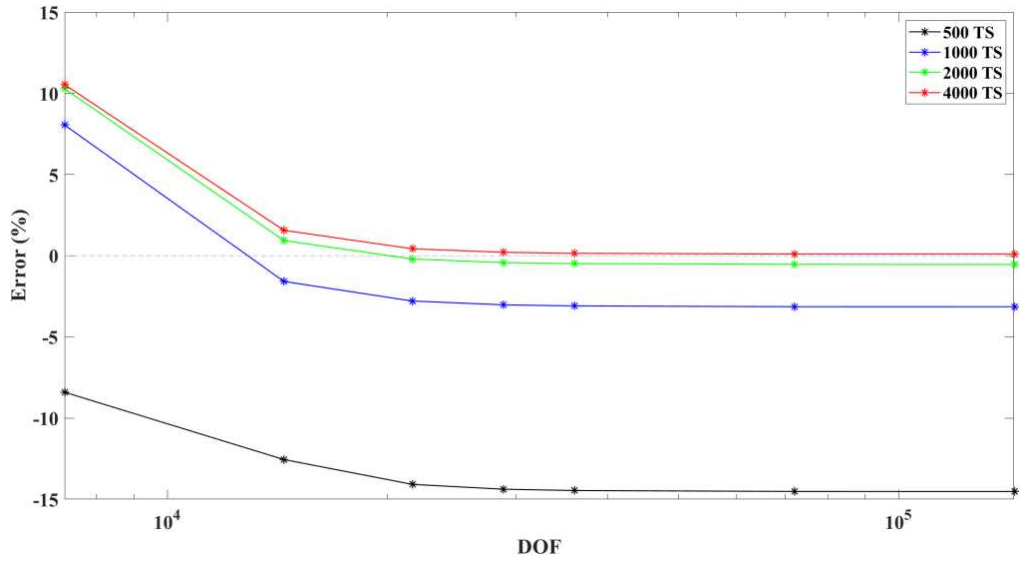

Figure 7. The effect of the number of timesteps (timestep estimate) on the convergence value

6. Conclusion

The numerical assessment of symmetric Lamb wave propagation using a Variable Kinematics model was studied for isotropic aluminum material on the premise of validating the model for further use in laminated and smart structures. The findings of this work show that this model can accurately predict the propagation of the symmetric Lamb waves in isotropic material. If

plate models were to be used, the most suitable element types would be either Q9 or Q16 elements, as Q4 elements are highly not recommended due to the low accuracy. The number of elements used differ according to the element type used, as Q16 elements can reach the same accuracy of Q9 elements for a lower number of elements but on the expense of DOF compared to that of Q9. As for the plate kinematics, or to-the-thickness expansion, the cubic to-the-thickness expansion (TE3 or LE B4) was enough. To reach a higher accuracy in modeling and convergence, a more refined timestep should be used, leading to the use of almost 4000 timesteps in the time domain of the model. To check the validity of the in general expressions mentioned in [4], with a timestep $\Delta t < \frac{1}{20\, f_{max}}$ and mesh size $L_{min} < \frac{\lambda}{10}$, and where $\lambda = \frac{c_y}{f}$. In order to get an error of less than 1%, according to our results it is better to choose a timestep $\Delta t < \frac{1}{30 f_{max}}$ with a cubic expansion to-the-thickness, as $\Delta t < \frac{1}{20\, f_{max}}$ gives a round 1200 timesteps, leading to a higher convergence error. The minimum mesh size is chosen to be $L_{min} < \frac{\lambda}{8}$ when using Q9 plate elements and $L_{min} < \frac{\lambda}{5}$ when using Q16 plate elements, thus a general mesh size of $L_{min} < \frac{\lambda}{10}$ as proposed in the reference before is acceptable.

Acknowledgements

The authors would like to thank the Hauts-de-France Region (France) and Politecnico di Torino (Italy) for the funding of this work as part of the doctoral thesis of Mr. Jamal NAJD (Agreement number 20003877, N◦ GALIS: ALRC2.0-000072).

1. References

1. Jollivet T, Peyrac C, Lefebvre F. Damage of composite materials. In: Procedia Engineering. Elsevier Ltd; 2013. p. 746–58.

2. Giurgiutiu V. Structural health monitoring with piezoelectric wafer active sensors. 16th International Conference on Adaptive Structures and Technologies. 2006. 94–100 p.

3. Carrera E, Cinefra M, Zappino E, Petrolo M. Two-Dimensional Shell Models with Nth-Order Displacement Field, the TE Class. In: Finite Element Analysis of Structures Through Unified Formulation [Internet]. John Wiley & Sons, Ltd; 2014. p. 231–51. Available from: https://onlinelibrary.wiley.com/doi/abs/10.1002/9781118536643.ch11

4. Carrera E, Cinefra M, Zappino E, Petrolo M. Two-Dimensional Models with Physical Volume/Surface-Based Geometry and Pure Displacement Variables, the LE Class. In: Finite Element Analysis of Structures Through Unified Formulation [Internet]. John Wiley & Sons, Ltd; 2014. p. 253–60. Available from: https://onlinelibrary.wiley.com/doi/abs/10.1002/9781118536643.ch12

5. Willberg C, Duczek S, Vivar Perez JM, Schmicker D, Gabbert U. Comparison of different higher order finite element schemes for the simulation of Lamb waves. Comput Methods Appl Mech Eng [Internet]. 2012;241–244:246–61. Available from: http://dx.doi.org/10.1016/j.cma.2012.06.011

6. GARCIA DE MIGUEL A. Hierarchical component-wise models for enhanced stress analysis and health monitoring of composites structucres. Politecnico di Torino; 2019.

7. Alem B, Abedian A, Nasrollahi-Nasab K. Reference-Free Damage Identification in Plate-

Like Structures Using Lamb-Wave Propagation with Embedded Piezoelectric Sensors. J Aerosp Eng. 2016;29(6):04016062.

  doi:10.5075/epfl-298799_978-2-9701614-0-0

ULTRA-THIN, HIGH POROUS PAPER SENSORS

Uwe Müller[a], Florian Egger[b], Martin Kaltenbrunner[b], Herfried Lammer[a], Arunjunai raj Mahendran[a], Franz Padinger[c], Melanie Steiner[a], Thomas Stockinger[b]

a: Kompetenzzentrum Holz GmbH (Wood K plus), Altenbergerstraße 69, 4040 Linz, AT
u.mueller@wood-kplus.at
b: Soft Matter Physics, Johannes Kepler University, Altenbergerstraße 69, 4040 Linz, AT
c: SCIO Holding GmbH, Franzosenhausweg 51, 4030 Linz, AT

Abstract: *Sensor technology in composites enables in-situ analysis of cross-linking, monitoring of material properties, communication between material, developer and end user, and integration of intelligent functions. For minimally invasive sensor integration, the sensors should be made of the same material as the end product or the resin must be able to penetrate the sensors. Furthermore, the sensors must be flexible as the sensors are often deformed with the product.*

In the paper industry, many highly porous or ultra-thin papers are produced for tea bags, overlays, sausage casings, capacitors, and so on. These papers contain no additives. In this work, we show that it is possible to print impedance sensors on commercial highly porous papers. These sensors can be integrated into composites, allowing unadulterated in-situ analysis of the cross-linking of the matrix. The printed sensors on such materials are a cost-effective and economical route for a wide range of applications.

Keywords: ultra-thin; high porous; paper; sensors

1. Introduction

Engineered wood, a high-tech material of the 21st century demonstrates the revival of timber for the construction of green urban eco-buildings. Moreover, gluing and composite technologies are innovative fields of interdisciplinary research, including fundamental investigations, development work and industrial applications. The mass timber architecture, carbon and glass fibre composites are examples, which benefit from progress of gluing and resin concepts, ranging from the development of high performance to robust, cost-, material- and time-efficient in-situ testing routines.

Nevertheless, testing of these materials still relies on methods known for centuries like pulling, bending and ripping. These techniques require strong manpower; they are ex-situ, destructive and incompatible with the Industrial Internet of Things (IoT). Commercially available impedance spectroscopy sensors allow in-situ analysis of curing [1], but in wooden glue joints or composites they do not only act as foreign bodies, they can also falsify the results.

We remove this dilemma in a frugal way [2] by developing a new generation of thin and ultrathin test sensors made from absorbent paper with printed surface electrodes, see Figure 1. Our sensors can be intimately integrated in glue lines, prepregs, coatings, enabling rapid in-line industrial performance analysis. They do not act as a defect and they can remain in the glue joint or composite as an integral element of the engineered wood or the composite part.

  doi:10.5075/epfl-298799_978-2-9701614-0-0

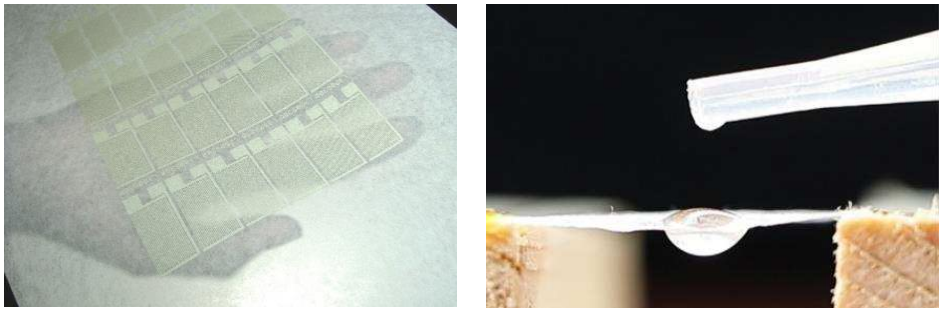

Figure 1. Printed sensors on high porous paper

2. Experimental

2.1 Materials

Commercial aqueous UF based or coloured mUF based glues and a commercial bio based epoxy prepreg were characterised by impedance and simultaneous impedance/DMA measurements.

For our experiments, we tested abaca papers from Glatfelter Gernsbach GmbH and Papierfabrik Wattens GmbH & Co KG, and compared the results with a special electronic printing paper (PES, Technocell) and prints on PET. The data for comparison have been already extensively investigated in an earlier publication [3].

2.2 Sensors

The sensors used for impedance measurements were printed by screen printing with a silver ink and varying line/spacing. The gaps between electrodes have a width of G while the fingers have a width of W. Sensors with the following W/G ratio were printed on each paper: 300/300; 250/250; 200/200; 150/150; 125/125; 100/100, all numbers [µm/µm]. Since the highly porous abaca papers cannot be fixed with a vacuum, they were fixed on copy paper and then printed. More experimental details on the printing and characterisation (microscopy, surface texture, penetration etc.) of the printed sensors can be found in the paper from Stockinger [3].

2.3 Impedance Spectroscopy

All impedance measurements were performed using an impedance spectrometer (Alpha-A High Performance Frequency Analyzer) from Novocontrol (Germany). Experimental details for the measurements in the hot press are described in the paper from Stockinger [3].

The use of impedance spectroscopy or dielectical analysis for the characterisation of the cross-linking is well described in literature. However, the problem is that these publications use different symbols and terms and there is no standardised designation [4].

By dielectric analysis, the impedance of the system is measured [5]. The impedance presents the resistance, the ratio of voltage to the current, in an alternating field. It was introduced by NETZSCH to express this resistance as so-called ion viscosity (IonVisc), defined as the multiplicative inverse of the conductivity Eq. (1). The area of the electrodes and the distance between the electrodes are considered. Immobilization of groups as a result of polymerization processes causes a decrease in the dielectric conductivity. Moreover, the relation between ion viscosity and resin viscosity is derived with the Eqs. (2) – (4) [6, 7].

$$\boldsymbol{IonVisc} = \frac{\mathbf{1}}{\boldsymbol{\sigma}} = \frac{\mathbf{1}}{\boldsymbol{\varepsilon_0 \cdot \omega \cdot \varepsilon''}} = R_P \cdot \frac{A}{d} \quad (1)$$

$$\boldsymbol{IonVisc} = \frac{\mathbf{1}}{\mu \cdot [C] \cdot q} \sim \frac{\mathbf{1}}{\boldsymbol{\sigma}} \quad (2)$$

$$\boldsymbol{\mu} \sim \frac{\mathbf{1}}{\boldsymbol{\eta}} \quad (3)$$

$$\boldsymbol{IonVisc} \sim \boldsymbol{\eta} \quad (4)$$

where σ is the conductivity, ε_0 is the permittivity of free space ($8.854 \cdot 10^{-12}$ F/m), $\omega = 2\pi\phi$ is the angular frequency, is f the frequency of the alternating electrical field, R_P is resistance, A is electrode area, d is the distance between electrodes, μ is the ion mobility, [C] the mobile ion concentration, q the charge of an ion and η is the viscosity.

2.4 Simultaneous Measurements

The measurement was combined with DMA (Q800 from TA Instruments, USA) by inserting the sandwich (see Figure 2) in a 3-point bending clamp. DMA tests were carried out with an oscillation frequency of 1 Hz at amplitude of 40 µm and heating rate of 1K/min. Low heating rates (1-5 K /min) are necessary to guarantee the heat exchange inside the sandwich.

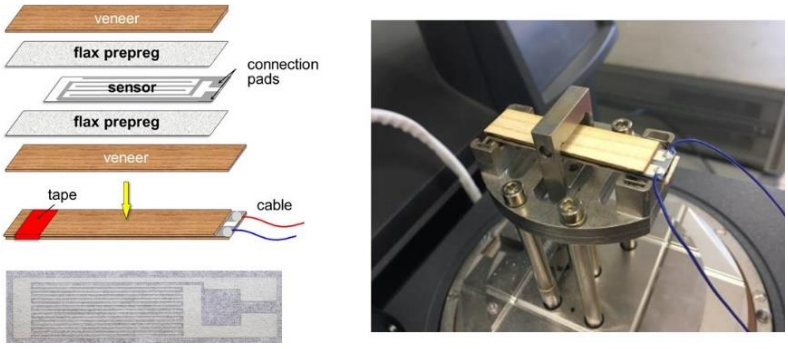

Figure 2. Experimental setup of the sandwich in the DMA with a small impedance sensor.

3. Results

3.1 Impregnation, Smoothness and Printability of the Paper

The papers investigated can also be divided into uncoated (abaca), coated (electronic printing paper), as well as long fibre papers (all abaca types). The surfaces of the papers differ more or less on type of surfaces either closed (coated), and open-pored (abaca papers). Especially the open-pored abaca papers differ extremely in air permeability. For example, the papers with 22 - 26 g/m^2 allow considerably less air to pass through (e.g. paper 5 >100 l/m²s) than the products with smaller grammage (>1600 l/m²s). The differences in the surface therefore suggest large differences in impregnation.

Surprisingly, we found that all papers can be impregnated with resin in less than 0.5 s. All open-pored abaca papers can be impregnated somewhat faster than the more closed electronic printing paper, but the differences are negligible.

Figure 3 shows the surface textures and printed silver lines with a W/G-ratio 300/300 [µm/µm] of an impedance sensor on one paper and on Polyethylene terephthalate (PET). The roughness (Ra) of the special electronic printing paper (PES) is almost twenty times higher than the PET-film (Ra = 0.11±0.04 (PET); 2.21±0.72 (PES). Nevertheless, the microscopic characterisation of a

  doi:10.5075/epfl-298799_978-2-9701614-0-0

300 µm printed silver line on many papers shows the edge sharpness, W/G ratio, and profile of the print are nearly similar to PET (see Figure 7).

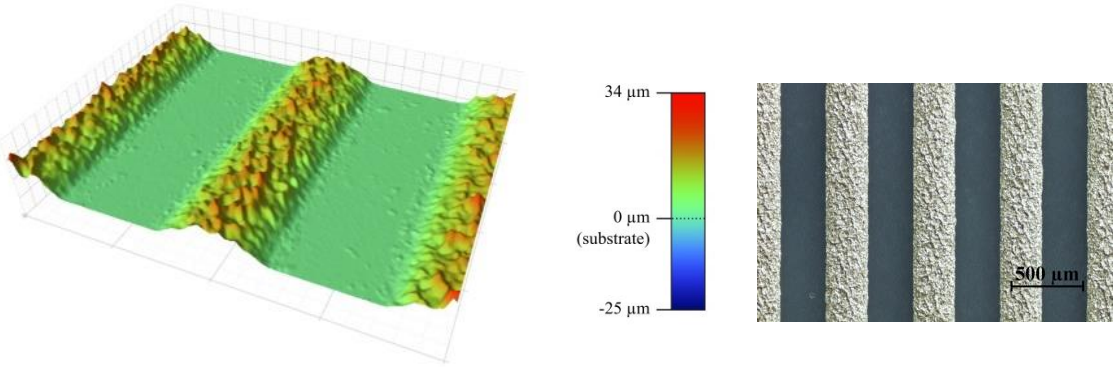

R_a = 0.11±0.04 µm

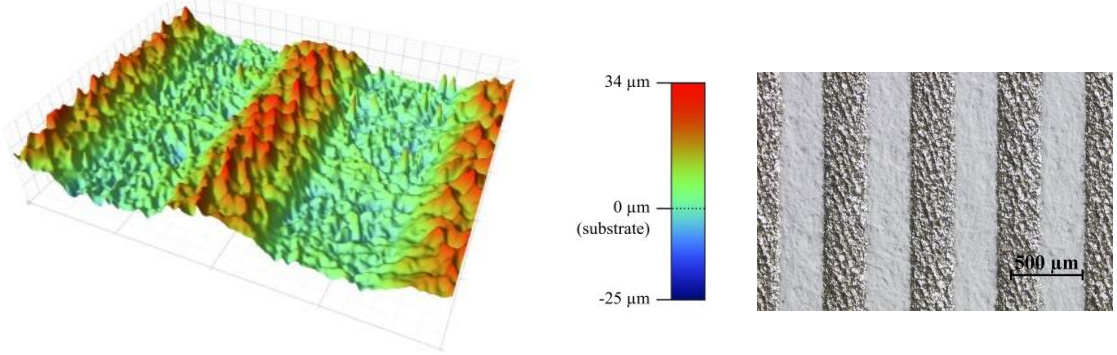

R_a = 2.21±0.72 µm

Figure 3. Surface textures and printed silver lines with a W/G-ratio of 300/300 [µm/µm] of an impedance sensor on PET (top) and the special electronic printing paper PES (bottom)

The microscopic examination of the prints on abaca paper (see Figure 4) showed that, the W/G ratio of the screen is poorly reproduced. The printed ink penetrates into the gap, which of course worsens the sharpness of the edges and leads to short circuits at low W/G ratios. However, this problem can be minimized by adjusting the screen (smaller lines, larger gaps). The test prints with narrower finger widths W (270; 285 µm) showed that with a W/G of 290/310 [µm/µm] on the higher density paper 300/300 [µm/µm] can be achieved in real terms.

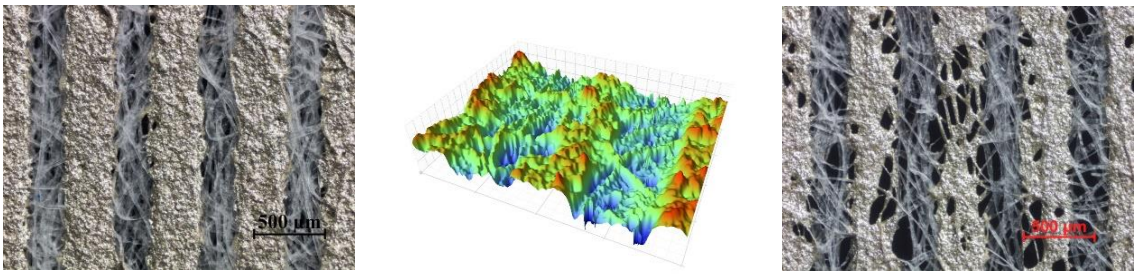

Figure 4. Microscope images of the print on 22g/m² (left) and 13g/m² Abaca paper (left) and surface structure (centre) of the 22g/m2 Abaca paper, where the blue areas show the holes.

The strong and crushed fibres of the abaca papers form pathways for the ink to flow into the free space (gap). This of course changes the edge sharpness and the measured W/G ratio of the

print. However, in Figure 4 it is observed that if there is higher grammage smaller holes can be bridged with the highly viscous ink.

We assessed the print quality by means of short-circuit tests. As reported in our previous article [3] all printed sensors on PET with a line to space (W/G) ratio ≥ 100/100 are short circuit free. In contrast to PET, the sensors are short-circuit-free ≥ 150/150. The higher density abaca papers are free of short circuits ≥ 250/250, and the high porous Abaca papers are free of short circuits ≥ 300/300.

3.2 Study of the cross-linking

Impedance spectroscopy can measure the mobility of ions or dipoles in a material with the help of an electrical alternating voltage. If the viscosity of the dielectric changes, e.g. through cross-linking or drying, and thus the conductivity of the material is reduced. This effect can be used to measure cross-linking reactions directly in the component or to detect moisture (increase or decrease of the water (dipole) content.

The curing of a UF resin in the glue joint during heat pressing with the help of impedance measurements is shown in Figure 5 and it show the influence of the paper substrate on the cross-linking curves. At least three measurements were taken for each sample and the average was calculated. The mean value of the standard deviation was used to determine the reproducibility of the measurement. For the low grammage abaca papers, six measurements were needed since some sensors failed under pressure (short circuit) or showed other artefacts. Figure 5 shows also the reproducibility of the results depending on the paper. The individual curves can either be close to each other and almost congruent. Therefore, all papers were divided into three groups (good (▲), still working (►), bad (▼)).The mean values of the standard deviation were used as criteria ▲ ≤ 0.125; 0.125 < ► < 0.20; ▼ ≥ 0.20; see also paper [3].

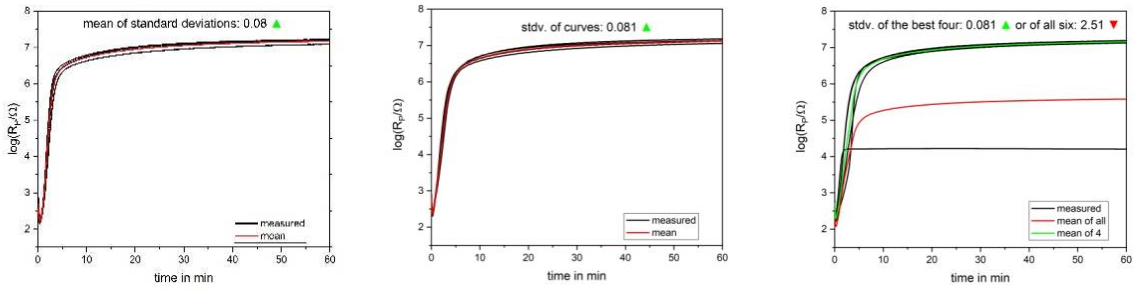

Figure 5. Typical measured cross-linking curves (black) and average of the single measurements (red or green) of a UF resin recorded using printed silver sensors on different paper substrates (left: PES, middle: 22 g/m² abaca paper, right: 13 g/m² abaca paper) in the hot

From our former paper [3] we know, that the paper influences the reproducibility, shape and slope of the curve. But it has no influence on the final conversion. Compared to our previous work [3], however, the difference between the individual substrates is not very large. This result is consistent with the fact that all papers have no additives or are almost neutral. Very poor reproducibility is obtained only when sensors fail during the measurement (prints on low density abaca papers). However, if one circles out these measurements, the reproducibility is acceptable, see Figure 5.

The causes for these effects on the low density abaca papers are speculative. Presumably, the high blurring of the printing edge on abaca papers plays an important role - abaca fibres form the tracks on which the ink flows into free space. A short circuit or leakage currents are then possible under pressure. The ink can also flake off on the printed individual fibres. This means that the sensor has fewer fingers, which then affects the signal level (see paper [3]).

Impedance spectroscopy with printed sensors on abaca papers allow unbiased in-line tracking of the cross-linking of glues or resins. As these sensors fulfil the criteria for integration in the bulk and they do not represent a foreign body that weakens the properties of the adhesive joint or the composite. The results correlates very well with DMA and infrared spectroscopy synchronous measurements [8]

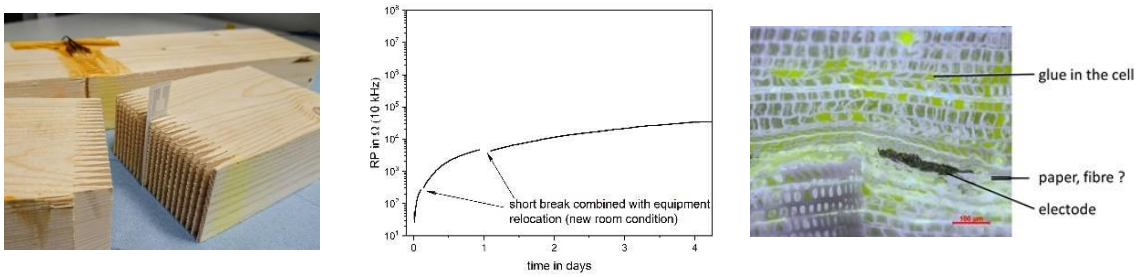

Figure 6. Experimental setup in the finger joints with a small impedance sensor (left), result of cross-linking measurement (middle) and a microscopic picture of the microtome cut of the glue joint

Figure 6 shows the cross-linking in the finger joint of a glued laminated beam at room temperature. The glue was only applied on one side. However, the microtome section of the glue joint shows that the glue is detectable in both joint parts. The sensor is penetrated and embedded with glue

Figure 7 shows the cross-linking in the body of a glass fibre epoxy prepreg during the production of a luge in a vacuum bag process with autoclaving process. The sensor was placed between two prepregs.

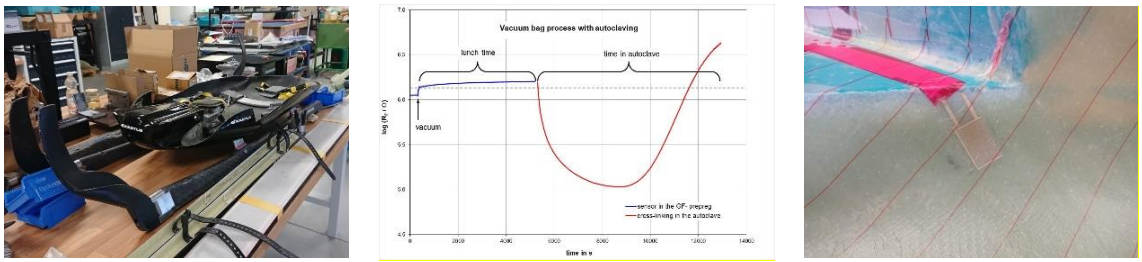

Figure 7. Cross-linking (middle) in the body of a glass fibre epoxy prepreg during the production of a luge (left) in a vacuum bag process with autoclaving. The right figure shows the full embedded sensor in the glass fibre body

The impedance curve in Figure 7 can be interpreted as follows. The log R_P value starts at a value above 6 and then increases as the vacuum is applied and the contact with the sensor improves. In the longer lunch break, one can also observe how R_P slowly increases during this time. As the room temperature was very high (hot summer day), this indicates the start of cross-linking. With

the introduction of the vacuum bag into the climate chamber, the R_P value drops very quickly and detects the decrease in the viscosity of the resin (increase in the mobility of the conductive particles). With the onset of cross-linking, this is restricted again and R_P increases (decrease in the mobility of the conductive particles by heat).

In a previous work of our group [8], we observed that paper sensors probably affect epoxy cross-linking and attributed this to the hydroxy groups, which terminate the chain reaction. Today we know that additives (such as calcium carbonates) in various papers are responsible for these effects. Neutral papers such as abaca papers do not influence the cross-linking kinetics. Figure 8 shows the crosslinking of a carbon prepreg (heating ramp 3K/min in a press) detected with a commercial IDEX sensor with a glass fibre diaphragm (protection against short circuit) and detected with a normal IDEX sensor and a diaphragm of 2 layers of abaca paper (22g/m^2). The minima and maxima are identical, so no influence of the paper on the kinetics of curing was detected.

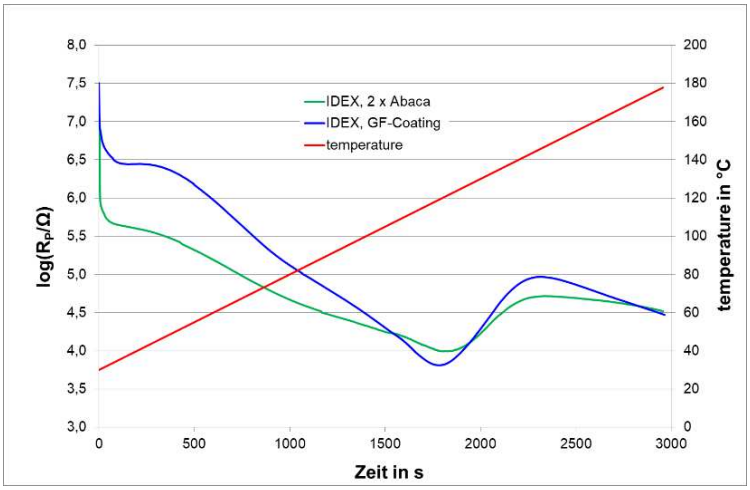

Figure 8. Cross-linking between 2 carbon prepregs in a press (heating ramp 3K/min).

Figure 9 shows a measurement of impedance in the heating chamber of DMA equipment. The start and end of the reaction are almost identical. This synchronous measurement shows that cross-linking can be detected very well online with the help of printed impedance sensors.

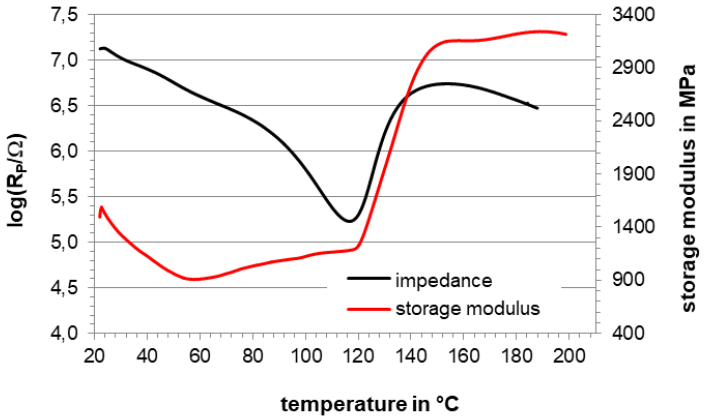

Figure 8. Cross-linking between 2 flax prepregs in in the heating chamber of a DMA equipment (1Pa = 1Kg/(m·s^2); heating ramp 1K/min).

Acknowledgements

This work was supported by the Austrian Research Promotion Agency GmbH (FFG) BRIDGE Project "Swips" under grant agreement no. 849442, by the Austrian Research Promotion Agency GmbH (FFG) BRIDGE Project "Interactive Wood" under grant agreement no. 874770, and within the Austrian Research Promotion Agency GmbH (FFG) COMET Modul "i^{3}Sense" under grant agreement no. FO999888361.

4. References

1. Müller U, Pretschuh C, Mitter R, Knappe S. Dielectric analysis as a cure monitoring system for UF particle boards. International Journal of Adhesion and Adhesives, 2017; 73C: 45-50.
2. Whitesides GM. The Frugal Way. The Economist - The World in 2012. 2011; 154.
3. Stockinger T, Liedl B, Steiner M, Schwödiauer R, Padinger F, Bauer S, Kaltenbrunner M, Müller U. Printed sensors on paper and wood – The frugal way of in-line detection to characterize the crosslinking behaviour of water based glues. Sensors and Actuators B: Chemical 2020: 324,128750
4. Liedl B. Printed and laser-structured impedance sensors in glue lines. Diploma Thesis University Vienna. 2018
5. Müller U, Pretschuh C, Zikulnig-Rusch E, Dolezel-Horwath E, Reiner M, Knappe S. Dielectric analysis as cure monitoring system formelamine-formaldehyde laminates, Progress in Organic Coatings 2016; 90: 277-283.
6. Zahouily K, Decker C, Kaisersberger E, Gruener M. Real-time UV cure monitoring: dielectric and infrared spectroscopy analyses show linear correlation. Eur. Coat. J. 2013; 11(3): 14–18.
7. Conway BE. Electrochemical Supercapacitors - Scientific Fundamentals and Technological Applications. Springer Science+Business Media New York. 1999; 13.4, 343-344.
8. Bauer S, Liedl B, Müller U, Schwödiauer R, Steiner M, Stockinger T, Tambe S, Inline cure monitoring in engineered wood with paper sensors – inspiration for carbon-prepregs, Proceedings of the thermosetting resins conference, 25 – 27 September 2018, Berlin, Germany.

  doi:10.5075/epfl-298799_978-2-9701614-0-0

NANOSTRUCTURED SELF-SENSING PIEZOELECTRIC COMPOSITE LAMINATE

Tommaso Maria Brugo[a], Davide Cocchi[a], Emanuele Maccaferri[b], Andrea Zucchelli[a], Davide Fabiani[c], Laura Mazzocchetti[b], Loris Giorgini[b]

a: Industrial Engineering Department - University of Bologna – tommasomaria.brugo@unibo.it
b: Industrial Chemical Department - University of Bologna
c: Electrical Engineering Department - University of Bologna

Abstract: *Structural Health Monitoring (SHM) systems need the integration of the composite laminate with bulky sensors, which often can dramatically reduce the inherent strength of the hosting material. In this work GLARE hybrid laminates (Glass Laminate Aluminum Reinforced Epoxy) were interleaved with PVDF-TrFE piezoelectric nanofibers and the aluminum sheets were exploited as electrodes to collect the piezoelectric signal. The nanostructured hybrid laminate so obtained is intrinsically a piezoelectric sensor, capable of detecting out-of-plane loads on its whole surface. Low-velocity impact tests were performed to investigate the real-time electrical response and impact resistance of the self-sensing laminate. A lumped electric model was applied to study and optimize the circuit electrical parameters and the sensing performances were evaluated in terms of linearity and spatial uniformity. The impact resistance was compared with the pristine non-self-sensing counterpart in terms of dynamic response and micrograph analysis.*

Keywords: smart material; sensing; piezoelectric; nanofiber; SHM.

1. Introduction

Composite laminates find massive application in the aerospace field thanks to their high specific resistance. However, they show remarkable limits in tolerating out-of-plane loads such as impacts, due to the laminar structure. During its service life, the component can be subject to even minor but repeated impacts, which cause the formation of micro-cracks. As a result of cyclic loads, these cracks can propagate between one sheet and another until they turn into delamination, the propagation of which can lead to sudden and catastrophic structural failure of the structure if not intervened in time. Therefore, it is currently necessary to carry out stringent and expensive scheduled maintenance plans to guarantee adequate safety standards, with consequent stoppage of the activities involved. It is therefore of great interest to develop strategies aimed at monitoring, in real-time, the state of health of the component (Structural Health Monitoring, SHM), as it allows to intervene promptly in the event of localized damage without spending time and money with frequent inspections [1].

In order to detect an impact event, various sensor systems have been developed, such as the use of Fiber Bragg Gratings (FBG), which, however, can reduce the intrinsic strength of the composite and themselves cause delamination triggering [2]. Recently, piezoelectric sensors, both ceramic and polymeric, have been developed to be used in the SHM field [3]. Although ceramic piezoelectric sensors can generate higher electrical signals than their polymeric

  doi:10.5075/epfl-298799_978-2-9701614-0-0

counterpart, they are difficult to integrate into FRP laminates, as they are extremely fragile and their breakage can cause crack nucleation and subsequently trigger delaminations [4] [5]. On the contrary, piezoelectric polymers, are more flexible and ductile and therefore potentially more suitable for integration into composite materials. Among these, polyvinylidene fluoride (PVDF) and the copolymer with tetrafluoroethylene (PVDF-TrFE) are the most widely used [6]. However, the interface strength between the sensor and the hosting matrix can be an issue especially if embedded in form of films [7]. Other issues to be overcome are the integration of the electrodes to collect the piezoelectric signal without reducing the inherent strength of the hosting material and the difficulties in shielding the sensor from electromagnetic and triboelectric noise to have a clean and reliable signal [8].

In this work, the integration of the composite laminate with a nanostructured piezoelectric sensor, based on PVDF-TrFE nanofibers and aluminum sheets as electrodes, proposed by the authors in [9] is investigated. Structurally, the resulting composite is a hybrid laminate consisting of aluminum sheets alternatively bonded to glass-fiber reinforced plastic (GFRP) prepreg layers and interleaved with PVDF-TrFE nanofibrous mats. Such lay-up belongs to a special class of hybrid laminates known as glass laminate aluminum reinforced epoxy (GLARE) and is well known for its superior impact strength [10]. Moreover, nanofibrous mat interleaving is a consolidated technique used to increase the fracture toughness of composite laminate [11], [12]. Hence, the resulting nanostructured hybrid laminate constitutes by itself a piezoelectric sensor capable of detecting an impact load on its whole surface. Low-velocity impact tests were performed to investigate the real-time electrical response and impact resistance of the self-sensing laminate. The sensing performances were evaluated in terms of linearity and spatial uniformity. The impact resistance was compared with the pristine non-self-sensing counterpart in terms of dynamic response and micrograph analysis.

2. Materials & Methods

This paragraph describes the process developed for the manufacture of the nanostructured hybrid laminate with self-sensing properties and the methodology with which the impact tests were conducted to evaluate its mechanical and electrical properties.

2.1 Electrospinning piezoelectric nanofibers

The PVDF-TrFE copolymer nanofibrous mats with piezoelectric properties were produced by electrospinning using a Spinbow machine equipped with 4 needles and a rotating drum collector. The copolymer PVDF-TrFE 70:30 mol % copolymer (Solvene®300 EAP, courtesy of Solvay S.p.A. Milan) was dissolved at 20% wt in a mixture of 55 wt% acetone and 45 wt% dimethylformamide. The process parameters used for electrospinning are as follows: electric potential 9 kV, flow rate 0.9 ml/h, needle-collector distance 15 cm, tangential velocity of the cylindrical collector equal to 0.2 m/s, temperature 24 °C and relative humidity 45% RH. The morphology of the nanofibrous mat so produced is shown in the scanning electron microscope (SEM) micrograph of Figure 1. The nanofibers are randomly deposited and their average diameter is equal to 320 nm, with a dispersion (σ) of 100 nm.

  doi:10.5075/epfl-298799_978-2-9701614-0-0

2.2 Stacking, Curing and Post-polarization

The laminate specimens consist of 4 aluminum sheets (Al 2024-T3, 60 x 70 x 0.5 mm) interspersed with 4 layers of woven Glass Fiber Reinforced Polymer (GFRP) prepreg (E-glass 8H Satin 300g/m2 - epoxy matrix, VV300S - DT121H-34 DeltaPreg, 80 x 90 x ~0.22 mm), as described in Figure 1. Before carrying out the lamination, the aluminum plates were subjected to etching treatment, according to ASTM D2651, to improve adhesion with the GFRP prepreg, then the cables were welded in the aluminum sheets to collect the piezoelectric signal. The nanofibrous mat was interleaved in the laminate midplane between the two central GFRP plies. In addition, a specimen free of nanofibers was produced and used as a reference laminate (Reference) to compare it with the self-sensing one (Piezo). The laminates were cured with a vacuum bag in autoclave with a curing cycle of 2 hours at 120 °C + 1 hour at 150 °C, with a constant pressure of 6 bar. The final thickness of the cured laminate was equal to 4.6 mm. At the end of the curing cycle, the specimens were post-polarized by applying an electric field of 10 kV/mm for 30 minutes at a temperature of 110 °C (above the polymer Curie temperature (Tc) of 103 °C), in order to align the piezoelectric dipoles.

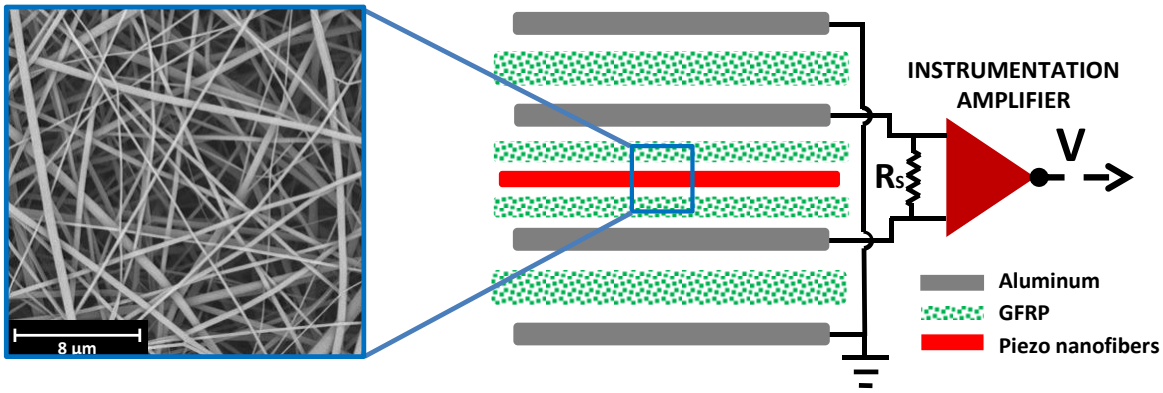

Figure 1 Left picture: SEM micrograph of the nanofibrous mat; right picture: self-sensing composite laminate stacking sequence and amplification circuit.

2.3 Impact Test and Signal conditioning system

The laminates were subjected to low-velocity impact tests to investigate the piezoelectric response and the mechanical strength. For this purpose, it was used a drop weight tower equipped with a 1.3 kg impactor mass and a hemispherical head with a diameter of 12.7 mm instrumented with a load cell Figure 2. The non-destructive pre-tests, were performed with an impact energy in the range of 0 - 0.5 J to evaluate the electrical response; while the destructive tests, were performed at 5, 10 and 20 Joules to evaluate the mechanical resistance. During the impact tests, in addition to the contact force measured by the load cell, the piezoelectric signal generated by the self-sensing laminate was acquired. The signal was pre-conditioned by a custom circuit composed of an instrumentation amplifier connected in parallel with an adjustable shunt resistance.

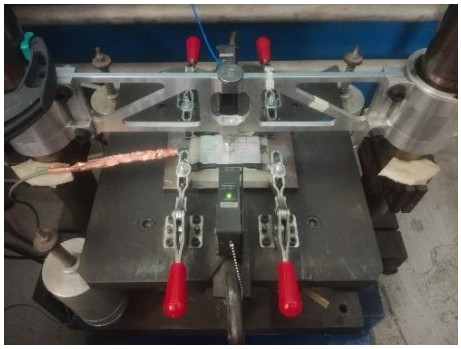

Figure 2 Low Velocity Impact test setup.

3. Results

The laminates were subjected to preliminary non-destructive impact tests to evaluate the electrical response of the integrated sensor and subsequently impacted at higher energy to evaluate their mechanical strength.

3.1 Non-destructive impact tests & Calibration

In order to study the electrical response of the self-sensing laminate and then calibrate it, each specimen was impacted at different energies with a maximum force of 0.5 kN, as it was lower than the damage threshold of the composite.

Figure 3 shows the trend of the piezoelectric signal (in mV) generated by the self-sensing composite during impact (red curve) and compared with the contact force (in kN) measured by the mounted load cell on the impactor (blue curve). As can be observed, the curves generally show a sinusoidal trend (except for negligible vibrations), an indication of purely elastic behavior and therefore free from damage phenomena. It is clearly noted that the curve associated with the piezoelectric signal (appropriately scaled) copies precisely the trend of the contact force measured by the reference cell, both during the ascent and descent phase. Only following the detachment of the impactor the piezoelectric signal take a few moments to return completely to zero, probably due to the oscillation of the specimen.

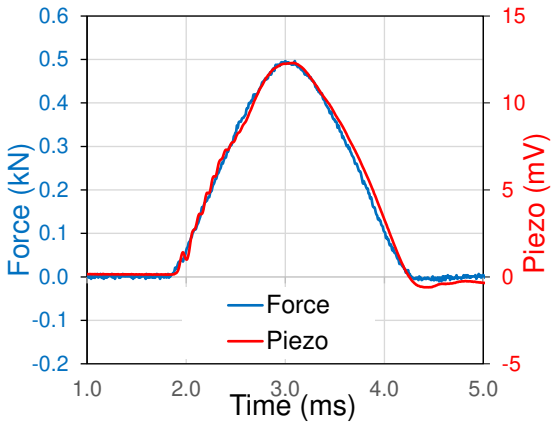

Figure 3 Piezoelectric response of the self-sensing laminate (continuous red curve) compared to the contact force measured by the impactor load cell (blue curve).

  doi:10.5075/epfl-298799_978-2-9701614-0-0

Figure 4 (a) on the right shows the peak values of the voltage generated by the self-sensing composite and the corresponding contact force measured during impact tests, repeated at different heights. In order to calibrate the sensor and evaluate its linearity, these values were interpolated with al linear regression through the origin. Its resulting sensitivity (slope of the line) is 25.2 mV/kN, while the coefficient of determination (R^2) is higher than 0.999, remarking the good linearity of the sensor.

The 3D scatter plot of Figure 4 (b) shows the sensitivity of the self-sensing laminate impacted in different spots on a grid of 3 x 3 with a 10 mm step. The calculated sensitivity has a confidence interval of ± 1.1 mV/kN, and a relative error of ± 4.6 %. The measured spatial accuracy should be considered acceptable for structural health monitoring purposes

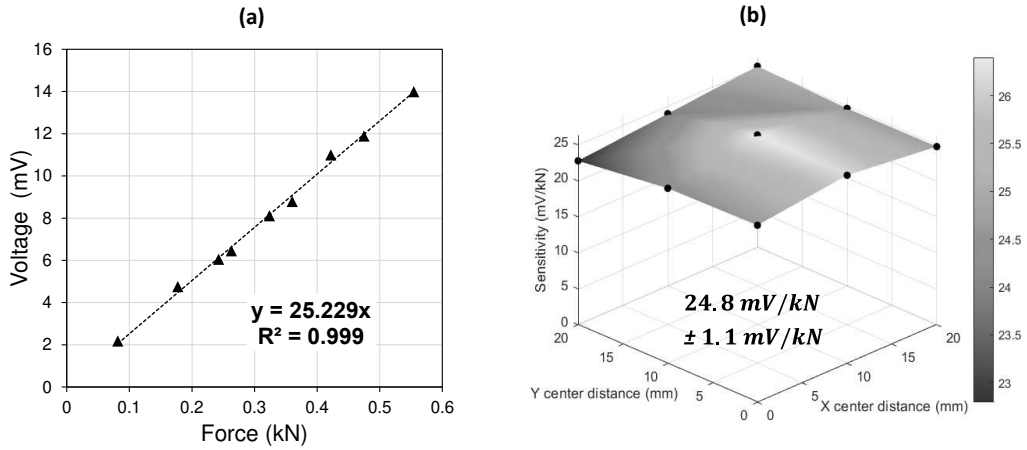

Figure 4 (a) Sensor linearity: piezoelectric voltage peak versus contact force peak for impacts performed at different magnitude levels. (b) Spatial uniformity: sensitivity of the self-sensing laminate impacted at different points on its surface.

3.1 Destructive impact tests

After the calibration of the self-sensing laminates, both Piezo and Reference laminates were impact tested at 3 different energy levels, 5, 10 and 20 J. In the graphs of Figure 5 are reported the force vs time and force vs displacement for the Reference (blue curve) and Piezo (red curve) laminates impacted at 20 joules.

Observing the graph on the left, for both laminates, there is a first force drop exceeding the 2 kN threshold, associated with the propagation of cracks and delaminations at the GFRP-GFRP and GFRP-aluminum interface [11]. Once the 5 kN threshold is exceeded, the graph on the right shows a change in the slope of the curve, associated with a stiffness change of the laminate, caused by more important damage such as breakage of the GFRP sheets and plasticization of the aluminum sheets [11]. Both return curves are not perfectly elastic due to the undergone damage. Comparing the curve of the Piezo laminate with the Reference, no particular differences are observed in the dynamic impact behavior with a slightly greater loss of stiffness in the case of the Reference laminate. The results of the dynamic analysis, shown in Table 1, confirm what has been observed. Indeed, the absorbed energy (Ea) is comparable while the permanent deformation is 7.3% lower for the self-sensing laminate.

  doi:10.5075/epfl-298799_978-2-9701614-0-0

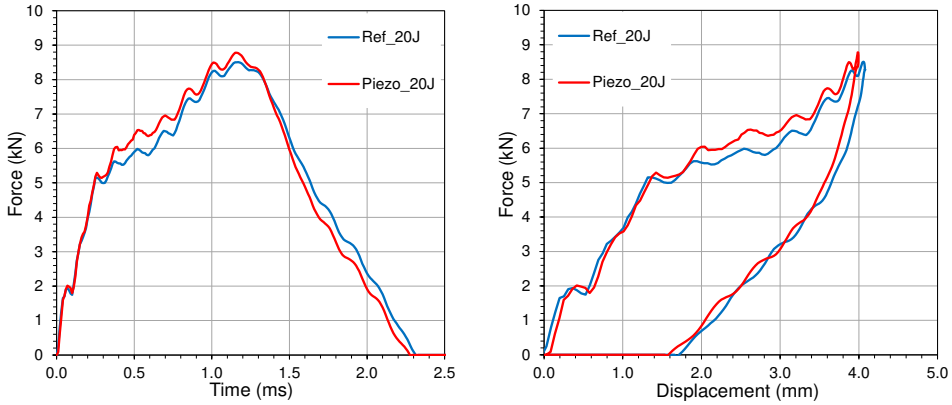

Figure 5 Destructive impact test response at 20J for Reference (blue curve) and Piezo (red curve) laminates: contact force measured by the impactor load cell with respect to time (left graph) and with respect to displacement (right graph).

Table 1 Salient impact response data

Sample	Ei (J)	Fmax (kN)		Smax (mm)		Sper (mm)		Ea (J)		Ti (ms)		Vi (ms)	
	Value	Value	Δ (%)	Value	Δ (%)	Value	Δ (%)	Value	Δ (%)	Value	Δ (%)	Value	Δ (%)
Reference	20.1	8.51	-	4.08	-	1.69	-	13	-	2.32	-	5.56	-
Piezo	20.1	8.78	3.2	4	-2	1.57	-7.3	13.01	0.1	2.28	-1.7	5.56	0.1

In Figure 6 the impact force detected by the self-sensing laminate (dashed curve), previously calibrated through a non-destructive impact test, is compared to the contact force measured by the commercial cell mounted on the impactor.

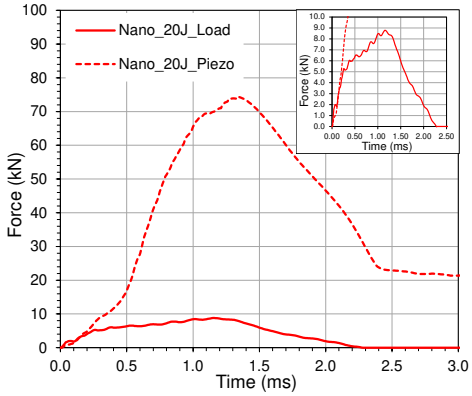

Figure 6 Comparison between the impact force measured by the self-sensing laminate (dashed curve) and the commercial load cell (continuous curve), for an impact at 20 J.

It can be observed that up to 5 kN the two curves are comparable. However, above this value, the force detected by the self-sensing laminate diverges from the reference one, reaching values up to an order of magnitude higher. The force value beyond which the drastic loss of proportionality of the self-sensing laminate is recorded coincides with the threshold value above which a loss of stiffness of the laminate occurs, which is correlated to the development of damage. Therefore, the divergence of the piezoelectric signal can be ascribed to the damage development resulting in friction of the fracture surfaces, which in turn generates a triboelectric signal. In other words, when the Piezo laminate exceeds the damage threshold value it loses its

structural and electrical functionality and hence its linearity (force vs piezo voltage proportionality). The so marked variation in the electrical response can be exploited in the SHM environment as a clear damage indicator alarm, thus allowing prompt intervention for repairing or replacing the component.

Figure 7 shows the cross-section micrograph at the impact point for the Reference (left) and Piezo (right) laminates, impacted with an energy equal to 20 J. For both laminates, comparable plastic deformation of the aluminum foils can be observed, with the top sheet coping the shape of the impactor. Moreover, matrix cracks can be observed for both samples, that propagate in the form of delaminations between the glass fiber sheets with a pattern known as the reverse pine-tree pattern, which suggests that the laminate works mainly in bending [13]. The differences in the delamination lengths between the two types of laminate can be considered within the variability of the experimental tests, as in these areas the two laminates do not show differences in the stacking sequence. Focusing on the mid-plane interface, in which the piezoelectric nanofibers have been interleaved, no delaminations were observed (the area in the case of the Piezo laminate is darker due to the presence of the nanofibers). It can therefore be asserted that the presence of the piezoelectric nanofibrous mat, necessary to give the laminate self-sensing properties, does not affect its resistance to impact.

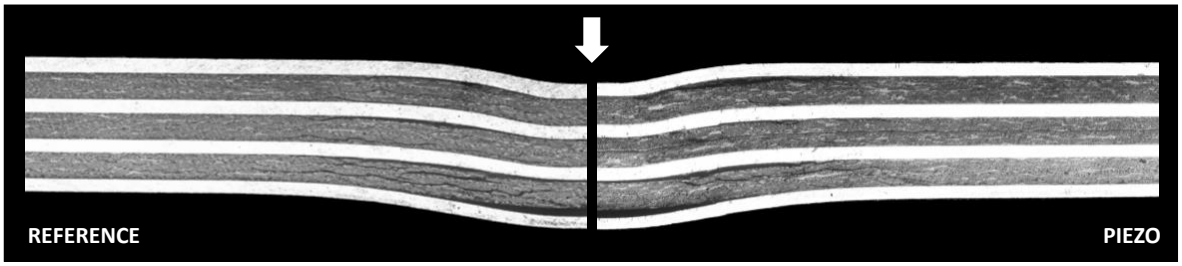

Figure 7 Cross-section micrograph analysis of Reference laminate (on the left) and Piezo laminate (on the right) impacted at 20 J.

4. Conclusions

In this work, the integration of the composite laminate with a nanostructured piezoelectric sensor, based on PVDF-TrFE nanofibers and aluminum sheets as electrodes, is investigated. The resulting nanostructured hybrid laminate constitutes by itself a piezoelectric sensor capable of detecting an impact load on its whole surface. At non-destructive impact forces, its piezoelectric response precisely copies the impact force measured by the commercial load cell mounted on the impactor, with remarkable linearity ($R^2 > 0.999$) and spatial uniformity (E%<5%). The impact resistance at 20 J of the piezoelectric laminate, evaluated by dynamic and micrograph analysis, is comparable to the reference non-self-sensing one. Therefore, the integration of the piezoelectric fabric has no negative effect on the strength of the hosting material, contrary to what generally happens when embedding commercial sensors. Once the critical load threshold for the development of damage has been exceeded, the piezoelectric signal generated by the self-sensing laminate rapidly diverges from the contact force, losing its proportionality. The so marked variation in the electrical response can be exploited in the SHM environment as a clear damage indicator alarm, thus allowing prompt intervention for repairing the component.

  doi:10.5075/epfl-298799_978-2-9701614-0-0

Acknowledgements

The research was funded by the European Union's Horizon 2020 Research and Innovation Programme – “MyLeg” (No. 780871, 2018).

5. References

1. Cai J, Qiu L, Yuan S, Shi L, Liu P, Liang D. Structural Health Monitoring for Composite Materials. In: Composites and Their Applications. 2012.
2. Shivakumar K, Bhargava A. Failure mechanics of a composite laminate embedded with a fiber optic sensor. J Compos Mater. 2005;39(9):777–98.
3. Masmoudi S, El Mahi A, Turki S. Use of piezoelectric as acoustic emission sensor for in situ monitoring of composite structures. Compos Part B Eng. 2015;
4. Cheng J, Qian C, Zhao M, Lee SWR, Tong P, Zhang TY. Effects of electric fields on the bending behavior of PZT-5H piezoelectric laminates. Smart Mater Struct. 2000;
5. Butler S, Gurvich M, Ghoshal A, Welsh G, Attridge P, Winston H, et al. Effect of embedded sensors on interlaminar damage in composite structures. J Intell Mater Syst Struct. 2011;
6. Bae JH, Chang SH. Characterization of an electroactive polymer (PVDF-TrFE) film-type sensor for health monitoring of composite structures. Compos Struct. 2015;
7. Chrysochoidis NA, Gutiérrez E. Evaluation of the sensitivity and fatigue performance of embedded piezopolymer sensor systems in sandwich composite laminates. Smart Mater Struct. 2015;
8. Coverley PT, Staszewski WJ. Impact damage location in composite structures using optimized sensor triangulation procedure. Smart Mater Struct. 2003;12(5):795–803.
9. Brugo TM, Maccaferri E, Cocchi D, Mazzocchetti L, Giorgini L, Fabiani D, et al. Self-sensing hybrid composite laminate by piezoelectric nanofibers interleaving. Compos Part B Eng. 2021;212(October 2020):108673.
10. Vlot A, Gunnink W. Fibre Metal Laminates: an Introduction. The Netherlands: Kluwer Academic Publishers. 2001.
11. Zarei H, Brugo T, Belcari J, Bisadi H, Minak G, Zucchelli A. Low velocity impact damage assessment of GLARE fiber-metal laminates interleaved by Nylon 6,6 nanofiber mats. Compos Struct. 2017;
12. Brugo T, Palazzetti R. The effect of thickness of Nylon 6,6 nanofibrous mat on Modes I–II fracture mechanics of UD and woven composite laminates. Compos Struct. 2016;
13. Abrate S. Impact on Composite Structures. Impact on Composite Structures. 1998.

  doi:10.5075/epfl-298799_978-2-9701614-0-0

RATE DEPENDENT ELECTROMECHANCAL CHARACTERIZATION AND MODELING OF GRAPHENE BASED FIBER REINFORCED POLYMER LAMINATES

Israr, ***Ud Din****, Yacob,* ***Medhin****, Naziha****, Aslam****,* *Mohamed Salman,* ***Sikandar Bathusha****, Rehan,* ***Umer****, Kamran A.,* ***Khan***

Department of Aerospace Engineering, Khalifa University of Science and Technology (KUST), Abu Dhabi, United Arab Emirate (UAE) – israr.uddin@ku.ac.ae

Abstract: *Fiber reinforced polymer (FRP) composite laminates are used in numerous structures that require high strength-to-weight ratio. The health status of these laminates is traditionally monitored using point strain gauge arrays, fiber optics etc. installed at critical locations. In this work, a composite laminate capable of sensing its own health has been developed using embedded fabric sensor. In this study, a manufacturing protocol is developed for in-situ reduction of graphene oxide (GO) coated fabric into rGO coated fabric. A vacuum assisted resin transfer molding process was used to fabricate the composite laminates with embedded rGO coated fabric sensors. The piezoresistivity of the composite laminate was measured both before and during fabrication. The in-plane tension tests were carried out at three different loading rates (0.2, 2, 20 mm/min) to determine the rate-dependent piezoresistive response of composite laminates. We recorded both the piezoresistivity and load-displacement data simultaneously to obtain the electromechanical response of the fabricated samples.*

Keywords: Graphene; rate dependency; fiber reinforced polymer; electromechanical; characterization

1. Introduction

The novel applications of graphene associated nanomaterials (GANs) to fabricate multifunctional structures have significantly increased over the years owing to their favorable properties such as higher thermal conductivity, higher electrical conductivity, and better electromagnetic interference shielding, etc. [1–4]. Electrically conductive fiber reinforced polymer (FRP) composite is one of such examples which is used for sensing purposes by introducing GANs into the FRP composite. In such case, the electrical networks formed by the GANs are not static and evolve continuously with external pressure and heat which imparts piezoresistivity to the structure. There are various manufacturing approaches used in the literature to introduce GANs into the FRP composite. One of the most important guidelines to keep in mind is how and where to add nanomaterials to get the desired performance, which ultimately determines the overall manufacturing process. As a prerequisite for scalability, the proposed manufacturing process should be able to be adapted to existing methods of manufacturing [5].

Conductivity of the FRP composite is enhanced by the addition of nanomaterials to the polymer matrix. This approach faces some serious challenges during manufacturing, such as an increase in viscosity that causes difficulties during infusion. Further, nanomaterials can also be filtered by the mesh nature of the fabric reinforcement and distributing media mesh that is generally used as consumables. In addition, nanoparticles in a liquid medium agglomerate over time, impairing

  doi:10.5075/epfl-298799_978-2-9701614-0-0

the even distribution of nanofillers in the matrix and the resulting multifunctionality [6–8]. As a result, serval alternative manufacturing techniques are preferred by depositing the nanofillers on the fabric reinforcement to form continuous electrical networks. These techniques comprise spraying, dipping/solution method, chemical vapor decomposition (CVD), and electrophoretic deposition, etc. [6, 7, 9, 10].

In this work, graphene based FRP composites have been manufactured and electromechanically characterized at various loading rates during in-plane tension. In the as received state, the plain weave E-glass fabric was coated with graphene oxide (GO) which was subsequently reduced to reduced graphene oxide (rGO) for better electrical conductivity. The coated fabric was then embedded within the laminate at a symmetric position. The piezoresistive laminate was manufactured using a vacuum assisted resin transfer molding (VARTM) process. The samples were prepared in accordance with the ASTM standard for FRPs in-plane tension testing. A simultaneous mechanical and piezoresistive response was measured during the mechanical testing at different load rates.

2. Materials

Graphene oxide (GO) paste was supplied by Abalonyx AS, Norway in form of aqueous solution. A Plain woven E-glass fabric with an aerial density of 202 g/m^2 provided by Gurit®, UK was used as reinforcement and substrate for GO coating by solution dipping method. For all the electrical connections commercially available copper tape and wire were used. In the VARTM process, epoxy resin and hardener (GURIT PRIME™ 20LV resin and PRIME™ 20 hardener) were mixed at a ratio of 100: 28 by weight.

3. Experimental

3.1 Specimen preparation

The samples were manufactured according to the ASTM D3039 standard. Accordingly, the in-plane tension test sample length and width were 200 mm and 20 mm respectively. The rGO-coated fabric was placed in a symmetrical position within the laminates consisting of eight plain woven glass fabrics. After that, VARTM process was used to fabricate the required laminates. The final laminate average thickness was measured as 1.7 mm. Throughout the VARTM process, resistance change was measured on each sample. E-glass tabs having a thickness of 1.7 mm each side were also attached with the help of cold compression to the samples for firm gripping and transfer of load during in-plane tension experiments. Finally, the samples were painted appropriately with speckle patterns to acquire a complete strain field using digital image correlation (DIC). Figure 1 illustrates the steps involved in fabricating in-plane tension test samples.

  doi:10.5075/epfl-298799_978-2-9701614-0-0

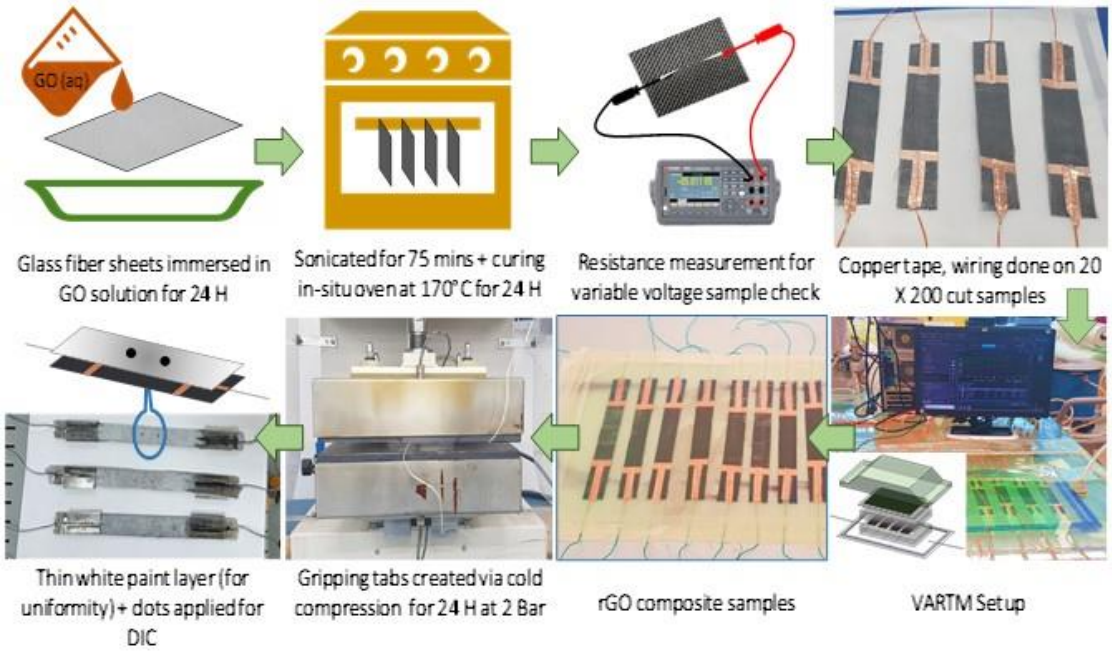

Figure 1. Steps followed in the fabrication of samples: starting from the raw materials until the final specimens.

3.2 Experimental testing procedures

3.2.1 In-situ piezoresistive measurement

Piezoresistivity is expressed as a fractional change in resistance (FCR) which was monitored during the various stages of the VARTM process including vacuum bag compaction, resin flow, and finally curing and post curing. For this purpose, BenchVue acquisition software was used along with the Keysight DAQ970A data acquisition system (DAQ) to display real time readings. It measures the instantaneous resistance change caused by the compaction of the vacuum and resin flow pressure in each sample placed transversely to the resin flow, as shown in Figure 1. The instantaneous resistance R is normalized by the characteristic resistance R_o measured prior in the absence of any external excitation (stress or strain) to compute FCR as given by Eq.(1):

$$FCR = \left(\frac{R-R_0}{R_0}\right) \times 100 \quad (1)$$

3.2.2 Electromechanical in-plane tension test

For all tension tests, the Instron 5969 with load cell capacity of 50/5 kN equipped with built-in DIC system was used. The in-plane tension tests were carried out at three different loading rates (0.2, 2, 20 mm/min) to determine the rate-dependent piezoresistive response of composite laminates. We tested three samples at each load rate. The electromechanical characterization test setup is shown in Figure 2 which records both the mechanical load vs. displacement data and resistance, simultaneously.

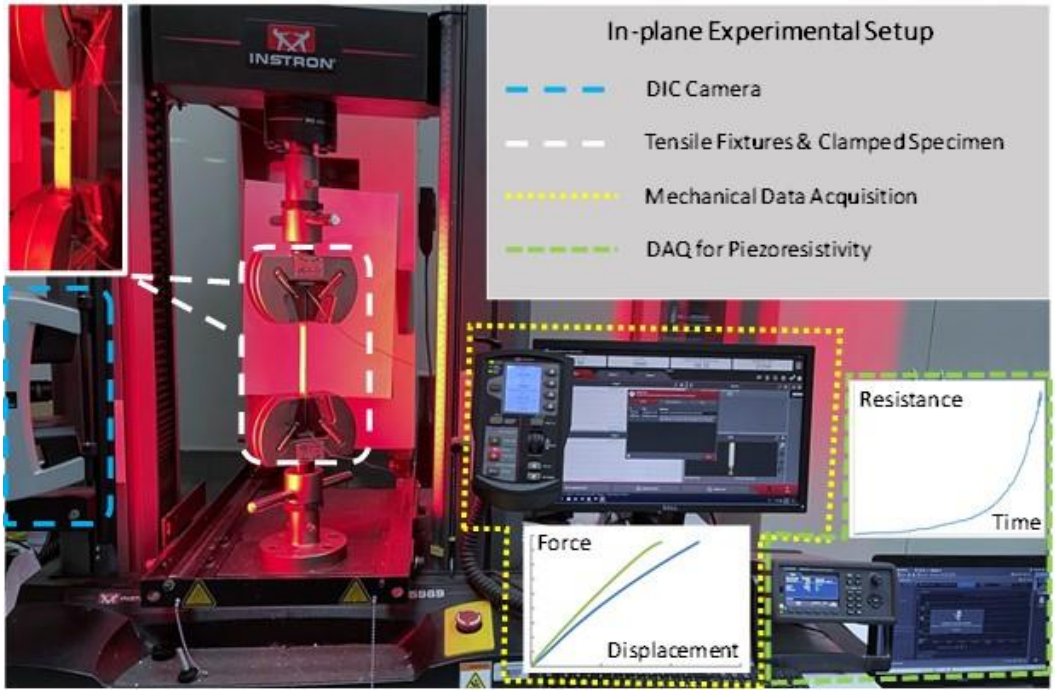

Figure 2. Electromechanical in-plane characterization test setup.

4. Results and discussion

4.1 In-situ VARTM piezoresistivity measurement

The instantaneous resistance R was measured for the rectangular sensors during the different stages of VARTM process such as vacuum compaction, resin flow and final curing as given in Figure 3. The positions of all six samples and resin flow fronts can be seen in Figure 3(a) where sample 6 is nearest to the resin inlet. The FCR evolution of all the samples showed a sudden drop in the percentage change upon vacuum application and resin flow over the rGO coated sensors. The vacuum application and resin flow compressed the rGO coated fabric sensors which in-turn decreased the inter-yarn gaps. Hence, this compaction enhanced the electrical network and decreased the resistance R. The maximum decrease was noted for the sensor located near the inlet having a value of 63.5%. This may be associated to the position of the sample in mold. After completing saturation of the fabric with resin and entry of the excess resin into the outlet duct, the resin entry was stopped by clamping at approximately 26 min. The differences in the FCRs of all samples in Figure 3 may be due to the minor variation in rGO coating.

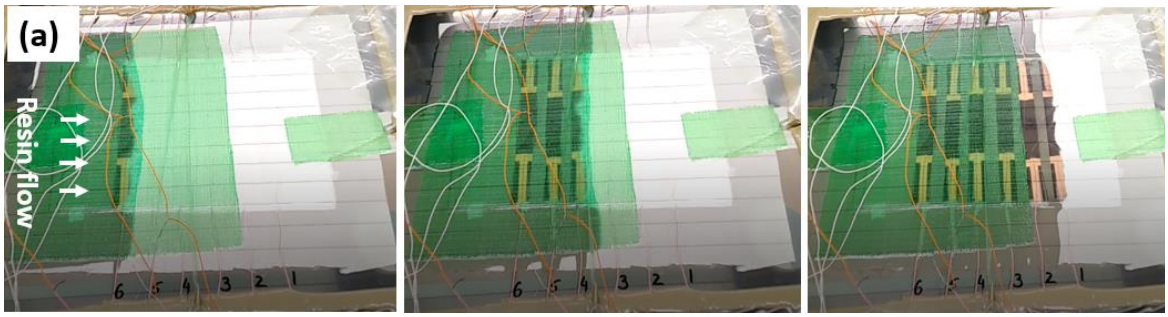

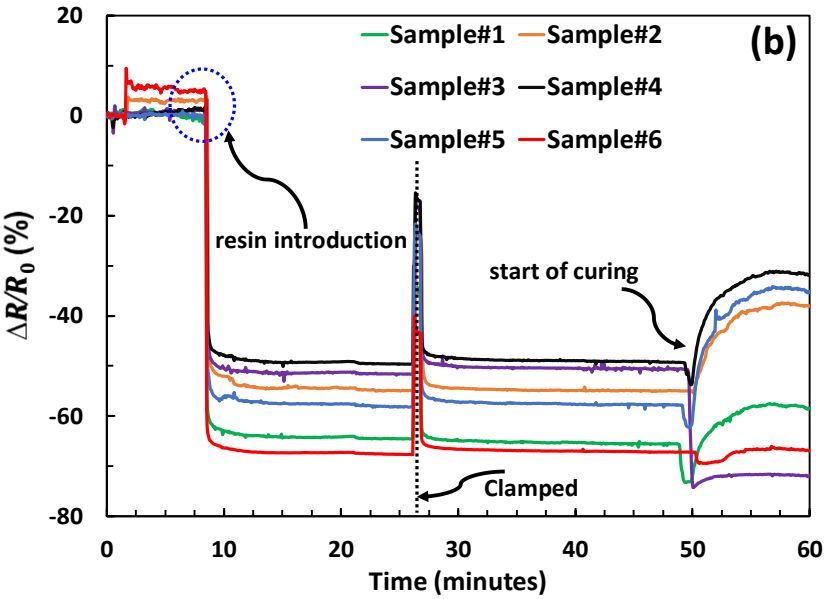

Figure 3. In-situ piezoresistivity measurement during the VARTM process, (a) resin flow fronts at sample 6, sample 4 and sample 1, (b) FCR measurement vs. time for six sensors.

4.2 In-plane tensile electromechanical characterization

Three samples per load rates (0.2, 2, 20 mm/min) were tested to record the scatter in the piezoresistivity of the developed sensors. The average stress (σ) vs. average strain (ε) in the fiber direction and the respective changes in the resistance are compared for the three load rates, as shown in Figure 4 (a). As the load rate is increased, the stress-strain behavior demonstrated the strain-hardening behavior which is very well documented for metals as well as FRP composites.

The piezoresistive behavior in the in-plane tension experiments were found in agreement with other researchers in similar experimental setup [10]. The FCR graphs started to rise with low slope within the strain of 0.5%. After that, a significant increase in FCR was observed as the strain increased beyond 0.5% in the elastic strain limit of the rGO coated fabric sensor. There is also a possibility of microscale partial localized fibers damage causing discontinuation in the electrical network. The end points of each stress-strain plot denote the catastrophic brittle fracture of the number of fiber yarns or the complete ply known as macro-level damage (see fractured samples in Figure 4-b). Upon this macro-level damage, a substantial increase in the FCR can be seen which is expected showing the overall discontinuation of the conducting network in the continuous rGO coated fabric sensor. Such piezoresistive behavior can be expressed with simplified exponential growth functions.

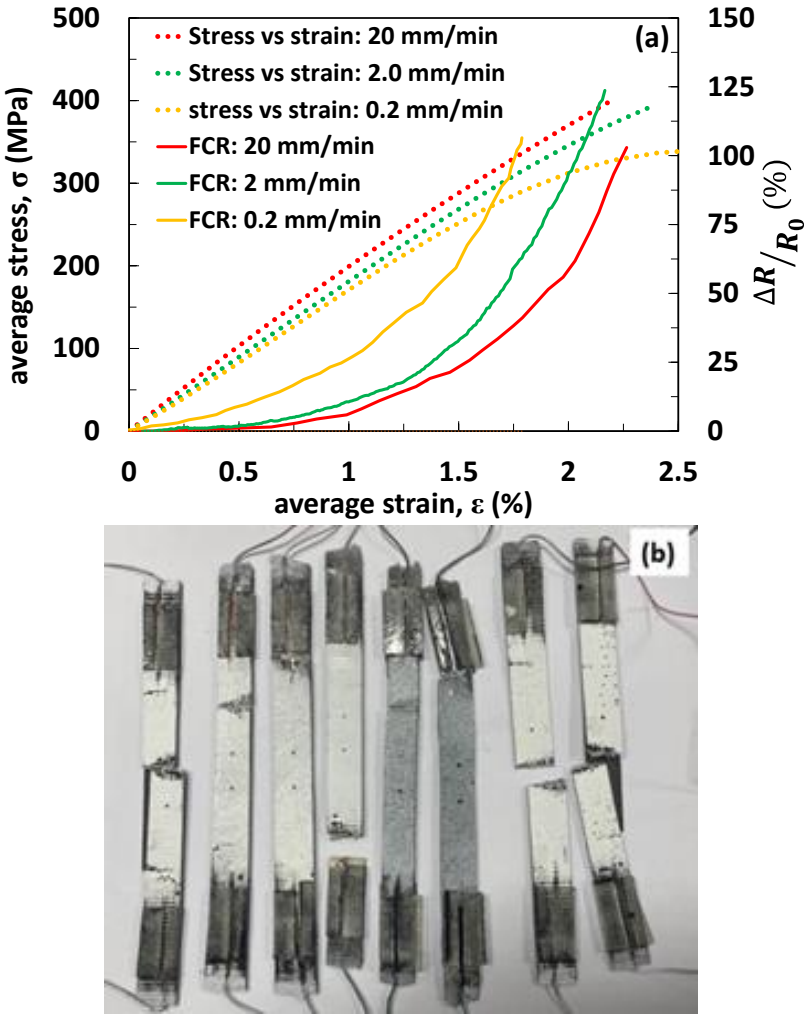

Figure 4. Simultaneous recordings of in-plane stress-strain in loading direction and FCR (a) comparison of the three load rates of 0.2, 2.0, and 20 mm/min, (b) some of the post-test fractured sensors.

The piezoresistive sensitivity for the three load rates were compared by determining the gauge factors: $k = (\Delta R/R_0)/\varepsilon$. These gauge factors (k) were calculated for the three load rates in the moderate slope region. Tangent lines were drawn to the exponential functions fitted in between the experimental upper and lower bounds given in Figure 5 (a) at strain of 1%. The percentage error based on the upper and lower bounds of the failure stress and FCR are shown in Figure 5 (b). The fitted functions describing the average FCR is given by Eq.(2).

$$FCR = (a + be^{\beta\varepsilon}) \times 100 \tag{2}$$

The corresponding constants and gauge factors are summarized in Table 1. Eq.(2) was constrained to $a = -b$ during fitting such that the initial conditions of FCR at $\varepsilon = 0$ must be satisfied. The slowest load rate of 0.2 mm/min resulted into a maximum gauge factor of 53 with respect to the other two cases. It can be noticed that the load rate is in inverse relation with the gauge factor.

Table 1: Fitted parameters and computed gauge factors

Load rate	(a)	(b)	(β)	Gauge factor

mm/min				(k)
0.2	-6.8	6.8	1.6	53
2.0	-2.3	2.3	1.9	29
20	-2.7	2.7	1.6	21

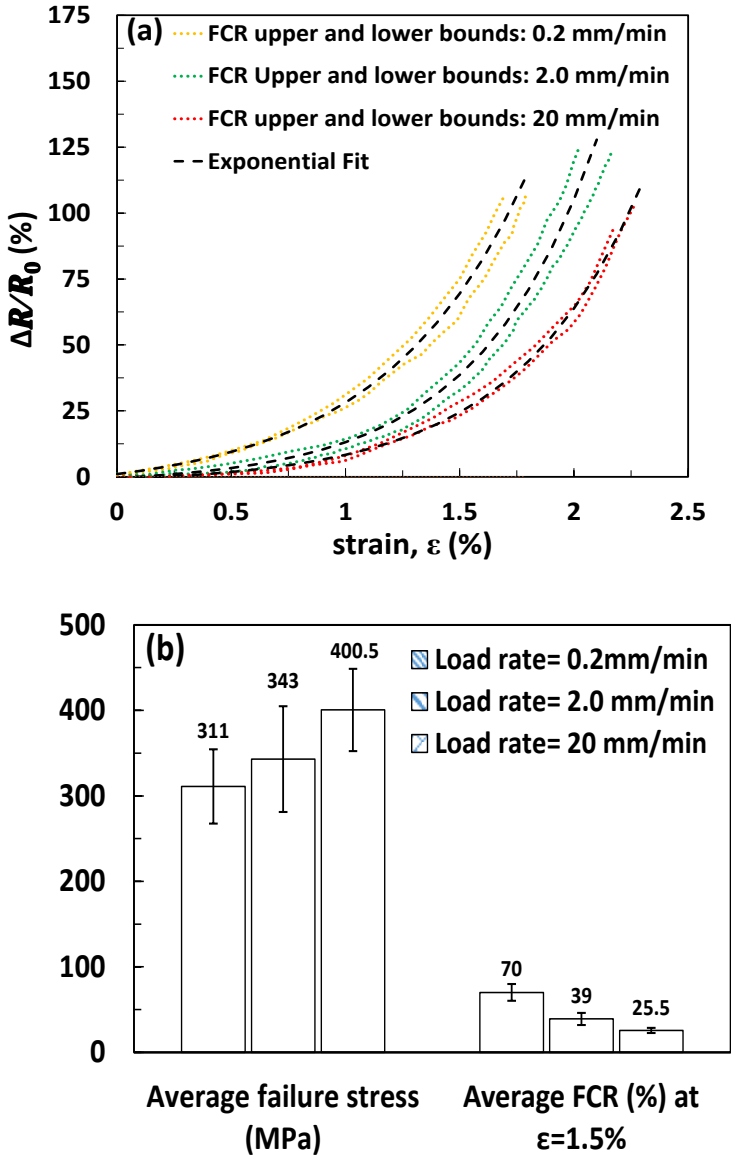

Figure 5. (a) Exponential growth model representation, (b) Fractured strength and FCR with percentage error.

5. Conclusions

Graphene enhanced coated fabric is inherited with obvious advantages to be embedded as sensor in advanced multifunctional fiber reinforced polymers composites as compared to the mixing of nanofillers in the matrix polymer material. Complete fabrication process of such multifunctional FRP composite was demonstrated by manufacturing samples for in-plane

  doi:10.5075/epfl-298799_978-2-9701614-0-0

tension tests using the VARTM process. The rGO coated fabric sensors were found capable to capture the various stages of the VARTM for process monitoring such as vacuum compaction, resin entry and flow, curing, and post-curing. Then, electromechanical characterization in in-plane tension tests were completed at three load rates of 0.2, 2.0 and 20 mm/min to evaluate the load rate dependency of piezoresistivity. The patterns of the piezoresistivity observed during the experiments were represented with exponential growth model. Besides, gauge factors were computed for each load rate in the elastic region. During in-plane mechanical tension tests, it was concluded that piezoresistivity and gauge factor are inversely proportional to the load rate.

Acknowledgements

This research work is supported by the Abu Dhabi Award for Research Excellence (AARE-2019) under project number 8434000349/AARE19-232.

6. References

[1] Kamar NT, Hossain MM, Khomenko A, et al. Interlaminar reinforcement of glass fiber/epoxy composites with graphene nanoplatelets. Composites Part A: Applied Science and Manufacturing 2015; 70: 82–92.

[2] Qin W, Vautard F, Drzal LT, et al. Modifying the carbon fiber-epoxy matrix interphase with graphite nanoplatelets. Polym Compos 2016; 37: 1549–1556.

[3] Ud Din I, Naresh K, Umer R, et al. Processing and out-of-plane properties of composites with embedded graphene paper for EMI shielding applications. Composites Part A: Applied Science and Manufacturing 2020; 134: 105901.

[4] Irfan MS, Khan T, Hussain T, et al. Carbon coated piezoresistive fiber sensors: From process monitoring to structural health monitoring of composites – A review. Composites Part A: Applied Science and Manufacturing 2021; 141: 106236.

[5] Zhang H, Peijs T. Multifunctional composites based on hierarchical micro–nanostructures: design, manufacturing, properties, and applications. In: Fiber-Reinforced Nanocomposites: Fundamentals and Applications. Elsevier, pp. 183–198.

[6] Yao X, Kinloch IA, Bissett MA. Fabrication and Mechanical Performance of Graphene Nanoplatelet/Glass Fiber Reinforced Polymer Hybrid Composites. Front Mater 2021; 8: 773343.

[7] Umer R. Manufacturing and Mechanical Properties of Graphene Coated Glass Fabric and Epoxy Composites. J Compos Sci 2018; 2: 17.

[8] Umer R, Li Y, Dong Y, et al. The effect of graphene oxide (GO) nanoparticles on the processing of epoxy/glass fiber composites using resin infusion. Int J Adv Manuf Technol 2015; 81: 2183–2192.

[9] Du X, Zhou H, Sun W, et al. Graphene/epoxy interleaves for delamination toughening and monitoring of crack damage in carbon fibre/epoxy composite laminates. Composites Science and Technology 2017; 140: 123–133.

[10] Mahmood H, Vanzetti L, Bersani M, et al. Mechanical properties and strain monitoring of glass-epoxy composites with graphene-coated fibers. Composites Part A: Applied Science and Manufacturing 2018; 107: 112–123.

TOWARD SUSTAINABLE ACTIVE CELLULOSE NANOCRYSTALS-BASED INK FOR STRUCTURAL HEALTH MONITORING

Adel, Alrai[a,b], Ersin, Beyhan[a,b], Amir, Asadi[c], Elif, Özden-Yenigün[d], Hülya, Cebeci[a,b]

a: Department of Aeronautics and Astronautics, İstanbul Technical University, 34469, Istanbul – adelalrai@gmail.com
b: ITU Aerospace Research Center, Istanbul Technical University, Istanbul, 34469, Turkey
c: Manufacturing and Mechanical Engineering Technology, Department of Engineering Technology and Industrial Distribution, Texas A&M University, MEOB 309, College Station, TX 77843, USA
d: School of Design, Textiles, Royal College of Art, London SW7 2EU, UK

Abstract: *Sustainable aqueous-based active inks can offer an environmental advantage by replacing hazardous volatile solvents with a friendly environmental option; water, and an ease of application for composite applications. This work studies the potential of piezoresistivity of carbon nanotubes (CNTs) and cellulose nanocrystals-based strain sensor that was simply coated on the surface of glass fiber reinforced polymer (GFRP). The rheological behavior of the developed inks and the morphology of the processed sensor were examined. The in-situ piezoresistive behavior was investigated by measuring the change of resistance during a tensile test. Sensitivities of 2.8 and 24.3 were calculated ($\Delta R/R_0\varepsilon$)) for the linear regions in elastic and plastic deformations, respectively.*

Keywords: Carbon Nanotubes; Cellulose Nanocrystals; Piezoresistivity; Strain Sensor; Composite

1. Introduction

Structural health monitoring through embedded sensors currently in composites faces obstacles that necessitate the need for an alternative. To demonstrate, optical fiber sensors, *e.g.* fiber Bragg grating (FBG) one of the widely used technology (1), incorporated with composites are only sensitive to localized damages and require noise cancelling analysis to enhance their resolution (2). Furthermore, the presence of the fiber in the matrix composite causes the increase of stress raisers that lead to various complications (3–5). In the last decade, the advancement made in synthesis of carbon-based nanomaterials paved the way for the development of piezoresistive-based strain sensors as an alternative approach (6).

Carbon nanotubes (CNTs) nanocomposites have been developed and exploited as self-sensing sensors due to their piezoresistivity which originates from reconstruction and deconstruction of CNTs network subjected to the strain changes. Several works demonstrated the feasibility of the approach for different polymer matrices (7–9). For instance, satisfactory and reliable sensitivity as high as 13 was demonstrated for graphene-glass fiber coated polymer composites (5); however, a decrease in mechanical properties was also noted.

Cellulose nanocrystals (CNCs), a product of natural occurring substances, *e.g.* wood, have emerged as an excellent stabilizer for CNTs in aqueous solutions. The ability of CNCs to stabilize

  doi:10.5075/epfl-298799_978-2-9701614-0-0

the hydrophobic CNTs have been attributed to its miscellaneous surface chemistry which encompasses surfaces of both hydrophobic and hydrophilic natures (10,11). Also, their mechanism to separate and isolate individual CNTs have been explained by their relatively smaller size compared with CNTs (12). As a result, in the past few years, an emerging research has been dedicated to apply the variant of their hybrid systems in different applications. For example, our previous work showed that screen-printed CNTs/CNCs inks had excellent flexible and electrical properties to function as a wearable antenna application for wireless communication (13).

This work studied the applicability of CNTs/CNCs-based strain sensor coated on a composite system. First, CNTs/CNCs ink was developed and applied on the surface of GFRP composites and dried to act as a functional strain sensor. The binder-free coated CNTs/CNCs layers strongly adhered to the surface of the composite. The CNTs/CNCs hybrid sensor showed an ohmic behavior. The in-situ piezoresistive behavior was investigated by measuring the change of resistance during a tensile test. Sensitivities of 2.8 and 24.3 were calculated for the linear regions in elastic and plastic deformations, respectively.

2. Experimental

2.1 Materials

Carbon nanotubes and cellulose nanocrystals were purchased from Sigma-Aldrich (United States of America), CelluForce (Canada), respectively. Epoxy resin LR160 and hardener LH160 (weight ratio of resin/hardener is 100:25) were purchased from DostKimya, Hexion (Turkey). All materials were used without purification. E-glass fabric (plane woven, 200 g/m^2) was purchased from Hexcel (USA). Silver paste was purchased from Nanografi (Turkey)

2.2 Fabrication of composites, inks, and strain sensor

Using resin vacuum infusion process, GFRP laminates were prepared. The final dimensions of a GFRP coupon were 1×25×250 mm^3. After CNCs were dispersed in water, CNTs were added to the mixture and ultrasonicated. The CNTs/CNCs ink was then applied on the middle surface of GFRP coupons with an area of 40x25 mm^2 through a roller blade, and was dried at elevated temperature of 40 °C. Copper electrodes were attached to the far ends by silver paint. The as prepared strain sensors were ready for further electromechanical testing. Table 1 shows the composition of all the prepared inks and the corresponding nomenclature.

Table 1: Compositions of the prepared ink.

Given name	CNT wt.%	CNC wt.%	Total concentration (wt.%)
1.0_ink	1.0	1.0	2

2.3 Characterization methods

Rheology tests of the developed inks were studied using a rheometer instrument. Morphology of the CNTs/CNCs sensors was examined using scanning electron microscopy (SEM). Tensile and tensile cyclic tests were carried out using Universal Testing Machine (UTM). Resistance data and electrical measurements were collected using Keithley (2400 SMU). Using two-probe

  doi:10.5075/epfl-298799_978-2-9701614-0-0

configuration, change in resistance was calculated based on $(R_i-R_0)/R_0$ where R_i and R_0 are instantaneous and initial resistances, respectively. The distance between the electrodes was 40 mm. The electrodes have a constant area of 25*5 mm^2.

3. Results and discussion

Rheological properties of the prepared of CNTs/CNCs ink with ratio of 1.0:1.0 are shown in Figure 1. The difference between the storage and loss moduli indicated that the ink is of solid-like nature, Figure 1a. The relatively large difference was attributed to applicability of the ink to be smoothly applied on the surface of the composite. Furthermore, the complex viscosity decreased as angular frequency increased which indicates the shear thinning behavior of the ink, Figure 1b. The shear thinning behavior of CNTs/CNCs ink was also attributed as an advantage to be exploited for coating applications. It is worth reporting that similar results of aqueous-based CNCs and polymeric-based CNTs dispersions were reported (14,15).

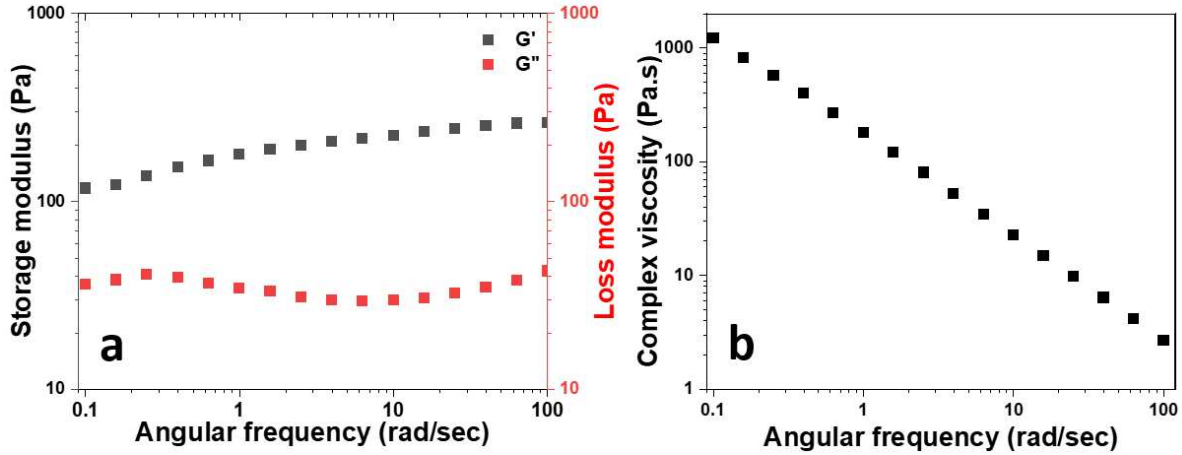

Figure 1: Rheological properties of CNTs/CNCs with ratio of 1.0:1.0 a) storage (G') and loss (G'') moduli and b) complex viscosity as function of angular frequency (rad/second).

Figure 2 shows surface morphology of the strain sensor prepared from 1.0_ink at two different magnifications. Figure 2a shows the surface of the CNT/CNC sensor at low magnification. Some agglomeration of CNC particles was seen which was attributed to the high load of CNC (12) which are highlighted in Figure 2b. X-ray photoelectron (XPS) analysis to be conducted to confirm the results.

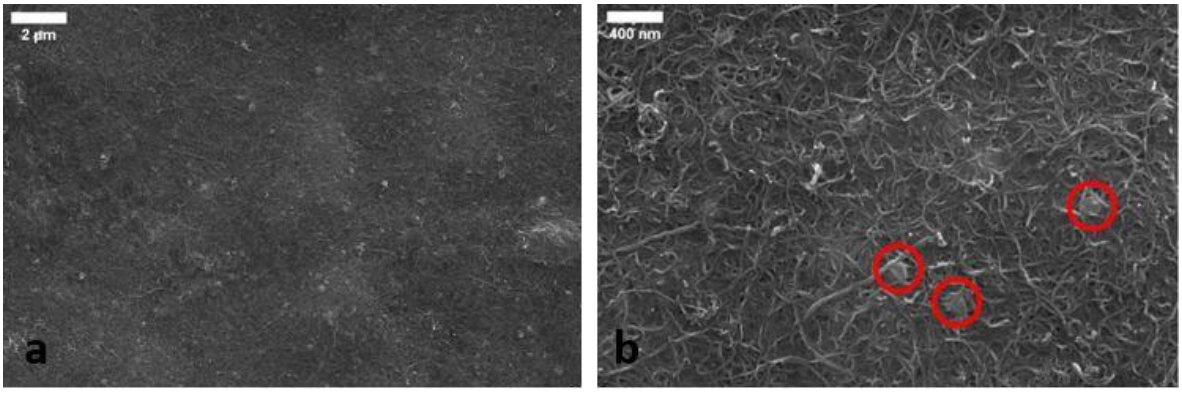

Figure 2: SEM images of 1.0_ink CNT/CNC strain sensor at two magnification a) 20KX b) 100KX.

  doi:10.5075/epfl-298799_978-2-9701614-0-0

Current-voltage curve of the prepared sensor is of ohmic nature as shown in Figure 3. This ohmic, linear, behavior of the CNTs/CNCs-based strain sensor is essential to behave as a piezoresistive sensor.

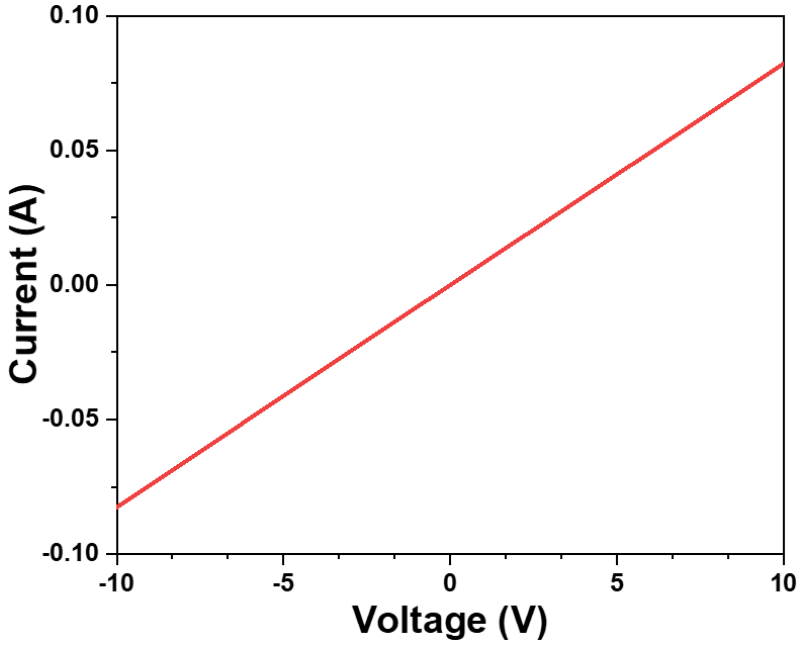

Figure 3: Current-voltage curve of 1.0_ink from -10 to 10 voltages in unloading state (0% strain).

Piezoresistive behavior of the as-prepared sensors were tested in tensile mode. The loading speed was set at 2 mm/min. The strain ranged up to 0.45% which encompassed both elastic and plastic regions. Samples were not strained until failure to avoid damage to the contact extensometer. Figure 4 shows the behavior of coated CNTs/CNCs-based strain sensor on the surface of the composite under tensile loading. The linearity of the sensor extends up to 0.1% strain while the elasticity of GFRP composite is still present to at least 0.2% strain. A gauge factor ($\Delta R/R_0\varepsilon$) of 2.8 was calculated for this linear region where the conductive network was under both reconstruction and deconstruction. In the plastic deformation, the linear region of the sensor between 0.4 to 0.45% strain has a gauge factor 24.3. The high gauge factor in plastic region was attributed to the irreversible increase in tunneling distance between CNTs due to deconstruction of network (16). It is worth emphasizing that the linearity of the GFRP, elasticity, did not completely match the linearity of the sensor.

  doi:10.5075/epfl-298799_978-2-9701614-0-0

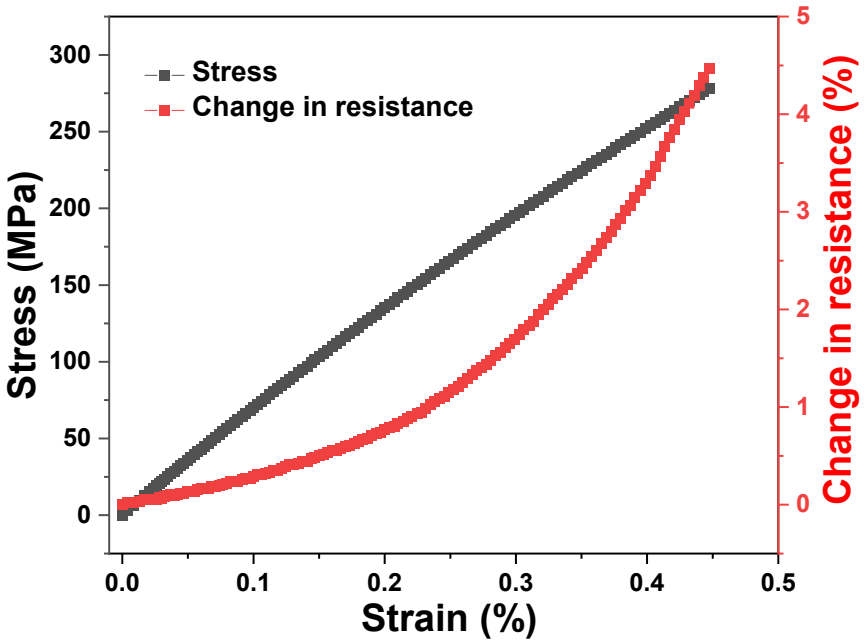

Figure 4: Tensile piezoresistive behavior of CNTs/CNCs based strain sensor coated on the surface of GFRP.

4. Conclusion and future work

This work presented here shows the potential of lightweight CNTs/CNCs-based strain sensor for composites. CNTs/CNCs-based ink was first formulated and applied on the surface of a GFRP to function as a strain sensor. Although the sensor showed noticeable electrical conductivity and potential tensile piezoresistive behavior, the linearity of the sensor only matched the initial part of the elastic region of the composite. Therefore, in an attempt to improve linearity, future work will focus on different CNT/CNC compositions (*e.g.* 1.0:0.5. 1.0:1.0, 0.5:1.0) and their effect on piezoresistivity. The hypothesis is that the variations in CNCs loading might influence the tunneling distance among CNTs particles. Slight changes in the tunneling distance, would impact sensitivity, conductive network paths, and the overall piezoresistive behavior. As a result, the underlaying mechanism of CNTs/CNCs hybrid strain sensor and the effect of CNCs on tunneling resistance will be fully addressed and, therefore, the potential CNT/CNC-based coated on the surface of composite for piezoresistive applications will be studied.

Acknowledgements

Adel ALRAI thanks and acknowledges support from Boeing-İTÜ ARC Student Scholarship Program. Adel ALRAI also acknowledges the support he received from Scientific and Technological Research Council of Turkey (TUBITAK) 2224-A Grant Program for Participation in Scientific Meetings Abroad to participate in ECCM20. The authors also would like to acknowledge the support received from Katip Çelebi - Newton Fund provided jointly by TÜBİTAK and Royal Academy of Engineering (Project number: 220N307) for material characterization.

5. References

1. Monastyreckis G, Stepura A, Soyka Y, Maltanava H, Poznyak SK, Omastová M, et al. Strain Sensing Coatings for Large Composite Structures Based on 2D MXene Nanoparticles. Sensors. 2021 Jan;21(7):2378.
2. Wang M, Li N, Wang GD, Lu SW, Zhao QD, Liu XL. High-sensitive flexural sensors for health monitoring of composite materials using embedded carbon nanotube (CNT) buckypaper. Composite Structures. 2021 Apr;261:113280.
3. Fedorov AY, Kosheleva NA, Matveenko VP, Serovaev GS. Strain measurement and stress analysis in the vicinity of a fiber Bragg grating sensor embedded in a composite material. Composite Structures. 2020 May 1;239:111844.
4. Kinet D, Mégret P, Goossen KW, Qiu L, Heider D, Caucheteur C. Fiber Bragg Grating Sensors toward Structural Health Monitoring in Composite Materials: Challenges and Solutions. Sensors. 2014 Apr;14(4):7394–419.
5. Reghat M, Mirabedini A, Tan AM, Weizman Y, Middendorf P, Bjekovic R, et al. Graphene as a piezo-resistive coating to enable strain monitoring in glass fiber composites. Composites Science and Technology. 2021 Jul;211:108842.
6. Zhang X, Xiang D, Zhu W, Zheng Y, Harkin-Jones E, Wang P, et al. Flexible and high-performance piezoresistive strain sensors based on carbon nanoparticles@polyurethane sponges. Composites Science and Technology. 2020 Nov;200:108437.
7. Yu S, Wang X, Xiang H, Zhu L, Tebyetekerwa M, Zhu M. Superior piezoresistive strain sensing behaviors of carbon nanotubes in one-dimensional polymer fiber structure. Carbon. 2018 Dec 1;140:1–9.
8. Bragaglia M, Paleari L, Lamastra FR, Puglia D, Fabbrocino F, Nanni F. Graphene nanoplatelet, multiwall carbon nanotube, and hybrid multiwall carbon nanotube–graphene nanoplatelet epoxy nanocomposites as strain sensing coatings. Journal of Reinforced Plastics and Composites. 2021 Sep;40(17–18):632–43.
9. Irfan MS, Khan T, Hussain T, Liao K, Umer R. Carbon coated piezoresistive fiber sensors: From process monitoring to structural health monitoring of composites – A review. Composites Part A: Applied Science and Manufacturing. 2021 Feb;141:106236.
10. Olivier C, Moreau C, Bertoncini P, Bizot H, Chauvet O, Cathala B. Cellulose Nanocrystal-Assisted Dispersion of Luminescent Single-Walled Carbon Nanotubes for Layer-by-Layer Assembled Hybrid Thin Films. Langmuir. 2012 Aug 28;28(34):12463–71.
11. Hajian A, Lindström SB, Pettersson T, Hamedi MM, Wågberg L. Understanding the Dispersive Action of Nanocellulose for Carbon Nanomaterials. Nano Lett. 2017 Mar 8;17(3):1439–47.
12. Shariatnia S, Kumar AV, Kaynan O, Asadi A. Hybrid Cellulose Nanocrystal-Bonded Carbon Nanotubes/Carbon Fiber Polymer Composites for Structural Applications. ACS Appl Nano Mater. 2020 Jun 26;3(6):5421–36.
13. Ibanez Labiano I, Arslan D, Ozden Yenigun E, Asadi A, Cebeci H, Alomainy A. Screen Printing Carbon Nanotubes Textiles Antennas for Smart Wearables. Sensors. 2021 Jan;21(14):4934.
14. Fan Z, Advani SG. Rheology of multiwall carbon nanotube suspensions. Journal of Rheology. 2007 Jul;51(4):585–604.
15. Qiao C, Chen G, Zhang J, Yao J. Structure and rheological properties of cellulose nanocrystals suspension. Food Hydrocolloids. 2016 Apr;55:19–25.
16. Cao X, Wei X, Li G, Hu C, Dai K, Guo J, et al. Strain sensing behaviors of epoxy nanocomposites with carbon nanotubes under cyclic deformation. Polymer. 2017 Mar;112:1–9.

  doi:10.5075/epfl-298799_978-2-9701614-0-0

Fiber reinforced polymer composites with self-powered sensing capabilities – An experimental and simulation study

A. Voudouris Itskaras[a], G. Karalis[a], L. Koutsotolis[a], K. Tsirka[α], E. Lambrou[a], L. N. Gergidis[a], A. S. Paipetis[a]

a: Department of Materials Science and Engineering, University of Ioannina, Ioannina 45500, GR - a.voudouris@uoi.gr

Abstract:

Smart structures represent an extremely interesting field of research on composite science and technology on account of their potential to perform more than one specific functions, such as structural health monitoring, strain or damage sensing, temperature control and energy harvesting. In this work, a multifunctional fiber reinforced polymer composite with self-powered sensing capabilities was manufactured. The thermal energy harvesting ability of the composite structure was endowed by the controlled deposition of nanomaterials onto reinforcing fibers. The thermal sensing capability was accurately correlated with the enhanced thermoelectric voltage of the multifunctional structure, by eliminating the need for "external" sensors. Both experimental and modeling work validated the thermoelectric performance.

Keywords: Fiber Reinforced Polymers; Multifunctional Composites; Energy-autonomous Structures; Self-sensing

1. Introduction

Thermoset polymers are the most common types of matrices regarding state-of-the-art advanced composite materials. With the progress of technology, fiber reinforced polymer matrix composites have replaced many conventional materials in numerous applications such as aerospace, automotive, wind turbines, solar systems, compressed gas storage, etc., due to their advantageous specific properties [1].

In the last two decades multifunctional materials have gained considerable attention in the field of composite science. The term "multifunctional" means that these materials beside their primary structural function (e.g., fracture toughness, strength, thermal stability etc.) exhibit another non-structural one without the integration or connection of an additional device. Some non-structural functions include sensing, joule heating, electromagnetic interference (EMI) shielding, energy harvesting and storage etc. [2].

Two of the most concerning issues that humanity is facing are the aggravation of environmental problems and energy crisis as a result of the reckless use of fossil fuels, overconsumption and overpopulation [3]. Therefore, one of the challenges that scientists must deal with in the field of composite materials is the evolution of multifunctional composites for energy harvesting from alternative energy sources, that could be extended into self-powered structures.

A proposed solution to these problems is the utilization of the large amounts of energy losses. This includes the thermal energy, most of which is released into the environment. Thus, the

development of thermoelectric materials and devices for energy harvesting and self-powered applications consist current topics for active research.

The operation of thermoelectric materials and devices is based on the thermoelectric effect known as Seebeck effect, which describes the direct conversion of a temperature difference between two dissimilar electrical conductors or semiconductors into electrical voltage. The potential difference that develops in a thermoelectric material by applying a temperature difference (ΔT) is equal to the product $S \cdot \Delta T$, where S is the Seebeck coefficient, an intrinsic property of the material, that depends on temperature and is related to its electrical properties. Seebeck coefficient is used for the calculation of power factor (PF) given by the formula $PF = \sigma \cdot S^2$. The efficiency of thermoelectric materials is described by the figure of merit ZT and is given by the equation $ZT = (\sigma \cdot S^2/\kappa)/T$. According to this formula, a thermoelectric material in order to exhibit high thermoelectric performance, it must feature a high electrical conductivity (σ), a high Seebeck coefficient (S) and a low thermal conductivity (κ)[4].

The most reported thermoelectric materials with high figure of merit values (ZT>1) are conventional inorganic materials. Nevertheless, these materials require high temperature differences for their optimal operation and are based on elements that are usually rare, expensive, inflexible, heavy and very often toxic as lead (Pb), bismuth (Bi) and tellurium (Te). In accordance with the above, it is necessary to search for low-cost thermoelectric materials, which are light, flexible and less-toxic for low temperature applications (300K<T<600K)[5].

Candidate materials for these applications are carbon-based materials and its allotropic forms, which possess a wide variety of energy gaps (e.g., graphene, carbon nanotubes, fullerene etc.) and due to their mechanical properties can lead to lightweight and high-strength thermoelectric devices. In addition, another advantage of such materials is the easy-process production of functional inks which can be employed through the use of various printing technologies (e.g., inkjet printing, screen printing etc.). As a result, printed functional films can be integrated into composite structures, importing desirable non-structural functions[6].

In many industrial or transport sectors, several thermal gradients are generally measured during operation lifetime using distributed temperature sensors. Typical temperature sensors are based on thermocouples or resistance elements[7]. However, these sensors are not always suitable for applications, especially in cases where liquids or gases are involved, e.g. pipelines, since their presence affects the flow itself. In this experimental and theoretical work, a multifunctional structural composite was carried out where the material itself can act as a sensor, exploiting the principles of thermoelectric materials and devices.

2. Results and Discussion

2.1 Materials

SWCNT powder was provided by OCSiAl (TUBALL, carbon content: >85 wt. %, CNT: ≥75 wt. %, outer mean diameter of CNT 1.8 ± 0.4 nm, length of CNT >5 μm, metal impurities <15 wt. %). Sodium dodecylbenzenesulfonate ((SDBS), 348.48 g/mol) and poly(ethyleneimine) solution ~50% in H_2O-PEI (M_r : 600 000−1 000 000) were purchased from Sigma-Aldrich. The PEDOT: PSS conductive polymer screen-printing ink (Orgacon ELP5015 with 2.5−5.5% wt. solid

content) was provided by Agfa. Silver paint was received from Agar scientific. Distilled water (DI water) and isopropyl alcohol (IPA) of ≥98% purity have been used throughout all of the different processes in this research work. A unidirectional (UD) glass fabric (GF) (320 gr/sqm) of 0.26 mm single ply thickness was used. The LY-5052 DGEBA-based epoxy resin and amine-based hardener by Huntsman Advanced Materials Inc. were utilized as the composite matrix (resin to hardener weight ratio 100:38 w/w) with $T_g \approx 131°C$. Curing was conducted under 3 MPa pressure using a hydraulic press at room temperature (RT) for 24 h and post curing at 100°C for 4 h.

2.2 Fabrication of multifunctional composite with sensing capabilities

The main goal of the research was to transform a conventional composite structure to a self-powered multifunctional laminate. For this purpose, the architecture of the multifunctional composite was designed to be able to exploit the untapped thermal energy based on the principles of the thermoelectric materials. Initially, the production of both p- and n-type thermoelectric inks was realized. The inks were integrated into the composite structure deposited on the glass fabrics by drop casting method, forming a single conductive path. The geometrical characteristics of this conductive pattern was designed, so that the p- and n- type thermoelements were electrically interconnected in series and thermally in parallel. Finally, the reinforcing layers of glass fabrics were impregnated using epoxy resin to form a stable structure, denoted as multifunctional composite laminate with thermoelectric generator (TEG) device characteristics (Figure 1).

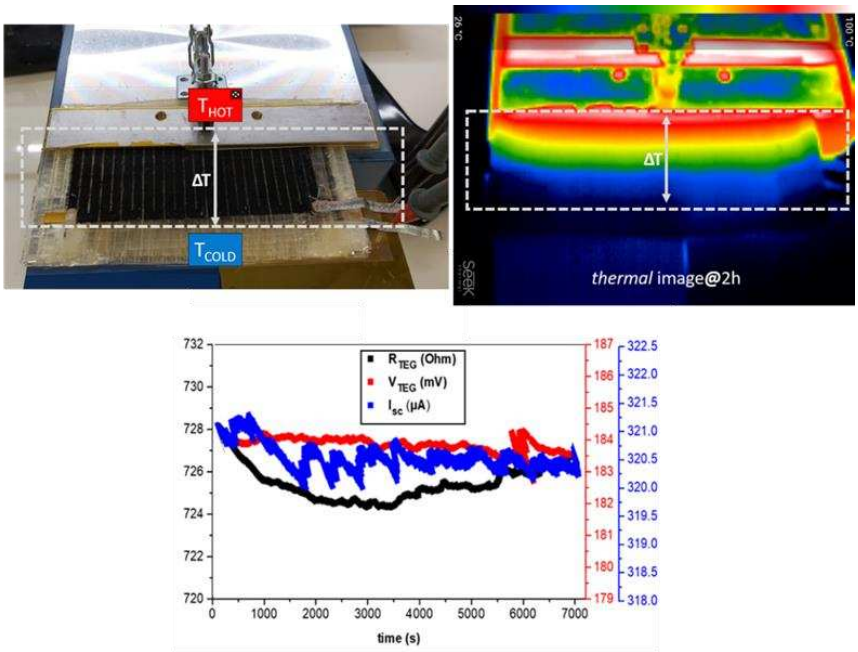

Figure 1. Visual (top left), thermal (top right) and electric-thermoelectric graph for the monitoring of the multifunctional composite performance upon exposure to a ΔT of 75 K for 2 h.

2.3 Finite Elements Simulation

The performance of the thermoelectric device was modeled using Finite Elements (FE) discretizations following the exact geometry and individual material properties such as thermal/ electrical conductivities, Seebeck coefficients of the TEG device used or measured in the experimental setup. Finite Elements numerical simulations were conducted for the solution of the thermoelectric coupled constitutive equations with the appropriate boundary conditions dictated also by the experimental setup. The temperature range used in the numerical simulations was between 25°C (298 K) and 125°C (398 K).

Temperature and electrical potential distributions, extracted from the numerical solution, were monitored in the discretized space of the device. Representative TEG's temperature distributions are given for the model device in Figure 2 showing a smooth behavior between the "cold" and "hot" aluminum heat baths.

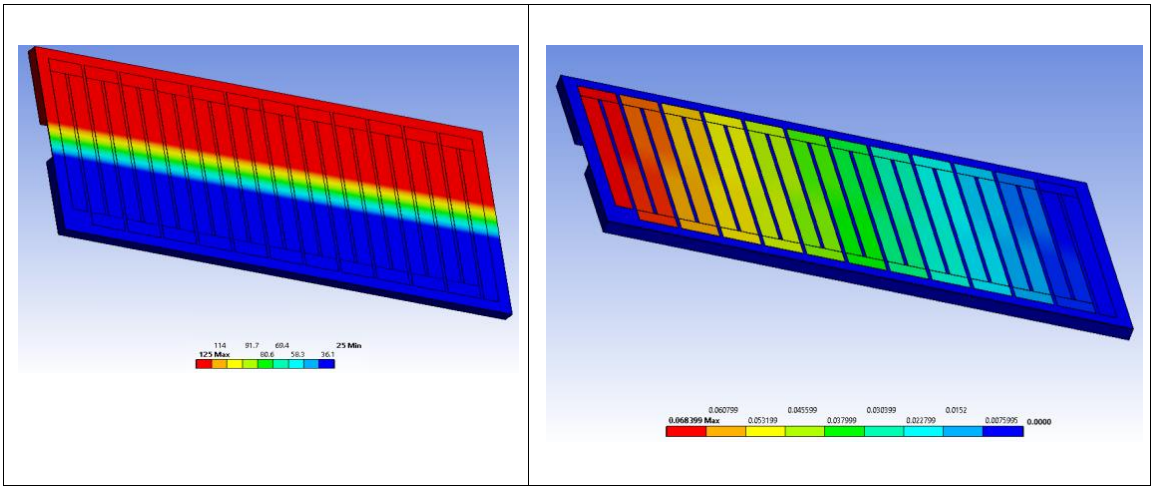

Figure 2. Temperature distributions (left) in the TEG device obtained from Finite Elements numerical simulations. The temperature values shown in the color bar are in Celsius degrees. Electrical potential distribution (right) obtained from FEM numerical computations. The color bar values are in Volts.

The calculated electrical potential distribution throughout the device is also shown in Figure 2. The voltage drop is clear as the electrons move through the serial connected n-, p-type semiconductor thermoelements. The electrical potential difference between the first and last thermoelement is intimately related to the open circuit voltage of the TEG device and can be promptly calculated for different temperature differences allowing the simulation of different operating conditions presented in Table 1.

Table 1: Output voltages measured experimentally and obtained from FE simulation.

T_{cold} (°)	T_{hot} (K)	ΔT (K)	ΔV_{sim} (mV)	ΔV_{exp} (mV)
298	398	100	66.35	52.5
298	373	75	51.30	45.75
298	348	50	34.20	27.5

The Finite Element analysis output voltages are in reasonable agreement with the measured voltages as can be seen in Figure 2 considering the thermal and electrical losses present in the experimental procedure.

2.4 Evaluation of the multifunctional structure as an infrared (IR) sensor

The satisfactory sensitivity and response of the multifunctional structure to the aforementioned environmental stimuli could enable it to be used as a sensor to detect changes in specific environmental conditions. The measured sensitivity for infrared form of radiation applied to the active surface of multifunctional structure was analyzed and characterized accordingly.

Figure 3a shows the set-up for evaluating the functionality of IR radiation sensor for the multifunctional structure. The FLIR A6750 MWIR thermal camera was used, with a resolution of 640×512 pixels and a frame rate of 60 Hz. In combination, 2×1000 W IR lamps were used as heat sources, activated either manually or by the Tektronix AFG3052C signal generator for the pulse thermography method. The ramp pulse lasted for 5 s and the peak-to-peak voltage was 9 V. The distance between the multifunctional FRP laminate and the array of lamps, as well as the distance between the laminate and the camera was 1 m.

In particular, Figure 3b presents the response of the multifunctional laminate upon the application of both IR pulsed and continuous radiation with the corresponding thermal images(Figure 3c) during heating and cooling cycles. For both cases, an immediate TE response was observed during the infrared radiation time period with an almost instantaneous increase of the produced TE voltage, e.g. from. 0.8 mV to 50 mV in 30 s of continuous application, while an expected direct drop of the generated TE voltage was occurred when the IR lamps were switched off.

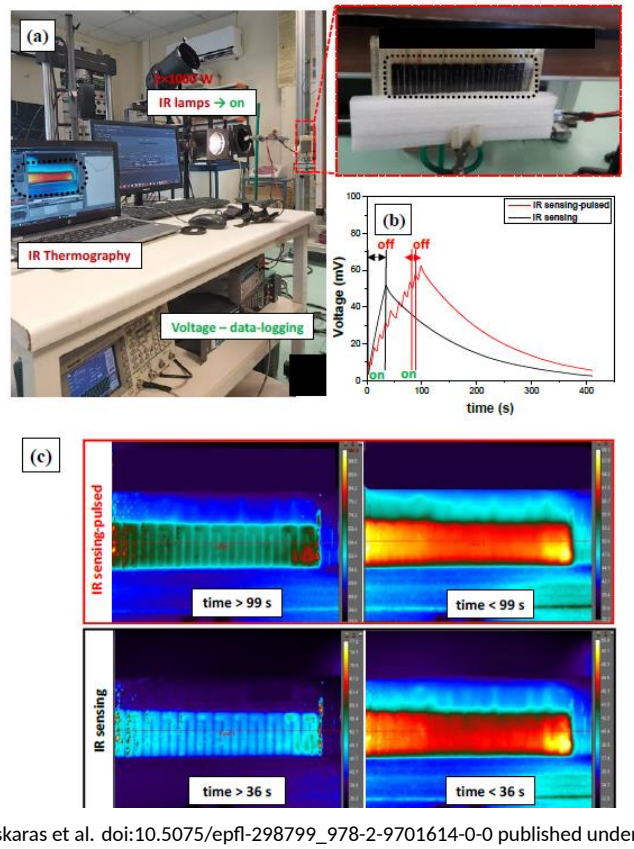

Figure 3. *(a) IR radiation sensing set-up for evaluating the multifunctional laminate performance, (b) data-logged TE response upon specific application of pulsed and continuous IR radiation, (c) thermal imaging captures of the multifunctional laminate for both pulsed and continuous IR during heating and cooling.*

3. Conclusions

In this research study, a self-powered multifunctional composite structure with sensing capabilities was reported. The additional thermal energy harvesting functionality was accomplished by the integration of nanostructured materials into the final structure through a printing technique. The evaluation of the thermoelectric performance was performed both experimentally, as well as by Finite Elements simulations. The capability of the multifunctional structure for infrared radiation detection based on the thermoelectric response was also validated. The obtained results showed an instantaneous increase and decrease of the generated voltage during the activation and deactivation of the IR lamps, respectively. This factenables the composite structure to acquire remarkable IR radiation sensing properties.

Acknowledgments

The research leading to these results has been part of complementary activities carried out at University of Ioannina to support the ATHENA project. This research has been co-financed by the European Union and Greek national funds through the Operational Program Competitiveness, Entrepreneurship and Innovation, under the call RESEARCH – CREATE – INNOVATE (project code: T1EDK 03480).

4. References

1. Kumar Sharma A, Bhandari R, Sharma C, Krishna Dhakad S, Pinca-Bretotean C. Polymer matrix composites: A state of art review. Mater Today Proc [Internet]. 2022;(xxxx). Available from: https://doi.org/10.1016/j.matpr.2021.12.592

2. Ali A, Andriyana A. Properties of multifunctional composite materials based on nanomaterials: a review. RSC Adv. 2020;10(28):16390–403.

3. Kumar P, Singh S, Hashmi SAR, Kim KH. MXenes: Emerging 2D materials for hydrogen storage. Nano Energy [Internet]. 2021;85(March):105989. Available from: https://doi.org/10.1016/j.nanoen.2021.105989

4. Karalis G, Tzounis L, Lambrou E, Gergidis LN, Paipetis AS. A carbon fiber thermoelectric generator integrated as a lamina within an 8-ply laminate epoxy composite: Efficient thermal energy harvesting by advanced structural materials. Appl Energy [Internet]. 2019;253(February):113512. Available from: https://doi.org/10.1016/j.apenergy.2019.113512

5. Wang H, Yu C. Organic Thermoelectrics: Materials Preparation, Performance Optimization, and Device Integration. Joule [Internet]. 2019;3(1):53–80. Available from: https://doi.org/10.1016/j.joule.2018.10.012

6. Hung NT, Nugraha ART, Saito R. Thermoelectric properties of carbon nanotubes.

Energies. 2019;12(23):1–27.

7. Shi Y, Wang Y, Deng Y, Gao H, Lin Z, Zhu W, et al. A novel self-powered wireless temperature sensor based on thermoelectric generators. Energy Convers Manag [Internet]. 2014;80:110–6. Available from: http://dx.doi.org/10.1016/j.enconman.2014.01.010

  doi:10.5075/epfl-298799_978-2-9701614-0-0

EMBEDDED CARBON NANOTUBES FOR LOCALIZED CURE MONITORING

Tobias Karlsson[a], Per Hallander[a,b], Malin Åkermo[a]

a: KTH, Department of Engineering Mechanics, KTH Royal Institute of Technology,
SE-11428 Stockholm, Teknikringen 8, Sweden – Tobiask2@kth.se
b: Saab Aerostructures, SE-58188 Linköping, Sweden

Abstract: *In this paper, non-intrusive vertically aligned carbon nanotubes forests have been used to monitor the cure locally in a glass fiber/epoxy laminate. Deposited on a prepreg surface, the resistance evolution of the conductive vertically aligned carbon nanotube forests is monitored during curing of a laminate. Distinguishable phases of the resistance evolution are observed, correlating to the material characteristics during the heating up and curing. The consolidation of the prepregs is initially seen, followed by the reduction in viscosity, initiation of crosslinking, chemical shrinkage, and gel point of the matrix. Rheological and thermal experiments have been performed to correlate and interpret the resistance evolution in the glass fiber/epoxy laminate during curing. Applying this method, quality control of manufactured components and cure cycle optimization for increased production efficiency and energy savings are envisioned.*

Keywords: Cure monitoring; Carbon Nanotubes; Viscosity; Chemical Shrinkage; Gel-point

1. Introduction

The high specific modulus and strength of fiber reinforced composites (FRPCs), as well as their corrosion resistance has increased the use of FRPCs within the aerospace, automotive, marine and energy sector to achieve larger and lightweight structures. With the more extensive use of FRPCs, it has become increasingly important to monitor the production procedure, in order to ensure quality control, locating defects and deviations during production; and increase efficiency in production for time and energy savings. Today, the design of curing processes relies on experimental data gathered *ex-situ* through Differential Scanning Calorimetry (DSC) [1,2], Dynamical Mechanical Analysis (DMA)[3,4] and rheologic measurements [2,5]. Only analysing small samples, the use of these techniques to monitor cure in real-time in components is not possible. Approaches to monitor curing in real time through embedded fiber optical [6] and dielectric analysis (DEA) [7] sensors have been developed. However, when designing a sensor for embedment into the composite structure, the size of the sensor is critical in order not to interfere with or deteriorate the mechanical structure. Ideally, a non-intrusive sensor embedded in the composite structure is desired, which may be used for *in-situ* online cure monitoring during production for quality control and cure cycle optimization. Subsequently, in the cured state, the sensor is ideally used for further sensing, i.e. for structural health monitoring (SHM). Further, to simplify recycling, it is desirable that the sensor does not bring foreign materials into the composite structure.

With the discovery of carbon nanotubes (CNTs) an interest of manufacturing new sensitive resistive sensors has appeared. Sensors for strain [8], temperature [9], pressure [10] and humidity [11] sensing have been presented. Work on cure monitoring of thermosets using CNTs

  doi:10.5075/epfl-298799_978-2-9701614-0-0

has appeared [12–14]. However few has been applied in thermoset prepreg material [15–17]. From these studies, it is clear that the morphology of the CNT network in the sensor is of paramount importance to the sensor's signal and sensitivity.
In this paper, Vertically Aligned Carbon Nanotube (VACNT) forests are presented for the first time for localized *in-situ* resistive real-time cure-monitoring of thermoset prepreg material. The VACNT forests are deposited on the prepreg surface prior to curing through a combined pressure and temperature deposition technique. Being deposited onto the prepreg, the VACNTs offers great liberty of quasi-distributed sensing. The resistive response of the embedded VACNT forests is measured over the course of a cure cycle, showing clear and distinguishable phases. These are interpreted and explained using supporting data from DSC and rheometric measurements.

2. Material and Experimental

2.1 Material

The VACNT forest used for resistive sensing is 20 µm high (Figure 1) and purchased from N12 Technologies. Grown on stainless steel substrates, the VACNT forests (V_f≈1% [18]) are delivered still attached to the substrate and are used without further modification. The glass fiber/epoxy prepreg used in this study is HexForce 120/HexPly 6376 glass fiber prepreg from Hexcel. To establish electrical contact to the embedded VACNT sensor, a non-woven, copper and nickel coated carbon fiber veil (Carbon 20444A, 34g/m^2, Technical Fibre Products Ltd) was chosen. For rheometric studies, a HexPly6376 epoxy film from Hexcel was used.

2.2 Deposition of VACNT forest

To successfully embed the VACNT forests into the composite structure, the VACNT forest was first deposited on the surface of a prepreg. The deposition makes use of capillary forces to infiltrate the inter-tube space between CNTs with epoxy, requiring both elevated temperatures and pressure. The deposition was performed in a set-up consisting of a heating plate, encapsulated by a vacuum bag connected to a vacuum pump. Using this set-up, both temperature and vacuum can be controlled and adjusted.

Figure 1 : (Left) VACNT forest on stainless steel substrate. (Right) VACNT forest deposited on prepreg surface.

To deposit the VACNT forest, the prepreg is placed on top of an heating plate followed by the stainless-steel substrate on top of the prepreg, allowing the VACNT forest facing the prepreg surface. A vacuum bag is thereafter added, covering the layup and sealed towards the layup table. The deposition procedure of the VACNT forest to the surface of HexForce 120/HexPly 6376 is initiated by increasing its temperature to 55°C. Upon reaching temperature, 890 mbar vacuum is applied and held for 2 minutes. After this, the vacuum bag was opened and the stainless-steel substrates removed, leaving the VACNT forest deposited on the prepreg surface, infiltrated by epoxy. Full VACNT deposition was not obtained due to the surface roughness from the 4-harness satin weave pattern used in the prepreg.

2.3 Curing of Sample

The sample prepared consisted of 20 layers of prepreg material, in-plane dimensions being 250x30 mm^2. In the midplane of the lamina, the two prepregs with VACNT forests was placed, allowing the VACNT deposited sides of the prepregs to meet and make up the midplane. To contact the VACNTs in the midplane, carbon fiber veil electrodes were inserted 50 mm into the lamina from each side during the lay-up. A potentiostat (SP-50, BioLogic) was connected to the electrodes, measuring the resistance evolution during curing. The curing of the sample was performed out-of-autoclave, inside a vacuum bag (800 mbar), placed inside an ACS FM340C climate chamber. The climate chamber was used to control the ramping of temperature. The cure cycle consisted of an initial temperature ramp 2°C/min up to 180°C, followed by a 2 hour dwell at 180°C. Temperature of the sample was measured through a thermocouple inserted into the vacuum bag. The cure monitoring has been repeated to assure reproducibility. However, presented here is a single representative sample.

2.4 Differential Scanning Calorimetry

A Mettler Toledo DSC820 was used to perform curing analysis on HexForce 120/HexPly 6376 glass fiber prepreg. The cure cycle of the sample was emulated, ramping the temperature by 2°C/min from 25 to 180°C. Subsequently the temperature was held for 2 hours. The test was performed in inert atmosphere with a flow of 50 ml/min of nitrogen.

2.5 Rheometry

Rheometry was performed on a pure HexPly 6376 epoxy film. The machine used was a DHR-2 from TA Instruments. The test was performed with parallel plates in oscillatory mode, maintaining a constant gap between the parallel plates and applying an angular frequency of 10 rad/s and 0.25% strain. Again, the cure cycle was emulated, ramping the temperature 2°C/min from 25 to 180°C. Thereafter, the temperature was held at 180°C for 2 hours.

3. Results and Discussion

The measured resistance of the embedded VACNT forest during curing is shown in figure 2. The curing has been divided into four phases - to facilitate the discussion. Initially, in phase I, a decrease of resistance is observed until 9 minutes into the process. Here, the decrease in resistance is due to two effects. First, the negative temperature coefficient (NTC) nature of [19,20] VACNTs, decreasing its resistance in response to temperature increase. Second, the consolidation of the prepreg stack. The consolidation is a time dependent process, the degree of contact between the prepregs increasing over time. Consequently, the VACNT

forests on the prepreg surface in the midplane achieves greater degree of contact, decreasing the resistance. This is also aided by the raise in temperature, which decreases the viscosity of the matrix, facilitating the consolidation of prepregs.

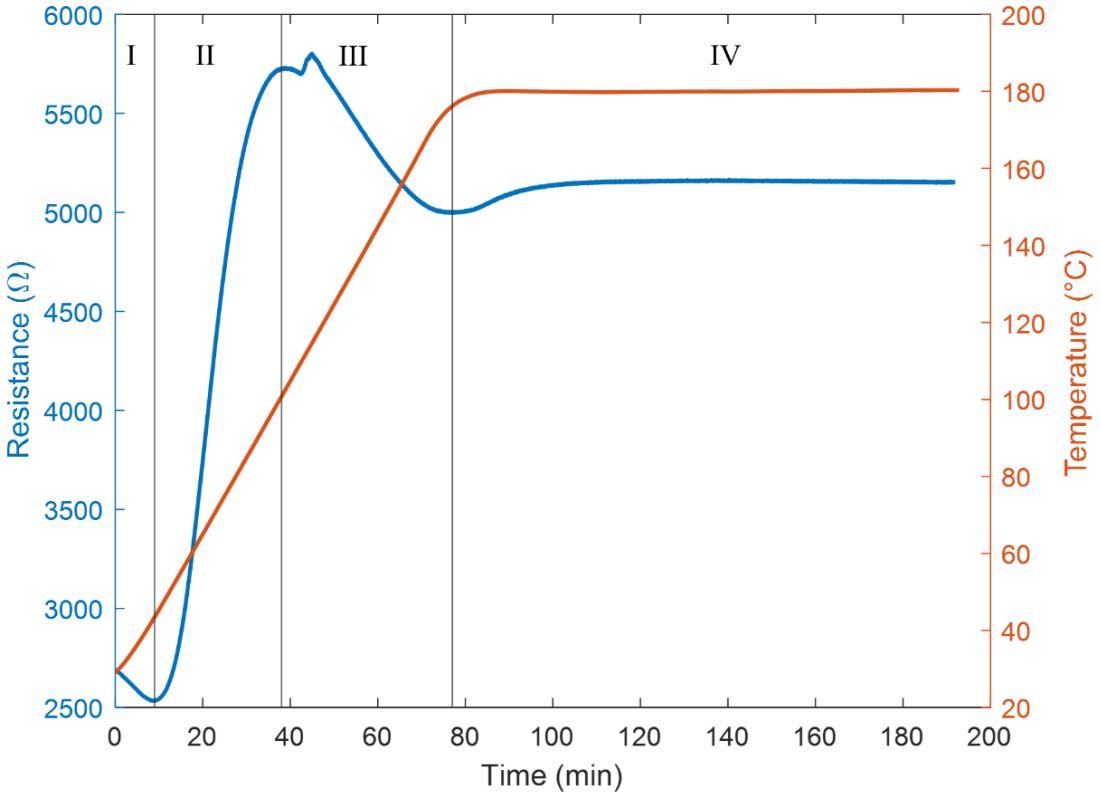

Figure 2 : Resistance of sensor over the curing cycle.

Phase I ends after 9 minutes into the curing cycle, as the resistance starts to increase rapidly in phase II. This dramatic increase in resistance is due to the rapid decrease in viscosity of the prepreg matrix. In figure 3, the measured resistance in phase I – III is plotted together with the complex viscosity of the HexPly 6376 epoxy film. Since reliable data below 60°C was not attained in the rheometric study, the obtained data is compared to data presented in [21]. The obtained data of the viscosity, presented in figure 3, is in good agreement with the viscosity presented in [21], where the viscosity of the HexPly 6376 epoxy film continues to increases up to 10 000 Pa*s at 30°C. The increase in resistance in phase II is due to this change in viscosity. As the viscosity is decreasing, the matrix will start to move, filling out voids in the laminate. As the matrix spreads out in the lamina, the CNTs are carried along in this motion. Consequently, the concentration of the carbon nanotubes will decrease locally, decreasing the volume fraction. As percolation theory states [22] the decrease in volume fraction will increase the resistance. The rapid decrease in viscosity starts to level out after about 90°C, at the same temperature as the resistance increase starts levelling out. The resistance peak after 38 minutes, ending phase II, is twofold. First, matrix viscosity has reached a plateau, decreasing its effect on the resistance increase. Second, the crosslinking of the matrix has initiated. Figure 4 shows the measured resistance evolution of the whole cure cycle together with DSC data from HexForce 120/HexPly6376 prepreg. In phase III, as the crosslinking continues and, cure induced shrinkage of the matrix appears. As the matrix continues to shrink due to crosslinking, the local volume

  doi:10.5075/epfl-298799_978-2-9701614-0-0

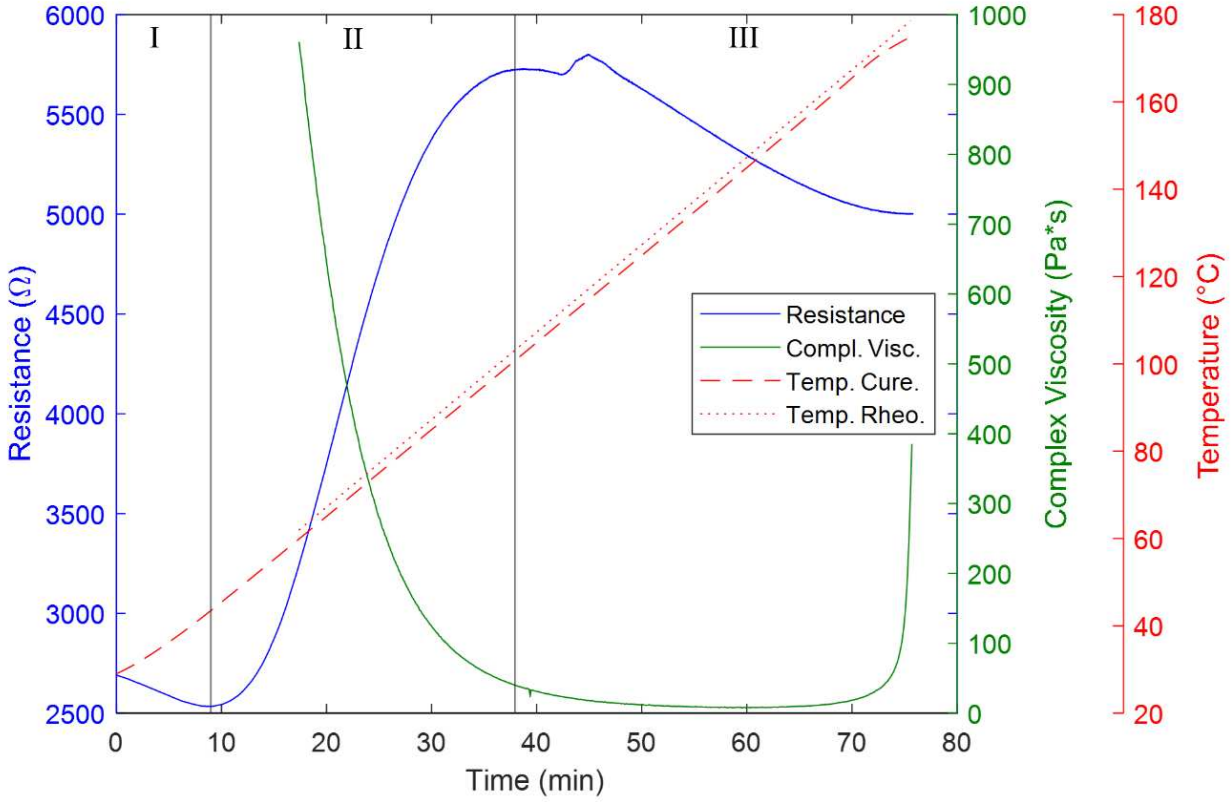

Figure 3 : Resistance of sensor and complex viscosity of HexPly 6376. Phase I, II and III.

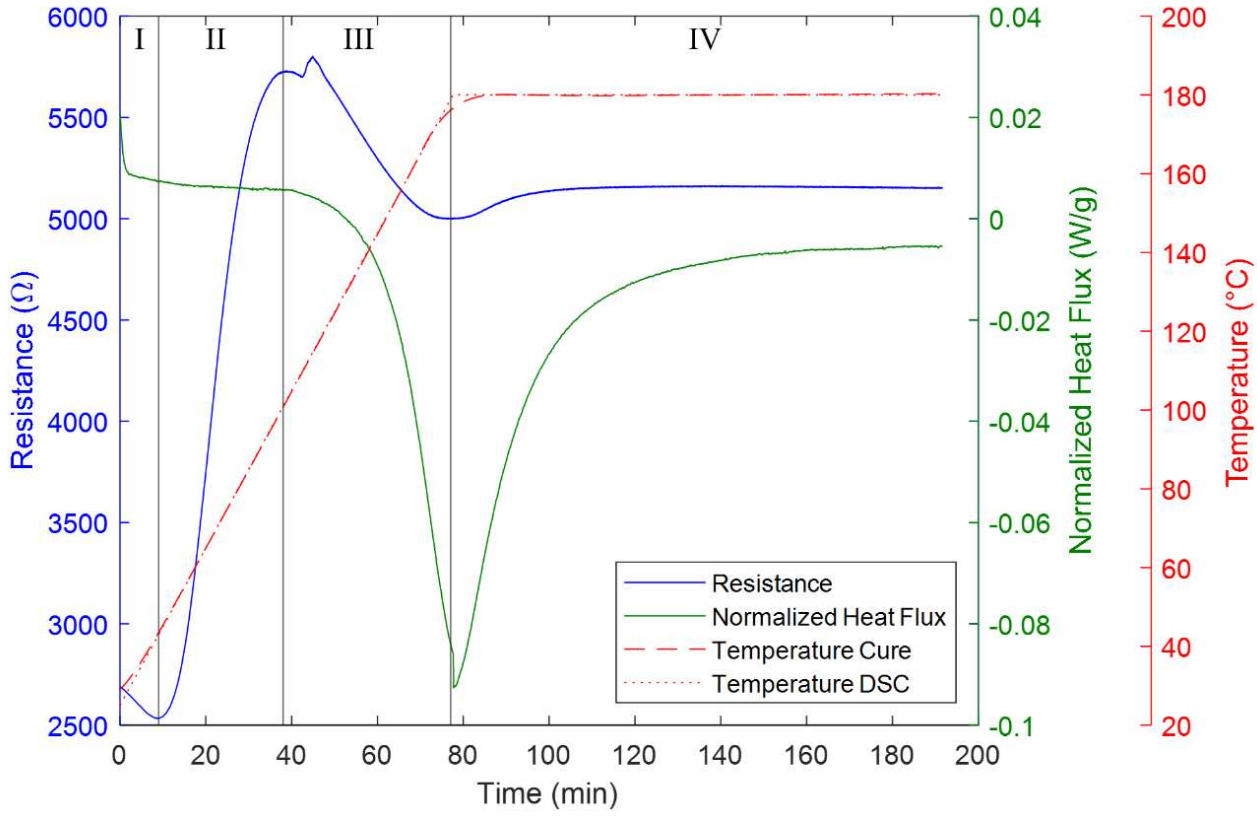

Figure 4 : Resistance of sensor and DSC data of HexForce120/HexPly6376 prepreg.

  doi:10.5075/epfl-298799_978-2-9701614-0-0

fraction of CNTs will increase, decreasing the resistance as the new percolated paths appear [13–15,17]. The decrease in resistance in phase III mirrors the rapid increase of the exotherm released by the matrix. As the cure induced shrinkage continues, the resistance deceases, until time reaches 76 minutes, when the bottom of the valleys in the resistance and DSC curves are reached. Again, observing figure 3, this valley corresponds to the rapid increase in viscosity towards infinity, indicating that the gel-point of the matrix has been reached [21]. The gel point occurring at the end of the temperature ramp has also been observed by Stark et al [3,4], using DMA. After the gel point is reached, we move into phase IV where curing continues, as shown by the DSC data. However, the cure rate is decreasing, caused by a decrease of mobility in the matrix as a gelled network has been formed. The increase in resistance in phase IV is yet not fully understood. Since the sample is still being cured after the gel point has been reached, the matrix experience continual cure shrinkage. Therefore, the resistance is expected to continue to decrease. A possible explanation is the introduction of residual stresses in the system, the matrix applying stress on the surface of the piezoresistive [23] carbon nanotubes. However, a continued study of this phase of the cure is required.

4. Conclusion

In this paper a novel method enabling following *in-situ* the cure evolution of a glass fiber/epoxy system with non-invasive vertically aligned carbon nanotube forests have been demonstrated. The cure evolution har been divided into clear phases, being characterized by the different physical events occurring during curing. First, the effect of consolidation of prepreg plies is observed by the VACNT forests as their resistance decreases due to more intimate contact between prepreg surfaces. Thereafter, the viscous behavior characterizes the second phase of the curing as the CNTs are dispersed due to viscous flow of the resin as its viscosity decreases. This is verified by a correlating rheological study of the HexPly6376 epoxy matrix used in the system. The transition to the third phase occurs as the viscosity of the matrix reaches its minimum viscosity simultaneously as the crosslinking of the matrix is initiated, which is verified by a correlating DSC study. Therefore, the third phase and its decreasing resistance is characterized by the chemical shrinkage of the matrix. The final phase of the curing is subject to continued work by the authors. Applying this method, quality control of manufactured components and cure cycle optimization for increased production efficiency and energy savings are envisioned. Later, in the cured state, the proposed sensor may be used for structural health monitoring.

  doi:10.5075/epfl-298799_978-2-9701614-0-0

5. References

1. Stark W, Jaunich M, McHugh J. Cure state detection for pre-cured carbon-fibre epoxy prepreg (CFC) using Temperature-Modulated Differential Scanning Calorimetry (TMDSC). Polym Test. 2013;32(7):1261–72.

2. Kiewiet S, Janssens V, Miltner HE, Van Assche G, Van Puyvelde P, Van Mele B. RheoDSC: A hyphenated technique for the simultaneous measurement of calorimetric and rheological evolutions. Rev Sci Instrum. 2008;79(2).

3. Stark W, Jaunich M, McHugh J. Carbon-fibre epoxy prepreg (CFC) curing in an autoclave analogue process controlled by Dynamic Mechanical Analysis (DMA). Polym Test. 2013;32(8):1487–94.

4. Stark W. Investigation of the curing behaviour of carbon fibre epoxy prepreg by Dynamic Mechanical Analysis DMA. Polym Test. 2013;32(2):231–9.

5. Núñez-Regueira L, Gracia-Fernández CA, Gómez-Barreiro S. Use of rheology, dielectric analysis and differential scanning calorimetry for gel time determination of a thermoset. Polymer. 2005;46(16):5979–85.

6. Marin E, Robert L, Triollet S, Ouerdane Y. Liquid Resin Infusion process monitoring with superimposed Fibre Bragg Grating sensor. Polym Test. 2012;31(8):1045–52.

7. Kahali Moghaddam M, Breede A, Chaloupka A, Bödecker A, Habben C, Meyer EM, et al. Design, fabrication and embedding of microscale interdigital sensors for real-time cure monitoring during composite manufacturing. Sensors Actuators, A Phys. 2016;243:123–33.

8. Rein MD, Breuer O, Wagner HD. Sensors and sensitivity: Carbon nanotube buckypaper films as strain sensing devices. Compos Sci Technol. 2011;71(3):373–81.

9. Loyola BR, Zhao Y, Loh KJ, La Saponara V. The electrical response of carbon nanotube-based thin film sensors subjected to mechanical and environmental effects. Smart Mater Struct. 2013;22(2).

10. Kim SY, Jee E, Kim JS, Kim DH. Conformable and ionic textiles using sheath-core carbon nanotube microyarns for highly sensitive and reliable pressure sensors. RSC Adv. 2017;7(38):23820–6.

11. Yoo KP, Lim LT, Min NK, Lee MJ, Lee CJ, Park CW. Novel resistive-type humidity sensor based on multiwall carbon nanotube/polyimide composite films. Sensors Actuators, B Chem. 2010;145(1):120–5.

12. Dai H, Thostenson ET. Scalable and multifunctional carbon nanotube-based textile as distributed sensors for flow and cure monitoring. Carbon. 2020;164:28–41.

13. Wang G, Wang Y, Luo Y, Luo S. Carbon nanomaterials based smart fabrics with selectable characteristics for in-line monitoring of high-performance composites. Materials. 2018;11(9).

14. Gnidakouong JRN, Roh HD, Kim JH, Park Y Bin. In situ process monitoring of hierarchical micro-/nano-composites using percolated carbon nanotube networks. Compos Part A Appl Sci Manuf. 2016;84:281–91.

15. Luo S, Obitayo W, Liu T. SWCNT-thin-film-enabled fiber sensors for lifelong structural health monitoring of polymeric composites - From manufacturing to utilization to failure. Carbon. 2014;76:321–9.

16. Lu S, Zhao C, Zhang L, Chen D, Chen D, Wang X, et al. Real time monitoring of the curing degree and the manufacturing process of fiber reinforced composites with a carbon nanotube buckypaper sensor. RSC Adv. 2018;8(39):22078–85.

17. Lu S, Chen D, Wang X, Shao J, Ma K, Zhang L, et al. Real-time cure behaviour monitoring of polymer composites using a highly flexible and sensitive CNT buckypaper sensor. Compos Sci Technol. 2017;152:181–9.

18. Wardle BBL, Saito DS, García EJ, Hart AJ, DeVilloria RG, Verploegen EA. Fabrication and Characterization of Ultrahigh-Volume- Fraction Aligned Carbon Nanotube – Polymer Composites. Adv. Mater.2008;20:2707–14.

19. Koratkar N, Modi A, Lass E, Ajayan P. Temperature effects on resistance of aligned multiwalled carbon nanotube films. J Nanosci Nanotechnol. 2004;4(7):744–8.

20. Lee J, Stein IY, Devoe ME, Lewis DJ, Lachman N, Kessler SS, et al. Impact of carbon nanotube length on electron transport in aligned carbon nanotube networks. Appl Phys Lett. 2015;106(5).

21. Davies LW, Day RJ, Bond D, Nesbitt A, Ellis J, Gardon E. Effect of cure cycle heat transfer rates on the physical and mechanical properties of an epoxy matrix composite. Compos Sci Technol. 2007;67(9):1892–9.

22. Bauhofer W, Kovacs JZ. A review and analysis of electrical percolation in carbon nanotube polymer composites. Compos Sci Technol. 2009;69(10):1486–98.

23. Tombler TW, Zhou C, Alexseyev L, Kong J, Dai H. Reversible electromechanical characteristics of carbon nanotubes under local-probe manipulation. Nature. 2000;405:769–72.

FULLY-INTEGRATED CARBON NANOTUBE EPOXY FILM SENSORS FOR STRAIN SENSING IN GFRP

Christina Buggisch[a], Nils Felmet[a], Dennis Gibhardt[a], Bodo Fiedler[a]

a: Institute of Polymers and Composites, Hamburg University of Technology, Denickestraße 15, 21073 Hamburg, Germany
christina.buggisch@tuhh.de

Abstract: *Structural health monitoring of fiber-reinforced polymer composites becomes more important to ensure a safe and reliable operation. This work demonstrates a method for local matrix modification of glass fiber-reinforced polymers with fully-integrated pre-cured carbon nanotube epoxy thin-film sensors enabling a piezo-resistive strain and damage monitoring. The film sensors were manufactured using a manual film applicator, partially pre-cured for 48 h under lab conditions, cut to shape, and placed on dry glass fiber fabrics before infusion in a resin transfer molding process. Three-point bending tests with sensor films under the upper ply, in the middle, and over the lower ply prove the sensor films' ability for localized strain monitoring. Furthermore, detection of critical buckling is possible in structural parts, as demonstrated in compression tests of coupon specimens and stringer components.*

Keywords: Structural Health Monitoring; Damage Detection; Multifunctional Composite

1. Introduction

Fiber-reinforced polymer composites exhibit a complex failure behavior due to their multi-scale nature. In-situ damage monitoring during operation, referred to as structural health monitoring (SHM), can significantly enhance safety and reliability. Many advanced SHM methods, e.g., fiber Bragg sensors, electrical measurements, acoustic emission, and wave propagation, have been developed and are part of ongoing research [1]. Most of these methods require skilled personnel or expensive measuring equipment. Therefore, standard surface-mounted strain gauges are still widely used for strain and damage monitoring of composite structures. However, surface-mounted strain gauges are susceptible to external influences, merely monitor small areas, and cannot monitor internal strains.

The intrinsic electrical conductivity of carbon fibers enables self-sensing of strain and damage detection in carbon fiber-reinforced polymers with electrical resistance measurements [2, 3]. Due to a lack of material conductivity, unmodified glass fiber-reinforced polymers (GFRP) do not exhibit such self-sensing behavior. However, a modification of the polymer matrix with conductive nanoparticles such as carbon nanotubes (CNTs) can enable electrical conductivity when the filler content is above the percolation threshold. Load application leads to a resistance change due to a change of the conductive CNT network paths known as piezo-resistive effect. The piezo-resistive strain-sensing ability of GFRPS with a fully nanoparticle-modified polymer matrix was studied by many researchers for different load cases [4, 5].

However, fully modifying the polymer matrix is expensive and does not allow localized damage monitoring. Surface-mounted CNT/polymer sensors have demonstrated promising results on various substrates but experience similar limitations as classic metal strain gauges [6]. Furthermore, different methods for localized integration of CNTs have been proposed, like

  doi:10.5075/epfl-298799_978-2-9701614-0-0

dipping selected dry glass fabrics in aqueous CNT dispersions [7], spray-coating CNTs on dry glass fiber fabrics [8], integrating aligned CNT sheets [9] or buckypapers [10], and applying CNTs using frictional roller sliding [11].
Within this work, fully-integrated pre-cured CNT/epoxy thin-film sensors for piezo-resistive strain and damage monitoring are demonstrated. The flexible film sensors can easily be cut to the desired shapes and integrated in standard industrial infusion processes. Therefore, the proposed method enables a tailored SHM via electrical resistance measurements.

2. Materials and Methods

2.1 Manufacturing of Sensor Films

A homogeneous paste containing the amine-based two-component epoxy system EPIKOTE™ Resin MGS™ RIMR 135 and EPIKURE™ Curing Agent MGS™ RIMH 137 (Hexion Inc., USA) and 0.5 wt.% OCSiAl Tuball™ SWCNT was manufactured using a three-roll mill process further described in [12, 13]. The film sensors with a thickness of 6 mils (152.4 µm) were applied on a polished steel plate covered in Polytetrafluoroethylene (PTFE) foil using a manual film applicator BYK 5358 (BYK-Gardner GmbH, Germany) and partially pre-cured for 48 h under lab conditions.

2.2 Manufacturing of Laminates

The pre-cured films were cut to the desired shapes, removed from the PTFE foil, and placed on dry non-crimp E-glass fiber fabrics UT-E250 and UT-E500 (Gurit Holding AG, Switzerland) before infusion in a vacuum-assisted resin transfer molding process using a closed aluminum mold. The two-component epoxy system used for film manufacturing was also used as infusion resin to achieve a sufficient chemical bonding between the integrated films and the surrounding polymer matrix. The unidirectional (UD) laminates were cured in a heat press at 50 °C for 16 h and post-cured in an oven at 80 °C for 16 h.

2.2 Manufacturing of Coupon Specimens

The specimens were cut to the dimensions specified in Table 1 using an ATM Brillant 265 precision saw (ATM Qness GmbH, Germany). The compression specimens were equipped with 1 mm-thick GFRP loading tabs before cutting. Therefore, the gripping areas and loading tabs were ground using 600 grit sanding paper and cleaned with isopropanol. The two-component epoxy paste adhesive UHU Endfest 300 (UHU GmbH & Co. KG, Germany) was used to bond the loading tabs to the specimens. The adhesive was cured for 60 min at 60 °C using a heat press. For electrical contacting, LiFy copper cables with a cross-section of 0.25 mm² were attached to the specimen edges using Acheson 1415 conductive silver paint (PLANO GmbH, Germany). Figure 1 shows the specimen configurations, including sensor film and contacting positions.

Table 1: Lay-up and film positions of unidirectional coupon specimens.

Specimen type	Size	Film Position
Bending	100x15x2 mm³	Under top ply, Middle, Above bottom ply
Compression	130x10x4 mm³	Middle

  doi:10.5075/epfl-298799_978-2-9701614-0-0

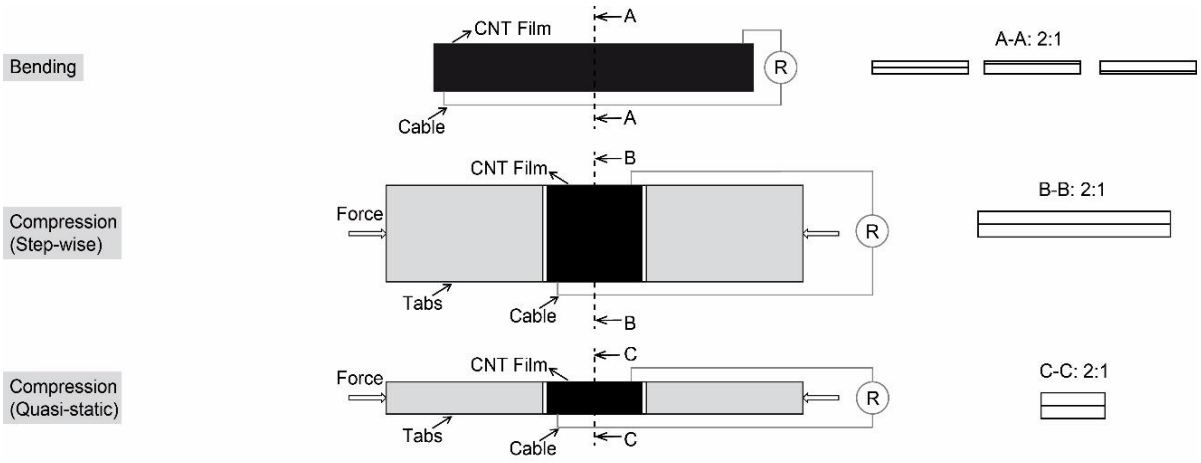

Figure 1. Schematics of coupon specimens including film and contacting positions

2.3 Manufacturing of Stringers

Stringers were manufactured in a vacuum-assisted infusion process on an open aluminum mold using a vacuum bag setup. The stringers had a $[\pm 45/0_3]_s$ lay-up consisting of bidiagonal ±45° glass fiber fabrics B320E-H (HP-Textiles GmbH, Germany) and UD UT-E250 (Gurit Holding AG, Switzerland) non-crimp glass fiber fabrics. The film sensors were integrated under the top ±45°-layer. The infusion resin was the same two-component epoxy system also used for film and laminate production. Curing was performed at room temperature for 48 h and post-curing took place in an oven at 80 °C for 16 h. The backing plate was manufactured as described in Section 2.2 using UT-E250 (Gurit Holding AG, Switzerland) fabrics and a $[0_2/90/0_2]_s$ lay-up. Stringer and backing plate were cut to a size of 245 x 127 mm² and adhesively bonded using the two-component epoxy paste adhesive UHU Endfest 300 (UHU GmbH & Co. KG, Germany) following the process described in Section 2.2. Curing of the adhesive was performed for 1 h at 60 °C in an oven. Afterward, both stringer ends were cast 30 mm deep in epoxy resin as load introduction elements. Furthermore, the backing plate was spray-painted with a random speckle pattern for digital image (DIC) correlation measurements. The electrical contacting was carried out in the same way as for the coupon samples. The positions of the film sensors and the electrical contacting are shown in Figure 4.

2.4 Test Setup

Force-controlled step-wise and quasi-static tests until final failure were conducted for three-point bending (TPB) and compression coupon tests. The TPB tests were performed on a Z10 universal testing machine (ZwickRoell GmbH & Co. KG, Germany) according to DIN EN ISO 14125 [14]. The support distance was 60 mm, the upper roller diameter 15 mm, and the lower roller diameters were chosen as 10 mm. The test speed was 2 mm min^{-1}. Compression tests on coupon specimens and the crippling test on the stringer were conducted on a Z400 universal testing machine (ZwickRoell GmbH & Co. KG, Germany). Compression tests were performed in shear mode following ASTM D3410 [15] using a hydraulic combined loading fixture. Crippling tests of the stringers were performed with a constant speed of 0.25 mm min^{-1}. An ARAMIS 4M DIC system was used to monitor the deformations and buckling of the stringers. The in-situ electrical resistance was measured during all tests using a Keithley 2601A (one film sensor – coupon specimens) or a Keithley 2602 (two film sensors – stringers). Therefore, a constant voltage of 1 V was applied and the current was measured.

  doi:10.5075/epfl-298799_978-2-9701614-0-0

3. Results and Discussion

3.1 Three-Point Bending Tests

Figure 2 shows representative results of step-wise TPB tests on UD specimens with CNT sensor films under the upper ply, in the middle of the laminate, and over the lower ply, including stress and resistance changes over time. The resistance change ΔR in % is calculated according to Equation (1)

$$\Delta R = \frac{R-R_0}{R_0} 100\,, \tag{1}$$

with initial resistance R_0 and current resistance R. In general, all three configurations show a different resistance change behavior. The resistance changes result from the piezo-resistive behavior of the CNT epoxy film sensors and the variation of the CNT network as a consequence of the loading.

Due to their placement above the neutral axis, the sensor films under the upper ply experience compressive stress resulting in an anti-proportional and negative resistance change which is fully reversible for small loads and increasingly irreversible with higher loads. The compressive strain leads to a formation of new conductive paths or a reduction of the tunneling resistance as CNTs are moved closer together [16, 17]. The irreversibility is caused by irreversible network changes inside the CNT film sensors, e.g., due to the indentation at the rollers.

Film sensors integrated in the middle of the laminate show a small and mixed positive and negative resistance change. As in theory only shear and no volume change is expected in the neutral axis during bending, the influence of the loading on the CNT network and the resistance change should be minimal for film sensors in the middle of the laminate. The measured resistance change is significantly smaller than in film sensors under the upper or above the lower ply. The small and mixed positive and negative resistance changes can be explained by deviations of the films with respect to the neutral axis due to, e.g., the films' thickness and manufacturing-related waviness.

Placing the film sensors over the lowest ply induces tensile stresses in the film that result in a positive resistance change proportional to the applied stress. Conductive paths inside the film sensors dissolve under tensile load as CNTs are pulled further apart or lose contact. The resistance change is fully reversible during the first three load steps. Afterward, the resistance drops below the initial resistance when fully unloading the samples, indicating more conductive paths or closer CNTs inside the sensors.

TPB tests generally reveal the sensor film's ability to detect local stresses inside the GFRP and monitor the applied stresses. Due to the piezo-resistive effect, monitoring the stress or strain inside the material is possible by measuring the resistance change. A threshold value of the resistance change can be specified to ensure a safe and reliable operation of the respective GFRP part. A more detailed analysis, including the sensor films' influence on the mechanical properties and the sensing results of bending and tensile tests of UD and cross-ply specimens, can be found in [13].

  doi:10.5075/epfl-298799_978-2-9701614-0-0

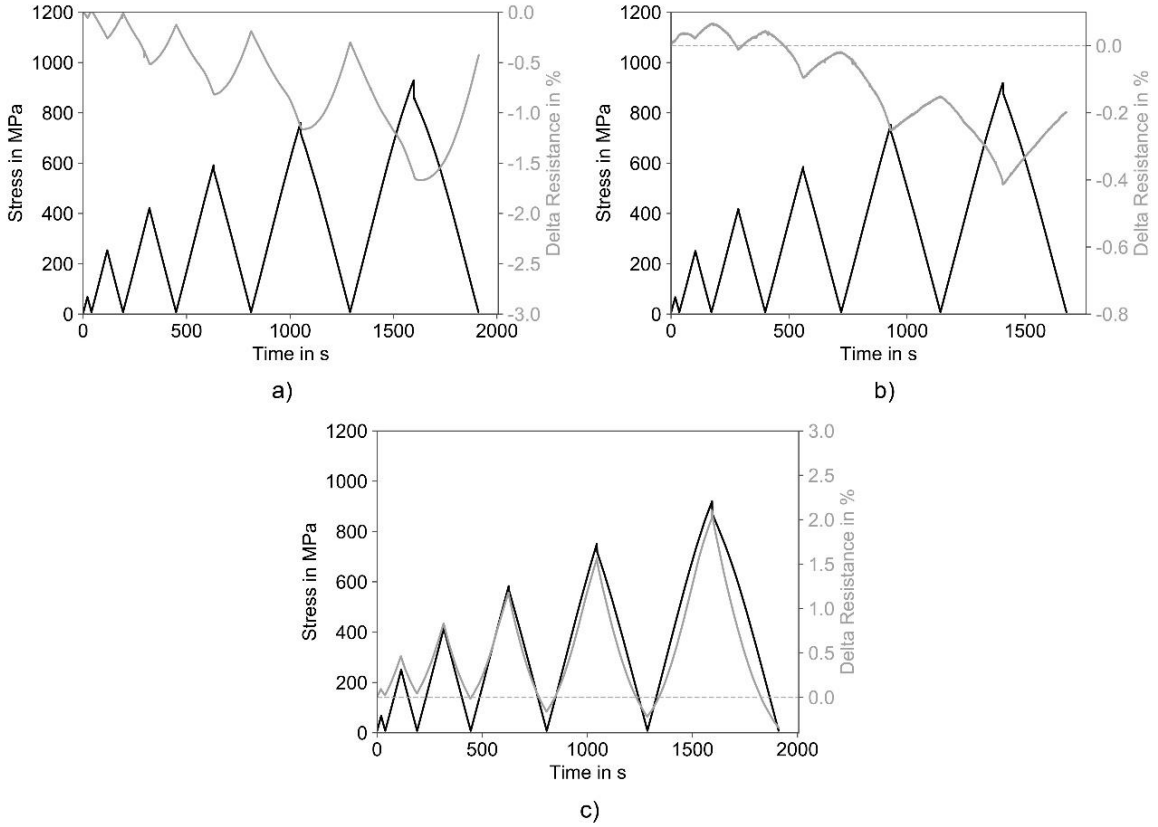

Figure 2. Representative results of quasi-static bending tests on UD specimens - a) Sensor film under the upper ply, b) Sensor film in the middle, c) Sensor film over the lower ply

3.2 Compression Tests

Representative results of step-wise and quasi-static compression tests until failure on UD coupon specimens are shown in Figure 3.

Following the findings of the bending tests and the piezo-resistive behavior, a stress anti-proportional resistance change is expected during compression tests. The step-wise tests (compare Figure 3 a)) show the expected anti-proportional agreement of the resistance change with the applied stress and a fully reversible resistance change during unloading, which implies no irreversible changes in the CNT network due to damages. No buckling or damaging of the specimens was observed in the step-wise tests.

To ensure failure in the shear loading setup, the specimens loaded until final failure were less wide (compare Table 1) and experienced visible buckling. As visible in the representative results in Figure 3 b), the measured resistance change is anti-proportional with the applied stress in the beginning but starts to increase after approximately 10 s. This increasing resistance change correlates with a slight slope change in the stress-time curve and with visible buckling of the specimens during the tests. As a result of the buckling, the sensor films no longer encounter a pure compressive load. Instead, the buckling introduces a bending of the integrated sensor films, which explains the resistance increase.

Consequently, buckling during compression tests can reliably be detected by an unexpected resistance increase without an associated load decrease.

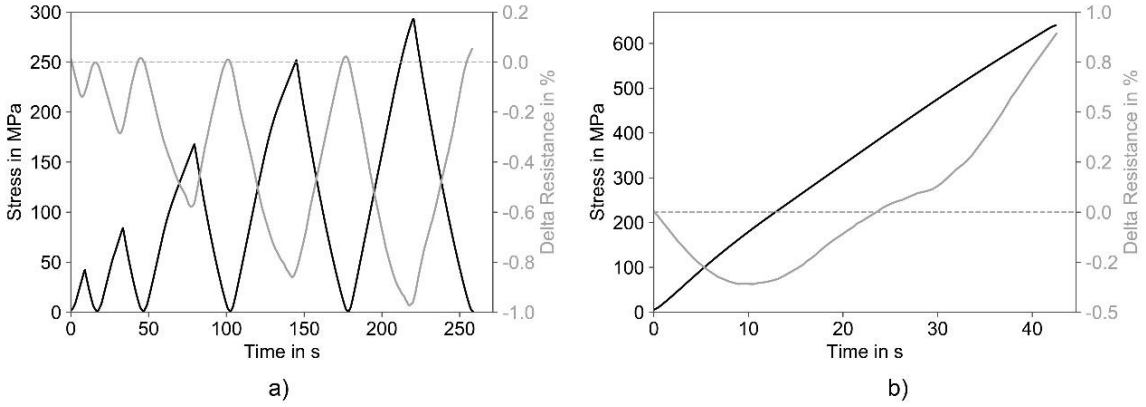

Figure 3. Representative results of quasi-static compression tests on UD specimens - a) Step-wise test, b) Until final failure.

3.3 Crippling Tests

Crippling tests on stringers were conducted to evaluate the sensor films' behavior in larger components. The results of a representative compression test on a stringer are shown in Figure 4, including force, resistance change, and corresponding DIC images. The DIC images show the z-displacement of the backing plate of the stringer.

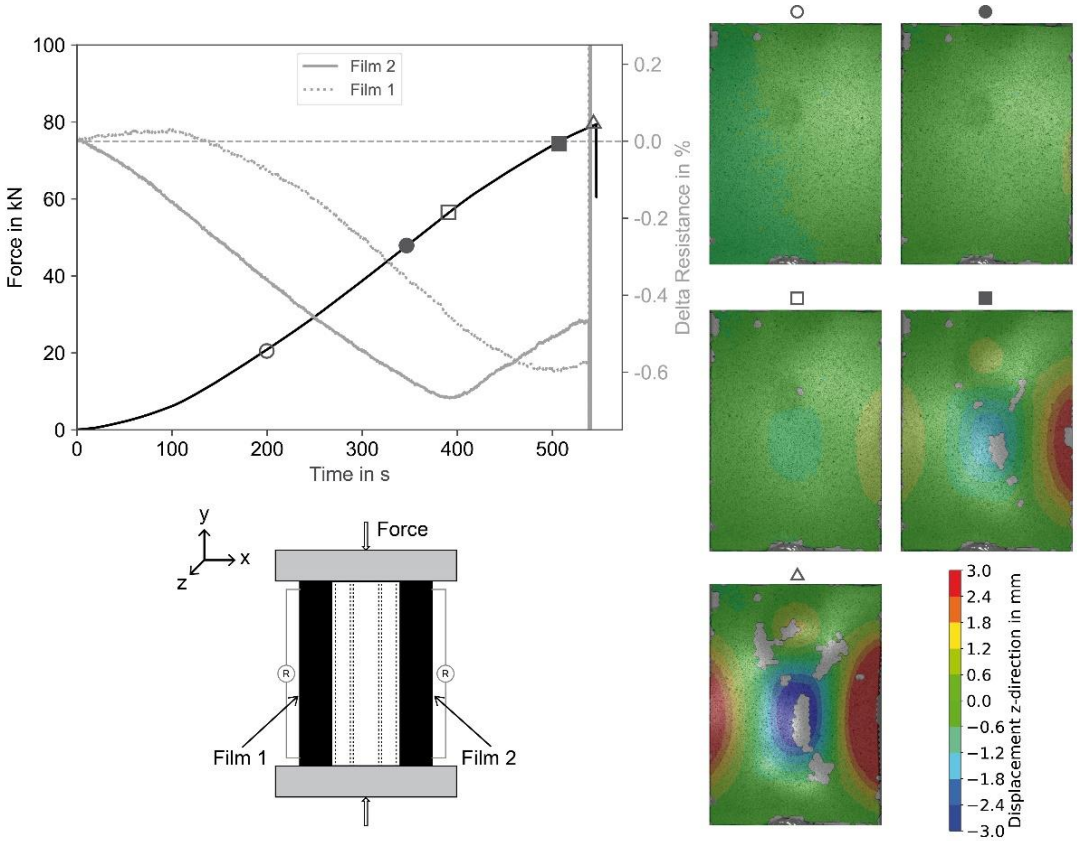

Figure 4. Results of crippling test on stringer component with two fully-integrated CNT/epoxy film sensors including force, resistance change, and digital image correlation images with displacement in z-direction.

At the beginning of the test, film sensor 2 shows a resistance change that is anti-proportional with the applied load and the DIC images reveal no buckling. From 400 s onwards, the resistance change starts to increase. At this time, the according DIC image reveals a significant z-displacement in the area of film 2 visible as a yellow area. The stringer starts to buckle. Until final failure, the buckling becomes more and more severe as visible by the growing z-displacement and the resistance change is increasing further.

The resistance change measured in film sensor 1 shows delayed behavior. Up to approximately 150 s, almost no resistance change is visible. After that, the resistance starts to decrease with a similar slope as observed for film sensor 2. The whole remaining course of the resistance change, including the resistance increase in film sensor 1, is measured with a time delay. The DIC images also reveal a delayed buckling in the area of film sensor 1. While no z-displacement is visible in the area of film sensor 1 at 400 s, film sensor 2 already displays a significant z-displacement. The time shift can be explained by a non-uniform load introduction.

The results prove the sensor films' ability to detect undesired critical buckling during compressive loading in coupon specimens and bigger components like the presented stringer.

4. Conclusion

The presented fully-integrated pre-cured CNT epoxy film sensors allow for piezo-resistive strain and damage monitoring of GFRPs. A reproducible piezo-resistive correlation between strain and resistance change is possible. Tensile stresses result in a strain-proportional resistance increase and compressive stresses in a resistance decrease which is anti-proportional to the applied stress.
Integration in different layers in TPB tests showed the potential for localized strain state evaluation inside the material.
Furthermore, the results of compression tests on coupon samples and crippling tests on stringers proved the reliable detection of critical buckling by a resistance increase during compressive loading.
In general, the thin-film sensors allow for tailored strain and damage monitoring of GFRP by offering large design freedom, including measurements at different material depths, over large sections, or in highly loaded areas. The flexible, pre-cured sensor films can easily be handled, cut to the desired shapes, placed on dry glass fiber fabrics, and thus be used in standard (industrial) vacuum infusion processes. Furthermore, the introduction of these fully integrated thin-film sensors does not lead to any strength reduction.

Acknowledgments

This research was funded by the German Research Foundation (DFG) within the project number 393868053.

5. References

1. Diamanti K, Soutis C. Structural health monitoring techniques for aircraft composite structures. Progress in Aerospace Sciences. 2010; 46:342–352.
doi: 10.1016/j.paerosci.2010.05.001.
2. Schulte K, Baron C. Load and failure analyses of CFRP laminates by means of electrical resistivity measurements. Composites Science and Technology. 1989; 36:63–76.
doi: 10.1016/0266-3538(89)90016-X.

3. Abry JC, Choi YK, Chateauminois A, Dalloz B, Giraud G, Salvia M. In-situ monitoring of damage in CFRP laminates by means of AC and DC measurements. Composites Science and Technology. 2001; 61:855–864. doi: 10.1016/S0266-3538(00)00181-0.
4. Thostenson ET, Chou T-W. Carbon Nanotube Networks: Sensing of Distributed Strain and Damage for Life Prediction and Self Healing. Adv. Mater. 2006; 18:2837–2841. doi: 10.1002/adma.200600977.
5. Böger L, Wichmann MHG, Meyer LO, Schulte K. Load and health monitoring in glass fibre reinforced composites with an electrically conductive nanocomposite epoxy matrix. Composites Science and Technology. 2008; 68:1886–1894. doi: 10.1016/j.compscitech.2008.01.001.
6. Kang I, Schulz MJ, Kim JH, Shanov V, Shi D. A carbon nanotube strain sensor for structural health monitoring. Smart Materials and Structures. 2006; 15:737–748. doi: 10.1088/0964-1726/15/3/009.
7. Gao S-L, Zhuang R-C, Zhang J, Liu J-W, Mäder E. Glass Fibers with Carbon Nanotube Networks as Multifunctional Sensors. Adv. Funct. Mater. 2010; 20:1885–1893. doi: 10.1002/adfm.201000283.
8. Rodríguez-González JA, Rubio-González C, Soto-Cajiga JA. Piezoresistive Response of Spray-coated Multiwalled Carbon Nanotube/Glass Fiber/Epoxy Composites under Flexural Loading. Fibers Polym. 2019; 20:1673–1683. doi: 10.1007/s12221-019-8711-8.
9. Aly K, Li A, Bradford PD. Strain sensing in composites using aligned carbon nanotube sheets embedded in the interlaminar region. Composites Part A: Applied Science and Manufacturing. 2016; 90:536–548. doi: 10.1016/j.compositesa.2016.08.003.
10. Slobodian P, Lloret Pertegás S, Riha P, Matyas J, Olejnik R, Schledjewski R, Kovar M. Glass fiber/epoxy composites with integrated layer of carbon nanotubes for deformation detection. Composites Science and Technology. 2018; 156:61–69. doi: 10.1016/j.compscitech.2017.12.012.
11. Kravchenko OG, Pedrazzoli D, Bonab VS, Manas-Zloczower I. Conductive interlaminar interfaces for structural health monitoring in composite laminates under fatigue loading. Materials & Design. 2018; 160:1217–1225. doi: 10.1016/j.matdes.2018.10.045.
12. Meeuw H, Wisniewski VK, Köpke U, Nia AS, Vázquez AR, Lohe MR, Feng X, Fiedler B. In-line monitoring of carbon nanoparticle epoxy dispersion processes. Prod. Eng. Res. Devel. 2019; 13:373–390. doi: 10.1007/s11740-019-00884-5.
13. Buggisch C, Gibhardt D, Felmet N, Tetzner Y, Fiedler B. Strain sensing in GFRP via fully integrated carbon nanotube epoxy film sensors. Composites Part C: Open Access. 2021; 6:100191. doi: 10.1016/j.jcomc.2021.100191.
14. DIN EN ISO 14125. Fibre-reinforced plastic composites - Determination of flexural properties; 2011.
15. ASTM D3410. Standard Test Method for Compressive Properties of Polymer Matrix Composite Materials with Unsupported Gage Section by Shear Loading. West Conshohocken, PA: ASTM International.
16. Hu N, Karube Y, Yan C, Masuda Z, Fukunaga H. Tunneling effect in a polymer/carbon nanotube nanocomposite strain sensor. Acta Materialia. 2008; 56:2929–2936. doi: 10.1016/j.actamat.2008.02.030.
17. Wichmann MHG, Buschhorn ST, Gehrmann J, Schulte K. Piezoresistive response of epoxy composites with carbon nanoparticles under tensile load. Phys. Rev. B. 2009; 80:667. doi: 10.1103/PhysRevB.80.245437.

FBG SENSORS FOR PROCESS AND STRUCTURAL HEALTH MONITORING OF A SMALL TYPE III COMPOSITE OVERWRAPPED PRESSURE VESSEL FOR UNMANNED AERIAL VEHICLE

Helena, Rocha[a,b], Paulo, Antunes[b], Ugo, Lafont[c], João P., Nunes[a]

a: Institute for Polymers and Composites, University of Minho, Guimarães, Portugal
b: PIEP – Innovation in Polymer Engineering, Guimarães, Portugal – paulo.antunes@piep.pt
c: European Space Agency, Noordwijk, The Netherlands

Abstract: *In this work, fibre Bragg grating (FBG) sensors were embedded in a 1-litre type III composite overwrapped pressure vessel (COPV) for an unmanned aerial vehicle (UAV), during its manufacturing for process and structural health monitoring (SHM). A single optical fibre having eight FBG sensors was fixed around an aluminium liner to form a grid network. The carbon fibre/epoxy composite layers were wound on top of it with a winding machine. The FBG sensors were able to follow the developed strain during winding, making it an important quality control tool. The same sensors were used to monitor impact tests, where the distances between real and predicted locations varied between 17 and 56 mm.*

Keywords: *Composite Overwrapped Pressure Vessel;* Filament Winding; *Fibre Bragg Grating Sensor; Impact Damage; Structural Health Monitoring*

1. Introduction

Alternatives to fossil fuels are being explored, especially, for the transportation sector, aiming to restrain global warming [1]. Hydrogen-powered fuel cell systems are regarded as one viable energy alternative solution [2]. Particularly, when compared to electrical batteries, Unmanned Aerial Vehicles (UAV) may benefit from it for longer flight times and autonomy, with short charging time, keeping downtime to a minimum [1]. The implementation of fuel cell systems usually utilizes Composite Overwrapped Pressure Vessels (COPV) for hydrogen storage. COPV are the most weight efficient solution among pressure vessels, where a fibre reinforced polymer composite overwrap is wound around a liner [3].

COPV may face some reliability issues due to the loading scheme complexity, the assortment of commercial construction solutions and material degradation. Yet, traditional non-destructive testing may fail to timely detect critical defects that may occur in between periodic inspections. Differently, COPV instrumentation and application of Structural Health Monitoring (SHM) systems offers added safety, as continuous data acquisition enables the real-time detection of critical defects. Hence, immediate repair, operation status downgrade or deactivation of the COPV can be instructed to prevent catastrophic bursting. Additionally, COPVs are also susceptible to low velocity impacts (LVI), causing barely visible impact damage (BVID). BVID can result in stiffness deterioration, which may reduce the lifetime of the COPV [4].

A small type III COPV was designed resorting to FEA and experimental burst testing was used for validation. The integration of FBG sensors in the COPV was demonstrated for winding process monitoring and further impact testing monitoring of the produced COPV.

  doi:10.5075/epfl-298799_978-2-9701614-0-0

2. Experimental Techniques

2.1 Design and Production of Smart COPV

A small COPV consisting of a 6061-T6 aluminium liner and a carbon fibre/epoxy composite overwrap was developed to withstand a nominal storage pressure of 350 bar. The COPV has a 1 litre volume capacity and internal diameter of approximately 75 mm. The layup configuration of the composite overwrap was optimized via FEA, using Abaqus 2020 software, with the burst testing being simulated. The COPV was modelled to have a burst pressure that is 3 times that of the nominal storage pressure (1050 bar). CADWIND software was used to find adequate winding patterns for the mentioned liner, which were used in the FEA model. This was an iterative process between the layup configuration (winding angles and number of layers) and the resultant modelled burst pressure. The Hashin failure criteria was used to identify damage initiation in the composite overwrap. The optimized configuration was found to be $[90_3/\pm15_2/90_3]$. Burst pressure tests were performed on three COPVs, according to the EN12245 European standard, to validate the FEA model. The obtained burst pressure was 1061 ± 26 bar.

An optical fibre with a FBG sensor array was fixed in the aluminium liner with X120 epoxy adhesive from HBM and left to cure at room temperature. Each optic fibre had 8 FBG sensors, with central wavelengths ranging from approximately 1535 to 1564 nm, each separated by about 4 nm. The optic fibres were polyimide coated with a diameter of 150 µm and having FC/APC connectors. The optic fibres were supplied by HBK FiberSensing, Portugal. The optic fibre was wound around the central cylindrical region of the liner. The OF at the FBG position was fixed at 90° to be aligned with the carbon fibres in the first circumferential layer, while the OF in between FBG sensor was wound at lower angles to decrease the length of the OF. The FBG sensors were distanced in a way that they were positioned in 3 lines along the longitudinal axis of the liner, equally separated by an angle of 120°, where each following sensor was placed in the next line, separated by 26 mm in the longitudinal direction of the liner from the previously fixed sensor, forming an equally distributed network grid (see figure 1).

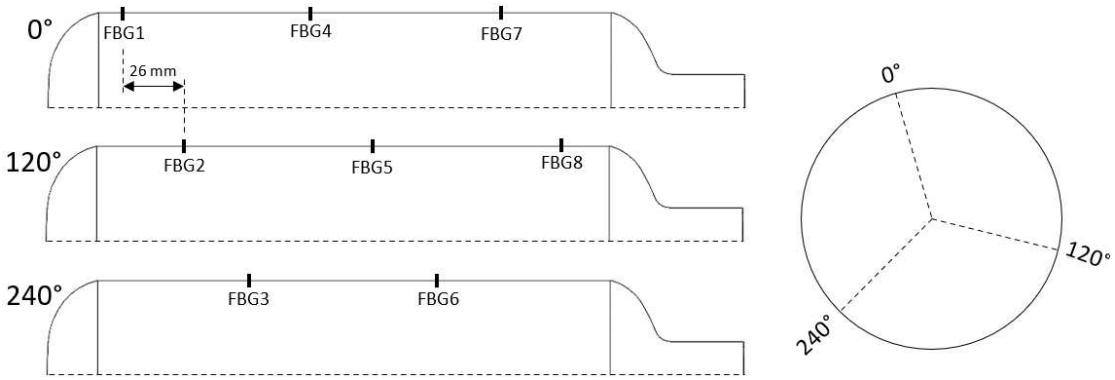

Figure 1: Schematic representation of FBG sensors on the liner surface

Winding process monitoring can be a valuable tool for quality control. The winding pre-tension plays an important role on the stiffness of the composite overwrap; lower winding pre-tension may not allow to use the full potential of tensile strength of the carbon fibres, while excessive pre-tension may cause fibre damage. A 150 mm long screw was adhesively bonded to the closed dome of the liner to attach the optic fibre interrogator and monitor the winding process (see figure 2(a)). The interrogator system, from Ibsen Photonics, comprised the DL-BP1 1501A super-

luminescent LED source and I-MON 256 USB High Speed interrogation monitor. The system has a wavelength fit resolution of 0.5 pm and acquired the FBG data during winding at a sampling rate of 50 Hz.

A filament winding machine, manufactured by Gislotica, Portugal, was used to produce the COPV. The filament winding machine has six axes of movement: three linear moving axes and two rotating axes of the carriage, and a rotating spindle, where the liner is fixed. Part program files were also generated by CADWIND software for each pattern (circumferential, helical and angle combinations) and fed to the winding machine. The prepreg tape was wound over the optic fibre on the liner surface to produce the composite overwrap. A 6 mm wide prepreg tape made of Tenax®-E ITS50 carbon fibre, from Teijin, and RCX0125 epoxy, from RED Composites, was used. After winding, the COPVs were cured with an initial holding stage at 90 °C for 60 min and a last holding stage at 150 °C for 90 min, as per suggestion of the resin manufacturer. An example of a produced COPV, with embedded FBG sensors, is shown in figure 2(b).

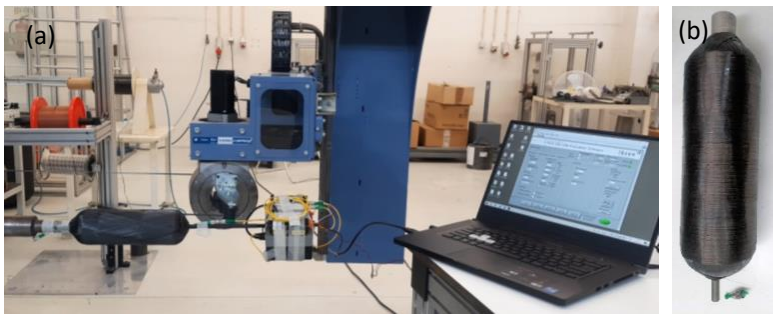

Figure 2: Production of the COPV by tape winding

2.4 Impact Testing and Localization

Drop-weight impact tests were performed on the Fractovis Plus impact testing equipment from CEAST. The impactor had a hemispheric shape with a 20 mm diameter and a mass of 5.045 Kg. Each COPV was impacted at 4 locations. The low velocity impacts were performed with the impactor head at an initial vertical distance of 305 mm and velocity of 2.446 m/s, to produce an impact energy of 15 J. The optical fibre data acquisition during impacts was taken at a sampling rate between 550 and 800 Hz, depending on the exposure time used in the interrogation system. The setup used for impact testing can be seen in figure 3.

Figure 3: Drop-weight impact testing setup with optical interrogation system

A simple residual strain amplitude method, similar to the one reported by Hiche et al. [5], was used to predict damage location on the circumferential section of the COPV. This method is based on the assumption that FBG sensors closer to the impact sight measure higher residual strain.

The residual strain values on each sensor, after impact, were normalized to calculate the strain ratio, r_{ij}, between each pair of sensors, according to Eq. 1.

$$r_{ij} = \frac{\bar{\varepsilon}_j}{\bar{\varepsilon}_j + \bar{\varepsilon}_i} \quad (1)$$

being $\bar{\varepsilon}_j$ and $\bar{\varepsilon}_i$ the normalized absolute maximum strain obtained from FBG_i and FBG_j sensors, respectively.

For the detection of each impact, only the four sensor pairs with highest strain magnitude, M_{ij}, were used (Eq. 2).

$$M_{ij} = \bar{\varepsilon}_j + \bar{\varepsilon}_i \quad (2)$$

The FBG sensors coordinates (ρ, ϕ, z) were initially inputted using cylindrical coordinate system. The linear surface distance between each of the selected sensor pairs, d_{ij}, was calculated following Eq. 3.

$$d_{ij} = \sqrt{\left(z_j - z_i\right)^2 + \left(\left(\Phi_j - \Phi_i\right)\left(\frac{\pi\rho}{180}\right)\right)^2} \quad (3)$$

The relative distance between FBG_i of the FBG_i/FBG_j sensors pair and the expected impact location, I_d, was calculated according to Eq. 4.

$$I_d = r_{ij} \times d_{ij} \quad (4)$$

The cartesian coordinates of the relative impact locations ($(I_{ij})_x$, $(I_{ij})_y$) were recorded, using the nearest FBG sensor as origin of the coordinate axes, considering the 2D flat projection of the cylinder region (as in figure 1(b)). The cartesian coordinates of the predicted impact location, ($I(p)_x$, $I(p)_y$), is finally obtained from the average of the relative impact positions of the four FBG sensor pairs previously selected, as given by Eq. (5).

$$\left[I(p)_x, I(p)_y\right] = \left[\frac{\sum_{k=1}^{4}\left(I_{ij}^k\right)_x}{4}, \frac{\sum_{k=1}^{4}\left(I_{ij}^k\right)_y}{4}\right] \quad (5)$$

3. Results and Discussion

3.1 Winding Process Monitoring

Figure 6 shows the strain variation measured by FBG4 during winding process. Up to approximately 10 minutes there are three main strain decreasing steps corresponding to the three wound internal circumferential layers. When the carbon fibres cover the FBG sensor, there is a sudden decrease of strain, followed by a strain plateau during the remaining time of layer winding, until the FBG is compressed again in the next wounded layer. The winding of the helical layers does not impose further compression on the FBG sensor (time between approximately 10 and 50 min), and instead there is a slight increase of strain during these steps. Next, three

  doi:10.5075/epfl-298799_978-2-9701614-0-0

sudden strain decreasing steps are also observable during winding of the external layers. At the moment that the carbon fibre covers the FBG the steep decrease of strain occurs, but it quickly recovers to a strain value similar to the one after winding of the helical layers, approximately -90 με. By the end of the winding process the FBG shows a strain of approximately -100 με. All the FBG sensors showed a very similar behaviour.

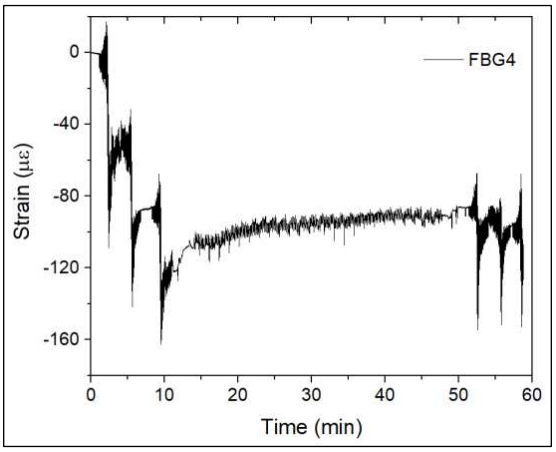

Figure 6: Strain change measured by FBG4 during COPV winding process

3.2 Impact Detection and Localization

The strain amplitude method explained in section 2.4 was used to locate impact events, based in the residual strain after impact. Figure 7 shows the location of the FBG sensors, “real” impact locations, predicted impact locations based on the residual strain between pairs of FBG sensors and averagely predicted impact location. Distances as small as 17 mm and up to 56 mm (Table 1) were measured between the predicted impact locations and the “real” impact locations. This proved to be a simple and inexpensive method to closely find the impact location. It should be mentioned that differences between the “real” and the predicted impact location may arise due to the misidentification of the FBG sensors location in the COPV after winding. The FBGs are fixed in the liner surface and a plastic jig mask is used to mark their position. However, after winding, as the diameter of the COPV increased comparatively to the liner diameter, an exact identification of the FBG sensors is not possible. After production of the COPV, only one of the three longitudinal lines with three sensors is marked on the surface of the COPV using the plastic jig mask, while the remaining sensor locations are identified by reference measurements on the COPV surface considering the 120° angle between each longitudinal line and the 26 mm longitudinal distance between consecutive sensors.

  doi:10.5075/epfl-298799_978-2-9701614-0-0

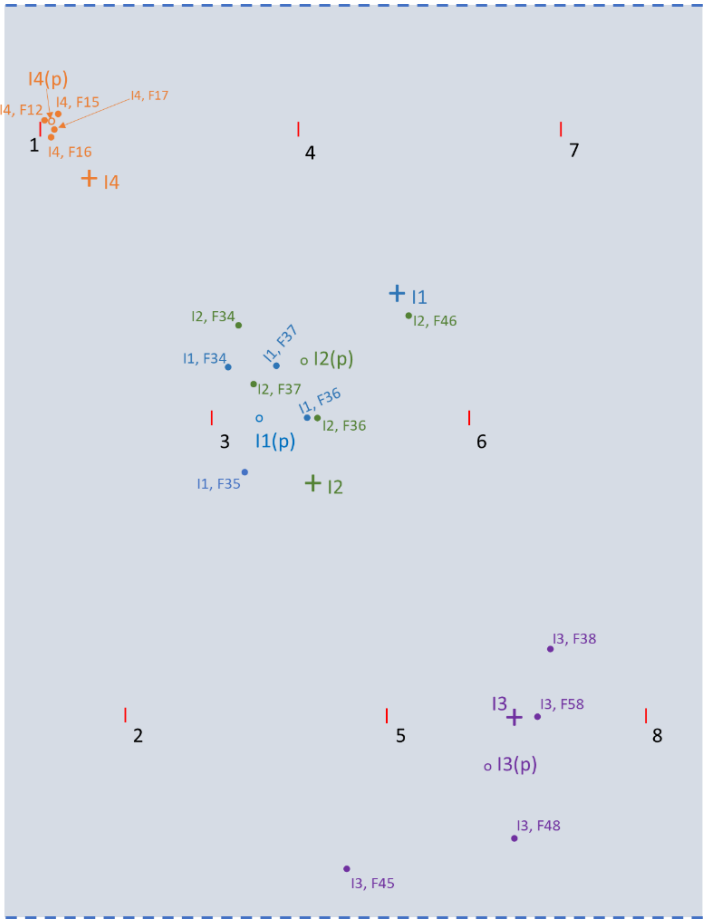

Impact	Real – Predicted distance (mm)
1	56
2	36
3	17
4	21

+ In - Impact location of impact number n

o In(p) - Average Impact location prediction

• In, F_{ij} - Impact location prediction between FBG sensors pair F_{ij}

Figure 7: Real and predicted Impact locations on the flat projection of the COPV cylindric region

4 Conclusions

An FBG sensor grid, consisting of 8 FBG sensors, was integrated in a small type III COPV for winding process monitoring and LVI detection and localization. The optical fibre with FBG sensors was wound around the cylindrical region of the liner to distribute the FBG sensors over this surface area. The FBG data clearly allows to identify the winding step of each layer. The winding of the inner circumferential layers produced a compression strain of about 130 με, while the strain slightly increases during winding of the helical layers. Further compressive strains are visible when winding the outer circumferential layers, where a final compressive strain of approximately 100 με is measured. The integration of the FBG sensors array in the liner is a valuable strategy to monitor the full production process, serving as a quality control tool.

After production completion of the COPV, the same FBG sensors were used to monitor LVI. A strain-amplitude based method was used to locate impact damage in between FBG sensor pairs. The used method was able to localize damage, with distances between the “real” impact location and the predicted impact location varying between 17 and 56 mm. These are short distances that would quickly enable the localization of the impact in a real life structure and to take preventive measures.

  doi:10.5075/epfl-298799_978-2-9701614-0-0

Acknowledgements

Helena Rocha would like to acknowledge the support of European Space Agency [Network/Partnering Initiative Program - ESA Contract 4000123315] and the ACE project founded by the European Union's Portugal 2020 founding program.

5 References

1. Pollet BG, Kocha SS, Staffell I. Current status of automotive fuel cells for sustainable transport. Curr Opin Electrochem. 2019;16:90–5.
2. Menon NC, Kruizenga AM, Alvine KJ, Marchi CS, Nissen A, Brooks K. Behaviour of Polymers in High Pressure Environments as Applicable to the Hydrogen Infrastructure. In: Proceedings of the ASME 2016 Pressure Vessels and Piping Conference. Vancouver; 2016. p. 1–14.
3. Abdalla AM, Hossain S, Nisfindy OB, Azad AT, Dawood M, Azad AK. Hydrogen production, storage, transportation and key challenges with applications: A review. Energy Convers Manag. 2018;165(April):602–27.
4. Weerts RAJ, Cousigné O, Kunze K, Geers MGD, Remmers JJC. A methodological approach to model composite overwrapped pressure vessels under impact conditions. Compos Struct [Internet]. 2021;276(December 2020):114482. Available from: https://doi.org/10.1016/j.compstruct.2021.114482
5. Hiche C, Coelho CK, Chattopadhyay A. A strain amplitude-based algorithm for impact localization on composite laminates. J Intell Mater Syst Struct. 2011;22(17):2061–7.

  doi:10.5075/epfl-298799_978-2-9701614-0-0

3D PRINTED POLYMER NANOCOMPOSITES ENGINEERED WITH GRAPHENE AND METALLIC NANOPARTICLES FOR OPTICAL DETECTION OF WATER POLLUTANTS

Sara Fateixa,[a] Johannes Schneider,[b] S. Kumar,[b] Robert Böhm[c]

a: Department of Chemistry – CICECO Aveiro Institute of Materials, University of Aveiro, 3810-193, Aveiro, Portugal.
b: James Watt School of Engineering, University of Glasgow, Glasgow, G12 8LT, UK
c: HTWK Leipzig, Faculty of Engineering, PF 30 11 66, 04251 Leipzig, Germany

Abstract: *The development of novel low-cost materials capable of exhibiting high performance, sensitivity and reproducibility are highly desirable for environmental quality monitoring of emerging chemical pollutants (ECPs). Their presence in water can be harmful and have unpredictable consequences for the environment and human health. Therefore, monitoring such ECPs is critical to improving water quality and preventing the increased incidence of several diseases. Here, we explore the performance of 3D printed polymer nanocomposites comprising graphene and gold nanoparticles (AuNPs) to detect ECPs in water using surface-enhanced Raman scattering (SERS). Fused filament fabrication additive manufacturing will fabricate samples using nanoengineered filaments comprising graphene and AuNPs. Nanoengineered filaments are prepared by melt blending using a twin-screw extruder. The composites' capability to detect the ECPs is evaluated using conventional and portable Raman instruments. Imaging techniques, namely confocal Raman microscopy, are used to optimize the Raman signal of the ECPs on the substrates.*

Keywords: 3D printed polymer nanocomposites; graphene; SERS; emerging pollutants.

1. Introduction

Emerging chemical pollutants (ECPs), also known as contaminants of emerging concern (CECs), are considered a severe problem worldwide. ECPs such as hormones, pharmaceuticals, pesticides and persistent organic pollutants are defined as new chemical compounds for which no regulation and monitoring protocols have been established yet. However, they can harm human health and the environment due to their persistence, resist biodegradation and bioaccumulation.[1,2] For example, antibiotics pose a significant concern because, even in vestigial amounts, they can cause health problems and contribute to antimicrobial resistance.[3,4] Typical analytical techniques such as high-performance liquid chromatography, capillary electrophoresis and liquid/gas chromatography-mass spectrometry have been used to detect vestigial amounts of ECPs.[5-7] However, these methods are time-consuming, cost-intensive and comprise complex laboratorial procedures. Therefore, novel technologies with high sensitivity, simple operations, in situ samplings, and portability are needed for detecting such environmental pollutants.

In this context, surface-enhanced Raman scattering (SERS) emerges as a promising method to monitor ECPs because it affords high sensitivity, spectroscopic fingerprints, easy sample preparation, and non-destructive analyses.[8-10] SERS is a vibrational spectroscopic technique for detecting molecules adsorbed on metal surfaces, typically Ag and Au.[11,12] Great progress was made to assemble such metals into nanostructures that act as stable, reproducible and

  doi:10.5075/epfl-298799_978-2-9701614-0-0

active SERS substrates to detect trace levels of molecules of interest.[13,14] These strategies envisage metal surfaces where an enhanced local electromagnetic field (hotspots) is observed. Hotspots have been proposed to occur in nanojunctions between closely spaced metallic nanoparticles (MNPs) by inducing colloidal aggregation in apexes of anisotropic nanostructures or decorating graphene sheets.[15-17] These hotspots originate highly enhanced local electromagnetic fields that allow Raman detection at the single-molecule level.[15,18,19] This makes SERS a valuable tool in the environmental detection of trace levels of ECPs, provided effective SERS substrates are available. Fateixa *et al*. have investigated a variety of hybrid structures for the optical detection of ECPs, including magnetic substrates,[20,21] inkjet printing paper-based platforms[22] and MNPs dispersed in a polymer matrix[23] or filter mambranes[24].

Fabricating highly sensitive, reproducible, stable, and cost-effective SERS templates remains an actively researched topic.[25-27] 3D SERS templates have recently gained particular interest due to their larger surface area, increasing the molecules uptake and, therefore, its detection.[28-31] By increasing the hotspots' number in the z-direction, the Raman signal of the ECP can be improved, and detection limits can be lowered.

Additive manufacturing (AM), also known as 3D-printing, has recently established itself as a technology that enables the production of new designs and materials and does not require expensive molds or tools, which makes it particularly valuable for prototyping, mass customizations, waste minimization and low processing costs.[32,33] Fused filament fabrication (FFF) is one of the most used and affordable 3D printing techniques, an extrusion-based process that enables layer-by-layer deposition of the thermoplastic polymers in x-y, and z direction to fabricate complex 3D structures. The filament feedstock can be tailored to improve materials properties such as stiffness, strength, and energy absorbing capabilities by adding micro- and/or nano-scale fillers, such as carbon fibers, carbon nanotubes or graphene nanoplatelets, which further can increase the materials electrical conductivity over several magnitudes and improve thermal conductivity, enabling new fields of application such as self-sensing devices for biomedical applications.[34-36] Carbon reinforced high performance composites are gradually replacing typical metallic materials due to their outstanding material properties and have excellent potential to significantly impact the manufacturing industry.[37]

Only one paper reports the fabrication of 3D-printed composites by FFF for SERS applications so far.[29] The authors have used 3D printing to fabricate highly sensitive reproducible SERS templates using a fluorenylmethyloxycarbonyl diphenylalanine hydrogel loaded with silver or gold NPs. The 3D-printed peptide-hydrogel composites were used to detect adenine molecules at concentrations as low as 100 pM. In this work, we use extrusion-based 3D printing method to fabricate 3D-SERS nanocomposites containing polylactic acid (PLA), graphene nanoplatelets (GNPs) and gold nanoparticles (AuNPs) as novel material technologies, envisaging their use for ECPs' extraction and detection in real complex water matrices (Figure 1). 3D-printed polymer composites are evaluated as SERS platforms for target antibiotics such as ciprofloxacin as a proof-of-concept for ECPs' monitoring. Confocal Raman microscopy is used to study the synergistic effect from the chemical mechanism between adsorbates on graphene-based materials and the local electromagnetic field formed by the AuNPs.

  doi:10.5075/epfl-298799_978-2-9701614-0-0

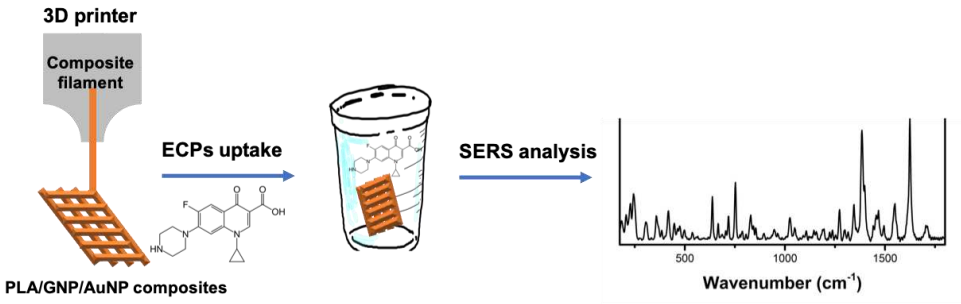

Figure 1. Preparation of PLA/GNP/AuNPs nanocomposites and the procedure for uptake and SERS detection of ECPs in water.

2. Experimental

2.1 Materials

The following chemicals were used as purchased: tetrachloroauric(III) acid trihydrate ($HAuCl_4 \cdot 3H_2O$, 99,9%, Sigma-Aldrich), ethylene glycol (EG, Aldrich, 99%), oleylamine (OA, Aldrich, 70%), Ciprofloxacin hydrochloride monohydrate (CIP, $C_{17}H_{18}FN_3O_3 \cdot HCl \cdot H_2O$, 99.0%, Sigma-Aldrich), Polylactic acid (4043D PLA pellets, Natureworks Ingeo), Graphene Nanoplatelets (2-10nm, ACS Material), Acetone (Sigma-Aldrich) .

2.2 Synthesis of organically capped-gold nanoparticles

Organically capped AuNPs were prepared using a modification of the polyol method described by Martins et al.[38] A solution containing $HAuCl_4 \cdot 3H_2O$ (0.15 M) in ethylene glycol (10 mL) was injected into a hot solution containing 40 mL of oleylamine (120 °C) for 30 min under a nitrogen stream. A dark red color solution is obtained after cooling to room temperature. The AuNPs were washed with 2-propanol and methanol and isolated by centrifugation (6000 rpm). The AuNPs were then dispersed in toluene.

2.3 Filament fabrication and 3D printing of PLA/Graphene blend and PLA/Graphene/AuNPs composites

The filaments are produced in-house with the Filabot EX6 extruder (Triex LLC dba Filabot), which has a three-stage extrusion screw made of hardened and polished stainless steel with a length-to-diameter ratio of 24:1. The feedstock is prepared by dry mixing PLA granules with the addition of GNPs and AuNPs, with the final mixing taking place in the extruder. Extruder temperatures are set at 167.5 °C, 166 °C, 165 °C and 40 °C for front, center, back and feed, respectively, using a 1.75 mm diameter die. To cool the extruded filament, it passes through the Filabot air path unit, using forced convection as it being extruded (fan speed 100%, Magnets: 5 used along airpath. end, center, front). The spool unit collects the filament and can be adjusted so that the filament diameter is precise within a range of 1.75±0.05 mm (settings used: drive–mid, traverse: 30%).

In this study, samples were fabricated using FFF technology, in which continuous thermoplastic filaments are fed from a spool through a heated nozzle, causing the material to melt and be deposited onto a heated print bed. The nozzle attached to the print head is able to move in-plane (x and y directions), while the print bed moves vertically (z direction), allowing the material to be applied layer by layer to form a final design. The 3D printer used is a Creator Pro (Zhejiang

  doi:10.5075/epfl-298799_978-2-9701614-0-0

Flashforge 3D Technology Co) with an extrusion temperature of 210 °C, a bed temperature of 60 °C, a layer height of 0.18 mm and an extrusion width of 0.48 mm (nozzle diameter 0.4 mm).

2.4 SERS studies

The sensitivity of 3D printing PLA/GNP/AuNPs composites was evaluated by SERS analysis coupled to Raman imaging. Raman images and spectra were acquired using a combined Raman-AFM-SNOM WITec alpha 300RAS+ microscopy. A Nd:YAG laser operating at 532 nm or a He:Ne laser operating at 633 nm were used as excitation sources.

Aqueous solutions of CIP with distinct concentrations (from 10^{-3} to 10^{-9} M) were prepared to establish the lower detection limit for the substrates used in SERS. The 3D printing PLA/GNP/AuNPs composites were placed in a vessel with the analyte solution to uptake the contaminant for several minutes (30min, 2h). Then, the composites were rinsed twice with distilled water to wash any unabsorbed analyte. The 3D printing PLA/GNP/AuNPs composites were transferred to a glass side and dried at room temperature before SERS analysis.

High-resolution Raman imaging was performed by taking 150 × 150 Raman spectra (in a total of 22500 spectra) in an area of 30 × 30 µm. A 100× objective was used to view samples, and the integration time for each spectrum was 0.05 s. Raman images were constructed by integrating the absolute area underneath the CIP Raman band at 1383 cm^{-1} (aromatic ring stretching) using WITec software (Project 5.0).

2.5 Instrumentation

TEM was carried out on a Hitachi H-9000 TEM microscope (Hitachi, Tokyo, Japan) operating at 300 kV. The TEM samples were prepared by placing a drop of the diluted AuNPs on a carbon-coated copper grid, and the solvent was left to evaporate in air. The 3D printing PLA/GNP/AuNPs composites were analyzed by scanning electron microscopy (SEM) using a SU-70 Hitachi instrument fitted with an energy- dispersive spectroscopy (EDS) accessory (EDS detector: Bruker AXS; software: Quantax), operated at 15 kV. Samples for SEM were placed on carbon tape and coated with carbon before the analysis in secondary electron (SE) and backscattered electron (BSE) modes. The XRD data were collected using a PAN analytical Empyrean X-ray diffractometer (PANanalytical, Almelo, The Netherlands) equipped with Cu K. The optical spectra were recorded using a GBC Cintra 303 UV/ VIS spectrophotometer. The spectra were recorded in diffuse reflectance mode using MgO as a reference for the 3D printing PLA/GNP/AuNPs composites. The corresponding absorption spectra were obtained by applying the Kubelka−Munk function to the experimental reflectance spectra.

3. Results

3.1 Characterization of the 3D printing of PLA/GNP/AuNPs composites

Organically capped Au NPs were prepared by reducing a gold salt in a mixture of long alkyl chain amines (e.g. oleylamine) and ethylene glycol. This reacting mixture promoted the formation of metal nuclei in a shorter period, resulting in AuNPs with an average size of around 25 nm. The TEM image of the AuNPs presents a spherical morphology of the particles with a significantly broader size distribution (Figure 2a). An average diameter of 24.7 ± 7.1 nm was obtained using the TEM image. The optical spectrum presented in Figure 2b shows an absorption band at 525 nm corresponding to the surface plasmon resonance (SPR) band characteristic for Au NPs.

  doi:10.5075/epfl-298799_978-2-9701614-0-0

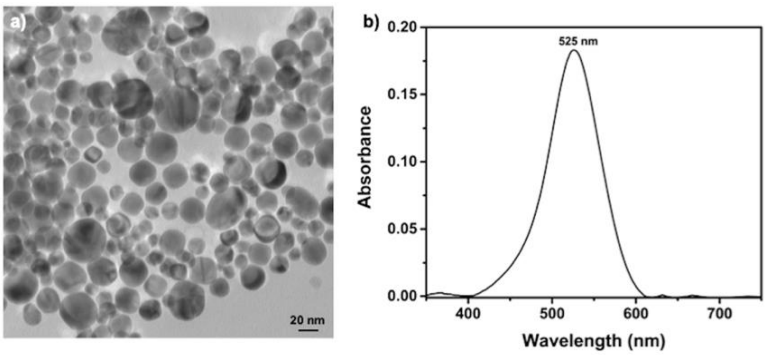

Figure 2. a) *Transmission electron microscopy (TEM) image of AuNPs and b) optical spectrum of organically capped Au NPs*

3.2 SERS studies

The as-prepared AuNPs were used as SERS substrates to detect CIP with a concentration of 10^{-5}M (pH 6). Figure 3A presents the SERS spectrum of CIP obtained using the AuNPs and the conventional Raman spectrum of CIP powder. It can be observed that the Raman spectrum of diluted CIP aqueous solution on the AuNPs is distinct from the pure solid analyte. The conventional Raman spectrum of CIP aqueous solution (10^{-5}M) did not present any Raman bands (data not shown). Therefore, the vibrational features observed in Figure 3Ab can only be explained by the SERS effect due to the presence of the AuNPs. The detection limit achieved for CIP using these AuNPs was lower as 10^{-7}M (Figure 3B).

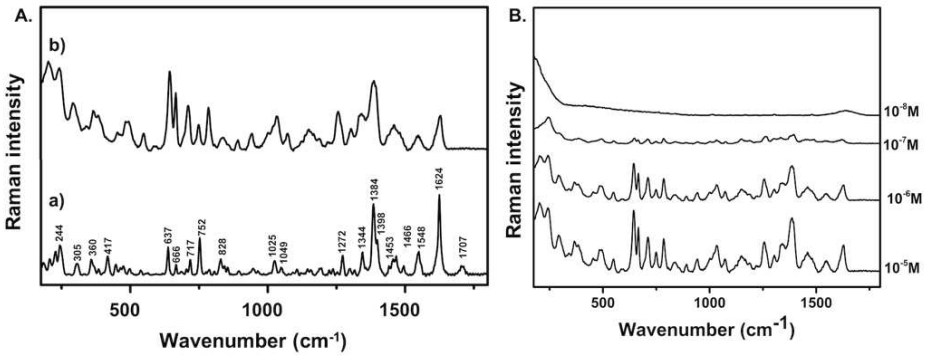

Figure 2. A. (a) Conventional Raman spectrum for CIP powder; (b) SERS spectrum of CIP aqueous solution (10^{-5} M) using the AuNPs; B. SERS spectra of CIP in distinct concentrations in AuNPs.

The incorporation of the AuNPs into graphene oxide sheets (Au/GO) can increase the CIP's Raman signal due to the synergistic effect between the graphene oxide (charge transfer) and AuNPs (enhancement of the electromagnetic field). The TEM image presented in Figure 4a shows bigger aggregates of AuNPs dispersed on the GO surface. These composites were used as nanosorbents to extract CIP from waters and analyzed by SERS imaging.

The Raman image shows the spatial distribution of CIP molecules (10^{-5}M) on the Au/GO surface (Figure 4b). The integration of the absolute area underneath the band at 1389 cm^{-1} (aromatic ring stretching) was used to establish the colour intensity and create the Raman image. Thus, the brighter colours in the image indicate regions with stronger SERS signal due to the presence of CIP molecules adsorbed in the AuNPs, simultaneously indicating the distribution of the AuNPs

  doi:10.5075/epfl-298799_978-2-9701614-0-0

over the GO sheets. The Raman image also shows that the AuNPs are evenly dispersed over the surface of the GO sheets, which agrees with the TEM results presented in Figure 4a.

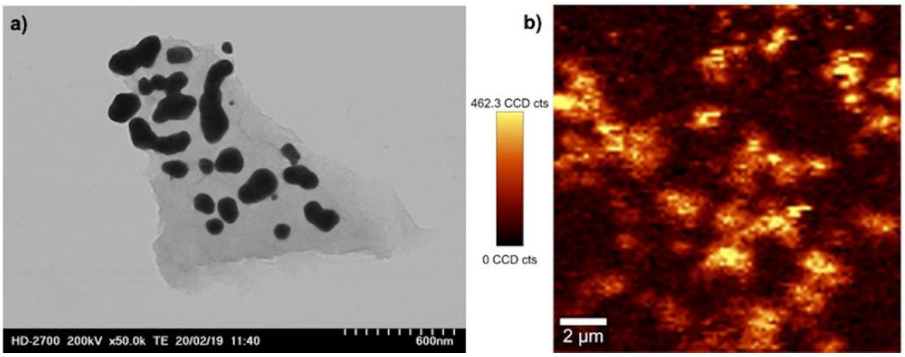

Figure 4. a) TEM image on Au/GO composite; b) Raman image obtained using the integrated intensity of the band at 1389 cm^{-1} in the SERS spectrum of CIP (10^{-5}M) using the Au/GO as substrates.

4. Conclusions

Preliminary results demonstrate that the AuNPs can be used as SERS substrates to detect CIP. The addition of AuNPs into the graphene-based materials results in highly stable composites with high sensitivity to extract and detect CIP from water. Further studies on 3D printing PLA/GNP/AuNPs composites must be performed to evaluate their sensitivity to uptake and detect CIP from water using SERS.

Acknowledgements

This work was developed within the scope of the project CICECO-Aveiro Institute of Materials, UIDB/50011/2020, UIDP/50011/2020 & LA/P/0006/2020, financed by national funds through the FCT/MEC (PIDDAC). S. F. thanks FCT for his research contract (REF-069-88-ARH-2018), which is funded by national funds (OE), through FCT-Fundação para a Ciência e a Tecnologia, I.P., in the scope of the framework contract foreseen in the numbers 4, 5, and 6 of the article 23, of the Decree-Law 57/2016, of August 29, changed by Law 57/2017, of July 19. The authors additionally acknowledge the support given by the European Commission via the COST Action CA19118 “High-performance carbon-based composites with smart properties for advanced sensing applications” (EsSENce). JS acknowledges EPSRC DTA PhD studentship [Award No: EP/R513222/1].

5. References

1. Lei M, Zhang L, Lei J, Zong L, Li J, Wu Z, Wang Z. Overview of emerging contaminants and associated human health effects. BioMed Res. Int. 2005; 2015:404796.
2. Tang Y, Yin M, Yang W, Li H, Zhong Y, Mo L, Liang Y, Ma X, Sun X. Emerging pollutants in water environment: Occurrence, monitoring, fate, and risk assessment. Water Environ. Res. 2019; 91:984.
3. Carvalho IT, Santos L. Antibiotics in the aquatic environments: A review of the European scenario. Environ. Int. 2016; 94:736.

  doi:10.5075/epfl-298799_978-2-9701614-0-0

4. Boxall ABA, Kolpin DW, Halling-Sørensen B, Tolls J. Are veterinary medicines causing environmental risks? Environ. Sci. Technol. 2003; 37:286A.
5. Petrie B, Youdan J, Barden R, Kasprzyk-Hordern B. Multi-residue analysis of 90 emerging contaminants in liquid and solid environmental matrices by ultra-high-performance liquid chromatography tandem mass spectrometry. J. Chromatogr. A 2016; 1431:64.
6. O'Sullivan-Carroll E, Howlett S, Pyne C, Downing P, Rafael A, Lynch M, Hogan AM, Moore EJ. Determination of Pharmaceuticals in Surface and Wastewater by Capillary Electrophoresis (CE): A Minireview. Anal. Lett. 2021; 55:1.
7. Gómez MJ, Gómez-Ramos MM, Agüera A, Mezcua M, Herrera S, Fernández-Alba AR. A new gas chromatography/mass spectrometry method for the simultaneous analysis of target and non-target organic contaminants in waters. J. Chromatogr. A 2009; 1216:4071.
8. Pinheiro PC, Daniel-da-Silva AL, Nogueira HIS, Trindade T. Functionalized Inorganic Nanoparticles for Magnetic Separation and SERS Detection of Water Pollutants. Eur. J. Inorg. Chem. 2018; 2018:3443.
9. Li DW, Zhai WL, Li YT, Long YT. Recent progress in surface enhanced Raman spectroscopy for the detection of environmental pollutants. Microchim. Acta 2014; 181:23.
10. Bodelón G, Pastoriza-Santos I. Recent Progress in Surface-Enhanced Raman Scattering for the Detection of Chemical Contaminants in Water. Front. Chem. 2020; 8:478.
11. Ding SY, Yi J, Li JF, Ren B, Wu DY, Panneerselvam R, Tian ZQ. Nanostructure-based plasmon-enhanced Raman spectroscopy for surface analysis of materials. Nature Rer. Mater. 2016; 1:1.
12. Langer J, *et al.* Present and Future of Surface-Enhanced Raman Scattering. ACS Nano 2020; 14:28.
13. Wang AX, Kong X. Review of recent progress of plasmonic materials and nano-structures for surface-enhanced raman scattering. Materials 2015; 8:3024.
14. Fateixa S, Nogueira HIS, Trindade T. Hybrid nanostructures for SERS: Materials development and chemical detection. Phys. Chem. Chem. Phys. 2015; 17:21046.
15. Chen T, Wang H, Chen G, Wang Y, Feng Y, Teo WS, Wu T, Chen H. Hotspot-induced transformation of surface-enhanced Raman scattering fingerprints. ACS Nano 2010; 4:3087.
16. Wei H, Xu H. Hot spots in different metal nanostructures for plasmon- enhanced Raman spectroscopy. Nanoscale 2013; 5:10794.
17. Zhu C, Zhao Q, Wang X, Li Z, Hu X. Ag-nanocubes/graphene-oxide/Au- nanoparticles composite film with highly dense plasmonic hotspots for surface- enhanced Raman scattering detection of pesticide. Microchem. J. 2021; 165:106090.
18. Mao, P, Liu C, Favraud G, Che Q, Han M, Fratalocchi A, Zhang S. Broadband single molecule SERS detection designed by warped optical spaces. Nat. Commun. 2018; 9:1.
19. Park WH, Kim ZH. Charge transfer enhancement in the SERS of a single molecule. Nano Lett. 2010; 10:4040.
20. Pinheiro PC, Fateixa S, Nogueira HIS, Trindade, T. Magnetite-supported gold nanostars for the uptake and SERS detection of tetracycline. Nanomaterials 2019; 2019:9.
21. Pinheiro PC, Fateixa S, Daniel-da-Silva AL, Trindade T. An integrated approach for trace detection of pollutants in water using polyelectrolyte functionalized magneto-plasmonic nanosorbents. Sci. Rep. 2019; 9:19647.
22. Martins NCT, Fateixa S, Fernandes T, Nogueira HIS, Trindade T. Inkjet Printing of Ag and Polystyrene Nanoparticle Emulsions for the One-Step Fabrication of Hydrophobic Paper-Based Surface-Enhanced Raman Scattering Substrates. ACS Appl. Nano Mater. 2021; 4:4484.

23. Fateixa S, Soares SF, Daniel-Da-Silva AL, Nogueira HIS, Trindade T. Silver-gelatine bionanocomposites for qualitative detection of a pesticide by SERS. Analyst 2015; 140:1693.
24. Fateixa S, Raposo M, Nogueira HIS, Trindade T. A general strategy to prepare SERS active filter membranes for extraction and detection of pesticides in water. Talanta 2018; 182:558.
25. Liu Y, Kim M, Cho SH, Jung YS. Vertically aligned nanostructures for a reliable and ultrasensitive SERS-active platform: Fabrication and engineering strategies. Nano Today 2021; 37:101063.
26. Mekonnen ML, Workie YA, Su WN, Hwang BJ. Plasmonic paper substrates for point-of-need applications: Recent developments and fabrication methods. Sensors Actuators B 2021; 345:130401.
27. Lee S, Choi, I. Fabrication Strategies of 3D Plasmonic Structures for SERS. Rev. Artic. BioChip. J. 2019; 13:30.
28. Almohammed S, Alruwaili M, Reynaud EG, Redmond G, Rice JH, Rodriguez BJ. 3D-Printed Peptide-Hydrogel Nanoparticle Composites for Surface-Enhanced Raman Spectroscopy Sensing. ACS Appl. Nano Mater. 2019; 2:5029.
29. Lee SY, Kim SH, Kim MP, Jeon HC, Kang H, Kim HJ, Kim BJ, Yang SM. Freestanding and Arrayed Nanoporous Microcylinders for Highly Active 3D SERS Substrate. Chem. Mater 2013; 25:2421.
30. Lee S, Hahm MG, Vajtai R, Hashim DP, Thurakitseree T, Chipara AC, Ajayan PM, Hafner JH. Utilizing 3D SERS active volumes in aligned carbon nanotube scaffold substrates. Adv. Mater. 2012; 24:5261.
31. García-Astrain C, Lenzi E, de Aberasturi DJ, Henriksen-Lacey M, Binelli MR, Liz-Marzán LM. 3D-Printed Biocompatible Scaffolds with Built-In Nanoplasmonic Sensors. Adv. Funct. Mater. 2020; 30: 2005407.
32. Schneider J, Kumar S. Multiscale characterization and constitutive parameters identification of polyamide (PA12) processed via selective laser sintering. Polym. Test. 2020; 86:106357.
33. Andrew JJ, Schneider J, Ubaid J, Velmurugan R, Gupta NK, Kumar S. Energy absorption characteristics of additively manufactured plate-lattices under low- velocity impact loading. Int. J. Impact Eng. 2021; 149:103768.
34. Arif MFF, Kumar S, Varadarajan KMK, Cantwell WJJ. Performance of biocompatible PEEK processed by fused deposition additive manufacturing. Mater. Des. 2018; 146:249.
35. Verma P, Ubaid J, Varadarajan KM, Wardle BL, Kumar S. Synthesis and Characterization of Carbon Nanotube-Doped Thermoplastic Nanocomposites for the Additive Manufacturing of Self-Sensing Piezoresistive Materials. ACS Appl. Mater. Interfaces 2022; 14:8361.
36. Andrew JJ, Alhashmi H, Schiffer A, Kumar S, Deshpande VS. Energy absorption and self-sensing performance of 3D printed CF/PEEK cellular composites. Mater. Des. 2021; 208:109863.
37. Koumoulos, E. P. *et al.* Research and Development in Carbon Fibers and Advanced High-Performance Composites Supply Chain in Europe: A Roadmap for Challenges and the Industrial Uptake. J. Composites Sci. 2019; 3:86.
38. Martins MA, Fateixa S, Girão AV, Pereira SS, Trindade T. Shaping gold nanocomposites with tunable optical properties. Langmuir 2010; 26:11407.

SELF-HEALING VITRIMER COMPOSITES FOR SOFT ROBOTICS

Jakob, Langenbach[a], Camille, Bakkali-Hassani[a], Quentin-Arthur, Poutrel[a], Antonia, Georgopoulou[b,c], Frank, Clemens[b], François, Tournilhac[a], Sophie, Norvez[a]

a: Molecular, Macromolecular Chemistry, and Materials, ESPCI Paris, PSL University, CNRS UMR7167, 75005 Paris, France – jakob.langenbach@espci.fr
b: Department of Functional Materials, Empa - Swiss Federal Laboratories for Materials Science and Technology, Überlandstrasse 129, 8600 Dübendorf, Switzerland
c: Brubotics, Vrije Universiteit Brussel (VUB), Pleinlaan 2, B-1050 Brussels, Belgium

Abstract: *Hybrid networks (i.e. including physical and chemical crosslinks) were synthesized from bio-sourced fatty acids, linked to each other by a controlled number of non-exchangeable ether bonds, exchangeable ester bonds and non-covalent hydrogen bonds. Mechanical properties are tuned by the acid/epoxy ratio. Their thermo-stimulated weldability was exploited to incorporate stretchable strain sensors by embedding electrically conductive fibers into the vitrimer matrix. The efficiency of welding at 80 °C and the tunability of mechanical properties are both attractive assets for effective incorporation of thermo-degradable conductive fibers while preserving their mechanical and electrical integrity. Mechanical and electrical behavior of the sensor composites were simultaneously tested in cyclic tensile experiments at 50 °C. The stress concentration in dog-bone shaped samples was investigated by observations in polarized light and shear stress calculations. The study emphasizes the importance of matching the Young's moduli of components in deformable composite samples, which is important for soft robotic applications.*

Keywords: soft robotics; matrix-sensor fiber laminates; deformation gradient; stiffness matching

1. Introduction

Soft robots have many advantages over conventional robots made of rigid materials, such as their high deformability (up to several hundred percent strain) and adaptability to their environment. However, soft materials are also intrinsically prone to damage, leading to an increasing research of self-healing elastomers for soft robots (1). Self-healing (SH) polymers can heal damage due to dynamic bonds in the network. In order to detect possible damage or to measure the robot's deformation, stretchable strain sensors have to be integrated into the robotic devices (2). Different manufacturing techniques are possible for the sensor integration, while self-healing polymers take advantage of exchangeable bonds in the network to promote the adhesion (3,4).

The strain sensors often consist of an elastomeric material with incorporated conductive fillers like carbon black particles, carbon nanotubes, etc. The electrically conductive filler modifies the mechanical properties of the strain sensor, which results in a stiffness mismatch between the elastic matrix and the integrated sensor fiber. The mismatch induces shear stresses at the fiber-matrix interface which has negative effects up to the rupture of the sensor fiber inside the matrix.

  doi:10.5075/epfl-298799_978-2-9701614-0-0

Herein, we report the integration of thin strain sensor fibers into hybrid networks (i.e., including physical and chemical crosslinks) with tunable mechanical properties. The matrix stiffness is adapted to reduce the shear stress at the fiber-matrix interface. Calculations and observations under polarized light suggest that small stiffness changes can significantly decrease the shear stress to prevent a fiber rupture, especially in areas with changing cross-section.

2. Results

The hybrid network materials (including physical hydrogen bonds and possibly exchangeable ester bonds) were synthesized in a facile two step synthesis (5) and the crosslinking density was adapted by the initial feed ratio acid/epoxy. An epoxy excess leads to homo-polymerization and the formation of non-exchangeable ether bonds (6). Nevertheless, the vitrimer nature of the materials was preserved, as indicated by creep and solubility measurements (7). The sensor-fiber composites (SFCs) were produced by cutting pairs of dog-bone shaped specimens and placing the thin sensor fiber (diameter 0.3 mm) in between (Figure 1). The sensor-fiber composite was assembled by using the thermally stimulated weldability, leading to a good integration of the thermo-degradable sensor fiber between the two laminates (7).

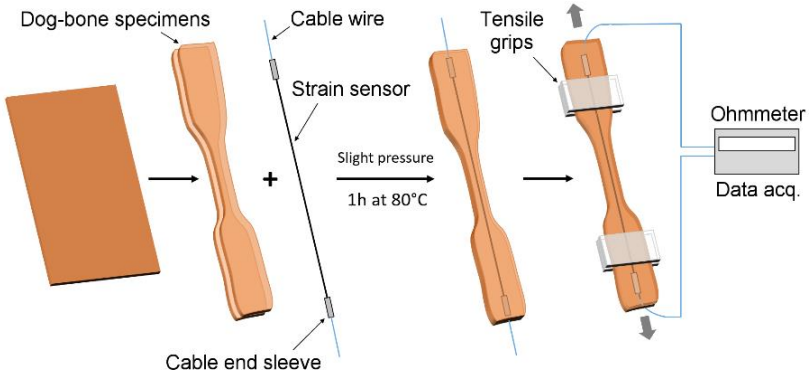

Figure 1. Scheme for the integration of electrically conductive sensor fibers in tunable hybrid networks by sandwich-welding. Sensor fibers are sandwiched between two dog-bones and sensor-fiber composite is welded at 80 °C for 1 h. Reprinted with permission from (7)*. Copyright 2022 American Chemical Society.*

The SFCs were tested under cyclic tensile experiments (0 – 20 % strain) at 50 °C, measuring simultaneously the tensile stress and electrical resistance of the sensor fiber. The glass transition temperature (T_g) of the hybrid networks is slightly below room temperature (12 – 16 °C), so the speed of elastic return at temperatures T around 25 °C is highly influenced by the distance T-T_g. The samples with 0 mol%, 5 mol% and 10 mol% epoxy excess are named **C_0epoxy**, **C_5epoxy** and **C_10epoxy**, respectively. Figure 2 displays 20 cycles of tensile stress of the composites and the relative resistance, which is the ratio of the change in resistance (R-R_0) divided by the resistance at rest (R_0):

$$Relative\ Resistance = \frac{R - R_0}{R_0} \quad (1)$$

All SFCs show buckling during cyclic tensile loading at room temperature due to the vicinity of glass transition. Nevertheless, the sensor fibers withstand the deformation without break. Of note, at this temperature, the stiffnesses of matrix and fiber are similar (see Young's moduli of sensor fiber and matrices in Figure 5a) (7).

At 50 °C, the hybrid networks get softer due to the increased distance from the T_g whereas the stiffness of the strain sensor remains almost the same. During cyclic testing at 50 °C, the sensor fiber in the matrix **C_0epoxy** breaks after 3 tensile cycles (shown by the dashed line of the relative resistance increasing abruptly in Figure 2a) and the fiber in **C_5epoxy** after 5 cycles (Figure 2b). However, the sensor fiber in **C_10epoxy** (Figure 2c) shows a linear response with only a small drift for all 20 tensile cycles. Consequently, an increase of the matrix stiffness correlates with extended cyclability before rupture of the sensor fiber inside the composite.

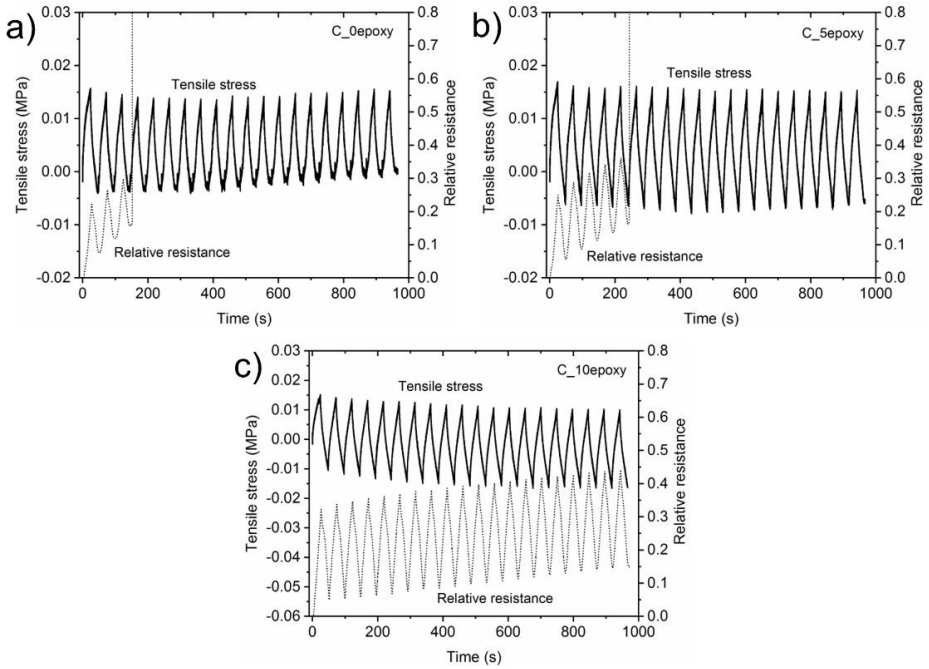

Figure 2. Cyclic tests (20 cycles at 0 – 20 % strain) for the three SFCs at a deformation rate of 50%.min^{-1}. Solid lines represent the stress values and dashed lines the relative resistance. a) ***C_0epoxy****, b)* ***C_5epoxy*** *and c)* ***C_10epoxy*** *at 50 °C.*

Images of stretched specimens are shown in Figure 3. The sensor rupture appeared in the shoulder region of the dog-bone samples in several cases (**C_5epoxy** in Figure 3a, b). For investigation of the stress concentration, a constant force of 1 N (to the bottom direction) was applied on a pristine sensor-fiber composite. When crossed polarizers are oriented at 45° with respect to the stretching direction, the darker area reflects the stress gradient in the lower part of the shoulder region (Figure 3c). When crossed polarizers are oriented along the stretching direction (Figure 3d), orange areas appear in both shoulders. Consequently, the dark spots in both images with polarized light show the region of highest stress concentration during tensile stretching (Scheme in Figure 3e).

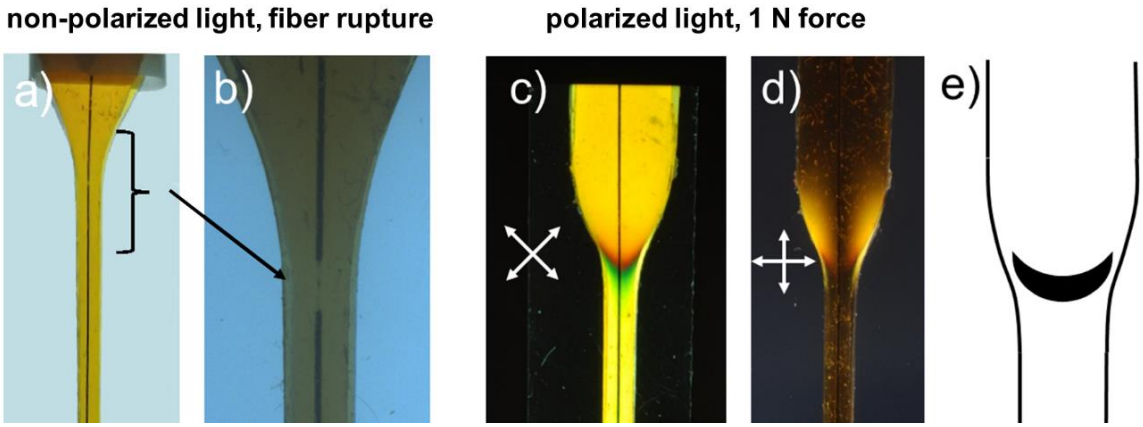

*Figure 3. a) Image of stretched **C_5epoxy** sample showing two spots of fracture of the sensor fiber. b) Zoom-in on the point of rupture in the shoulder region observed with a binocular magnifier. c, d) A SFC sample bearing with 1 N weight observed in polarized light between crossed polarizers oriented at 45° or parallel to the stretching direction. e) Scheme of dog-bone region with area of highest stress concentration due to extensive deformation.*

As described by G'sell *et al.* in the case of neck formation during bar stretching, the stress concentration in the region of changing cross-section depends on the area of convex or concave curvature (8). At the root of the shoulder, in the concave part, the triaxial stress is in tension in all directions, causing a phenomenon of cavitation that possibly initiates rupture (see Figure 4a).

To describe quantitatively the situation of rupture in our samples, the difference of stiffness between fiber and matrix must be considered, in addition to triaxiality effects appearing in the shoulder region of the dog-bone sample. Indeed, as the dog-bone is made of components having different stiffnesses, a shear stress τ is generated along the interface S_T between fiber and matrix in the shoulder region. τ may be written as the difference of forces Δf applied on the fiber in the narrow (f_1) and large (f'_1) parts divided by the interfacial surface S_T in the shoulder region (Figure 4b):

$$\tau = \frac{\Delta f}{S_T} \tag{2}$$

The overall force f applied to the dog-bone bar may be decomposed into partial forces f_1 and f_2, f'_1 and f'_2, applied to the fiber and to the matrix, in both extremities of the shoulder:

$$f = f_1 + f_2 = f'_1 + f'_2 \tag{3}$$

and the variation Δf expressed as:

$$\Delta f = f_1 - f'_1 = f_2 - f'_2 \tag{4}$$

Introducing strains ε and ε' in narrow and large parts of the bar, (3) may be written as:

$$f = S_1 E_1 \varepsilon + S_2 E_2 \varepsilon = S'_1 E_1 \varepsilon' + S'_2 E_2 \varepsilon' \tag{5}$$

  doi:10.5075/epfl-298799_978-2-9701614-0-0

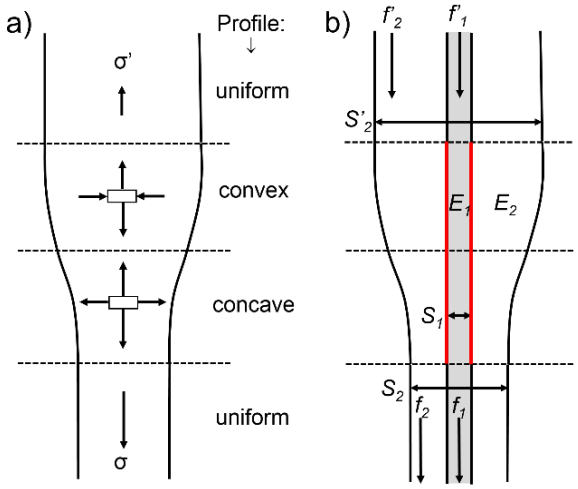

Figure 4. a) Scheme of stress profile (dark arrows) in shoulder region of a dog-bone sample. Bi-axial stress profile in convex (extensive and compressive) and in concave (all tensile) areas. b) Parameters for calculation of shear stress during stretching: E_1, E_2, Young's moduli of fiber, matrix, respectively; S_1, S_2, cross-sections of fiber, matrix. The projection of fiber-matrix surface S_T is underlined in red; f_1, f_2 partial strengths applied to fiber, matrix. The (') symbol accounts for parameters in the large part of the specimen.

Assuming the fiber cross-section remains constant during stretching, $S_1 = S'_1$ implies:

$$f = (S_1E_1 + S_2E_2)\varepsilon = (S_1E_1 + S'_2E_2)\varepsilon' \quad (6)$$

and:

$$\Delta f = f_1 - f'_1 = S_1E_1\varepsilon - S_1E_1\varepsilon' = S_1E_1(\varepsilon - \varepsilon') \quad (7)$$

Combining (6) and (7) leads to:

$$\frac{\Delta f}{f} = S_1E_1\left(\frac{1}{S_1E_1 + S_2E_2} - \frac{1}{S_1E_1 + S'_2E_2}\right) = \alpha \quad (8)$$

where α describes the relative variation of the force when the composite sensor is under strain. Plotting α against E_2 clearly shows that this ratio passes through a maximum value for a Young's modulus of the matrix around 0.025 MPa and drops rapidly with softer or stiffer matrices (Figure 5b). This extremum corresponds also to a maximum of the shear stress τ. The E_2 values measured for the three matrices at 50 °C were 0.07 MPa, 0.085 MPa and 0.13 MPa for 0 %, 5 %, and 10 % epoxy excess, respectively. Those matrix moduli may seem quite similar and far from the one of the fiber (9 MPa at 50 °C). However, their difference makes them more or less close to the maximum of α values, as shown in the plot of Figure 5b. The sample **C_0epoxy** experiences the highest shear stress, with decreasing shear for raising epoxy excess. This may explain why samples **C_0epoxy** and **C_5epoxy** broke at 50 °C while **C_10epoxy** sample did not, as the formers suffered much more shear stress during cyclic experiments.

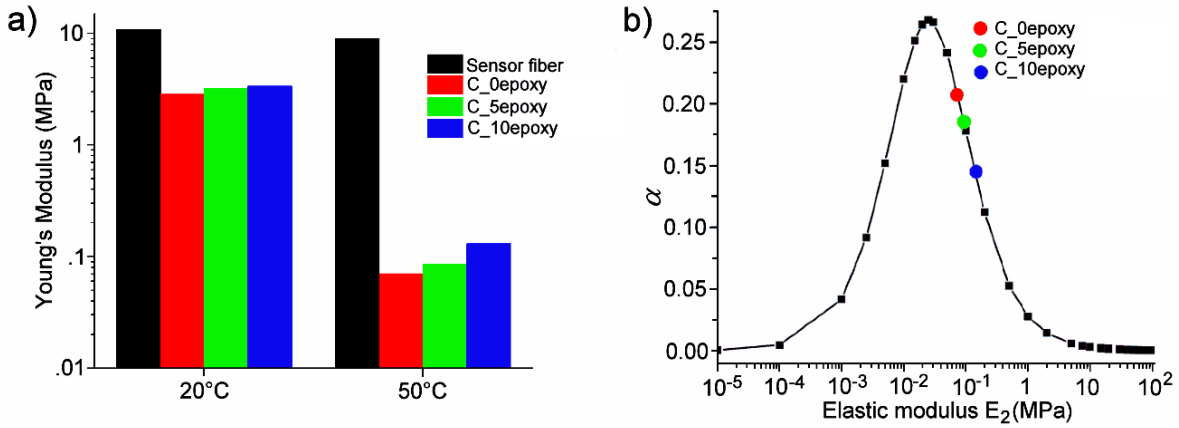

Figure 5. a) Compared Young's moduli of the sensor fiber and the three vitrimer matrices, at 20 °C and 50 °C. b) Dependence of the ratio α= Δf /f at the sensor-matrix interface on E_2, the Young's modulus of the elastomer matrix. E_1 = 10 MPa, S_1 = 0.07 mm², S_2 = 16 mm² and S'_2 = 48 mm² (Figure 4b). Reprinted with permission from (7). *Copyright 2022 American Chemical Society.*

The dog-bone shape of the specimen, useful to apply strong elongation while avoiding break in the clamps, has underlined the importance of matching the Young's moduli of matrix and fiber. This problem is important to integrate sensors in soft robotics grippers whose shapes are rarely rectangular. This also raises the question of matrix glass transition temperature. A glass transition temperature well below room temperature is desirable for improving the mechanical properties of the matrix (faster return, less drift, in particular), but meanwhile possibly worsens the Young's moduli mismatch with a fiber of high stiffness.

3. Conclusions

In this work, the integration of strain sensor fibers into self-healing matrices is reported. The stiffness mismatch of hybrid network material and sensor fiber induces shear stresses at the fiber-matrix interface. Moreover, the stiffness of the matrix is highly temperature dependent, which causes a premature rupture of the softest matrix, **C_0epoxy** at 50 °C. A slight epoxy excess leads to a stiffness increase of the matrix and avoids early fiber rupture (**C_10epoxy**). Moreover, the shear stress is concentrated in the concave shoulder region of the SFC, shown by images between crossed polarizers. The calculations show that even a slight change of matrix stiffness may have a significant impact on the interfacial shear stress. The matching of Young's moduli of matrix and integrated sensor fibers is thus an essential requirement for the development of long-lasting soft robots made of self-healing materials.

4. Experimental section

4.1 Hybrid network synthesis

The hybrid networks **C_*n*epoxy** were synthesized in the form of flat sheets. Desired quantities of DGEBA, TGMDA and supramolecular polymer precursor SP50 were introduced in a PTFE beaker, that was heated to 100 °C while mixing with a metallic stirrer until phase miscibility took place. 2-Methylimidazole (2-MI) was then added, and the mixture was stirred for two minutes before casting into a rectangular PTFE mold. After degassing under vacuum, the mold was put

  doi:10.5075/epfl-298799_978-2-9701614-0-0

in an oven and flushed with an inert atmosphere during curing at 130 °C for 3 h. Table 1 summarizes the hybrid network samples synthesized, with the different total quantities of di-(DGEBA) and tetra-(TGMDA) epoxide introduced. The molar quantity of the total epoxides in the network is shown in the last column. The crosslinking accelerator 2-MI was used at 6 mol%/COOH group for all formulations.

Table 1: Quantities of reactants for the preparation of hybrid network sheets.

Name	SP50 [g]	DGEBA [g]	TGMDA [g]	COOH [mmol]	Epoxy [mmol]
C_0epoxy	15.00	2.85	0.589	22.3	22.3
C_5epoxy	15.00	2.99	0.619	22.3	23.5
C_10epoxy	15.00	3.13	0.648	22.3	24.5

4.2 Strain sensor fiber synthesis

For the piezoresistive strain sensor fiber, a styrene-based triblock copolymer by Kraiburg TPE (Waldkraiburg, Germany) was combined with carbon black obtained from TIMCAL (Bodio, Switzerland). The two components were mixed in a 1:1 mass ratio (50 wt% carbon black), using torque rheometer HAAKE Polylab Rheomix 600 from Thermofisher (Karlsruhe, Germany). Sensor fibers with a diameter of 0.3 mm were extruded using a capillary rheometer RH7 from NETZSCH (Selb, Germany). The temperature used for the mixing and the extrusion was 190 °C. The sensor fiber fabrication and properties have been reported elsewhere (9). The sensing mechanism is based on rotation of the conductive particles, as well as on tunneling and hopping.

Acknowledgements

This work was funded by the European Union's Horizon 2020 FET Open Project Self-Healing Soft Robotics [grant agreement no. 828818]. The authors thank ESPCI-PSL, CNRS, and EMPA for the supportive financial environment, as well as Arkema for kindly gifting UDETA.

1. References

1. Terryn S, Langenbach J, Roels E, Brancart J, Bakkali-Hassani C, Poutrel Q-A, et al. A review on self-healing polymers for soft robotics. Materials Today. 2021;47:187–205.

2. Georgopoulou A, Clemens F. Piezoresistive Elastomer-Based Composite Strain Sensors and Their Applications. ACS Appl Electron Mater. 2020;2(7):1826–42.

3. Chabert E, Vial J, Cauchois J-P, Mihaluta M, Tournilhac F. Multiple welding of long fiber epoxy vitrimer composites. Soft Matter. 2016;12(21):4838–45.

4. Roels E, Terryn S, Iida F, Bosman AW, Norvez S, Clemens F, et al. Processing of Self-Healing Polymers for Soft Robotics. Advanced Materials. 2022;34(1):2104798.

  doi:10.5075/epfl-298799_978-2-9701614-0-0

5. Sordo F, Mougnier S-J, Loureiro N, Tournilhac F, Michaud V. Design of Self-Healing Supramolecular Rubbers with a Tunable Number of Chemical Cross-Links. Macromolecules. 2015;48(13):4394–402.

6. Tangthana-umrung, K, Poutrel Q-A, Gresil M. Epoxy homopolymerisation as a tool to tune thermo-mechanical properties and fracture toughness of vitrimer. Macromolecules. 2021;54(18):8393–406.

7. Langenbach J, Bakkali-Hassani C, Poutrel Q-A, Georgopoulou A, Clemens F, Tournilhac F, Norvez S. Adhesion and Stiffness Matching in Epoxy-Vitrimers/Strain Sensor Fiber Laminates. ACS Appl Polym Mater. 2022;4(2):1264–75.

8. G'sell C, Aly-Helal NA, Jonas JJ. Effect of stress triaxiality on neck propagation during the tensile stretching of solid polymers. J Mater Sci. 1983;18(6):1731–42.

9. Melnykowycz M, Koll B, Scharf D, Clemens F. Comparison of Piezoresistive Monofilament Polymer Sensors. Sensors. 2014;14(1):1278–94.

  doi:10.5075/epfl-298799_978-2-9701614-0-0

SOFT CARBON-BASED MULTI-SENSORY RESISTIVE RECEPTORS

Antonia Georgopoulou[a,b], Louisa Marie Eckey[a], Frank Clemens[a]

a: Department of Functional Materials, Empa – Swiss Federal Laboratories for Materials Science and Technology, Überlandstrasse 129, 8600 Dübendorf, Switzerland
b: Brubotics, Vrije Universiteit Brussel (VUB) and Imec, Pleinlaan 2, B-1050 Brussels, Belgium

Abstract: *Living organisms are equipped with several types of sensory receptors, a key aspect of survival, adaptability and the evolution of life on earth. Soft resistive sensors are developed to mimic the natural sensory receptor response, by combining a carbon conductive filler with a thermoplastic elastomer matrix. The resulting composites can be used to detect different stimuli in soft robotic applications; piezoresistive sensors can be used to detect mechanical deformation similar to mechanoreceptors; thermoresistive sensors can detect the changes in the temperature, attributing thermoreception; chemiresistive sensors can detect the presence of vapors and solvents, resembling the sense of olfaction. The additive manufacturing technique of pellet-based fused deposition modeling was used for integration of single sensory threads in the soft bending actuator elements. Selectivity to a specific stimulus can be tuned by adjusting the concentration of the conductive filler and the type of thermoplastic elastomer matrix. Considering these two parameters, a multi-sensory receptor approach can be achieved, while maintaining selectivity in detecting each specific stimulus. Therefore, multi-sensing soft robots for more efficient control and improved functionality can be created.*

Keywords: sensors, conductive composites, carbon-based composites, additive manufacturing, soft robots

1. Introduction

The sensory functions allow natural organisms to interact with the world and perceive their internal and external conditions(1–3). Senses are a key issue for the evolution of life and are a necessary tool for the adaptation and survival of living organisms(4). Using the natural senses as inspiration, artificial sensors are being developed and they are able to detect different stimuli, like temperature, deformation and the presence of chemical species(1,5,6). For natural sensory receptors, flexibility is an important requirement because it allows large deformations and the ability to conform to complex surfaces, a concept often adopted in soft robotics(7–10). Soft resistive sensors can be made with the combination of a thermoplastic elastomer with a carbon filler, like carbon black(11). The advantage of using thermoplastic elastomers is the fact that parts can be reshaped and reused, minimizing the number of waste products and scraps produced during the manufacturing process(12,13).

Mechanoreceptors are a type of sensory receptor involved in the senses of tactility and proprioception (body awareness)(14). Mechanoreceptors can be mimicked by piezoresistive sensors and this type of receptor has been used in the past for monitoring the motion of soft robotic modules(15–17). Nonetheless, it is possible to develop other types of sensory receptors based on soft resistive composites. Thermoreceptors record changes in the temperature and are associated with the sense of tactility(18). These receptors can be mimicked by elastomer and carbon nanofillers and detect changes in temperature by thermal expansion of the polymeric matrix(19–21). Chemoreceptors are associated with the senses of gustation and

  doi:10.5075/epfl-298799_978-2-9701614-0-0

olfaction and can be mimicked with the use of chemiresistive sensors. Thermoplastic elastomers like styrene based co-polymers exhibit a swelling behavior in the presence of solvents that result in a change of the electrical resistance(22-23).

In this study, mechano-, thermo- and chemoreceptive sensors are combined in one soft robotic actuator module. The target is to demonstrate the detection of different stimuli and selective response to the specific stimulus on a multi-materials 3D printed tendon soft robotic module. Thermoplastic printing is an alternative to casting or direct ink writing and allows a faster fabrication process. For demonstration, thermoplastic polyurethane (TPU) was selected as a matrix material for the soft thermoreceptive sensor (TR sensor), because of the good thermal expansion of the TPU(24). A styrene-based co-polymer (TPS) was selected for the chemoreceptive sensor (CR sensor), because of the swelling response of TPS in the presence of toluene solvent. Finally, a composite based on TPS and a high carbon black concentration was selected for the mechanoreceptive sensor (MR sensor), because of the piezoresistive behavior reported in previous studies(16). Due to the specific sensor compositions, the different sensors will exhibit a sensitive sensor response for each specific stimulus, and mimicking multi-sensory functions of natural organisms for 3D printed soft structures is demonstrated.

2. Figures, Tables, and citations

2.1 Preparation of the resistive conductive composites

The thermoplastic elastomer styrene-based tri-block co-polymer (TPS) was obtained by Kraiburg TPE (Waldkraiburg, Germany) in Shore hardness 50A. Thermoplastic polyurethane (TPU) with Shore hardness 85A was obtained by BASF (Ludwigshafen, Germany). Carbon black Ensaco 250G was obtained from Imerys (Paris, France). For the MR sensor, the TPS was mixed with the carbon black of concentration 50% w/w. For the TR sensor, the TPU was mixed with the carbon black of concentration 20% w/w. For the CR sensor, the TPS was mixed with the carbon black in concentration 25% w/w. The mixing was performed with the torque rheometer from Thermofisher (Karlsruhe, Germany). After the mixing, the conductive composites were extruded with a capillary rheometer from Netzsch (Selb, Germany). After the extrusion process, the extruded filaments were cut into 3mm pellets.

2.2 Fabrication of the TR sensor sensing elements

Because the TR sensor elements were positioned post printing to the robotic modules, single sensing elements with dimensions of 10 x 1.2 x 0.4 mm were printed with the Voladora Nx+ FDM pellet printer (International Technology 3D Printers S.L., Valencia, Spain), as described in a previous study (16). The nozzle temperature was fixed to 250°C and the printing speed to 15 mm/s. A temperature of 45°C was used for the printing bed.

2.3 Fabrication of the tendon-based actuator module with the integrated sensing elements

For the fabrication of the sensorized actuator module, the PR and CR sensors were printed first and on top of those sensor elements printing of the actuator body was continued. The printing was performed with the parameters described in 2.2. The body of the tendon-based actuator module was fabricated with the FDM 3D printer Bigfoot 200 Pro (International Technology 3D Printers S.L., Valencia, Spain), using thermoplastic polyurethane (TPU) with Shore hardness 90A

  doi:10.5075/epfl-298799_978-2-9701614-0-0

from Spectrum Group (Pecice, Poland). A nozzle temperature of 230°C and a printing speed of 15 mm/s was used. The temperature of printing bed was fixed to 45°C. For the actuation, a stainless steel tendon wire with 0.5 mm diameter and a Dynamixel AX-12A servomotor from Robotis (Lake Forest, Illinois, USA) were used. An Arduino microcontroller was used for the actuation and the recording of the sensor signal. Different analog channels were used for the different sensor types. A conductive yarn was used for the electrical connections between the sensing elements and the Arduino, with the help of metallic crimps and silicone glue.

After printing of TR sensor strips, they were fixed on the tip of the bending actuator by fusing with the finishing tool Modifi3D (Steelmans 3D, Coalville, UK) at a temperature of 220°C.

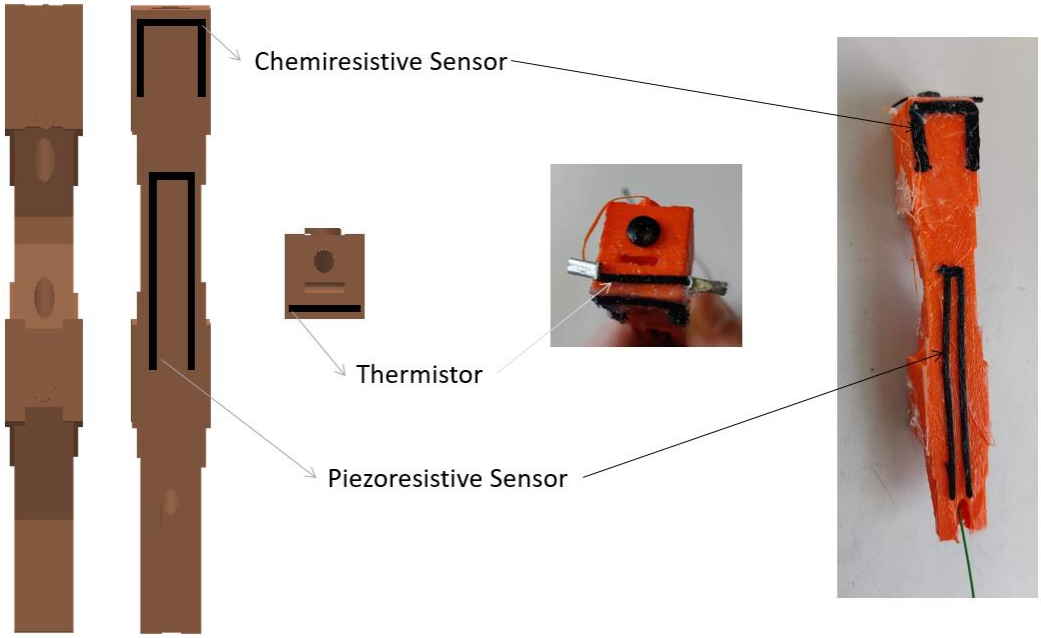

Figure 1: CAD design and photograph of the robotic actuator with the different integrated resistive sensors.

2.4 Testing the sensing response of the sensing elements

To evaluate the sensor performance, a bending test was performed with the soft robotic actuator module. For the deformation experiments, the soft robotic actuator module was cycled ten times while the sensor signal was recorded. For the thermal test, the signal of the sensors was recorded while the tip of the soft bending actuator was in contact with a heating plate. The temperature was measured with a thermocouple type K and the data logging device Testo 735 from Testo (Lenzkirch, Germany). The thermocouple measured the temperature of the heating plate next to point of contact of the thermistor element. For better comparison, the change of the relative resistance was investigated vs. the temperature measured with the thermocouple. For the detection of the chemical species, the solvent toluene was selected. In this case, the sensor signal was recorded for five minutes, while the soft actuator was exposed to toluene solvent.

3. Results

For the detection of the mechanical deformation during cyclic bending, a repeating bending motion was programmed (Figure 2a and 2b). The sensor signal response was recorded over ten

  doi:10.5075/epfl-298799_978-2-9701614-0-0

bending cycles and it was seen that the response was monotonic. The reproducibility of the MR sensor response was good with a drift of 1% between the first and the tenth cycle (Figure 2c). During the test, the CR Sensor showed a very small change of the sensor signal, which was attributed to the motion of the soft actuator. Even though the CR sensor was not placed above the hinge of the actuator, a deformation in the thicker part of the soft actuator can be expected due to the hyperelastic properties of the actuator material. The TR sensor exhibited flat signal without any noise, but with low signal drift (1%).

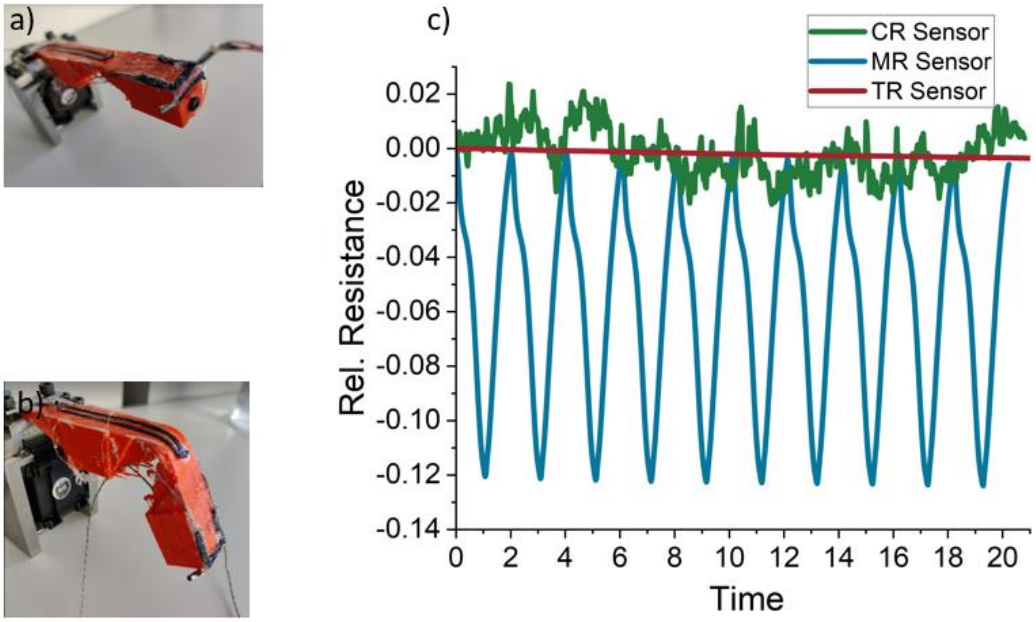

Figure 2: The soft robotic actuator module in potion a) straight and b) bent c) the response of the sensor signal during the bending test for the different types of resistive sensors.

For the assessment of the temperature response, the bending actuator was in contact with a heating plate and the sensor signal was recorded during touching the heated surface after bending (Figure 3a). At the same time, the temperature of the heating plate was recorded. For this type of sensing, the thermal expansion of the matrix is responsible for the sensing mechanism. From the response of the sensor signal (Figure 3b), it was seen that the TR sensor signal increased with a sharp increase above 70°C. This behavior is known as the PTC (positive temperature coefficient) effect and it can be explained by the increase of the interparticle distance, caused by the thermal expansion of the matrix. As expected, the sensor signal of the two other sensor types does not change significantly. These sensors are not directly exposed to the heating plate, and due to the low thermal conductivity and the thermal mass of the soft actuator structure, the heating will be damped. In comparison to the MR sensor, the CR sensor is closer to the heating source and at the end of the experiment, a negative slope can be observed. This behavior is known as the negative temperature coefficient (NTC) effect and it has been attributed to intramolecular changes in the polymer that can cause a re-arrangement of the conductive filler(25). Nonetheless, the change was significantly smaller than the change in the TR sensor.

  doi:10.5075/epfl-298799_978-2-9701614-0-0

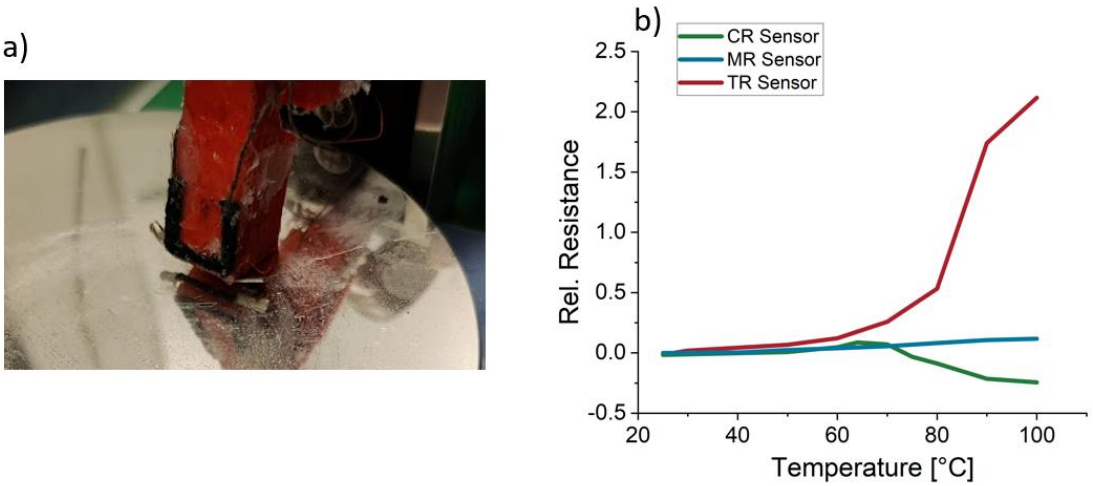

Figure 3: a) Heating test for the robotic actuator module and b) the response of the integrated sensors during the thermal test.

For the assessment of the chemical response, the actuator module was immersed in toluene solvent for five minutes (Figure 4a). It is worthwhile to mention that based on the sensor placement, the CR and TR sensors will be immersed in the toluene solvent, whereas the MR sensor will be exposed to the toluene vapor. For chemoreceptive sensors, the sensing response depends on the swelling of the thermoplastic elastomer matrix of the sensing element. Because of the swelling, the interparticle distance of the conductive network increases and the resistance of the electrical signal increases. For that purpose, a low carbon black concentration (20 wt%) was selected for the CR sensor composite. From the sensor response (Figure 4b), it was seen that the CR sensor had a significant change in the relative resistance in comparison to the two other sensing elements. The MR element consists of the same thermoplastic elastomer and therefore, the change in the relative resistance was expected. Due to the differences in the exposure (liquid/vapor) and the different content of carbon filler for the MR and CR sensor, the relative resistance increased only moderately. TPU does not exhibit swelling behavior under exposure to toluene solvent and therefore the sensor signal did not significantly change. For mimicking the sense of olfaction in soft robots, setting up a threshold (for example relative resistance of 2) can be crucial for detecting the presence of chemical species. It is worth to mention that even though toluene was used in this study, in the future, the same concept can be expanded for other solvents.

  doi:10.5075/epfl-298799_978-2-9701614-0-0

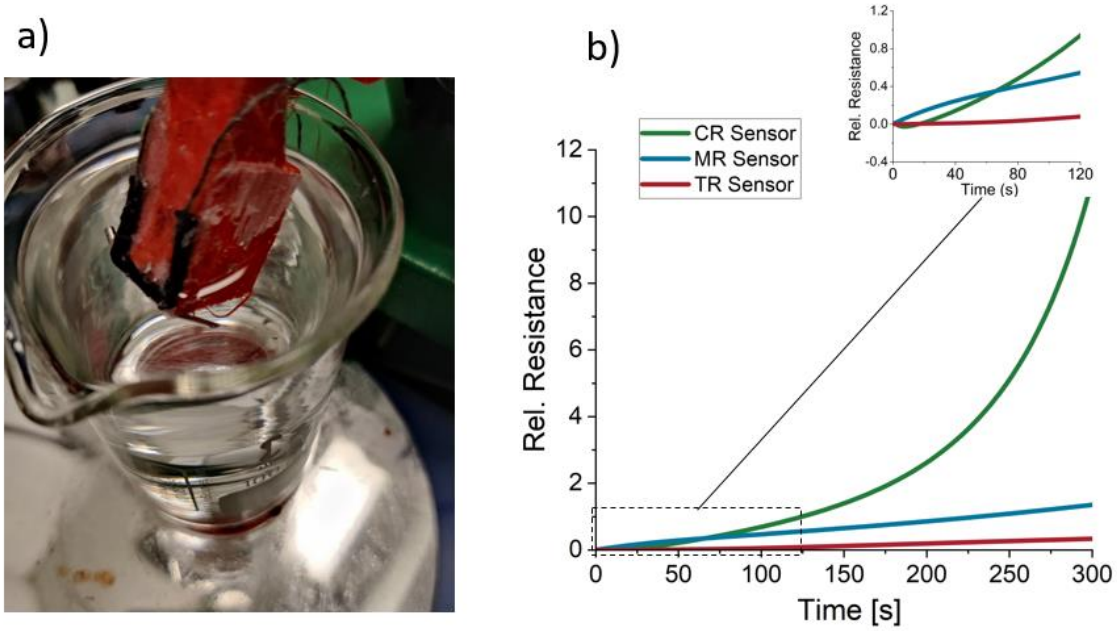

Figure 4: a) Solvent contact test for the robotic module and b) the response of the integrated sensors during the solvent contact test.

Table 1 compares the response during the different experimental cases of the three different sensors. It can be seen that the range of values is very different for each case. In every case, one of the resistive sensors is at least ten times more sensitive than the other two and based on this response, selectivity to the specific stimulus can be achieved. The same concept can be found in sensory receptors in biological organisms. Selectivity to a specific stimulus in nature is often achieved by different ranges in the activation energy, required to stimulate the sensory receptor. In the case of this study, the activation of the sensor is also affected by the placement of the sensor on the soft bending actuator module. Due to the FDM printing, it is possible to investigate the effect of the sensor elements systematically in the future. Additionally, intelligent machine learning algorithms can help to improve the sensor signal analysis and to establish reliable closed-loop control in soft robots.

Table 1: Comparison of the sensitivity of the different sensing elements during the bending test, heating test and solvent contact test.

Sensing element	ΔR_{rel} (Bending test)	ΔR_{rel} (Heating test)	ΔR_{rel} (Solvent contact test)
MR sensor	**0.12**	0.1	1.3
TR sensor	0.01	**2.1**	0.3
CR sensor	0.02	-0.2	**11**

4. Conclusion

In this study, a soft robotic actuator equipped with three different types of resistive sensors was fabricated by multi-material extrusion based additive manufacturing method, also known as fused deposition modelling (FDM). A soft robotic bending actuator with integrated sensor

  doi:10.5075/epfl-298799_978-2-9701614-0-0

elements to demonstrate the sensory receptors concept, found in nature, was successfully manufactured. A mechanoreceptive sensor element based on TPS and a high filler content of carbon black was used to monitor the bending motion of the actuator. A thermoreceptive sensor composed of thermoplastic polyurethane was used to detect the heating of the soft actuator by an external heat source. A chemoreceptive sensor was able to detect the presence of toluene, because of the swelling of the styrene-based copolymer matrix. In comparison to the mechanoreceptive sensor, a low filler content of carbon black was used for the chemo- and thermoreceptive sensor. For all cases, the specified sensor showed a sensor response with sensitivity at least ten times higher than the other two sensors, showing selectivity to the specified stimulus. In this study, the different sensors where at certain places and the demonstrator design already shows that this will affect the sensing behavior too. With the multi-material 3D printing, it is possible to investigate the effect of sensor placement in soft robot actuator modules to be able to sense proprioception, tactility and olfaction, while maintaining selectivity to each stimulus. We expect that multi-sensor material approach will help to establish intelligent closed-loop control functions to increase the functionality and autonomy of soft robotic modules.

Acknowledgement

This project has received funding from the European Union's Horizon 2020 research and innovation programme under grant agreement No 828818 (SHERO Project).

References

1. Bar-Cohen Y. Biological Senses as Inspiring Model for Biomimetic Sensors. IEEE Sens J. 2011 Dec;11(12):3194–201.
2. Fulkerson M. Rethinking the senses and their interactions: the case for sensory pluralism. Front Psychol. 2014 Dec 10;5:1426.
3. Macpherson F. The Senses: Classic and Contemporary Philosophical Perspectives. Oxford University Press; 2011. 425 p.
4. Elliott P. The senses and survival: using a sensory homunculus to stimulate an exploration of adaptation. 1996;
5. Svechtarova MI, Buzzacchera I, Toebes BJ, Lauko J, Anton N, Wilson CJ. Sensor Devices Inspired by the Five Senses: A Review. Electroanalysis. 2016;28(6):1201–41.
6. Lema MA, Antonakoglou K, Sardis F, Sornkarn N, Condoluci M, Mahmoodi T, et al. 5G case study of Internet of Skills: Slicing the human senses. In: 2017 European Conference on Networks and Communications (EuCNC). 2017. p. 1–6.
7. Coyle S, Majidi C, LeDuc P, Hsia KJ. Bio-inspired soft robotics: Material selection, actuation, and design. Extreme Mech Lett. 2018 Jul 1;22:51–9.
8. Laschi C, Mazzolai B. Bioinspired materials and approaches for soft robotics. MRS Bull. 2021 Apr 1;46(4):345–9.
9. Kim S, Laschi C, Trimmer B. Soft robotics: a bioinspired evolution in robotics. Trends Biotechnol. 2013 Mai;31(5):287–94.
10. Jung YH, Park B, Kim JU, Kim T. Bioinspired Electronics for Artificial Sensory Systems. Adv Mater. 2019;31(34):1803637.
11. Georgopoulou A, Clemens F. Piezoresistive Elastomer-Based Composite Strain Sensors and Their Applications. ACS Appl Electron Mater. 2020 Jul 28;2(7):1826–42.

  doi:10.5075/epfl-298799_978-2-9701614-0-0

12. Fazli A, Rodrigue D. Waste Rubber Recycling: A Review on the Evolution and Properties of Thermoplastic Elastomers. Materials. 2020 Jan;13(3):782.
13. Markarian J. Processing and recycling advantages drive growth in thermoplastic elastomers. Plast Addit Compd. 2004 Nov 1;6(6):22–5.
14. Macefield VG. The roles of mechanoreceptors in muscle and skin in human proprioception. Curr Opin Physiol. 2021 Jun 1;21:48–56.
15. Georgopoulou A, Vanderborght B, Clemens F. Fabrication of a soft robotic gripper with integrated strain sensing elements using multi-material additive manufacturing. Front Robot AI. 2021;8:326.
16. Georgopoulou A, Egloff L, Vanderborght B, Clemens F. A Sensorized Soft Pneumatic Actuator Fabricated with Extrusion-Based Additive Manufacturing. Actuators. 2021 May;10(5):102.
17. Shih B, Christianson C, Gillespie K, Lee S, Mayeda J, Huo Z, et al. Design Considerations for 3D Printed, Soft, Multimaterial Resistive Sensors for Soft Robotics. Front Robot AI. 2019 Apr 30;6:30.
18. Schepers RJ, Ringkamp M. Thermoreceptors and thermosensitive afferents. Neurosci Biobehav Rev. 2010 Feb 1;34(2):177–84.
19. Noh J-S. Conductive Elastomers for Stretchable Electronics, Sensors and Energy Harvesters. Polymers. 2016 Apr;8(4):123.
20. Singh S, Buchanan RC. Sensor properties of SBS block copolymer and carbon composite film structures. Plast Rubber Compos. 2007 Feb;36(1):42–6.
21. Wang X, Zhang G. PTC effect of carbon fiber filled EPDM rubber composite. J Mater Sci Mater Electron. 2008 Nov 1;19(11):1105–8.
22. Gao J, Wang H, Huang X, Hu M, Xue H, Li RKY. A super-hydrophobic and electrically conductive nanofibrous membrane for a chemical vapor sensor. J Mater Chem A. 2018 May 29;6(21):10036–47.
23. Wang X, Li Y, Pionteck J, Zhou Z, Weng W, Luo X, et al. Flexible poly(styrene-butadiene-styrene)/carbon nanotube fiber based vapor sensors with high sensitivity, wide detection range, and fast response. Sens Actuators B Chem. 2018 Mar 1;256:896–904.
24. Somdee P, Lassú-Kuknyó T, Kónya C, Szabó T, Marossy K. Thermal analysis of polyurethane elastomers matrix with different chain extender contents for thermal conductive application. J Therm Anal Calorim. 2019 Oct 1;138(2):1003–10.
25. Voet A. Temperature Effect of Electrical Resistivity of Carbon Black Filled Polymers. Rubber Chem Technol. 1981 Mar 1;54(1):42–50.

  doi:10.5075/epfl-298799_978-2-9701614-0-0

CHARACTERIZATION OF A SOFT MAGNETIC COMPOSITE FOR USE IN ROAD-EMBEDDED WIRELESS-CHARGING SYSTEMS

Kai-Yeung Li [a], Bill Trompetter[b], Maedeh Amirpour[c], Tom Allen[a], Simon Bickertoa[a], Piaras Kelly[c]

a: Centre for Advanced Composite Materials, University of Auckland, 314-390 Khyber Pass Road, Newmarket, Auckland, New Zealand 1023
kli063@aucklanduni.ac.nz
b: National Isotope Centre, GNS Science, 30 Gracefield Road, Gracefield, New Zealand 5010
c: Engineering Science, University of Auckland, 70 Symonds Street, Grafton, Auckland New Zealand 1010

Abstract: *A soft magnetic composite (SMC) composed of a flexible polyurethane and ferrite particles was manufactured as an alternative to ferrite for use as a magnetic core inside road embedded wireless-charging systems. An experimental investigation was conducted into the trade-offs between the mechanical, thermal and magnetic properties at ferrite volume fractions between 46% and 81%. The investigation showed a trade-off between the increase in magnetic permeability and the reduction in ductility as ferrite volume fraction increased. Nevertheless, the strain-to-failure of the composite was 20 times higher than that of ferrite even at the highest volume fraction, indicating that the SMC was successful in providing a more ductile and flexible alternative. Based on the properties of the composite with 74 vol% ferrite, it was chosen for further mechanical characterization at temperatures from 0°C to 100°C. A linear reduction in strength was observed with increasing temperature, with no significant change in failure strain.*

Keywords: particulate composite; multi-functional composite; soft magnetic composite; ferrite

1. Introduction

Road-embedded wireless charging systems have the potential to promote the mainstream uptake of electrical vehicles (EV's) by increasing their effective range and reducing their battery size. This is done by transferring power over an air-gap to a moving EV, using the principle of Inductive Power Transfer (IPT). In order for this solution to be economically viable however, it is imperative that these road-embedded systems, referred to as 'IPT pads', have a robust mechanical design to survive cyclic traffic wheel loads [1] at operating temperatures of up to 100°C [2]. At elevated temperatures, these systems would also experience mechanical stress from the mismatched thermal expansion of its internal components.

One of the core components of an IPT pad is its ferrite magnetic core [3]. Ferrite is particularly susceptible to failure by fracture due to its brittle nature (failure strain of only 0.02-0.03%), and its high stiffness (140 GPa), which also makes it the primary load bearing member of the structure. The durability requirements of IPT pads, combined with the brittleness of ferrite has motivated the development of alternative materials for use as the magnetic core. Soft magnetic composites (SMCs) are a class of composite comprising of a ferromagnetic filler with an electrically insulating matrix. By using an SMC composed of ferromagnetic particles within a ductile polymer matrix, the ductility of the pad magnetic core would be significantly higher than that of the corresponding bulk ferrite, while potentially still having the required magnetic properties for efficient power transfer.

  doi:10.5075/epfl-298799_978-2-9701614-0-0

SMCs have been the subject of a large amount of research from novel manufacturing methods [4], to the use of novel electrically insulating materials [5], to the effect of magnetic volume fraction and particle size [6], [7]. However, the vast majority of these studies have been conducted with a focus on optimizing magnetic properties (i.e. permeability, core-loss, magnetic saturation), with limited investigation into their mechanical properties [4], [5].

It is also crucial to understand the mechanical behavior of the magnetic core at elevated temperatures due to the heating of an IPT pad during operation. Studies on neat polymers have been conducted which show the high dependency of strength and modulus on temperature [8]. Epoxy with up to 60% volume fraction inorganic filler was also tested in compression at up to 80°C [9], while polyurethane rubber with 20% filler was tested in tension at up to 65°C [10].

Given the lack of literature regarding the multi-functional characterization of flexible magnetic core materials for IPT pads, the objective of this study was two-fold. First, SMCs composed of a flexible polyurethane and crushed ferrite for use in an IPT pad were investigated, as well as the trade-off between the mechanical, thermal and magnetic properties at a range of ferrite volume fractions. Because the magnetic core would be subjected to multiple modes of loading (i.e. wheel loading, thermal loads), mechanical characterization was performed in both bending and uniaxial tension to gain a more complete picture of its structural performance. In the second part of the study, one volume fraction was chosen based on the trade-off of properties and its mechanical behavior was further characterized in tension from 0°C to 100°C.

2. Materials and manufacturing

In this study, crushed ferrite (Cosmo CF295) was used as the magnetic filler. The particles had a wide size distribution: 80% of the magnetic particles were 0.5-1.4 mm in size, while the remaining 20% were 63-125 µm. A highly flexible polyurethane, WEVO PD52, was chosen as the binding matrix material due to its ability to impart increased ductility to the composite.

The composite was manufactured at ferrite volume fractions between 46% and 81% using a compression moulding process. To manufacture the composite, the required amount of resin, hardener and ferrite was mixed, poured evenly into an aluminium mould, and compacted for 15 hours in a pre-heated press at 60°C. The pressure required to compact the composite increased exponentially with volume fraction, as shown in Table 1. Each mixture had an additional 10 vol% of polyurethane which was squeezed out through runners in the mould during the compaction process. The extra resin provided additional lubrication between the particles, allowing for more effective packing and reduced void content. Because tensile dogbone specimens were longer than flexural specimens, a larger mould was manufactured to produce the former. Due to the larger area of that mould, tensile specimens could only be compacted to a maximum volume fraction of 74% using the maximum force available on the press.

Microscopy images of the SMC at the highest and lowest volume fractions are shown in Figure 1, demonstrating good dispersion of small particles (63-125 µm) around the larger (0.5-1.4 mm) particles, as well as confirming generally low void content. Minor particle breakage was seen at 75 vol% and significant particle breakage was seen at 81 vol% due to the large pressure required for compaction. Breakage occurred predominately across the short side of the particles, thus reducing their aspect ratio.

  doi:10.5075/epfl-298799_978-2-9701614-0-0

Table 1. Average pressure required to compact samples to each volume fraction

Vol%	46	55	65	75	81
Pressure (MPa)	0	4	20	80	180

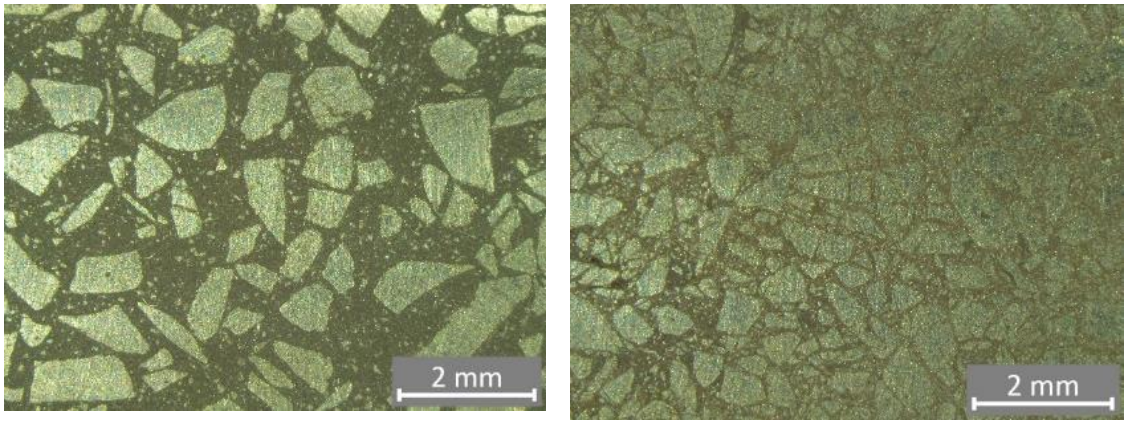

(a) (b)

Figure 1. Microscopy images of composite at (a) 46% and (b) 81% ferrite volume fraction

3. Experimental methods

Flexural properties were measured in 4-point bending on rectangular specimens with length 110 mm, width 15 mm and thickness 7 mm. An Instron 5567 was used, with a crosshead speed of 1 mm/min, a support span of 90 mm and a loading span of 45 mm. The test methodology was based on ASTM C1161. Tensile properties were measured using dogbone samples of the same thickness, in accordance with ASTM D638. An Instron 5567 was used with a cross-head speed of 0.5 mm/min for room temperature tests. Non room temperature tensile tests were performed on the larger Instron 1185 in order to have enough space for an environmental chamber (Instron 3119-600 series) to fit inside the Instron frame. Tensile tests were performed from 0°C to 100°C in 20°C increments. A thermocouple was attached to the specimen to verify that it had reached ±1°C of the target temperature prior to testing.

The methodology for measuring relative magnetic permeability was adopted from [11]. Measurements were taken using an LCR meter on toroidal samples with an inner radius 7.5 mm, outer radius 15 mm and a nominal thickness (t) 7 mm. A low B-field was used; hence, the initial relative magnetic permeability was obtained. Thermal conductivity was measured using the transient hot wire method with the Mathis TC 30, on flexural specimens prior to the bending test.

4. Effect of ferrite volume fraction

4.1. Mechanical properties

Figure 2(a) presents the typical stress-strain curves in 4-point bending at volume fractions between 46% and 81%, and Figure 2(b) presents the stress-strain curves in tension at volume fractions between 46% and 74%. A large increase in both flexural and tensile stiffness with volume fraction was observed. The shape of the curves was similar for both modes of loading. All curves had a high degree of non-linearity across a large range of strain, characterized by a gradual downward softening of the composite. This can be attributed to a combination of non-

linearity of the polymer itself, which was revealed through tensile tests, and dewetting. Dewetting occurs when the matrix and particles gradually de-bond and the matrix loses the structural support of the filler, resulting in the loss of stiffness [12].

It was observed that the 46 vol% flexural samples were able to bend so much that they were bending 'through' the support pins towards the end of each test. The reduction in stress at around 7% strain was a result of this, as opposed to a failure in the actual material. As a result, only an accurate flexural modulus (calculated at low strain) for the 46 vol% samples was obtained. Measured flexural strength and strain-at-maximum-stress could only be interpreted as the lower limits of those properties.

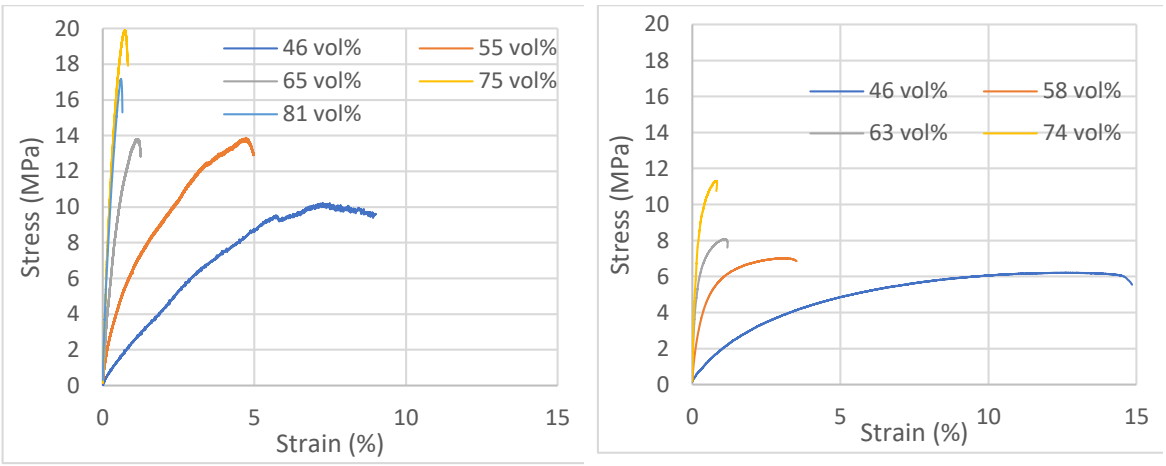

Figure 2 Stress-strain curve of the composite at different ferrite volume fractions tested in (a) 4-point bending and (b) uniaxial tension

The effect of ferrite volume fraction on flexural and tensile strength is presented Figure 3 (a). Both increased as volume fraction increased to 75%, indicating strong particle-matrix adhesion, and good stress-transfer between the ferrite and polyurethane. The percentage increase was also similar under both modes of loading, increasing 80-100% between 46 vol% and 75 vol%. This is in agreement with Yilmazer, who also measured an increase in strength of polyurethane rubber with an increasing volume fraction of glass beads [12]. Flexural strength was 60%-80% higher than tensile strength at all volume fractions. This was expected: since maximum tensile stress only occurs on the bottom surface of flexural specimens, as oppose to the entire cross-section of dogbone specimens, they are less sensitive to defects within the composite which are detrimental to its strength. The reduction in flexural strength from 75 vol% to 81 vol% can be attributed to the loss in reinforcement through particle breakage during compaction.

Ductility is a crucial property of the composite, as it prevents possible early brittle fracture, as occurs in ferrite. Strain at maximum stress, presented in Figure 3(b), was used as a measure of ductility. As expected, strain at maximum stress in both bending and uniaxial tension had approximately an inverse relationship to volume fraction. Unlike with strength, both modes of loading had a similar strain across a large range of ferrite volume fractions, with the exception of specimens at 46 vol%. The largest reduction in strain was measured in tension between 46 vol% and 58 vol%, where strain reduced from 12.2% to 3.2%. The difference in strain at the higher volume fractions was relatively small. In bending, strain decreased from 0.70% to 0.66% between 75 vol% and 81 vol%. It is important to note that even at the highest volume fraction,

  doi:10.5075/epfl-298799_978-2-9701614-0-0

strain-at-maximum-stress was 20 times higher than that of ferrite, meaning the composite was successful in providing a more ductile alternative.

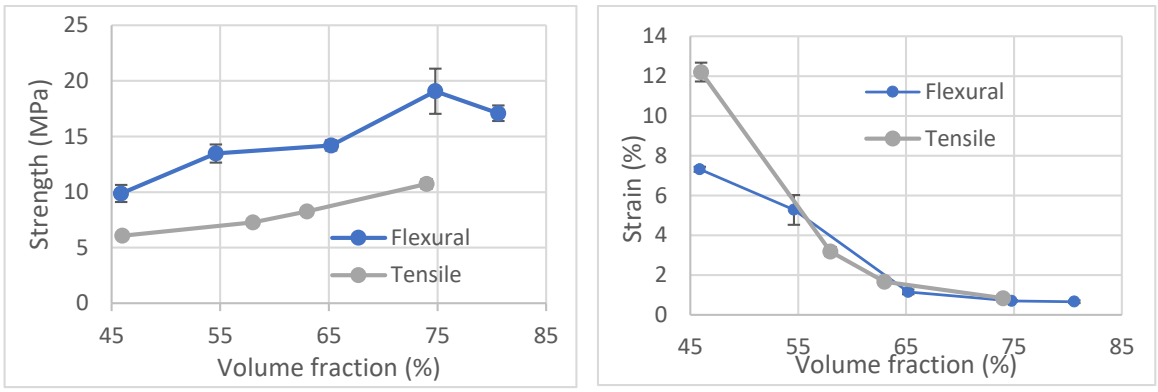

(a) (b)

Figure 3. (a) Composite strength at each volume fraction, (b) Strain at maximum stress in bending and tension

4.2. Thermal conductivity

It can be seen in Figure 4, that thermal conductivity increases monotonically with ferrite volume fraction due to the higher bulk conductivity of ferrite, with the exception of the 81 vol% sample. This levelling off at the highest volume fraction is likely due to significant particle fracture during compaction. Smaller particles are not as effective at facilitating heat transfer through the composite because of the slight thermal barrier created by the interfacial surface area [13].

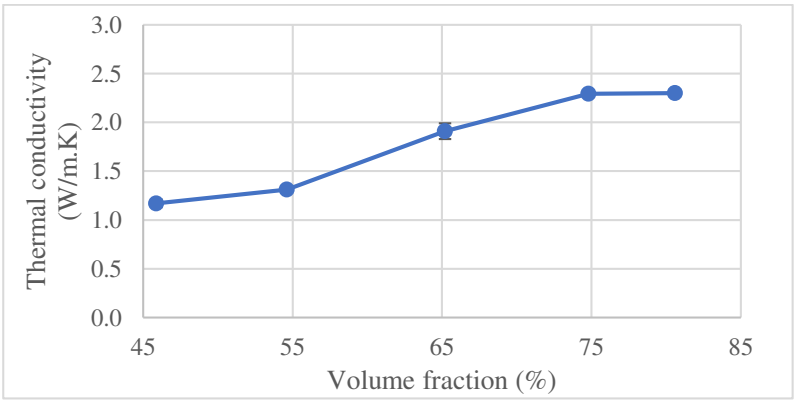

Figure 4. Thermal conductivity at each ferrite volume fraction

4.3. Initial relative magnetic permeability

Initial relative magnetic permeability is greatly enhanced by increasing ferrite volume fraction, as seen in Figure 5. However, the relative permeability of the SMCs even at the highest volume fraction were still two orders of magnitude lower than that of bulk ferrite. This is a key trade-off when considering the use of SMCs within IPT pads. As such, it is crucial that IPT pads with SMCs are optimized for lower permeability materials and evaluated for its electromagnetic performance relative to traditional ferrite-based pads. Similar to mechanical and thermal properties, a leveling off of permeability was measured between 75 vol% and 81 vol% despite all analytical models predicting an exponential increase with volume fraction [7]. Analogous to thermal conductivity, this was also likely due to the detrimental effect of reduced particle size and aspect ratio [14] on the flow of magnetic field through the composite.

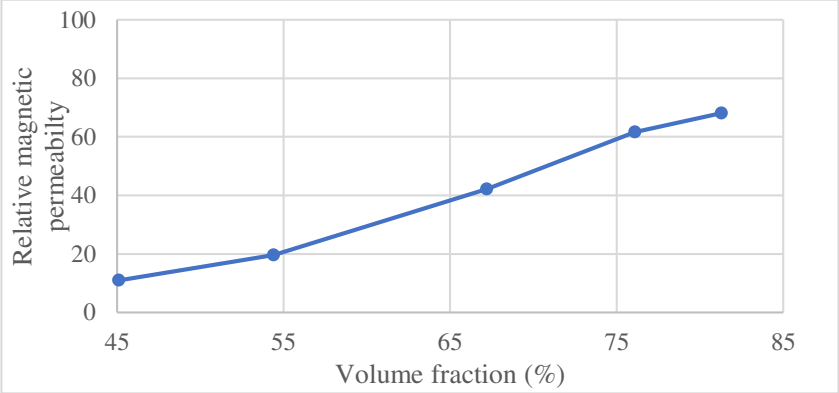

Figure 5. Relative initial magnetic permeability at each volume fraction

5. Discussion of trade-offs in the context of its application in road-embedded IPT pads

In general, the main trade-off with volume fraction was between mechanical properties and magnetic permeability. As volume fraction increased, the ductility (i.e. strain at maximum stress) of the composite was greatly reduced. Meanwhile, an SMC will become a higher load carrying member of the structure as modulus was greatly increased, increasing induced stresses for a given wheel load. This was only partially compensated for by a relatively small increase in strength. These factors mean that the SMC would be more susceptible to mechanical failure as volume fraction increases. However, magnetic permeability was also seen to greatly increase with volume fraction, meaning that the composite would be more effective in enhancing the magnetic field generated by the litz wire. All things being equal, this would increase the power transfer efficiency of the system. The increase in thermal conductivity with volume fraction is another benefit, improving heat conduction and lowering the steady-state operating temperature of the IPT pad.

It is clear from the results, that there was not a significant change in mechanical, thermal, and to a lesser extent, magnetic properties between 75 vol% and 81 vol%. Much of this could be attributed to the extensive particle fracture seen under microscopy. A large increase in pressing force was required however (see Table 1). This implies that the economical processing limit lies somewhere between 75 and 81 vol%, under which gains in composite performance could still be achieved with the proposed material composition. Just below the processing limit however, at 75 vol%, the composite demonstrated good overall properties for IPT applications. Between 65% and 75% ferrite volume fraction, magnetic permeability increased by 45%, flexural strength increased by 30% and thermal conductivity increased by 20%. Tensile strength also increased 29% between 63 vol% and 74 vol%, however, this was traded off with a 50% reduction in strain at maximum stress. Given the importance of magnetic permeability in this application and the relatively high strength of the composite, it was decided to conduct further multi-temperature tensile tests at a ferrite volume fraction of 74%.

6. Effect of temperature on mechanical properties

Figure 6 shows the typical stress-strain curves for the 74 vol% composite at temperatures ranging from 0°C to 100°C. The composite demonstrated similar stress-strain behaviour across the operating temperature of the pad, however, a clear monotonic decrease in stiffness was

observed with temperature. Likewise, tensile strength, shown in Figure 7(a), decreased linearly with increasing temperature, from 11.9 MPa at 0°C to 3.96 MPa at 100°C. This softening behaviour is well known in polymers [10], [15]. The change in strain at maximum stress is shown in Figure 7(b). It is clear that temperature did not have an effect on the ductility of the composite. Visual inspection of the fracture surfaces indicated a similar failure mechanism at all temperatures, with particle pull-out seen in most specimens. This stability in the composite's mechanical properties over the operating temperatures of the IPT pad is ideal because it allows the structural behaviour of the magnetic core to be accurately predicted, thus guaranteeing the durability of a particular pad design. This stability in mechanical properties is likely attributable to the glass-transition temperature of the polymer being significantly lower than 0°C.

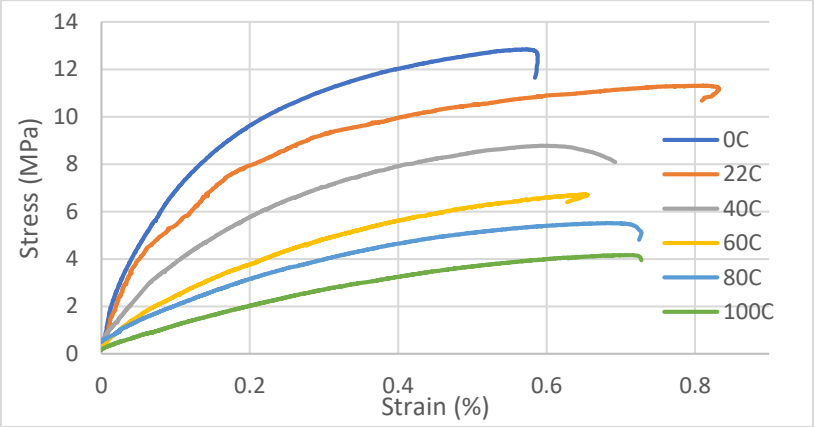

Figure 6. Tensile stress-strain curve of the 74 vol% composite at temperatures from 0°C to 100°C

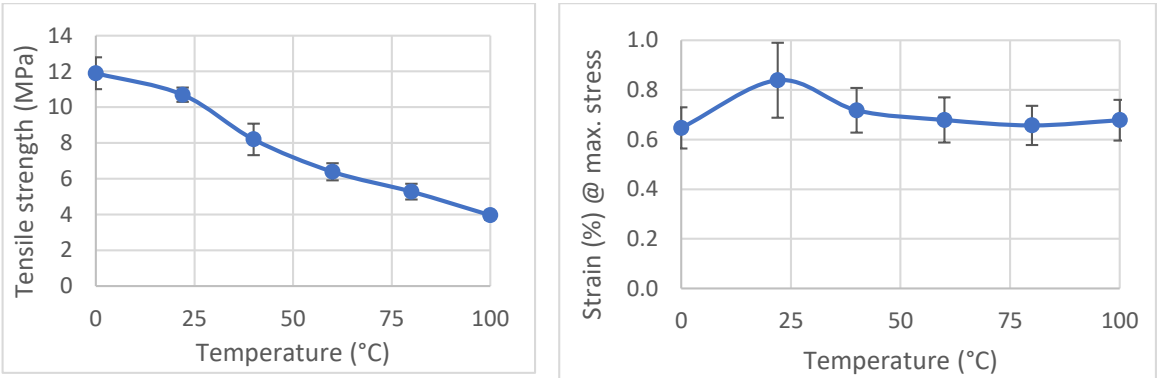

(a) (b)

Figure 7. (a) Tensile strength and (b)strain at maximum stress for 74 vol% in uniaxial tension from 0°C to 100°C

7. Conclusion

In this work, low-porosity SMCs composed of ferrite particles inside a polyurethane matrix were manufactured using compression moulding to a maximum volume fraction of 81%. An investigation was conducted into the trade-off between magnetic and mechanical performance with increasing ferrite volume fraction. Strain-at-maximum stress was approximately proportional to the inverse of volume fraction, however, a 0.66% bending strain at 81 vol% was still a significant improvement over that of ferrite. Meanwhile, magnetic permeability, strength and thermal conductivity all increased with volume fraction. A notable plateau of all properties was observed between 75 and 81 vol%, indicating the processing limit of this particular material system. Just below the processing limit, at 75 vol%, high magnetic permeability, strength and

thermal conductivity was obtained, while still having 20 times the strain of ferrite. Thus, that volume fraction was chosen for further mechanical characterization across the operating temperatures of the charging pad. A predictable softening and linear decrease in tensile strength was observed with increasing temperature, while no notable change was observed in strain at maximum stress. This stability of its mechanical performance is ideal because it allows for accurate prediction of the structural reliability of the magnetic core during in-road use.

8. References

[1] F. Chen, N. Taylor, and N. Kringos, "Electrification of roads: Opportunities and challenges," *Appl. Energy*, vol. 150, pp. 109–119, 2015.

[2] M. Amirpour, S. Kim, M. P. Battley, P. Kelly, S. Bickerton, and G. Covic, "Coupled electromagnetic-thermal analysis of roadway inductive power transfer pads within a model pavement," *Appl. Therm. Eng.*, vol. 189, no. February, p. 116710, 2021.

[3] G. A. Covic and J. T. Boys, "Modern trends in inductive power transfer for transportation applications," *IEEE J. Emerg. Sel. Top. Power Electron.*, vol. 1, no. 1, pp. 28–41, 2013.

[4] J. Li *et al.*, "The preparation and magnetic performance of the iron-based soft magnetic composites with the Fe@Fe3O4 powder of in situ surface oxidation," *J. Magn. Magn. Mater.*, vol. 454, pp. 103–109, 2018.

[5] K. J. Sunday and M. L. Taheri, "NiZnCu-ferrite coated iron powder for soft magnetic composite applications," *J. Magn. Magn. Mater.*, vol. 463, no. May, pp. 1–6, 2018.

[6] H. Shokrollahi and K. Janghorban, "The effect of compaction parameters and particle size on magnetic properties of iron-based alloys used in soft magnetic composites," *Mater. Sci. Eng. B Solid-State Mater. Adv. Technol.*, vol. 134, no. 1, pp. 41–43, 2006.

[7] M. Anhalt and B. Weidenfeller, "Magnetic properties of polymer bonded soft magnetic particles for various filler fractions," *J. Appl. Phys.*, vol. 101, no. 2, 2007.

[8] R. Mark and W. N. Findley, "Nonlinear Creep of Polyurethane Under Combined Stresses and Elevated Temperature.," *Trans Soc Rheol*, vol. 18, no. 4, pp. 563–582, 1974.

[9] M. M. Khotbehsara *et al.*, "Effect of elevated in-service temperature on the mechanical properties and microstructure of particulate-filled epoxy polymers," *Polym. Degrad. Stab.*, vol. 170, p. 108994, 2019.

[10] Y. cui, J. E. Campbell, M. burley, M. patel, K. hunt, and T. W. Clyne, "Effects of temperature and filler content on the creep behaviour of a polyurethane rubber," *Mech. Mater.*, vol. 148, no. February, 2020.

[11] W. J. Trompetter *et al.*, "Investigation of New Zealand's natural magnetic minerals for application in inroad charging systems," *Int. J. Mod. Phys. B*, vol. 34, no. 01n03, p. 2040018, Jan. 2020.

[12] U. Yilmazer and R. J. Farris, "Mechanical behavior and dilatation of particulate-filled thermosets in the rubbery state," *J. Appl. Polym. Sci.*, vol. 28, no. 11, pp. 3369–3386, 1983.

[13] D. P. H. Hasselman, K. Y. Donaldson, and A. L. Geiger, "Effect of Reinforcement Particle Size on the Thermal Conductivity of a Particulate-Silicon Carbide-Reinforced Aluminum Matrix Composite," *J. Am. Ceram. Soc.*, vol. 75, no. 11, pp. 3137–3140, Nov. 1992.

[14] Y. Y. Zheng, Y. G. Wang, and G. T. Xia, "Amorphous soft magnetic composite-cores with various orientations of the powder-flakes," *J. Magn. Magn. Mater.*, vol. 396, pp. 97–101, 2015.

[15] P. Y. Huang, Z. S. Guo, and J. M. Feng, "General Model of Temperature-dependent Modulus and Yield Strength of Thermoplastic Polymers," *Chinese J. Polym. Sci. (English Ed.*, vol. 38, no. 4, pp. 382–393, 2020.

THERMOELECTRIC 0D/1D CEMENT COMPOSITES FOR FUTURE LARGE-SCALE THERMAL ENERGY HARVESTING

Ioanna Vareli[a], Aikaterini Gkaravela[a], Alkiviadis S. Paipetis[a], Nektaria-Marianthi Barkoula[a]

a: Department of Materials Science & Engineering, University of Ioannina, Ioannina, Greece – i.vareli@uoi.gr

Abstract: *This study reports on the utilization of carbon materials as nanoadditives in a cementitious matrix, resulting into a new class of functional cementitious nanocomposites for waste energy harvesting. Here, single wall carbon nanotubes (SWCNTs) and nano-Carbon Black (nCB) with inherent positive (p-type) semiconductor characteristics were introduced into the cementitious matrix while the Seebeck coefficient (S) and Power Factor (PF) for different SWCNT/nCB loadings were determined at the 28th day of the cement hydration. Cementitious nanocomposites with 0.5 wt.% loading of SWCNT and 0.25 wt.% loading of nCB exhibited the highest performance in terms of S (+1780 μV/K) and PF (5.05×10³ μW/mK²), with the PF being the highest amongst other carbon nanoadditive-based cement thermoelectric nanocomposites to date. These materials can be further used for the fabrication of a thermoelectric generator (TEG) device.*

Keywords: Cement-based nanocomposites ; thermal energy harvesting ; green construction ; sustainable buildings ; carbon black, CNTs

1. Introduction

Sustainable development is one of the most substantial challenges of the 21st century. For this reason, the global community has set 17 goals to open the way towards a more sustainable future for next generations. Among these 17 goals, the 7th goal is to guarantee access to affordable, reliable, and sustainable energy. In this direction, thermoelectric materials appear as an ideal candidate for harvesting the wasted heat energy paving the way towards an efficient sustainable outcome [1].

Heat energy, among all different types of wasted energy is the most abundant, existing almost everywhere. Thermoelectric devices can convert thermal energy into electricity via the well-known Seebeck effect, illustrated by the Seebeck coefficient (S), or thermoelectric power (TEP), which is the direct conversion of thermal to electrical energy [2]. The Seebeck coefficient, in units of μV/K, is expressed by the following equation (Eq. 1):

$$S = {}^{\Delta V}/_{\Delta T} \qquad (1)$$

Where V_{OC}, in μV is the open circuit potential or the generated thermovoltage per unit temperature difference (ΔT, in K) between a hot and cold point.

The Seebeck coefficient is positive for p-type and negative for n-type semiconductors. Furthermore, the power factor is another important entity, commonly used for the comparison of TE materials' efficiency and is given by the following equation (Eq. 2):

$$(PF = \sigma \times S^2) \quad (2)$$

  doi:10.5075/epfl-298799_978-2-9701614-0-0

Where *PF* is the power factor, in units of W/mK^2 and σ is the conductivity in units of S/m.

Till now, in the thermo-electric (TE) society, inorganic low band-gap semiconductors such as Bi_2Te_3 [3], have been used for thermoelectric generator (TEG) devices however, their extensive application is obstructed by their relative high cost, and the fact that they consist of rare and toxic elements, etc. [4]. Recently, low-dimensional functional carbon nanomaterials such as graphene [5], nano carbon black (nCB) [6] and carbon nanotubes (CNTs) [7], have also been proposed as potential TE materials due to their excellent carrier conducting properties. Great TE power factors were estimated in single-walled carbon nanotubes (SWCNTs) and graphene [8], both experimentally and theoretically, but a big challenge in the enhancement of TE performance of carbon-based TE materials is the overall interdependence of the TE properties (for example, the Seebeck coefficient decreases while increasing electrical conductivity, whereas the overall thermal conductivity increases with improved electrical conductivity).

Concrete and other cement-based composites are the most used materials for construction and buildings as they have a variety of attributes, such as versatility, durability, and availability. Advanced energy efficiency in construction is a crucial feature determining human induced emissions worldwide, while modern materials with advanced large-scale ambient thermal energy harvesting capabilities have been in the spotlight of the applied energy research. Thermal energy harvesting in buildings suggests a new strategy towards the reduction of human-activity's energy emissions. The thermal energy loss can be likewise captured and converted into electricity by thermoelectric cement composites which could be constructed as coatings on exterior walls of existing building [9].

The thermoelectric effect in cement-based materials was firstly introduced by Sun et al. in 1998 in cement paste with short carbon fibers [10] whereas the use of conductive carbon nanomaterials in cementitious matrices has received an explosive interest over the past years [11]. For instance, cementitious nanocomposites with p- and n- type CNTs have shown amongst others enhanced mechanical properties, variable electrical conductivity (σ), piezoresistive strain sensor property, as well as thermoelectric functionality as recently reported [12]. However, the final properties of the cement composites are highly dependent on the possible alignment and level of carbon materials dispersion in the cementitious matrix.

In the study at hand, two types of carbon-based nano materials, namely nCB and SWCNTS, were introduced into cement matrix, while the Seebeck coefficient (S), electrical conductivity (σ), and power factor (PF) were defined. The SWCNTs content was kept constant at 0.5 wt. % by cement's mass, while the influence of nCB content on the thermoelectric properties of the cement / nanocomposites at an age of 28 days was examined. All nano-modified cementitious composites exhibited a p-type semiconductor behavior. Due to their excellent electrical properties SWCNT/nCB fillers, are potential candidates for smart and multifunctional cement-based materials. Indeed, this study demonstrates, that the 0D nCB and the 1D SWCNTs provide a synergistic combination effect resulting in enhanced TE response, which cannot be otherwise obtained by adding alone nCB or SWCNTs.

2. Experimental

2.1 Materials

  doi:10.5075/epfl-298799_978-2-9701614-0-0

SWCNTs in the form of powder were provided by OCSiAl (TUBALL, carbon content: >85 wt.%, mean diameter of 1.8±0.4 nm, length> 5 μm, metal impurities <15 wt.%). SDBS (Sodium dodecylbenzene sulfonate) was purchased from Sigma Aldrich. nCB with particle size of 60-70nm and surface area of 254 m^2/g was purchased from Nanocyl SA. Ordinary Portland cement (OPC) CEM I 42.5R has been provided by TITAN S.A. GREECE. Deionized water was used to prepare all nanocomposites in this study.

2.2 Preparation of cement-SWCNT/nCB paste and nanocomposite specimens

To ensure adequate dispersion of SWCNTs in DI water, SDBS, an anionic surfactant was employed. The stock solution/dispersions contained predetermined amount of nCB 0.25 wt.% and 1.0 wt.% by weight of cement, while the ratio of SWCNT/SDBS was kept constant at 1:1. Based on a previous work, the addition of 0.5 wt.% SWCNT in the cementitious paste results in optimized electrical and thermoelectrical properties [13]. Thus, in this study 0.5 wt.% SWCNT is used in the preparation of the two different 0D/1D cement nanocomposites. Ultrasonication was performed for 60 min at 25% (~8kJ) using the UP400S tip-ultrasonic probe processor (Hielscher Ultrasonics). Cementitious nanocomposites were prepared by mixing the SWCNT/nCB dispersions with cement at a water-to-cement ratio (w/c) of 0.5.

All cement composites were prepared by a standard mixing procedure using an IKA® EUROSTAR control 200P4 equipped with an R1381 propeller stirrer. The SWCNT/nCB dispersions were introduced in a plastic container and the cement powder was added gradually during mixing at 320 rpm. After 5 min of total mixing time, the homogenous slurry was casted in 10x10x60 mm^3 oiled steel moulds. The specimens were subsequently sealed in a plastic bag at 23-25 °C until testing. For electrical and thermoelectric measurements, the samples were measured at an age of 28 days. The samples are denoted according to their nanofiller content; for instance, the cement-SWCNT/nCB nanocomposite, which contains SWCNT at 0.5 wt.% and nCB at 1.0 wt.% will be denoted as cement-SWCNT(0.5)/nCB(1.0). For comparison reasons, the current study also presents data for cement-based composites with 0.5 wt.% SWCNTS (designated as cement-SWCNT(0.5)) taken from a previous study [13].

2.3 Characterization techniques

A typical 4-probe technique using a commercial four-point probe system (Ossila Ltd.) was employed for the determination of the electrical conductivity (σ) of the cement-SWCNT/nCB nanocomposites, based on the formula:

$$\sigma = {}^{1}/_{R_s} \times {}^{L}/_{S} \times \left({}^{ln2}/_{\pi}\right) \quad (3),$$

where Rs is the measured 4-probe sheet resistance (Ohm per square), L is the length (m) and S is the cross-section (m^2) of each sample.

For measuring the sheet resistance (Rs) of the cement-based nanocomposites, silver paste was deposited between the material's surface and the probes of the employed four-point probe system to improve their physicochemical contact and increase the accuracy of the measurement.

The Seebeck coefficient of the cement-SWCNT/nCB nanocomposites (specimen dimensions: 10×10×30 mm^3) was determined using a custom-made set-up. To enable the generation of a

temperature gradient, all the samples were mounted on two metal blocks. For every measurement, the one block was kept at room temperature (T_{cold}, at 25 °C), while the other block (T_{hot}) was heated up via calibrated temperature-controlled resistors, allowing the generation of temperature difference (ΔT). For the thermoelectrically driven voltage measurement, Ag wires were wrapped around the two end-point perimeter of the samples. Silver paste was also applied between the Ag wire and the sample surface to minimize and plausible contact resistance. The Ag wires were connected to an Agilent 34401A 6½ digital multimeter to measure the generated thermovoltage (ΔV). The Seebeck coefficient (S) was derived then from the $\Delta V/\Delta T$ ratio (see equation 1).

Fig. 1 shows schematically the process towards the development of SWNT/nCB dispersions (Fig. 1a), and the mechanical mixing of the p-type SWCNT dispersion, and cement towards the fabrication of 10×10×60 mm^3 cement-SWCNT/nCB nanocomposites (Fig. 1b). Samples of cement-SWCNT/nCB nanocomposites (10×10×30 mm^3) with Ag contacts deposited at the ends of each specimen were used for the S measurements.

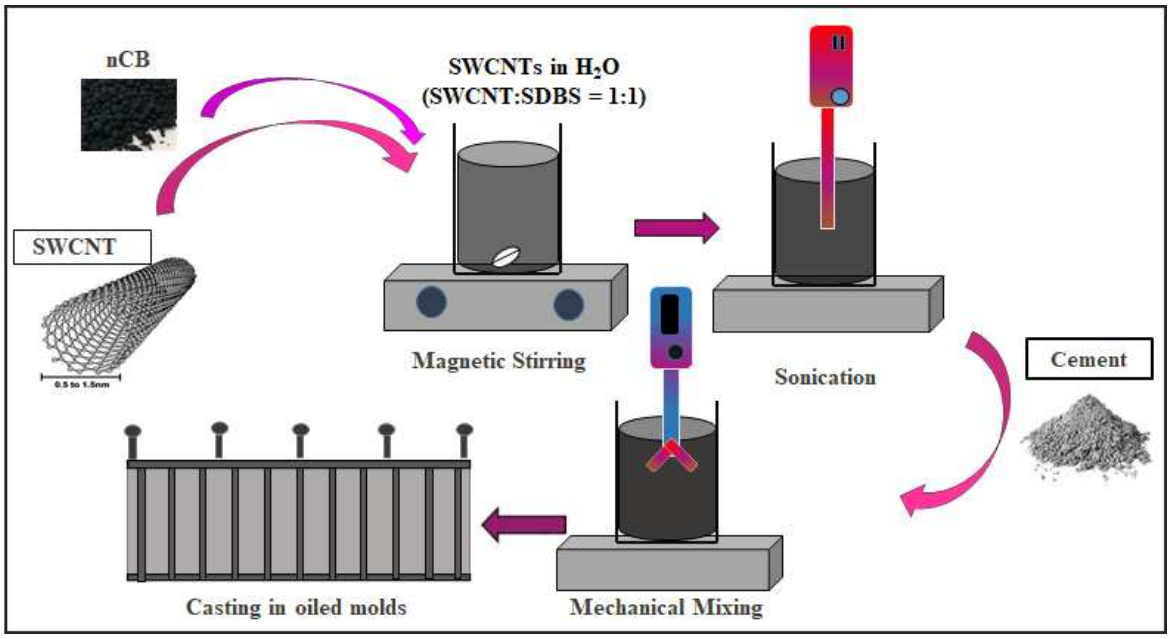

Figure 1. Schematic representation of the process towards the preparation of SWCNT/nCB solution/dispersion and the fabrication of cement-SWCNT/nCB composites i.e., mechanical mixing of the p-type SWCNT/nCB dispersion and cement followed by casting resulting in 10×10×60 mm^3.

3. Results and Discussion

3.1 Electrical and Thermoelectrical properties of cement-SWCNT/nCB

Figures 2a and 2b indicate the S and the calculated PF together with the corresponding standard deviation values for the 0D/1D nanocomposites at 28 days. The positive sign of the S suggests that the cement nanocomposites are, in analogy to solid state semiconductors, p-type semiconductors, meaning the cations thermodiffuse easier than the anions along with the prevalence of holes over electrons as the major electronic charge carriers. An extremely high Seebeck coefficient can be observed at low doping level of nCB in the 0D/1D nanocomposites.

The Seebeck coefficient in cement nanocomposites enhanced with carbon nanomaterials, derive from a superposition of the thermo-diffusion of electronic charge carriers (holes and electrons) and the diffusion of ions (anions and cations). Holes, in our case, reach the contacts and are capable of further surpassing the contact to an external circuit while the ions tend to accumulate to the contacts. Therefore, the potential is high due to both the holes and the ions.

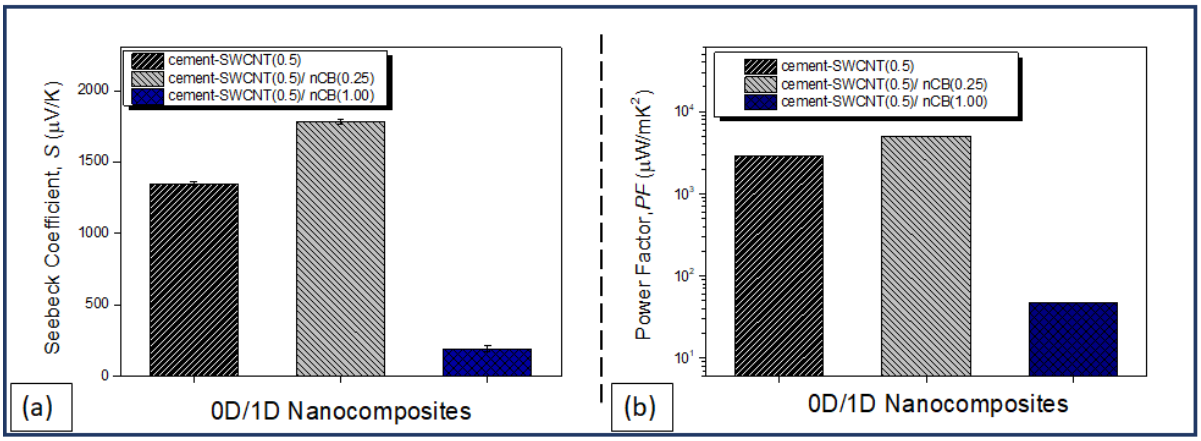

Figure 2. Thermoelectric properties (a) S and (b) PF of cement-SWCNT/nCB nanocomposites with three different nanofiller loadings at 28 days. Data for cement-SWCNT(0.5) were taken from a previous study [13].

A possible explanation of the enhanced TE response obtained here can be given via the energy filtering induced by the defects that exist in the cement nanocomposites or by the different Fermi levels in the 0D/1D electronic materials when in contact. When the percentage of the nCB surpasses the one of the SWCNT, instead of advancing the electrical conductivity, nCB acts as a barrier, interrupting the conductive network, thus the TE properties appeared decreased. Table 1 reviews indicative studies from the existing literature on the thermoelectric properties of cement based composite reinforced with carbon materials.

Table 1: Summary of the Seebeck coefficient for cement based composites with carbon and metallic inclusions.

Materials	Concentration(wt.%)	S (μV/K)	Ref
Carbon Fibers	2.0	+5.5	[14]
Expanded Graphite	15	-54.5	[15]
Fe_2O_3	5.0	+2500	[16]
SWCNT/nCB (This study)	**0.5 /0.25**	**+1780**	

In conductive cement nanocomposites with carbon-based nanofillers, the experimentally measured electrical conductivity has a contribution both from the electrons (electronics charge carriers), as well as ions (ionic charge carriers) in a mixed electrical transport carrier transport mechanism. During the first days of the cement hydration ionic conductivity is dominant due to the high amount of available water. As the hydration of cement proceeds free pore water

  doi:10.5075/epfl-298799_978-2-9701614-0-0

decreases, and the electrical conductivity is promoted due to the contribution of the electronic charge carriers. In addition, as cementitious crystals nucleate, they repel the electrostatically self-assembled SWCNT/nCB to the boundaries developing an enhanced conductive network. The self-assemblance of the SWCNT/nCB conductive network is depicted in Figure 3.

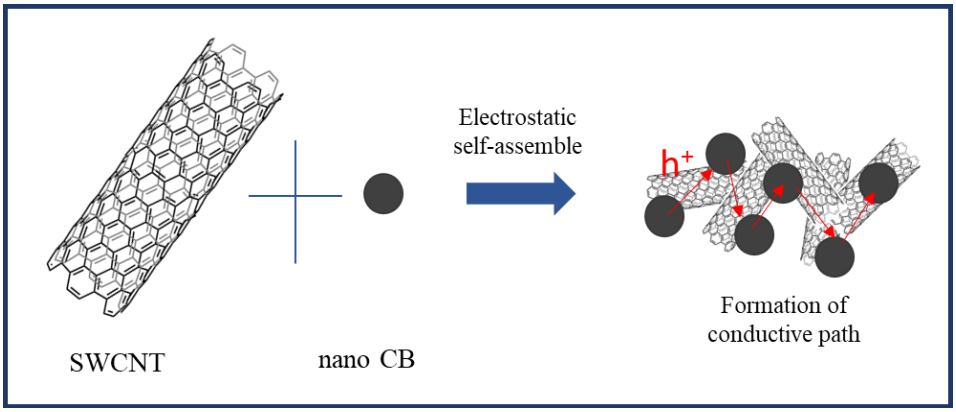

Figure 3. Evolution of the conductive path in the 0D/1D thermoelectric cement nanocomposites.

As observed, the 0D/1D cement nanocomposites developed in this study, are promising for the fabrication of a cementitious thermoelectric generation device (TEG).

4. Conclusion

0D/1D cement nanocomposites with p-type thermoelectric characteristics were evaluated with respect to their potential use as thermoelectric materials for energy harvesting applications. Cement-SWCNT/nCB nanocomposites demonstrate exceptionally high values of Seebeck coefficient (+1780 μV/K) and power factor (5.05×10^3 μW/mK^2) at a single thermoelement level compared to other carbon-based cement nanocomposites found in the literature. It is expected that this work will give rise to more in-depth understanding to the TE properties of these materials.

Acknowledgements

This research has been co-financed by the European Union and Greek national funds through the Operational Program Competitiveness, Entrepreneurship, and Innovation, under the call RESEARCH-CREATE-INNOVATE (HICOTEG-T1EDK-03482).

5. References

1. Caballero-Calero O, Ares JR, Martín-González M. Environmentally Friendly Thermoelectric Materials: High Performance from Inorganic Components with Low Toxicity and Abundance in the Earth. Adv Sustain Syst. 2021 Nov 1 ; 5(11):2100095.
2. Vineis CJ, Shakouri A, Majumdar A, Kanatzidis MG. Nanostructured Thermoelectrics: Big Efficiency Gains from Small Features. Adv Mater. 2010 Sep 22; 22(36):3970–80.
3. Kanatzidis MG. Nanostructured thermoelectrics: The new paradigm? Vol. 22, Chemistry of Materials. 2010. p. 648–59.

  doi:10.5075/epfl-298799_978-2-9701614-0-0

4. Freer R, Powell A V. Realising the potential of thermoelectric technology: a Roadmap. J Mater Chem C. 2020 Jan 2; 8(2):441–63.
5. Liu C, Huang X, Wu YY, Deng X, Liu J, Zheng Z, et al. Review on the research progress of cement-based and geopolymer materials modified by graphene and graphene oxide. Nanotechnol Rev. 2020 Jan 1; 9(1):155–69.
6. Han J, Wang D, Zhang P. Effect of nano and micro conductive materials on conductive properties of carbon fiber reinforced concrete. Nanotechnol Rev. 2020 Jan 1; 9(1):445–54.
7. Mendoza Reales OA, Dias Toledo Filho R. A review on the chemical, mechanical and microstructural characterization of carbon nanotubes-cement based composites. Vol. 154, Construction and Building Materials. Elsevier Ltd; 2017. p. 697–710.
8. Yun J-S, Choi S, Im SH. Advances in carbon-based thermoelectric materials for high-performance, flexible thermoelectric devices. Carbon Energy. 2021; p. 1–42.
9. Ghosh S, Harish S, Ohtaki M, Saha BB. Enhanced figure of merit of cement composites with graphene and ZnO nanoinclusions for efficient energy harvesting in buildings. Energy. 2020 May 1; 198.
10. Sun M, Li Z, Mao Q, Shen D. Thermoelectric percolation phenomena in carbon fiber-reinforced concrete. Cem Concr Res. 1998 Dec 1; 28(12):1707–12.
11. Li W, Dong W, Guo Y, Wang K, Shah SP. Advances in smart/functional cementitious composites incorporating various carbon nanomaterials. Cem Concr Compos. 2022 Feb 20; 104454.
12. Tzounis L, Liebscher M, Fuge R, Leonhardt A, Mechtcherine V. P- and n-type thermoelectric cement composites with CVD grown p- and n-doped carbon nanotubes: Demonstration of a structural thermoelectric generator. Energy Build. 2019 May 15; 191:151–63.
13. Vareli I, Tzounis L, Tsirka K, Kavvadias IE, Tsongas K, Liebscher M, et al. High-performance cement/SWCNT thermoelectric nanocomposites and a structural thermoelectric generator device towards large-scale thermal energy harvesting. J Mater Chem C. 2021 Oct 28; 9(40):14421–38.
14. Sun M, Li Z, Mao Q, Shen D, Thermoelectric percolation phenomena in carbon fiber-reinforced concrete. Cem. Concr. Res. 1998 December 28; 1707–1712.
15. Wei J, Zhao L, Zhang Q, Nie Z, Hao L. Enhanced thermoelectric properties of cement-based composites with expanded graphite for climate adaptation and large-scale energy harvesting. Energy Build. 2018 Jan 15; 66-74.
16. Ghosh S, Harish S, Ohtaki M, Saha BB. Thermoelectric figure of merit enhancement in cement composites with graphene and transition metal oxides. Mater Today Energy. 2020 Dec 1;18.

  doi:10.5075/epfl-298799_978-2-9701614-0-0

Evaluating viscoelastic shear properties in clear wood via off-axis compression testing and digital image correlation

Rhodel Bengtsson, Reza Afshar, Mahmoud Mousavi and E. Kristofer Gamstedt

Department of Materials Science and Engineering, Division of Applied Mechanics
Uppsala University (UU), rhodel.bengtsson@angstrom.uu.se

Abstract: *Anisotropic materials like wood and unidirectional polymer composite structures are sensitive to shear deformations, in particular close to joints. Large wooden structures in buildings and e.g. wind turbine blades are designed to last for decades, and hence susceptible to unwanted creep deformations. For improved structural design, the shear creep properties of the material are needed. These are rarely available in the literature, maybe because of technical difficulties to achieve a well-defined shear stress state in test specimens. For cost-efficient testing this goal of a pure stress state necessarily needs to be compromised. In the present study, we propose a simple test method based on uniaxial compression on wooden cubes, but equally applicable for fibre composites. The viscoelastic shear properties of Norway spruce (Picea abies) under off-axis creep compression tests are characterized. The tests are performed in a controlled climate chamber and the creep strains are captured using digital image correlation.*

Keywords: Viscoelasticity; Experiment; Shear Creep; Wood; Composites

Introduction

Since prehistoric times, wood has been used as a building material due to its unrivalled properties and abundance. It is still considered as an excellent building material due to its high stiffness to weight ratio, flexibility and damage tolerance. Recently, wood is seeing a renaissance as a renewable and sustainable building material, where characterising its structural properties is important.

Large wooden structures in buildings and e.g. wind turbine blades are designed to last for decades, and hence susceptible to unwanted creep deformations [1,2]. For improved structural design, the shear creep properties of the material are needed.

Wood can be considered as an orthotropic material with three material directions: longitudinal (L), radial (R) and tangential (T). There has been numerous research on the static and time-dependent behaviour of wood in the normal directions i.e. the L-, T-and R-directions [3]. A methodology to find the normal creep properties of wood was developed using small cubic samples under compression in [4]. However, despite the importance of knowing the full three-dimensional behaviour of materials, the time-dependent shear behaviour of wood in the different planes i.e. LT, LR and RT are rarely available in literature.

Shear testing of materials often leads to challenges with experimental setup and test performance. In principle, it is inevitable that both normal and shear stresses exist in the material plane being tested. It is therefore very difficult to perform a, so called, "pure shear test".

To the knowledge of the authors, there have only been two studies on the shear creep behaviour of wood. In [5], plate shear tests were made according to the ASTM Designation D 805-63

  doi:10.5075/epfl-298799_978-2-9701614-0-0

standard, which were extended into a creep test. The experiments were done with Douglas fir wood in a constant climate room with 50% relative humidity (RH) and 22 C. The shear creep compliances were later obtained by using the deflection in relation to the point loads on the plate samples. In [6], an off-axis tensile test was extended into a creep test. Rectangular specimens with fibres oriented at a certain angle with respect to the applied load, were subjected to a constant tensile load. The creep strains were obtained using strain gauges and post-processed to get the shear creep compliance using well-known tensor transformation laws. Similarly to [5], the experiments of [6] were also performed in a constant climate at 25 C and 30% RH.

Due to the extremely scarce data on the time-dependent shear behaviour of wood, it is hard to cross-verify the aforementioned methods described above. Additionally, there are plenty of numerical works in literature regarding linear viscoelasticity in wooden structures that estimates the shear creep behaviour via various assumptions or simplifications, resulting into possible errors outputted from their numerical models. Thus, there is a need of adding more experimental shear creep data (in LR, LT and RT) and methodologies for various wood species.

In the present study, we propose a simple test set up based on uniaxial compression on wooden cubes. We use the same experimental setup used in [2], as shown in Fig. 2, in a constant climate chamber to perform our shear creep experiments. Similarly, to the off-axis tests in [6], the wooden cube samples have the radial direction oriented at a given angle with respect to the applied compression load, allowing us to use transformation laws to determine the shear creep compliance in the RT-plane, J_{RT}. The extension of this method to the other planes LR and LT requires only modifications of the material orientation in the wooden cubes. Therefore, this method can be generalized to determine the other shear creep compliances, J_{LR} and J_{LT}. Unlike [6], we use digital image correlation (DIC) to determine the creep strains as well as providing shear creep compliance in the RT-plane, which has not been available in literature to the knowledge of the authors before.

Method

The methodology of this study is as follows: A cubic specimen of Norway Spruce (15mm x 15mm x 15 mm) with material directions orientated such as in Fig. 1, is provided.

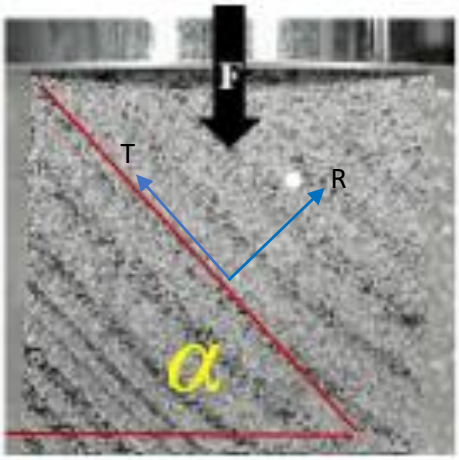

Figure 1: RT plane of a wooden sample loaded with a compression force F.

The cube sample is then inserted into the setup shown in Fig. 2. The setup itself is contained inside a climate chamber with a constant temperature of 24 C and 65% RH. Knowing the weights in the far ends of the experimental setup, the compression load in Fig. 1 can be calculated using force and moment equilibrium equations described in [2].

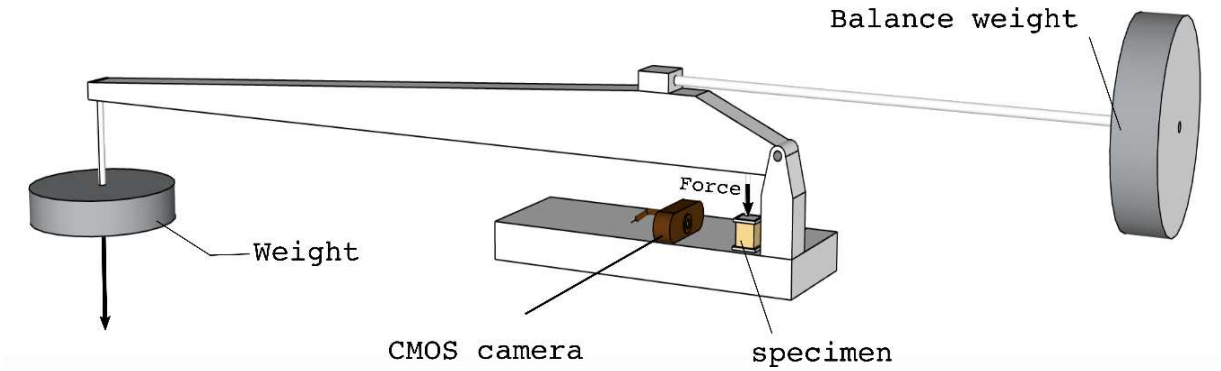

Figure 2: Experimental setup for creep test on wooden cube samples. Designed by Vorobyev et al [3].

Images of the surface with the RT-plane are continuously taken with 30-minute intervals in a 20-hour period with the camera as seen in Fig. 2. The global strain fields (ε_x, ε_y and ε_{xy}) of the surface are later provided by NCORR, an open source DIC software [7]. Note that global y-coordinate system is parallel to the compression force, the x-coordinate is along the width of the cube specimen, and z-coordinate is parallel to the L-direction which is normal to the RT-plane. Due to the inhomogeneity of wood, the strains will not be homogenous on the surface as seen in Fig. 3. To simplify the post-processing of obtaining the material properties, the strain fields are averaged and further mentions of strains in the text will be referred as the average equivalence.

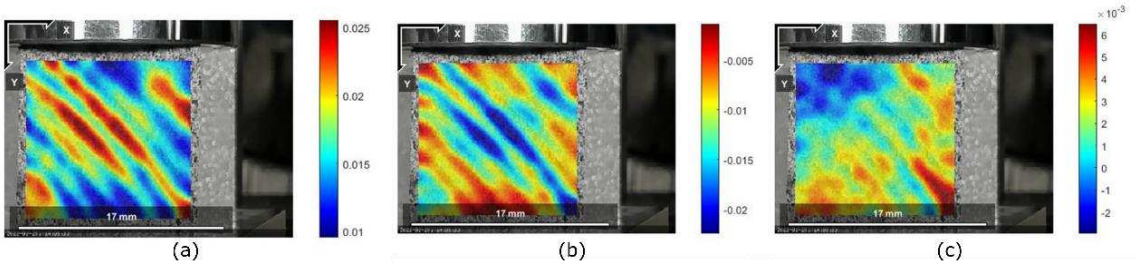

Figure 3: Strain fields ε_x (a), ε_{xy} (b) and ε_y (c) on one of the samples at the end of the creep test. The strains are obtained by post-processing the images using NCORR [7].

Since the compressive force and the area of the surface it is applied onto are known, the compressive stress σ_y is readily available and assumed to be homogenous throughout the specimen.

Knowing the global stress and strains of our specimen, the tensor fields according to the LTR-coordinate system are obtained by the following well-known transformation equations:

$$\varepsilon_{RT} = (\varepsilon_x - \varepsilon_y) sin\alpha \cos a + \varepsilon_{xy} \cos 2\,\alpha \quad (1)$$

$$\sigma_{RT} = (\sigma_x - \sigma_y) sin\alpha \cos a + \sigma_{xy} \cos 2\,\alpha \quad (2)$$

  doi:10.5075/epfl-298799_978-2-9701614-0-0

The relation between the evolution of creep strain and constant load is described by the constitutive equation:

$$\varepsilon(t) = J(t)\sigma_0 \quad (3)$$

In our case, ε(t) is our shear creep strains ε_{RT}, J(t) is shear creep compliance J_{TR} and σ_0 is our constant compressive stress σ_y.

Using Eq. (1) and Eq. (2), allow us to solve Eq. (3) for J(t).

Results and Discussion

Six samples were prepared and tested with their creep compliances J_{TR} presented in Fig. 4. Using sample 6 as the median curve, there is a consistent variation of 15% throughout the whole test duration for all samples. This variation is expected since wood is a natural composite, where the composition of constituents inside one sample may differ to another.

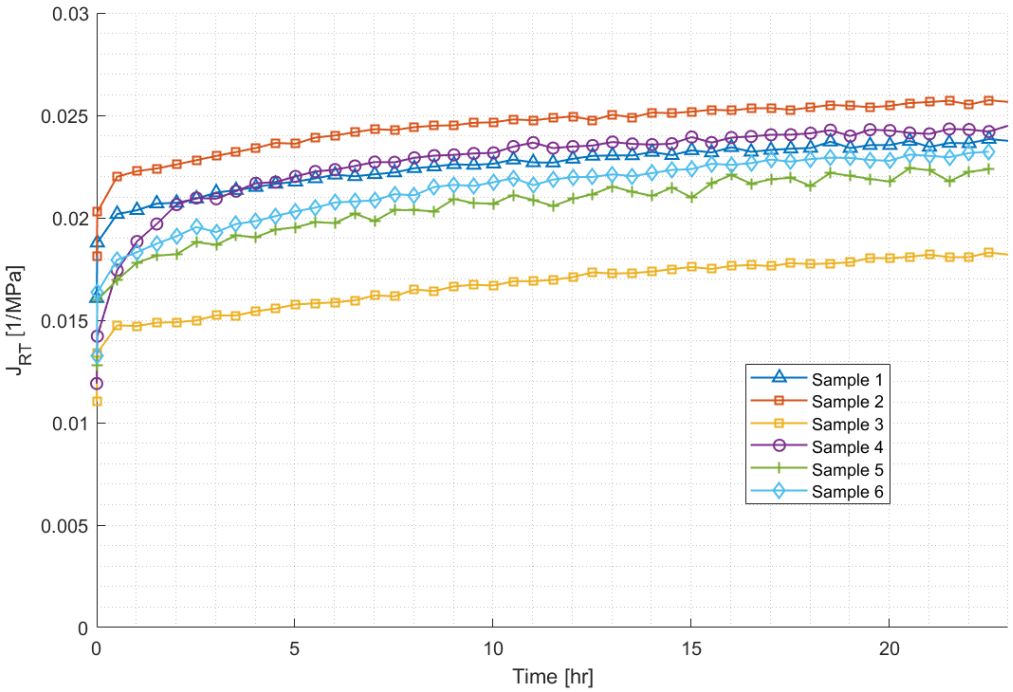

Figure 4: The resulting creep compliances from six different samples of Norway Spruce.

Since the shear creep compliance in the RT-plane for Norway Spruce are not available in literature, it is not possible to fully verify the curves in Fig. 4 as they are the first of its kind presented. However, we obtained the elastic shear modulus G_{RT} for our samples as we have the initial strain fields and compared them to literature values [8,9] for Norway Spruce. The shear modulus values are presented in Table 1.

Table 1: *Shear modulus values obtained at t=0 for all samples 1-6. Literature values ranges from 53-90 MPa for Norway Spruce using various methods under different climate conditions.*

	Sample 1	Sample 2	Sample 3	Sample 4	Sample 5	Sample 6	Average	Literature Values [8,9]
G_{RT} [MPa]	62.3	57.7	91.1	85.7	75.5	76.4	74.8	53-90

Using DIC and only obtaining the strain fields on the surface may produce some errors in the results as the field may not be consistent throughout the thickness of the specimen due to inhomogeneity as well as boundary effects of the specimen. One may suggest the using digital volume correlation to get the accurate description of the strain fields for the whole volume. This however will require far more equipment and larger data quantities to handle. A far simpler solution is to have thinner wood samples of which the plane stress assumption is appropriate, but further studies will need to be made to avoid the buckling phenomena from the current compression setup.

  doi:10.5075/epfl-298799_978-2-9701614-0-0

Concluding Remarks

The authors have presented a viable creep setup to obtain the shear creep compliance of wooden samples for the RT-plane by a uniaxial compression. No intricate test jigs or equipment are required for this method, as the setup only relies on the orientation of the material directions inside the wooden cube. Furthermore, the method can be generalized for the other planes LT and LR by simply modifying the orientation inside the wooden cube specimens. Albeit, the method was presented with using Norway Spruce, it is equally applicable for other types of tree species as well as other composite materials.

The J_{RT} curves for Norway such as presented in Fig. 4 have not been presented elsewhere to the knowledge of the authors, and hopefully can be verified by other types of shear creep methods developed in the future. The only kind of verification made so far are the comparison of the elastic shear modulus in Table 1, which are well within range of the values from literature.

References

1. Heinrichs TD, Naughton BT. Radar Friendly Blades. Sandia National Lab.(SNL-NM), Albuquerque, NM (United States); 2014 Mar 1.
2. Holzer SM, Loferski JR, Dillard DA. A review of creep in wood: concepts relevant to develop long-term behavior predictions for wood structures. Wood and Fiber Science. 1989;21(4):376-92.
3. Vorobyev A. Static and time-dependent mechanical behaviour of preserved archaeological wood: Case studies of the seventeenth century warship Vasa (Doctoral dissertation, Acta Universitatis Upsaliensis).
4. Afshar R, Cheylan M, Almkvist G, Ahlgren A, Gamstedt EK. Creep in oak material from the Vasa ship: verification of linear viscoelasticity and identification of stress thresholds. European Journal of Wood and Wood Products. 2020 Nov;78(6):1095-1
5. Schniewind AP, Barrett JD. Wood as a linear orthotropic viscoelastic material. Wood Science and Technology. 1972 Mar;6(1):43-57.
6. Hayashi K, Felix B, Le Govic C. Wood viscoelastic compliance determination with special attention to measurement problems. Materials and Structures. 1993 Jul;26(6):370-6.
7. Blaber J, Adair B, Antoniou A. Ncorr: open-source 2D digital image correlation matlab software. Experimental Mechanics. 2015 Jul;55(6):1105-22.
8. Ehrhart T, Brandner R. Rolling shear: Test configurations and properties of some European soft-and hardwood species. Engineering Structures. 2018 Oct 1;172:554-72.
9. Keunecke D, Sonderegger W, Pereteanu K, Lüthi T, Niemz P. Determination of Young's and shear moduli of common yew and Norway spruce by means of ultrasonic waves. Wood science and technology. 2007 Apr;41(4):309-27.

SELF-SENSING PROPERTIES OF DIFFERENT CARBON NANOMATERIAL BASED COMPOSITES FOR SUSTAINABLE INFRASTRUCTURES

İmirza Okay Altuntaş[a], Oğuzhan Öztürk[a], Alexander Kahnt[b], Christian Wagner[b], Robert Böhm[c]

[a]*Konya Technical University, Department of Civil Engineering, Konya, Turkey*

[b]*HTWK Leipzig, Faculty of Civil Engineering, Leipzig, Germany*

[c]*HTWK Leipzig, Faculty of Engineering, Leipzig, Germany, robert.boehm@htwk-leipzig.de*

Abstract: *Recently, various studies have focused on the cement-based composites doped with carbon-based materials to provide non-structural functional properties without compromising engineering properties. Some of the most important non-structural functional properties are self-sensing performance of cement-based composites, such as damage, strain, structural vibration, and durability monitoring. Generally, the term attained as "self-sensing" is related to the function of cement-based material to exhibit its piezoresistive ability. Accordingly, self-sensing capability of the cement-based composites can be attained and structural or/and material health monitoring can be provided without the need external integrated. In this study, the mixtures of cement-based composites functionalized with self-sensing ability was addressed. The paper focuses on the production techniques, engineering performance and multifunctionality properties of small-size specimens to large-scale trial specimens. Challenges of the current methods as sensory materials are also discussed together with other cement-free composites.*

Keywords: Carbon-based materials; Multifunctionality; Self-sensing; Structural Health Monitoring.

1. Introduction

Measurements obtained as a result of structural/material health monitoring are used by engineers in diagnosing structural problems and evaluating the inspection of damage. These applications are useful for the required repair activities and re-evaluation of the infrastructures' remaining service life through life cycle models. Structural/material health monitoring is used to mean the evaluation of the parameters that affect the properties of the materials and overall quality assurance and quality control of the infrastructure [1]. Continuous health monitoring of the infrastructures also provides more precise approaches for the design of new infrastructures. In summary, it is of great importance to constantly monitor the damages in concrete structures in order to reduce possible hazards in case of damages caused by mechanical loads, earthquake, wind, ocean wave, live loads and environmental loads. Examples of structure/material properties evaluated within the scope of structural/material health monitoring are parameters of strength, elastic modulus, strain, permeability, and the condition of reinforcement corrosion.

Structural health monitoring (SHM) covers a wide range of approaches such as strain gauges [2], optical fibers [3], impedance-based transducers [4], acoustic emission or electromagnetic

  doi:10.5075/epfl-298799_978-2-9701614-0-0

emission [5] and magnetoelastic sensor-based techniques [6]. Current approaches require SHM applications for entire infrastructures as it is sometimes challenging to evaluate the locations of damage. For this reason, research to develop the intrinsic structural element sensor function itself by modification of the electrical properties of the composite material is of great interest. A piezo-resistive behavior of cement-based composite materials was introduced a few decades ago [7]. In this regard, the "self-sensing" function of composites is attributed to the continuous change of relative electrical resistivity under strain change. However, a traditional cement-based matrix has a bulk electrical resistivity of around 10^1-10^5 Ωm [8] and requires a special mixture design by adding electrically conductive fillers to act as a piezo-resistive composite. These fillers are generally carbon-based materials such as carbon nanotubes (CNT) [9], carbon fibers [10], carbon black [11], or nanographenes [12]. Those carbon-based materials are not only expected to be used to tailor electrical properties but also contribute to improving mechanical and durability properties of cement-based composites. On the other hand, besides Portland cement (PC) based composites, non-cementitious composites having similar structural properties are started to grow in construction industry. For example, geopolymer-based composites having beneficial functions compared to ordinary PC-based composites are nowadays available in the construction market [13]. The production of geopolymers does not require the calcination of limestone in contrast to PC, thus a significant amount of released CO_2 (up to around 80 %) can be limited [14]. Recently, the structural properties and piezo-resistivity of geopolymer composites with carbon-based materials is investigated in several studies [15-17]. It has been suggested that geopolymer composites show better electrical properties compared to OPC-based materials. For example, the ionic conductivity of geopolymer composites is likely to sustain more piezo-resistive behavior as stated in the current studies [18]. The current paper deals with review of cement-based and cement-free structural composites having piezo-resistive behavior under strain change. The review initially addresses the effective distribution of conductive fillers into cementitious and geopolymer matrices. Then, the use of conductive fillers was undertaken in terms of mechanical compatibility and the minimum required filler ratio for the electrical performance. The paper also covers the self-sensing ability of structural composites under different levels of applied loads and environmental conditions together with large-scale production possibilities of such materials.

2. The use of carbon-based materials in the cement-based composites

2.1. Mixing procedure of the carbon-based fillers

Carbon-based materials are mostly used to improve the electrical properties of cement-based composites which are generally regarded as non-conductive composite material. Different micro or nano carbon filler materials significantly change the electrical properties of traditional cement-based materials, provided that they are used in appropriate mixing and optimum usage rates. However, besides the high costs of such micro and nanoscale carbon-based materials, there are two main parameters that are significantly influential in the electrical modification. For example, homogeneous mixing problems and bond properties between the matrix and the carbon-based material is of great interest for the reliable tailoring of electrical performance. The high surface area/volume ratios of such materials make them prone to pull each other under the influence of van der Waals forces and form agglomerates. For this reason, the distribution

and separation of such materials in both cement-based and geopolymer-based matrices is difficult [19]. In the case of a weak non-uniform dispersion, carbon-based particles create weak zones in the mixtures together with the inadequate electrical properties. This adversely affects the mechanical performance of cement/geopolymer based composites. Carbon-based materials (carbon nanotube, carbon black and nano graphene particles, carbon fiber) have been widely discussed in terms of type and size, and a wide knowledge has been gained [20]. For example, a mixing procedure was proposed in the collaborative studies of researchers for both small and large-scale specimens [10]. Although it comprises a slightly different mechanical stirring rate due to very high specific surface of carbon-nano tubes, the proposed mixing procedure (Figure 1) using with sodium hydroxide (NaOH) as a surfactant exhibited promising results in alkali-activated composites as well [15].

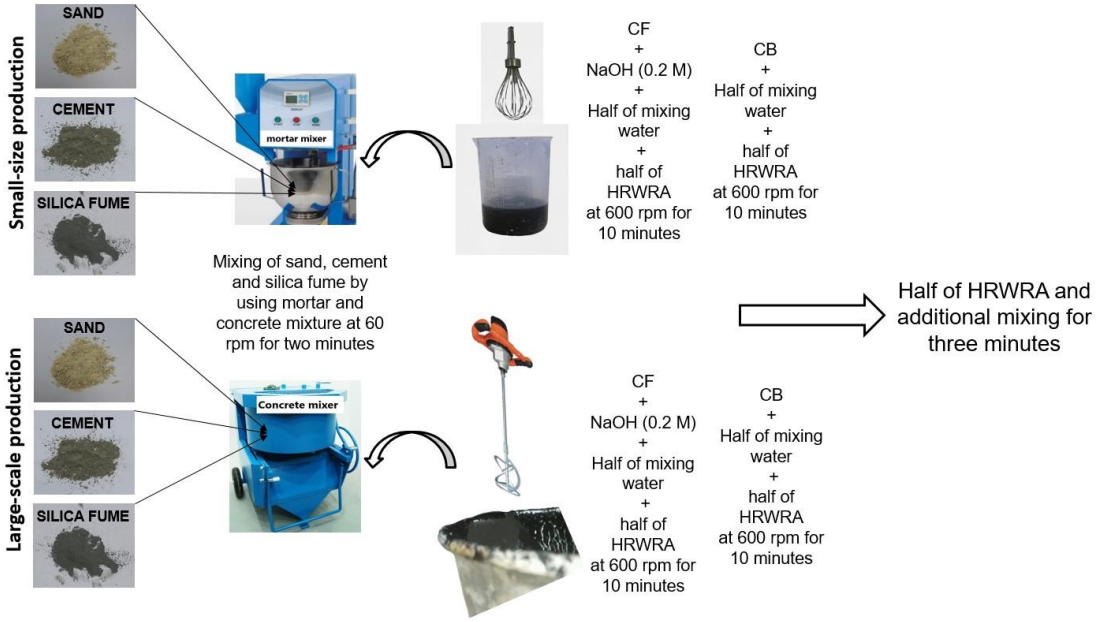

Figure 1. Different mixing methods for the small- and large-scale specimens

2.2. Measurement of self-sensing performance

Self-sensing ability of different cement-based composites is significantly improved with the addition of carbon-based fillers although the extent of improved piezo-resistivity was dependent on individual conductivity of the specimens [21]. On the other hand, self-sensing ability of cement-based composites are very related to the applied load and the tested configurations [22]. Accordingly, it can be suggested that configuration of the self-sensing tests should be decided according to the experimental design. Figure 2a-b presents the one of the examples of self-sensing test configurations under flexural and compressive loading conditions. Besides characteristics of cracks and capability of individual carbon-based materials in the piezoresistive behavior, the experimental configuration and electrical resistivity measurement device are also important factors together with the proposed loading conditions.

Besides loading configuration, curing ages of the specimens are also another parameter as different maturation of the matrix present different piezoresistive behavior. On the other hand, carbon-fiber (CF) incorporation seems more feasible in terms of cost and performance aspects in large-scale elements while nano fillers seem more appropriate in small-scale applications. In

  doi:10.5075/epfl-298799_978-2-9701614-0-0

addition to the filler type, reversibility of piezoresistivity is one of the challenging topics in the studies related to self-sensing. Although some studies suggest the utilization of carbon nanotubes (CNT) and carbon black (CB) compared to CF for reversible self-sensing purposes [22], some studies utilized hybrid use of CF with other nano fillers for better reversible self-sensing purpose and cost considerations [10].

Addition of various carbon-based materials within cement-based mixtures generally improves the engineering properties of specimens, however, the level of improvement is highly related with the uniform dispersion and optimum bond strength between hydrated cement matrix and the inert carbon fillers. Therefore, electrical performance which evaluated through figuring out the percolation threshold of the matrix should be addressed with mechanical compatibility resulting in “multifunctionality” of such composites.

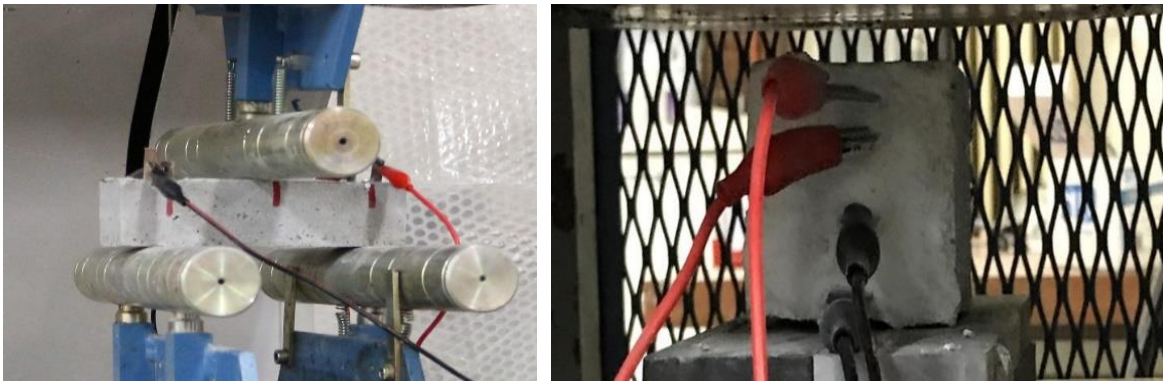

Figure 2. Self-sensing tests under flexural loading (at left) and compressive loading (at right)

3. Measurement of self-sensing performance in cement-free composites

Geopolymers differ from traditional building materials (PC-based) with their alkaline active-matrix properties. One of these properties is that the ionic content in the matrix of geopolymer-based matrix that contains more favorable conditions for electrical properties. Compared to PC-based materials, geopolymers having various advantages for higher electrical conductivity (alkaline, water and hydroxyl ions), have the potential to be adapted with desired electrical properties with more practicality and less cost. In addition, it is seen that various conductive filler materials (mostly carbon-based materials) added to PC-based mixtures have laborious mixing methods and that the developed mixtures have unstable electrical properties at different curing ages. The potential to adapt the electrical properties of geopolymer-based composites at a higher stability may tailor such materials more advantageous in a variety of applications that require structural and non-structural properties. In addition, it is thought that such materials may be promising for providing more stable and reliable multifunctional solutions. In addition, simultaneous regulation of crack control of geopolymers may also exhibit more value added self-sensing performance compared to their traditionally brittle structure similar to PC-based counterparts.

Although studies on the electrical properties of geopolymers are limited in the literature, recent studies show that composites with geopolymer binders have some advantages over PC-based materials in terms of tailoring the electrical properties [23]. For example, it has been stated that NaOH, which is used in geopolymer design, acts as an electrolyte in the matrix and facilitates electron transitions. It is also reported that alkaline solutions (used as surfactants) facilitate

homogeneous mixing of conductive fillers (usually carbon-based materials) used to improve electrical properties [24]. Similarly, other studies dealing with self-sensing behavior of geopolymers also suggest that alkaline solutions which are already used in matrix as ingredient provide easier distribution of conductive fillers [15].

4. Conclusion

The carbon-based materials used in different matrices and the electrical properties (piezoresistivity) that are changed after the applied strain can provide self-sensing functions to the structural elements allowing structural health monitoring. In this study, studies on piezoresistive responses of cementitious mixtures with different compositions and properties are presented. In addition, the difficulties, and solutions in the addition of carbon-based materials to cement-based mixtures are presented. Comprehensive studies on the evaluation of reversible and non-reversible (damage) strains in large and small-scale specimens using multifunctional cement-based composites are further needed for the reliable self-sensing capability. Following results can be drawn from the study:

- In the development of multifunctional cement-based composites, the homogeneous addition of carbon-based materials into the mixtures is significant for the pre-targeted self-sensing performance.
- Evaluation of the critical carbon-based filler ratio is important in terms of economic, mechanical and damage monitoring performance. Hybrid use of carbon-based fillers may be also promising for reduction in cost and increasing piezo-resistivity performance.
- Addressing reversible and non-reversible strains separately from each other is one of the most important and challenging aspects in designing reliable multifunctional structures.
- As knowledge is gradually increasing on the subject, it is expected that the self-sensing performance of structural elements such as large-scale columns / beams will reach higher levels in the coming years.

5. References

1. Chung, D. D. L. Composites get smart. Materials today, 2002 ; 5(1), 30-35.

2. De Backer H, De Corte W, Van Bogaert P. A case study on strain gauge measurements on large post-tensioned concrete beams of a railway support structure. Insight Non-Destructive Test Cond Monit 2003;45:822-826+830. https://doi.org/10.1784/insi.45.12.822.52987.

3. Leng JS, Winter D, Barnes RA, Mays GC, Fernando GF. Structural health monitoring of concrete cylinders using protected fibre optic sensors. Smart Mater Struct 2006;15:302–8. https://doi.org/10.1088/0964-1726/15/2/009.

4. Taha H, Ball RJ, Paine K. Sensing of Damage and Repair of Cement Mortar Using Electromechanical Impedance. Materials (Basel) 2019;12:3925. https://doi.org/10.3390/ma12233925.

5. Shchegel, G.O.; Böhm, R.; Hornig, A.; Astanin, V.V.; Hufenbach, W.: Probabilistic damage modelling of textile-reinforced thermoplastic composites under high velocity impact based on combined acoustic emission and electromagnetic emission measurements. International Journal of Impact Engineering 69 (2014), pp. 1-10

6. Olivera J, González M, Fuente JV, Varga R, Zhukov A, Anaya JJ. An Embedded Stress Sensor for Concrete SHM Based on Amorphous Ferromagnetic Microwires. Sensors. 2014; 14(11):19963-19978. https://doi.org/10.3390/s141119963

7. Chen PW, Chung DDL. Carbon fiber reinforced concrete as an electrical contact material for smart structures. Smart Mater Struct 1993;2(3):181-8. https://doi.org/10.1088/0964-1726/2/3/006.
8. Chung DDL. Electrical conduction behavior of cement-matrix composites. J Mater Eng Perform 2002;11:194–204. https://doi.org/10.1361/105994902770344268.
9. Mendoza O, Sierra G, Tobón JI. Influence of super plasticizer and Ca(OH)2 on the stability of functionalized multi-walled carbon nanotubes dispersions for cement composites applications. Constr Build Mater 2013;47:771–8. https://doi.org/10.1016/j.conbuildmat.2013.05.100.
10. Öztürk, O., Koçer, M., Ünal, A. Multifunctional behavior of composite beams incorporating hybridized carbon-based materials under cyclic loadings. Engineering Structures, 2022; 250, 113429.
11. Öztürk, O., Ünal, A., Koçer, M. Piezo-resistivity of Cement-based Mortars Doped with Carbon black and Carbon Fibers for Self-sensing Behavior, International Conference on Engineering Technologies, 2021, Konya, Turkey.
12. Ozbulut O, Jiang Z, Harris DK. Exploring scalable fabrication of self-sensing cementitious composites with graphene nanoplatelets Smart Mater. Struct.2018; 27 115029.
13. Geopolymer Market: Global industry trends, share, size, growth, opportunity and forecast 2019-2024 (Technical Report) ID: 4753123, 2019, IMARC Group.
14. Raijiwala D.B, and Patil H.S. Geopolymer concrete, a green concrete Institute of Electrical and Electronics Engineers, 2nd Int. Conf. on Chemical, Biological and Environmental Engineering, 2010, Cairo, Egypt.
15. Öztürk, O. Multifunctional behavior of CNT-and CB-based composite beams, Constr. and Build. Mater. 2021; 296,123453.
16. Payakaniti P., Pinitsoontorn S., Thongbai P., Amornkitbamrung V., Chindaprasirt P. Electrical conductivity and compressive strength of carbon fiber reinforced fly ash geopolymeric composites Constr. and Build. Mater. 2017, 135 164–176.
17. Saafi M., Tang L., Fung J., Rahman M., Sillars F., Liggat J. Zhou X. Graphene/fly ash geopolymeric composites as self-sensing structural materials Smart Mater. Struct. 2014, 23 065006.
18. Saafia M. Gullanea A. Huanga B. Sadeghib H. Yea J. Sadeghic F. Inherently multifunctional geopolymeric cementitious composite as electrical energy storage and self-sensing structural material Compos. Struct. 2018, 201 766–778.
19. H.M. Khatera and H.A. Abd el Gawaad, Characterization of alkali activated geopolymer mortar doped with MWCNT Advances in Materials Research, 2015, 4, 1 45-61.
20. B. Han, S. Ding, X. Yu Intrinsic self-sensing concrete and structures: A review Meas J Int Meas Confed, 59 2015, 110-128.
21. Öztürk O., Yıldırım G, Keskin, U.S, Siad H, Şahmaran M, Nano-tailored multi-functional cementitious composites, Composites Part B: Engineering, 2020, 182, 107670.
22. G. Yıldırım, O. Öztürk, A. Al-Dahawi, A. A. Ulu, M. Şahmaran Self-sensing capability of engineered cementitious composites : effects of aging and loading conditions Constr. Build. Mater., (2020), 231, 117132.
23. Saafi M., Andrew K., Tang P.K. et al., Multifunctional properties of carbon nanotube/fly ash geopolymeric nanocomposites, Constr. Build. Mater., 2013, 49, 46-55.
24. Heister E, Lamprecht C, Neves V, Tîlmaciu C, Datas L, Flahaut E, Soula B, Hinterdorfer P, Helen M. Coley, S. Ravi P. Silva, McFadden J ACS Nano 2010 4 (5), 2615-2626

Composites Meet Sustainability – Proceedings of the 20th European Conference on Composite Materials,
ECCM20. 26-30 June, 2022, Lausanne, Switzerland

DEVELOPMENT OF METHODOLOGY FOR EXPERIMENTAL PARAMETER IDENTIFICATION FOR INELASTIC 3D MATERIAL MODEL

Liva Pupure[a], Janis Varna[a,b], Rihards Gailitis[a], Zainab Al-Maqdasi[b], Leonids Pakrastins[a]

a: Institute of Structural engineering, Riga Technical University – liva.pupure@rtu.lv
b: Group of Polymeric Composite Materials, Lulea University of Technology

Abstract: *Lately due to advancement of materials, structures and modeling capacities demand for 3D nonlinear material models implemented in commercial software's and codes have increased. In order to obtain such implemented model, firstly the model itself and the methodology for experimental parameter identification have to be established. The overall goal is to create a 3D material model, that could account for viscolpasticity, viscoelasticity and damage. Within this study the viscoplastic behavior in axial and lateral direction will be analyzed, thus obtaining the materials 3D viscoplastic behavior. Experimental data for various materials are analyzed. The results showed that viscoplastic strain has the same time and stress dependency in axial and lateral direction. The only difference is in the ration of axial and lateral strain, which is characterized by a single multiplication factor within viscoplastic material model.*

Keywords: Nonlinearity; 3D; viscoplasticity; strain recovery; creep

1. Introduction

In recent years there has been a great advancement made in more sustainable material choices and increased effectiveness of currently used materials and structures. For example, bio-based materials offer more sustainable alternative to glass fiber composites for a wide range of applications. However, research has shown, that they exhibit highly nonlinear behavior [1-2]. Similarly, there have been an increasing number of studies focusing on composites, in hopes to use them at elevated temperatures. One of the applications for such composites could be substitute parts of jet engines. This would further reduce the weight of airplanes and in return the fuel consumption and carbon emissions. However, similarly to bio-based composites, composites at high temperatures tend to be more nonlinear exhibiting irreversible strains. Thus, there is a great need to develop more complex material models, that could capture the nonlinearity of these materials.

Moreover, the structures themselves are becoming more and more geometrically complicated. This increases the need for different simulations tools, for example, finite element modeling. Most of the nonlinear models are developed for 1D cases. For example, the Scapery's nonlinear viscoelastic 3D material model [3-5], modified in [6] to include Zapas model for viscoplasticity [7] and damage has been widely used to simulate the 1D time dependent behavior of different materials [6,8]. Even if some of the models are developed for 3D cases, methodologies for parameter experimental identification for these models are lacking. In the best-case scenario, there is a theoretical description of how such parameters could be obtained.

In order to simulate material behavior in 3D, the nonlinearity of isotropic material has to be studied not only in the loading direction but also in the transverse direction. In the case of anisotropic material, the number of experiments significantly increases, due to fact that each

  doi:10.5075/epfl-298799_978-2-9701614-0-0

direction has to be studied separately. Another challenge for nonlinear modeling of complex geometrical structures is the need to find the nonlinear functions and parameters for the model in both loading modes - tension and compression.

In the current paper the viscoplasticity for 3D material model subjected to uniaxial tensile load will be analyzed. The viscoplasticity model developed by Zapas [7] will be used. The experimental data for various materials has been analyzed and overall trend between the VP strain in axial and lateral direction found. Links or a lack of them between parameters in both directions will be identified and simplifications for VP material model in 3D, when possible, is made.

2. Nonlinear modeling

Viscoplasticity is the first step in understanding the time-dependent behavior of materials. After removing the viscoplastic (VP) strain component from recorded data, the pure nonlinear viscoelasticity can be analyzed. It has been demonstrated for various materials [8-14] that the Zapas model presented in eq. (1) for case of uniaxial loading in direction 1, can be used to characterize the VP behavior in direction 1, when $i = 1$

$$\varepsilon_i^{VP}(\sigma, t) = C_{i1}^{VP}\left\{\int_0^{\frac{t}{t^*}}\left(\frac{\sigma_1(\tau)}{\sigma*}\right)^{M_i} d\tau\right\}^{m_i} \qquad \text{i=1,2} \qquad (1)$$

where C_{i1}^{VP}, M_i and m_i are material constants determined experimentally, t/t^* is normalized time and t^* and σ^* are arbitrary chosen characteristic time and stress constants. In most of the study cases these values are chosen to have more simplistic calculations, therefore t^* is chosen as the sum of the creep loading time for one stress level and σ^*=1 MPa. In this work we broaden the application of (1), applying it also for lateral VP strains, i=1,2. In [9] two different experimental methods for determining VP parameters have been discussed: using a different specimen for each stress level (further in the text will be referred as "DS method") and using single specimen for all stress levels (in the text referred as "SS method").

In case of DS method, when constant stress is applied (creep $\sigma_1 = \sigma_0$) and there has not been any previous loading history the VP strain dependence on the duration of the creep test (time interval Δt_1) obeys the following power function:

$$\varepsilon_i^{VP}(\sigma_0, \Delta t_1) = C_{i1}^{VP}\left(\frac{\sigma_0}{\sigma*}\right)^{M_i m_i}\left(\frac{\Delta t_1}{t*}\right)^{m_i} \qquad \text{i=1,2} \qquad (2)$$

Thus, if the Zapas model is applicable, the time dependence of VP strain in constant stress test (creep) should follow a power function:

$$\varepsilon_i^{VP}(\sigma_0, \Delta t_1) = A_i\left(\frac{\Delta t_1}{t*}\right)^{m_i} \qquad \text{i=1,2} \qquad (3)$$

where A has a power law dependence on the applied stress level in the creep test:

$$A_i = C_{i1}^{VP}\left(\frac{\sigma_0}{\sigma*}\right)^{M_i m_i} \qquad \text{i=1,2} \qquad (4)$$

In case of the SS method, the determination of VP parameters becomes more complicated, due to previous loading history. For the first stress level there are no changes, but for the *k*-th stress level $n_k\sigma_0$, (n_1=1) if previous stress levels have the same total creep time duration Δt_0, VP strain is obtained as follows:

  doi:10.5075/epfl-298799_978-2-9701614-0-0

$$\varepsilon_i^{VP}(n_k, \Delta t_1) = C_{i1}^{VP}\sigma_0^{M_i m_i}\left(\frac{\Delta t_0}{t*} + n_2^{M_i}\frac{\Delta t_0}{t*} + n_3^{M_i}\frac{\Delta t_0}{t*} + \cdots + n_k^{M_i}\frac{\Delta t_1 - (k-1)\Delta t_0}{t*}\right)^{m_i} \quad (5)$$

One method for obtaining VP parameters is to plot the experimental data in ln-ln axis, where experimental data have linear trend. For the DS method first Eq. (2) ca be plotted in ln-ln axis, where VP strain have linear trend with respect to time. Then similarly Eq. (3) can be plotted in ln-ln axis where VP strain has linear fit with strain. For SS method this approach could be used with Eq. (4), but in this case the linear trend is not as easily obtained as with DS method. More detailed description of the methodology for parameter identification for both methods can be found in [9].

All this has been proven to work in uniaxial loading for VP strains in the loading direction, but when developing nonlinear 3D models, not only strains in loading direction has to be analyzed, but also in lateral direction. The lateral VP strain has not been widely analyzed. Within small amount papers some quantitative lateral strain analysis has been done. In some rare cases the VP parameters have been identified also for lateral direction, but they have not been linked with parameters and VP strains for axial direction. This study will try to identify and link the VP parameters between axial and lateral orientation.

3. Materials and experimental method

3.1 Experimental methodology

In order to obtain VP parameters C_i^{VP}, M_i and m_i described in section 2 the specimens were subjected to sequence of tensile uniaxial loading ramps in direction 1 each consisting of uploading to constant stress; keeping the stress constant for a fixed time; unloading the specimen and waiting for viscoelastic strain to recover. This loading ramp has to be performed for each material at several stress levels, to obtain the VP dependence on stress. At the end of each recovery the strains in two directions axial ε_1^{VP} and lateral ε_2^{VP} were assumed as pure VP strains. Detailed information on this experimental methodology can be found in previously published studies [6,8,10].

Since large number of experimental data have been analyzed within this paper, the experimental set-up can vary from study to study. More information on particular set-up can be found in the material reference paper given in the next section.

3.2 Materials

In order to obtain complete picture of the viscoplasticity, it is crucial to analyze several materials and see if the assumptions that have been made for one material apply also for others. The list of materials used in this study has been summarized in table 1. More detailed description of constituents, manufacturing methods and experimental set-up of these materials can be found in the corresponding supplied reference.

4. Results and discussion

The first part of the data analysis was to perform analysis of VP strains in both directions separately and obtain the parameters for material model. The obtained results showed that the best overall fit was obtained using different values of parameters for axial and lateral direction. In Figure 1 the experimental data of HDPE with different amount of GNP is presented and the obtained VP parameters are presented in Table 2. The data fitting was done using the SS method.

  doi:10.5075/epfl-298799_978-2-9701614-0-0

Even though for some materials the fit between the experimental data and modeling is not ideal the overall agreement is good. This trend was observed for all materials listed in section 3.2.

Table 1: Summary of studied materials

Material abbreviation	Short description of material	Ref.
HDPE HDPE+2%GNP HDPE+6%GNP HDPE+15%GNP	High density polyethylene with different amount of graphene nanoplatelets (GNP).	[10]
PP	Recycled Polypropylene	[11]
CF/PP	Recycled carbon fiber (volume fraction ~30%) reinforced polypropylene	[12]
Epoxy	LY5052 epoxy resin system	[13]*
GF/PP	Short glass fiber polypropylene composite	**

* The raw materials and manufacturing of epoxy in done similar manner as for the composite reported within this paper.

** Due to confidentiality detailed information on this material cannot be disclosed. Therefore, absolute values for this particular material will not be given, only the overall trends discussed.

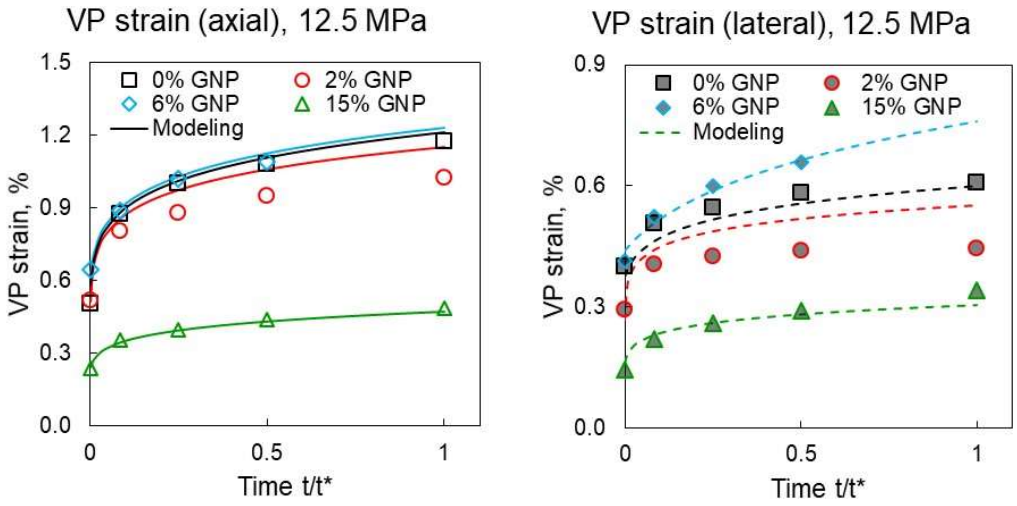

Figure 1. The experimental VP strain and the modeling curves with obtain parameters presented in table 2 at 12.5 MPa in axial (left) and lateral (right) direction.

From the simulation point of view, it would significantly reduce the complexity of models if some VP parameters would not differ between axial and lateral direction, for example $m_1 = m_2$ or $M_1 = M_2$. From table 2 it can be seen that the parameters *m* and *M* are rather close in values.

These parameters show the material's VP strain dependence on time and stress in two directions. If it could be proven that values in both directions are the same or are linked somehow, the characterization and VP simulations in 3D would be rather simplified – the only difference between axial and lateral direction would be in the parameter C_i^{VP} which represents the ratio of VP strains. Therefore, the parameter determination in Eq. (1) was modified enforcing to have the same m_i and M_i values for both directions. The obtained results are presented in Figure 2, where the experimental data and modeling for HDPE with different amount of GNP is presented. The adjusted VP parameters are presented in table 3, where product of parameters *m* and *M*, representing the VP strain dependence on stress are given.

Table 2: VP parameters for HDPE with different amounts of GNP

Material	m_1	m_2	M_1	M_2	C_1^{VP} (%)	C_2^{VP} (%)
HDPE	0.13	0.11	25	19	$3.29 \cdot 10^{-4}$	$3.05 \cdot 10^{-3}$
HDPE+2%GNP	0.12	0.09	30	36	$1.29 \cdot 10^{-4}$	$1.54 \cdot 10^{-4}$
HDPE+6%GNP	0.11	0.09	22	28	$1.46 \cdot 10^{-3}$	$7.41 \cdot 10^{-4}$
HDPE+15%GNP	0.13	0.115	23	25	$2.47 \cdot 10^{-4}$	$2.13 \cdot 10^{-4}$

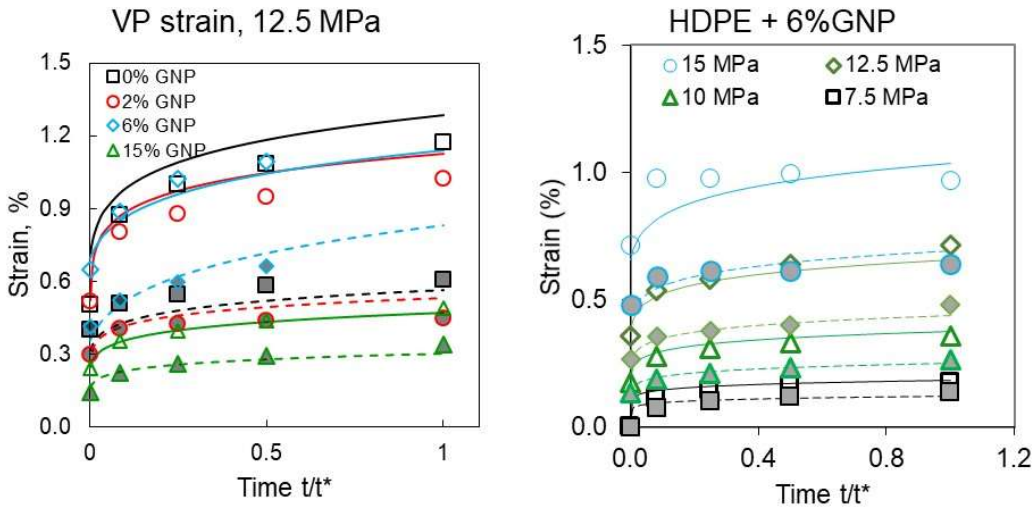

Figure 2. The experimental VP strain and the modeling curves with the same m and M values for both direction for HDPE with different amount GNP at 12.5 MPa (left) and HDPE+6%GNP (right). The solid lines and empty markers represent the axial direction and dashed lines with filled markers the lateral direction

It can be seen that for some stress levels the adjusted (unified) parameters show slightly reduced agreement between experimental data and modeling, but the overall fit of the data is good regardless of the enforced equality of fitting of parameters m_i and M_i. It also can be seen that the VP parameter C_i^{VP} is larger for axial direction and smaller for lateral, which is logical since the parameter scales the VP strain and the strain in axial direction for isotropic materials is larger than in transverse direction. It can also be seen that the stress dependence is increasing slightly

with increase amount of GNP. The only exception is HDPE with 2% GNP which shows significantly higher value of *mM*. However, this material also showed worse overall fit with experimental data, independently if the fit was done with or without forcing $m_1 = m_2$ or $M_1 = M_2$.

Table 3: Adjusted VP parameters for HDPE with different amounts of GNP

Material	*m*	*M*	*mM*	C_1^{VP} (%)	C_2^{VP} (%)
HDPE	0.12	22	2.64	$1.63 \cdot 10^{-3}$	$7.18 \cdot 10^{-4}$
HDPE+2%GNP	0.105	33	3.465	$1.78 \cdot 10^{-4}$	$8.43 \cdot 10^{-5}$
HDPE+6%GNP	0.10	25	2.50	$1.19 \cdot 10^{-3}$	$7.95 \cdot 10^{-4}$
HDPE+15%GNP	0.12	24	2.88	$3.25 \cdot 10^{-4}$	$2.09 \cdot 10^{-4}$

The assumption that VP strain in axial and transverse direction follow the same time and stress dependence, but differ in the overall scale, has to be tested on more than one type of material. The above results showed that parameters m and M can be adjusted to have the same values for both direction and the overall fit between the experimental data and modeling will be acceptable. Figure 3 shows the results for Epoxy analyzed using SS method and Figure 4 shows the results of PP and short fiber composite CF/PP analyzed using DS method. All studied materials presented in table 1 showed similarly good agreement between experimental data and modeling, as is presented in Figures 2-4, even if the VP parameters m_i and M_i are forced to be constant in axial and in lateral direction at the same time. This indicates that VP strain in lateral direction follows the same time and stress dependence as in axial direction and the total VP strain values are only scaled. Since in most of the cases the overall strain in lateral direction is smaller than in axial direction the parameter C_i^{VP} in lateral direction will be smaller.

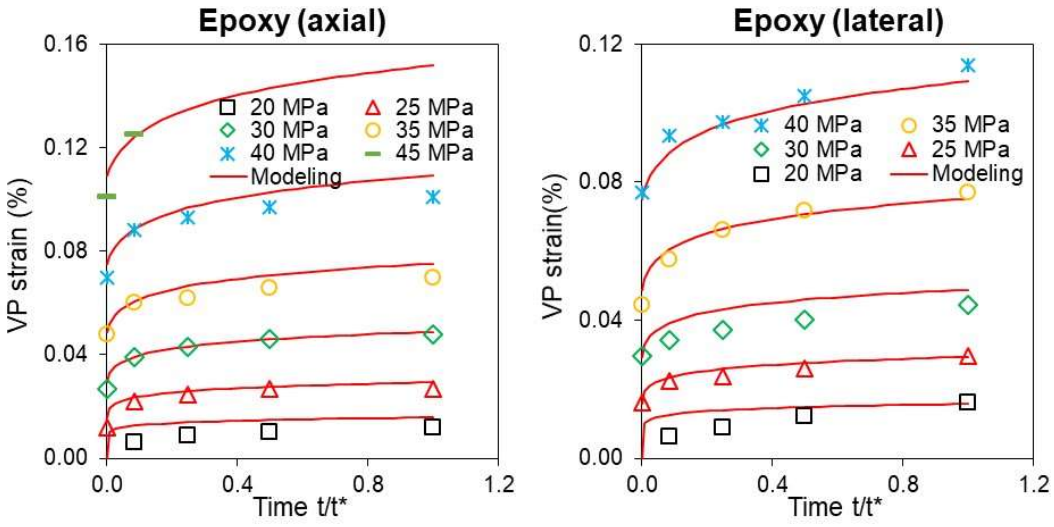

Figure 3. The experimental VP strain and the modeling curves for epoxy resin in axial (left) and lateral (right) direction.

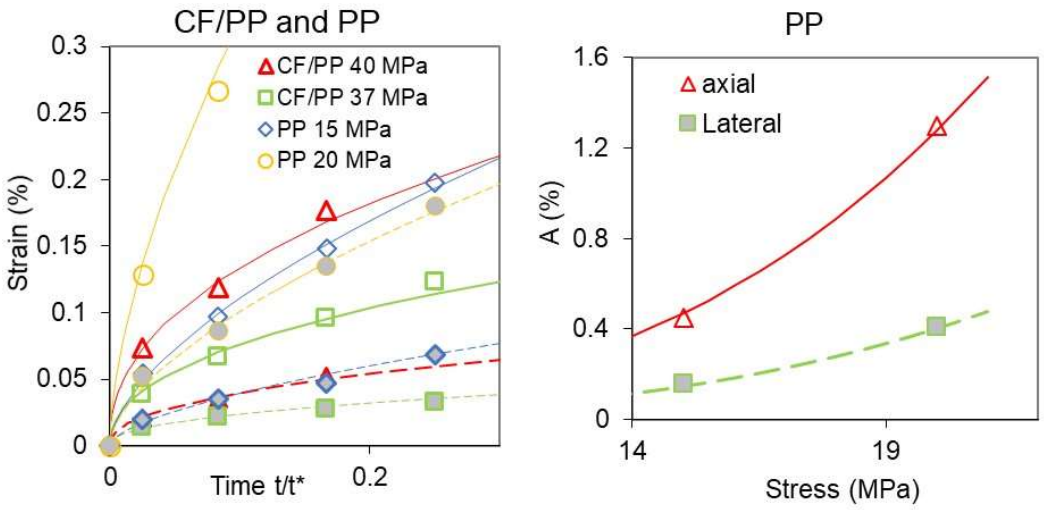

Figure 4. The experimental VP strain and the modeling curves for PP and CF/PP composite dependence on time (left) and PP VP strain dependence on stress (right) .

5. Conclusions

Experimental data of VP strain in both axial and lateral direction for large number of materials have been analyzed within this study. Zapas model for viscoplasticity has been proven to be applicable for VP strain simulation in both axial and lateral direction for all of the studied material systems. Although initially the best overall fit was obtained using different parameters for axial and lateral VP strain, forcing the parameters m_i and M_i to be the same in both directions did not reduce the overall fit between the experimental data and modeling. These parameters characterize the irreversible stain dependence on time and stress, thus it can be concluded that material VP strain in lateral direction follows the same trend as for axial direction.

The only difference in parameters were observed for parameter C_i^{VP} which is a constant that is used to multiply the time and stress dependent part of viscoplasticity. Since for the most materials strain in lateral direction is smaller than in axial direction, the parameter C_i^{VP} will also be smaller for lateral direction. These finding will help to simplify characterization for developing 3D material models for nonlinear material behavior with irreversible strains. The next step of the analysis will be to subtract the VP strain component from the total creep strain, obtaining pure nonlinear viscoelastic behavior and analyze the nonlinear viscoelasticity.

Acknowledgements

This work has been supported by the European Regional Development Fund within the Activity 1.1.1.2 “Post-doctoral Research Aid” of the Specific Aid Objective 1.1.1 “To increase the research and innovative capacity of scientific institutions of Latvia and the ability to attract external financing, investing in human resources and infrastructure” of the Operational Programme “Growth and Employment” (No.1.1.1.2/VIAA/4/20/646).

  doi:10.5075/epfl-298799_978-2-9701614-0-0

6. References

1. Almgren KM, Gamstedt EK, Varna J. Contribution of wood fibres to the moisture-induced dimensional instability of composite plates. Polymer Composites 2010; 31: 762-771.
2. Pupure L, Doroudgarian N and Joffe R. Moisture uptake and resulting mechanical response of biobased composites. I. constituents. Polymer Composites 2014; 35(6): 1150-1159.
3. Schapery RA. Nonlinear Viscoelastic and Viscoplastic Constitutive Equations Based on Thermodynamics. Mechanics of Time-Dependent Materials 1997; 1: 209-240.
4. Lou YC and Schapery RA. Viscoelastic characterization of a nonlinear fiber-reinforced plastic. Journal of Composite Materials 1971; 5: 208-234.
5. Schapery RA. On the Characterization of nonlinear viscoelastic materials. Polymer Engineering and Science 1969; 9(4): 295-310.
6. Marklund E, Eitzenberger J, Varna J. Nonlinear viscoelastic viscoplastic material model including stiffness degradation for hemp/lignin composites. Composite Science and Technology 2008; 68(9): 2156-2162
7. Zapas LJ and Crissman JM. Creep and Recovery Behavior of Ultra-high Molecular Weight Polyethylene in the Region of Small Uniaxial Deformations. Polymer 1984; 25: 57-62.
8. Nordin L-O, Varna J. Nonlinear viscoelastic behavior of paper fiber composites. Composites Science and Technology 2005; 65(10): 1609-1625.
9. Pupure L, Varna J, Joffe R. On viscoplasticity characterization of natural fibres with high variability. Advanced Composite Letters 2015; 24(6): 125-129.
10. Al-Maqdasi Z, Pupure L, et. al. Time-dependent properties of graphene nanoplatelets reinforced high-density polyethylene. Journal of Applied Polymer Science 2021; 138(30), 50783.
11. Szpieg M, Giannadakis K, Varna J. Time-dependent nonlinear behavior of recycled polypropylene in high tensile stress loading. Journal of Thermoplastic Composite Materials 2011; 24(5): 625–652
12. Szpieg M, Giannadakis K, Asp LE. Viscoelastic and viscoplastic behavior of a fully recycled carbon fiber-reinforced maleic anhydride grafted polypropylene modified polypropylene composite. Journal of Composite Materials 2012; 46(13): 1633–1646
13. Pupure L, Saseendran S, et. al. Effect of degree of cure on viscoplastic shear strain development in layers of [45/−45]s glass fibre/ epoxy resin composites. Journal of Composite Materials 2018; 52(24): 3277–3288.
14. Vadivel HS, Al-Maqdasi Z, et. al. Time-dependent properties of newly developed multiscale UHMWPE composites. Polymer Testing 2022;105: 107400.

  doi:10.5075/epfl-298799_978-2-9701614-0-0

LIFE CYCLE ASSESSMENT AND LIFE CYCLE COSTING ON RECYCLED POST-INDUSTRIAL COMPOSITE WASTE

Anastasia Gkika[a], Foteini Petrakli[a], Anestis Vlysidis[a], Panagiotis Karagiannis[a], Sandy Moisan[b], Elias Koumoulos[a]

a: IRES—Innovation in Research & Engineering Solutions, Rue Koningin Astridlaan 59B, 1780 Wemmel, Belgium – agkika@innovation-res.eu
b: Institut de Recherche Technologique Jules Verne, Chemin du Chaffault, 44340 Bouguenais

Abstract: *Due to the rapidly increasing use of carbon fibre-reinforced composite (CFRP) materials in numerous industries, such as aerospace, automotive, and energy, cost-effective and environmentally responsible methods of CFRP recycling are becoming increasingly significant. Composite scraps, such as uncured or semi-cured prepreg, offers a great opportunity for recycling as the recovered carbon fibres have not yet been subjected to aging. This study presents a 'cradle-to-gate' Life Cycle Assessment and Life Cycle Costing, aiming to quantify the potential environmental and cost impacts of recovered carbon fibres applying for the first time extraction with supercritical CO_2, an already industrial technology used to obtain valuable compounds from natural sources. Inventory data at laboratory and pilot production scale have been assessed, presenting the cost-efficiency and the lower energy intensiveness benefits for the scaling-up of technology. Initial results compared to virgin carbon fibre impacts and costs reveal that extraction with supercritical CO_2 can offer great potentials to composite recycling.*

Keywords: Life cycle assessment; Life cycle costing; composites; recycling;

1. Introduction

Recycled carbon fibre market is considered a fast growing market driven by the intensive demand of high-performance, environmental-friendly and low-cost composites in many industrial applications like automotive, aerospace, sports, renewable energy. For the years 2021-2026, an average annual growth rate of 12% is given (1). Currently, there are three dominant technologies for composite recycling; the mechanical, the thermal and the chemical recycling (2), (3). Mechanical recycling has given results with poor-quality, short length and low tensile modulus CF, while thermal processes, more specifically pyrolysis, creates char on the surface and requires high temperatures. Chemical recycling uses hazardous solvents that have a negative impact on environment. Up to now chemical recycling with supercritical fluids (solvent or water) provides high quality recovered carbon fibres without mechanical degradation (4) (5). Carbon fibre reinforced polymer (CFRP) composite scraps (e.g uncured prepregs, semi-finished products) may be subjected to appropriate post-processing treatments, allowing recycled carbon fibres to retain the mechanical properties of the virgin carbon fibre and become an added-value product. Life cycle assessment studies (LCA) have revealed that the production of virgin CF is an energy-intensive process and therefore, the embodied energy of CF appears to be higher compared to other structural materials (6). Indicatively, the calculated embodied energy for CF is 183–286 MJ/Kg, whether the embodied energy of glass fibre and stainless steel ranges between 13–32 MJ/Kg and 110–210 MJ/kg, respectively (7) (8). The presence of hazardous emissions during production stage such as hydrogen cyanide (HCN), ammonia (NH3), carbon monoxide (CO), carbon dioxide (CO_2), nitrogen oxide (NOx) and volatile

  doi:10.5075/epfl-298799_978-2-9701614-0-0

organic compounds (VOCs) has been referred in several studies (9) (10) (11) that need to be treated appropriately during the process. On the contrary, LCA studies focused on recycled carbon fibre through various recycling methods, have indicated a much lower embodied energy of the recycled carbon fibre (rCF) compared to virgin (12) (13). Although research and commercial interest has turned to the chemical recycling option for recovering CF, great barriers have yet to be overcome. Resin degradation can be achieved by solvents under critical and suitable conditions by focusing on concentration, pressure, catalysts and reaction time (14). Those solvents, can be considered harmful chemicals to human health and environmental, whether water supercritical conditions require high temperature and pressure (15), (16). Further, difficulties appeared relating to remanufacturing composites with recycled CFs with high mechanical characteristics. Supercritical CO_2 (sc-CO_2) extraction is an industrial scale process usually applied as "green chemistry" to obtain valuable compounds from natural sources (17), (18), (19). For the first time, it is used to retrieve not only carbon fibres from uncured composite waste, but also to extract organic part of the thermoset resin. This study focuses on the environmental and cost assessment of this technology and present initial results on the potential environmental and economic impacts of the recycled carbon fibre under extraction with sc-CO_2.

2. LCA and LCC methodologies

Life cycle assessment (LCA) is a methodology to assess the environmental loads of a system, process or product and quantify the allocated impacts. To effectively and adequately perform the LCAof the examined recycling process, we have followed the general framework provided by the ISO standards 14040:2006 & 14044:2006 (20) (21), including in our study the four main phases of an LCA:

- Goal and scope: definition of the main study choices, such as the goal the study, the system boundaries, the functional unit and the lifetime of the product or system(s);
- Life cycle inventory analysis: description of the product system/process, inputs and outputs flows of the examined product or system(s);
- Life Cycle Impact assessment: characterization and classification of the inventory flows into impact categories to evaluate the significance of the potential environmental impacts of the product or system(s) under study
- Interpretation of results: evaluation and validation of the results, indicative conclusion derived

Life Cycle Costing (LCC) methodology systematically accounts all the costs of a product or system incurred over its entire life cycle to assist the decision-making process towards more sustainable and cost-efficient options (22). Life Cycle Cost studies are performed according to the general framework provided by ISO 15686-5:2017 (23) and SETAC guidelines on Life Cycle Costing (24). Life Cycle Cost in this study is structured in such way to complement LCA, so that its framework follows the four LCA phases (25).

3. LCA and LCC on recycled CF via extraction with supercritical CO_2

3.1. Goal and scope of the study

The goal of the current study is to evaluate the environmental and cost performance of the recycling technology applied to recover CFs and by-products from post-industrial unidirectional (UD) prepreg waste at laboratory and scaled-up production. The system boundaries of the

process follow a “cradle-to-gate” approach, including the feedstock and the recycling process. The scope of the study is to support decision-makers on the future exploitation of this technology for semi-finished composite parts, end-of-life CFRPs and manufacture scraps from several applications. This LCA study is conducted following the attributional approach in modeling concerning data used and allocations of environmental loads along the life cycle stages considered. The functional unit (FU), selected for this study, is set as the production of 1 kg of recycled CF at 6 mm length. Life Cycle costing complements LCA results at the same functional unit and assesses the total costs of the recycling process across the different production volumes.

3.2. Inventories and System description

UD prepreg waste has been provided to IRT Jules Verne premises by a composite aircraft manufacturer. Prepregs are initially chopped using a Zund cutting equipment at 6 mm length. The chopped prepregs are then placed in a 4L reactor (fully filled in with 0,885kg prepreg) and treated under supercritical fluid chemistry. The supercritical CO_2 is selected as “green solvent” to recover not only carbon fibres but also to extract a fraction of the prepreg matrix. Liquid CO_2 is first compressed and heated up until the respective supercritical conditions (40°C, with an extraction pressure of 290 bars) are achieved. The CO_2 is recycled by 95% in a closed loop process. UD prepreg is composed by carbon fiber (IMA type) and thermoset resin (M21E) at composition rate of 34% resin by weight. The prepreg has to be stored under -18 °C to avoid polymerization reaction before entering the reactor. The system boundaries are illustrated in Figure 1. The reaction is stopped when 100 kg/kg of CO_2 ratio is obtained. . Inventories are provided at low and high production volumes, as shown in Table 1. For the scale up production, a recycling pilot scale system that processes ~145 tons/year with 8.000 annual operating hours and a lifetime of 30 years was selected.

General assumptions have been introduced at different stages of this life cycle assessment. Electricity is considered country-specific as the recycling plant is located in France. Transportation has not been accounted due to nearby sites of composite manufacturer/waste provider and the recycling plant. Maximum capacities of additional equipment (cutting tool) are allocated to the functional unit. The UD prepreg waste is assumed as a “zero impact” material for the respective assessment. Bisphenol A obtained from ecoinvent database has been used as proxy for the organic monomers retrieved after extraction.

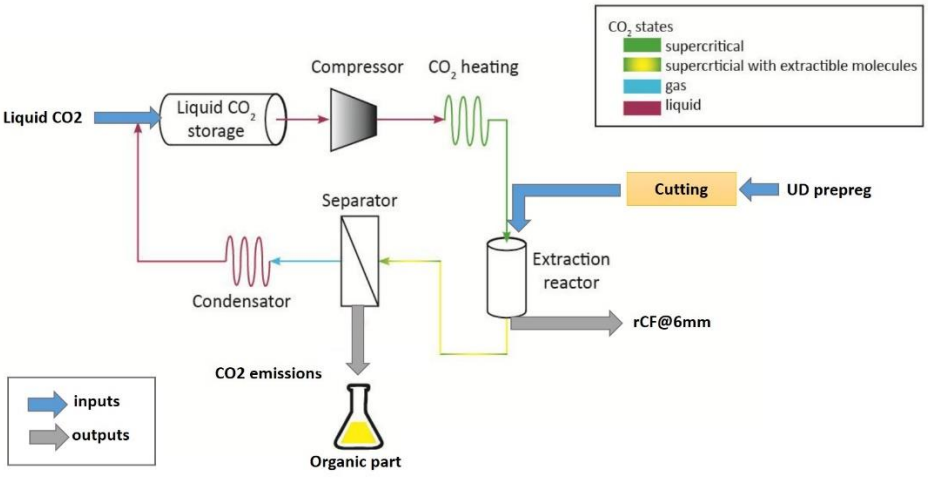

Figure 1 System boundaries of extraction with supercritical CO_2 process

Table 1 Life cycle Inventory for functional unit of 1 kg recovered CF

Input	Experimental data
UD prepreg	0.752 kg
Paper	0.248 kg
CO_2 liquid	100 kg
Electricity (cutting & extraction)	226.55 kWh
Output	
Organic part	4.75 kg
CO_2 emissions	5 kg
Paper waste	0.248 kg

3.3. Life Cycle Impact Assessment

The LCA is performed using a set of impact categories sourced from the characterisation methods of the ILCD 2011 Midpoint+ (v1.11). The ILCD 2011 Midpoint method was released by the European Commission, Joint Research Centre in 2012 (26). It supports the recommended default characterisation factors and models for impact assessment as evaluated in the ILCD guidance document (27). The ILCD 2011 Midpoint+ method classifies impacts in 16 midpoint categories. For the current impact assessment, only global warming potential (GWP) impact category, based on the Intergovernmental Panel on Climate Change's (IPCC) 2007 report for a 100-year period has been selected and it is in consistency with the goal and scope of the study. Ecoinvent "cut-off" library (v3.6) is selected for modelling the inventory flows of the system in the SimaPRO software (v9.1.1.7). For the secondary data, the allocations of Ecoinvent Database 3.6 have been applied.

4. LCA and LCC results

The environmental assessment results on 1 kg of recovered carbon fibre using extraction with sc-CO_2 for the GWP impact indicator are presented below. As shown in Figure 2 (a) contribution per process in Climate change impact is higher for the closed loop of CO_2 recycling (approximately 90%) at lab scale inventory, whether cutting process share dominates by 70% at scale up production. Linear approach has been followed for the scale up of the energy consumption of the cutting process, thus resulting at very high share in the total impact. Comparing both inventory scales, it is evident that when scale up is considered, climate change impact can be as low as 90% for the defined functional unit. In net values, this reduction is one order of magnitude lower, illustrated in Figure 2 (b). Bisphenol A, considered as avoided co-product in LCA modelling, has very low contribution in Climate Change impact, almost 1% in scale up recycling process and much lower at laboratory scale (<0.5%). Analysing further per individual input/output, electricity appears to be the main hotspot with the highest environmental burden in both scales, ranging from 90-97%, as shown in Figure 3 (a). Sensitivity analysis on energy consumption for cutting process on scale up production that presented in Figure 3 (b) indicates an exponential decrease in the total climate change impact (when energy is decreased by 75%, climate change is by approximately 50% lower).

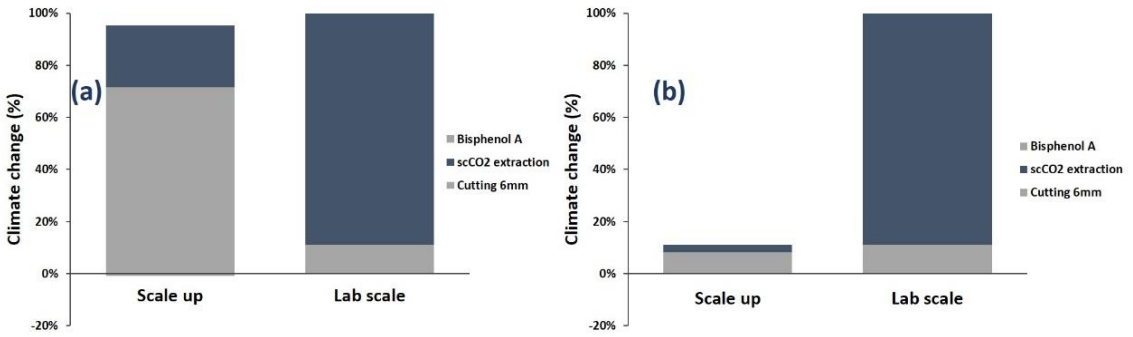

Figure 2 Contribution (%) per process in Climate change impact (a) and comparative assessment at different scales of extraction with sc-CO_2 technology (b) per functional unit

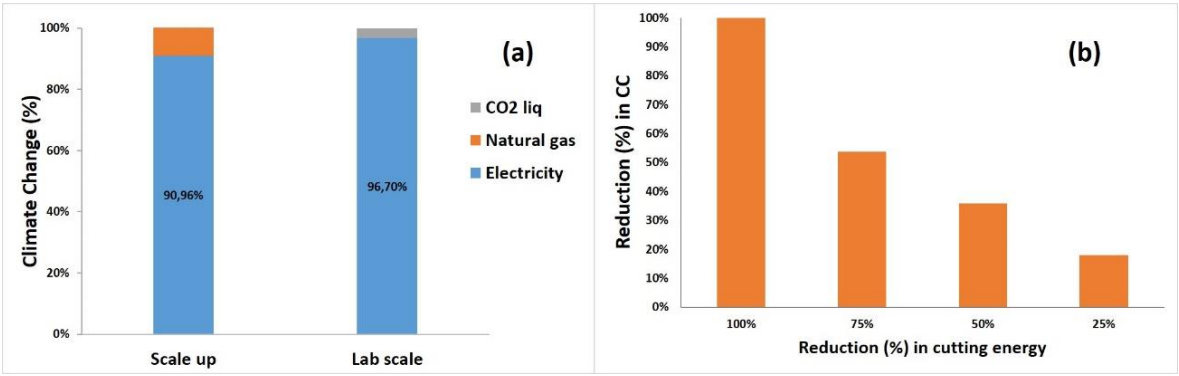

Figure 3 Hotspot analysis (left) in Climate change impact (%) and sensitivity analysis (right) on cutting energy at scale up production per functional unit

The most commonly used literature inventories of virgin carbon fibre, used in LCA studies on composites (10) (11) (28), have been chosen to compare initial results from this study and have a first evaluation, as illustrated in Figure 4.

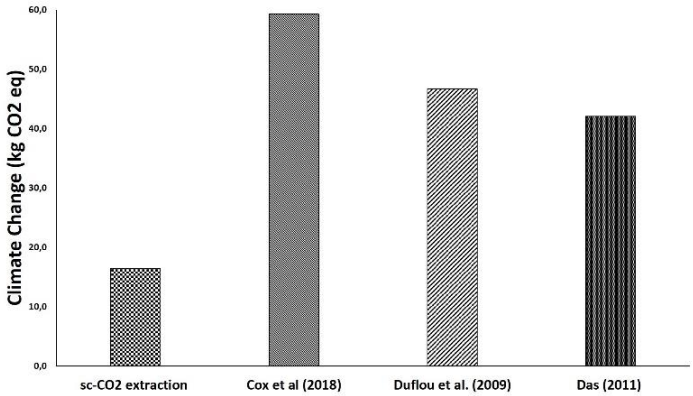

Figure 4 Comparative assessment of recycled CF under sc-CO_2 extraction virgin CF

Initial comparative assessment to virgin CF production indicates that recovered CF under sc-CO_2 extraction have lower climate change impact, ranging from 61-72%. However, Extraction with sc-CO_2 seems to be a promising and energy-efficient alternative to substitute virgin CF in composite manufacture. For the cost assessment, the most important categories are included such as cost of raw materials, cost of manufacture, utilities cost and labour cost. Initial cost breakdown analysis results at different scales are illustrated in Figure 5. The higher cost impact category at both scales is the utilities cost (mainly energy), whether at scale up production annuity CAPEX and cost of operating labour are the ones contributing by approx. 20-25%. The

total LCC per functional unit, defined the same as in LCA, when compared at different scales indicate a significant reduction at higher productivity volumes by approximately 70% .

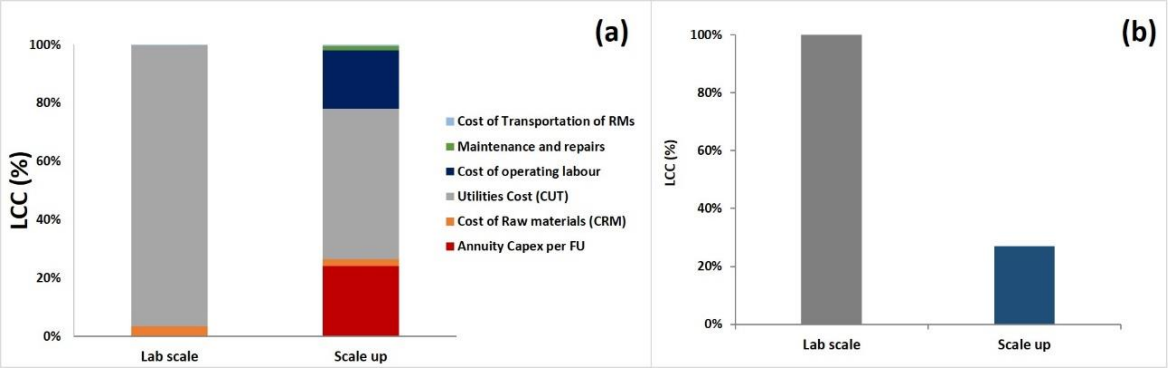

Figure 5 Cost breakdown analysis (LCC %) at different scales (a) and Comparative LCC (%) results at different scales per functional unit (b)

5. Conclusions

Life cycle assessment and life cycle costing are methodological tools to quantify and assess the environmental and cost impacts of a system or product across its entire life cycle. This study constitutes an initial assessment to evaluate the environmental and cost performance of an industrial technology that is used for the first time in the frame of REPAIR3D H2020 funded project (29), to recover not only carbon fibres, but, partially the organic part of the thermoset resin, sourced from uncured UD prepreg waste. Initials results indicate that the referred technology using supercritical CO_2 extraction can be considered as promising future alternative in composite scrap recycling with great opportunities for further market exploitation.

Acknowledgements

This research is conducted in the frame of the project “REPAIR3D-Recycling and Repurposing of Plastic Waste for Advanced 3D Printing Applications” that has received funding under the European Union's Horizon 2020 research and innovation programme with Grant agreement N° 814588 and in the frame of “Carbo4Power - New generation of offshore turbine blades with intelligent architectures of hybrid, nanoenabled multi-materials via advanced manufacturing” that has received funding under the European Union's Horizon 2020 research and innovation programme with Grant agreement N° 953192.

6. References

1. Recycled Carbon Fiber Market by Type (Chopped Recycled Carbon Fiber, Milled Recycled Carbon Fiber), Source (Aerospace Scrap, Automotive Scrap), End-use Industry and Region (North America, Europe, APAC, MEA and Latin America) - Global Forecast to 2026, Onl.

2. Pimenta S, Pinho ST (2011). Recycling carbon fibre reinforced polymers for structural applications: technology review and market outlook. Waste Management 31, 378–392. DOI:10.1016/j.wasman.2010.09.019.

3. Giorgini, L., Benelli, T., Brancolini, G., Mazzocchetti, L., 2020. Recycling of carbon fiber reinforced composite waste to close their life cycle in a cradle-to-cradle approach. Current Opinion in Green and Sustainable Chemistry 26. https:// doi.org/10.10.

4. Butenegro JA, Bahrami M, Abenojar J, Martínez MÁ. Recent Progress in Carbon Fiber Reinforced Polymers Recycling: A Review of Recycling Methods and Reuse of Carbon Fibers. Materials. 2021; 14(21):6401. https://doi.org/10.3390/ma14216401.

5. Karuppannan Gopalraj, S., Kärki, T. A review on the recycling of waste carbon fibre/glass fibre-reinforced composites: fibre recovery, properties and life-cycle analysis. SN Appl. Sci. 2, 433 (2020). https://doi.org/10.1007/s42452-020-2195-4.

6. Rhys J. Tapper, Marco L. Longana, Andrew Norton, Kevin D. Potter, Ian Hamerton, An evaluation of life cycle assessment and its application to the closed-loop recycling of carbon fibre reinforced polymers,.

7. Young S. Song, Jae R. Youn, Timothy G. Gutowski, Life cycle energy analysis of fiber-reinforced composites, Composites Part A: Applied Science and Manufacturing,.

8. F. Meng, J. McKechnie, T.A. Turner, S.J. Pickering, Energy and environmental assessment and reuse of fluidised bed recycled carbon fibres.

9. E. Griffing and M. Overcash, Chemical Life Cycle Database, www.environmentalclarity.com, 1999 - present (2010 last updated).

10. Das, S. Life cycle assessment of carbon fiber-reinforced polymer composites. Int J Life Cycle Assess 16, 268–282 (2011). https://doi.org/10.1007/s11367-011-0264-z.

11. J.R. Duflou, J. De Moor, I. Verpoest, W. Dewulf, Environmental impact analysis of composite use in car manufacturing.

12. Y.F. Khalil, Sustainability assessment of solvolysis using supercritical fluids for carbon fiber reinforced polymers waste management.

13. Angela Daniela La Rosa, Sebastiano Greco, Claudio Tosto, Gianluca Cicala, LCA and LCC of a chemical recycling process of waste CF-thermoset composites for the production of novel CF-thermoplastic composites. Open loop and closed loop scenarios.

14. Kumar, S., Krishnan, S. Recycling of carbon fiber with epoxy composites by chemical recycling for future perspective: a review. Chem. Pap. 74, 3785–3807 (2020). https://doi.org/10.1007/s11696-020-01198-y.

15. Krauklis AE, Karl CW, Gagani AI, Jørgensen JK. Composite Material Recycling Technology—State-of-the-Art and Sustainable Development for the 2020s. Journal of Composites Science. 2021; 5(1):28. https://doi.org/10.3390/jcs5010028.

16. Karuppannan Gopalraj, S., Kärki, T. A review on the recycling of waste carbon fibre/glass fibre-reinforced composites: fibre recovery, properties and life-cycle analysis. SN Appl. Sci. 2, 433 (2020). https://doi.org/10.1007/s42452-020-2195-4.

17. Feral Temelli, Perspectives on supercritical fluid processing of fats and oils, The Journal of Supercritical Fluids, Volume 47, Issue 3, 2009, Pages 583-590, ISSN 0896-8446, https://doi.org/10.1016/j.supflu.2008.10.014.

18. Wilson V. Vasquez, Diego Martín Hernández, Joaquín Navarro del Hierro, Diana Martin, M. Pilar Cano, Tiziana Fornari, Supercritical carbon dioxide extraction of oil and minor lipid compounds of cake byproduct from Brazil nut (Bertholletia excelsa) beverage.

19. Sandra Gonçalves, Anabela Romano, Chapter 4 - Application of supercritical CO2 for enhanced oil recovery, Editor(s): Inamuddin, Abdullah M. Asiri, Arun M. Isloor, Green Sustainable Process for Chemical and Environmental Engineering and Science, Elsevier,.

20. ISO, 2006a. ISO 14040: Environmental management – Life cycle assessment. Principles and framework, Geneva.

21. ISO, 2006b. ISO 14044: Environmental management – Life cycle assessment – Requirements and guidelines. Geneva.

22. David G. Woodward, Life cycle costing—Theory, information acquisition and application, International Journal of Project Management,.

23. ISO 15686-5:2017(en) Buildings and constructed assets — Service life planning — Part 5: Life-cycle costing.

24. Swarr, Thomas & Hunkeler, David & Klöpffer, Walter & Pesonen, Hanna-Leena & Ciroth, Andreas & Brent, Alan & Pagan, Robert. (2011). Environmental Life-Cycle Costing: A Code of Practice. The International Journal of Life Cycle Assessment. 16. 389-391. 10.10.

25. Sara Toniolo, Roberta Chiara Tosato, Fabio Gambaro, Jingzheng Ren, Chapter 3 - Life cycle thinking tools: Life cycle assessment, life cycle costing and social life cycle assessment,.

26. European Commission, Joint Research Centre, Institute for Environment and Sustainability. Characterisation factors of the ILCD Recommended Life Cycle Impact Assessment methods. Database and Supporting Information. First edition. February 2012. EUR 25167. .

27. European Commission-Joint Research Centre - Institute for Environment and Sustainability: International Reference Life Cycle Data System (ILCD) Handbook- Recommendations for Life Cycle Impact Assessment in the European context. First edition November 2011.

28. Brian Cox, Wojciech Jemiolo, Chris Mutel, Life cycle assessment of air transportation and the Swiss commercial air transport fleet,.

29. REPAIR3D webpage, https://www.repair3d.net/.

ADDITIVE MANUFACTURING OF MULTILAYERED POLYMER COMPOSITES: DURABILITY ASSESSMENT

Ali, Payami Golhin [a], Chaman, Srivastava [a], Jens Fossan, Tingstad [b], Aditya Suneel, Sole [b], Are, Strandlie [a], Sotirios, Grammatikos [a]

a: Laboratory for Advanced and Sustainable Engineering Materials (ASEMlab), Department of Manufacturing and Civil Engineering, Norwegian University of Science and Technology, 2815 Gjøvik, Norway – ali.p.golhin@ntnu.no
b: Department of Computer Science, Norwegian University of Science and Technology, 2815 Gjøvik, Norway

Abstract: *This study examines the impact of additive manufacturing (AM) settings on the durability of 3D-printed polymer composite objects in terms of object color appearance and corresponding mechanical properties when subjected to simulated environmental conditions using accelerated aging. For this purpose, the AM pre-processing factors that influence the performance of the composite material, such as build platform position, color, and finishing configurations, are discussed. The experimental campaign was designed according to the Taguchi method to minimize the color difference and maximize the mechanical parameters. The results indicate that the best factor parameters for each performance characteristic differ following the design goal. Accordingly, black-on-white with a glossy-on-matte finish manufactured on the outer swath demonstrated the best color and mechanical performance fidelity, where the studied properties were not altered significantly due to aging.*

Keywords: PolyJet 3D printing, Accelerated aging, Structural degradation, Object appearance, Color change

1. Introduction

The new r-theta rotating build platform approach with a fixed print head was recently introduced as an alternative to traditional XYZ build platform 3D printers. The stated reasons for the disc-shaped build platform include increased reliability, easier maintenance, and a smaller footprint. However, the distinct layering mechanism and pattern compared to other AM machines necessitates new considerations in the design, appearance, and durability evaluation. In particular, a close inspection of the various assembled models printed on a rotary build platform reveals a few broken and glued small parts, indicating that the commercial PolyJet printer currently in use produces rigid and brittle parts with microscopic textures [1, 2]. In addition, while Material jetting (MJT)-printed products represent a desirable appearance, their durability is vital due to their prohibitive costs and environmental impact, especially for engineering applications [3].

The surface quality of 3D-printed objects can be affected by various process parameters. According to the Taguchi approach in the design of experiments, the process variables can be reduced, and the mean values must be adjusted to a target value. Orthogonal arrays are used to execute the tests and measure process quality. Thus, the signal-to-noise (S/N) ratios can

  doi:10.5075/epfl-298799_978-2-9701614-0-0

assess the quality of the production process designed for regular application in testing, surgical planning, and tooling [4].

In this work, we present the results of an investigation into the optical and mechanical properties of 3D-printed bi-layer polymer specimens manufactured under various parametric conditions. The effect of three 3D printing parameters, including color, the position of the piece on the build platform (swath selection), and finishing on the mechanical and appearance variables, was investigated using the Taguchi methodology. The novelty of the work presented herein lies in the unique linkage between appearance and long-term mechanical properties, providing new insight into assessing the durability of AM products.

2. Materials and methods

A Stratasys J55 PolyJet 3D printer has been used to manufacture samples under different conditions. The characteristics of the VeroPureWhite (RGD837), VeroBlackPlus (RGD875), VeroCyan (RGD843), VeroYellow (RGD836), and VeroMagenta (RGD851) photo-resins (Stratasys Ltd., USA) are investigated in this study. These rigid polymers mainly consist low-viscosity acrylic oligomer, exo-1,7,7-trimethylbicyclo [2,2,1] hept-2-yl acrylate, (octahydro-4,7methano-1H-indenediyl) bis(methylene) diacrylate, and 4-(1-oxo-propenyl)-morpholine [5].

Parts were designed with a minimum thickness of 2 mm when a 1 mm white background was covered by 1 mm of colored material. The reference materials for color studies were the same as-printed samples before aging. For mechanical testings, the specimens were selected from the magenta samples printed on the middle swath and glossy on the glossy (GoG) finish. According to the datasheet for used photo-resins [6], the Vero materials family shares similar mechanical, thermal, and electrical properties.

To investigate the impact of 3D printing parameters on the variables, an L8(4^1 2^2) orthogonal array was chosen for three parameters of color, swath, and finishing process. As a result, 63 specimens were manufactured for 8 runs and as references. The process parameters and their levels are summarized in Table 1.

Table 1: Taguchi factors and their levels.

	Factor		
Run	Color	Swath	Finish
1	Cyan	Inner	Glossy on Glossy
2	Cyan	Outer	Glossy on Matte
3	Magenta	Inner	Glossy on Glossy
4	Magenta	Outer	Glossy on Matte
5	Yellow	Inner	Glossy on Matte
6	Yellow	Outer	Glossy on Glossy
7	Black	Inner	Glossy on Matte
8	Black	Outer	Glossy on Glossy

  doi:10.5075/epfl-298799_978-2-9701614-0-0

For the assessment of mechanical performance, tensile and viscoelastic testing were considered (Figure 1).

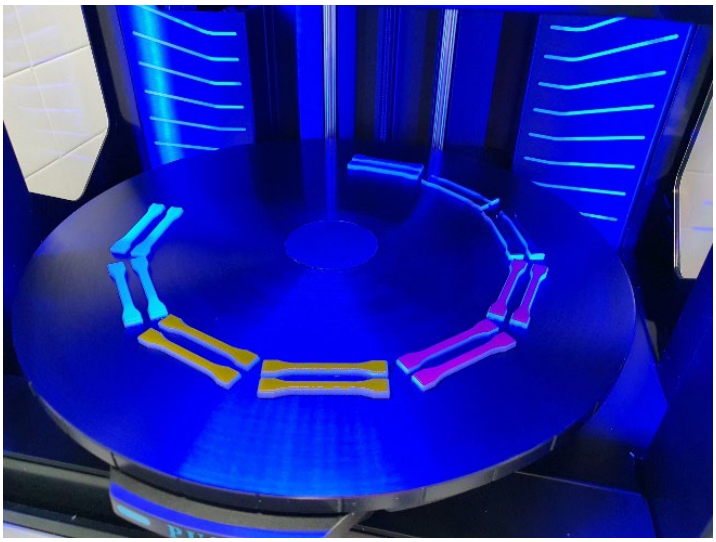

Figure 1. Reference tensile specimen in the middle swath of the rotary build platform.

To determine the durability of the polymeric specimens, the specimens were aged in a QUV chamber from QLab for a maximum duration of 2 weeks. The aging regime representing natural weathering was selected according to the ASTM G154 standard. The weathering cycle had a UV exposure at 0.8 W/m^2 for 6 hours at 60 °C, followed by condensation at 40 °C and spray at 24 °C, where the humidity is set at 60% and 100%, respectively.

A Konica Minolta CS-2000 tele-spectroradiometer (TSR) was used to measure appearance by recording radiance at the specimen surface within the 380-780 nm spectral range. The optical resolution and physical sampling intervals were 1 and 10 nm, respectively. The device was placed 50 cm in front of the target object, normal to the surface (Figure 2). The measurement field of view was set to 0.2 degrees to avoid error due to targeting areas covered by stains or dust. The surface of the 3D-printed specimen was studied using a 45°:0° viewing geometry according to CIE Publication 15.2 [7]. The spectral results of targets were calibrated using the standard spectralon white ceramic patch. The colorimetric values were calculated using the computational color science toolbox in MATLAB R2021a [8].

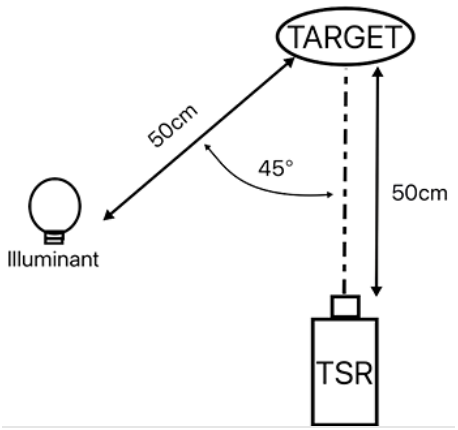

Figure 2. Schematic view of the color appearance measurement setup.

  doi:10.5075/epfl-298799_978-2-9701614-0-0

Dynamic Mechanical Analysis (DMA) of the polymer coupons is carried out to determine the glass transition temperature (T_g) and the relative shift in the T_g as a function of the aging time and temperature [9]. The test was performed on Discovery DMA 850 from TA instruments, as per the ASTM D4065 standard. The specimen dimensions were 60 × 13 × 3 mm^3. A temperature ramp test was performed at a heating rate of 2 °C. The test temperature range was set from 20°C to 95°C, which was below the degradation temperature of the material. The amplitude of the test was set to 20 µm with a frequency of 1 Hz. The maxima of the tan δ curve and its corresponding temperature are referred to as the T_g reported in the paper.

To determine the tensile modulus and the strength of the polymer material as a function of aging duration, ISO 527-02 was used [10]. The dimensions of the dog bone specimens were 75 × 10 × 2 mm^3. Uniaxial tensile testing was performed on Instron 5966 universal testing machine, and the strain was measured using an AVE2 virtual extensometer. The loading rate was set to 2 mm/min. The force-displacement curves were used to determine the tensile chord modulus, and the ultimate tensile stress was chosen as the tensile strength of the bi-layer material.

3. Results and discussions

Figure 3 depicts the color difference for DMA coupons after two weeks of accelerated weathering. According to CIEDE2000 colorimetric difference [7], in Figure 3a, magenta samples are notably altered in color compared to reference samples. On the other hand, cyan and yellow samples represent noticeable color differences compared to the control parts and at a lower level. Similar advantages for cyan color over red feedstock were described before for fused deposition modeling (FDM) [11]. In magenta and yellow samples, significantly higher color differences were observed for the GoG samples.

On the other hand, cyan and black objects respond in reverse as their average CIEDE2000 has slightly decreased. The redness (a*) and yellowness (b*) shifts in the CIE L*a*b* values at a constant lightness of 90 suggest yellower yellow samples, less red magenta samples, and bluer/greener cyan samples after two weeks of aging (Figure 3b). The color of the black objects did not change enough to be recognized without measurement.

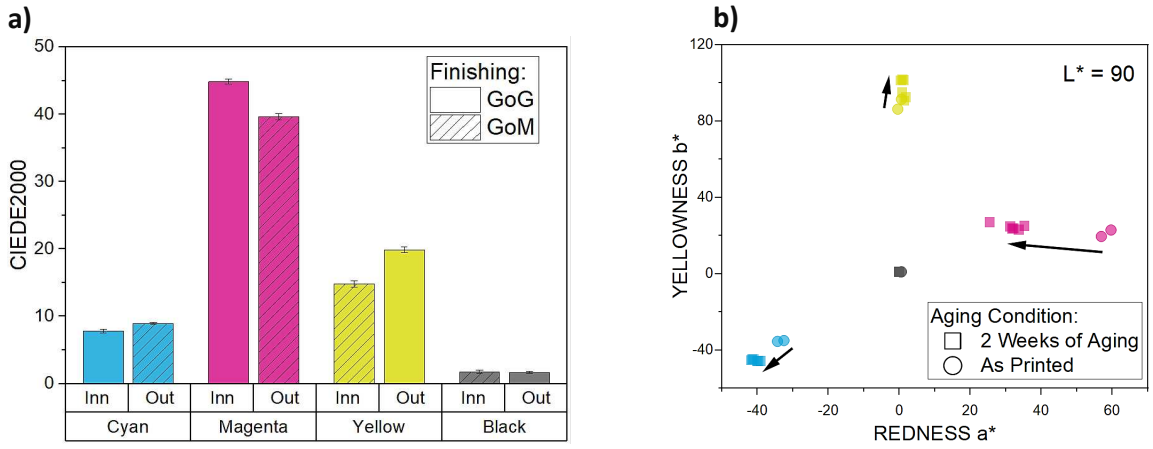

*Figure 3. a) CIEDE2000 color difference and associated root mean square error (RMSE) bars, and b) shift in the a*b* values after the aging process.*

  doi:10.5075/epfl-298799_978-2-9701614-0-0

The DMA coupons after two weeks of weathering are depicted in Figure 4. In magenta samples, the marginal dark-red area represents the original color obscured by the sample holders. As seen from the edges, the color differences for magenta samples were significant, while the color differences for cyan and yellow pieces were barely noticeable after aging.

Figure 4. DMA specimens after two weeks of weathering exposure.

Figure 5a depicts representative stress-strain curves for each type of specimen aged and tested. The results are compared with the reference specimens before aging. It is observed that the tensile modulus of the polymer specimen increases during the 2 weeks aging regime, which complements the findings from the DMA analysis and in conjunction with the stiffness increase. The table shown in Figure 5b populates the results for glass transition temperature measurements from the tan δ curve from the DMA analysis. It is observed that the glass transition temperature of the polymeric material has increased significantly to a range of 80-84°C for each specimen, where the reference value of 53°C is taken from the reference manual for the feedstock material. The sharp increase in the change in the T_g of the material is very anomalous. This can be attributed to the material being cured during 3D printing, pre-aging due to storage, and weathering process, where the T_g increased slowly.

a)

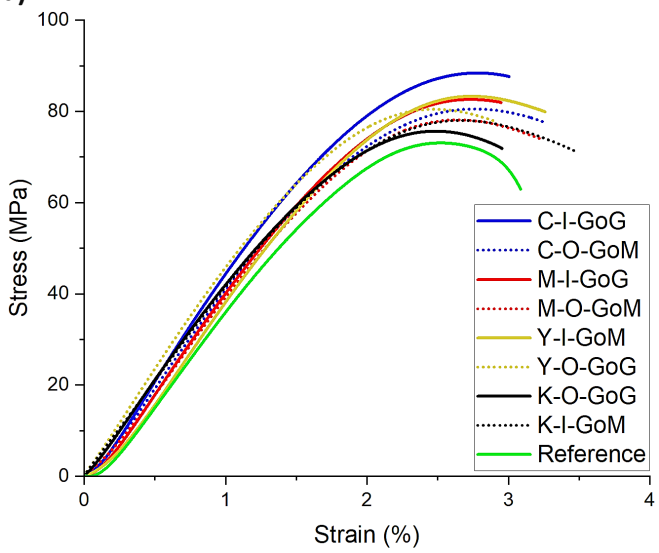

b)

Sample	Elastic Modulus [GPa]	T_g [°C]
Reference	3.99 ± 0.03	73.29
C-I-GoG	4.51 ± 0.12	83.18
C-O-GoM	4.15 ± 0.20	83.00
M-I-GoG	4.23 ± 0.13	82.88
M-O-GoM	4.09 ± 0.08	80.55
Y-I-GoM	4.29 ± 0.11	80.88
Y-O-GoG	4.37 ± 0.07	81.30
K-I-GoM	4.00 ± 0.08	80.36
K-O-GoG	4.07 ± 0.14	81.67

Figure 5. a) Stress-strain curves for tensile specimens, and b) E modulus and T_g results; C: Cyan, M: Magenta, Y: Yellow, K: Black, I: Inner Swath, O: Outer Swath, GoG: Glossy on Glossy finish, GoM: Glossy on Matte finish.

  doi:10.5075/epfl-298799_978-2-9701614-0-0

According to the S/N ratio plots in Figure 6a, color, as expected, had the most significant influence on the color difference. In contrast, swath and finishing had no considerable impact on this variable. However, after two weeks of weathering, the choice of outer swath and GoG finish resulted in more stable color difference calculations (Figure 6 b)). In terms of color, black and then cyan samples demonstrated significantly more reliable color fidelity than magenta and yellow samples after aging.

On the other hand, S/N ratio plots for mechanical properties (Figures 6c and d) revealed, in addition to color, that the swath and finishing significantly influenced the elastic modulus and T_g of the studied samples. Accordingly, the inner swath and GoG finish resulted in higher elastic modulus and T_g. Cyan provided higher E and T_g than black, while magenta and yellow samples demonstrated unstable behavior in mechanical testing. The ultraviolet (UV) absorbance of samples during the weathering test can explain the possible effect of post-curing behind these mechanical behaviors of the studied specimens, resulting in more rigid materials with altered mechanical properties and color appearances.

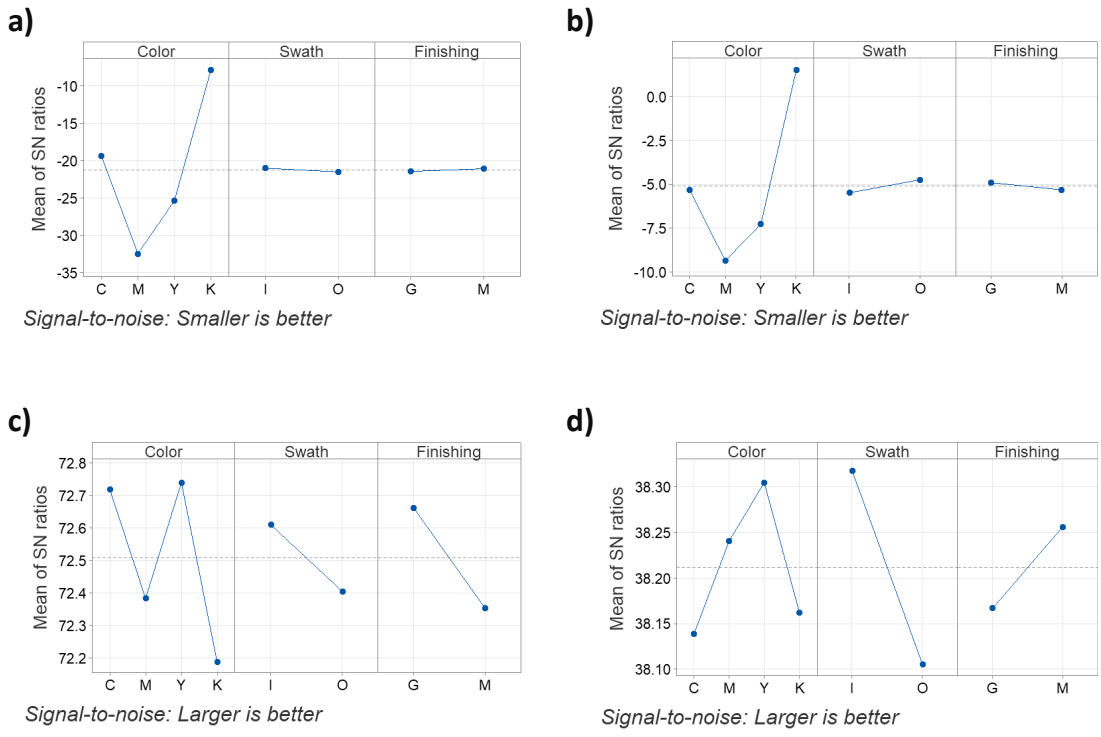

Figure 6. Main effects S/N plots for a) CIEDE2000, b) RMSE for CIEDE2000, c) Elastic modulus, and d) T_g.

  doi:10.5075/epfl-298799_978-2-9701614-0-0

4. Conclusions

A durability study was conducted to investigate the effect of processing parameters, including color, the position of the piece on the build platform (swath), and finishing on the long-term mechanical properties and appearance of photo resin samples made using the Stratasys Vero family after two weeks of accelerated aging in a weathering chamber. Based on the results, the color factor solely dominated the color appearance results compared to other studied parameters. On the other hand, the swath and finishing selections, in addition to color, also significantly affected the mechanical properties.

Compared to as-printed control samples, all aged coupons showed altered mechanical properties. However, the black-on-white with a glossy-on-matte finish manufactured on the outer swath offered the best color fidelity and stable mechanical behavior after weathering. In contrast, the magenta samples had the weakest durability response due to the possible excessive UV post-curing in the QUV chamber. Furthermore, the durability assessment in a harsh environment for yellow and cyan samples revealed their unstable behavior due to their color appearance, which should be considered in the design process. The results demonstrated the importance of the color study as a primary parameter when investigating weathering and UV exposure, which is necessary for engineering applications.

5. Future studies

The nature of the weathering test is to age the samples over an extended period. Therefore, further research on the response of variables over a more extended aging period allows for a better balance of all studied parameters to be discovered. To this end, our next step is to conduct a long-term study on the samples to reduce the impact of measurement uncertainty and provide more details to improve the durability of an object in MJT additive manufacturing.

Acknowledgments

We would like to acknowledge support from the ApPEARS-ITN project funded by the European Union's H2020 research and innovation program under the Marie Skłodowska-Curie grant agreement No. 814158 and from the LIFETIME project, Ref: 309943, funded by the Research Council of Norway.

6. References

1. Elber G, Kim MS. Synthesis of 3D jigsaw puzzles over freeform 2-manifolds. Comput Graphics (Pergamon). 2021.
2. Payami Golhin A. Generation of micro-and nano-textured surfaces. Brussels: European Commission; 2021.
3. Li Y, Linke BS, Voet H, Falk B, Schmitt R, Lam M. Cost, sustainability and surface roughness quality – A comprehensive analysis of products made with personal 3D printers. CIRP J Manuf Sci Technol. 2017;16:1-11.

  doi:10.5075/epfl-298799_978-2-9701614-0-0

4. Camposeco-Negrete C. Optimization of FDM parameters for improving part quality, productivity and sustainability of the process using Taguchi methodology and desirability approach. Prog Addit Manuf. 2020.
5. Tee YL, Peng C, Pille P, Leary M, Tran P. PolyJet 3D printing of composite materials: experimental and modelling approach. Jom. 2020;72(3):1105-17.
6. Vero: Realistic, Multi-Color Prototypes in Less Time. 2022.
7. l'Éclairage CId. Colorimetry CIE 015:2004: Commission Internationale de l'Éclairage; 2004. p. 1-82.
8. Westland S, Ripamonti C, Cheung V. Computational colour science using MATLAB: John Wiley & Sons; 2012.
9. Das SC, Paul D, Grammatikos SA, Siddiquee MAB, Papatzani S, Koralli P, et al. Effect of stacking sequence on the performance of hybrid natural/synthetic fiber reinforced polymer composite laminates. Compos Struct. 2021;276.
10. Plastics - Determination of tensile properties. Part 2: Test conditions for moulding and extrusion plastics: International Organization for Standardization ISO/TC 61/SC 2 Mechanical behavior; 2012.
11. Payami Golhin A, Strandlie A, John Green P. The Influence of Wedge Angle, Feedstock Color, and Infill Density on the Color Difference of FDM Objects. J Imaging Sci Technol. 2021;65(5):050408-1–-15.

  doi:10.5075/epfl-298799_978-2-9701614-0-0

MATERIAL DESIGN-FOR-EXCELLENCE (OR M-DFX) – NEW METHODOLOGICAL APPROACH APPLICABLE TO COMPOSITE MATERIALS

Susana, P.B. Sousa[a], António, J.Baptista[a], António, Torres Marques[a,b], Paulo Nóvoa[,b], Helena Soares[,b], Margarida Bastos[,b]

a: INEGI - Institute of Science and Innovation in Mechanical and Industrial Engineering
b: FEUP - Faculty of Engineering of the University of Porto – marques@fe.up.pt

Abstract: *Material Design-for-eXcellence (M-DfX) is a novel approach to support the assessment of material performance in a systematic and visual way, through the evaluation of material properties ("X" dimensions) and characteristics in a normalized form. It manages the material composition complexity in different scales, adopting a modular configuration analogy. In this work it is made a demonstration example of M-DfX for the framework testing in the Composite Materials field, comparing a carbon fibre versus other fibres based in a real case application, for the BMW i3 vehicle. It was possible to observe that basalt fibre could be a good sustainable fibre for the automotive sector. Future developments and research lines for M-DfX were also described, including the development and characterization of bulk and dough moulding compounds from non-metallic fractions recovered from printed circuit boards.*

Keywords: Performance; Advanced materials; Eco-efficiency; Sustainability; Materials Life Cycle.

1. Introduction

In an increasingly globalized world, there is growth in travelling and transports. This expansion in the transport sector does not tend to stop. However, 96% of the transport vehicles are dependent of petroleum-based fuels, so this will result in significant rise in global fuel demand and greenhouse gas (GHG) emissions (1, 2). The transport sector is responsible for about a quarter of the total GHG emissions in Europe. Road vehicles are the biggest contributors to global emissions (3). Transport industry is one of the main pillars of the global economy, so the companies must move forward together to achieve "carbon neutrality", using sustainable products, reducing energy consumption, trying to reduce emissions, tracking the carbon footprint, among other measures (4).

Currently, polymers represent less than 12% of the average weight of a car vehicle, saving up to 30 times more energy over the life cycle of this vehicle than the energy needed to produce it. While in an aircraft, weight reduction using carbon fibre reinforced polymers (CFRP) could potentially reduce CO_2 emissions by 20% during use. Therefore, reducing vehicle weight represents considerable savings in fuel/energy and emission reduction (1, 2). So, in the last years the polymer composites have been known as instrumental to reduce the transports sector footprint, due to their structural performance and low weight that leads to lower fuel consumption and, thus, better environmental benefits (5-7). However, manufacturers also struggle to provide low-cost, high-performance and reduction of CO2 emissions. There for, the material design becomes an essential element of competitive advantage that can impact the industries businesses competitiveness, particularly in terms of productivity, circularity, safety, sustainability, and quality (8).

  doi:10.5075/epfl-298799_978-2-9701614-0-0

Nevertheless, each year the challenges for this industry are more complex. Moreover, recently there is a shortage of raw materials because of environmental catastrophes, natural disasters, pandemics, wars, and other, making them seek for holistic solutions, which guarantee the reduction of the environment impact, leads to less material consumptions, reduce time in the product development process, has higher product quality, reduce overall costs and fulfilling customers' requirements. To achieve all these requirements, companies must use new models that certify design efforts, customer, and societal needs from product ideation until its end-of-life (9). It is essential to look for methodologies to develop the best recycling routes to obtain non-metallic waste from different sources such as Printed Circuit Boards – PCBs used in the automotive industry, followed by the processing study of molding compounds with the inclusion of the residue as a reinforcing filler, and using the residue from the resin of PCBs (10). Nevertheless, there is a lack for straightforward material performance methods allowing for an easy and multi-dimensional assessment for the material properties, relating to the inner structure of the material to a Life-Cycle assessment orientation (11-13).
The BMW i3 is an example of a vehicle that is already on the market and has carbon fibre structural components to be more sustainable. However, BMW i Ventures has been studying the feasibility of developing and using natural-based high-performance composites. Therefore, in this study we will analyse the true sustainability of the current carbon fibre composite solution compared to other potential bio-based solutions (14-17). So, in this study it is proposed a new methodology applicable to composite materials that can contribute to the optimization of design based on the Design for X (DFX) approach, which considers several requirements through different factors Xs, to improve the product design as well as the design process (9). The aim of this methodology is to make the product better suited for the different life phases and increase the general product performance.

2. Materials and Methods

2.1 Material Design-for-eXcellence

The Material Design-for-eXcellence conceptual framework was created upon state-of-art methodologies developed by INEGI, for complex product development multi-dimensional assessment (18) and production systems resource and operational efficiency assessment (19). In M-DfX framework two essential aspects are assessed in and combined way: i) the material behaviour and its multiple characteristics assessment, and ii) the manufacturing processes efficiency. By using these two aspects, the material performance can be assessed in a holistic and life cycle-oriented form. The framework considers the analogy of product design holistic approaches, as Design-for-X, to organize and assess the multi-dimensional performance for each "X" Material Property (Figure 1) (20).
Besides, the M-DfX framework is structured in four fundamental pillars, which also corresponds to the base sequence for the methodology formulation (**Error! Reference source not found.**) (20).
The first pillar corresponds to the physical arrangement decomposition of the material. The second pillar of the framework is the cornerstone to the approach since it holds a key part of the formulation behind the calculus for either the effectiveness aspect and efficiency and eco-efficiency assessment. The third pillar is the visual management of the different attributes (represented for the four-color scheme and legend for effectiveness levels). And the last pillar considers a graphical comparison of the two performance components, effectiveness (assessing

  doi:10.5075/epfl-298799_978-2-9701614-0-0

the properties characteristics) and (eco)efficiency (assessing the resources efficiency along the life cycle), in the form of a Quadrant Graph, for a more sensible overall comparison of the materials in comparison (20).

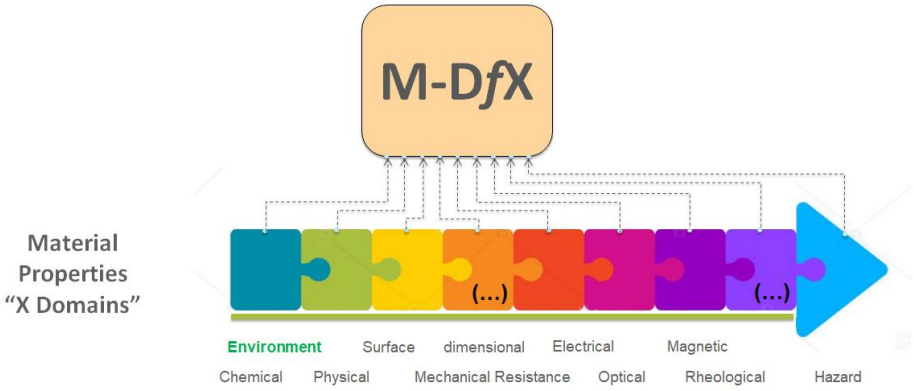

Figure 1. M-DfX multi-dimensional overview regarding material life cycle and material properties "X" examples.

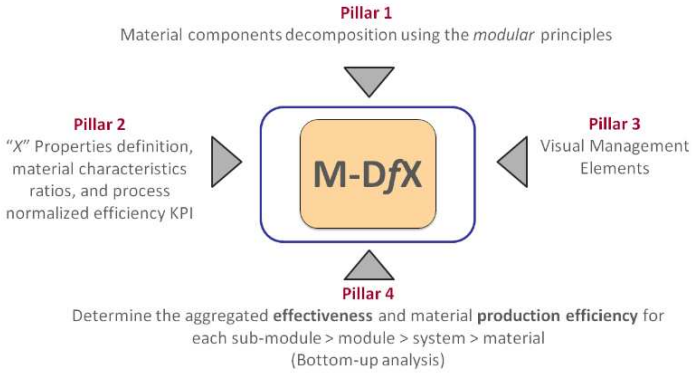

Figure 2. M-DfX framework pillars.

2.2 Applications for composites

The example here proposed is based on a BMW i3 vehicle that has structural components in CFRP (Carbon Fibre Reinforced Plastics). The production of the CFRP are complex and involve several materials and production technologies. Since the use of natural based materials in composites have expressively lower properties than the "artificial ones," especially the bio-based thermosetting resins, in this research, to try to overcome this main drawback, a compromise/hybrid solution is proposed, analysing only the kind of fibre and production method.

In the **Error! Reference source not found.** presents the relevant properties of the main raw materials, based on the information of CES EduPack 2021 (21) and commercial datasheets.

Error! Reference source not found. presents the relevant properties of the composites based on the rule of mixtures, considering 50% of fibre and matrix volume fraction (the most common obtained with the vacuum assisted resin infusion process).

There are several processes for the FRP production components, where the selection is driven by the design requirements of the application. To obtain higher properties, normally autoclave process is chosen, although lately out of autoclave (OoA) processes have been optimized leading to similar performance and lower energy consumption (22, 23). In the **Error! Reference source**

not found. presents the relevant data of the main FRP production methods, based on the information of CES EduPack 2021.

Table 1. Main average properties of the main raw materials (21).

Properties		Matrix		Fibres			
		Epoxy	Bio-Epoxy*	Carbon	Glass	Basalt	Flax
Mechanical	Young's Modulus (GPA)	2,41	2,86	242,50	89,50	90,50	53,50
	Tensile Strength (MPa)	67,30	67,17	4600,00	4750,00	3165,00	845,00
	Elongation (% strain)	4,50	6,33*	1,85	5,25	3,20	2,20
Thermal	Maximum service temperature (ºC)	130,00	99,44**	555,00	310,00	675,00	120,00
	Glass transition temperature (ºC)	117,00	89,50	-	-	-	-
	Thermal conductivity (W/mºC)	0,19	0,15**	140,00	1,28	0,03	0,25
Physical	Density (kg/m^3)	1255,00	1152,00	1820,00	2495,00	2695,00	1470,00
Cost	Price (€/kg)	3,62	6,81	25,00	22,25	2,13	1,50
Primary production	Energy (MJ/kg)	128,50	79,67**	286,00	51,80	0,91	11,05
	CO_2 (kg/kg)	6,60	4,09**	20,30	3,00	0,06	0,44
	Water (l/kg)	28,00	17,36**	7,40	296,00	13,70	3150,00
Recycle fraction	Currently (%)	0,71	0,71**	4,98	0,10	0,00	0,1
Production in Europe	Yes/No	Yes	Yes	No	Yes	Yes	Yes

***Based on average values of a commercial 38% bio-epoxy resin**

**** Estimated values**

The use phase refers to the period of a vehicle component, which it is functioning in its predetermined application. This phase dominates the energy consumption of automobile, primarily due to impacts of its weight, i.e., fuel economy. Therefore, the lightness benefits are especially recognised in the use stage. Until now, landfill has been the most common disposal route for composite materials. However, more recently, recycled processes have been developed and used for these materials, with different energy and CO_2 results (Table 4).

The predominant treatments are mechanical (Grinding), thermal (Pyrolysis), and chemical (Solvolysis) process. Solvolysis treatments are normally used to recuperate from the composite materials the carbon fibres with higher properties (24-26). The grinding method is the most common and profitable for glass fibres composites to be used at a large-scale, due to the low cost, obtaining at the end of this process crushed particles, which can be used as reinforcement in new materials (24, 27-29). Since basalt fibres have high temperature resistance, the most adequate process to recover these kind of fibres from the composite is the pyrolysis (30, 31). The grinding method probably will be also the most adequate method to recycle flax composites, since the natural fibres have low chemical and thermal properties. Despite this practice, the environmental aspects of the technique, particularly its process energy demand must be considered (20). In manufacturing, recycling and remanufacturing electrical energy demand dominates the environmental burden and global warming potential of this process (25, 26). Future research will consider different processing routes for the use of recycled fibres and resins as moulding compounds.

Table 2. Main average properties of the resultant composites.

Properties		Standard based composite				Bio based composite			
		Carbon	Glass	Basalt	Flax	Carbon	Glass	Basalt	Flax
Mechanical	Young's Modulus (GPA)	122,46	45,96	46,46	27,96	122,68	46,18	46,68	28,18
	Tensile Strength (MPa)	2333,65	2408,65	1616,15	456,15	2333,59	2408,59	1616,09	456,09
	Elongation (% strain)	3,18	4,88	3,85	3,35	4,09	5,79	4,77	4,27
Thermal	Maximum service temperature (ºC)	342,50	220,00	402,50	125,00	327,22	204,72	387,22	109,72
	Glass transition temperature (ºC)	117,00	117,00	117,00	117,00	89,50	89,50	89,50	89,50
	Thermal conductivity (W/mºC)	70,10	0,74	0,11	0,22	70,08	0,72	0,09	0,20
Physical	Density (kg/m^3)	1537,50	1875,00	1975,00	14700	1486,00	1823,50	1923,50	1311,00
Cost	Price (€/kg)	14,31	12,94	2,88	2,56	15,91	14,53	4,47	4,16
Primary production	Energy (MJ/kg)	207,25	90,15	64,71	69,78	182,84	65,74	40,29	45,36
	CO_2 (kg/kg)	13,45	4,80	3,33	3,52	12,20	3,55	2,08	2,27
	Water (l/kg)	17,70	162,00	20,85	1589,00	12,38	156,68	15,53	1583,68
Recycle fraction	Currently (%)	2,85	0,41	0,36	0,41	2,85	0,41	0,36	0,41
Production in Europe	Yes/No	No	Yes	Yes	Yes	No	Yes	Yes	Yes

Table 3. FRP production process analysis (21).

Process	Energy (MJ/kg)	CO_2 (kg/kg)	Water (l/kg)
Autoclave	21,95	1,76	17,00
Resin transfer moulding (RTM)	12,80	1,03	6,34
Vacuum assisted resin infusion (VARI)	10,21	0,82	11,18
Total	44,96	3,61	34,52

Table 4. Environmental impact of the main EOL treatments (25, 26).

Process	Energy (MJ/kg)	CO_2 (Kg/kg)
Grinding	1.12	-36.00
Pyrolysis	37.36	8.60
Solvolysis	38.39	–
Total	76,87	-27,4

3. Results and discussion

In the research work it was adopted the "Relative best" approach to the normalization of the effectiveness ratios, and for the (eco) efficiency along the macro-phases selected. For this case study diverse number of characteristics were selected for each proprietary, being the ones that were considered more relevant for the project design. In Figure 3 is presented the aggregated results for carbon composite material ("Material 1") application to BMW3i, when compared with the other composites for normalization, for the effectiveness.

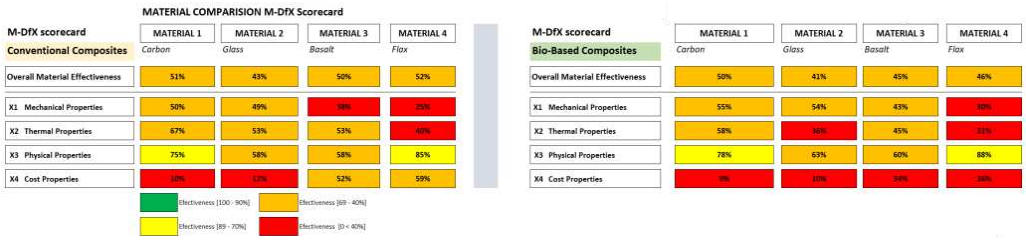

Figure 3. M-DfX Efectiveness scorecard.

For the (eco)efficiency analysis four KPI were selected: Energy Efficiency (MJ/kg), CO_2 Emissions (kg CO_2/kg), H_2O consumption (l/kg) and Recyclability (%). Not all KPI could be mapped for all Macro Phases, either for absence of data available or if it is not applicable (N.A.). Figure 4 presents results for carbon composite, where the normalization was done phase by phase, according the relative best reference material. The results are integrated column by column, assessing the macro-phase (eco)efficiency and the overall result is computed by averaging the macro-phases figures.

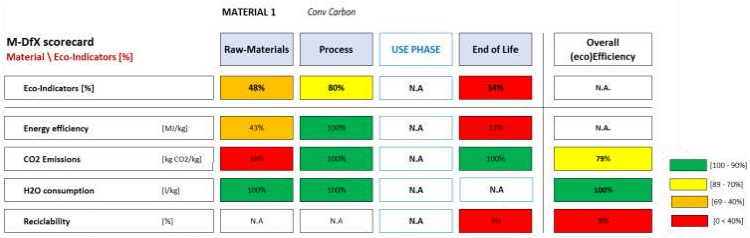

Figure 4 - M-DfX (eco)Efficiency scorecard for carbon composite material.

The carbon bio-composite performs slightly better than the others, with significant lower results for the H_2O consumption in Raw-Materials extraction and CO_2 Emissions in End-of-Life (EOL). Nonetheless, it is clearly worse in Energy Efficiency in Raw Materials phase. It was considered that both materials are processed by infusion, and that's the reason that both share the same 100% result in production phase. In synthesis, the M-DfX identify that carbon composite is gets worse results in Raw-Materials phase, but much better in EOL, regarding the other composites. In Use-Phase, carbon laminates show slightly better results, but the others composites hold also a very good result. However, bio-based basalt fibre composite also presents high effectiveness and (eco)Efficiency, that could be an indicator to a large uses of these eco-materials.

4. Conclusions

Material Design-for-eXcellence Framework presents an original approach to address the challenge of evaluating material performance with a multi-dimensional assessment for the material properties, relating to the inner structure of the material in a multi-scale proposition supported by a Life-Cycle Assessment mindset for different macro-phases. M-DfX formulation encompasses a systematic and visual way – through the evaluation of material properties and related characteristics in a normalized form. It manages the material composition complexity in different scales, adopting a modular configuration analogy. The integrated analysis of material performance is attained via an effectiveness assessment of the properties' characteristics cross-evaluated with efficiency/eco-efficiency aspects, within a Life Cycle approach, resulting in new original M-DfX Scorecards and Quadrants Graphs tools. A demonstration example of M-DfX was given for the framework demonstration in the Composite Materials field, comparing several kind of composites to be potentially used in the BMW i3 vehicle. It was possible to observe that the bio based solution with basalt fibre could be a good sustainable alternative for the automotive sector. In a very near future, Material Design-for-eXcellence Framework must include other parameters such us social impacts, ethics and an evaluation of social acceptance for all the stakeholders. Bearing in mind the need for a sustainable planet, a new paradigm for product development will have to appear. It will be required that the products have a longer life and to be able to receive new technological updates. Hence, the M-DfX Framework will have to include a Design for update. A high potential manufacture process, the additive

manufacturing hybridized with subtractive technologies, and an innovative product, high performance composites parts produced without moulds and with tailored properties presents a new challenge. Both process and products hold a high potential of, in the future, converting into tradable goods fostering the industry in particular and the economy in general. M-DfX will have to deal with the development of expeditious ways of creating hybrid materials or combinations. Bearing in mind that researchers are creating, in a fast way, more and more new materials, having a diversity of properties at different scales, Material Design-for-eXcellence must also consider these factors. Hence, additional studies are thus foreseen to explore and develop this new tool, so that they achieve higher performance without significant costs increase, to ensure widespread use of this developed sustainable solution.

Acknowledgements

The financial support of FEDER funds through COMPETE2020 (under Research Project PTDC/EAM-MIN/31041/2017 Waste Zero-PCBs: A sustainable and practically non-waste technology for recycling printed circuit boards – POCI-01-0145-FEDER-031041) is gratefully acknowledged.

References

1. Al-Lami A, Hilmer P, Sinapius M. Eco-efficiency assessment of manufacturing carbon fiber reinforced polymers (CFRP) in aerospace industry. Aerospace Science and Technology. 2018;79:669-78.
2. Mayyas A, Qattawi A, Omar M, Shan D. Design for sustainability in automotive industry: A comprehensive review. Renewable and sustainable energy reviews. 2012;16(4):1845-62.
3. EEA. Greenhouse gas emissions from transport 2022 [Available from: https://www.eea.europa.eu/ims/greenhouse-gas-emissions-from-transport
4. Huang Q, editor Analysis of Global Policy and Impact on Automobile Industry under Carbon Neutrality. E3S Web of Conferences; 2021: EDP Sciences.
5. Tan X, Wang J, Xu Y, Curran R, Raghunathan S, Gore D, et al., editors. Cost-Efficient Materials in Aerospace: Composite vs Aluminium2008; London: Springer London.
6. Pervaiz M, Panthapulakkal S, Sain M, Tjong J. Emerging trends in automotive lightweighting through novel composite materials. Materials Sciences and Applications. 2016;7(01):26.
7. Scelsi L, Bonner M, Hodzic A, Soutis C, Wilson C, Scaife R, et al. Potential emissions savings of lightweight composite aircraft components evaluated through life cycle assessment. Express Polymer Letters. 2011;5(3).
8. Barbosa GF, Carvalho J. Analytical model for aircraft design based on Design for Excellence (DFX) concepts and use of composite material oriented to automated processes. International Journal of Advanced Manufacturing Technology. 2013;69(9-12):2333-42.
9. Benabdellah AC, Benghabrit A, Bouhaddou I, Benghabrit O. Design for relevance concurrent engineering approach: integration of IATF 16949 requirements and design for X techniques. Research in Engineering Design. 2020;31(3):323-51.
10. Research Project PTDC/EAM-MIN/31041/2017Waste Zero-PCBs. A sustainable and practically non-waste technology for recycling printed circuit boards – POCI-01-0145-FEDER-031041.
11. Rao RV, Davim JP. A decision-making framework model for material selection using a combined multiple attribute decision-making method. The International Journal of Advanced Manufacturing Technology. 2008;35(7-8):751-60.

12.Alemi-Ardakani M, Milani AS, Yannacopoulos S, Shokouhi G. On the effect of subjective, objective and combinative weighting in multiple criteria decision making: A case study on impact optimization of composites. Expert Systems with Applications. 2016;46:426-38.
13.Milani A, Eskicioglu C, Robles K, Bujun K, Hosseini-Nasab H. Multiple criteria decision making with life cycle assessment for material selection of composites. Express Polymer Letters. 2011;5(12).
14.Bledzki AK, Seidlitz H, Krenz J, Goracy K, Urbaniak M, Rösch JJJP. Recycling of carbon fiber reinforced composite polymers—Review—Part 2: Recovery and application of recycled carbon fibers. 2020;12(12):3003.
15.Gfrerrer M. Integration of Carbon Fiber Reinforced Plastic Components in a Car Body Structure: University of Leoben; 2020.
16.Jacob AJRP. Carbon fibre and cars–2013 in review. 2014;58(1):18-9.
17.Sovacool BK, Rogge J-C, Saleta C, Masterson-Cox EJEi, transitions s. Transformative versus conservative automotive innovation styles: Contrasting the electric vehicle manufacturing strategies for the BMW i3 and Fiat 500e. 2019;33:45-60.
18.Atilano L, Martinho A, Silva MA, Baptista AJ. Lean Design-for-X: Case study of a new design framework applied to an adaptive robot gripper development process. Procedia CIRP. 2019;84:667-72.
19.Lourenço E, Pereira J, Barbosa R, Baptista A. Using multi-layer stream mapping to assess the overall efficiency and waste of a production system: a case study from the plywood industry. Procedia CIRP. 2016;48:128-33.
20.Sousa S, Baptista A, Marques A. Material Design-for-eXcellence Framework–Application to Composites. 2021.
21.Granta Design Limited [Internet]. 2021.
22.Naresh K, Khan K, Umer R, Cantwell WJJM, Design. The use of X-ray computed tomography for design and process modeling of aerospace composites: A review. 2020;190:108553.
23.Sapuan S, Mansor MR. Design for Sustainability: Green Materials and Processes: Elsevier; 2021.
24.Karuppannan Gopalraj S, Kärki T. A review on the recycling of waste carbon fibre/glass fibre-reinforced composites: Fibre recovery, properties and life-cycle analysis. SN Applied Sciences. 2020;2(3):1-21.
25.Tapper RJ, Longana ML, Norton A, Potter KD, Hamerton I. An evaluation of life cycle assessment and its application to the closed-loop recycling of carbon fibre reinforced polymers. Composites Part B: Engineering. 2020;184:107665.
26.Meng F, Olivetti EA, Zhao Y, Chang JC, Pickering SJ, McKechnie JJASC, et al. Comparing life cycle energy and global warming potential of carbon fiber composite recycling technologies and waste management options. 2018;6(8):9854-65.
27.Job S. Recycling glass fibre reinforced composites–history and progress. Reinforced Plastics. 2013;57(5):19-23.
28.Mamanpush SH, Li H, Englund K, Tabatabaei AT. Recycled wind turbine blades as a feedstock for second generation composites. Waste Management. 2018;76:708-14.
29.Sommer V, Becker T, Walther G. Steering Sustainable End-of-Life Treatment of Glass and Carbon Fiber Reinforced Plastics Waste from Rotor Blades of Wind Power Plants. Resources, Conservation and Recycling. 2022;181:106077.
30.Bhat T, Fortomaris D, Kandare E, Mouritz A. Properties of thermally recycled basalt fibres and basalt fibre composites. Journal of Materials Science. 2018;53(3):1933-44.
31.Pucci MF, Seghini MC, Liotier P-J, Sarasini F, Tirilló J, Drapier S. Surface characterisation and wetting properties of single basalt fibres. Composites Part B: Engineering. 2017;109:72-81.

GREEN CARBON / CARBON WITH CVI – POSSIBLE OR NOT?

Denny Schüppel[a], Florian Halter[b], Tobias Schneider[a], Dr. Lars Wietschel[b], Dr. Andrea Thorenz[b], Prof. Dr. Axel Tuma[b], Prof. Dr. Dietmar Koch[a]

a: Augsburg University, Institute of Material Ressource Management, Chair Materials Engineering; denny.schueppel@mrm.uni-augsburg.de
b: Augsburg University, Institute for Business Administration, Chair Production & Supply Chain Management

Abstract: *In recent decades, the development efforts on ceramic composites (CMC) have mainly focused on improving the mechanical, chemical, and thermal properties as well as on optimizing cost-effective production routes. Recently, more and more application areas for CMC have emerged outside of aerospace engineering, where environmental impacts and emissions are increasingly relevant. These impacts have hardly been studied so far but are attracting growing interest due to the increasing awareness of environmental impacts. The project team of the CU EcoCeramic joint research project is now focusing on these questions using C/C (carbon fiber reinforced carbon) as a generic example to show what the environmental footprint of C/C manufacturing looks like along the chemical vapor infiltration (CVI) route. On one hand, the key performance indicators (KPI) are considered. Secondly, realistic future scenarios are calculated, such as the use of regenerative process energy and the further development of manufacturing technology. Finally, current approaches and ideas are discussed as to what a holistic regenerative approach to C/C using CVI might look like when biobased carbon fibers and green process gases are used. The environmental impact is determined by a life cycle assessment (LCA).*

Keywords: CMC, CO_2-Footprint, CVI, Carbon/Carbon, LCA

1. Introduction

The present work and the associated research project CU EcoCeramic [1] deal with the life cycle assessment and economic evaluation of fiber-ceramic composite structures, so-called Ceramic Matrix Composites (CMC). The aim is to overcome existing obstacles in the use of CMC and to achieve a real closure of the recycling loops. The research objective is to consolidate and expand the acceptance of CMC. In doing so, a robust and transparent presentation of the current and future ecological footprint of CMC can help the broad SME sector to use this class of materials in the future as an "enabler" for necessary technological solutions in such ways that they can contribute to achieving the Paris 2050 climate targets [2].

The production, processing, and use of CMC for new applications are predominantly carried out by SMEs in Germany [3]. High material costs combined with ignorance of eco-efficiency and sustainability lead to a reluctance to use CMC, which hinders innovation. While large companies are increasingly preparing their own life cycle assessments and employ specialists in environmental management, research and development or other central areas of the company, SMEs in particular are unable to keep pace. The results achieved in this project thus enable SMEs

  doi:10.5075/epfl-298799_978-2-9701614-0-0

in the long term to market their products quickly and in an ecologically or economically sensible manner.

In the medium term, it can be assumed that new materials will only become widely established if they meet minimum requirements in terms of ecological compatibility and recyclability. In addition, solutions must be identified to enable the landscape to sequestrate carbon dioxide from the earth's atmosphere on a large scale, store it and bind it permanently in carbon sinks.

Ceramic matrix composites based on carbon fibers with a carbon matrix seem to be an option for the future. Initial research activities are being conducted into carbon fibers made from green hydrogen. At the same time, green process gases for the CVI process are also being researched. Accordingly, the guiding or research question of this article is: Is it worth thinking about "sustainable" carbon/carbon materials (see also figure 1) from an ecological point of view, or does the energy-intensive manufacturing process obscure the benefits of the materials used?

It also remains to be seen, weather the environmental benefits of novel applications enabled by carbon/carbon materials (see also figure 1) outweigh the environmental impacts caused the energy-intensive manufacturing process of CMCs.

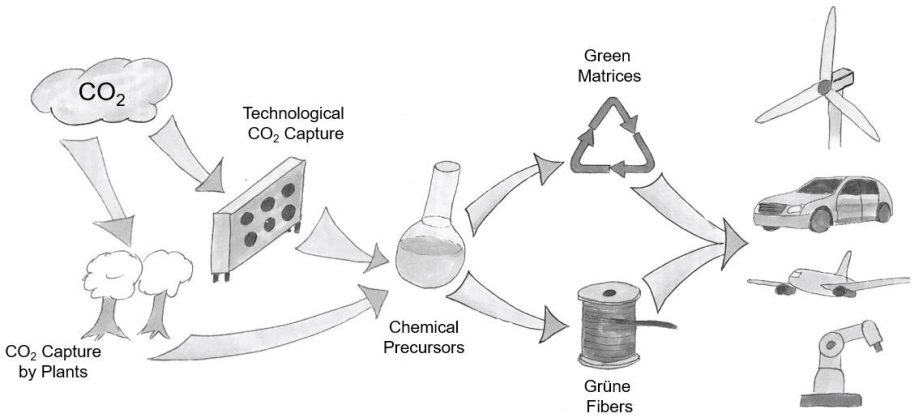

Figure 1: Generic sustainable production route for sustainable ceramic matrix composites, source: Ceramic Compoistes, Composite United e. V.

Ceramic matrix composites with a carbon fiber and a carbon matrix (C/C) are the most common CMC in terms of production volume. In aircraft alone, approx. 10,000 to 20,000 tons of brake discs are installed annually [4]. Most of these materials are produced by the chemical vapor infiltration (CVI) process route. In this process, an alkane, e.g., methane, flows around a "dry" carbon fiber preform in a furnace. Under highly specialized processing conditions, the carbon atoms of the alkane are deposited on the preform and thereby build up the matrix.

The build-up of a carbon matrix depends on many success factors: Gas flow rate, total pressures, partial pressures, gas composition, carrier gas mixtures, duration of gas flow, furnace temperature and many more. CVI is a highly complex process that only a few companies worldwide have mastered so far. However, if successful, high temperature resistant high-performance components can be produced, see figure 2.

  doi:10.5075/epfl-298799_978-2-9701614-0-0

Figure 2: Exemplary components made of C/C, produced with CVI. Source: CV-Technology GmbH.

Here you can see only a few examples of C/C components. In Europe, there are ten companies that operate a CVI commercially while four of them are located in Germany. The process differs within these companies as there is no "standard" CVI process. The entire setup changes when components and, above all, geometries change. For example, small components can be flowed through well while the flow through large components is more difficult. Depending on the availability of the plant, the geometry of the components and the component requirements, other plant configurations result, which has to be considered for the life cycle assessment. According to this, it is generally not possible to speak of a C/C component that has been manufactured using CVI.

2. Approach

Through a systematic variation of relevant material, process and production parameters, the range of decision variables as well as the corresponding interactions are demonstrated, and the most important levers are elaborated. To display the variety of applications despite the lack of a standard C/C component, several component types were analyzed. Assumptions and scenarios must help to describe the reality abstractly and generically on the one hand, but well-founded and resilient on the other. For this reason, generic structures of different degrees of complexity have been defined in the present work, see also Fig. 3. A basic distinction can be made between "profile-shaped" and "shell-shaped" structures. Profile-shaped components can, for example, be manufactured by means of braiding processes. Shell-shaped components are produced by weaving, among other methods. Five different levels of complexity have been defined for this purpose: Starting from complexity level 1: plane plate or plane tube up to complexity level 5: multiple curved shell or skeletal structure.

Figure 3: Illustration of the different levels of complexity. Here: complexity level 1 for a plane plate and 3 of a shell structure.

  doi:10.5075/epfl-298799_978-2-9701614-0-0

Expert panels were held for all generic geometries to discuss realistic process parameters. The discussed parameters serve as a database for the subsequent Life Cycle Inventory. Based on these values, the global warming potential was calculated for eight different scenarios. 1) State of the art (average) 2) Realistic favourable [slightly thinner, smaller, less complex] 3) Realistic unfavourable [slightly thicker, larger, more complex] 4) Gas recovery 5) Gas flow optimized 6) Production in Austria 7) Production in Norway 8) Realistic favourable 2030.

There is already a whole series of scientific publications from the world of carbon fibre-reinforced plastics on which this work bases. Hohmann et al. for example, have published several papers that take a generic look at the environmental footprint of carbon fibre and the preforming process, as described above [5-7]. These point out, that the ecological footprint of carbon fibre alone varies greatly. In addition, the production margins and general conditions vary greatly. Some fibre manufacturers use a more electricity driven energy input for oxidation and carbonization, while others use a more gaseous energy input [5-7].

In the preceding research study MAI Enviro [5], a generic HT fiber was determined using SGL Carbon and (at that time) Toho Tenax. Furthermore, life cycle assessments were performed for all other production processes of CFRP [5][6]. The values determined in this study are used as input for this present work.

In the area of data collection, this paper therefore deals primarily with all process steps that have not been covered in MAI Enviro - here using the CVI process as an example. All secondary processes (provision of gases, heat, cooling, other mass flows) were balanced individually, see also Figure 4. In addition to each individual input and output stream, realistic minimum and maximum values were parameterized in such a way that the estimation of the CO_2 footprint can be made as a function of the degree of complexity.

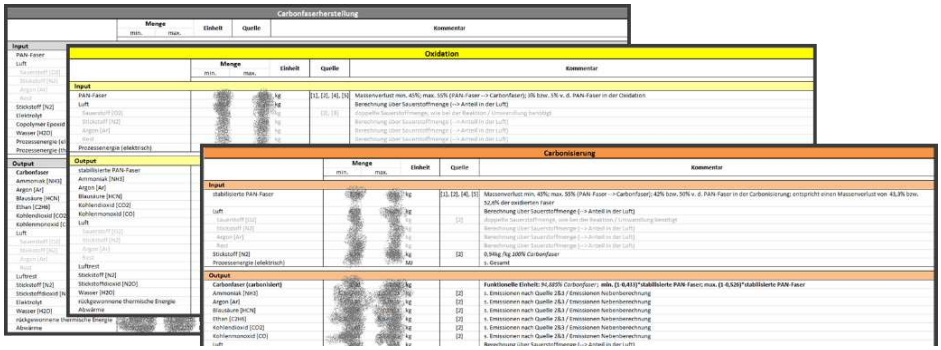

Figure 4: Sample data collection for various missing processes along CVI process route

Furthermore, central boundary and framework conditions were defined for the subsequent CO_2 analysis. It is always important to note that the figures presented here are based on series production. However, there are also CVI plants that are primarily used for research and development. For research and development, however, the furnaces are often oversized, which leads to a biased environmental assessment. In addition, sometimes several prototypes must be produced for one component. All these development steps are neglected in the present work.

  doi:10.5075/epfl-298799_978-2-9701614-0-0

3. Results

Figure 5 shows an average state-of-the-art process of series components in the left bar. The complexity level is three and the surface type is shell-shaped. The number of pieces is rather high compared to the CVI process with approx. 500 pieces per year. It can be seen that the carbon fiber accounts for only a very small share of the GWP of this generic component at 2.1% (orange). Preforming and other logistical processes, in this case nonwoven production (gray), account for another 0.27%. The main share of the ecological footprint here is accounted for by the CVI process and all its secondary processes. In particular 69.5 % of the GWP is attributable to use of electricity for the CVI process. (German electricity mix 2021). In addition, alkanes, such as methane, ethane, etc., which are used to build up the matrix account for 20%. The remaining part of the GWP is made up of carrier and other gases with approx. 8 %. These include: Nitrogen for purging, the use of inert gases such as argon, or gases to adjust the partial pressure, e.g. hydrogen. Neglected here: The reprocessing of CVI systems. Especially in series production, CVI systems have to be maintained frequently. However, these maintenance intervals are massively dependent on the manufactured product and can therefore not be considered in such an approach.

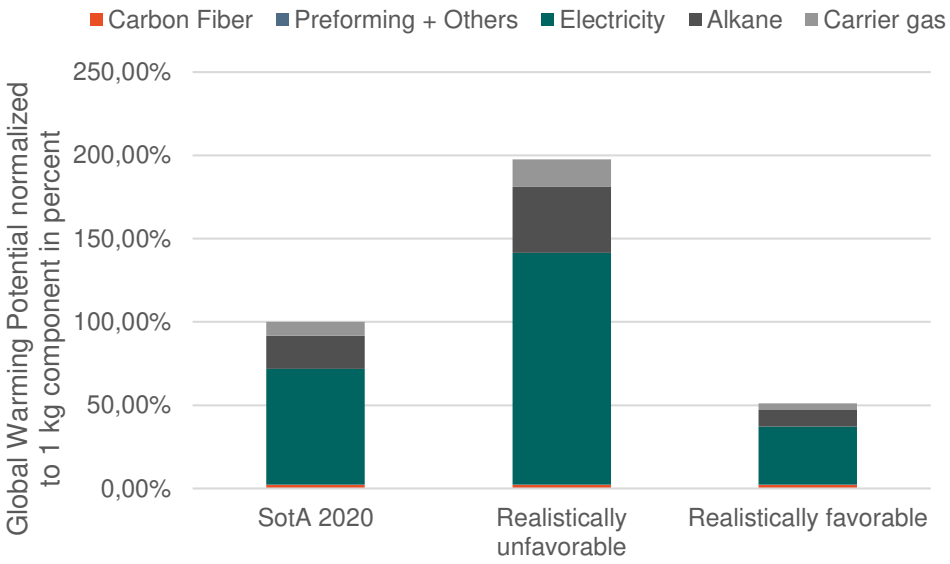

Figure 5: Normalized GWP - State of the Art Process and Realistically Unfavorable / Favorable

As described in chapter 2: GWP is strongly dependent on the processes used and the manufactured components. In Figure 5, the geometries of the manufactured generic semi-finished products were simulated unfavorably and favorably using the example of the middle and right bars. Component thickness (slightly thicker, slightly thinner), component size (slightly larger, slightly smaller) and component complexity (five and 1) were simulated. For this purpose, the thermal furnace load was reduced and increased by 20 % respectively (to approx. 90 % of the maximum load). The results imply that marginal and general conditions of the manufacturing process have a very significant influence. This is why it is not possible to speak of a generalized CVI, but why the marginal and general conditions should always be included. Therefore, the component type and the furnace utilization are decisive for the CO_2 emissions.

  doi:10.5075/epfl-298799_978-2-9701614-0-0

Knowing the significant ecological variation of the different boundary and framework conditions shown in Figure 5, further investigations of the ecological factors influencing a C/C via the LSI route were done and illustrated in Figure 6. The left bar shows the state of the art values from Figure 5. Based on this, different scenarios were considered.

First of all, the influence of Gas treatment or gas recovery is determined. In the CVI process, significant amounts of alkanes are passed through the textile preform at high temperatures. These can be different alkanes. Taking methane (CH4) as an example, only a single-digit percentage of the methane introduced is converted in the reactor to carbon, which builds up the matrix, and additionally hydrogen. More than 90 % of the methane leaves the CVI process unreacted, enriched with alkanes of higher carbon content. The state of the art process assumes that all exhaust gases go to controlled combustion and are emited to the environment. In contrast, in Scenario 2 "Gas Recovery" it is assumed that a functioning methanizer exists at the gas outlet, which proportionally captures the outflowing hydrogen, enriches it with CO2 and produces methane. This methane is to be fed back into the process as recycled feedstock. This additional gas treatment step requires approx. 1 % - 3 % more electricity, but saves up to 81 % alkane. Thus, this step alone reduces the CO2 emissions of the entire production process by 16 %.

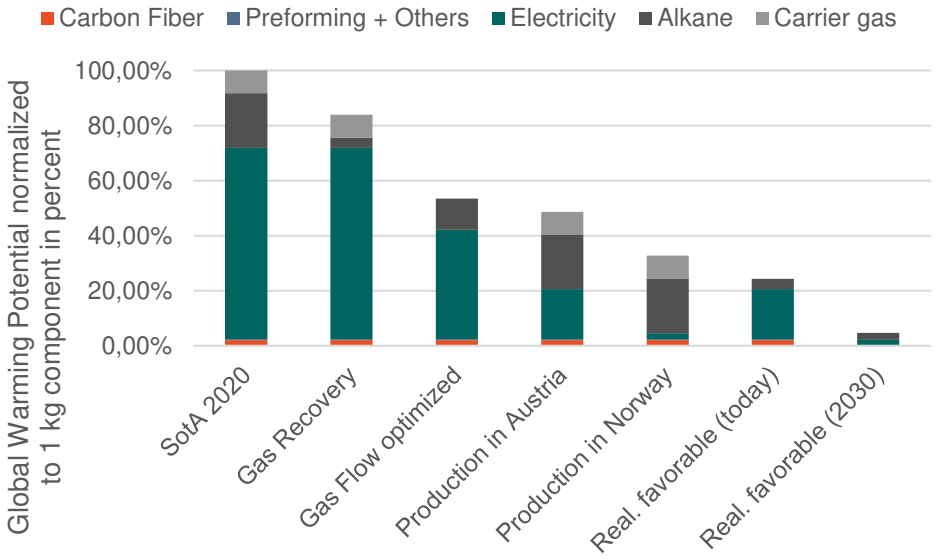

Figure 6: Ecological optimization potentials in comparison to the State of the Art 2020

The 3rd bar from the left, shows the optimization potential of an optimized gas flow. There are a lot of possibilities to optimize the gas flow. However, this optimization is also dependent on the geometries of the components and thus the degrees of complexity. In order to remain comparable with the state of the art, optimization potentials in complexity level 3 were presented for flat semi-finished products. This representation differs in other degrees of complexity. Optimized gas flow can be achieved by means of gas flow aids in the reactor, adjustment of the partial pressures and temperature setting. The composition of the alkane is also decisive. If methane is used, for example, a certain purity of well over 90 % must be available depending on the process. As Figure six shows the optimized gas flow causes the matrix to build up faster in this example. As a result, the process can be run for a shorter time (43 % less

  doi:10.5075/epfl-298799_978-2-9701614-0-0

electricity required), less alkane (-42 %) is needed and carrier gases can be completely omitted. This reduces the CO_2 footprint by 47 % compared to the state of the art.

Bars 4 and 5 show the ecological optimization potential for production cities (meaning exclusively the CVI process) outside of Germany (state of the art, left bar), but in Austria (electricity mix 2021) or Norway (electricity mix 2021). Due to the comparatively more ecologically sensible electricity mixes (more electricity from hydropower/wind power, less electricity from coal and gas), significant reduction potentials based on location alone can be found: Austria - 51% and Norway - 67% compared to Germany.

Many companies that want to launch semi-finished products or finished products on the market are already being asked about the carbon footprint of their products. As a result, many companies are already active in this area. In addition to reducing costs and increasing component performance, the ecological production margins and framework conditions are becoming increasingly relevant. Together with the project consortium [1], a possible generic C/C production was defined, which reflects the state of the art today as reasonably as possible as shown in Figure 5, realistically favorable today. This scenario is state of the art for some manufacturing companies. The second bar from the right shows the state of the art if the following conditions are also met (compared to the left bar): Vapor recovery, optimized gas flow, no carrier gas, Austrian electricity mix. Individual companies thus already achieve a CO_2 reduction potential of 76% compared to other companies.

The last Scenario determined the “Realistically Favorable in the year 2030”. In the past, it has become established in the forerunner projects to also define realistic assumptions for the future. For example, it can be assumed that the use of biogases (methane) instead of natural gases will become established. This will only lead to minimal adjustments to the process and can be implemented technologically or is already being investigated today due to the political unrest in Eastern Europe. In addition, the European electricity mixes will change until 2030. Furthermore, process optimizations of 20% (faster) have been assumed as well as the use of a bio-based carbon fiber [7]. It can therefore be assumed that the ecological optimization potential can once again drop by approx. 80 % compared to the favorable scenario today.

4. Conclusion

The main influencing factor for a generic CO_2 investigation of the CVI process is, that the scope must be clearly defined as Fig. 5 shows. To this end, it can be pointed out, that compared to other materials such as steel, aluminum, titanium, plastics or CFRP, C/C has a higher average CO_2 footprint via the CVI route. However, if the process is optimized in a technically clever way, almost 40% of greenhouse gas emissions can be avoided, compare Figure 7, left. However, the leverage of the production site is the highest due to the underlying electricity mix. Germany does not have a particularly favorable electricity mix in 2021. Austria or the European pioneer country Norway, on the other hand, do. The location alone has an influence of around 50% on CO_2 emissions in production. Green precursors, especially biogas compared to natural gas, have just under 20% influence on the CO_2 footprint of C/C products via the CVI route.

  doi:10.5075/epfl-298799_978-2-9701614-0-0

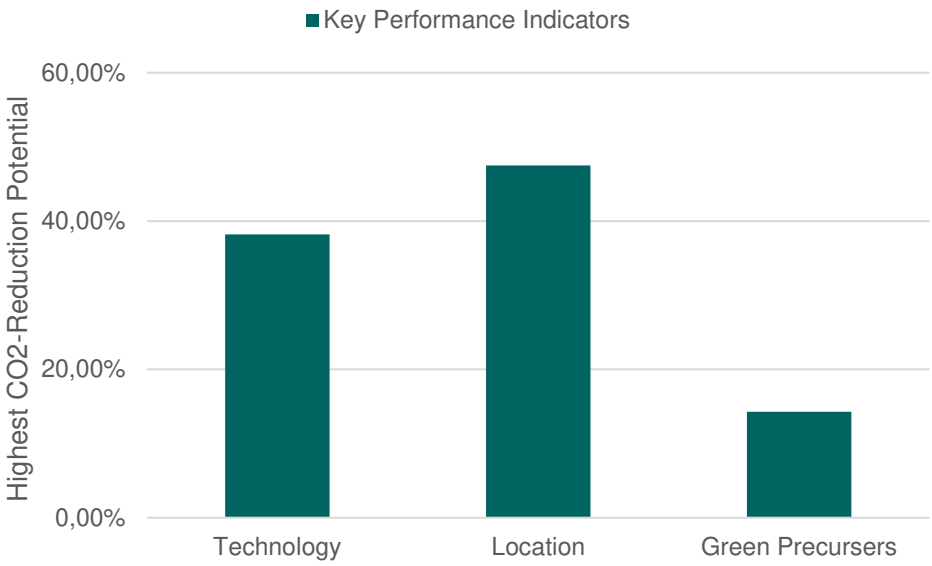

Figure 7 : Key Performance Indicators

The answer to the question, "Possible or not?" with respect to "Green C/C" is: yes, but. Yes, it is possible, but it strongly depends on which components are manufactured, how and where. Furthermore, it is crucial how innovative the manufacturing companies are and how advanced the production processes are already today.

5. Outlook

The next steps are to corroborate these collected life cycle inventory data sets by the broader industry. The absolute figures are then to be published. A rough shift of the relative proportions is not to be expected. However, a slight absolute adjustment may still happen, depending on the common understanding of the state of the art. In addition, correlations between ecological and economic footprint or ecological footprint and component performance will be established. Finally, some German companies are already working on the production of "own" methane, from hydrogen from the CVI process and CO_2 from the environment. Powered by renewable electricity, the question arises: will we even achieve a CO_2 sink one day?

6. References

1. Website of CU EcoCeramic (2020): https://composites-united.com/projects/cmc-enviro/
2. Paris 2050 climate targets (2016): https://www.bmuv.de/fileadmin/Daten_BMU/Download_PDF/Klimaschutz/klimaschutzplan_2050_bf.pdf
3. List of members of the Network of Ceramic Composites (2020): https://composites-united.com/cluster/ceramic-composites/
4. Composited United Market Report (2021), M. Sauer, D. Schüppel; https://composites-united.com/cfk-marktberichte-des-cu/

  doi:10.5075/epfl-298799_978-2-9701614-0-0

5. MAI Enviro: Vorstudie zur Lebenszyklusanalyse mit ökobilanzieller Bewertung relevanter Fertigungsprozessketten für CFK-Strukturen (2015): A. Hohmann, B. Schwab, D. Wehner, S. Albrecht, R. Ilg, D. Schüppel, T. v. Reden; ISBN: 978-3-8396-0929-3
6. Recommendations for resource efficient and environmentally responsible manufacturing of CFRP products. Results of the Research Study MAI Enviro 2.0.(2017): A. Hohmann, S. Albrecht, J. P. Lindner, D. Wehner, M. Kugler, T. Prenzel, T. Pitschke, M. Seitz, D. Schüppel, S, Kreibe, T. von Reden; Buch des Spitzenclusters MAI Carbon; ISBN: 978-3-9818900-0-6
7. Nachhaltige Verbundwerkstoffe für Hochleistungsfasern, Abschätzung der Umweltwirkungen und Möglicher Reduktionspotentiale; A. Hohmann, Technologietag Leichtbau, 09. November 2021

  doi:10.5075/epfl-298799_978-2-9701614-0-0

ENERGY EFFICIENCY-ORIENTED DECISION-MAKING FOR ADDITIVE MANUFACTURING WITH CARBON-FIBRE-REINFORCED POLYAMIDE 12

Thibault Le Gentil[a,b], Daniel Therriault[b], Olivier Kerbrat[a,c]
[a] ENS Rennes, Bruz, France
[b] Laboratory for Multiscale Mechanics (LM2), Department of Mechanical Engineering, Polytechnique Montreal, Canada – thibault.le-gentil@polymtl.ca
[c] Civil and Mechanical Engineering Institute (GeM), CNRS, Rennes University, Rennes, France

Abstract: *Additive manufacturing (AM) technologies have transformed manufacturing, in particular, owing to its versatility and higher mechanical performances, AM with composite materials has grown exponentially over the past few years. Although it is seen as a promising solution for improving resource efficiency and environmental sustainability, the literature showing the advantages of AM over conventional manufacturing is case-specific. Furthermore, to support industrial applications, it is important to analyse all the economic, technical, and environmental aspects. For this reason, we designed an experimental method, focused on fused filament fabrication, for measuring the impact of temperature parameters on total cost, energy consumption, and ultimate tensile strength. Results provided an overview of this impact, yielding information to support optimization investigations.*

Keywords: Fused filament fabrication; Manufacturing cost; Energy consumption; Sustainability; Multiple-criteria decision analysis

1. Introduction

Additive manufacturing (AM) refers to a family of manufacturing techniques that adopt a layer-by-layer approach to producing parts and has attracted interest from both academia and industry. Among the processes in this family, fused filament fabrication (FFF) is one of the most popular ones, as it enables flexibility in both design and supply chain, and allows parts to be made that are impossible to produce in conventional manufacturing [1]. Advantages of AM include reducing raw material consumption and waste during the process [2]. Additionally, in the context of Industry 4.0 and sustainability, AM is seen as one of the many means of bringing about this transition [3]. In particular, the combination of AM and carbon-fibre-reinforced polymer opens up the possibility of producing parts with a high strength-to-weight ratio [4], whilst reducing total mass through complex designs [5].

However, regarding sustainability, AM has several potential drawbacks, depending on its use [6]. There are two major issues, the first being the high energy demand during the manufacturing phase, and the second, the reduced productivity, compared with conventional processes [7]. Given the rapid growth of AM in industry, and the importance of ensuring sustainable development, there is a real need to investigate the relationship between energy consumption, cost, and the quality of the produced parts. In the present study, we therefore sought to develop a methodology for connecting these three aspects in the case of FFF of carbon-fibre polyamide 12. The latter has found numerous engineering applications, especially in the aerospace industry, owing to its good mechanical properties and thermal stability [8].

  doi:10.5075/epfl-298799_978-2-9701614-0-0

2. Relevant literature on energy and cost assessment

2.1. Energy assessment and specific energy consumption

Initially designed for subtractive processes by Kara and Li [9], the specific energy consumption (SEC) indicator has since been applied to AM as a way of comparing and quantifying the energy efficiency of different processes or machines. It is defined as the ratio of total energy consumption to the mass deposited, and can be used to quantify energy efficiency in material deposition. Compiled data available in the literature [7], underlines the differences in performance, depending on the printer's architecture (industrial grade or semi-professional; some with an enclosed printing area, others not), the materials, the process parameters, and the geometric complexity. The warm-up phase has been identified as the part of the process that consumes the most energy [10], hence a second indicator, specific printing energy (SPE; i.e. SEC during deposition phase), can be determined to focus on the printing phase. Energy consumption during fabrication can be divided into two categories: energy for the preparation of the printing (E_p), and energy directly needed for the fabrication phase (E_f).

2.2. Cost assessment

In contrast to energy assessment, cost assessment for AM is well established. Based on the literature [11–14], six distinct cost categories can be identified: 1) materials (including support); 2) electricity (e.g., warm-up, build-up, calibration); 3) workforce (software and hardware); 4) pre- and postprocess (including quality control); 5) indirect cost (e.g., investment, maintenance); and 6) consumables.

2.3. Motivation for the present approach

As seen in the literature, energy and cost assessments have mainly focused on polymer AM. In the case of composite materials, especially fibre-reinforced polymers, the demand for high performance and high mechanical properties requires the technical quality of the produced parts to be assessed. The method we devised, first establish the total manufacturing cost gives an indication of the parameters that can be optimised. Modifications made from an *economic point-of-view* have impacts that need to be assessed from an *environmental point-of-view*. Finally, to ensure the industrial viability of the process, the impact on mechanical performance needs to be estimated from a *technical point-of-view*.

3. Modelling approach

3.1. Materials and equipment

We used a Raise 3D Pro2 FFF printer, an enclosed printer. To assess the mechanical properties of the printed part, we selected a tensile specimen type 1A, from standard ISO 527-2:2012. The filament material was CarbonX™ Nylon-CF Gen 3 from 3DXTech. We used a Fluke 289 multimeter to measure the electrical current. The voltage was measured upstream and assumed to remain constant throughout the experiment.

3.2. Cost model

Previously identified cost categories made it possible to obtain a generic formula for the total cost (variables defined in Table 1):

  doi:10.5075/epfl-298799_978-2-9701614-0-0

$$C_{\mathrm{tot}} = C_{\mathrm{part}}.M_{\mathrm{part}} + C_{\mathrm{sup}}.M_{\mathrm{sup}} + C_{\mathrm{elec}}.\left(P_{\mathrm{p}}.t_{\mathrm{p}} + P_{\mathrm{f}}.t_{\mathrm{f}}\right) + C_{\mathrm{op}}^{\mathrm{hard}}.\left(t_{\mathrm{f}} + t_{\mathrm{post}}\right) + C_{\mathrm{op}}^{\mathrm{soft}}.t_{\mathrm{soft}} + \frac{C_{\mathrm{soft}}}{t_{\mathrm{soft}}} + \frac{\frac{C_{\mathrm{m}}}{\alpha}+M}{t_{\mathrm{hr}}.\beta}.\frac{1}{t_{\mathrm{f}}+t_{\mathrm{p}}} + \sum_{1}^{N_{\mathrm{cons}}} C_{\mathrm{cons}}.\frac{t_{\mathrm{cons}}}{T_{\mathrm{cons}}} \quad (1)$$

Table 1: FFF cost terminology

Parameter	Definition [unit]	Parameter	Definition [unit]
C_{part}	Base material part cost [€/kg]	$C_{\mathrm{op}}^{\mathrm{soft}}$	Software operator cost [€/hr]
M_{part}	Base material part mass [kg]	t_{soft}	Software (slicing) time [hr]
C_{sup}	Support cost [€/kg]	C_{m}	Machine cost [€]
M_{sup}	Support mass [kg]	α	Machine lifetime [hr]
C_{elec}	Base electricity cost [€/Whr]	M	Maintenance cost [€]
P_{p}	Preparation power [W]	t_{hr}	Annual working hours [hr]
t_{p}	Preparation time [hr]	β	Percentage of use time [%]
P_{f}	Fabrication power [W]	N_{cons}	Total number of consumables
t_{f}	Fabrication time [hr]	C_{cons}	Consumables cost [€]
$C_{\mathrm{op}}^{\mathrm{hard}}$	Hardware operator cost [€/hr]	t_{cons}	Use time of consumables [hr]
t_{post}	Post-process time [h]	T_{cons}	Tool lifetime [hr]

Eq. (1) can be further developed and readjusted, in a gate-to-gate scope. Materials, electricity and consumables cost becoming the main categories and can be described as follow :

$$Cost = [C_{\mathrm{part}}.M_{\mathrm{part}} + C_{\mathrm{sup}}.M_{\mathrm{sup}}] + \left[C_{\mathrm{elec}}.\left(P_{\mathrm{p}}.t_{\mathrm{p}} + P_{\mathrm{f}}.t_{\mathrm{f}}\right)\right] + \left[C_{\mathrm{printhead}}.\frac{t_{\mathrm{printhead}}}{T_{\mathrm{printhead}}} + C_{\mathrm{heatbed}}.\frac{t_{\mathrm{heatbed}}}{T_{\mathrm{heatbed}}}\right] \quad (2)$$

This equation presents the different factors an operator can modify during the fabrication phase, namely the material, electricity, and consumables (here, the printhead and heatbed). The material cost remains constant for the desired part design, and the consumables cost is only related to printing duration. Consequently, the electricity cost is the only variable that can be controlled by the operator through printing parameters. Divided into preparation and fabrication consumption, as seen previously, those two phases of energy consumption are related to power demand and duration (P_{p}, P_{f}, t_{p} and t_{f}). Reducing these variables through printing parameters (e.g. temperature) can reduce the total cost.

3.3. Energy model

In the context of industrial transition, it is particularly crucial to consider the impact of decisions about energy consumption. Given that the two elements identified above are directly related to power consumption, it is necessary to identify and measure these quantities. Additionally, the power profile can give qualitative information about the distribution of the power demand. provides an example of power profiles plotted as a function of process time. Seven different process phases can be identified: 1) idle and file launching; 2) heatbed warm-up; 3) printhead warm-up; 4) calibration and printing; 5) end and return to 0; and 6) idle. Phases 2) and 3) are temperature (hence material) dependent. Phase 4) is design dependent. Finally, Phases 1) and 5) are operator dependent. *Preparation energy* corresponds to the sum of the switch-on, file launch, heating (heatbed and printhead), calibration, return to 0 and idle phases. While

fabrication energy corresponds to the energy used to keep the elements warm and displace them. As shown in Figure 1, the terms for fabrication energy E_f are directly given by the power demand in Phase 4), without the need to measure each displacement or heating energy term. Additionally, energy consumption for the warm-up and E_f are related to temperatures for both the printhead and heatbed.

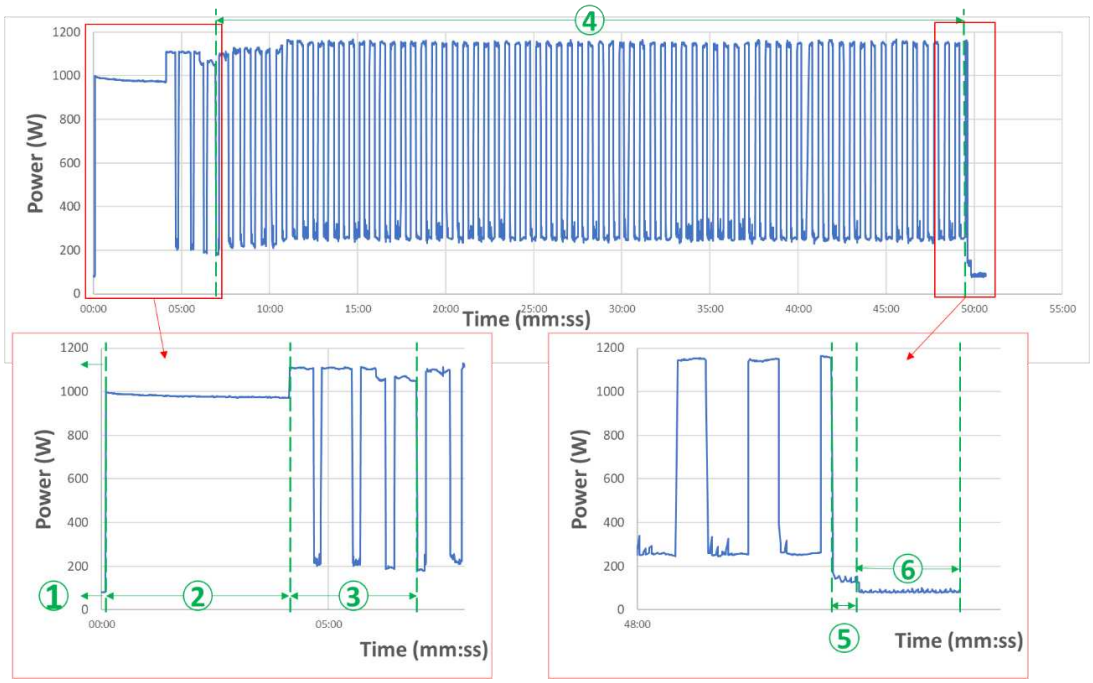

Figure 1: Power profile and identification of main printing phases. This profile corresponds to the printing of a specimen A1, polyamdide12-carbon fibre at 260 °C printhead and 100% heating at 80 °C for the heatbed.

3.5. Mechanical performance

Carbon-fibre-reinforced polymer can be used in AM to improve material properties, but it is essential to control the quality of the part. In particular, if replacing a metallic part with a composite one means a drastic loss in mechanical performances, any reductions in cost and energy are irrelevant.

4. Results

4.1. Experimental setup

To illustrate the impact of printing parameters on energy consumption and cost, as seen with Eq. (3), we selected two factors: printhead temperature, and heatbed heating strategy. As the recommended temperature for the printhead is 240-270 °C, we selected 245 °C, 250 °C, and 260 °C as our values. For the second parameter, we chose three levels depending on the number of heated layers relatively to the total number of layers printed (in percentage): full heating of the heatbed (100%), heating stopped at half the total layers (50%), and no heating (0%). In total, we performed nine different tests, with four repetitions for each test. Throughout the experimental tests, deposition speed is set at 80 mm/s, for 0.2 mm layer thickness and a nozzle diameter of 0.4 mm. An 80 °C was applied to the heatbed temperature and the infill percentage of each samples was 100 %.

4.2 Cost data

The first step was to calculate, from Eq. (2) the change in cost, depending on the condition. From supplier sources, 52.78 EUR/500g base material part cost is assumed, 227.49 EUR for printhead cost and 109.19 EUR for heatbed cost. Expected lifetime for both consumables are estimated to be 1 year. 0.32 EUR/kWhr as base electricity cost is extracted from public data [15]. Total cost and cost distribution between materials, electricity and consumables are shown in Figure 2. Materials represented the main cost, ranging from 74% to 94% of the total cost, depending on the experiment. As material consumption was roughly the same across all experiments, the absolute value of the material cost remained constant. It was therefore the differences in energy consumption that were responsible for the changes in total cost. Differences in power demand meant that the electricity cost represented between 5% and 20% of the total cost. As printing duration was equal for each experiment, the cost of consumables was not affected.

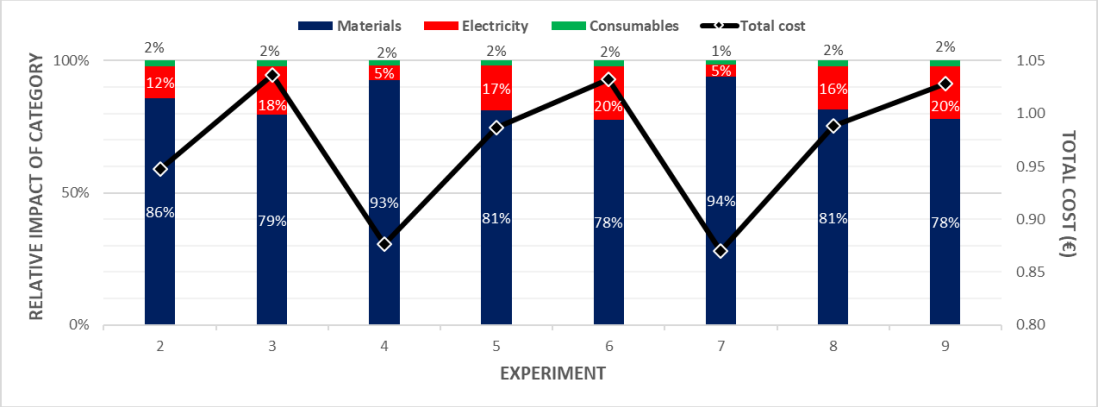

Figure 2: Total cost and cost distribution for each test.

4.3 Energy data

The second step was to measure the impact on energy consumption. Table 2Table 2 shows the different results and measures, with total duration, printed mass, specific energy consumption (all six phases described in Figure 1), and specific printing energy (Phase 4 only). While SEC was related to total energy consumption, SPE corresponded to fabrication energy. As expected, energy consumption increased as the temperature increased. The difference in energy was, however, smaller between 50% and 100% than between 0% and 50%. In the case of Experiments 1 and 4, the adhesion between the part and the heatbed does not allow a proper deposition of the materials. The printhead temperature in Experiment 1 was insufficient to print the parts, while in Experiment 4 only two samples were successfully printed.

Table 2: Mean data of printing duration, part mass, SEC and SPE for each experiment.

#	Printhead temperature [°C]	Heatbed strategy	Duration [s]	Mass [g]	SEC [kWhr/kg]	SPE [kWhr/kg]
1	245	0%	*Failed to print*			
2	245	50%	2971	7.7	45	30
3	245	100%	3009	7.8	75	52
4	250	0%	2195	7.7	19	18
5	250	50%	2572	7.6	54	38
6	250	100%	3035	7.6	84	57

  doi:10.5075/epfl-298799_978-2-9701614-0-0

7	260	0%	1671	7.75	15	14
8	260	50%	2883	7.625	64	42
9	260	100%	3168	7.8	89	58

4.4 Tensile test data

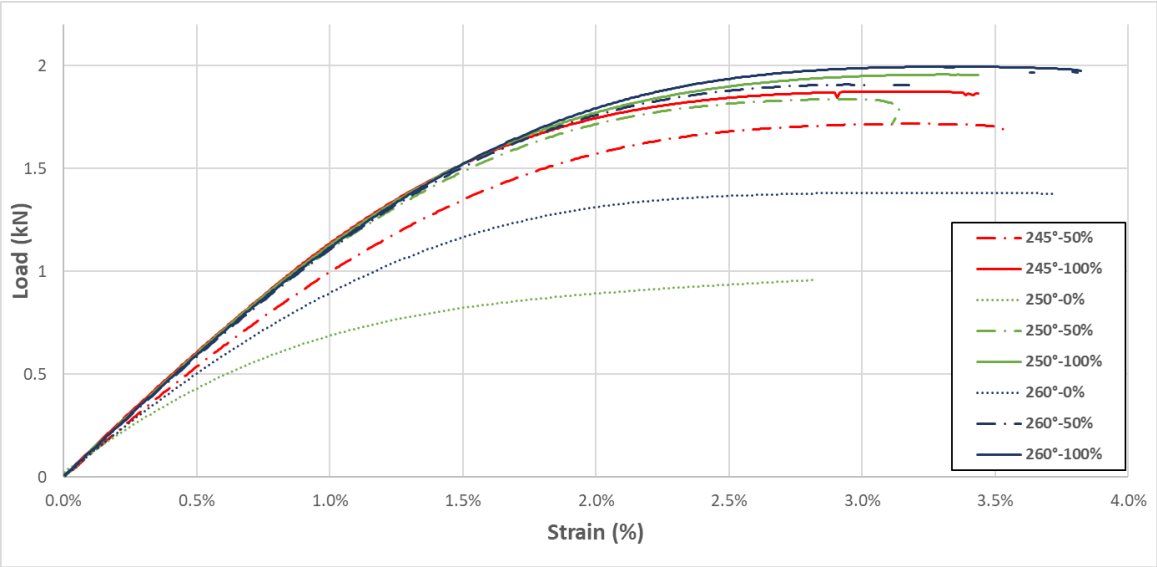

Figure 3: Mean data from tensile tests.

Third and last, each of the 36 tensile specimens was tested. Means for each variation of the test are plotted in Figure 4. Results revealed a substantial drop-off for experiments without heatbed heating (n°4 and n°7), and higher ultimate tensile strength for Experiments 6, 8 and 9. Experiments 6 and 9 corresponded to full heating of the heatbed, but Experiment 8 yielded higher tensile strength than Experiment 3, even though the heatbed was only heated for half the fabrication time.

5. Discussion

In the cost assessment, the two parameters we assessed (printhead temperature and heatbed strategy) were compared on three cost categories: materials, electricity, and consumables. The materials cost remained constant and was higher than that of the other two categories, while electricity was the most variable cost, ranging from 5 to 20% of the total cost. The change in total consumption according to the different parameters was as expected, reflecting a total energy that was more than four times higher when the heatbed was heated, increasing linearly across half and total heating. SEC and SPE underwent similar changes, as the temperature of the printhead and the heating strategy of the heatbed influenced both preparation power and fabrication power. Additionally, the unsuccessful printing in Experiment 1 indicated a trade-off value or combination of the two parameters, determining the printability or otherwise of a part. The results of tensile tests on the printed specimens also changed as expected: heating positively increased ultimate tensile strength. However, the change in strength between the different heating strategies was not linear. Whereas a printing strategy of 0% for the heatbed considerably reduced tensile strength, the difference between a 50% strategy and full heating was relatively small. In particular, the combination of 260 °C and half heating of the heatbed

  doi:10.5075/epfl-298799_978-2-9701614-0-0

(Experiment 8) was a better solution in all three aspects, compared with 260° and full heating (Experiment 3).

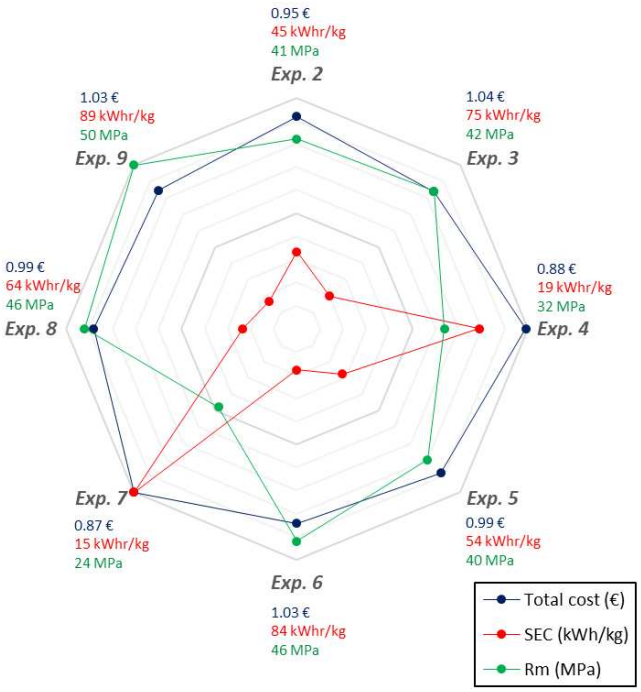

Figure 4: Radar charts for Experiments 2-9. Values are normalized, 100% being the optimum value (maximum for ultimate tensile strength and minimum for total cost and SEC).

The results of Experiments 5 and 9 seems to indicate a possible means of optimizing energy consumption with a relatively small reduction in mechanical strength. Figure 4 summarizes all the economic (total cost), technical (ultimate tensile strength), and environmental (SEC) results for each variation in the parameters. In this graph, results are normalized as 100% for the best performance. It shows that Experiment 4 was the most cost effective, while Experiment 7 had the lowest energy consumption but the worst ultimate tensile strength. Finally, Experiment 9 was the most efficient in terms of ultimate strength, but had the highest energy consumption and was one of the most expensive.

6. Conclusion

The aim of the present study was to develop an experimental method for gauging the impact of FFF printing parameters on three key indicators: total cost, specific energy consumption, and ultimate tensile stress. Analysis of the flows involved in the process highlighted several economic variables. To optimize the process in terms of cost and energy, both duration and power demand were identified as variables. As duration is dependent on part design and desired mechanical strength, an optimization study would involve assessing both printing parameters and redesign, making it harder to assess. By contrast, power demand is directly linked to printing parameters, making it much simpler to adjust for the operator. The present study therefore focused on a quick impact analysis of two parameters that influence the power demand for both the preparation phase and the printing phase: printhead temperature and heatbed heating strategy. With a few measurements, an overview of all cost, energy and mechanical impacts can be estimated. Hence, the proposed methodology can be used to present solutions and strategies for optimizing the process, depending on the operator's requirements.

  doi:10.5075/epfl-298799_978-2-9701614-0-0

Acknowledgements

The authors gratefully acknowledge the financial support provided by Brittany Regional Council for the mobility of the PhD student.

7. References

1. Suárez L, Domínguez M. Sustainability and environmental impact of fused deposition modelling (FDM) technologies. International Journal of Advanced Manufacturing Technology. 2020;106(3–4):1267–79.
2. Paris H, Mokhtarian H, Coatanéa E, Museau M, Ituarte IF. Comparative environmental impacts of additive and subtractive manufacturing technologies. CIRP Annals - Manufacturing Technology. 2016;65(1):29–32.
3. Mabkhot MM, Ferreira P, Maffei A, Podržaj P, Mądziel M, Antonelli D, et al. Mapping industry 4.0 enabling technologies into united nations sustainability development goals. Sustainability (Switzerland). 2021;13(5):1–35.
4. van de Werken N, Tekinalp H, Khanbolouki P, Ozcan S, Williams A, Tehrani M. Additively manufactured carbon fiber-reinforced composites: State of the art and perspective. Additive Manufacturing. 2020;31(July 2019):100962.
5. Herrmann C, Dewulf W, Hauschild M, Kaluza A, Kara S, Skerlos S. Life cycle engineering of lightweight structures. CIRP Annals. 2018;67(2):651–72.
6. Saade MRM, Yahia A, Amor B. How has LCA been applied to 3D printing? A systematic literature review and recommendations for future studies. Journal of Cleaner Production. 2020;244:118803.
7. Lunetto V, Priarone PC, Galati M, Minetola P. On the correlation between process parameters and specific energy consumption in fused deposition modelling. Journal of Manufacturing Processes. 2020;56(June):1039–49.
8. Salmoria G V., Paggi RA, Lago A, Beal VE. Microstructural and mechanical characterization of PA12/MWCNTs nanocomposite manufactured by selective laser sintering. Polymer Testing. 2011;30(6):611–5.
9. Kara S, Li W. Unit process energy consumption models for material removal processes. CIRP Annals - Manufacturing Technology. 2011;60(1):37–40.
10. Ma Z, Gao M, Wang Q, Wang N, Li L, Liu C, et al. Energy consumption distribution and optimization of additive manufacturing. International Journal of Advanced Manufacturing Technology. 2021;116(11–12):3377–90.
11. Luo Y, Ji Z, Leu MC, Caudill R. Environmental performance analysis of solid freeform fabrication processes. IEEE International Symposium on Electronics and the Environment. 1999;1–6.
12. Yosofi M, Kerbrat O, Mognol P. Energy and material flow modelling of additive manufacturing processes. Virtual and Physical Prototyping. 2018;13(2):83–96.
13. Junk S, Côté S. A practical approach to comparing energy effectiveness of rapid prototyping technologies. Proceedings of AEPR'12. 2012;(June):12–4.
14. Kellens K, Mertens R, Paraskevas D, Dewulf W, Duflou JR. Environmental Impact of Additive Manufacturing Processes: Does AM Contribute to a More Sustainable Way of Part Manufacturing? In: Procedia CIRP. Elsevier B.V.; 2017. p. 582–7.
15. Ministère de l'Énergie et des Ressources naturelles du Québec. Prix de l'électricité.

COMPARATIVE LIFE CYCLE ASSESSMENT OF THERMOPLASTIC AND THERMOSETTING CFRP IN AEROSPACE APPLICATIONS.

Chizoba Josphine, Ogugua[a], Jos, Sinke[a], Clemens, Dransfeld[a]

a: Aerospace Manufacturing Technologies, Faculty of Aerospace Engineering, Delft University of Technology, Kluyverweg 1, 2629 HS Delft, The Netherlands

Abstract: *This work quantifies and compares the environmental impact of a thermoset CFRP aircraft skin panel to that of a thermoplastic CFRP panel. This comparison is done using a cradle to gate life cycle assessment including impacts from raw material extraction, manufacturing and end of life. In addition, a hotspot analysis was performed to identify processes with the highest contribution to environmental impacts of the panels. The results show that the thermoplastic panel performed better in three endpoint damage categories including damage to human health, ecosystem and resources. The results also identify carbon fibre production, electricity usage for curing/consolidation and prepreging as the major contributors to the life cycle impacts of both panels. This provides decision makers with insights on where to focus on for future improvement actions aimed at reducing the environmental footprint of CFRP structures.*

Keywords: Life Cycle Assessment (LCA); Environmental Impact; Carbon Fibre Reinforced Polymers (CFRP); Thermoset (TS); Thermoplastic (TP).

1. INTRODUCTION

The drive for sustainable aviation has raised increasing interest in Carbon Fibre Reinforced Polymers (CFRP). This is due to their excellent specific strength and stiffness which are desirable properties in aerospace structures. According to C. Soutis, [1] weight reduction of over 20% can be achieved by replacing metals with CFRP in both primary and secondary structures. This results in a significant improvement in fuel efficiency of aircrafts and is projected to contribute up to 15% of aviation CO2 reduction targets by 2050 [2][2].

CFRP parts can be manufactured using either a thermoset or thermoplastic matrix system. So far, most CFRP aircraft structures are realised with thermosetting matrix. This is due to their low processing viscosity, low curing temperature and moderate non-recurring cost. Although these properties make thermoset (TS) CFRP suitable for small volume production, there are still challenges associated with their joining methods, low fracture toughness and end of life. Due to these limitations, interest in thermoplastic (TP) CFRP have increased significantly in recent years[3]. TP CFRP provide potentials for better recycling, alternative joining methods and better intrinsic fracture toughness. However, their high processing temperatures is a major downside. Thermoplastic CFRP are manufactured at significantly higher temperatures than thermoset CFRP. Which may lead to more energy consumption and use of special moulds to withstand high temperature conditions. The question is “is the overall environmental performance of TP CFRP better than TS CFRP, despite its limitations in manufacturing?”. This question cannot be answered without taking a life cycle perspective.

Some studies have assessed the environmental impact of CFRP used in aerospace applications. Most of these studies have focused on the impacts of thermoset CFRP in comparison to other

  doi:10.5075/epfl-298799_978-2-9701614-0-0

materials including aluminium and steel [4][5]. Others have assessed the impact of different processing routes for thermoset CFRP [6]. However, with the advent of thermoplastic CFRP in aerospace applications, only a few studies have assessed their overall life cycle impacts and compared them to thermoset CFRP. Katsiropoulos et.al., [7] compared life cycle impact of a helicopter's canopy made with Carbon Fiber /epoxy to that from Carbon Fibre/PEEK. Although this study included impacts from raw material extraction, manufacturing and end of life of the panels, it only considered one impact category – Global Warming Potential (GWP). Also, the primary data used in this study was obtained only from literature.

The goal of this study is to benchmark the environmental impact of an aircraft skin panel made from thermoset CFRP against a thermoplastic CFRP panel. Also, to identify hotspots or high impact activities throughout the life cycle of the compared panels. This would guide future impact reduction efforts.

2. METHODOLOGY

2.1 Life Cycle Assessment Methodology

Life cycle assessment (LCA) is a standardized framework for assessing the impact of a product system on human health, ecosystem quality and natural resources. It involves the collection and evaluation of the inputs, outputs and the potential environmental impacts of a product system throughout its life cycle [8]. LCA also covers a wide range of environmental issues, allowing most environmental impacts associated with a process or system to be identified instead on focusing on just one impact for instance climate change. In this study, the impacts of a thermoplastic CFRP panel was bench marked against that of a thermoset CFRP panel. This was done in accordance with ISO 14044 and 14400 and include the following steps: goal and scope definition, inventory analysis, life cycle impact assessment (LCIA) and interpretation.

2.2 Goal and Scope Definition – Functional Unit and System Boundary

Functional unit is the quantitative reference for comparison and provides the same functional performance for the systems compared. In this study, functional Unit is defined as 450X450X2mm aircraft skin panel with a fiber volume fraction Vf of 55%. Raw material and manufacturing data for the carbon fibre (CF) prepregs used in the two panels were normalized to have similar panel areal weight, panel thickness, fiber volume fraction and fiber orientation to ensure comparable strength and stiffness [9]. In this study, a cradle to gate system boundary was adopted considering three phases: raw material extraction, manufacturing and EOL. We assumed the compared panels have only a small weight variation and have similar maintenance therefore the use phase would be identical. The joining methods and assembly steps for the two panels were not considered.

2.3 Life Cycle Inventory Analysis

Inventory analysis quantifies elementary flows from all process steps in the studied product system. In this study, the energy and material flows for each processes in the raw material stage, manufacturing and end of life were quantified using data from literature, databases or direct measurements. Details are shown in subsections below.

2.3.1 Raw Material Stage

  doi:10.5075/epfl-298799_978-2-9701614-0-0

The raw materials needed to manufacture a CFRP panel is mainly the carbon fibre, polymer matrix and consumables. For this study, carbon fibre prepregs were used. For thermoset CF/Epoxy panel, Deltapreg M30Sc-150-DT was used and for the thermoplastic CF/PPS panel, Toray T300JB was used. Inventory data for the polymer matrices (Epoxy and PPS) and consumables were obtained from the ecoinvent 3.5 database [10]. However, details of the manufacturing process used to produce these consumables were obtained from Witik et.al. [11]. LCI data for carbon fibre production is not represented in ecoinvent database, so process steps for CF production was modelled in this study using process description and data obtained from Das [12] and Pillain et al. [13]. The quantity of consumables and CF-prepregs used during manufacturing were obtained by direct measurement. However, the CF/Matrix weight compositions were obtained using fiber areal weight provided in the prepreg manufacturer data sheet alongside panel size, and weight of cured laminate.

2.3.2 Manufacturing Stage

Panel manufacturing was carried out at the Delft Aerospace Structure and Materials Laboratory (DASML), TU Delft. CF/Epoxy panel was manufactured using manual collation and autoclave curing while the CF/PPS panel was fabricated using manual collation and forming in a hot press. The process steps for each panel is shown in figure 1.

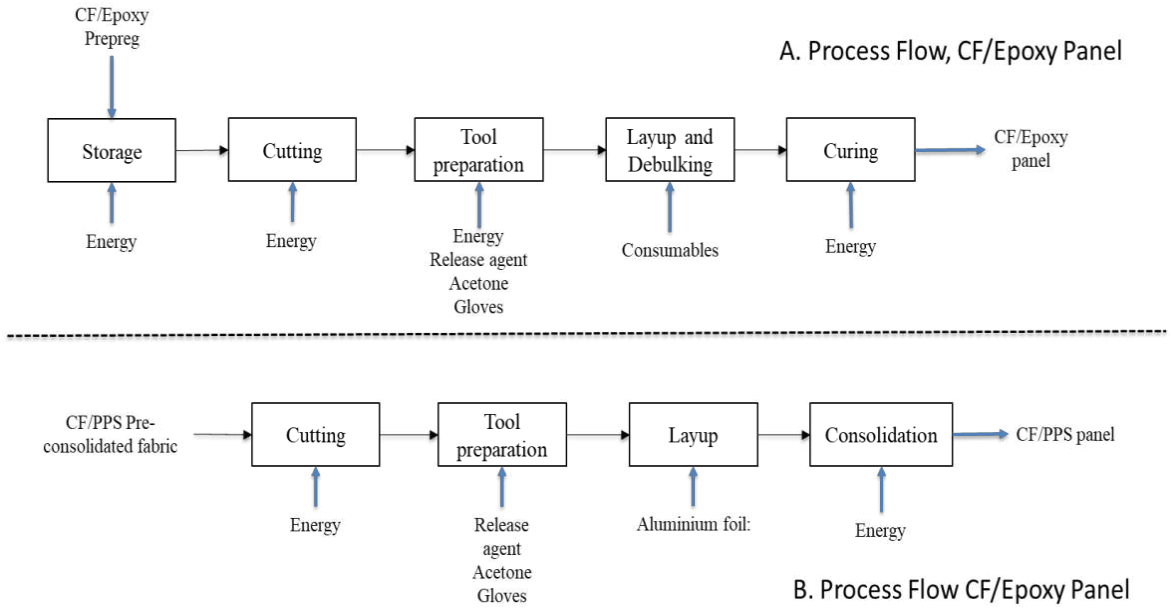

Figure 1 Process flow chart for Manufacture of CFRP Panel. product A = CF/Epoxy panel and product B is CF/PPS Panel

The prepreg/preconsolidated fabrics and consumables were cut into desired part shape and dimension using a CNC automated Gerber cutting machine. Energy use of the cutting machine during operation was measured using a power meter. The cut composite plies were manually laid up on aluminum moulds and consumables for each process were added, these were weighed and recorded prior to layup. Vacuum pump was used at interval when collating the thermoset plies to suck out excess air (debulking) and to ensure the vacuum bag was properly sealed prior to curing. The energy consumption of the vacuum pump was measured and recorded. Once layup was completed, the thermoset laminate stack was placed in the autoclave

  doi:10.5075/epfl-298799_978-2-9701614-0-0

to cure while the thermoplastic stack was placed in between hot press plates to consolidate. Electrical energy consumption of the autoclave and the hot press were monitored during curing and consolidation using a power meter. Once cure and consolidation cycles were completed, the panels were cooled and weighed. After the manufacturing stage, the parts are usually moved to a joining facility for assembly. Joining methods were not considered in this study.

2.1.1 EOL Stage

Average lifespan of composite panel used in aircraft skin was assumed to be 30 years which is similar to the average operational service life of an aircraft[14] . The EOL for both panels were modelled as incineration of mixed plastics with energy recovery and data was obtained from ecoinvent 3.5 database [10].

2.2 Life Cycle Impact Assessment (LCIA)

In this stage, the elementary flows quantified from life cycle inventory are converted to environmental impacts. LCIA results in this study were calculated using two impacts assessment methods including Cumulative Energy Demand CED and ReCiPe 2016 Hierarchist method [15]. These two methods are integrated in the SimaPro 9.2 software. ReCiPe 2016 includes 18 impact categories at midpoint level and three damage end point categories.. The end point indicators cumulate these midpoint impacts into three damage categories including impact on human health in DALY, ecosystems in species.yr and resources in USD2013 [15]. Raw materials extraction and manufacturing of CFRP panel are energy intensive, hence CED was adopted to give an overview of quantity of energy utilized for each process.

3. RESULTS AND DISCUSSIONS

3.1 LCIA results

The environmental impacts of CF/Epoxy and CF/PPS panels throughout their lifecycle- (raw material production, manufacturing and end of life) is shown in figure 2.

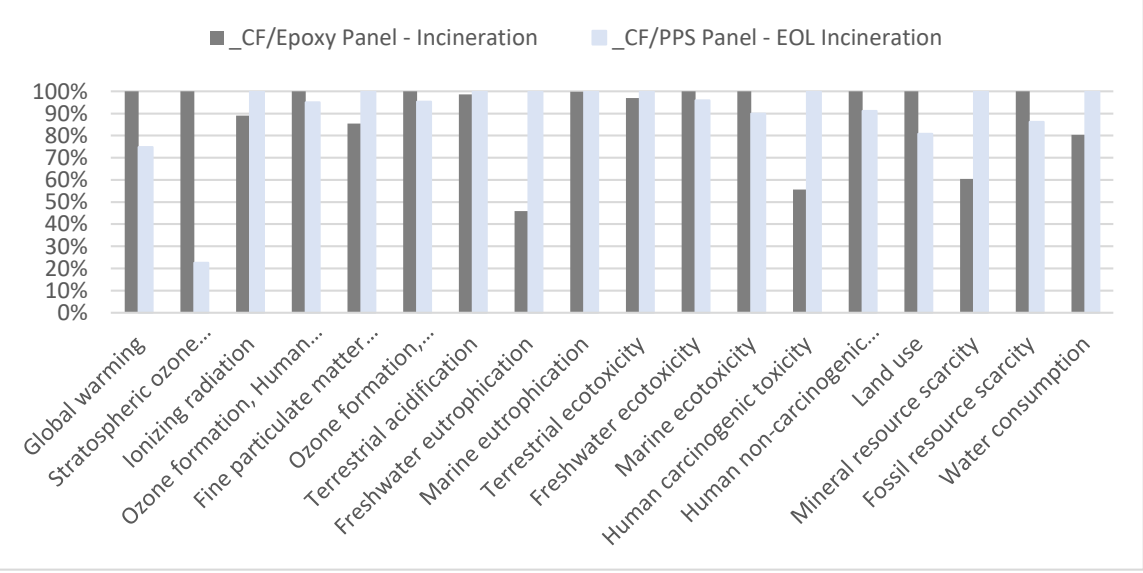

Figure 2 Environmental Impact assessment of raw material production and manufacturing of CF/Epoxy Panel and CF/PPS panels

  doi:10.5075/epfl-298799_978-2-9701614-0-0

Impacts from CF/PPS were higher in nine impacts categories including water Consumption, however it had lower impacts than CF/Epoxy in nine other impact categories including global warming. LCA studies in the aerospace industry have mostly focused on GWP impact category, presenting their results in CO_2 equivalent. However, the results in figure 2 show that although CF/PPS performed better in the global warming category, it was worse in some other impact categories. This shows the importance of taking into account a number of impacts as it provides a better representation of the environmental performance of a product system.

Figure 3 shows the end point damage categories using Recipe H method. The endpoint results show the damage to human health, ecosystem and resources and provide a more real-life perspective of the impacts. CF/PPS performed in all three damage categories including impact to human health, ecosystem and resources.

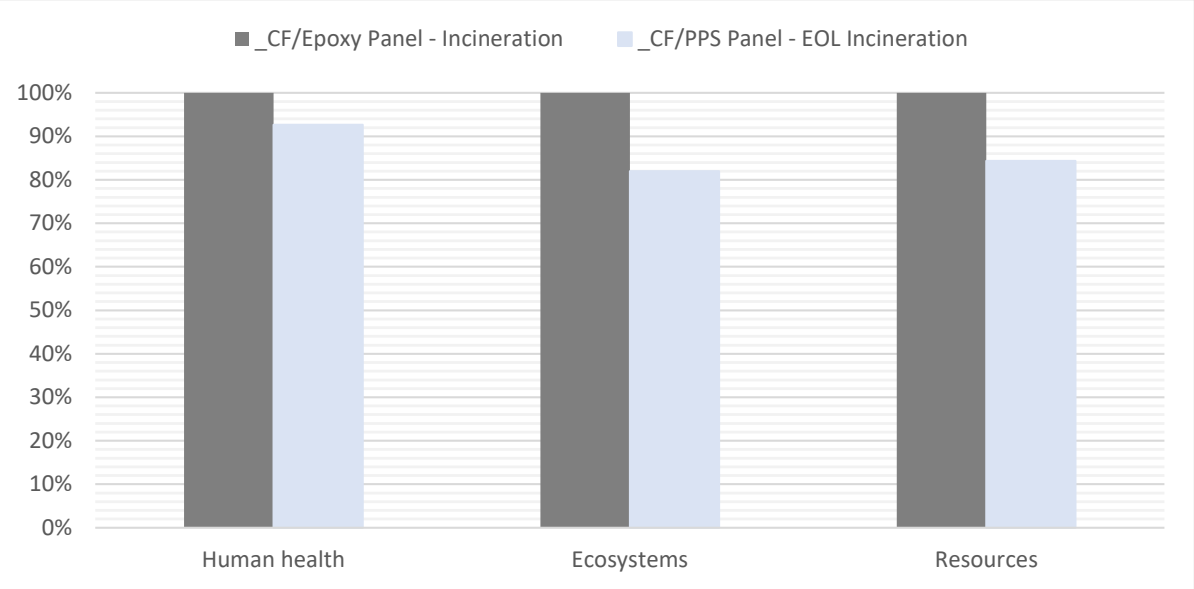

Figure 3:Cradle to gate environmental impact comparison between CF/Epoxy and CF/PPS panels.

3.2 Hotspot Analysis

Hotspot analysis is used to identify processes in a product system that contribute significantly to the environmental impact. It serves as a decision support tool that points out areas to focus on when planning to reduce environmental footprint of a product system. Cumulative Energy Demand (CED) 1.11 single score method and SimaPro 9.2 software was used in this section.

Figure 4 compares the CED of CF/Epoxy to CF/PPS throughout the lifecycle stages considered in this study. As seen, The raw material stage had the highest contribution for the two panels, followed by manufacturing. The figure also shows that at the raw material stage, the CED for CF/PPS was higher than that of CF/Epoxy. However, in the manufacturing stage, the reverse was the case. Overall, the total CED of CF/Epoxy was higher than CF/PPS by 15%.

  doi:10.5075/epfl-298799_978-2-9701614-0-0

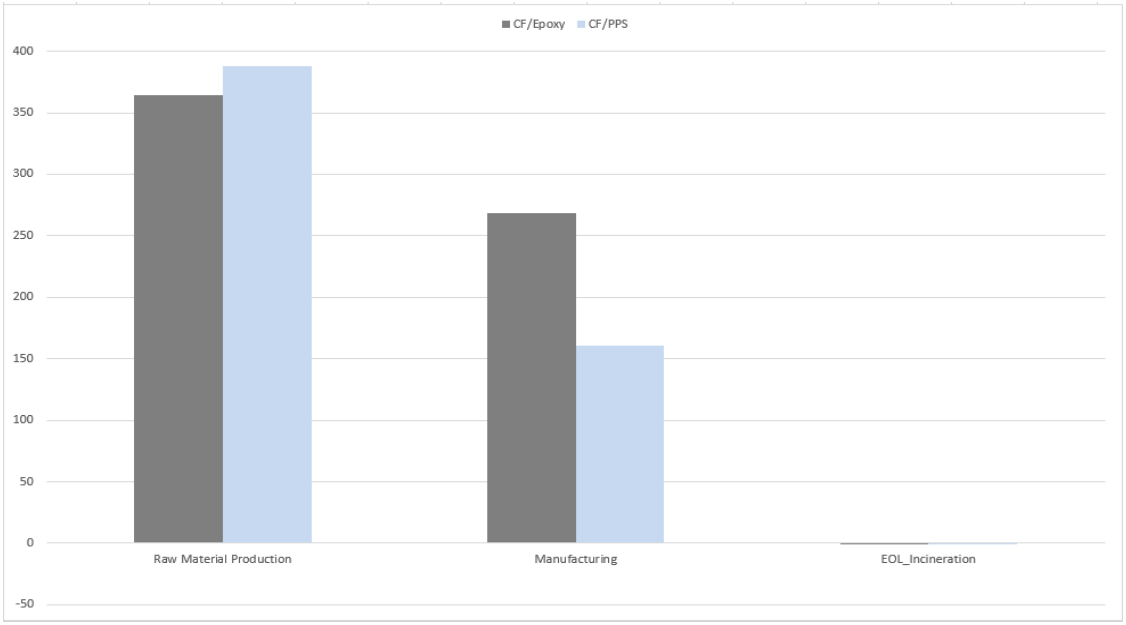

Figure 4: Life Cycle Cumulative Energy Demand of CF/PPS and CF/Epoxy

Figure 5 shows the sub-processes in CF/PPS product system that contribute to its environmental footprint for raw material production and manufacturing. Production of the CF/PPS fabric was the highest contributor to the CF/PPS product system taking up 71% of its cumulative energy demand. Consolidation of the CF/PPS panel contributed 26% of the overall CED and includes only the electricity consumed by the press during consolidation. Figure 5 further breaks down the process steps of the raw material production. This breakdown shows that production of carbon fiber contributed 57.5% to raw material production and 41% to the overall CED of CF/PPS panel.

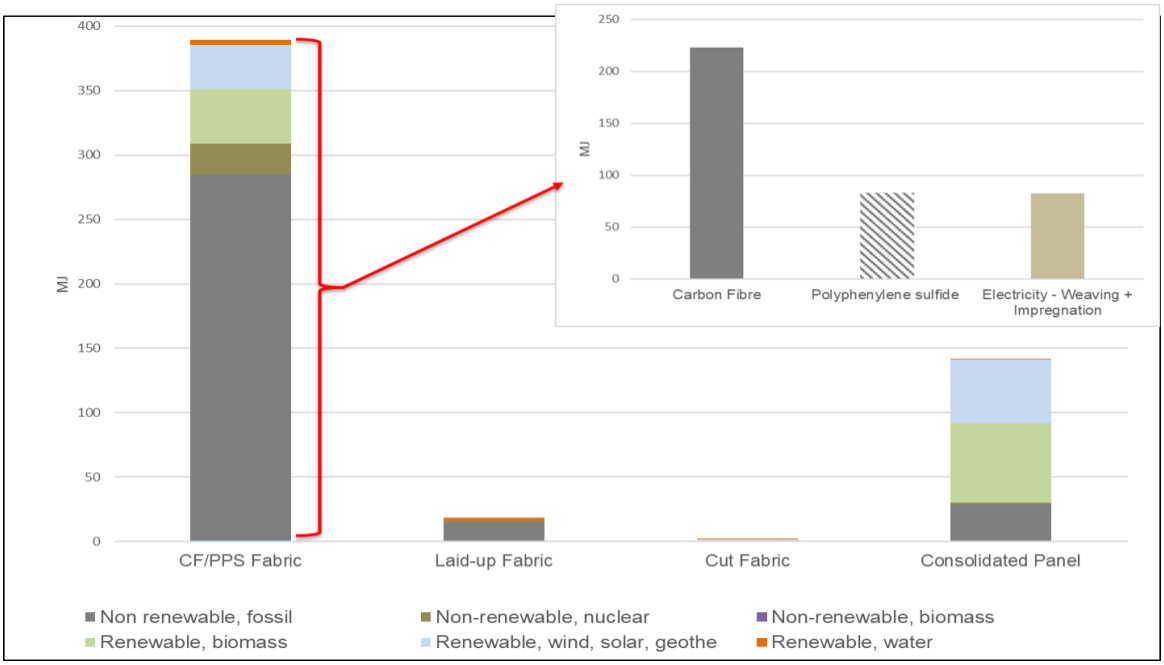

Figure 5 Process contribution for CF/PPS product system.

  doi:10.5075/epfl-298799_978-2-9701614-0-0

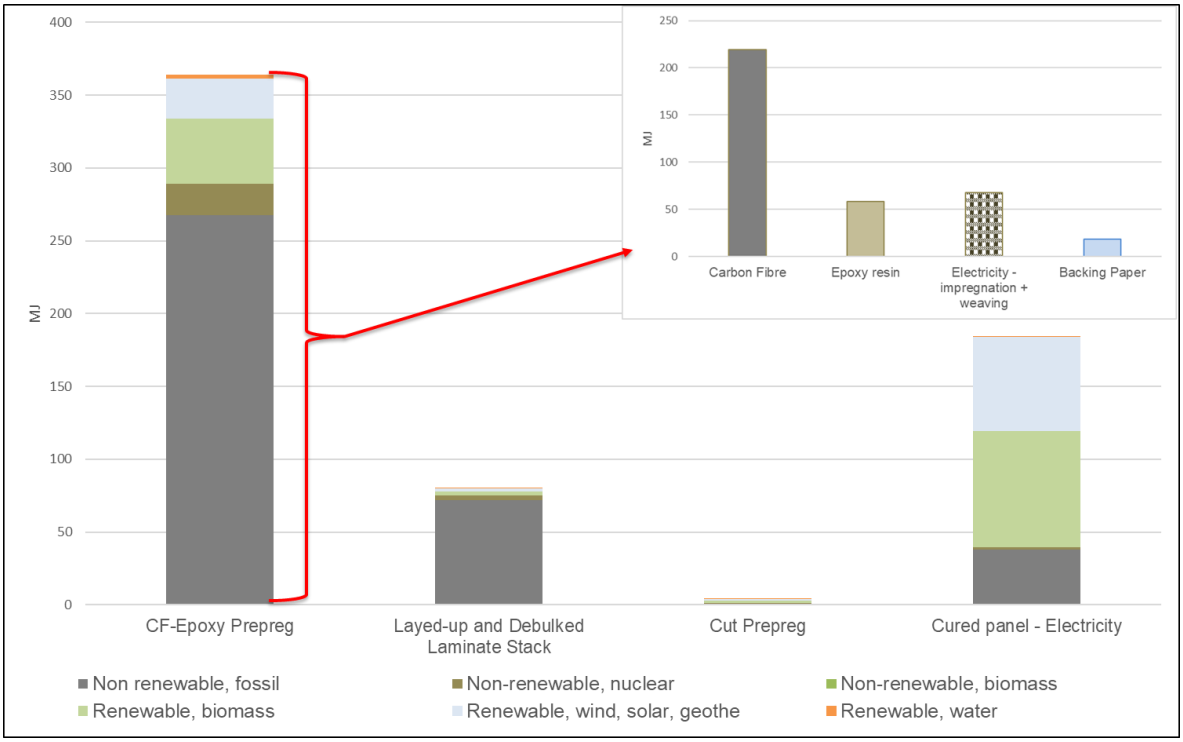

Figure 6 Process Contribution for CF/Epoxy product System.

Figure 6 on the other hand shows the process in the CF/Epoxy panel product system that contribute to its total footprint in the raw material and manufacturing stages. Again, raw material production of the CF/Epoxy prepreg had the highest contribution consuming 42% of the total cumulative energy demand. Curing of panel contributed 29% of the total energy and this includes only the electricity used by the autoclave. Layup and debulking contributed 13% of the total impacts. A breakdown of the raw material production process shows that carbon fibre production contributed 60% to raw material production and 35% of overall CED of CF/Epoxy Panel. Production of epoxy resin as well as electricity for weaving and prepreging also contributed 9% and 11% respectively to the overall CF/Epoxy panel impact.

CONCLUSION

This study compares the life cycle impact of two aircraft skin panels made from thermoset CF/Epoxy and thermoplastic CF/PPS. The results showed that at midpoint level, the TS panel performed better in nine impact categories and the TP panel was better in nine other impact categories including global warming. When impacts were aggregated at the end point levels, the thermoplastic panel performed better in all three damage categories including impact to human health, ecosystem and resources. LCA studies in the aerospace industry have mostly focused on global warming potential, presenting their results in CO2 equivalent. However, the results from this study reiterates the importance of taking into account a number of impacts as it provides a better representation of the environmental performance of a product. A hotspot analysis was also carried out to identify processes within the product systems that contributed significantly to the overall environmental impacts of the panels. Carbon fiber production contributed almost 30% to the total cumulative energy demand of the two panels considered. A strategy to reduce this impact would be recycling the CFRP parts instead of incineration or landfilling. Recycling methods for TS CFRP are still at their incipient stage, but potentials for improvement by the next

  doi:10.5075/epfl-298799_978-2-9701614-0-0

30 years (the panel lifespan considered in this study) is still there. Further studies including recycling methods as EOL pathways instead of incineration will provide more insight to their environmental benefits. Electricity consumption during curing and prepreging contributed almost 40% of cumulative energy demand for CF/Epoxy panel. Most of the electricity were sourced from the Dutch electricity grid, hence about 60% of the electricity came from non-renewable energy sources. Strategies to reduce energy consumption or to promote the use of more renewable energy sources can reduce the carbon footprint of CFRP manufacturing.

REFERENCES

[1] C. Soutis, "Use of carbon fiber-reinforced plastics in aircraft construction," *Mater. Sci. Eng. A*, vol. 412, no. 4, pp. 171–176, 2005.

[2] L. Zhu, N. Li, and P. R. N. Childs, "Light-weighting in aerospace component and system design," *Propuls. Power Res.*, vol. 7, no. 2, pp. 103–119, Jun. 2018.

[3] G. A. Vincent, "Recycling of thermoplastic composites laminates The role of processing," University of Twente, the Netherlands, 2019.

[4] S. Howe, A. J. Kolios, and F. P. Brennan, "Environmental life cycle assessment of commercial passenger jet airliners," *Transp. Res. Part D Transp. Environ.*, vol. 19, pp. 34–41, Mar. 2013.

[5] A. J. Timmis *et al.*, "Environmental impact assessment of aviation emission reduction through the implementation of composite materials," *Int. J. Life Cycle Assess.*, vol. 20, no. 2, pp. 233–243, 2015.

[6] R. A. Witik, F. Gaille, R. Teuscher, H. Ringwald, V. Michaud, and J.-A. E. Månson, "Economic and environmental assessment of alternative production methods for composite aircraft components," *J. Clean. Prod.*, vol. 29–30, pp. 91–102, Jul. 2012.

[7] C. V. Katsiropoulos, A. Loukopoulos, and S. G. Pantelakis, "Comparative environmental and cost analysis of alternative production scenarios associated with a helicopter's canopy," *Aerospace*, vol. 6, no. 1, Jan. 2019.

[8] Dansk Standard, "DS/EN ISO 14040:2008 Miljøledelse - Livscyklusvurdering - Principper og struktur," 2008.

[9] J.-A. E. MÅNSON, M. D. WAKEMAN, and N. BERNET, "Composite Processing and Manufacturing—An Overview," in *Comprehensive Composite Materials*, Elsevier, 2000, pp. 577–607.

[10] "ecoinvent 3.7.1 – ecoinvent." [Online]. Available: https://www.ecoinvent.org/database/ecoinvent-371/ecoinvent-371.html. [Accessed: 29-Jun-2021].

[11] R. A. Witik, R. Teuscher, V. Michaud, C. Ludwig, and J. A. E. Månson, "Carbon fibre reinforced composite waste: An environmental assessment of recycling, energy recovery and landfilling," *Compos. Part A Appl. Sci. Manuf.*, vol. 49, pp. 89–99, 2013.

[12] S. Das, "Life cycle assessment of carbon fiber-reinforced polymer composites," *Int. J. Life Cycle Assess.*, vol. 16, no. 3, pp. 268–282, 2011.

[13] B. Pillain *et al.*, "Positioning supercritical solvolysis among innovative recycling and current waste management scenarios for carbon fiber reinforced plastics thanks to comparative life cycle assessment," *J. Supercrit. Fluids*, vol. 154, p. 104607, Dec. 2019.

[14] "Operating life | Airbus." [Online]. Available: https://www.airbus.com/en/products-services/commercial-aircraft/the-life-cycle-of-an-aircraft/operating-life. [Accessed: 15-Apr-2022].

[15] "LCIA: the ReCiPe model | RIVM." [Online]. Available: https://www.rivm.nl/en/life-cycle-assessment-lca/recipe. [Accessed: 01-Jul-2021].

  doi:10.5075/epfl-298799_978-2-9701614-0-0

ENVIRONMENTAL IMPACT ASSESSMENT OF THERMO-STAMPING CARBON FIBRES REINFORCED POLYPHENYLENE SULFIDE COMPOSITE PARTS

V. Lacoma[a,b], J.-L. Bailleul[c], S. Moisan[b], C. Binetruy[a], O. Kerbrat[d]

a: Nantes Université, Ecole Centrale Nantes, CNRS, GeM, UMR 6183, F-44000 Nantes, France – vincent.lacoma@ec-nantes.fr
b: Nantes Université, IRT Jules Verne, F-44000 Nantes, France
c: Nantes Université, CNRS, Laboratoire de thermique et énergie de Nantes, LTeN, UMR 6607, F-44000 Nantes, France
d: Univ Rennes, ENS Rennes, CNRS, Gem, UMR 6183, F-35000 Rennes, France

Abstract: *The use of composite materials instead of metals for aircraft parts has long been identified as a way of improving their environmental performance, as the weight savings reduce fuel consumption. In the context of environmental transition, it is important to improve the environmental impact of each step of the lifecycle. However few studies have described the environmental performance of composite part manufacturing. In the present study, we therefore conducted a complete environmental analysis of the thermo-stamping of carbon-fibre-reinforced polyphenylene sulfide (CF/PPS) composite parts using a Life Cycle Assessment based framework. First, to define the system's boundaries, the manufacturing process was described as a unit process sequence associated with the consumption and waste of materials and energy (i.e. elementary flows). Data were then collected from experimental measurements, databases, and literature for each flow. These data were used to produce an environmental assessment, highlighting the environmental impact hotspots of CF/PPS part thermo-stamping.*

Keywords: Environmental impact; manufacturing process; thermoplastic composites; thermo-stamping

1. Introduction

Polymer composites reduce the weight of structural parts, owing to their good strength-to-weight ratio compared with traditional materials such as metals. In aircraft, weight reduction reduces fuel consumption, meaning that composite parts have a smaller environmental impact across their life cycle [1]. Therefore, polymer composites have long been identified as an efficient way of reducing the environmental impact of the aeronautical sector. In the current context of environmental transition, everyone involved in the life cycle of aeronautical parts needs to find ways of reducing their environmental impact, and this includes the impact of the manufacturing stage. To this end, we carried out an environmental impact assessment of the carbon fibres reinforced polyphenylene sulfide (CF/PPS) thermo-stamping process. This process was chosen because it is already used in the aeronautical industry.

To the best of our knowledge, few articles have so far focused on the environmental impact of the thermo-stamping manufacturing process, in terms of detailed inventory data and associated environmental assessments. In a recent comparison of manufacturing processes, Wegmann *et al.* undertook an environmental assessment of a polycarbonate/glass fibre car

  doi:10.5075/epfl-298799_978-2-9701614-0-0

bonnet manufactured by thermo-stamping [2]. The authors used inventory data yielded by thermodynamic calculations and picked from the ecoinvent database. However, their environmental assessment of the manufacturing step was energy-oriented and did not include other elementary flows. Several studies have involved the environmental analysis of processes close to thermo-stamping, including the preform matched die process [3], cold diaphragm forming process [4], and automated tape laying coupled with thermoforming [5], but again focusing mainly on energy consumption. The lack of environmental data for the thermo-stamping process makes it difficult to identify its environmental hotspots and thus to set the priorities for enhancing its environmental performance. In the present study, we therefore conducted an environmental assessment of CF/PPS part thermo-stamping.

After introducing the context, we describe the methodology used for the environmental assessment of the CF/PPS thermo-stamping process (Section 2). This is followed by a comprehensive inventory analysis and environmental assessment (Section 3), after which we discuss our results (Section 4), and present our conclusions (Section 5).

2. Methodology for the environmental analysis of the CF/PPS thermo-stamping process

This article is based on the Life Cycle Assessment (LCA) framework, the standardized methodology (ISO 14040 and ISO 14044) for environmental analysis.

2.1. Scope of the study

The material used in this study was semi-crystalline CF/PPS (Toray Cetex® TC1100), in the form of consolidated sheets of 14 ply and 4.34 mm thick. The stamp-forming process we studied allows finished parts to be manufactured from semi-finished reinforced composite sheets, as shown in Figure 1. Preform heating was performed using a Sopara infrared (IR) composite oven. A 75T SCAMEX press was used for the stamping step. The process also involved preform cutting using an OMAX ProtoMAX abrasive water jet (AWJ), robot arm handling, and post-process machining. For each unit process, we listed the consumption and waste of all the materials and energy (i.e. elementary flows). All the elementary flows considered in the environmental analysis are shown in Figure 1. As the thermo-stamping process heats thermoplastic materials to high temperatures to soften the polymer matrix, emissions to air may take place as a result of material degradation and material additive vaporization mechanisms [6]. Two types of emissions may occur: particulate matter (PM) and gaseous compound such as volatile organic compounds (VOCs). According to the literature, the gases emitted during PPS degradation are mainly hydrogen sulfide (H_2S) and benzenethiol [7].

In the present study, our functional unit was a 250 x 200 x 4.34 mm CF/PPS part, manufactured in France using the thermo-stamping process. The composite was heated to 370 °C in the IR oven and then stamped in a mould at 100 °C with a 200 kN closing force. These process parameters are representative of real-world CF/PPS part thermo-stamping [8]–[12]. We assumed that scraps would mainly be generated at the preprocessing step (90%), and only a few at the postprocessing step (10%). Based on industrial observations, we expected successive part production cycles to overlap. In other words, while one part was being stamped, the next preform would be heated in the IR oven. As a consequence, machine idling time would be shorter.

  doi:10.5075/epfl-298799_978-2-9701614-0-0

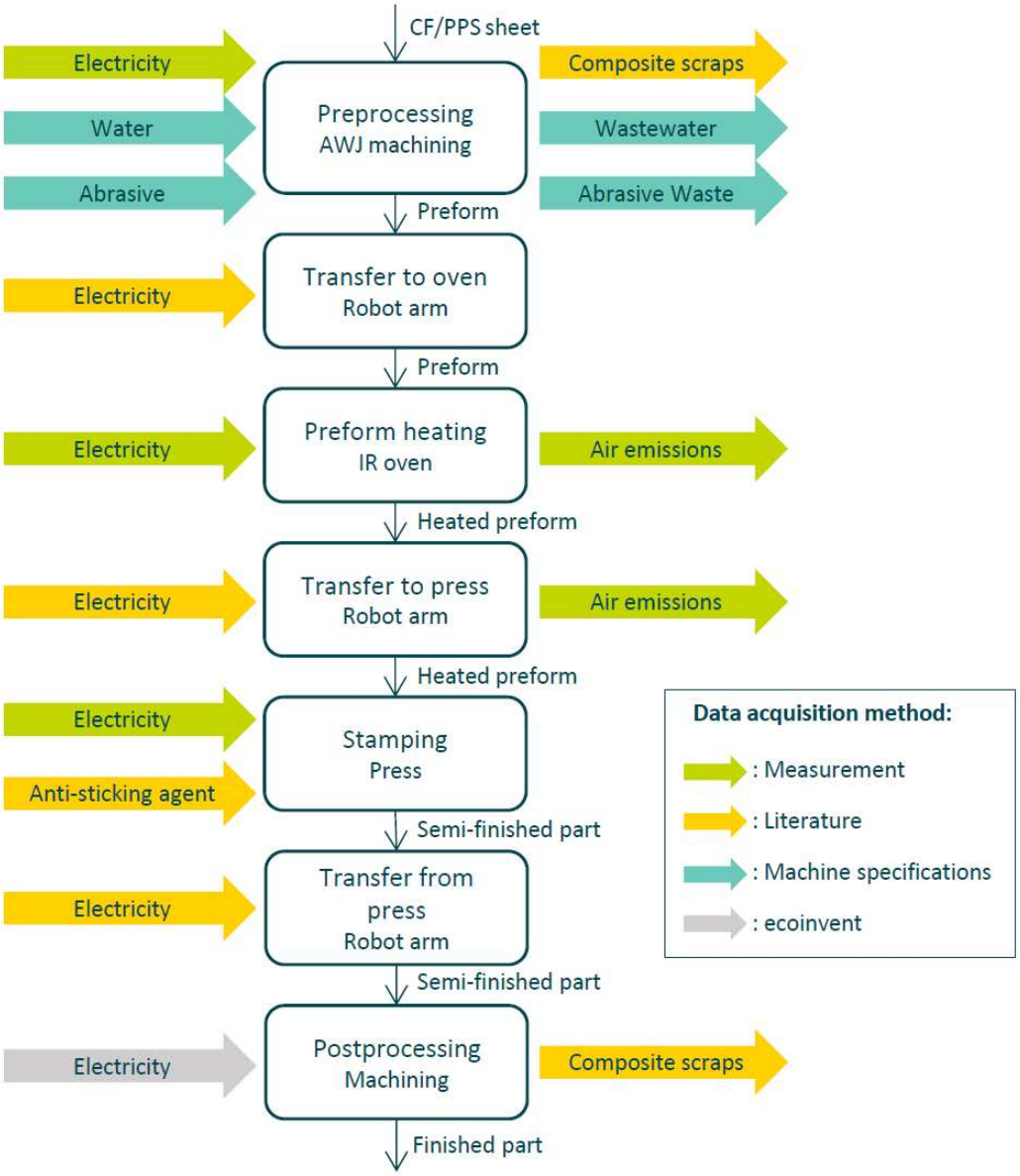

Figure 1: Thermo-stamping process description

2.2. Inventory data collection

Inventory data related to the process described in Figure 1 were collected through experimental measurements and from machine specifications, published studies, and ecoinvent databases. In Figure 1, the origins of the data for each elementary flow are colour-coded. Electrical energy consumption and air emissions were measured experimentally. The active power consumed by the machines was measured with a Fluke 434 II power quality and energy analyser with Fluke i30s current clamps. A Q-Trak (TSI) indoor air quality monitor with 987 VOC probe capable of detecting H_2S and benzenethiol was used to measure gaseous compound emissions. A DUSTTRAK (TSI) was also used to detect 0.1-10 µm PM emissions. Measurements with both instruments were performed at the output of the IR oven exhaust system during CF/PPS heating tests. As emissions from thermoplastics increase with the temperature [13], the temperature of the different tests was set to the maximum (370 °C) used for CF/PPS thermo-stamping [8]–[12], to maximize emissions during the tests.

  doi:10.5075/epfl-298799_978-2-9701614-0-0

2.3. Environmental assessment

The environmental impact was assessed using SimaPro software with the ecoinvent v3.5 database and the Impact 2002+ v2.15 method. Robot handling steps were summed as a single unit process. Material consumption was considered separately from the unit processes. Transport steps were excluded, and landfill was chosen as the waste treatment scenario. Polydimethylsiloxane was chosen as the anti-sticking agent, in line with Wegmann *et al.* [2]. To assess the environmental impact of the CF/PPS semi-finished material, we only considered PPS and CF production and not the semi-product manufacturing step. PPS production was modelled using ecoinvent v3.5. We computed the environmental impact of carbon fibre production using the data from Khalil *et al.* [14] and Duflou *et al.* [15] aggregated by Forcellese *et al.* in [16]. Our environmental analysis only included CF/PPS overconsumption. We adopted this approach in order to focus on improving the manufacturing process. Thus, the amount of CF/PPS used for the part was excluded from the elementary flows, as no actions on this flow are possible at the manufacturing stage: it can only be improved at the part design stage, which was beyond the scope of the present study.

3. Environmental results

3.1. Inventory analysis

The results of the inventory analysis of the CF/PPS thermo-stamping process are shown in Table 1. First, part material and scraps across the whole process were summed to obtain CF/PPS material consumption. Scrap data were extracted from the literature for different processes [17]–[25] and averaged to obtain the total scrap rate (34%). Using this rate, CF/PPS consumption was estimated at 5.1E-1 kg.

Air emission measurements were inconclusive, as no gaseous compound or PM emissions were detected. Anyway, emissions data have been computed assuming that the emissions are approximately equal to the detection threshold of the measuring devices and occur above the PPS melting temperature. Thus, the gaseous compound detector detection threshold and standard deviation of the PM measurements were assumed to be the emission values. To overestimate the environmental impact of the air emissions, we chose the worst scenario: hydrogen sulfide (H_2S) as the only emitted gaseous compound and 2.5 µm as the maximum diameter for PM emissions.

Table 1: Inventory dataset for the part thermo-stamping step
(E_i: Electrical energy consumption in Step i; m_i: mass of i flow; V_i: volume of i flow)

Unit process	Inventory data	Data collection methodology
AWJ preform cutting	$E_{AWJ\ cut}$ = 8.93E+05 J	Scaled on experimental measurements on the OMAX ProtoMAX AWJ machine
	V_{water} = 3.2 L	Scaled on OMAX ProtoMAX AWJ machine specifications
	$m_{abrasive}$ = 4.37E-01 kg	
	$m_{AWJ\ scraps}$ = 1.56E-01 kg	Arbitrary value set at 90% of total scrap
	$V_{wastewater}$ = 3.2 L	Set equal to water and abrasive input
	$m_{abrasive\ waste}$ = 4.37E-01 kg	
IR oven heating	E_{oven} = 3.07E+06 J	Scaled on experimental measurements on the SOPARA IR oven
	$m_{oven\ H2S}$ = 4.27E+02 mg	Based on experimental measurements and measuring machine specifications
	$m_{oven\ PM\ 2.5}$ = 2.45 mg	

Robot arm handling	E_{robot} = 8.17E+04 J	Computed with Chemnitz *et al.* model for Comau SMART SiX robot arm energy consumption during an 8 s motion [26]
	$m_{robot\ H2S}$ = 7.60E+01 mg	Based on experimental measurements and measuring machine specifications
	$m_{robot\ PM\ 2.5}$ = 4.36E-01 mg	
Stamp forming	E_{press} = 5.37E+06 J	Scaled on experimental measurements on 75T Scamex press
	$m_{anti\text{-}stick}$ = 1.22E-03 kg	Scaled using averaged literature data for anti-sticking agent consumption in different composite manufacturing processes [2], [16], [18], [27], [28]
Machining	$E_{machining}$ = 1.99E+05 J	Taken from ecoinvent v3.5 database model for chromium steel milling, because of its higher energy consumption factor than other metal milling models found in ecoinvent v3.5
	$m_{machining\ scrap}$ = 1.73E-02 kg	Arbitrary value set at 10% of total scrap

3.2. Environmental assessment

Environmental impact assessment results are set out in Figure 2. CF/PPS material overconsumption was identified as the primary contributor to environmental impact. Regarding the global warming impact category, 90% of the computed impact came from the material overconsumption flow. The heating and stamp-forming steps each had also a significant environmental impact. For the global warming impact indicator, 3% of the impact was caused by the IR heating and 6% by the stamp forming steps. It was the energy consumption flow that drove the environmental impact of these two unit processes. Focusing on air emissions, these two elementary flows accounted for three environmental impact indicators: $PM_{2.5}$ emissions contributed to around 0.11% of the respiratory inorganics environmental impact; and H_2S emissions contributed to 0.19% of non-carcinogens and 5.7% of aquatic acidification environmental impacts.

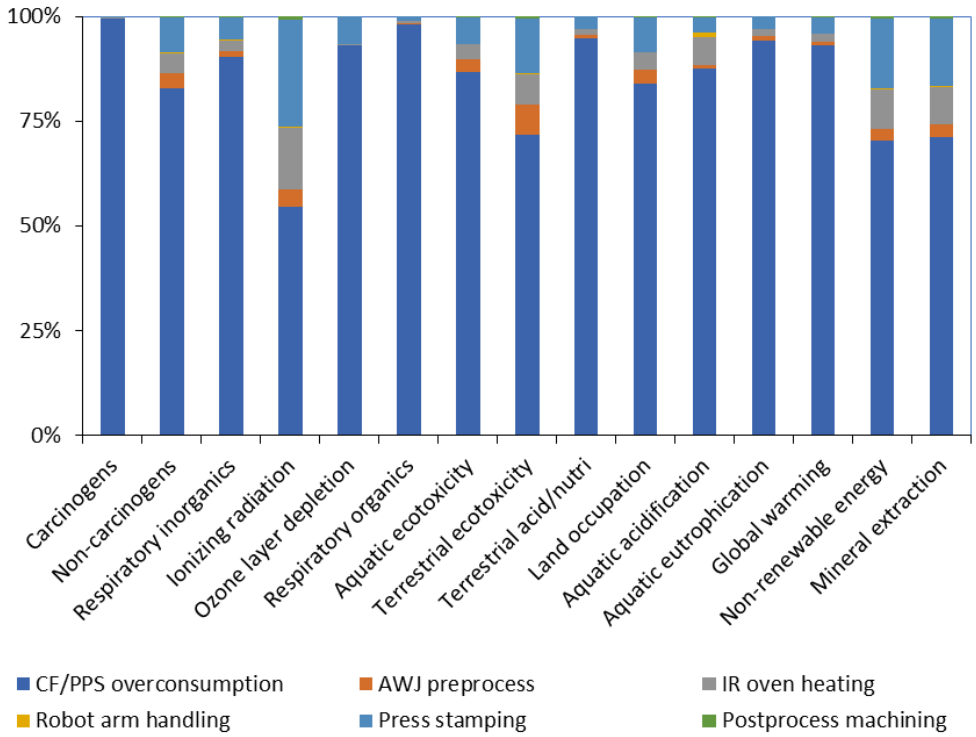

Figure 2: Environmental impact assessment of CF/PPS part manufacturing

  doi:10.5075/epfl-298799_978-2-9701614-0-0

4. Discussion

In the present study, we conducted an environmental assessment of CF/PPS part thermo-stamping. Results showed that CF/PPS material overconsumption was by far the greatest contributor to environmental impact, despite the underestimation of the environmental impact of CF/PPS production (PPS and CF production was considered, but not semi-product manufacturing). The energy consumption for the heating and stamping unit processes was also the source of significant impacts. In order to develop efficient environmental impact improvement strategies, the focus needs to be on the environmental hotspots we identified. However, our results need to be interpreted with care, as CF/PPS overconsumption was based on literature data. Furthermore, process specificities and part geometry were not considered, even though these two aspects strongly influence material consumption. For example, the blank holders used in the process caused material overconsumption. Expected part geometry also affected the preform's in-plane shear deformation on the mould, which was correlated with material consumption.

As experimental measurements were inconclusive, we estimated air emissions by coupling these inconclusive results with the specifications of the measuring machines. This led to overestimated emissions. Despite this, computing the associated environmental impact showed that air emissions had a negligible influence on the environmental impact of the process. This was still an advance, as very few studies have considered air emissions in thermoplastic composite manufacturing environmental assessments.

Our conclusions should be treated with caution, as the environmental results we computed pertain to a single case study of part manufacturing with a fixed set of parameters. Thus, the results cannot easily be generalized to the thermo-stamping process.

5. Conclusion

The use of composite materials has long been identified as a solution for decreasing the environmental impact of aircraft parts, thanks to the fuel savings afforded by the lighter structures. In the context of environmental transition, the environmental impact of composite parts has to be improved across their lifecycle. The present study focused on the environmental impact of the CF/PPS thermo-stamping process. Based on a complete description of this process, we assessed inventory data for each elementary flow we identified, using various strategies (experimental measurements, database and literature data). Using these data, we assessed the environmental impact of each part manufacturing step. This assessment highlighted two environmental hotspots: CF/PPS material overconsumption and energy consumption during the heating and stamping unit processes. Therefore, the present study helped to make up for the lack of environmental data for the thermo-stamping process. Nevertheless, it only focused on one part with one set of process parameters, which is not enough to draw general conclusions about the process.

Acknowledgements

This research was part of a PhD thesis supported by the PERFORM program of IRT Jules Verne.

  doi:10.5075/epfl-298799_978-2-9701614-0-0

6. References

1. Duflou JR, Deng Y, Van Acker K, Dewulf W. Do fiber-reinforced polymer composites provide environmentally benign alternatives? A life-cycle-assessment-based study. MRS Bull. 2012 Apr 9; 37(4):374–82.
2. Wegmann S, Rytka C, Diaz-Rodenas M, Werlen V, Schneeberger C, Ermanni P, et al. A life cycle analysis of novel lightweight composite processes: Reducing the environmental footprint of automotive structures. J Clean Prod. 2022 Jan; 330(October 2021):129808.
3. Suzuki T, Takahashi J. Prediction of energy intensity of carbon fiber reinforced plastics for mass-produced passenger cars. Proc 9th Japan Int SAMPE Symp. 2005;14–9.
4. Katsiropoulos C V., Loukopoulos A, Pantelakis SG. Comparative Environmental and Cost Analysis of Alternative Production Scenarios Associated with a Helicopter's Canopy. Aerospace. 2019 Jan 3; 6(1):3.
5. Brecher C, Schmitt R, Lindner F, Peters T, Emonts M, Böckmann MG. Increasing Cost and Eco Efficiency for Selective Tape Placement and Forming by Adaptive Process Design. Procedia CIRP. 2016; 57:769–74.
6. Patel SH, Xanthos M. Environmental issues in polymer processing: A review on volatile emissions and material/energy recovery options. Adv Polym Technol. 2001; 20(1):22–41.
7. Zuo P, Tcharkhtchi A, Shirinbayan M, Fitoussi J, Bakir F. Overall Investigation of Poly (Phenylene Sulfide) from Synthesis and Process to Applications—A Review. Macromol Mater Eng. 2019 May 7; 304(5):1800686.
8. McCool R, Murphy A, Wilson R, Jiang Z, Price M, Butterfield J, et al. Thermoforming carbon fibre-reinforced thermoplastic composites. Proc Inst Mech Eng Part L J Mater Des Appl. 2012 Apr 16; 226(2):91–102.
9. Han P, Butterfield J, Price M, Buchanan S, Murphy A. Experimental investigation of thermoforming carbon fibre-reinforced polyphenylene sulphide composites. J Thermoplast Compos Mater. 2015 Apr 22; 28(4):529–47.
10. Joppich T, Doerr D, van der Meulen L, Link T, Hangs B, Henning F. Layup and process dependent wrinkling behavior of PPS/CF UD tape-laminates during non-isothermal press forming into a complex component. In: AIP Conference Proceedings. 2016. p. 170012.
11. Jamin T, Dubé M, Laberge Lebel L. Effect of stamp-forming parameters and bend radius on the mechanical performance of curved beam carbon fiber/polyphenylene sulfide specimens. J Compos Mater. 2016 Apr 11;50(9):1213–25.
12. Abbassi F, Elfaleh I, Mistou S, Zghal A, Fazzini M, Djilali T. Experimental and numerical investigations of a thermoplastic composite (carbon/PPS) thermoforming. Struct Control Heal Monit . 2011 Nov;18(7):769–80.
13. Yamashita K, Yamamoto N, Mizukoshi A, Noguchi M, Ni Y, Yanagisawa Y. Compositions of Volatile Organic Compounds Emitted from Melted Virgin and Waste Plastic Pellets. J Air Waste Manage Assoc. 2009 Mar 24; 59(3):273–8.
14. Khalil YF. Eco-efficient lightweight carbon-fiber reinforced polymer for environmentally greener commercial aviation industry. Sustain Prod Consum. 2017 Oct; 12(April):16–26.
15. Duflou JR, De Moor J, Verpoest I, Dewulf W. Environmental impact analysis of composite use in car manufacturing. CIRP Ann. 2009; 58(1):9–12.
16. Forcellese A, Marconi M, Simoncini M, Vita A. Life cycle impact assessment of different manufacturing technologies for automotive CFRP components. J Clean Prod. 2020 Oct; 271:122677.

  doi:10.5075/epfl-298799_978-2-9701614-0-0

17. Rybicka J, Tiwari A, Alvarez Del Campo P, Howarth J. Capturing composites manufacturing waste flows through process mapping. J Clean Prod. 2015 Mar; 91:251–61.
18. Vita A, Castorani V, Germani M, Marconi M. Comparative life cycle assessment and cost analysis of autoclave and pressure bag molding for producing CFRP components. Int J Adv Manuf Technol. 2019 Dec 11; 105(5–6):1967–82.
19. Zhang J, Chevali VS, Wang H, Wang C-H. Current status of carbon fibre and carbon fibre composites recycling. Compos Part B Eng. 2020 Jul;193(December 2019):108053.
20. Mativenga PT, Sultan AAM, Agwa-Ejon J, Mbohwa C. Composites in a Circular Economy: A Study of United Kingdom and South Africa. Procedia CIRP. 2017; 61:691–6.
21. La Rosa AD, Recca G, Summerscales J, Latteri A, Cozzo G, Cicala G. Bio-based versus traditional polymer composites. A life cycle assessment perspective. J Clean Prod. 2014 Jul; 74:135–44.
22. Dér A, Kaluza A, Reimer L, Herrmann C, Thiede S. Integration of Energy Oriented Manufacturing Simulation into the Life Cycle Evaluation of Lightweight Body Parts. Int J Precis Eng Manuf Technol. 2022 Jan 3.
23. Loukopoulos A, Katsiropoulos CV, Pantelakis SG. Carbon footprint and financial evaluation of an aeronautic component production using different manufacturing processes. Int J Struct Integr. 2019 Jun 10; 10(3):425–35.
24. Al-Lami A, Hilmer P, Sinapius M. Eco-efficiency assessment of manufacturing carbon fiber reinforced polymers (CFRP) in aerospace industry. Aerosp Sci Technol. 2018 Aug; 79:669–78.
25. Witik RA, Gaille F, Teuscher R, Ringwald H, Michaud V, Månson JE. Economic and environmental assessment of alternative production methods for composite aircraft components. J Clean Prod. 2012 Jul; 29–30:91–102.
26. Chemnitz M, Schreck G, Kruger J. Analyzing energy consumption of industrial robots. In: ETFA2011. IEEE; 2011. p. 1–4.
27. Forcellese A, Mancia T, Simoncini M, Gentili S, Marconi M, Vita A, et al. Comparative life cycle assessment of carbon fiber reinforced composite components for automotive industry. ESAFORM 2021. 2021 Apr 2; 06:1–12.
28. Hann Chua M, Smyth BM, Murphy A, Butterfield J. Understanding aerospace composite components' supply chain carbon emissions. In: Irish Manufacturing Conference. 2015.

  doi:10.5075/epfl-298799_978-2-9701614-0-0

EFFECTS OF THE HYGROTHERMAL AGING HISTORY ON EPOXY RESINS AND GFRP COMPOSITES

Dennis Gibhardt[a], Devin Meyer[a], Lennart Braun[a], Christina Buggisch[a], Bodo Fielder[a]

a: Hamburg University of Technology, Institute of Polymers and Composites, Denickestraße 15, 21073 Hamburg, dennis.gibhardt@tuhh.de

Abstract: *As the success of fiber reinforced polymers (FRP) has reached a wide range of industries, sustainability, reliability, and durability are increasingly important requirements. Complex processes occur in the polymeric matrices and the multiscale composites, especially under challenging conditions (humidity, water, temperature). Due to the variety of available constituents (fibers, sizings, resins) and the high time pressure for new products and innovations, long-term property predictions rely mostly on accelerated aging procedures. However, since the available materials can differ considerably in their characteristics, aging effects need to be understood better. Therefore, long-term studies on four epoxies demonstrate the importance of the hygrothermal aging temperature affecting their thermo-mechanical properties by plasticization and physical aging processes. Additional investigations on several glass fiber composites under the same aging conditions reveal that the matrix and interphase dominated properties are likely to develop differently from neat epoxy. The sizing durability is essential here.*

Keywords: Glass fiber; Durability; Interphase; Sizing; Long-term properties

1. Introduction

In order to make a decisive contribution to the efficient and sustainable use of raw materials and energy, the potential of lightweight composites must be exploited even better in the future. To achieve this, it is necessary to extend the operating life of structures and components even under harsh environmental conditions while at the same time ensuring safe operation. Therefore, it is essential for composites and their polymer matrices to know how their mechanical properties develop over time under the influence of water, moisture, and different temperatures. In the past, academia and industry regularly concentrated on accelerated aging procedures at elevated temperatures aiming to make reasonable estimations for the long-term properties of polymers and composites [1]. However this approach produces quick results, but there is a danger of overestimating or generating effects that do not occur in the field. It is known and expected that thermo-mechanical properties of epoxies and composites might suffer from water absorption and aging. Loss of strength [2], decrease of the glass transition temperature (T_g) [3] or swelling induced cracks and defects [4] are typical phenomena. Accordingly, in the present study, the changes of the mechanical properties of epoxy resins due to water absorption (water bath/climate chamber) over a wide temperature range and long aging periods are investigated in detail. Tensile tests, DMTA, and FTIR investigations allow, for example, to reveal the current material condition and predict the development of strength as a function of environmental conditions and aging time [5]. Time-dependent investigations impressively show under which conditions the plasticizing effect of water is determinant and under which the polymer relaxation and water-network interaction [5, 6]. A comparison of four commercially widely used epoxies within this study points out commonalities and differences.

  doi:10.5075/epfl-298799_978-2-9701614-0-0

Alongside the changes in matrix properties, the fiber-matrix interphase plays a decisive role in composites' durability [7]. Therefore, the interphase properties' changes were investigated similarly in the second part of the study. Transverse tensile tests on numerous fiber-matrix combinations examine the unique role of fiber sizing for the performance and durability of glass fiber reinforced polymer (GFRP) composites. In principle, the transverse tensile strength develops first similarly but over time more and more contrary to the matrix strength. With increasing water absorption, a plasticizing and at elevated temperatures detrimental damage appears, which does not recover over time. Furthermore, the composite properties are not reversible by re-drying and rejuvenation to the same extent as those of the epoxy matrices [5, 6, 8]. In summary, the study will help enhance predictions regarding the effects of various environmental conditions on epoxy and epoxy composites in the future. For both neat polymers and GFRP composites, the importance of the time-temperature-humidity history concerning their operational durability is highlighted.

2. Materials and Methods

2.1 Epoxy resins and glass fibers

In total, four low viscosity epoxy resin systems based on compositions of bisphenol A diglycidyl ether (DGEBA) or bisphenol F diglycidyl ether (DGEBF) and amine-based hardeners were selected to investigate the hygrothermal aging behavior of epoxies and GFRP composites. All systems are applicable for infusion and resin transfer molding (RTM) processes and are widely used in the wind and maritime industry. Due to their chemical formulations, the chosen systems differ in the extent of their water absorption under constant environmental conditions. The epoxy resin system primarily investigated for long-term aging is EPIKOTE™ Resin MGS™ RIMR 135 and the amine hardener EPIKURE™ Curing Agent MGS™ RIMH 137 (Hexion Inc., USA). Additionally, EPIKOTE™ Resin MGS™ RIMR 035c and the hardener EPIKURE™ Curing Agent MGS™ RIMH 037 (Hexion Inc., USA), Araldite® LY 1568 and the hardener Aradur® 3489 (Huntsman, USA), and CeTePox® AM 3329 A/B (CTP Advanced Materials GmbH, Germany) were studied.

Glass fiber fabrics made of different fiber inputs (E-glass, ECR-glass, and R-glass) and finished with different commercial fiber sizings were used to manufacture unidirectional GFRP composite laminates. Different fibers and matrix systems were combined to study the impact of material selection on the hygrothermal durability of the composites. A detailed overview of all used fiber types and fabrics is given in Table 1.

Table 1 : Overview of the glass fiber fabrics structures and properties. All fabrics are sized with epoxy compatible sizes according to the manufacturers' data sheets.

Supplier	Fabric	Fiber	Manufacturer	Type	Areal weight in g/m²	0°-share
Saertex	UE1182	SE 2020	3B, Belgium	ECR-Glass	1182	97 %
Saertex	UE1192	W 2020	3B, Belgium	R-Glass	1192	97 %
Saertex	UVE1166	Hybon 2002	NEG, Japan	E-Glass	1166	99 %
Gurit	UE-500	ER469L	CPIC, China	ER-Glass	500	99 %

  doi:10.5075/epfl-298799_978-2-9701614-0-0

2.2 Manufacturing processes and specimen preparation

All neat epoxy plates and GFRP laminates were manufactured using vacuum-assisted RTM processes (VARTM). A two-part, polished aluminum mold was used in combination with frames of either 0.5 mm (neat epoxy) or 2.0 mm (GFRPs) thickness. The fiber fabrics were cut to size and placed unidirectional and parallel to the long side into the mold. The resins were mixed and degassed for 30 minutes according to the mixing ratios provided by the manufacturers' data sheets using a vacuum stirrer. The infusion process was done at 50 °C (RIMR135 and RIMR035c) or 40 °C (LY1568 and CeTePox 3329A/B) mold temperature and held for 15 hours. The ambient pressure of the trap side was only a few mbar during infusion and curing. The plates and laminates were demolded and subsequently post-cured at 80 °C for 15 hours (RIMR135 and RIMR035c) or 10 hours (CeTePox 3329A/B), or at 100 °C for 5 hours (LY1568). Rectangular GFRP transverse tensile specimens of 250x25x2 mm³ were cut using aluminum-oxide blades on a Brillant 265 (QATM, Germany) semi-automatic saw. Dogbone-shaped neat epoxy specimens for tensile tests and DMA investigations were elaborated using a Euromod 35 (Isel Germany AG, Germany) CNC-mill with a 1.8 mm diamond bit. The cutting edges of neat epoxy were polished with SiC sandpaper up to a grit-size of P2500, to minimize the effects of edge roughness. The specimen geometries and dimensions are given in Figure 1.

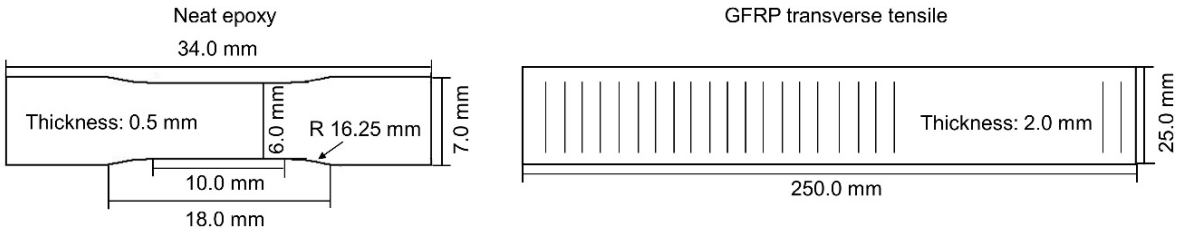

Figure 1. Specimen dimensions and geometries.

3. Results and Discussion

3.1 Water absorption and impact of aging temperature on epoxy strength

The water absorption process in highly cross-linked thermosets like epoxy resins is nowadays known to be mainly a result of the polymers' structure and chemical composition [9, 10]. For non-hydrolyzable epoxies, the process is regularly modelled with the Fickian absorption model [11]. Differences during isothermal water absorption result from molecular interactions between absorbed water molecules and polar groups within the polymers [10]. Therefore, the molar attraction and volume define hydrophilicity. Furthermore, the diffusion rate and, to some extent, the maximum content of absorbed water are temperature dependent [5, 12]. The isothermal water absorption process in a water bath at 8 °C is representatively shown with experimental data, and Fickian absorption models in Figure 2A for all studied neat epoxies. It is revealed that even though the epoxies are quite similar in terms of their main molecular components, the maximum water content at saturation shows differences of up to 1.0 m% due to the different chemical compositions. The effects of the water absorption on the tensile yield strength were analyzed for water bath and humid air aging temperatures between 8 °C and 70 °C. In Figure 2B, the residual strength is displayed exemplarily for aging at 8 °C and 40 °C related to the amount of absorbed water at saturation. The results demonstrate that the tensile strength of all epoxies decreases due to the plasticizing effect of water.

  doi:10.5075/epfl-298799_978-2-9701614-0-0

Furthermore, it becomes clear that the extent of the strength depression is, on the one hand, directly related to the amount of absorbed water and, on the other hand, also associated with the aging conditions (temperature and time). Based on the same gradients of the isothermal linear regressions, it can be concluded that the effects of water absorption on the strength are identical for all epoxies tested. The higher the water absorption of a system, the higher the strength loss. However, for specimens tested directly after reaching saturation, the impact of the aging temperature is significant. While aging at cold temperatures can lead to a strength loss of up to 9.57 (±0.39) MPa/m%, the impact is only about half as big for aging at 40 °C. This is because relaxation (physical aging) and polymer-water interaction (e.g. hydrogen bonding) co-occur with water absorption and, in contrast to plasticizing, increase the strength. Aging at elevated but sub-Tg temperature significantly accelerates the physical aging processes [5, 6]. As a result, aging in cold water leads almost entirely to a decrease in strength due to plasticization, while aging at elevated temperatures counteracts the strength reduction.

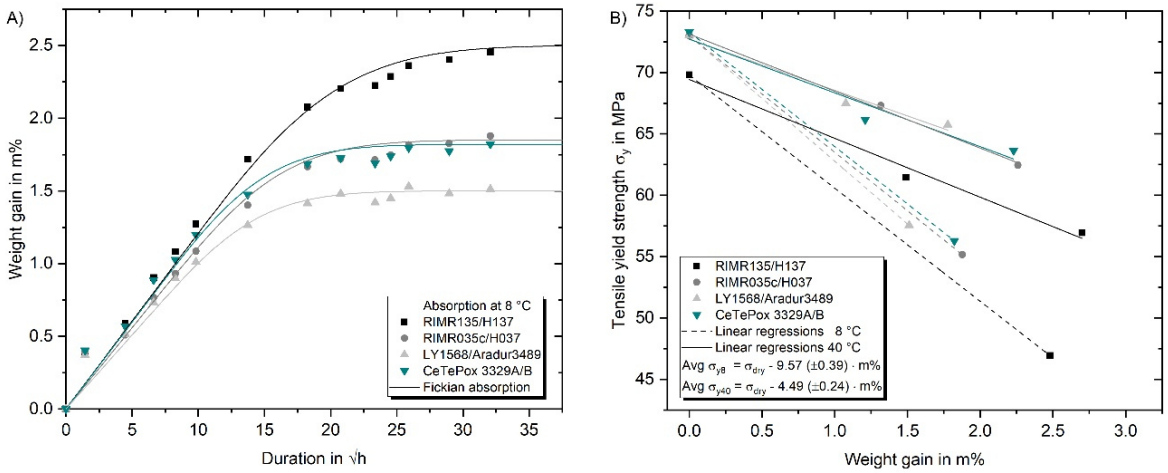

Figure 2. A) Weight gain curves of all neat epoxies for aging in 8 °C water. B) Correlation between tensile yield strength and amount of absorbed water at 8 °C and 40 °C. Tensile tests were performed as soon as saturation was reached.

As a consequence of these results, it can be deduced that the epoxy strength depends on the amount of absorbed water and on the time-temperature history of the environmental conditions. Assuming that the physical aging process and the formation of strong water-polymer bonds follow an Arrhenius like temperature relation, the Kohlrausch-Williams-Watts (KWW) correlation can be used to describe the strength evolution $\sigma_y(t,T)$ as follows [6]:

$$\sigma_y(t,T) = \sigma_0 + \Delta\sigma\,(1 - e^{-\left(\frac{t}{\tau(T)}\right)^{\beta}}), \tag{1}$$

where σ_0 is the plasticized strength without additional aging, $\Delta\sigma$ is the maximum strength change due to physical aging, t is the aging duration, β is a stretching parameter and $\tau(T)$ is the temperature-dependent relaxation time. Taking into account that the epoxies are in an unknown physical aging state after manufacturing, but that the increase of physical aging at cold temperatures is negligible for short durations, σ_0 can be designated based on the strength evolution shown in Figure 2B as:

$$\sigma_0 = \sigma_{dry} - 9.57\,(\pm 0.39) \cdot \mathrm{M}_{\infty}, \tag{2}$$

  doi:10.5075/epfl-298799_978-2-9701614-0-0

with the initial dry strength σ_{dry} and the amount of absorbed water at saturation M_∞. $\Delta\sigma$ can be determined experimentally with aging at elevated but sub-T_g temperatures within a short time. In Figure 3A, the strength evolution is shown exemplarily for the epoxy with the highest water absorption and most significant strength variations (RIMR135/RIMH137) for aging at four different temperatures of up to 6200 hours. The lines represent the KWW model predictions according to the given values of $\tau(T)$ and with constant values of $\beta = 0.5$ and $\Delta\sigma = 18.6$ MPa. The Arrhenius plot of the relaxation time is shown in Figure 3B, revealing an activation energy of 137.8 kJ/mol. This implies that an increase of the aging temperature by 10 K accelerates the aging process by a factor of more than five. Thus, if the strength is predicted for a service temperature of 10 °C using accelerated aging at 50 °C, this corresponds to an acceleration factor of 915. In other words, it also means that the strength achieved after less than eight days in a hot water bath, will take more than 20 years of service use. These enormous accelerations should be critically checked and reconsidered if accelerated aging is used to estimate long-term properties.

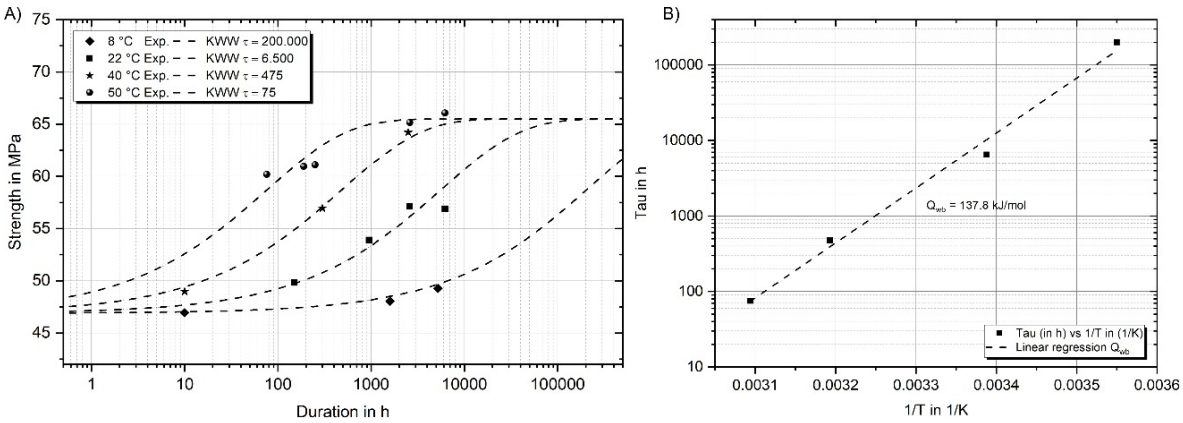

Figure 3. Tensile yield strength development over aging time for aging in water at four different temperatures of the RIMR135/RIMH137 neat epoxy. Kohlrausch-Williams-Watts (KWW) models with respective relaxation times τ are shown with lines.

3.2 Relation between epoxy strength and glass transition temperature

The linear relation between the T_g and the amount of absorbed water is shown in Figure 4A for all investigated epoxies. The plasticizing effect of the water molecules absorbed into the polymer structure decreases the T_g by about 8.4 °C/m% to 9.9 °C/m% and corresponds well with reported values [13]. Accompanying with the change of the T_g, a change of the polymer strength is expected and typically described by the Kambour or Eyring relationship [14]. Therefore, in Figure 4B, the RIMR135/RIMH137 epoxy strength is presented concerning the distance between the testing temperature and the T_g. The expected linear relationship can be verified for dry epoxies tested at various environmental temperatures. But for the wet-aged epoxy, clear deviations can be found. The two main characteristics affecting the strength and the T_g are the aging time and temperature. While the strength increases significantly with long-term aging (indicated by arrows) and elevated aging temperatures as shown in Figure 3 and Figure 4B, the T_g does not to the same extent. For this reason the Eyring prediction can only provide an approximate dimension by estimating wet properties based on tests with dry material. Wet-aging at cold temperatures (without additional physical aging) depresses the strength more than expected and wet-aging at elevated temperatures depresses the strength less than expected.

  doi:10.5075/epfl-298799_978-2-9701614-0-0

As described in more detail in Gibhardt et al. [5], the results show that the epoxy strength is particularly affected by plasticization and physical aging, while the T_g is mainly affected by the plasticization.

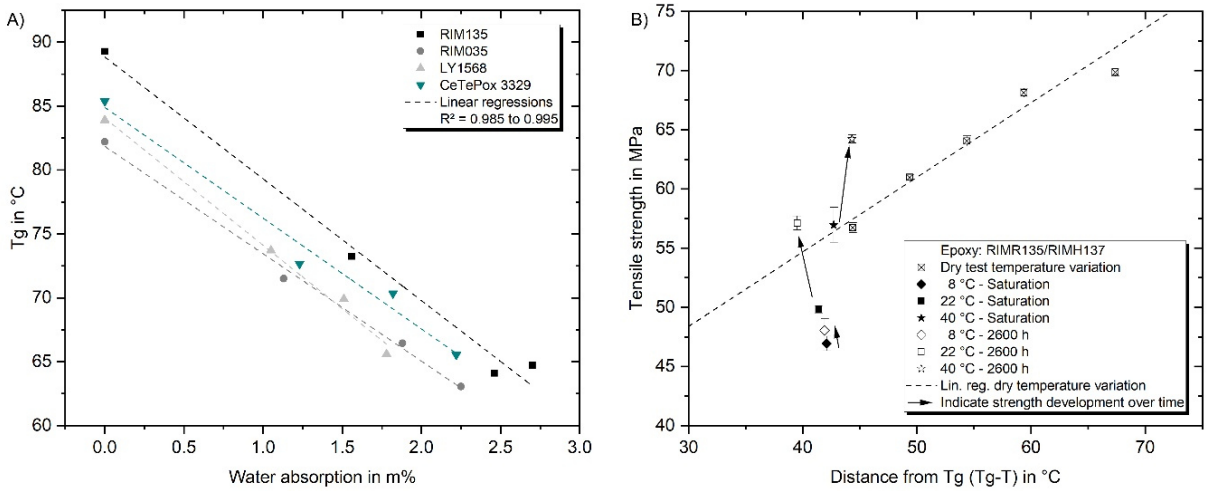

Figure 4. A) Relation between T_g and water absorption for all epoxies after aging in water between 8 °C and 40 °C. B) Tensile strength in relation to the distance between testing temperature and T_g of RIMR135/RIMH137. Line represents Eyring relationship of dry tests.

3.3 Aging history effects on transverse tensile strength of GFRP

Following the studies on epoxies, the question arises of how the aging behavior of the polymers affects the matrix and interphase dominated strength of GFRP composites. Therefore, transverse tensile specimens of four different fiber inputs were likewise aged in water baths at temperatures of 8 °C to 50 °C. The initial absolute transverse tensile strengths and the developments during aging are presented in Figure 5. First, the initial dry strength comparison shows significant differences between the four composites and highlights the importance of good interaction between fiber sizing and epoxy resin. As the dry epoxy strength is considerably higher than the transverse strength, it is reasonable to assume that the interphase strength limits the measured strength. While the SE 2020 and W 2020 composites perform well with an initial strength of about 55.0 MPa, the 25.0 MPa found for the NEG 2002 composites is relatively low.

The long-term wet-aging at different temperatures reveals different resistances to a water-induced reduction of the interphase strengths. When aged in 8 °C cold water (to about half-saturation within 3000 h), all systems' strength reductions are lowest. In fact, the strength of the SE 2020 composite was decreased by only 1.5 MPa (3.0 %), which is even less than 3.0 MPa (5.5 %) of the W 2020 or 4.9 MPa (20.0%) of the NEG 2002 composites. Taking the long-term epoxy strength at saturation at low temperatures into account (< 50 MPa), it is expected that the transverse strength will remain in this range during long-term aging (or service conditions) for the fiber-matrix combinations with the highest interphase strengths (SE 2020 and W 2020). Aging up to saturation at 30 °C, which is still about 30 °C lower than the wet-Tg of the epoxy, leads to a more pronounced strength reduction. While the NEG 2002 composite already loses about 13.0 MPa (53.0 %) and thus only has a minimal residual strength, the loss of all other systems is still moderate with about 6.0 MPa. Even though accelerated aging at 50 °C results in the most severe interphase strength reductions, huge differences arise. In contrast to the NEG

  doi:10.5075/epfl-298799_978-2-9701614-0-0

2002 and ER469L composites, which almost completely lose their integrity, the SE 2020 composite continues strong and has a residual interphase strength of about 48.0 MPa.

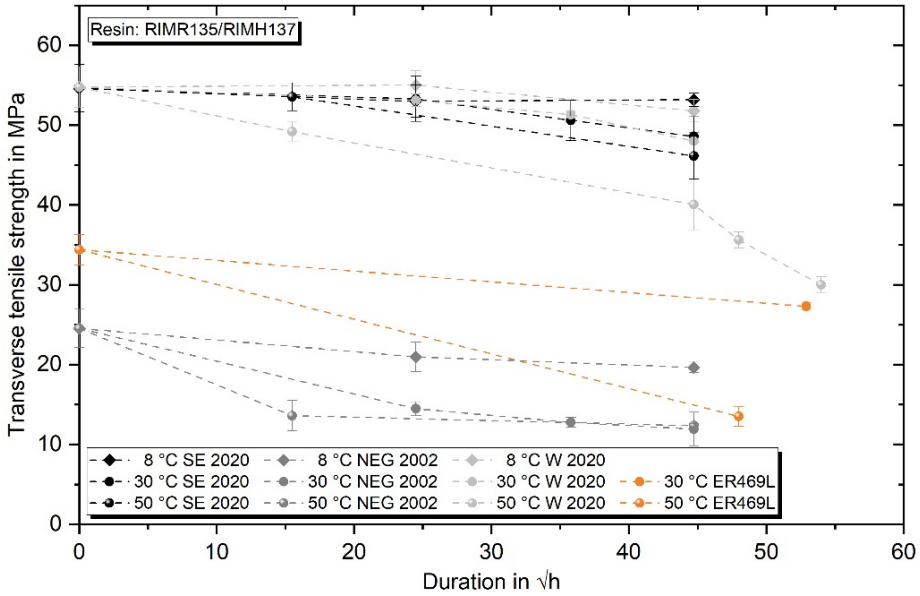

Figure 5. Transverse strength development of four different GFRPs for aging in water bath conditions from 8 °C to 50 °C over a period of up to 3000 h.

4. Conclusions

Long-term aging demonstrated a very similar behavior for all studied epoxies. It could be shown that the plasticizing effect on strength and T_g is primarily dependent on the amount of absorbed water. Based on the results, the KWW relationship for strength development was extended by the water absorption dependent initial strength prediction and verified for a wide temperature range. Overall, the identified changes of the epoxy strength during aging have been shown to have rather negligible effects on the transverse strength of the composites. Here, instead, the sizing-dominated interphase strength is of importance. Sizing and, therefore, interphase related durability differences could be uncovered considering the investigated temperature range. While water-induced plasticization at cold or moderate aging temperatures results in minor impacts in the majority of cases, elevated temperatures often severely affect the interphase integrity. In contrast to the water-polymer interactions increasing the strength by physical aging processes inside the neat epoxies, the interphase region seems not to be subjected to these processes. The complex combination of matrix polymer and various sizing components appears to be significantly more susceptible to water-induced weakening than the neat epoxy. The main reason for this could be an increased water affinity of polar components in the interphase and possible hydrolysis reactions of the silanes at high temperatures as highlighted by Thomason et al. [7]. For GFRP composites with wet-aging resistant interphase, matrix aging plays a more important role. The changes in strength and stiffness, the decrease in T_g and strong changes in elongation at break could affect the lifetime performance significant, especially under fatigue loads. However, this needs to be investigated further in the future.

  doi:10.5075/epfl-298799_978-2-9701614-0-0

5. References

1. Rocha IBCM, Raijmaekers S, Nijssen RPL, van der Meer FP, Sluys LJ. Hygrothermal ageing behaviour of a glass/epoxy composite used in wind turbine blades. Composite Structures. 2017; 174:110–22. doi:10.1016/j.compstruct.2017.04.028.
2. Dawson M, Davies P, Harper P, Wilkinson S. Composite Materials in Tidal Energy Blades. In: Davies P, Rajapakse YDS, editors. Durability of Composites in a Marine Environment 2. Cham: Springer International Publishing; 2018. p. 173–194. doi:10.1007/978-3-319-65145-3_10.
3. Zhou J, Lucas JP. Hygrothermal effects of epoxy resin. Part II: variations of glass transition temperature. Polymer. 1999; 40:5513–22. doi:10.1016/S0032-3861(98)00791-5.
4. Gibhardt D, Doblies A, Meyer L, Fiedler B. Effects of Hygrothermal Ageing on the Interphase, Fatigue, and Mechanical Properties of Glass Fibre Reinforced Epoxy. Fibers. 2019; 7:55. doi:10.3390/fib7060055.
5. Gibhardt D, Buggisch C, Meyer D, Fiedler B. Hygrothermal Aging History of Amine-Epoxy Resins: Effects on Thermo-Mechanical Properties. Frontiers in Materials 2022. doi:10.3389/fmats.2022.826076.
6. Le Guen-Geffroy A, Le Gac P-Y, Habert B, Davies P. Physical ageing of epoxy in a wet environment: Coupling between plasticization and physical ageing. Polymer Degradation and Stability. 2019; 168:108947. doi:10.1016/j.polymdegradstab.2019.108947.
7. Thomason JL. Glass fibre sizing: A review. Composites Part A: Applied Science and Manufacturing. 2019; 127:105619. doi:10.1016/j.compositesa.2019.105619.
8. Krauklis AE, Gagani AI, Echtermeyer AT. Hygrothermal Aging of Amine Epoxy: Reversible Static and Fatigue Properties. Open Engineering. 2018; 8:447–54. doi:10.1515/eng-2018-0050.
9. Bellenger V, Verdu J, Morel E. Structure-properties relationships for densely cross-linked epoxide-amine systems based on epoxide or amine mixtures. J Mater Sci. 1989; 24:63–8. doi:10.1007/BF00660933.
10. Colin X. Nonempirical Kinetic Modeling of Non-fickian Water Absorption Induced by a Chemical Reaction in Epoxy-Amine Networks. In: Davies P, Rajapakse YDS, editors. Durability of Composites in a Marine Environment 2. Cham: Springer International Publishing; 2018. p. 1–18. doi:10.1007/978-3-319-65145-3_1.
11. Gagani AI, Krauklis AE, Echtermeyer AT. Orthotropic fluid diffusion in composite marine structures. Experimental procedure, analytical and numerical modelling of plates, rods and pipes. Composites Part A: Applied Science and Manufacturing. 2018; 115:196–205. doi:10.1016/j.compositesa.2018.09.026.
12. Elkebir Y, Mallarino S, Trinh D, Touzain S. Effect of physical ageing onto the water uptake in epoxy coatings. Electrochimica Acta. 2020; 337:135766. doi:10.1016/j.electacta.2020.135766.
13. Fernández-García M, Chiang MYM. Effect of hygrothermal aging history on sorption process, swelling, and glass transition temperature in a particle-filled epoxy-based adhesive. J. Appl. Polym. Sci. 2002; 84:1581–91. doi:10.1002/app.10447.
14. Le Gac P-Y, Arhant M, Le Gall M, Davies P. Yield stress changes induced by water in polyamide 6: Characterization and modeling. Polymer Degradation and Stability. 2017; 137:272–80. doi:10.1016/j.polymdegradstab.2017.02.003.

EVALUATING THE SUSTAINABILITY OF LIGHTWEIGHT DRONES FOR DELIVERY: TOWARDS A SUITABLE METHODOLOGY FOR ASSESSMENT

Sinéad Mitchell[a,b,e], Juliana Steinbach[a,e], Tomas Flanagan[c], Pouyan Ghabezi[a,e], Noel Harrison[a,b,e], Simon O'Reilly[d], Stephen Killian[d], William Finnegan[a,e]

a: Mechanical Engineering, School of Engineering, College of Science and Engineering, NUI Galway, Ireland sinead.mitchell@nuigalway.ie
b: I-Form, the SFI Research Centre for Advanced Manufacturing, Ireland
c: Engineering Department, ÉireComposites Teo, Inverin, Co. Galway, Ireland
d: Manna Drone Delivery Ltd, NovaUCD, UCD, Belfield Innovation Park, Dublin, Ireland
e: Ryan Institute for Environmental, Marine and Energy Research, NUI Galway, Ireland

Abstract: *Drone technology is widely available and is rapidly becoming a crucial instrument in the functions of businesses and government agencies worldwide. The demand for delivery services is accelerating particularly since the Covid-19 pandemic. Both companies and customers want these services to be efficient, timely, safe, and sustainable, but these are major challenges. Last-mile delivery by lightweight short-range drones has the potential to address these challenges. However, there is a lack of consistency and transparency in assessing and reporting the sustainability of last-mile delivery services and drones. This paper presents a critical review of published assessments (specifically lifecycle assessment and circularity). The study reveals a lack of comprehensive studies, and a need to examine composite and battery manufacturing developments and provides key considerations for future study development.*

Keywords: Drone delivery; LCA; circularity; sustainability; composite.

1. Introduction

The transport sector is responsible for 25% of net anthropogenic GHG emissions in the EU (1) and 15% globally (2). The EU Green Deal aims for a 90% reduction in emissions from transport by 2050 (3). In Ireland the transport sector is the fastest-growing source of emissions, increasing by 100% since 1990, representing 18% of GHG emissions and 90% attributed to road transport (4). Ireland's climate action plan aims to reduce emissions by 42-50% to transport modes with lower energy consumption (5).

Unmanned Aerial Vehicles (UAVs), or drones, are a relatively new transport technology, and a growing number of delivery services are expected to enter the market (6). Drones for delivery could displace some road-dominated delivery modes (mainly cars and vans) and in turn, contribute to emission reduction targets. However, the technology is in its infancy and there is a dearth of knowledge on environmental impacts. New disruptive technologies should consider sustainability aspects for future scenarios as companies plan to scale the production and use of drones (7). Future designs should align with the European Green Deal for industry (8) and the EU Circular Economy Action Plan (CEAP) (9). Composite materials play a key part in reducing the weight of aerospace materials, which in turn help to reduce fuel, energy, and emissions. However, most composites are not widely recycled or designed with sustainability considerations.

This paper explores the sparse but growing body of research in understanding the sustainability of lightweight drones and drone delivery services. There is currently no agreed best practice

  doi:10.5075/epfl-298799_978-2-9701614-0-0

methodology and there has been little scrutiny of the parts production and composite material contribution to date.

2. Methodology

This paper seeks to synthesise emerging studies on the sustainability assessments of drone technologies, including the drone itself (as a product) and the delivery service a drone provides (as a product system). The study involved a review of the select body of literature, as a full systematic review was deemed unfitting because there are very few targeted studies. A critical analysis of the literature will describe the main findings with the main focus on methodological approaches. This research wishes to answer two research questions:

- RQ1. What can the emerging literature on the sustainability assessments of drone technologies tell us about established methodological approaches?
- RQ2. How should drone products and services be assessed for their sustainability impacts and what are the key considerations?

These questions guided the research strategy and focus on the collection, screening, and synthesis. The inclusion criteria for the literature were *peer-reviewed journal and conference articles in the English language with a focus on sustainability assessments of drones and drone delivery*. The analysis incorporated a similar analysis to Webster and Watson's "concept matrix" (10) to record variations in previous sustainability assessments. This involved an analysis of past LCAs conducted, comparing vehicle and type, system boundary, functional unit, drone payload, delivery criteria, and parts production input. Furthermore, industry partners on the MiDrone project were consulted about inputs and primary data collection.

3. Assessing the sustainability of drones, delivery systems, and composites

2.1 Life Cycle Assessment to assess the sustainability of drones

Life Cycle Assessment (LCA) is an analytical tool to measure and compare the environmental impacts of a product, process, system, or service. LCAs are used for decision-making for designers, manufacturers, researchers, and policymakers. The outputs can identify impact hotspots and have the potential to make robust comparisons between different scenarios (11). LCA studies examine emissions along life cycles or phases: from the extraction of raw materials, transportation, materials processing, manufacturing, distribution, product use, and disposal or recycling at the end of life (EoL) (12) (see Figure 1). LCA studies can be carried out on the entire life cycle such as a cradle-to-grave or a cradle-to-cradle study. Otherwise, LCA studies examine part of a life cycle such as a cradle-to-gate, a gate-to-gate, or a gate-to-grave.

An LCA consists of four iterative phases beginning at the goal definition and scope, followed by Life Cycle Inventory Analysis (LCI), Impact assessment, and interpretation (13). To define the goal and scope of a product (such as a drone) all the phases in Figure 1 should be considered (13). For a drone delivery service study, it is necessary to understand the operational model of the delivery business and a systems perspective is important. Drone delivery services are operated by businesses that are complex and dynamic. A systems approach can capture important interactions and feedback (14). Furthermore, the functional unit (e.g. a drone or a fleet of drones) employed in any LCA must align with the goal and scope for suitable comparisons (13).

  doi:10.5075/epfl-298799_978-2-9701614-0-0

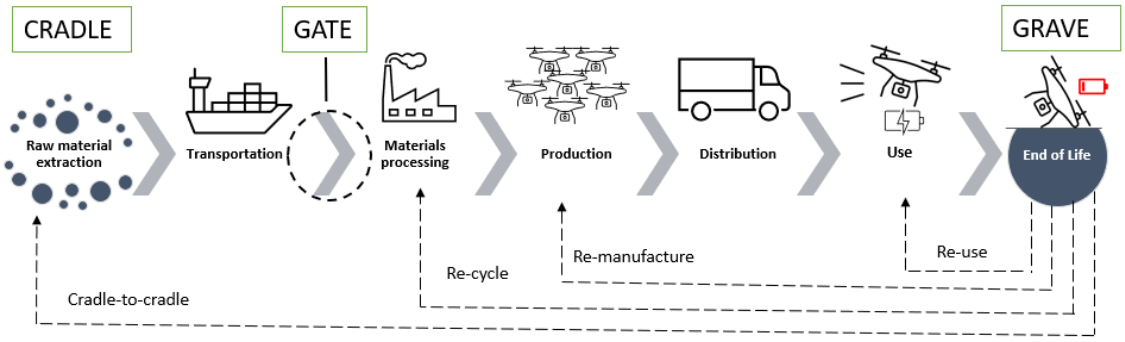

Figure 1: Phases in LCA of a drone to measure impact from raw material extraction to end of life. LCA studies can be conducted from cradle-to-cradle, cradle-to-grave, cradle-to-gate, gate-to-gate, and gate-to-grave depending on the goal and scope of the study.

The most critical phase of a robust LCA study is the Life Cycle inventory (LCI) analysis. Data is collected by retrieving primary evidence from companies and/or using established databases (15) that are continuously updated to reflect evolving realities (15). A lack of established data on recycling processes has made conducting comparative LCAs difficult when determining favourable scenarios (16). There is a lack of quantitative, transparent models for handling aircraft and drones at the end of life (17). The composite materials often end up in landfills, which has led to batteries being a major focus of drone LCAs to date (18). However, carbon fibre production represents an important aspect of LCA impact categories (such as human toxicity, freshwater aquatic ecotoxicity, marine aquatic ecotoxicity, and terrestrial ecotoxicity) (19), hence more research is needed in this area.

3.2 Drones, composite materials, and circularity

Government policies and action plans for a circular economy (CE) are driving change in the dominant model of the take-make-waste linear economy. CE offers a framework to improve the sustainability of drones by designing out waste and pollution in all phases, making more durable products to extend the use phase. A CE model can focus attention on designing products for repair, reuse, and remanufacturing as a priority before the consideration of recycling.

Aircraft contain large volumes of fibre-reinforced composites and are mostly landfilled when they are retired (20). The impact can depend on manufacturing processes, additives, the carbon intensity of the grid, recycling (and displacing virgin production), and EoL treatment methods (16). Composite materials for aircraft are highly challenging in the recovery and recycling phases (21). Pyrolysis recovery of carbon or glass fibres is positive, as it consumes only 5-10 % of the energy required to produce real carbon or glass fibre (22). However, while composites recycling can reduce impacts, it is often not economically viable (16) outside of non-structural light-weighting applications that do not demand high levels of purity and feedstock quality (16,23).

4. Discussion on selected LCA studies of UAV v Ground vehicles

The most comprehensive LCA studies were selected and critically analysed. Table 1 summarises the matrix of concepts and considerations used to make a UAV v ground vehicle comparative analysis. There was a general lack of transparency in the data, however, several important considerations were identified.

  doi:10.5075/epfl-298799_978-2-9701614-0-0

Table 1: LCA concept matrix of studies on drones and drone delivery systems

Delivery criteria	System boundary	Functional unit	Used vehicle and type	Drone payload	Parts production input	Ref.
One-to-many	Cradle to gate	Transportation of a payload within a 5-mile radius delivering 300 packages per day for two years	Multirotor UAV, Fixed-wing UAV, Truck	1kg	Multirotor frame, Battery, Charger, Motor, PCB, Transmitter, Optical Sensor	Neuberger (2017) (24)
One-to-one + One-to-many	Cradle to grave: production, operation, disposal	1 package delivered	Multirotor UAV, electrical tricycle, and diesel van	5.0kg	Battery Vehicle	Figliozzi (2017) (25)
One-to-one + One-to-many	Gate to gate + battery manufacturing for drone and electric vehicle + warehouse emissions	1 package delivered	4 multirotor UAV, 8 multirotor UAV, Personal electric vehicle, Personal car, Gasoline delivery van, Electric truck, Gasoline helicopter drone, Diesel truck, Natural gas truck	0.5 and 8,1kg	Battery	Stolaroff et. al. (2018) (18)
One-to-one	Gate to gate	1 pizza delivered	Multirotor UAV Motorcycle Electric Motorcycle	-	Out of System boundary	Park et. al. (2018) (26)
One-to-one	Cradle to gate	1 package delivered per km; Lifespan: 5000h	Multirotor UAV	5kg	Frame, Servo motor, Cargo box, Propeller, Electronic speed control Batteries	Koiwanit (2018) (19)
One-to-many	Gate to gate	Delivery of parcels to recipient addresses in circular service zones	Multirotor UAV Truck	-	Out of System boundary	Goodchild and Toy (2018) (9)
One-to-one	Cradle to grave	Number of deliveries made by a fleet of 10 UAV in 2 years	Multirotor UAV BEV ICE	20.4kg	Electricals, Plastic parts, Metal parts, PCB, Battery, Corrugated cardboard	Yowtak et. al. (2020) (28)

  doi:10.5075/epfl-298799_978-2-9701614-0-0

4.1 One-to-one v one-to-many considerations

To compete with ground vehicles, a drone delivery company need fleets of drones, not single units (28) which can cause difficulty comparing LCA scenarios. *One-to-one* delivery services are the most common model for food delivery, which is directed by a customer wanting an order within a short time (26). Ground vehicles for *one-to-one* delivery services are based on their low load capacity, therefore, motorcycles and cargo bikes are an ideal mode, followed by private cars (29). Stolaroff et al's (2018) *one-to-one* scenario simulated a same-day goods delivery system. The model represents the delivery embedded in a distribution logistics system and incorporates a drone hub (17). Park et al. compared the use phase in a *one-to-one* scenario of drone delivery and a motorcycle (26). A *one-to-many* service mainly depends on the ground vehicle load capacity and is not usually delivering ready-to-eat food.

4.2 Functional unit considerations

The functional unit has major consequences for the LCA inputs, and there is currently no consistency across key studies. In a *one-to-one* scenario for drones, there is a sequence of depot-costumer-depot. However, since UAV flight depends on a fully charged battery to operate one round trip (30), it is necessary to evaluate the number of batteries the system will require to operate. A well-maintained battery can hold 1000 recharge cycles (31). The battery lifespan can add more complexity to a drone's life cycle (25), as more than one drone would have to be included in the system to operate successfully (19).

Park et al. modelled their study on a pizza delivery as the functional unit (26), which is most similar to Figliozzi et al, who used a package delivered (weighing 5kg) to determine the relative energy efficiency of UAVs. However, Figliozzi et al examined both *one-to-one* and *one-to-many* models (25). Goodchild and Toy's study was based on the electricity for the batteries to receive 1W-hour (Wh) of charge (9). Yowtak e. al's functional unit was based on the drone's life span, 2 years, carrying 20.4 kg, and worked with a fleet of 10 drones to achieve an equivalent number of deliveries made by a Battery Electrical Vehicle (BEV) without having to recharge (28). Koiwanit estimated the impacts of a drone delivering a 5 kg package per kilometre with a lifespan of 5000 hours equivalent to 250,000 km (19). Neuberger presented the most comprehensive functional unit for a *one-to-many* delivery system and adapted the functional unit to a time frame of 2 years (drone's lifespan) (24).

4.3 Temporal dimension considerations

The inclusion of temporal dimension has been an uncommon practice in LCA (32). Neglecting timing in the analysis can influence outcomes and is related to the functional unit. Varying from one delivery being performed to one day of deliveries, to deliveries made under the drone's life span and finally, the deliveries made under a motorcycle/truck lifespan can differ significantly in terms of materials input that a poor decision at an early stage of the analysis can potentially lead to bogus outcomes.

While each of these studies contributes to the growing literature, providing their particular inputs and framework, the multiplicity of approaches taken creates difficulties when comparing different assessments to assess the suitability of each. LCA is very much a user-specific evaluation making a comparison of LCAs on similar topics (like last-mile delivery) complex and regularly impractical (33).

  doi:10.5075/epfl-298799_978-2-9701614-0-0

5. Conclusion

The study has revealed a lack of reliable data in past LCA studies, including a lack of robust data regarding parts production and end-of-life phases. None of the studies examined parts production in detail and considerations of composites were absent. However, the literature examined has revealed key relationships and dependencies established between the functional unit, the time frame of operation, and the operational model. For this reason, a functional unit suitable for a generic case study should include the transportation of cargo, payload mass, distance covered by the delivery, number of deliveries, and period, which aligns mostly with the Neuberger study (24). The attention to the particularities associated with the different business models is a key element to establish a fair comparison between UAVs and ground vehicle deliveries. The industry input from MiDrone has revealed the importance of understanding the operations in the manufacture and operation of drones when planning an LCA study. For example, the emissions related to composite manufacturing of airframes may vary considerably by manufacturing facility, such as energy use and waste production.

Key considerations for future studies are; (1) ensure models are like-for-like comparisons by choosing an appropriate functional unit; (2) start with simple studies such as gate-to-gate and build from there; (3) keep up to date with emerging technologies in manufacturing, battery, and composite developments; (4) consider the temporal dimension; (5) use primary data for accuracy; (6) for a systems approach ensure the delivery operations are well understood, observations of operations are recommended, and (7) develop new studies to examine circularity to overcome LCA limitations.

Acknowledgments: This work is funded by the Department of Business, Enterprise, and Innovation and administered by Enterprise Ireland under the Disruptive Technologies Innovation Fund, MI-DRONE Project (Contract Ref: DT 2020 0221). The authors would like to acknowledge the support from Science Foundation Ireland (SFI), through the MaREI Research Centre for Energy, Climate and Marine (Grant no. 12/RC/2302_2) and the I-Form Advanced Manufacturing Research Centre (Grant no. 16/RC/3872).

Author contributions: SM conceptualisation, study design, methodology, data collection, analysis, writing, supervision. JS. Conceptualisation, data collection, analysis, writing. TF Industry lead on composite manufacturing and input on process data. NH & PG input on composite materials and manufacturing. SO'R & SK Industry input on lightweight drone design and operation. NH, PG WF review and edit. WF MI-DRONE Project Management.

References

1. European Commission. Transport and the Green Deal | European Commission [Internet]. Transport and the Green Deal. 2022 [cited 2022 Apr 28]. Available from: https://ec.europa.eu/info/strategy/priorities-2019-2024/european-green-deal/transport-and-green-deal_en
2. IPCC. Climate Change 2022: Mitigation of Climate Change [Internet]. Climate Change 2022 Mitigation of Climate Change Summary for Policymakers. 2022 [cited 2022 Apr 28]. Available from: https://www.ipcc.ch/report/ar6/wg3/
3. European Commission. Sustainable & Smart Mobility Strategy. Brussels; 2020 Dec.

  doi:10.5075/epfl-298799_978-2-9701614-0-0

4. EPA. Transport | Environmental Protection Agency [Internet]. 2020 [cited 2022 Apr 28]. Available from: https://www.epa.ie/our-services/monitoring--assessment/climate-change/ghg/transport/
5. Department of the Environment C and C. Climate Action Plan 2021 [Internet]. Dublin; 2022 Apr [cited 2022 Apr 28]. Available from: https://www.gov.ie/en/publication/6223e-climate-action-plan-2021/
6. Gupta A, Afrin T, Scully E, Yodo N. Advances of UAVs toward Future Transportation: The State-of-the-Art, Challenges, and Opportunities. Future Transportation. 2021 Sep 1;1(2):326–50.
7. Heutger M, Kückelhaus M. Unmanned Aerial Vehicles in Logistics/ A DHL perspective on implications and use cases for the log. Troisdorf; 2020.
8. European Commission. A New Industrial Strategy for Europe [Internet]. Brussels; 2020 Mar [cited 2022 May 5]. Available from: https://eur-lex.europa.eu/legal-content/IT/TXT/?qid=1593086905382&uri=CELEX%3A52020DC0102
9. European Commission. A new Circular Economy Action Plan [Internet]. 2020 [cited 2021 Apr 2]. Available from: https://www.un.org/sustainabledevelopment/sustainable-consumption-production/
10. Webster J, Watson RT. Analyzing the Past to Prepare for the Future: Writing a Literature Review on JSTOR. MIS Quarterly [Internet]. 2002 Jun [cited 2022 May 3];26(2):xiii–xxiii. Available from: https://www-jstor-org.nuigalway.idm.oclc.org/stable/4132319?seq=1
11. Hellweg S, Canals LMI. Emerging approaches, challenges, and opportunities in life cycle assessment. Science (1979) [Internet]. 2014 Jun 6 [cited 2022 May 3];344(6188):1109–13. Available from: https://www-science-org.nuigalway.idm.oclc.org/doi/full/10.1126/science.1248361
12. Calisir D, Ekici S, Midilli A, Hikmet Karakoc T. A review on environmental impacts from the aviation sector in terms of life cycle assessment. Vol. 22, Int. J. Global Warming. 2020.
13. ISO. ISO 14040-2006. ISO 14040-2006 Environmental management — Life cycle assessment — Principles and framework. 2020.
14. Maani Kambiz, Cavana RY. Systems thinking, system dynamics : managing change and complexity. 2007;278.
15. Crawford RH, Bontinck PA, Stephan A, Wiedmann T, Yu M. Hybrid life cycle inventory methods – A review. Vol. 172, Journal of Cleaner Production. Elsevier Ltd; 2018. p. 1273–88.
16. Meng F, Olivetti EA, Zhao Y, Chang JC, Pickering SJ, McKechnie J. Comparing Life Cycle Energy and Global Warming Potential of Carbon Fiber Composite Recycling Technologies and Waste Management Options. ACS Sustainable Chemistry and Engineering. 2018 Aug 6;6(8):9854–65.
17. Ribeiro JS, de Oliveira Gomes J. Proposed framework for end-of-life aircraft recycling. In: Procedia CIRP. Elsevier B.V.; 2015. p. 311–6.
18. Stolaroff JK, Samaras C, O'Neill ER, Lubers A, Mitchell AS, Ceperley D. Energy use and life cycle greenhouse gas emissions of drones for commercial package delivery. Nature Communications. 2018 Dec 1;9(1).
19. Koiwanit J. Analysis of environmental impacts of drone delivery on an online shopping system. Advances in Climate Change Research. 2018 Sep 1;9(3):201–7.

  doi:10.5075/epfl-298799_978-2-9701614-0-0

20. Onwudili JA, Miskolczi N, Nagy T, Lipóczi G. Recovery of glass fibre and carbon fibres from reinforced thermosets by batch pyrolysis and investigation of fibre re-using as reinforcement in LDPE matrix. Composites Part B: Engineering. 2016 Apr 15;91:154–61.
21. Maaß S, Scholz ID. Project Aircraft Recycling-A Literature Review. 2020; Available from: https://doi.org/10.15488/11549
22. Kireitseu M. Environmental Strategies for Sustainable Manufacturing Process of Composites. In: IOP Conference Series: Materials Science and Engineering. Institute of Physics Publishing; 2017.
23. Deviatkin I, Grönman K. Carbon Footprint of Waste-Derived Composites. In: Encyclopedia of Materials: Composites. Elsevier; 2021. p. 245–51.
24. Neuberger B. An Exploration of Commercial Unmanned Aerial Vehicles (UAVs) An Exploration of Commercial Unmanned Aerial Vehicles (UAVs) Through Life Cycle Assessments [Internet]. Available from: https://scholarworks.rit.edu/theses
25. Figliozzi MA. Lifecycle modelling and assessment of unmanned aerial vehicles (Drones) CO2e emissions. Transportation Research Part D: Transport and Environment. 2017 Dec 1;57:251–61.
26. Park J, Kim S, Suh K. A comparative analysis of the environmental benefits of drone-based delivery services in urban and rural areas. Sustainability (Switzerland). 2018 Mar 20;10(3).
27. Goodchild A, Toy J. Delivery by drone: An evaluation of unmanned aerial vehicle technology in reducing CO2 emissions in the delivery service industry. Transportation Research Part D: Transport and Environment. 2018 Jun 1;61:58–67.
28. Yowtak K, Imiola J, Andrews M, Cardillo K, Skerlos S. Comparative life cycle assessment of unmanned aerial vehicles, internal combustion engine vehicles and battery electric vehicles for grocery delivery. In: Procedia CIRP. Elsevier B.V.; 2020. p. 244–50.
29. Corporate Partnership Board CPB How Urban Delivery Vehicles can Boost Electric Mobility Decarbonising Transport [Internet]. Available from: www.itf-oecd.org
30. Gupta A, Afrin T, Scully E, Yodo N. Advances of UAVs toward Future Transportation: The State-of-the-Art, Challenges, and Opportunities. Future Transportation. 2021 Sep 1;1(2):326–50.
31. Peters JF, Baumann M, Zimmermann B, Braun J, Weil M. The environmental impact of Li-Ion batteries and the role of key parameters – A review. Vol. 67, Renewable and Sustainable Energy Reviews. Elsevier Ltd; 2017. p. 491–506.
32. Lueddeckens S, Saling P, Guenther E. Temporal issues in life cycle assessment—a systematic review. Vol. 25, International Journal of Life Cycle Assessment. Springer; 2020. p. 1385–401.
33. Tapper RJ, Longana ML, Norton A, Potter KD, Hamerton I. An evaluation of life cycle assessment and its application to the closed-loop recycling of carbon fibre reinforced polymers. Vol. 184, Composites Part B: Engineering. Elsevier Ltd; 2020.

  doi:10.5075/epfl-298799_978-2-9701614-0-0

STATIC AND FATIGUE BEHAVIOR OF FLAX/EPOXY COMPOSITE: IMPACT OF THE PROCESS OF MANUFACTURING

F. Batouche[a], M.F. Ameur[a], R. Zitoune[ab], L. Toubal[c] , M.H. Saihi[a], A. Djabali[c]

a: Laboratoire des Technologies Innovantes, Ecole Nationale Supérieure de Technologie d'Alger, Algeria – faycalameur@gmail.com , f_batouche@enst.dz

b: Institut Clément Ader, UMR CNRS 5312, University of Toulouse, Toulouse, France.

c: Centre de Recherche sur les Matériaux Lignocellulosiques, Université du Québec à Trois-Rivières, Trois-Rivières, QC, Canada.

Abstract: *The aim of this study is to investigate the defects generated by different machining processes (conventional machining, abrasive water jet machining) and their impact on the mechanical behavior of composite materials made of flax/epoxy in static and fatigue tests under flexural loads. A 3D Finite Elements Method model is proposed to predict the ultimate deflection as well as the damage distribution in the composite. The validation of this model is conducted by performing three points bending tests. The obtained results have shown that, the flax/epoxy laminates have a linear behavior in the beginning of the loading then a nonlinear behavior until failure. In addition, the cartographies of the damage predicted by the model using Hashin criteria reveal that, Damage has occurred first in at tensile part of the laminate due the matrix cracking and fibers breakage and then smooth fracture in the compressed one.*

Keywords: *Abrasive water jet machining; Conventional machining; Fatigue behavior; Damages; Natural fiber reinforced composites.*

1. Introduction

Natural fiber composites are currently very popular in the field of engineering, due to their excellent mechanical and physical properties and low manufacturing costs unlike the most used synthetic fibers (carbon fiber, glass, Kevlar) [1]. However, natural FRP (NFRP) composite materials are in their nascent stages of development which includes addressing challenges in manufacturing and machining.

In industry, composite parts are usually fabricated to near net shape. However, after demolding, to obtain the required geometrical tolerances necessary for assembly, trimming is the first machining operation performed on composite structures. Two most commonly processes are used for trimming to obtain the final shape, namely: conventional machining by cutting tool, and nonconventional machining by abrasive water jet [2,3].

However, the composite materials are inhomogeneous and anisotropic because these materials are a combination of minimum two different phases. These properties make the machinability of composite materials very complex. Indeed, the physics of material removal in composite materials are accompanied by several defects. In addition, the nature and magnitude of these defects are strongly influenced by the process of machining used [2]. In fact, during conventional trimming, the defects occurring along the free edges of the machined surface are delamination, burrs and uncut fibers, while the defects appearing on the machined

  doi:10.5075/epfl-298799_978-2-9701614-0-0

surface are thermal and mechanical matrix degradation as well as craters, and fibers pull-out [3,4]. When the abrasive water jet process is used, defects such as craters on the machined surface, striations on the exit of the water jet and abrasive particles embedded between the layers are generated [5,6]. Moreover, the occurrence of machining damage has an impact on the mechanical behavior of the machined composite structures.

If we refer to the literature, most of studies correlate the surface quality of the machined structures with the mechanical properties. In addition, the machined surface quality is characterized by the surface roughness criteria (Ra, Rz). However, the use of surface roughness to characterize machining quality and define her relationship with mechanical behavior in composite materials is ambiguous [4,7]. This led many researchers to find new criteria for characterizing the quality of machined surfaces.

Many studies have shown that when the quality of machined surface is quantified in terms of machining induced defects an effective correlation between machining quality and mechanical behavior is obtained.

Recent study by Nguyen-Dinh et al. [3] has proposed new criterion namely crater volume (Cv) and depth of damage (D) to quantify the damages under machined surface when trimming of CFRP specimens and correlating them to compressive strength. The obtained results have shown clearly that the (Cv) and the (D) criteria are more representative of the machining quality compared to the surface roughness criteria. Hence, extensive study on the nature of the machining defects and their multi-scale characterization is necessary for reliable prediction of mechanical behavior.

The main focus of this paper is to investigate the defects generated by different machining processes (namely conventional machining, abrasive water jet machining) and their impact on the mechanical behavior of composite materials made of flax/epoxy in static and fatigue tests under flexural loads.

2. Experimental procedure

2.1 Material preparation

The flax/epoxy prepreg used in this study was supplied from LINEO, Belgium. The prepreg is a unidirectional (UD) flax fiber prepared by a patented sizing and drying process (US Patent NO. 8080288) and impregnated with partially cured epoxy resin system (Huntsman LY5150). The flax/epoxy prepreg has an area density of 180 g/m² and contains 50% weight content of epoxy. 32 layers of prepregs corresponding to the dimension of 300 mm X 300 mm were stacked together to create plates with a thickness of 8.32 mm and a stacking sequence of $[90/45/0/-45]_{4s}$. Compression molding process was used to manufacture flax/epoxy laminates using an automatic hydraulic press. The cure cycle for these laminates was carried out at 150 °C for 60 min during which the pressure maintained at 4 bars and the expected glass transition temperature (Tg) was 139 °C to 147 °C.

2.2 Bending tests

Three points bending testing is done to understand the Flexural Stress, and Flexural Strain of flax/epoxy material. The composite specimens were prepared using abrasive water jet (AWJ) cutting. It can be noticed that specimens were prepared according to the ASTM D 790

  doi:10.5075/epfl-298799_978-2-9701614-0-0

standard. The recommended dimensions for the bending test of each specimen are 162 mm X 16 mm X 8.32 mm and a span of 133 mm. The bending test machine used to carry out the three-point bending test is shown in figure 1, with a 50 kN load cell and a testing speed of 2 mm/min. Each sample was loaded until failure and the average of three samples is reported.

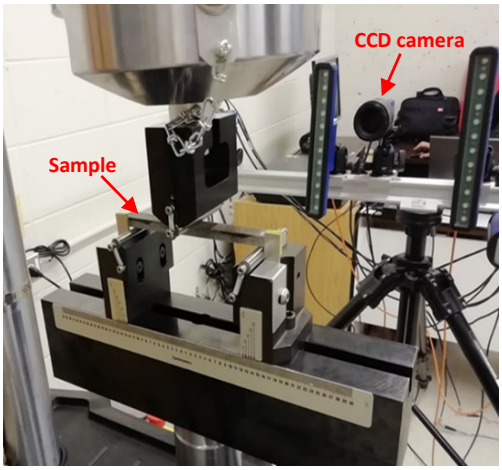

Figure 1. Experimental setup for bending test

2.3 Fatigue tests

The failure evolution of the specimens under fatigue loading was investigated by conducting X-ray computed tomography analysis on specimens subjected to 10,000 sinusoidal cycles of bending-bending loads. Four different displacement amplitudes equal to 15%, 25%, 35% and 45% of maximum mid-span quasi-static deflection. The device used in this work was an infrared camera with a spectral response covering the range from 3 to 5 µm (FLIR Ax5 from the FLIR Systems company). The detector spatial resolution was 320 × 256 pixels and the temperature sensitivity could reach to less than 50 mk. The IR camera was also utilized to measure the variation of the test specimen surface temperature in-situ and in real time.

3. Numerical model

Three-dimensional finite element models were developed in Abaqus following the dimensions and the composite layup of test samples. In this FE modelling the plate were exposed to three points bending test configuration, with main objective to compare this study with the experimental one and see where the failure takes place and how far the plate's deflection can get and also to visualize the longitudinal strain variation curve along the thickness of the plate.

3.1 Mesh and Boundary conditions

The FE model was similar to the experimental test by adding cylindrical rollers, a static displacement was applied in the middle of the sample (above the loading roller) and the two support rollers was fixed.

The workpiece was modelled as continuum shell using linear hexahedral element type SC8R. This element is an 8-node quadrilateral in-plane general-purpose continuum shell, reduced integration with hourglass control, finite membrane strains. Each two ply of the workpiece is modeled by one mesh element (16 elements through plate's thickness) and with a number of

  doi:10.5075/epfl-298799_978-2-9701614-0-0

elements about 64640 elements. The rollers were modelled as rigid elements. The mesh and the boundary conditions used in this model are represented in the Figure 2.

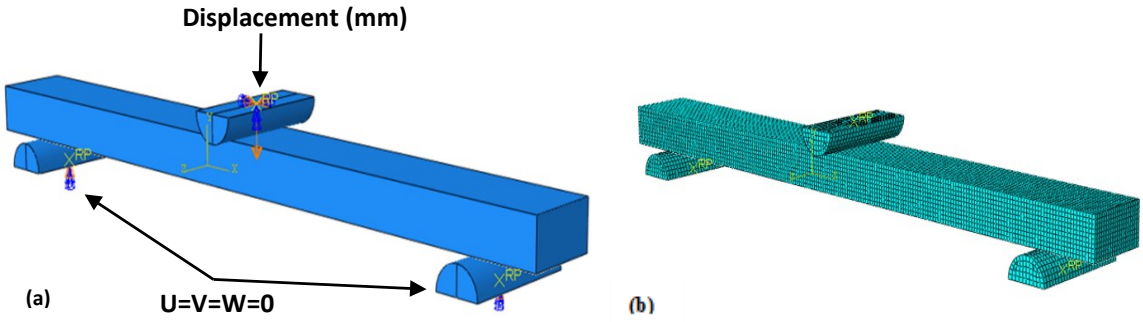

Figure 2. Numerical model proposed. With: (a) geometry and the boundary conditions, (b): mesh characteristic.

3.2 Material and damage modeling

The material parameters used to simulate the behavior of the unidirectional flax-epoxy laminated composite which considered as an orthotropic material are listed in Table 1.

Table 1: Mechanical properties of the flax/epoxy unidirectional ply [8].

E_1(Gpa)	E_2(Gpa)	E_3(Gpa)	G_{12}(Gpa)	G_{13}(Gpa)	G_{23}(Gpa)	v_{12}	v_{13}	v_{23}
17	5.6	5.6	1.5	1.5	1.5	0.36	0.36	0.06

In a lamina, the failure theories are based on the stresses in the material or local axes because a lamina is orthotropic and its properties are different at different angles, unlike an isotropic material.

In the case of a unidirectional lamina, there are two material axes: one parallel to the fibers and one perpendicular to the fibers. Thus, there are four normal strength parameters for a unidirectional lamina, one for tension and one for compression, in each of the two material axes directions. The fifth strength parameter is the shear strength of a unidirectional lamina.

the Hashin damage initiation criterion used in the present work takes into account four possible failure modes: (i) fiber tensile failure, (ii) fiber compression failure, (iii) matrix tensile failure and (iv) matrix compression failure [9].

The parameters of Hashin's damage for the FFRP are shown in Table 2.

Table 2: Hashin damage of the flax/epoxy [8].

X_t(Mpa)	X_c(Mpa)	Y_t(Mpa)	Y_C (Mpa)	S_{12} (Mpa)	S_{13} (Mpa)	S_{23} (Mpa)
287	127	34	80	21	21	21

4. Results and discussion

The representative stress versus strain behaviors for all the studied samples are shown in Figure 3. All specimens exhibit a non-linear behavior. The flexural modulus was determined in the strain interval 0-0.005. In all specimens, failure occurred inside the fiber bundles between fiber–fiber interfaces along the tensile surfaces in followed by progressive delamination and buckling of flax plies.

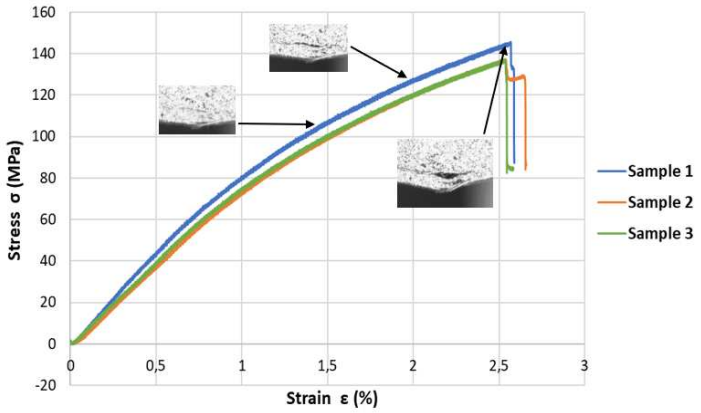

Figure 3. Flexural stress versus strain curve

Figure 4 shows the force vs. displacement curve of the three specimens and a comparison between the experiments and the numerical model. The ultimate deflection is about 9 mm and the maximum loading force equals 800±40 N.

It can be seen that the curve force-displacement of the numerical model fits very well with the experimental data until the displacement reaches about 4mm, but there is no large difference between the two curves, with about 880N as maximum load until failure.

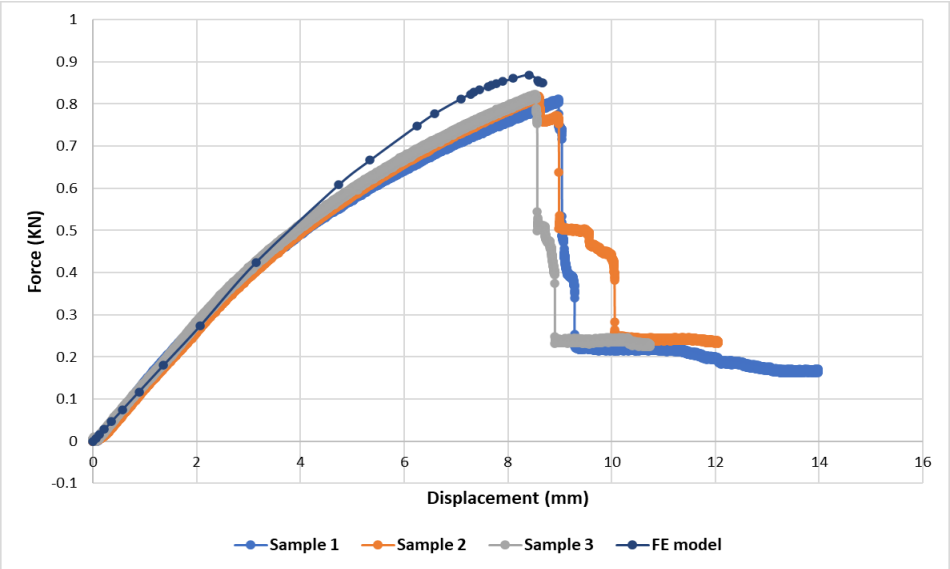

Figure 4. Typical load versus displacement curve

In the figure 5 we represent the cartographies of damage in the composite predicted by the model. These damages which concerns the fibers and the matrix are calculated based on Hashin failure criteria. It is clear that, the upper part of the plate's matrix compresses unlike the lower part (under the neutral axis) will be tended which confirms always the experiments. the damage of the matrix by compression and by tensile is located on a relatively large part of the plate, and we can say that these results are familiar ones according to the experimental tests.

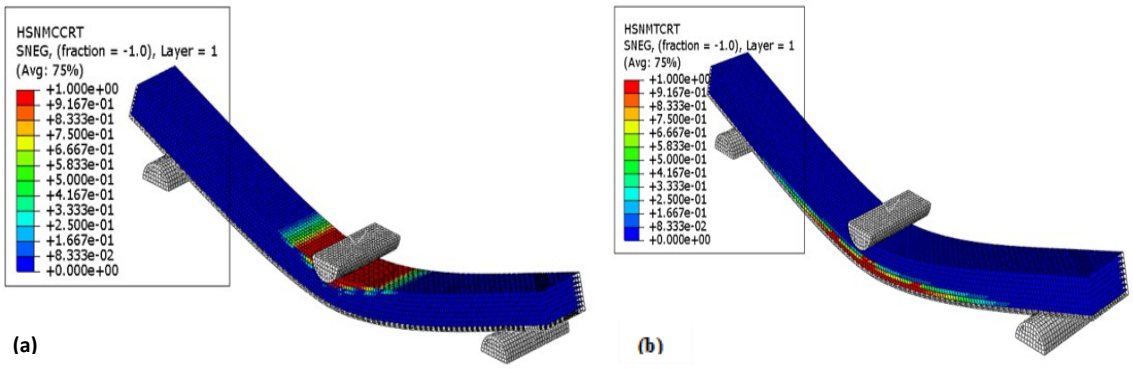

Figure 5. Hashin matrix failure criteria distribution. (a) Hashin matrix compression. (b) Hashin matrix traction

Figure 6 shows the comparison between compressive and tensile longitudinal strains of the three models of flax-epoxy plate with different deflection levels, it is clear from this figure that the compressive and tensile strains of the plate increase with increasing of deflection level. The reason for this increase could be attributed to the increase in the applied moment on the beams with increasing of deflection values. And also, the neutral axis can be predicted from longitudinal strain distribution curve. The strain curves have a linear behaviour in the beginning of the test, then it tends to change its behavior to non-linear both in compression and in the tensile part of the plate due the shear deformation, the maximum tensile strain recorded was approximately 0.0095, and the maximum compressive strain was about -0.0125.

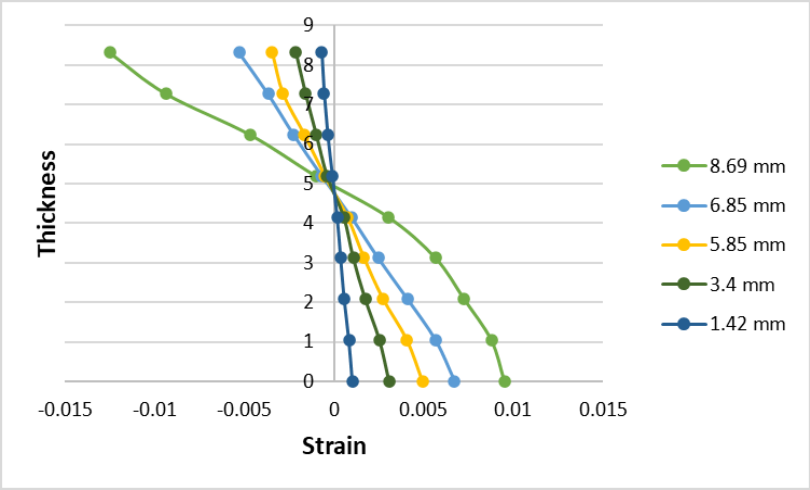

Figure 6. The longitudinal strain distribution along the plate's thickness

The plots of the temperature versus the applied displacement level (in % of maximal deflection) are presented in Figure 7. The bilinear nature of the data can be well seen from these graphs. We used a linear regression for each part of the plots and determined the endurance limit which according to this technique corresponds to the intersection of the two linear parts of the plot. The endurance limit determined by the IR thermography method was 25 % of the maximum deflection, about 2.2 mm.

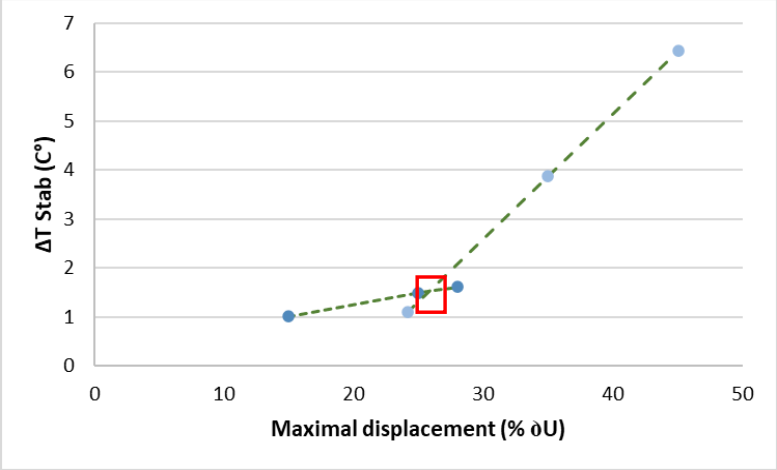

Figure 7. Average stabilized temperature versus the maximum applied displacement

The damage initiation in flax/epoxy laminates seem to occur inside the fiber bundles between fiber–fiber interfaces which justifies temperature increasing. During our cyclic loading, cracks will initiate and propagate through the interface between the elementary fibers within the bundles when applying a displacement near 50% of the maximal deflection till failure, that's why these tests have been carried out with loadings less than 50% of maximum deflection. The damage initiation and the final fracture are shown in Figure 8.

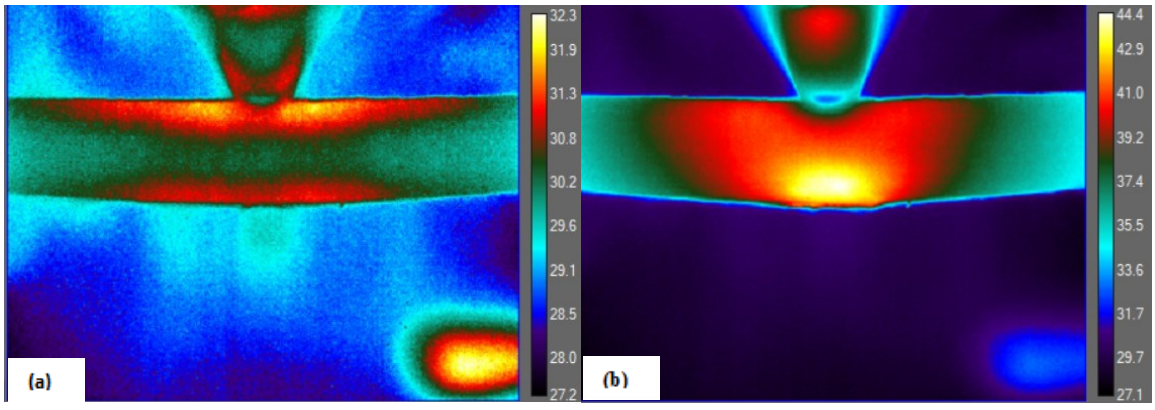

Figure 8. Images obtained by the infrared camera during cyclic loading on a tested specimen (a) damage initiation (b) final fracture

5. Conclusions

From the experimental and numerical study on the three points bending test of flax/epoxy composite, the following conclusions can be drawn:

- Flax/epoxy laminates have a linear behavior in the beginning of the loading then a nonlinear behavior until failure.
- Damage has occurred first in at tensile part of the laminate due the matrix cracking and fibers breakage and then smooth fracture in the compressed one according to hashin failure criteria distribution.
- We noticed a good correlation between the FE model and the experimental resalts in terms of ultimate deflection and damage distribution.
- The endurance limit determined by the IR thermography method was 25 % of the maximum deflection, about 2.2 mm.

6. References

1. El Sawi I, Bougherara H, Zitoune R, Fawaz Z. Influence of the manufacturing process on the mechanical properties of flax/epoxy composites. Journal of Biobased Materials and Bioenergy 2014; 8(1):69-76.

2. Haddad M, Zitoune R, Bougherara H, Eyma F, Castanié B. Study of trimming damages of CFRP structures in function of the machining processes and their impact on the mechanical behavior. Composites Part B: Engineering 2014; 57:136-143.

3. Nguyen-Dinh N, Bouvet C, Zitoune R. Influence of machining damage generated during trimming of CFRP composite on the compressive strength. Journal of Composite Materials 2020; 54:1413-1430.

4. Sheikh-Ahmad J, Shahid A. Effect of edge trimming on failure stress of carbon fibre polymer composites. International Journal of Machining and Machinability of Materials 2013; 13:331-347.

5. Shanmugam D.K, Nguyen T, Wang J. A study of delamination on graphite/epoxy composites in abrasive waterjet machining. Composites Part A: Applied Science and Manufacturing 2008; 39:923-929.

6. Hejjaji A, Zitoune R, Toubal L, Crouzeix L, Collombet F. Influence of controlled depth abrasive water jet milling on the fatigue behavior of carbon/epoxy composites. Composites Part A Appleid Science Manufacturing 2019; 121:397–410.

7. Ghidossi P, Mansori ME, Pierron F. Influence of specimen preparation by machining on the failure of polymer matrix off-axis tensile coupons. Composites Science and Technologie 2006; 66:1857–1872.

8. Ameur MF, Hadj Djilani A, Zitoune R, Krishnaraj V, Sheikh-Ahmad J, Toubal L, Bougherara H. Experimental and numerical investigations of the damages induced while drilling flax/epoxy composite. Journal of Composite Materials 2021 ; 0 :1–18.

9. Xu J, Lin T, Li L, Ji M, Paulo Davim J, Geier N, Chen M. Numerical study of interface damage formation mechanisms in machining CFRP/Ti6Al4V stacks under different cutting sequence strategies. Composite Structures (2022).

  doi:10.5075/epfl-298799_978-2-9701614-0-0

HOW CAN CFRP PREPREG SCRAPS BE REUSED? THE "CIRCE" LIFE PROJECT

Iacopo Bianchi[a], Alessio Vita[a], Vincenzo Castorani[b], Valerio Alessi[c], Dotoli Rosario[d], Lucia Delledonne[e], Damiana Cafagna[f]

a: Università Politecnica delle Marche, Ancona – i.bianchi@pm.univpm.it
b: HP composites, Ascoli Piceno
c: Alci, Ascoli Piceno
d: CETMA, Brindisi
e: Petroceramics, Stezzano
f: Base Protection, Barletta

Abstract: *Prepreg scraps generated during the cutting phase of virgin Carbon Fiber Reinforced Polymers parts typically account about 30% of the total prepreg produced. At present, these scraps end up in landfill or in incineration facilities, with relevant consequences in terms of costs and environmental impacts. In this context, a solution has been proposed within the CIRCE (Circular Economy Model for Carbon Fibre Prepregs) EU LIFE project. 5 Italian companies are collaborating to identify possible solutions to successfully reuse prepreg scraps. The companies have tested an industrial process that transform the scraps and prepare them to be processed as secondary raw material. To validate the recovery process, the manufacturing of three different composite products has been addressed: toe caps for safety footwear, carbo-ceramics brakes and automotive parts. The preliminary results demonstrated that this recovery process can be successfully employed to produce high mechanical properties composite parts with low environmental impacts.*

Keywords: Circular economy; Prepreg scraps; Sustainability; CFRP

1. Introduction

In the last years, the demand of composite materials is constantly growing in different industrial fields where lightness and resistance are required, such as automotive, marine, energy and sporting equipment sectors[1].

These materials are commonly defined as a combination of two or more distinct materials, each of which maintains its own distinctive properties, to create a new material with properties that cannot be achieved by any of the components acting alone. Due to this combination, composite materials are characterized by low weight and high performance in terms of specific stiffness and strength. Among these materials, Carbon Fiber Reinforced Polymers (CFRPs) are widely used for their relevant engineering properties, such as high stiffness and strength, low density, thermal and electrical insulation and corrosion and chemical resistance [2–4].

The increasing demand for composites is expected to reach 194 kt (kilo tones) in 2022, while, for carbon fibers, is predicted a demand of 117 kt. Mostly of CFRPs use can be attributed to the transport sector, where composites allow to reduce the emissions related to the useful life by reducing fuel consumption [5,6].

However, CFRPs are also associated to significant environmental impacts: most of them are related to the manufacturing process of carbon fiber. It accounts for about 70% of the total

  doi:10.5075/epfl-298799_978-2-9701614-0-0

environmental loads of a composite product and it is mostly due to the high energy consumption required for the raw material production [7].

Another issue associated to this increasing demand of CFRPs is the generation of prepreg scraps, wastes produced during the cutting phase of laminates manufacturing, which constitute between 20-50% of the virgin prepreg used[8]. Nowadays, these scraps typically end up in landfill or incinerator with negative impacts on the environment and high costs. These end of life strategies are adopted because, even though several recycling methods for CFRPs prepreg based on mechanical, thermal (e.g. pyrolysis and fluidises bed process), and chemical process have been developed, the properties of the recycled materials are very poor despite to the very high recycling costs [9,10]. Indeed, due to the cross-linked structure of thermoset matrix, it cannot be remelted and easily reshaped and reused [11]; when it is recovered it is typically used as filler, fuel or chemical feedstock [12]. In terms of recovered carbon fibers they are reduced in size and usually show a reduction in mechanical properties, with respect to vCF.

These issues have made necessary the development of methodologies that allow the recover the residual end-of-life value of CFRPs prepreg scraps. Indeed, these scraps, due to the presence of continuous carbon fibers and uncured thermoset matrix, can be reintroduced in the manufacturing process for the realization of high-quality composite components.

A possible solution has been proposed within the CIRCE (Circular Economy Model for Carbon Fiber Prepregs) EU LIFE project, developed as a collaboration between five Italian companies (HP Composites, Alci, Base Protection, Cetma, and Petroceramics). The project goal was to develop a recovery system for uncured prepreg scarps and to find suitable production processes and products for the new raw secondary material [13]. This project is based on a zero-waste approach, reusing scraps produced during the cutting operation of virgin prepreg rolls, in a circular economy model that allows to reduce the environmental impacts of products, costs and gives a second life to these materials that otherwise would go to landfill or incinerator. This allows to reach a 100% valorization of the waste, recovering completely the uncured waste[14,15]. Three case studies to be realized with the recovered scraps have been identified: a component for the automotive sector, toe caps for safety footwear and carbo-ceramic brakes. To quantify the advantages related to the new recovery process environmental impacts, costs, cost-benefits (CBA) and business model analyses have been conducted on the products realized.

The cost and impacts analyses are carried out following the international standards for Life Cycle Assessment (LCA) and Life Cycle Costing (LCC), in order to evaluate which processes are the most beneficial and identify critical issues and improvement possibilities.

In this paper, the CIRCE project and its main results are presented, highlighting potentialities and problems related to the recovery of carbon fiber prepreg scraps in the proposed applications.

2. Methodologies

The recovery process developed within the CIRCE project consists in an innovative solution, based on specific automated machines, able to transform the CFRPs prepreg scraps into a ready-to-use raw secondary material.

  doi:10.5075/epfl-298799_978-2-9701614-0-0

The recovery process consists in the shredding of the prepreg scraps and in the removing of backing paper. This process is performed by exploiting innovative and patented systems which allow to obtain ready-to-use chips of uncured prepreg. The thermoplastic backing paper is collected and treated as recyclable waste, while the chips are conveyed into a dedicated collector. If their use is not immediate, they have to be stored in an industrial refrigerator to avoid complete curing of the resin and adhesion of the chips.

In the first phase of the reclaim process, a cutting machine is employed for the sizing and shredding of the scraps, allowing to produce small pieces of prepreg characterized by almost uniform size and shape. In particular, the prepreg scarps, still covered with the backing paper, are first cut into linear strips and then into chips by means of rotary cutters.

The chips are then fed into the peeling machine that automatically removes the polyethylene backing paper, making the scraps ready for their reuse as reclaimed raw material. This process exploits the friction generated on the surfaces of the release films to allow easy and automated removal of the backing paper from both the faces of the chips.

Subsequently, the thermoplastic backing paper is collected and treated as recyclable waste, while the chips are conveyed into a dedicated collector. If their use is not immediate, they have to be stored in an industrial refrigerator to avoid complete curing of the resin and adhesion of the chips.

The reclaimed material can be employed in a wide range of applications and production processes. Three different alternatives for the preperg scraps use proposed and developed within the CIRCE project are:

- Automotive components

The solution proposed by HP Composites consists in the use of the recovered CFRP in an under-press process similar to the standard compression molding (CM) to obtain structural and aesthetic automotive components. In this process, metal mold and countermold are covered with a release agent and the reclaimed chips are placed inside the mold cavity. Thanks to a heated plates press, the prepreg material is cured under controlled temperature and pressure conditions. The part is then cooled down and removed from the mold and the production cycle can start again.

In the first stage of the project, in order to assess the mechanical properties of the recovered material, tensile and flexural specimens were produced by exploiting the CFRP scraps in a CM process. Tensile tests were carried out according to the ASTM D3039 standard for composite materials while flexural tests were conducted in line with the ASTM D7264 standard for polymer matrix composite material. A MTS universal testing machine equipped with a uniaxial extensometer was employed to carry out the tests and obtain stress-strain curves. The mechanical properties of the newly developed material were compared to those of a 6061-T6 aluminum alloy. This material was selected as it is one of the most commonly used aluminum alloy for general purpose use and automotive applications.

- Safety toe caps

A second application for the prepreg scraps is being developed by Base protection and CETMA to produce composite toe caps for work footwear. These safety equipment components are

  doi:10.5075/epfl-298799_978-2-9701614-0-0

crucial to prevent injuries to the frontal area of the foot and they must have adequate compression and impact resistance. At present, the toe caps are produced by means of an injection molding process by using a granulated thermoplastic compound mainly composed of polycarbonate. The goal of the project is to substitute the thermoplastic toe caps with recovered CFRPs ones; the latter are being produced by means of a compression molding process similar to that described for the automotive sector components. CETMA is evaluating the feasibility of the process in terms of the mechanical properties of the reclaimed products. In this context, the toe caps were tested to ensure compliance with the UNI EN 20345 standard in terms of impact and compression resistance.

- Carbon ceramics brakes

The third proposed solution for the reuse of prepreg scraps deals with the production of carbon ceramic brakes by Petroceramics. These ceramic matrix composite products are currently being produced by exploiting a liquid silicon infiltration (LSI) process; the first phase of LSI consists in the production of a green part by compression molding. At present, a patented compound constituted of thermoset resin and short virgin carbon fibers is employed as raw material. The project proposal is to substitute up to 10% of the virgin fibers with the prepreg scraps, leaving the rest of the production process unchanged.

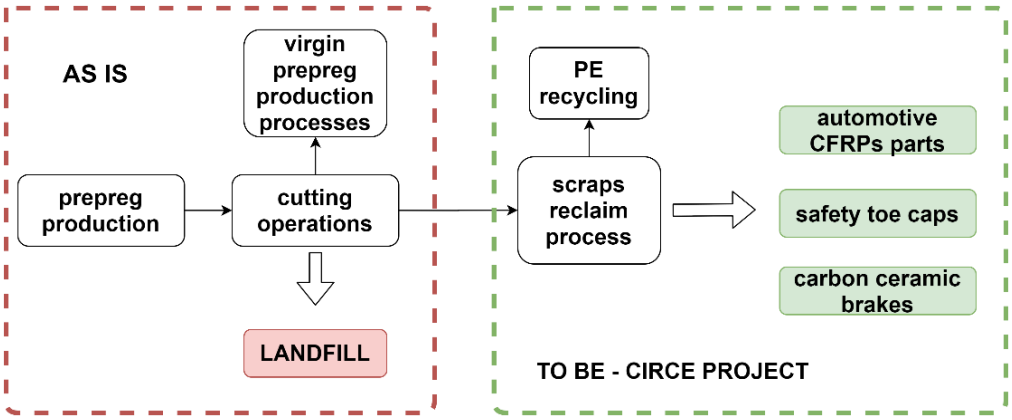

Figure 1 CIRCE project scenarios

In all the proposed applications, the reuse of prepreg waste allows to reduce the amount of virgin materials employed in compression molding processes (either virgin SMC or carbon fibers). Moreover, it prevents the CFRPs waste to be sent to landfills; overall, there are strong possible benefits in terms of environmental sustainability and cost reduction. In previous literature studies, Life Cycle Assessment analyses were carried out to evaluate the possible environmental impacts reduction that can be obtained by means of the proposed solutions. Overall, the recovery process showed negligible environmental impacts due to the low energy consumption required by the recycling system[16]. Great environmental benefits were showed for the reuse of the prepreg scraps for the production of CFRPs automotive and personal safety components.

For what concerns the carbon ceramic brakes production, an approximated evaluation of the emissions reduction obtained within the CIRCE project can be calculated by considering the environmental impacts of the virgin carbon fibers and of the reclaim process. In fact, as stated above, the production phases of the LSI process will remain unmodified except for the raw

  doi:10.5075/epfl-298799_978-2-9701614-0-0

materials mix employed for the compression molding operations. Hence, preliminary impacts reduction results can be obtained by comparing literature LCA analyses of the modelling of the raw materials footprints [16,17].

One of the main advantages of the CIRCE project will be the possibility of scaling up the process and globally extending the use of the new technology. The expected quantity of CFRP prepreg that will be produced in 2025 is equal to 250'000 tons; assuming an optimistic average nesting efficiency of 80%, about 50'000 tons of uncured waste will be disposed of in 2025. This is a relevant issue, in particular if the high environmental impacts and production costs of CFRPs are considered. In this context, the advantages of the CIRCE project could be extended to the global waste production of CFRP uncured waste, with important advantages in terms of CO_2 emission and costs reduction.

3. Results

3.1 Mechanical characterization

Figure 2 reports the results of the mechanical characterization in terms of specific tensile strength and specific flexural strength (i.e. the flexural and tensile strength divided by the density of each tested material). The reclaimed prepreg showed a specific tensile strength about 4.5% lower than that of the aluminum alloy. For what concerns the specific flexural strength, the recycled composite exhibited an average value 40% higher that that of the metal alloy alternative. This is a remarkable result considering the high mechanical properties of the 6061 aluminum alloy; the CIRCE reclaim process is able to transform the prepreg scraps into a raw secondary material with mechanical properties comparable with those of virgin prepreg. For this reason, the new material can be employed in a wide range of application in substitution to aluminum alloys and virgin SMC. The lower density of the recovered prepreg (about 1.5 g/cm^3) could also reduce the weight of transport sectors components that are currently produced by using metal alloys. Moreover, the innovative material could be used as a replacement for a large variety of unreinforced plastic parts with possible advantages in terms of weight reduction and improved mechanical performances.

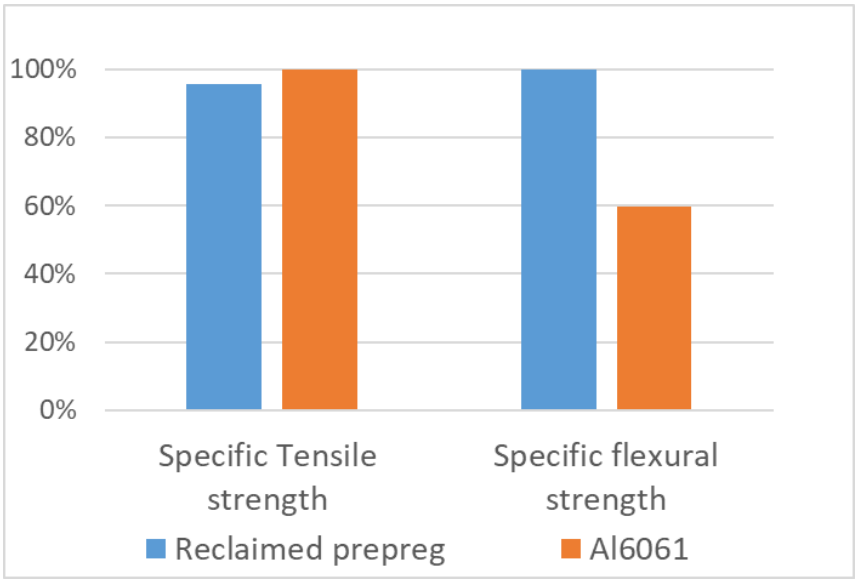

Figure 2 Results of the mechanical tests in terms of tensile and flexural strength

3.2 Environmental impact assessments

Environmental impact assessments were carried out for the three possible applications of the recovered material.

The reclaim process has almost zero environmental impacts if compared to virgin material production; specifically, the scraps preparation process has a cumulative energy demand (CED) equal to 5.8 MJ and a global warming potential (GWP) of 0.15 kg eq CO_2 per kg of waste processed (negligible if compare with 440.4 MJ and 24.40 kg CO_2 eq of virgin carbon fibers).

Considering CFRPs automotive components, the use of the reclaimed scraps can provide a reduction in energy use of 602 MJ and a reduction of equivalent CO_2 emissions of 37.4 kg per kg of CFRPs recovered waste[18]. The recovered material has slightly lower mechanical properties with respect to virgin SMC; hence, in order to guarantee the same mechanical performances of the automotive components, the recycled products are heavier than the virgin alternatives. This implies heavier molds and higher energy consumption for the curing phase of the reclaimed parts. However, virgin SMC has a strong carbon footprint and represents the main contribution on the impacts of virgin CFRPs parts; the CIRCE projects allows to substitute the high impacts virgin prepreg with a practically zero impacts recycled prepreg, with subsequent environmental benefits.

In the case of safety footwear components, the recovered scraps are employed as a substitute for a thermoplastic compound for an injection molding process. Overall, a reduction in CO_2 equivalent emissions of 2.5 kg can be obtained per kg of used reclaimed prepreg. This value is not as high as for the automotive components because the scraps are used to replace a raw material (polycarbonate) with relatively low carbon footprint. The reclaimed prepreg has better mechanical properties with respect to the thermoplastic material; hence, lighter toe caps can be produced with consequent ergonomic improvements of the safety footwear.

For what concerns the production of carbon ceramics brakes the expected reduction in impacts in terms of CED and GWP are equal to 434.6 MJ and 24.25 kg CO_2 eq per kg of scraps reused. These values were calculated by considering the environmental impacts of virgin carbon fibers and those of the CIRCE recovery process. The reuse of prepreg scraps in ceramic matrix composites does not require any changes in the production process with the exception of the raw materials. Therefore, these environmental benefits can be easily obtained without affecting the production line or the products quality.

If compared with other CFRPs recycling system, the environmental savings obtained by the uncured prepreg recovery system are even greater[12]. In fact, the CIRCE process allows to completely recover the scraps (both matrix and fibers), with a 100% valorization of the waste. On the other hand, the thermosetting composite recycling processes that are currently available on the market typically provide only a partial recovery of the products; in fact, recycled carbon fibers are usually reduced in size and they have deteriorated mechanical properties while the cured matrix are recovered in forms of fillers, fuel or chemical feedstock.

Considering the expected production of uncured CFRP waste in 2025 and the average impacts reduction that will be obtained by means of the CIRCE recovery process, the CO_2 equivalent emissions reduction that could be obtained globally every year is about 1.5 million of tons. This

  doi:10.5075/epfl-298799_978-2-9701614-0-0

estimate can give an idea of the potential that the project has to improve the environmental sustainability of composite products. Moreover, the project has strong economic repercussions because the reclaim process has very low costs and the reclaimed scraps can be employed to replace expensive virgin prepreg materials.

4. Conclusion

This manuscript had the objective of describing an innovative reclaim process for uncured prepreg scraps developed within the European CIRCE project. The system has the potential to improve the economic and environmental sustainability of composite products by recovering the scraps generated during the cutting phase of virgin prepreg and transforming them into a high technological value raw secondary material. The innovative technologies and three possible applications of the recovered material were presented; mechanical characterization and environmental assessments results were also reported.

The main outcomes of the paper can be summarized as follows:

- The reclaim material is suitable for a wide range of applications; recovered automotive and personal equipment sector components were developed within the project.
- The mechanical properties of the recovered scraps are similar to those of virgin sheet molding compound. If compared to a 6061 aluminum alloy, the recovered material has specific tensile strength about 4% lower and a specific flexural strength 40% higher.
- From an environmental perspective, the reclaim process has almost zero impacts and the prepreg secondary material can be used as replacement for high-carbon footprint virgin materials.
- Considering a global exploitation of the new technology, an annual reduction in emissions equal to 1.5 million of tons equivalent of CO_2 can be achieved by 2025.

For future development of the work, new structural applications of the recovered prepreg will be considered and analyzed. The recovery process will be optimized and improved to obtain a raw secondary material with even better mechanical properties. A large-scale diffusion of the process is expected with consequent improvements of the sustainability of composite products.

Acknowledgements

This research was founded by the EU LIFE project “CIRCE – CIRcular economy model for Carbon fibrE prepregs” LIFE18 ENV/IT/000155

5. References

[1] Zhang J, Chevali VS, Wang H, Wang CH. Current status of carbon fibre and carbon fibre composites recycling. Compos Part B Eng 2020;193:108053. https://doi.org/10.1016/j.compositesb.2020.108053.

[2] Holmes M. Carbon composites continue to find new markets. Reinf Plast 2017;61:36–40. https://doi.org/10.1016/j.repl.2016.12.060.

[3] Akbarpour H, Akbarpour M. Finite Element Modeling of Axially Loaded CFRP-Confined Rectangular Reinforced Concrete Columns. Civ Eng J 2016;2:414–25. https://doi.org/10.28991/cej-2016-00000046.

[4] Ebrahimpour Komleh H, Maghsoudi AA. Analytical Assessment of Bending Ductility in

  doi:10.5075/epfl-298799_978-2-9701614-0-0

FRP Strengthened RHSC Beams. Civ Eng J 2018;4:2719. https://doi.org/10.28991/cej-03091194.

[5] Das S. Life cycle assessment of carbon fiber-reinforced polymer composites. Int J Life Cycle Assess 2011;16:268–82. https://doi.org/10.1007/s11367-011-0264-z.

[6] Duflou JR, De Moor J, Verpoest I, Dewulf W. Environmental impact analysis of composite use in car manufacturing. CIRP Ann - Manuf Technol 2009;58:9–12. https://doi.org/10.1016/j.cirp.2009.03.077.

[7] Wilson A. Vehicle weight is the key driver for automotive composites. Reinf Plast 2017;61:100–2. https://doi.org/10.1016/j.repl.2015.10.002.

[8] Nilakantan G, Nutt S. Reuse and upcycling of aerospace prepreg scrap and waste. Reinf Plast 2015;59:44–51. https://doi.org/10.1016/j.repl.2014.12.070.

[9] Pickering SJ. Recycling technologies for thermoset composite materials-current status. Compos Part A Appl Sci Manuf 2006;37:1206–15. https://doi.org/10.1016/j.compositesa.2005.05.030.

[10] Oliveux G, Dandy LO, Leeke GA. Current status of recycling of fibre reinforced polymers: Review of technologies, reuse and resulting properties. Prog Mater Sci 2015;72:61–99. https://doi.org/10.1016/j.pmatsci.2015.01.004.

[11] Wang S, Xing X, Zhang X, Wang X, Jing X. Room-temperature fully recyclable carbon fibre reinforced phenolic composites through dynamic covalent boronic ester bonds. J Mater Chem A 2018;6:10868–78. https://doi.org/10.1039/c8ta01801d.

[12] Meng F, Olivetti EA, Zhao Y, Chang JC, Pickering SJ, McKechnie J. Comparing Life Cycle Energy and Global Warming Potential of Carbon Fiber Composite Recycling Technologies and Waste Management Options. ACS Sustain Chem Eng 2018;6:9854–65. https://doi.org/10.1021/acssuschemeng.8b01026.

[13] CIRCE | Circular Economy Model for Carbon Fibre Prepregs n.d.

[14] Souza CSR, Candido GM, Alves W, Marlet JMF, Rezende MC. Morphological and mechanical analyses of laminates manufactured from randomly positioned carbon fibre/epoxy resin prepreg scraps. Mater Res Express 2017;4:105601. https://doi.org/10.1088/2053-1591/aa8d3f.

[15] Wu M-S, Centea T, Nutt SR. Compression molding of reused in-process waste-effects of material and process factors. Compos Sci 2018;4:1–12. https://doi.org/10.1080/20550340.2017.1411873.

[16] Bianchi I, Forcellese A, Simoncini M, Vita A, Castorani V, Arganese M, et al. Life cycle impact assessment of safety shoes toe caps realized with reclaimed composite materials. J Clean Prod 2022;347:131321. https://doi.org/10.1016/J.JCLEPRO.2022.131321.

[17] Forcellese A, Marconi M, Simoncini M, Vita A. Life cycle impact assessment of different manufacturing technologies for automotive CFRP components. J Clean Prod 2020;271. https://doi.org/10.1016/j.jclepro.2020.122677.

[18] Bianchi I, Forcellese A, Marconi M, Simoncini M, Vita A, Castorani V. Environmental impact assessment of zero waste approach for carbon fiber prepreg scraps. Sustain Mater Technol 2021:e00308. https://doi.org/10.1016/j.susmat.2021.e00308.

ECONOMIC ASSESSMENT OF CARBON FIBER PREPREG SCRAPS REUSE IN AUTOMOTIVE COMPONENTS

Iacopo Bianchi[a], Marco Cucculelli[a], Archimede Forcellese[a], Serena Gentili [a], Tommaso Mancia[a], Michela Simoncini[a], Alessio Vita[a], Marco Chiaromonte [a],Vincenzo Castorani[b]

a: Università Politecnica delle Marche, Ancona, Italy – s.gentili@pm.univpm.it
b: HP Composites, Ascoli Piceno, Italy

Abstract: An innovative reclaim system for Carbon Fibers Reinforced Polymers prepreg scraps was investigated from an economic point of view. The reclaim system was developed within the LIFE-EU research project CIRCE (Circular Economy Model for Carbon Fiber Prepreg Scraps) with the goal of completely recovering the uncured scraps produced during the cutting operations of virgin prepreg. Composite structural parts were produced using the raw secondary material in a compression molding process. The innovative developed process was compared with traditional compression molding of virgin prepreg. The economic analysis was carried out by means of the Life Cycle Costing methodology: both production and service life phases were investigated. The analysis proved that the CIRCE system can guarantee a production cost reduction; savings are expected to increase when high production rates and heavier parts are produced.

Keywords: Sustainability; prepreg scraps; zero waste technology; composite; recycling.

1. Introduction

Carbon Fiber Reinforced Polymers (CFRPs) are composite materials characterized by low density and high specific mechanical properties such as stiffness and strength. A large variety of applications are possible for these materials; some examples can be found in sectors such as automotive, aerospace, nautical, energy production and sport (1). The decrease in production cost of composite products is leading to a sensible growth of the use of CFRPs, with an expected global demand of 194 kt (kilotonnes) for these materials in 2022 and a global demand for carbon fibers (CF) equal to 117 kt (2).

The use composite materials in parts of employed in transports contributes to reducing the fuel consumption during the useful life. Thus, remarkable cost and CO_2 emission savings can be obtained. However, these benefits are counterbalanced by the high costs and environmental impacts related to these products' manufacturing. In fact, both CFRPs raw materials production and molding processes are cost and energy intensive (3). Hence, developing an efficient system to recycle polymer matrix materials is mandatory and several technologies have been developed throughout the years.

Typically, thermosetting matrix composites are characterized by higher mechanical properties with respect to thermoplastic matrix alternatives. As a matter of fact, during the curing process, covalent bonds are generated between the polymer molecules, strongly improving the characteristics of the material. The curing process is based on irreversible reactions, so no remelting or reshaping is possible once the material is cured; this makes it difficult the complete recycling of the composite (4). Indeed, most of the recycling processes, currently available on the market, allows only a partial recovery of the material: the reinforcement phase is recovered

  doi:10.5075/epfl-298799_978-2-9701614-0-0

in the forms of short fibers with deteriorated mechanical properties while the matrix, when possible, is recovered as a filler or as a chemical feedstock. Recycling is not always convenient from an economic point of view, especially considering that the recovered materials are not usually suitable for structural applications.

Among possible composite raw materials, prepreg is one of the most used for high-end applications, with a forecasted global market value of 11.5 billion USD for the next three years; preperg is typically constituted by pre-impregnated composite sheets in which fibers are embedded in a partially cured thermosetting matrix (B-stage resin). Composite parts are built by stacking several layers of prepreg that are previously cut in order to match the mold geometry. Complete curing of the parts is obtained by applying high temperature and pressure in an autoclave or out-of-autoclave molding processes. One of the main issues related to prepreg environmental sustainability is determined by the waste produced during the cutting operations of the virgin material; in fact, due to the complexity of the cut shapes, nesting efficiency usually ranges between 50% and 70%, leading to a high volume of uncured waste in form of off-cuts, trim waste and end-roll waste (5). At the present moment, these wastes end up in landfill facilities of incineration plants without ever being effectively utilized. Considering the high purchase cost of virgin prepreg, the high quantity of scraps generated during the nesting phase results not only in serious environmental concerns but also in economic issues.

A solution for this problem was proposed within the CIRCE (Circular Economy Model for Carbon Fiber Prepreg Scraps) project, funded through the LIFE-EU programme. The main goal of CIRCE was to develop a recovery process able to transform the uncured prepreg scraps into a ready-to-use raw secondary material, with a 100% valorization of the composite wastes. The new-developed process turns long fibers virgin prepreg trims into short fibers small chips of recovered material with almost uniform size and shape. Since the prepreg scraps are not cured yet, both the fibers and the matrix can be fully recovered and the secondary material can be employed in compression molding (CM) manufacturing processes as a replacement for virgin fabric prepreg or sheet molding compound (SMC).

Several literature studies evaluated the feasibility of the reuse of the prepreg scraps in different applications but they were mainly focused on the mechanical properties of the recycled materials (6). Moreover, the analyzed recovery processes were primarily executed by hands, without any industrial automatization. The CIRCE reclaim process was investigated only from an environmental point of view by means of Life Cycle Assessment analyses that quantified the reduction in environmental impacts that can be achieved by substituting virgin material with the recycled alternative (7). However, no economic evaluations of the automated reclaim process are available in scientific literature. In this context, this paper aims at evaluating the economic aspects of the CIRCE recycling process to verify that environmental sustainability is paired with cost-effectiveness. To this purpose, Life Cycle Costing (LCC) analysis was performed considering all the costs related to the innovative reclaim process (e. g. labor costs, mold manufacturing, etc.). The results were compared with those obtained by considering the manufacturing cost of a traditional CM process based on prepreg virgin material.

2. Methodologies

2.1 Processes description

  doi:10.5075/epfl-298799_978-2-9701614-0-0

The innovative recovery process is based on the use of an automated system. It allows to shred the prepreg scraps in small chips and to remove the polyethylene release paper that is used in virgin prepreg manufacturing processes to prevent undesired sticking of the uncured material. The backing paper can be collected at the end of the process to be sent to plastic recycling plants. As for virgin prepreg, once the secondary raw material is ready, it has to be kept in an industrial refrigerator to prevent the complete curing of the matrix and adhesion of chips. The peeled chips can be used as a replacement for virgin materials in an autoclave and out of autoclave processes. In this study, a compression molding process was considered. The chips are removed from the refrigerator and are manually placed into a steel mold. A release agent is applied to the mold surfaces (mold and countermold) to allow easy removal of the finished products. The composite part is cured through a heated plates press under controlled temperature and pressure conditions. Once cooled down, the molded part is then manually removed from the mold.

The molding process of virgin materials (prepreg fabric or SMC) is similar to the one described for the recycled scraps. Virgin material is taken out from the refrigerator and a computer numerical control (CNC) machine is used to cut the prepreg to match the mold geometry. Virgin material scraps are usually disposed of in landfill or incinerators. As for the previously described process, the material is manually placed into a mold and complete curing is achieved by applying heat and pressure.

2.2 Life Cycle Costing

The economic evaluation of the new reclaim process was conducted by means of a Life Cycle Costing (LCC) analysis. This methodology allows to consider the costs incurred during multiple phases of the life cycle of a product or a process (the system boundaries, for example the manufacturing and useful life phases). The LCC analysis is referred to a functional unit, i.e. a quantified description of the performance requirements of the systems to which all the inputs and outputs are related. Once the scenarios are clearly defined, the cost inventory data are gathered and employed to evaluate the product's cost. In this particular case, a parametric approach was employed: several parameters, identified as cost drivers, are used to evaluate the cost of unitary activities (8).

As mentioned above, the CIRCE reclaim process was already analyzed from the environmental point of view in a previous literature Life Cycle Assessment study. In that case, the functional unit was defined as the production of a CFRP sample with defined top and bottom surface areas (0.0056 m^2 and 0.0057 m^2) and tensile strength between 5 and 5.7 kN. The same functional unit was utilized for the economic evaluation. Two different scenarios were considered:

- Scenario 1 deals with the production of the functional unit by using virgin prepreg in a compression molding process.
- Scenario 2 considers the production of the functional unit with the reclaimed scraps as raw secondary material and a compression molding process.

To fulfill the functional unit requirements, the two scenarios lead to sample with different weights. Specifically, Scenario 1 sample weights 0.06 kg while Scenario 2 sample weights 0.07 kg (7).

  doi:10.5075/epfl-298799_978-2-9701614-0-0

In the presented model, all direct and depreciation costs were considered to assess the scenarios manufacturing processes costs. Moreover, further evaluations were conducted to consider the parts useful life. As a matter of fact, prepreg and other composite materials are widely used for automotive applications and it is a goal of the study to determine whether or not the new reclaim process is suitable for the production of structural or aesthetic automotive components.

Most of the inventory data were provided by the company involved in the CIRCE project and were retrieved by means of direct measurements or purchase data. Some examples are the cost of raw materials, the energy cost per kWh, the molds, the machines used, the hourly cost of labour and the cost for waste disposal.

The energy consumptions of the industrial refrigerator, the press, the sytem for the prepreg recovery, the cutting CNC machine for virgin prepreg were directly measured during the samples production. The quantity of each material used (prepreg, scraps, and the release agent) were measured as well as the time required for the manual lay-up. The deprecation costs of the machines were allocated to the functional unit by considering their purchase price, their capacity, their estimated useful life, and the time of use of the machines per production cycle. The molds cost was calculated considering their purchase cost and the number of molding cycles that they can safely run before substitution is needed.

For what concerns the useful life phase, automotive structural components with the same weights of the scenarios samples were considered. The only cost item considered for the useful life is fuel consumption. Fuel cost was allocated to the composite parts by considering their weight with respect to the total weight of the car. A model, initially proposed by Hakamada et al (9) for environmental sustainability analyses, was repurposed for economic evaluations:

$$Use\ cost\ \left(\frac{€}{kg}\right) = \frac{e_c \times life\ \ time}{\varepsilon \times M} \quad (1)$$

Where:

- M is the curb weight of the vehicle (kg). A value of 1400 kg was considered as the initial value.
- e_c is the cost of the gasoline per litre (€/L). Average price in Italy updated to February 2022 was considered.
- ε is the fuel efficiency (km/L). According to International Energy Agency data, average fuel consumption for European Union light-duty vehicles equal to 16.7 km/L was considered (10).
- Life time expresses the useful life of the vehicle in km. 200’000 km were considered according to Duflou et al (11).

Costs related to the useful life of the two scenarios were calculated by multiplying the use cost obtained in Eq. (1) by the weight of each sample.

3. Results and discussion

Table 1 reports the costs related to the manufacturing process of the functional unit for the two considered scenarios. Table unitary values were obtained considering an optimal deprecation of the tools (i.e. considering a production volume that minimizes the mold costs). Figure 1 shows

  doi:10.5075/epfl-298799_978-2-9701614-0-0 published under CC BY-NC 4.0 license

the cost contribution for the samples production in terms of cost of the molds, of labor, and of materials and energy; different production volumes were considered as possible industrial cases.

Table 1 Cost inventory data and results for the two considered scenarios.

	Cost	Scenario 1 Production cost for one sample	Scenario 2
Raw materials			
Prepreg	80 €/kg	5.33 €	/
Prepreg waste disposal	0.65 €/kg	0.02 €	/
Release agent	20 €/kg	0.02 €	0.02 €
Labour	20 €/h	20.00 €	22.00 €
Mold and countermold			
Scenario 1	950 €	1.26 €	/
Scenario 2	1140 €	/	1.52 €
Machine deprecation			
Press	15000 €	0.32 €	0.32 €
Other machines			~ 0 €
Energy consumptions			
Press	0.17 €/kWh	0.17 €	0.20 €
Storage		0.01 €	0.01 €
Cutting CNC			~ 0 €
Recovery scrap			
Total		27.15 €	24.09 €

Scenario 2 is the best economic alternative and it guarantees a cost reduction per part produced of 3.06 € with respect to Scenario 1. This is mainly due to the low cost of the prepreg recovery process; this is a remarkable result considering the high technological value of the reclaimed scraps. The process has a high production rate and deprecation cost is negligible due to the long expected useful life of the recovery system. On the other hand, virgin prepreg is very expensive and determines about 20% of the total costs of Scenario 1.

Tools and manpower costs are higher for Scenario 2. This is due to the fact that more material is needed to fulfill the functional unit requirements; however, this price increment is fully compensated by the use of an almost zero-cost recycled material. For low production rates, Scenario 2 is the most expensive alternative because the tools' costs are divided by an insufficient number of parts. In fact, tools represent the main cost item for low production volumes; if only one part is produced, the cost of the mold would determine 98% of the total cost of the sample in Scenario 2. The percentage contribution lowers to 67% of the total in the case of 25 parts produced and it goes down to 6% if the production rate goes up 1500 parts. In industrial applications production processes that require expensive dedicated tools are preferred only if the production rates are high enough. In the considered analysis, a break-even point (BEP) between the two scenarios is reached for a production volume of 57 units; this value

  doi:10.5075/epfl-298799_978-2-9701614-0-0

is the minimum production rate that makes the reclaimed material a cheaper alternative in structural applications and the cost reduction increases as the production volume increases.

In this study, labour can determine even more than 90% of the total costs of the two scenarios This is in line with what was proved in previous literature analyses: in fact, high-end composite parts are typically produced by strongly relying on manpower for the lay-up phase (12). The development of automated lay-up systems for CFRP prepreg parts could contribute to improving their cost-effectiveness, making them an even more valuable alternative to traditional materials.

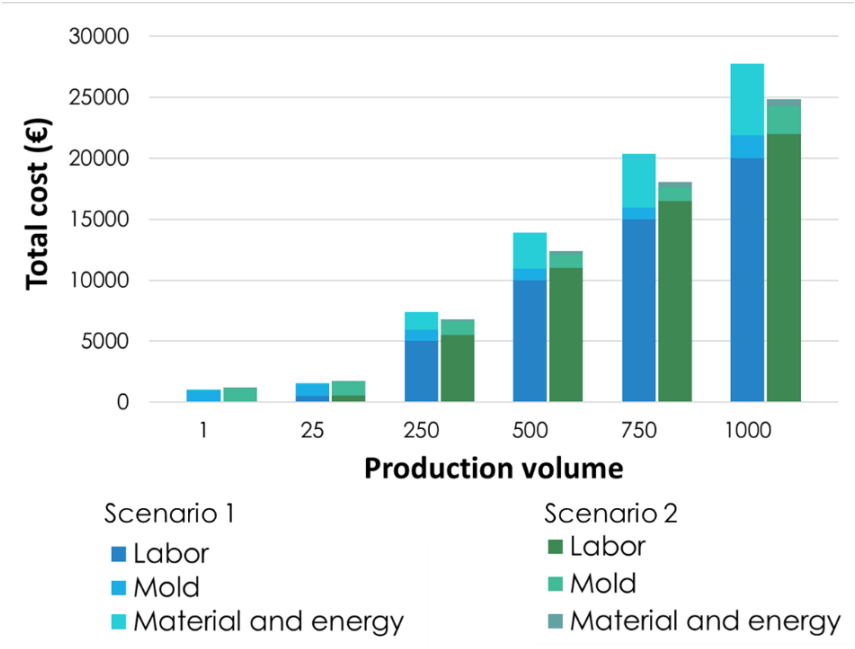

Figure 1 Production costs for the two scenarios in relation to the production volume

As far as the useful life of the considered components is concerned, Scenario 2 leads to a higher cost related to gasoline consumption (0.96 € for Scenario 1 vs 1.12 € for Scenario2, with an estimated cost per kg of 16 €). In fact, in the proposed model, gasoline cost consumption is linear with the weight of the part, so Scenario 2 has a useful life cost 20% higher than the virgin prepreg alternative. Service life is not a major cost item in the two scenarios as it contributes for only 3.5% in Scenario 1 and 4.6% in Scenario 2. So, even if the recovered scraps part has is heavier, overall its life cycle cost is still the lowest, with a total life cycle cost reduction of 2.9€ with respect to the virgin prepreg alternative.

The functional unit of this study is a structural component that has a weight between 0.06 kg and 0.07 kg; however, in industrial applications, it is not unusual to produce automotive components with considerable higher weight (up to tens of kg) (13). Hence, some evaluations were carried out to assess the total production costs of virgin prepreg and recovered scraps automotive components with different weights. Molds costs and labor time were estimated in collaboration with the involved company experts and by considering similar products production processes. Materials cost is assumed to be linear with the used quantity. Figure 2 reports the results of the weight analysis and shows that, as the produced components weight increases,

  doi:10.5075/epfl-298799_978-2-9701614-0-0

the CIRCE recovery process guarantees higher cost reductions. In Scenario 1, the percentage contribution of the raw materials increases as the part weight increase. For example, for a 1 kg component, the raw material contribution is 49.6% of the total cost (80 € out of 161.07 €). The corresponding component obtained by using the reclaimed scraps (with a weight of 1.2 kg) has a total cost of only 79.53 € and the raw material cost is almost negligible.

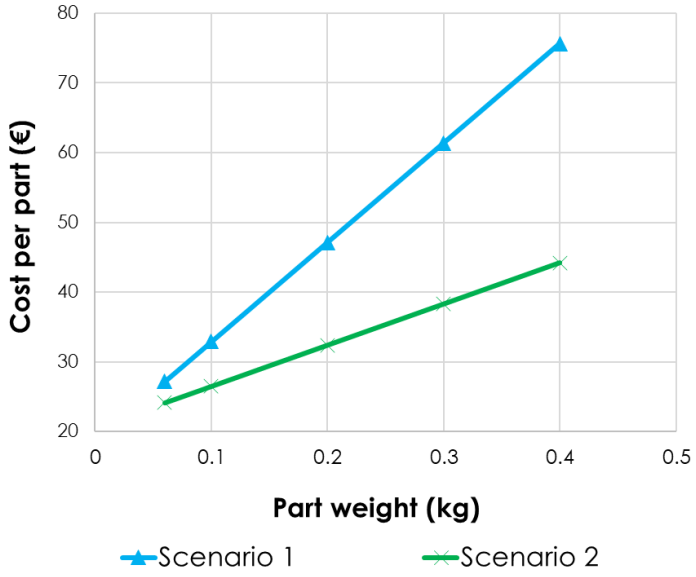

Figure 2 Manufacuring cost with respect to the parts weight

4. Conclusions

In this paper, an innovative reclaim process for prepreg scraps was investigated from an economic point of view. The process is based on the use of a new specifically designed system that allows to fully recover the prepreg scraps, with a 100% valorization of both the fibers and the matrix. In order to assess the economic sustainability of the new system, a Life Cycle Costing analysis was conducted. The functional unit was identified as a sample with defined mechanical properties and two different scenarios were analyzed: a virgin prepreg sample produced via compression molding was compared to a sample produced by using the reclaim material. The main results are summarized as follows:

- The CIRCE process allows recovering a raw secondary material with an high technological value with almost zero cost.
- The recovered scraps can be employed as a substitute for virgin prepreg in structural applications with economic advantages. A reduction in production cost equal to 3.06 € is achieved by using the recovered scraps for each produced sample.
- For low production volumes, the higher cost of the molds makes the recovery scenario the most expensive one. A break-even point is reached for a production rate of only 57 units.
- Due to its higher weight, the recovered sample has higher costs associated with its useful life. However, fuel consumption costs determine a little contribution on the Life

  doi:10.5075/epfl-298799_978-2-9701614-0-0

Cycle cost of the considered samples (less than 5%) so, despite being heavier, the recovered material sample has a lower life cycle cost.

- Economics savings are expected to increase as heavier parts are produced.

The reclaim material proved to be an optimal solution not only from an environmental point of view but from an economic perspective too. Future works could carry out a detailed economic investigation of industrial application of the CIRCE process. In addition, a comparison with other CFRPs recycling technology can be made.

Acknowledgements

- This research was founded by the EU LIFE project "CIRCE – CIRcular economy model for Carbon fibrE prepregs" LIFE18 ENV/IT/000155.

References

1. Holmes M. Carbon composites continue to find new markets. Reinf Plast [Internet]. 2017;61(1):36–40. Available from: http://dx.doi.org/10.1016/j.repl.2016.12.060
2. Dr Elmar Witten TK. Composites Market Report 2017. 2017;(September):1–44.
3. Meng F, Olivetti EA, Zhao Y, Chang JC, Pickering SJ, McKechnie J. Comparing Life Cycle Energy and Global Warming Potential of Carbon Fiber Composite Recycling Technologies and Waste Management Options. ACS Sustain Chem Eng. 2018;6(8):9854–65.
4. Wang S, Xing X, Zhang X, Wang X, Jing X. Room-temperature fully recyclable carbon fibre reinforced phenolic composites through dynamic covalent boronic ester bonds. J Mater Chem A. 2018;6(23):10868–78.
5. Nilakantan G, Nutt S. Reuse and upcycling of aerospace prepreg scrap and waste. Reinf Plast [Internet]. 2015;59(1):44–51. Available from: http://dx.doi.org/10.1016/j.repl.2014.12.070
6. Souza CSR, Candido GM, Alves W, Marlet JMF, Rezende MC. Morphological and mechanical analyses of laminates manufactured from randomly positioned carbon fibre/epoxy resin prepreg scraps. Mater Res Express. 2017;4(10):105601.
7. Bianchi I, Forcellese A, Marconi M, Simoncini M, Vita A, Castorani V. Environmental impact assessment of zero waste approach for carbon fiber prepreg scraps. Sustain Mater Technol [Internet]. 2021;e00308. Available from: https://linkinghub.elsevier.com/retrieve/pii/S2214993721000634
8. Duverlie P, Castelain JM. Cost estimation during design step: Parametric method versus case based reasoning method. Int J Adv Manuf Technol. 1999;15(12):895–906.
9. Hakamada M, Furuta T, Chino Y, Chen Y, Kusuda H, Mabuchi M. Life cycle inventory study on magnesium alloy substitution in vehicles. Energy. 2007;32(8):1352–60.
10. Fuel economy in the European Union – Analysis - IEA [Internet]. [cited 2022 Mar 3]. Available from: https://www.iea.org/articles/fuel-economy-in-the-european-union
11. Duflou JR, De Moor J, Verpoest I, Dewulf W. Environmental impact analysis of composite use in car manufacturing. CIRP Ann - Manuf Technol. 2009;58(1):9–12.
12. Vita A, Castorani V, Germani M, Marconi M. Comparative life cycle assessment and cost analysis of autoclave and pressure bag molding for producing CFRP components. Int J Adv Manuf Technol. 2019;105(5–6):1967–82.
13. Forcellese A, Marconi M, Simoncini M, Vita A. Life cycle impact assessment of different manufacturing technologies for automotive CFRP components. J Clean Prod. 2020;271.

  doi:10.5075/epfl-298799_978-2-9701614-0-0

ABSTRACT: The abstract should appear in italics in a justified text one line after the affiliations. Text size 11pt. The abstract should contain 100 to 150 words and no figures and/or tables. This abstract can differ from the abstract that was initially submitted electronically to ECCM20, however should describe the same work. The title of the full paper should be identical to the title of the abstract submitted electronically to the ECCM20, since both will appear on line during and after the conference. All manuscripts must be in English. Name your file ***"AbstractID_Fullpaper_Lastname_Firstname"*** *and submit a* ***.pdf*** *and a* ***.docx*** *version.*

This template includes complete descriptions of the number of pages, layout, fonts, spacing, and related information for producing the proceedings manuscripts. Papers not adhering to the guidelines of this template will not be included in the proceedings and relevant works will not be presented at the conference. Prepare your paper using this template only, **without making any adjustments to the font styles, colors and margins.**

Paper length is 6-8 pages including title, abstract, figures, tables and references. This will be a "camera ready" paper, therefore **do not write outside the margins and do not change the page layout neither the font type!** The manuscript font type is "Calibri Body" and the text size is 11pt, except from the **TITLE (14pt – Bold and CAPITAL) and the major headers (12pt - Bold).** Subheadings are in bold, 11pt.

In case you copy/paste (unpublished) text to this template from other documents in your computer, use the "Paste Special" option to paste the text as unformatted text (see Fig. 1 in next section).

Use SI units everywhere. If the work has been performed using Imperial unit, add SI units in brackets. Please use the "spell-check" and similar functions of your word processor to avoid errors.

5. Figures, Tables, and citations

2.1 Figures and Tables

Figures of good quality should be embedded in the manuscript text and arranged so as not to affect the manuscript flow/layout. Avoid long spaces between text and pages due to figures or tables.

Figures must be centered and followed by an appropriate figure caption also centered, immediately below the figure and in the same page. All figures should be cited in the manuscript in the order of their appearance.

  doi:10.5075/epfl-298799_978-2-9701614-0-0

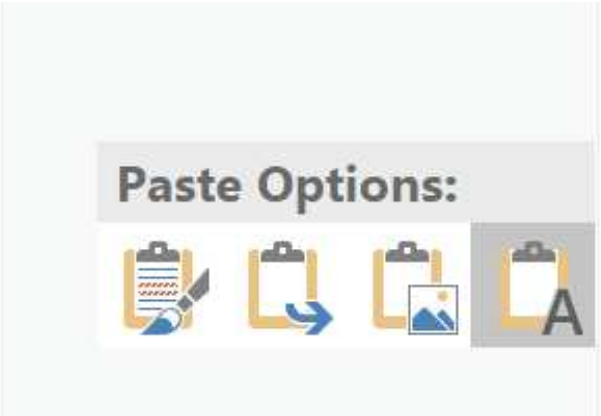

Figure 1. Use the option "Unformatted text" when copying/pasting text from other sources

A Table title should be provided before each table and all tables must be cited in the text, see an example in Table 1. Leave a blank space after each table. Introduce tables as text and not as images and avoid using vertical rules.

Table 1: Example of table layout.

ID number	Test type	Loading rate [mm/min]	Failure load F [kN]
1	Quasi-static	0.1	1.8
2	Quasi-static	5	2.4
3	Quasi-static	50	2.6
4	Quasi-static	100	2.9

2.2 Citations and references

List and number all bibliographical references at the end of the paper using the "Vancouver style". The references must be numbered in order of appearance in the document. When referring to them in the text, type the corresponding reference number in square brackets, e.g., as was described in [1], … Example of reference list is provided at the end of this document.

6. Other guidelines

3.1 Equations

Equations are implemented inline throughout the manuscript. Number equations in parenthesis aligned at the right margin. Do not use blank lines between the text and the equations. Example:

$$\frac{4}{3} = \frac{-b \pm \sqrt{b^2 - 4ac}}{2a} \quad (1)$$

Refer to any equation in the text with the number and Eq., e.g. "Solving Eq. (1) for …"

Always check the equations after conversion of the Word document to pdf.

3.2 Lists

  doi:10.5075/epfl-298799_978-2-9701614-0-0

Lists must be implemented in the manuscript text by using bullets, letters, numbers, … The following format should be adopted.

- List level 1
    - List level 2
        - List level 3

3.3 Page numbers and footnotes

Do not add page numbers and do not alter the header/footer of the template. Do not add any footnotes. Page numbers and the footnotes related to DOI will be added automatically at a later stage.

Acknowledgements

This research was founded by the EU LIFE project “CIRCE – CIRcular economy model for Carbon fibrE prepregs” LIFE18 ENV/IT/000155.

7. References

1. Mays GC, Hutchinson AR. Adhesives in civil engineering. Cambridge University Press. 1992.
2. Sims FA. Applications of resins in bridge and structural engineering. International Journal of Cement Composites and Lightweight Concrete 1985; 7:225-32.
3. Michels J, Sena-Cruz J, Czaderski C, Motavalli M. Structural strengthening with prestressed CFRP strips with gradient anchorage. Journal of Composites for Construction 2013; 17:651-661.
4. …

  doi:10.5075/epfl-298799_978-2-9701614-0-0

TRANSIENT THERMAL ANALYSIS AND THERMAL AGEING BEHAVIOR OF CARBON FIBRE REINFORCED PLASTICS FOR "GREEN" MOULDING OF AEROSPACE GRADE COMPOSITES

Thomas Schmidt, Raimund Grothaus, Johannes Neuling

EAST-4D Carbon Technology GmbH – t.schmidt@east-4d.de

Abstract: *Carbon fibre reinformced plastics are mainly produced using metallic mould systems. In recent years also CFRP mould materials have been assessed more deeply. For resin transfer moulding processes high mechanical and thermal loads need to be considered for this new class of moulding materials. For aerospace grade CFRP moulding processes tight process tolerances occur for the homogenity of process temperatures also during instationary heating steps. Transient thermal modelling of CFRP moulds with an orthotropic material behaviour are required, therefore. Next to these thermal requirements also the life and the life prediction itself of CFRP moulds are technological key elements. A new experimental proposal for life time prediction of CFRP mould has been assessed. Having in place the digital model of the CFRP tool and experimental ageing data of the tool material on the other side, a life time prediction of the mould made of CFRP is feasible for different process conditions. The basics of a specially developed CFRP ageing modell will be presented for this purpose.*

Keywords: CFRP; failure analysis; resin transfer moulding; thermal ageing

1. Introduction

For serial production of carbon fibre reinforced plastics (CFRP) the resin transfer moulding (RTM) process is a widely used technology in aerospace and automotive. Metallic moulds are the baseline technology due to the high mechanical loadings by preform compaction as well as the RTM injection pressure. Metallic moulds are reasonably convenient for high cycles and high temperature processes, but heavy mould weights and the high heat capacities provide a significant input to the CO_2 foot print of the RTM manufacturing process. Additionally, long process times and a high energy consumption for the heating and curing process steps gives strong economic disadvantages for metallic moulds.

Sustainable RTM manufacturing processes and significant CO_2 emission benefits can be achieved by CFRP tools which offer a factor of 5 improvement of energy efficiency in comparison to steel moulds [1]. The specific energy capacity of CFRP materials is only 20 % of the steel value. In addition, the CFRP moulds offer better handling capabilities due to the significantly lower weight. The high geometrical accuracy of RTM CFRP tools is another strong benefit due to the match of thermal expansion behavior between the mould and the CFRP part itself. Significantly more expensive Invar based tools are the competitor material for this challenging feature of thermal matching behavior.

An innovative manufacturing approach by sustainable design principles of the RTM mould has mainly accomplished some of the disadvantage of the reduced life time for CFRP moulds in comparison to steel moulds. The technical innovation by smart material set-up – adapted

  doi:10.5075/epfl-298799_978-2-9701614-0-0

mould design – integrated electrical heating system – advanced simulation methods add significant value to the composites industry. Sustainable design principles lead to new CFRP-tools with proven lifetimes of 500 – 1000 production cycles already. Current technology targets aim for 10,000 cycles in the near future, which is a sufficient mould life for many aerospace CFRP structures. For this life target a reliable RTM temperature – lifetime modelling is the key element and has been established to achieve sustainability targets for "green" CFRP production processes with a factor of 5 reduced CO_2 footprints in comparison to metallic tools. The ageing behavior analysis is demonstrated for a CFRP mould, which is used for aerospace grade CFRP mouldings according to the manufacturing set-up shown in Fig. 1.

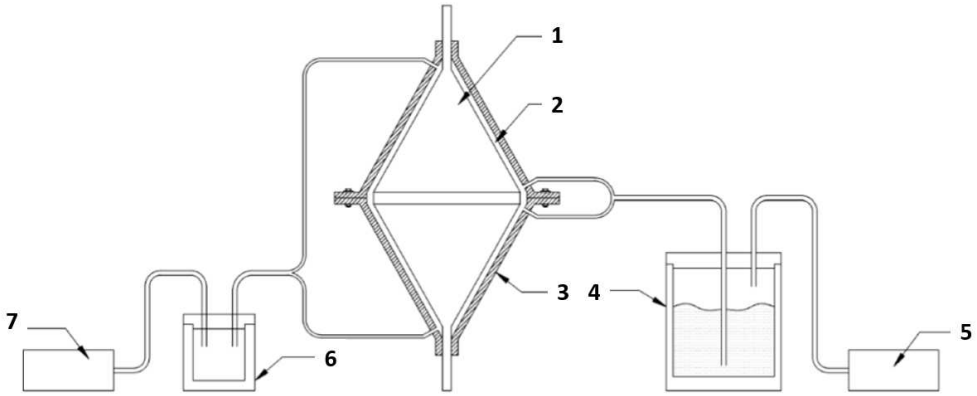

Figure 1. Schematic structure of a RTM tool system for aerospace grade composite moulding

2. Transient thermal analysis

In order to determine the ageing of the tooling material, a transient thermal analysis is carried out in the first step, which maps the complex temperature profile actually occurring in the individual layers. As shown in Fig. 2, only a 45° partial segment of the upper mold half is calculated due to symmetry. The input data for the thermal analysis are listed in Table 1:

Table 1: Input data of the thermal analysis for all components of the RTM mould

Property	$\rho\ \left[\frac{g}{cm^3}\right]$	$\kappa_{\parallel}\ \left[\frac{W}{m\,K}\right]$	$\kappa_{\perp}\ \left[\frac{W}{m\,K}\right]$	$c_p\ \left[\frac{J}{kg\,K}\right]$
Moulded part (GF+CF)	1,73	5,57	0,6	710
CFRP Mould/ Winding Mandrel	1,55	10,29	0,65	1188
Steel	7,83	55,7	-	434
Air (sea level)	1,2E-3	2,4E-2	-	1005
Polyurethane Foam	4,5E-2	3,5E-2	-	1500
GFRP Isolation	1,97	0,84	0,55	1204

  doi:10.5075/epfl-298799_978-2-9701614-0-0

The density ρ, thermal conductivity parallel $\kappa_{\parallel}$, and transverse $\kappa_{\perp}$ to the fibre direction and the specific heat capacity c_p are given here. The number of different material properties shows the thermal complexity of this tool system and the need for a numerical solution strategy. The glassfibre reinforced plastic (GFRP) and polyurethane foam are insulating layers of the actual tooling made of CFRP and surrounded by air. The tooling also has an integrated heating system. The part made of CF and GF hybrid material is positioned inside the mould. The innermost layer is the winding mandrel made of CFRP with a steel core construction.

For the numerical simulation the solver NX Nastran (solvertype "SOL 159 Transient Nonlinear Heat Transfer") of the software Simcenter NX is used. The result of the transient thermal analysis is the temperature distribution shown in Fig. 2 (right) for a heating time of 5,868 sec. The superior isolation behavior of the CFRP RTM mould is clearly visible by the low surface temperatures.

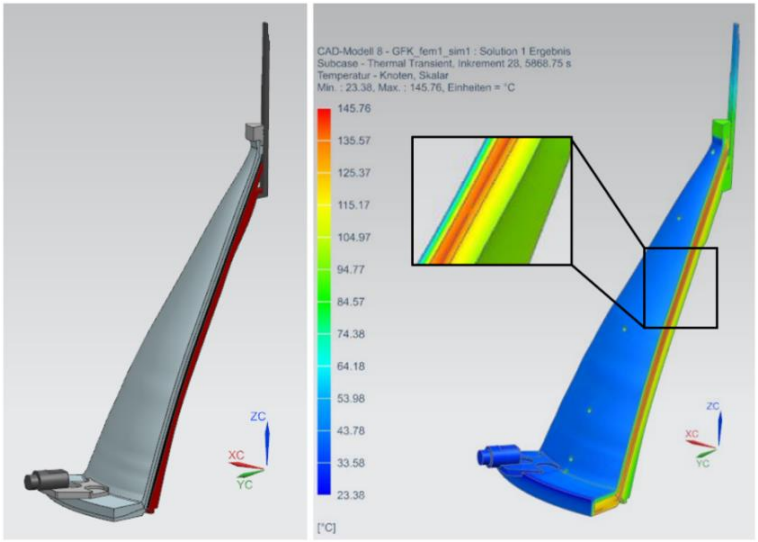

Figure 2. Pre-Processing model of 45° tooling segment (left), Post-Processing contour of temperature distribution (right)

3. Principals of ageing simulation

Based on the transient temperature distribution of the thermal FE model, the time- and temperature-dependent degradation of the tooling material can be estimated efficiently using an phenomenological model. The resulting degraded material properties can be used in an fatigue model to determine damage in the tooling system depending on the number of cycles and thus the expected life time [2]. Fig. 3 shows the flow chart of the progressive damage fatigue model used in this work, where m_r and R_r are the normalized residual mass and strength which depend on the temperature T and time t, respectively. The ageing factor λ, damage parameter δ, damage variable D, deflection ε and leakage rate q_P are used, furthermore. The subsection flow chart of the phenomenological thermal-oxidative ageing model to determine the ageing factor is presented in Fig. 4. The simplified ageing factor $\frac{P}{P_0}$ is a shortcut when ageing prediction into the future is not required, where P is any property of interest and P_0 its static initial value. This model is originally based on the work of *Flore* [3] and was modified and further developed to be used for lifetime prediction of composite RTM-tooling systems and arbitrary 3D stress states.

  doi:10.5075/epfl-298799_978-2-9701614-0-0

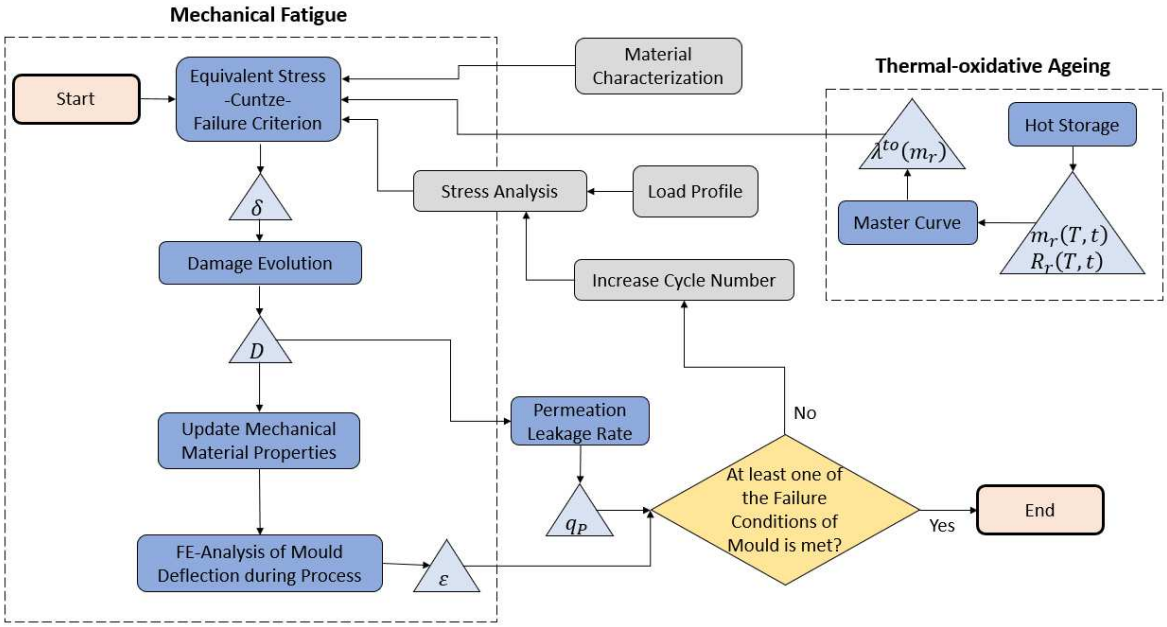

Figure 3. Flow chart of the progressive damage fatigue model used for lifetime prediction of composite tooling systems with integrated thermal-oxidative ageing model

The model meets the following criteria:

- Consideration of any multi-axial load conditions and stress states
- Consideration of relevant influences such as mean stress, temperature and fibre volume fraction
- Simple integration of ageing factor λ
- Introduction of a damage variable D as a measure of the degree of damage at any point in the service life
- Mapping of stiffness degradation over lifetime
- Efficiency of the calculation under fulfillment of above mentioned criteria

To investigate the thermal-oxidative aging factor (Fig. 4), accelerated thermal aging tests are performed in the first step with samples in ovens and characteristic residual mass curves versus time are determined for 6-7 different temperatures typically in the range of 70 % - 115 % of the glass transition temperature (T_g) of the matrix system. Subsequently, the curve of residual strength over time at one high temperature is needed only. A certain residual strength is always associated with a certain residual mass, regardless of the ageing history. Therefore, the master curve can also be constructed with only one residual strength curve. *Flore* [3] already showed this behavior for epoxy resin composite specimens and Fig. 5 confirms this relationship also for bismaleimide (BMI) resin composite specimens at ageing temperatures up to 115 % of T_g.

The prediction of the residual mass trends is carried out with the aid of the temperature-time superposition principle (TTS) [4], which is based on the *Arrhenius* law, i.e. the increase in the reaction rate and thus the aging with an increase in temperature. Thus, an acceleration factor AF can be formulated according to Eq. (1),

  doi:10.5075/epfl-298799_978-2-9701614-0-0 published under CC BY-NC 4.0 license

$$AF\left(T, T_{ref}\right) = exp\left(\frac{E_a}{k} \times \left(\frac{1}{T_{ref}} - \frac{1}{T}\right)\right) \tag{1}$$

where E_a is the activation energy, k is the *Boltzmann* constant, and T_{ref} is a reference temperature. An equivalent time can be calculated from Eq. (2) [5],

$$t_{eq} = t_{ref} \times AF\left(T, T_{ref}\right) \tag{2}$$

i.e. the time to reach a property level, whereby this time is known for a different temperature. In this relation, the activation energy is assumed to be constant, which according to *Arrhenius* is only permissible for temperatures $\leq T_g$ of the matrix. However, as shown in Fig. 6 using the interlaminar shear strength (ILSS) samples with a BMI matrix and high strength carbon fibres, the temperature-time superposition for up to 115 % of T_g nevertheless leads to a straight curve and is thus applicable because the deviation of the activation energy is only small and disappears on the logarithmic time axis.

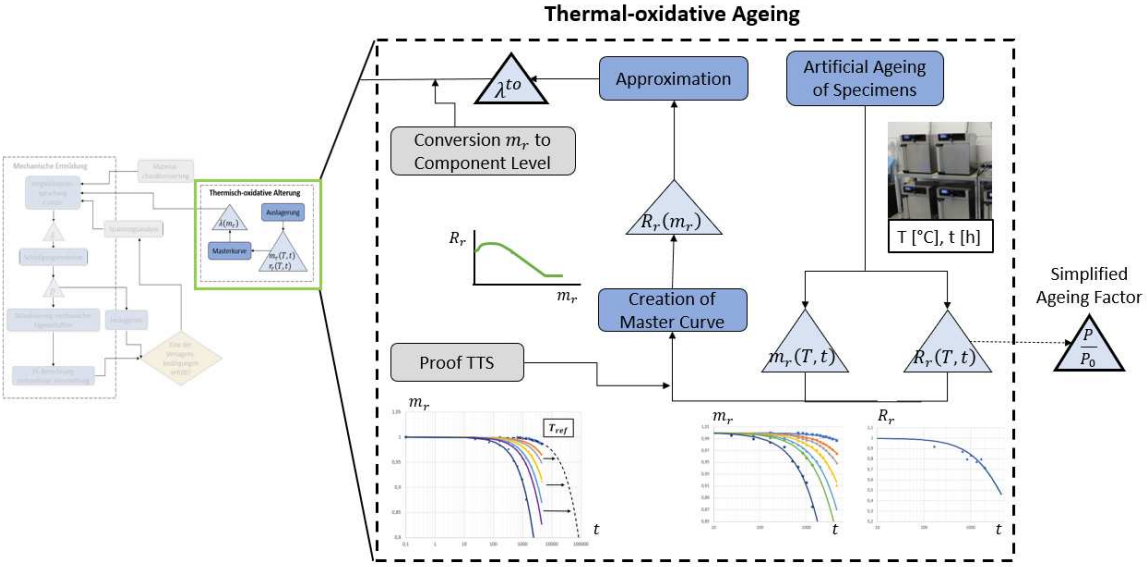

Figure 4. Subsection flow chart of the phenomenological thermal-oxidative ageing model

By creating the master curve and the subsequent linear approximation, the thermal-oxidative ageing factor can be determined directly, which is defined in Eq. (3),

$$\lambda^{to}\left(m_{r,sp}(T,t)\right) = R_r = \frac{R}{R_0} \tag{3}$$

where the indicator sp stands for the residual strength on specimen level. The main differences between specimen and component level that is relevant for the oxidative ageing mechanisms are the different surface-to-volume-ratios. By scaling the ratios, oxidative damage can be estimated at the component level. This thermal-oxidative ageing factor is than used multiplicatively in the progressive damage fatigue model from Fig. 3 so that it weakens the corresponding base strength. Since the *Cuntze* failure criterion [6] is used as basic equation, Fig. 7 shows the 5 failure modes of the 3D-*Cuntze* criterion with the inclusion of the newly obtained thermal-oxidative ageing factors. From these equations, the damage parameters δ can be calculated, which take into account the influence of the mean stresses [3].

  doi:10.5075/epfl-298799_978-2-9701614-0-0

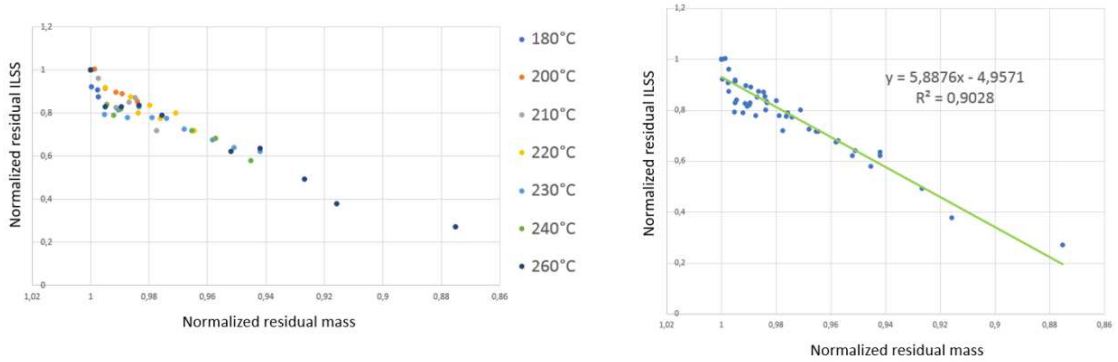

Figure 5. Master curve from the plot of residual strength versus residual mass of ILSS specimens (CFRP with BMI matrix)

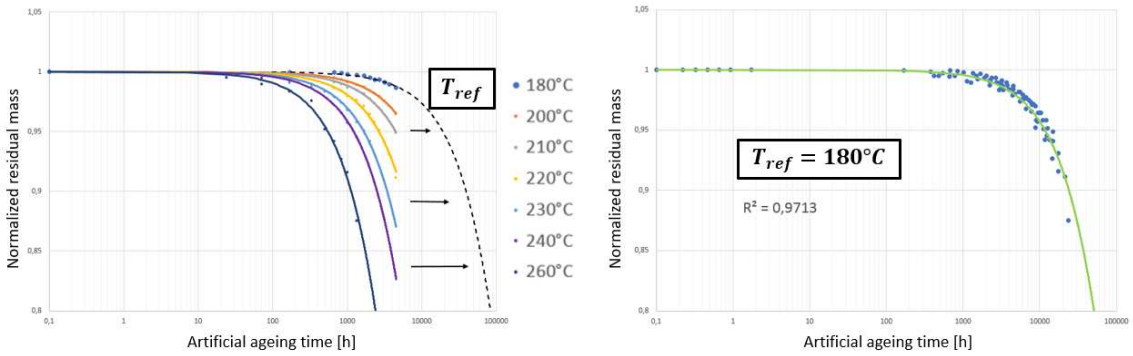

Figure 6. Horizontal shift of residual mass curves of ILSS specimens (CFRP with BMI matrix) to a reference temperature using temperature-time superposition

Using a suitable equation for the damage evolution, the damage variable D can then be calculated, which is a measure of the degree of damage in the material and is defined from 0 (no damage) to 1 (totally damaged). The damage variable D is then used to update and check the failure-related process variables (deflection due to injection pressure ε and leakage rate of air into the tooling q_P) for each cycle.

$$\text{FF1: } Eff^{\parallel\sigma} = \sigma_{eq}^{\parallel\sigma} / R_{\parallel}^{t} \quad \text{mit} \quad \sigma_{eq}^{\parallel\sigma} = \varepsilon\, E_{\parallel}^{t},$$

$$\text{FF2: } Eff^{\parallel\tau} = \sigma_{eq}^{\parallel\tau} / R_{\parallel}^{c} \quad \text{mit} \quad \sigma_{eq}^{\parallel\tau} = \varepsilon\, E_{\parallel}^{c},$$

$$\text{IFF1: } Eff^{\perp\sigma} = \sigma_{eq}^{\perp\sigma} / R_{\perp}^{t} \quad \text{mit} \quad \sigma_{eq}^{\perp\sigma} = \left[(\sigma_2+\sigma_3) + \sqrt{(\sigma_2-\sigma_3)^2 + 4\tau_{23}^2}\right],$$

$$\text{IFF2: } Eff^{\perp\tau} = \sigma_{eq}^{\perp\tau} / R_{\perp}^{c} \quad \text{mit} \quad \sigma_{eq}^{\perp\tau} = \left[b_{\perp\perp} \cdot \sqrt{(\sigma_2-\sigma_3)^2 + 4\tau_{23}^2} + (b_{\perp\perp}-1)(\sigma_2+\sigma_3)\right],$$

$$\text{IFF3: } Eff^{\perp\parallel} = \sigma_{eq}^{\perp\parallel} / R_{\perp\parallel} \quad \text{mit} \quad \sigma_{eq}^{\perp\parallel} = \left\{\frac{\left[\sqrt{b_{\perp\parallel}^2 I_{23-5}^2 + 4 R_{\perp\parallel}^2 \left(\tau_{31}^2+\tau_{21}^2\right)^2} + b_{\perp\parallel} I_{23-5}\right]}{2 R_{\perp\parallel}^3}\right\}^{0.5},$$

$$Eff^{m} = \sum_1^5 Eff^{mode} = \left(\frac{\sigma_{eq}^{\parallel\sigma}}{R_{\parallel}^{t} \times \lambda_{\parallel,t}^{to}}\right)^{m} + \left(\frac{\sigma_{eq}^{\parallel\tau}}{R_{\parallel}^{c} \times \lambda_{\parallel,c}^{to}}\right)^{m} + \left(\frac{\sigma_{eq}^{\perp\sigma}}{R_{\perp}^{t} \times \lambda_{\perp,t}^{to}}\right)^{m} + \left(\frac{\sigma_{eq}^{\perp\tau}}{R_{\perp}^{c} \times \lambda_{\perp,c}^{to}}\right)^{m} + \left(\frac{\sigma_{eq}^{\perp\parallel}}{R_{\perp\parallel} \times \lambda_{\perp\parallel}^{to}}\right)^{m}$$

Figure 7. The five failure modes for fibre fracture (FF) and inter-fibre fracture (IFF) of Cuntze failure criterion according to [6] with newly integrated thermal-oxidative ageing factors λ^{to}

The integration of D into the material law by an update of the material properties is widely understood for the analysis of component deflection using finite element analysis [7]. The

  doi:10.5075/epfl-298799_978-2-9701614-0-0 published under CC BY-NC 4.0 license

efficient calculation of q_P depending on D is a new feature of high interest and will be discussed in chapter 4, therefore.

4. Permeation leakage behavior of aerospace grade composite tools

The cyclic thermo-mechanical loads during the RTM process lead to ageing and fatigue of CFRP tooling materials which results in the formation of IFF micro cracks. These cracks are the main reason for the degradation of mechanical properties of the tooling. They also form paths which allow more easy permeation of air. This fatigue cracking behavior can also be observed for the permeation leakage rate data presented in Fig. 8 for different temperatures and CFRP systems. The wide scatter between academic and industrial leakage allowable standards is obvious and reflects the strong demand for future research work to this matter.

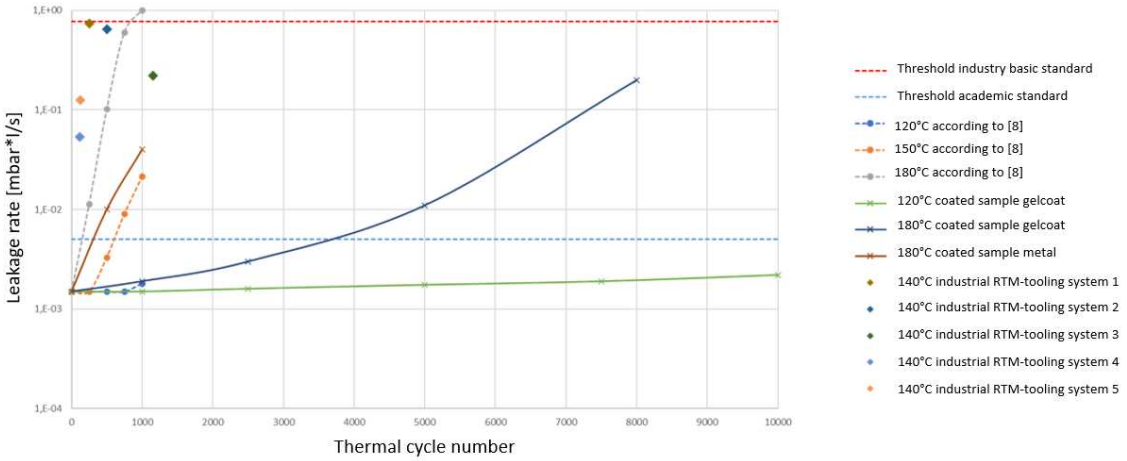

Figure 8. Industrial and academic allowables for air permeation leakage rates and experimentally measured leakage rates of CFRP tooling and material systems depended on temperatures and thermal cycles

The results of *Kammerhofer* [8] show the close relation between micro crack density or rather damage state induced by thermal-oxidative ageing and permeation leakage rate. The equation for the permeation leakage rate is shown in Eq. (4) [9],

$$q_P = \frac{P_A \times A \times \Delta p}{l} \tag{4}$$

with the permeation coefficient P_A, cross-sectional area of the permeation path A, pressure gradient Δp and material thickness l. Considering P_A as a function of D and using the results from [8] to approximate the relation between those variables one can estimate the value of P_A for a specific ageing history. With the permeation coefficient value a finite element analysis can be carried out to calculate q_P. Due to the similarity of permeation leakage rate and heat flux which can be calculated according to Eq. (5),

$$q_h = \frac{\kappa \times A \times \Delta T}{l} \tag{5}$$

with the thermal conductivity κ and temperature gradient ΔT, a thermal flow analysis through an identical geometry is feasable to calculate the permeation rate from the resulting heat flux. For this procedure the characteristic relation between P_A and κ is calibrated once. The numerical assessment of the permeation leakage behavior of complexly shaped tool

  doi:10.5075/epfl-298799_978-2-9701614-0-0

geometries could be performed using this approach. Next to RTM moulds also hydrogen pressure vessels could be assessed regarding their CFRP leakage characteristics.

5. Summary and outlook

The life limitations of CFRP moulds can be accomplished by a deep understanding of the ageing behavior of the CFRP mould material. This ageing behavior is closely aligned to the thermal history of the mould material especially for mould working conditions close to the T_g of the CFRP mould material. Within this paper a process is presented, which is based on a numerical analysis of the thermal profile of the tool. This thermal profile specifies the ageing conditions of the mould material. Using the principles of the *Arrhenius law* the life time of a CFRP mould can be predicted. This life is typically limited by resin fatigue which causes matrix cracks with consequent air leakage of the RTM mould afterwards. The presented workflow gives the opportunity to assess this composite failure behavior for the high temperature application of the CFRP mould. The principles of this analysis procedure allow a better usage and exploitation of this innovative and sustainable CFRP tooling proposal for future aerospace grade CFRP structures in low to medium volume production scenarios using the RTM technology. The high accuracy moulding capability of these CFRP moulding tools is next to the superior CO_2 footprint a significant system advantage. Future demand for more energy efficient production processes will further accelerate this innovative moulding material and tool design.

Acknowledgements

Some parts of this research work have been funded by the German ministry of education and research (BMBF) and by the state bank of Saxony (SAB).

6. References

1. Arikan E, Kammerhofer P, Reppe M, Weiland J. Project Report LEEToRB. 2015. https://cordis.europa.eu/docs/results/325/325936/final1-3_leetorb_final_publishable_summary_report.pdf
2. Eulitz J, Kroll S, Grothaus R. Computational methods for fatigue life design of modern fibrous composite materials: overview and perspectives; NAFEMS Seminar 2010 Wiesbaden
3. Flore D. Experimentelle Untersuchung und Modellierung des Schädigungsverhaltens faserverstärkter Kunststoffe unter thermomechanischer Langzeitbeanspruchung. Dissertation ETH Zurich. 2017.
4. Gates T. The physical and chemical ageing of polymeric composites. In: Ageing of Composites. Elsevier; 2008. P. 3-33.
5. Cardon A, Fukuda H, Reifsnider K. Progress in durability analysis of composite systems. Materials Science. 1996 A.D.
6. Koord J. Grafische Benutzeroberfläche für das Versagenskriterium nach Cuntze im ebenen Spannungszustand. Deutsches Zentrum für Luft- und Raumfahrt. 2018.
7. Matzenmiller A, Lubliner J, Taylor RL. A constitutive model for anisotropic damage in fiber-composites. Mechanics of Materials. 1995 A.D.
8. Kammerhofer P. Analyse der Haltbarkeit von Werkzeugen aus carbonfaserverstärkten Kunststoffen. Dissertation TU München. 2018.
9. Schlick-Hasper E. Analyse, Charakterisierung und Modellierung der Gasleckageraten repräsentativer Bauarten von Gefahrgutverpackungen. Dissertation Nr.161 BAM. 2018.

  doi:10.5075/epfl-298799_978-2-9701614-0-0

SENSITIVITY FACTOR ANALYSIS AND OPTIMIZATION OF RECYCLED GLASS FIBRE COMPOSITE WASTE REINFORCED FE-RICH INORGANIC POLYMER USING TAGUCHI AND ANOVA METHODS

Yixue Zhang[a,b], Yiannis Pontikes[a], Larry Lessard[b], Aart Willem Van Vuure [a]

a: KU Leuven, Department of Materials Engineering –yixue.zhang@mail.mcgill.ca
b: McGill University, Department of Mechanical Engineering

Abstract: *This work develops an optimized recycling route that provides a solution for two forms of waste. Mechanically recycled glass fibre reinforced composite (GFRP) waste (including all resin residues) was coldly incorporated into a Fe-rich inorganic polymer (IP), a by-product of the non-ferrous metal industry, to produce sustainable reinforced cementitious material. Different mechanical techniques to improve the efficiency of the grinding process and retain fibre length have been investigated. Sensitivity factor analysis on the mechanical performance of the final products was conducted by using a Taguchi design method and ANOVA, and a proposed reasonable optimization was suggested. The flexural strength enhancement compared to the state-of-the-art stands out, reaching a gain of 215% (amounting to 27MPa); the improvement in compressive strength is at a more moderate level of about 28% (reaching 101MPa) at 7-day curing. The results show the success of the optimization actions for the recycling route.*

Keywords: Glass fibre waste; Inorganic polymer; Mechanical recycling; Taguchi design

1. Introduction

The world needs a low carbon revolution, and processes to recycle end-of-life (EoL) glass fibre reinforced polymer (GFRP) with a thermoset matrix are integral to sustainable development. Due to the characteristics of GFRP recycling, such as the non-remoulding nature of thermoset resins, the low price of virgin fibres (2€/kg), low calorific value and high left-over burnt ash content, mechanical recycling shows more promise in practice [1].

To improve the cost-effectiveness of mechanical recycling, a recycling route with low energy input and end-use applications with high performance is highly desired. The current research group has optimized a promising recycling route based on previous work [2] by replacing the disc milling with a roller mill, where the recycled GFRP materials (including resin) are cold blended into a Fe-rich inorganic polymer (IP) (a by-product of the non-ferrous metal industry) to produce sustainably reinforced cementitious materials. By using roller milling, a higher percentage (79 wt.%) of recycled slender glass fibres (rGFs) (32 mm, aspect ratio of 23) was yielded, compared to 22 wt.% of fibrous recyclate with a maximum fibre length of around 2-5mm and an aspect ratio of 5-6, obtained by disc milling.

To further optimize the mechanical performance of recycled GFRP reinforced inorganic polymer (rGF-IP), grasping the effects of the different parameters on the mechanical properties of rGF-IP is necessary. However, insufficient research has been carried out so far on the parameter sensitivity analysis of rGF-IP. According to the authors, the available data are restricted in three ways. First, the Fe-rich inorganic polymer in this paper is a novel secondary product of non-ferrous metal industries; many of its properties have not been studied widely. Its high iron content (48.7 wt%) leads to different fresh/hardened matrix properties compared with OPC

  doi:10.5075/epfl-298799_978-2-9701614-0-0

(Ordinary Portland Cement) or commonly-used geopolymers, such as metakaolin and fly ash. Secondly, past studies mainly focused on incorporating pure/virgin glass fibres in cement, with little use of various GFRP waste (fibre, powder, mixture and scrap) simultaneously. These wastes generally have more complex characteristics, such as multiple length distribution, fluffiness, and irregular resin residues attached to the fibres. The type of reinforcements, fibre content, orientation and distribution, the pore structure of the cementitious matrix and fibre-matrix interaction all matter in the final performance. Lastly, previous studies mainly obtained results with a particular production method, and those studies did not explore the effects of different mixing technologies on the composites[2,3]. Parameters such as mixing technology, sequence, time, speed and temperature can alter the paste's entrapped air and fibre dispersion [4].

From the previous analysis, many factors affect the rGF-geopolymer and sometimes interact, and the relationship between various factors is complex and difficult to determine through the results of experiments. Therefore, a sensitivity factor analysis of the mechanical properties of rGF-IP through experiments is necessary. The Taguchi method was used to design experiments and, together with Analysis of Variance (ANOVA), to explore the significance of various factors on the final composites' properties. Effects of three parameters, including the fibre aspect ratio, fibre content and the producing method, on the flexural/compressive strength, Young's modulus, porosity distribution, and fibre orientation of the rGF-IP were analyzed, and a reasonable optimization suggestion was proposed.

2. Materials and methodology

2.1 Materials

The Fe-rich inorganic polymer (IP) used in this study originates from a secondary non-ferrous metallurgical process. An activating solution (SiO_2/K_2O = 2 and H_2O/K_2O = 20, by molar ratio) was employed to synthesize the IP. The GFRP waste samples were acquired from in-house GFRP flat panels with epoxy resin and E-glass fabric (52wt.%). The optimized milling route for mechanical processing of in-house GFRP waste includes (Figure 1 (1)): (1) primary shredding of GFRP; (2) roller milling of the shredded material; (3) mixing the crushed material with medium speed for 3mins with water in the mixing container; and (4) drying the milled GFRP waste at 50°C for 24h, then sieving by multiple staged sieves with varying mesh sizes.

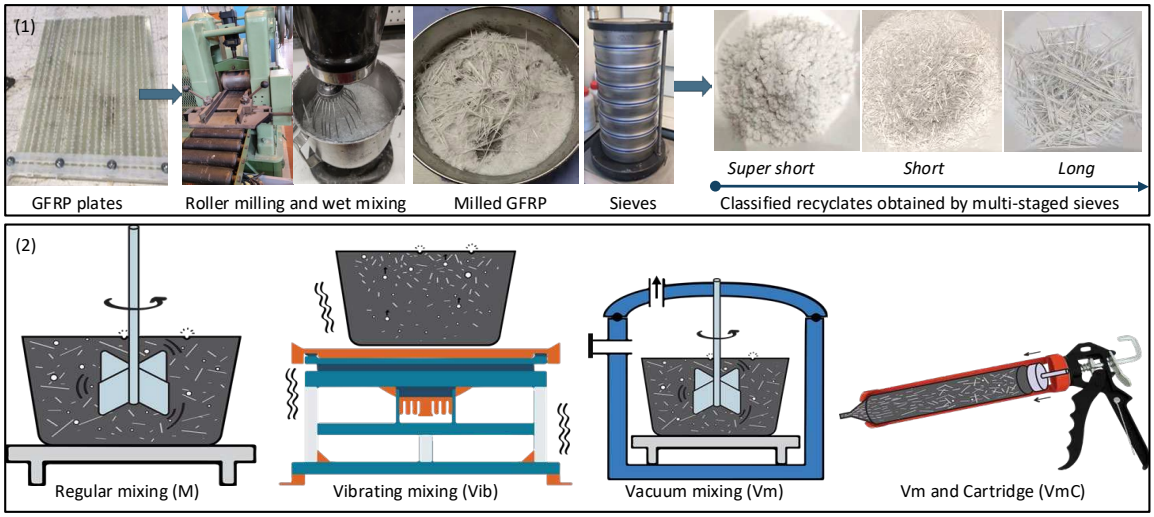

Figure 1. (1) Mechanical milling processes of the GFRP waste; (2) mixing technologies.

2.2 Taguchi orthogonal design

Factor sensitivity analysis was achieved by using the Taguchi orthogonal method with three parameters and four levels (Table 1). The producing method (Pm), rGFs aspect ratio (Ar), and fibre content (Fn) were selected as affecting parameters. Settings of parameters were determined by the L_{16} (4^3) orthogonal array with four levels and four specimens for each combination, giving 64 specimens in total.

Table 1. Experimental range and levels of variables

Control variables	Symbol	Unit	Levels			
			1	2	3	4
Producing method	*Pm*	-	M	Vib	Vm	VmC
rGFs aspect ratio	*Ar*	mm/mm	N/A	SS	S	L
rGFs content	*Fn*	vol%	0.5	1.5	3.5	6

M: Regular mixing Vib: Vibrating mixing Vm: Vacuum Mixing VmC: Vacuum mixing and cartridge.

Mixtures of different recyclates and contents underwent different mixing technologies: regular mixing (M), vibrating mixing (Vib), vacuum mixing (Vm), and vacuum mixing with a cartridge to squeeze the paste out into the mould (VmC) (illustrated in Figure 1(2)). The regular mixing time was set to 5mins. For samples made by Vib, a vibrator was used after mixing; the mixture was placed on a shaker table and vibrated for 5mins at a medium speed to release the entrapped air before casting. In the case of Vm, a reduction from ambient pressure to 100 mbar was established by a vacuum pump, and the 100 mbar was kept until the end of the mixing procedure. In terms of VmC, the smooth mixture was placed in a cartridge and was squeezed out into the mould (2cm*2cm*8cm). All samples were cured under controlled conditions (20±2°C and relative humidity not less than 50%) for 24h before demolding and left to cure until the curing time (7 days). In the second stage, experiments were performed. Response values, porosity (P) in the matrix, fibre orientation distribution (α), flexural strength (Fs), compressive strength (Cs), and Young's modulus (Es) were obtained. Minitab 19 was used for analyzing the experimental results. The rank of selected parameters in terms of contribution to response values was done via signal-to-noise ratios (S/N) and analysis of variance (ANOVA). Here, "signal" implies the (wanted) mean value while "noise" represents the (unwanted) standard deviation term [5]. A higher S/N ratio indicates lower variability in the process is ensured by maximizing the response.

2.3 Testing methods

Effects of fibre orientation are considered by using a so-called orientation factor α, obtained by Eq.(1), which represents how freely the fibre can rotate in all directions in the bulk zone. The lower the α, the higher the isotropy of the analyzed cross-sectional surface. For example, a value of 0.5 represents a 3D isotropic condition where fibres could rotate freely in all directions [6].

$$\alpha = \frac{n}{th} = n\frac{A_f}{V_f A} \quad (1)$$

Where n is the number of observed fibres, th is the theoretically expected number of fibres, A_f is the average cross-sectional area of the observed fibres, V_f is the fibre volume fraction, and A is the total cross-sectional area of the composite. The measurements of n and A_f are challenging by visual counting, as individual fibre diameter is around 15 μm and the recycled fibre bundles have irregularity and varying cross-sections. An easy recycled fibre counting

  doi:10.5075/epfl-298799_978-2-9701614-0-0

method that can automatically and spatially detect fibres was developed by micro-computed tomography (µ-CT). The reconstructed images were analyzed by Avizo software (Figure 2).

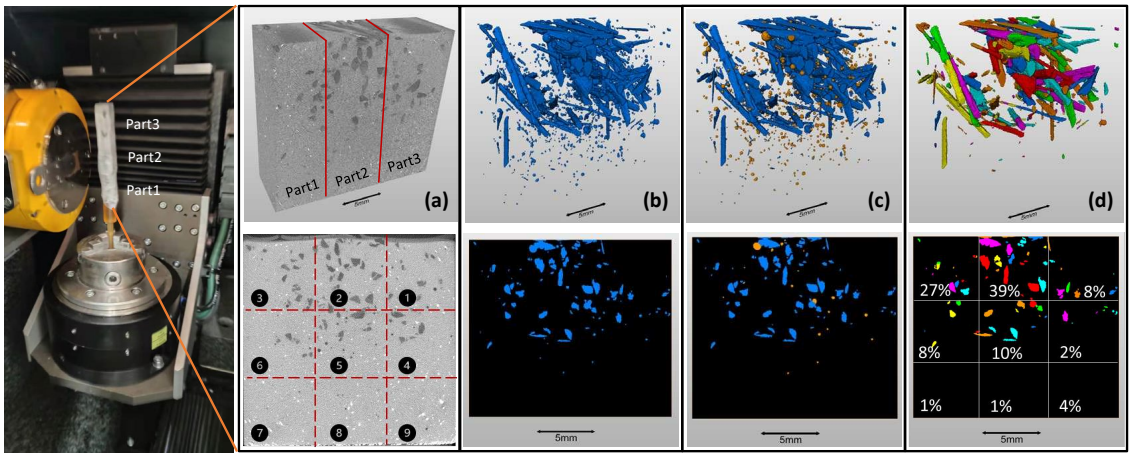

Figure 2. (a) IP block was sawn into nine parts and scanned; (b) a dual-threshold binarisation removed IP grains; (c) pores were further removed by sieving out sphere-like objects; (d) the recycled fibres were separated, and numbers (n) and cross-sectional areas (Af) were measured.

The porosities for hardened reinforced samples were measured before the mechanical test by µ-CT and mercury intrusion porosimetry (MIP). µ-CT was used to detect macro air voids (>200µm); MIP was used to analyze capillary pores and micropores (4nm-200µm). Their sum up is the total porosity of the sample. The mechanical tests of rGFs-IP composite samples were performed according to European standard EN 196-1:2005 [7]. In the bending case, 3D digital image correlation (3D DIC) determined the strain fields of rGFs-IP samples. The slope of the stress-strain curve at the initial linear stage was measured as Young's modulus.

3. Results and discussion

The S/N ratio and contribution of selected factors to rGFs-IP performance are shown in Figure 3.

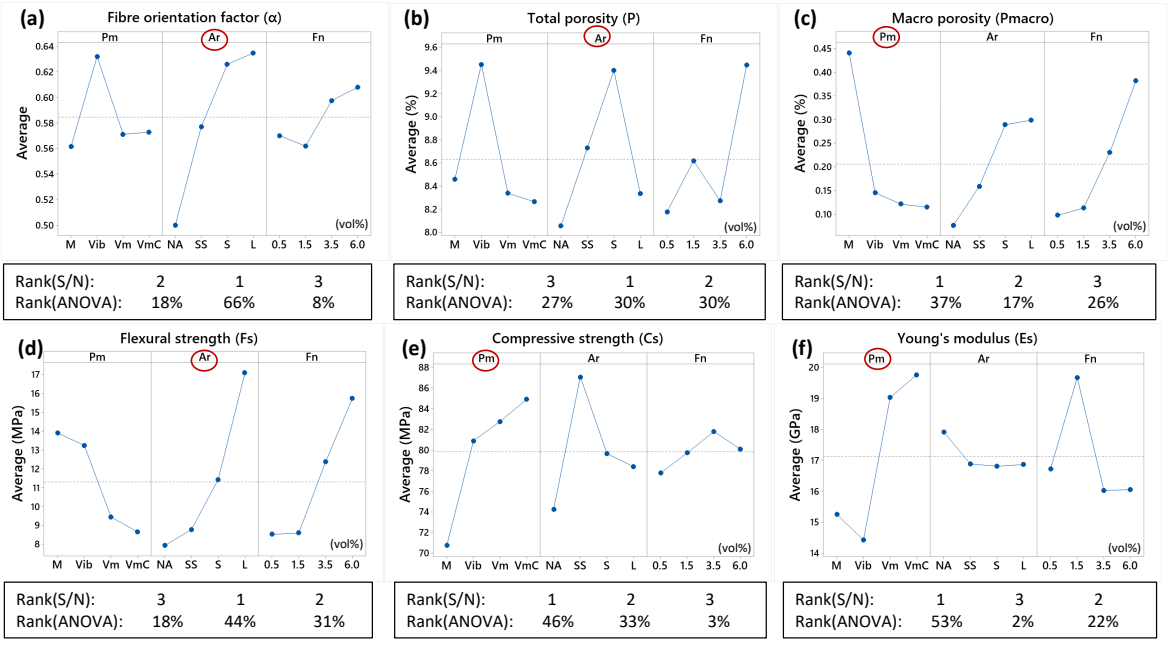

Figure 3. Effects of selected parameters on the rGFs-IP performance.

3.1 Fibre orientation distribution (α)

The contribution percentages in ANOVA and the S/N ratio indicated that the fibre aspect ratio (Ar) was the primary affecting parameter for the fibre orientation distribution. As the fibre length increases, the direction of glass fibre in the mixture moves further away from a 3-D random condition and tends to approach a 2-D alignment due to the influence of the mould wall. This effect was even more apparent in the case of L-type rGFs, whose average fibre length was close to or exceeded the width of the mould. During the casting, the boundaries restricted the random orientation of the fibres, forcing fibres (especially near the edge) to align longitudinally.

The production method (Pm) was the second significant factor affecting fibre orientation. Samples produced by vibration (Vib) had the highest average fibre orientation factor values compared to the other three methods. It is worth noting that the vibration period was 5mins in the current study. Since the impregnated glass fibre is much lighter than the IP paste when the fibre IP mixture vibrates, the fibres tend to float up and reorientate horizontally during the vibration process. In the current case, the fibre content (Fn) seems to be a negligible factor, and this was probably due to the sufficient mixing time and the good workability of the fresh IP mixture, which allowed rGF to be dispersed in the paste well.

3.2 Porosity and pore distribution (P)

MIP showed that most pore volumes were related to micropores and capillaries for pure IP samples. These originated from the mixing operations between the solid components of the hydrated slurry, with only 0.2%-0.5% porosity by volume above 15 μm, regardless of the production method. Figure 3(b) shows that all selected parameters significantly affected the total porosity (P). Both S/N ratio and ANOVA showed that the fibre length (Ar) was marginally the most influential factor for P. This is because long fibres tend to get inhomogeneously dispersed and form agglomerates, leading to excessive void formation due to poor compaction. The results also pointed out that S-type rGFs introduced more porosity than L-type rGFs. The S-type has a rougher surface with curling and branching and can be easily agglomerated, resulting in significantly more pores entrapped between fibre bundles. Surprisingly, in terms of exploring production methods (Pm) to reduce porosity, the average porosity value indicated vibration as ineffective for removing micropores and capillaries. As shown in Figure 3(c), Pm was found to significantly alter the number of large macro voids trapped in the matrix. The current study observed an approximately 72% decrease in air content by vacuum mixing. Studies on concrete in the open literature confirmed that mixing the concrete under a reduced air pressure decreases the macro voids [4]. Using a cartridge to place the paste after vacuum mixing can further eliminate the large visible pores, which is attributed to the breakage of air bubbles in the IP touching the cartridge walls under the effects of the squeezing motion.

3.3 Flexural and compressive strength (Fs, Cs)

Figure 3 (d) and (e) depict the effects of selected parameters on means of Fs and Cs. Trends of the influence of selected parameters showed a big difference in the composite's flexural and compressive strength. It can be seen that Fs increased with rises in fibre length and fibre content. Pure IP pastes typically fail in opening mode (mode 1), and the addition of fibre can overcome such failure by providing a higher resistance to crack formation and expansion. The rGFs used in

  doi:10.5075/epfl-298799_978-2-9701614-0-0

this study, such as S- and L-types, were usually bifurcated fibre bundles and partially covered by resin residues. The ruggedness and roughness increase the mechanical interlocking and friction resistance between the fibres and IP concrete. A larger fibre aspect ratio ensures effective stress transfer over a larger section of fibre, while increasing the fibre content generally leads to enhanced composite strength, e.g., an enhanced fibre bridging effect. In the present study, Fs increased when the fibre aspect ratio increased to the maximum level of 23, and the fibre content ranged from 0.5 to 6 vol%. Even though adding a high content of long fibres introduced pores and heterogeneity, the fibre-IP binder interaction was sufficient to overcome the weakness due to the porous structure in the abovementioned fibre length/content range. This follows the laws of composites mechanics and is confirmed by the literature, where the flexural strength of composites increases when the fibre content is increased to values less than 8 vol%, regardless of the fibre type [8].

However, Cs demonstrated more irregular trends with the increase in fibre length and fibre content, as observed in the literature [9]. Compression strength at the fibre levels used is dominated by the matrix (IP) strength and for the rest strongly depends on the fibre/matrix interaction, strength and dispersion of the fibres and defects present in the material. Above a fibre content of 3.5%, adverse effects of fibres appeared, which led to a significant increase in porosity and poor fibre dispersion. This effect was more severe in multifilament (e.g. type S and L rGFs) than in single fibres (type SS). Compression strength increased significantly upon introduction of the fibres, but at higher Ar apparently, the more slender fibres buckled more easily, leading to a decrease in Cs.

The S/N ratio and ANOVA results agreed: fibre aspect ratio (Ar) was the most significant factor affecting the flexural strength (Fs), whereas producing method (Pm) contributed most to compressive strength (Cs). Although Pm showed a minor contribution to Fs, its low P-value (<0.1) indicates importance. Furthermore, opposite effects of Pm were observed on Fs and Cs: from regular mixing to combo methods, such as Vib, Vm and VmC, Fs strongly decreased whereas Cs increased significantly, which was due to their different sensitivities to the local and overall properties of the material.

3.4 Young's modulus (Es)

As shown in Figure 3(f), the elastic modulus at the initial uncracked stage (Es) was predominately governed by Pm. In contrast, the ultimate horizontal strain for the multi-cracking phase was highly dependent on the Ar. The measured flexural stress-strain curves showed quite different behaviour for the various reinforced IP materials (*Figure 4*): unreinforced IP showed a brittle character with abrupt fracture of the specimen, while rGFs-IP showed a more elastoplastic behaviour. The first stage represented a linear elastic segment with a steep slope, which represents the uncracked response of the sample. This was similar for all samples tested since apparently, in this stage, the behaviour of the prism was mainly dominated by the unreinforced IP material with an E-modulus of around 18 GPa, and the amount of added reinforcement was apparently too small to have an apparent effect; please note that glass fibre reinforced epoxy rods would have an E-modulus of approximately 35 GPa and only a few percent of these were added to the IP. As the applied load increased, the reinforced materials did not fatally crack but showed a remarkably ductile behaviour due to crack bridging by the fibres, leading to remarkably higher strength and strain-to-failure values than for the unreinforced material. As the specimen underwent multiple cracking stages, only fibres bore the load until failure due to

  doi:10.5075/epfl-298799_978-2-9701614-0-0

rupture or sliding, resulting in the formation of multiple microcracks instead of several large cracks. As a result, the ductility of the material increased. This explains the observation in Section 3.3 that fibre-related characteristics (Ar, Fn) determined Fs. Longer fibres (Ar) and a higher content of fibres (Fn) will all benefit crack bridging and lead to a higher strain to failure.

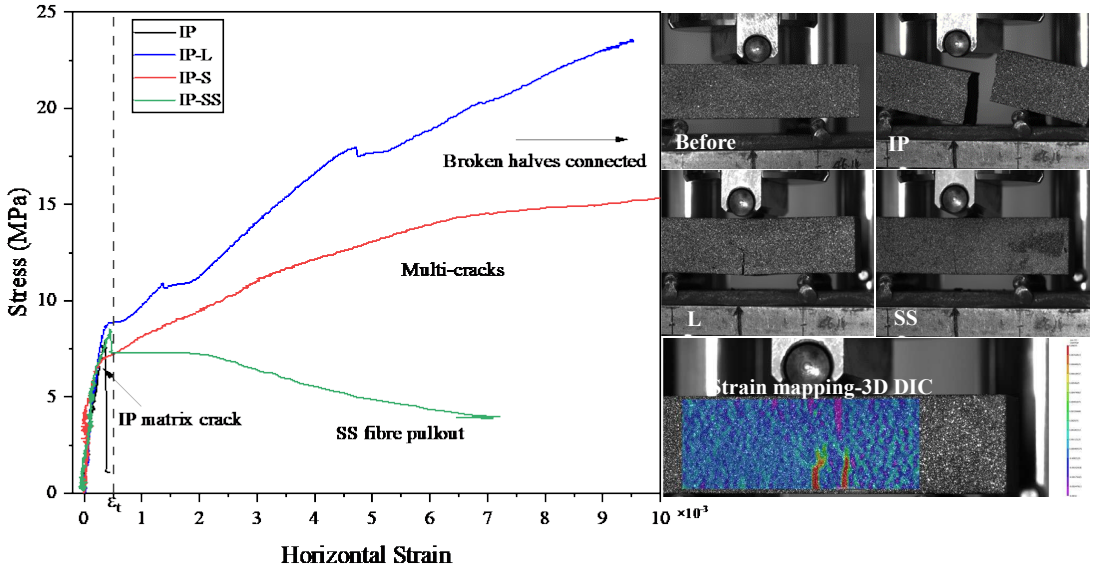

Figure 4. Typical stress-strain curves and fracture patterns for specimens.

3.5 Selection of optimum parameters and their effectiveness

Using the Taguchi method, it was found that the predicted optimum parameters to obtain a high compressive strength (expected value was 93 MPa) was the addition of 3.5 vol% of super short rGFs to the IP and the use of vacuum mixing to mix and a cartridge to place the mixture (SS-3.5%-VmC). The best parameters to obtain high flexural strength (predicted value was 24 MPa) were the addition of 6 vol% of long rGFs and vibratory placement of the mixture (Vib-L-6%). For validating the Taguchi predicted optimum conditions, confirmation tests were conducted. The measured compressive strength for the SS-3.5%-VmC sample reached 101 MPa (std. 6.7MPa, Fs 9.1MPa) and the flexural strength for Vib-L-6% amounted to 26.7 MPa (std. 0.9 MPa, Cs 68.6MPa) at 7 days of curing.

Outcomes of the current optimized recycling route for GFRP waste-reinforced Fe-rich inorganic polymers are promising: the flexural strength enhancement compared to the state-of-the-art stands out, reaching a gain of 215%; the improvement in compressive strength is at a moderate level of about 28%. The absolute strength exceeds the reported properties of fibre-reinforced cementitious materials, of which the flexural strength and compressive strength range from 3 to 12 MPa and from 20 to 70 MPa [2,3,9,10], respectively.

4. Conclusions

To improve the recycling efficiency and explore the new end-application possibilities of the GFRP recyclates with high-performance gains, this research group proposes a promising recycling route where roller milling recycled GFRP waste, including resin residues, is used as reinforcement for iron-rich inorganic polymers produced from non-ferrous metallurgical residues, which have only recently been evaluated for valorization in building materials.

  doi:10.5075/epfl-298799_978-2-9701614-0-0

The proposed recycling route was optimized by a sensitivity factor analysis. It was found that fibre orientation and distribution in the matrix were mainly influenced by the fibre aspect ratio (Ar) due to the mould wall effect. The porosity of the matrix was most affected by Ar and producing method (Pm). The processing steps, such as vibrating (Vib), vacuum mixing (Vm) and cartridge (VmC), considerably reduced the number of large voids trapped in the matrix. Compression strength and initial elastic modulus were mainly affected by choice of the Pm, followed by the Ar; they greatly modified the macropore structure and fibre dispersion in the matrix. Flexural strength and post-cracking behaviour were highly dependent on the fibre-related parameters- Ar, followed by fibre content (Fn), and lastly Pm. The measured compressive strength for the optimized product- SS-3.5%-VmC sample- reached 101 MPa (std. 6.7MPa, Fs 9.1MPa) and the flexural strength for Vib-L-6% amounted to 27 MPa (std. 0.9 MPa, Cs 68.6MPa, so with outstanding overall properties) at 7 days of curing. The flexural strength enhancement compared to the state-of-the-art stands out, reaching a gain of 215%; the compressive improvement is at a moderate level of 28%.

5. References

1. Shuaib NA, Mativenga PT. Energy demand in mechanical recycling of glass fibre reinforced thermoset plastic composites. Journal of Cleaner Production 2016;120:198–206.
2. Zhang Y, Pontikes Y, Lessard L, van Vuure A. Recycling and valorization of glass fibre thermoset composite waste by cold incorporation into a sustainable inorganic polymer matrix. Composites Part B: Engineering 2021;223:109120.
3. Coppola L, Cadoni E, Forni D, Buoso A. Mechanical Characterization of Cement Composites Reinforced with Fiberglass, Carbon Nanotubes or Glass Reinforced Plastic (GRP) at High Strain Rates. AMM 2011;82:190–5.
4. Dils J, Boel V, Schutter G de. Vacuum mixing technology to improve the mechanical properties of ultra-high performance concrete. Mater Struct 2015;48(11):3485–501.
5. Sivaiah P, Chakradhar D. Modeling and optimization of sustainable manufacturing process in machining of 17-4 PH stainless steel. Measurement 2019;134:142–52.
6. Parviz Soroushian and Cha-Don Lee. Distribution and Orientation of Fibers in Steel Fiber Reinforced Concrete. MJ 1990;87(5).
7. EN 196-1:2005. Methods of testing cement - Part 1: Determination of strength. Brussels: EUROPEAN STANDARD; 2005.
8. Ranjbar N, Talebian S, Mehrali M, Kuenzel C, Cornelis Metselaar HS, Jumaat MZ. Mechanisms of interfacial bond in steel and polypropylene fiber reinforced geopolymer composites. Composites Science and Technology 2016;122:73–81.
9. Alomayri T, Low IM. Synthesis and characterization of mechanical properties in cotton fiber-reinforced geopolymer composites. Journal of Asian Ceramic Societies 2013;1(1):30–4.
10. Fox TR. Recycling wind turbine blade composite material as aggregate in concrete. Graduate Theses and Dissertations, Iowa State University; 2016.

  doi:10.5075/epfl-298799_978-2-9701614-0-0

SUSTAINABLE SCRAPPING METHOD OF THERMOPLASTIC COMPOSITE MATERIALS

Alejandro Sandá [a], Rocío Ruiz [b], José Vicente Izquierdo [b], Jon Ander Sarasua [a], Miguel Ángel Mafé [b]

a: Tekniker, Basque Research and Technology Alliance (BRTA)– alejandro.sanda@tekniker.es
b: Technology Department, AIMPLAS Research Center– rruiz@aimplas.es

Abstract: *In this work, a new method for recycling thermoplastic composite materials is presented and more eco-efficient manufacturing methods are proposed to reprocess the recovered materials for a compression moulding process. For the recycling of carbon fiber reinforced thermoplastics (CFrTP), an innovative mechanical scrapping process has been conceived through simulation and experimentation by analyzing the properties of the scrap waste obtained. Thus, a cutting tool has been developed for the delamination of the input material so that long fibers can be kept in the resulting scrap. Different processing approaches have been evaluated aiming to obtain manageable scrap that can be subsequently used for a compression moulding process. Additionally, different methods have been evaluated to manage the scrap and perform the corresponding lay-up. The ultimate goal of this study is to use this scrap with longer carbon fibers to manufacture high-quality thermoplastic composite products with recycled materials.*

Keywords: composite: thermoplastic; recycling; sustainability; aerospace

1. Introduction

Transport is in a critical transition sector nowadays. The European Commission (EC), according to the Paris Agreement [1], intends to reduce greenhouse gas emissions by 80% below 1990 levels in 2050 [2]. Due to the growing concerns about the environment and energy, it is driven the widespread adoption of new lightweight materials such as polymer composites in transport sector, crucial issues being performance, cost efficiency, multifunctionality and recyclability [3]. Carbon Fibers Reinforced Plastic (CFRP) composites are high added value materials used in many manufactured products. They have been used as raw material for years by the aerospace sector to replace the aluminum of lightweight structures. The growing demand of CFRP composites in aerospace industry, at a CAGR of 10.5% during 2020-2025 [4], as a high-performance, light-weight materials is a result of their high specific strength, high specific stiffness, high fatigue resistance, good corrosion resistance, high durability, and low density [5].

Currently, there is no legislation that regulates the handling of end-of-life aircraft. Recycling of aircraft components is voluntary nowadays [8], but the European Parliament established as priority objective, to turn the Union into a resource-efficient, green and competitive low-carbon economy [9].

To achieve this objective, new technologies should be developed in order to improve the handling and recycling of end-of-life aircraft by increasing the recycling rate and consequently reducing the environmental impact.

  doi:10.5075/epfl-298799_978-2-9701614-0-0

Composites are challenging to recycle, especially CFRP composites due to their hardness and chemical stability. Nevertheless, finding ways to recover long high modulus fibers is worth the effort as opposed to the conventional way to handle composite waste, that is incineration or disposal in landfills [7].

In commercial FRPs, the matrix phase can be classified as either thermoset or thermoplastic. Thermosetting polyesters and vinyl esters are primarily used in FRPs due to the good balance of low cost and mechanical properties. Epoxies are the most important resins in the market, particularly in structural and aerospace applications, as they can perform under various temperatures and conditions. Fibre reinforcements of short (< 1 mm) or long (> 1 mm) fibres including glass fibre, carbon fibre, and polyaramid fibres are the main type of materials useful for the reinforcement of FRPs.

For aerospace applications, the most used FRPs are those polymers or plastics reinforced with filaments or fibres (FRPs) allowing to an increase in the properties. Typically, they consist of an epoxy-based system and a large percentage of high-performance continuous (> 100 mm) fibres.

Thermoplastics matrix can be heat-softened, melted and re-shaped repeatedly. From manufacturing point of view, the processing of thermoplastics is easier and faster compared to thermosets. Thermoplastic composites (TPCs) in contrast to CFRP with a thermoset matrix, have better perspective for a sustainable manufacturing and assembling and what is more, they can be recycled, remoulded and repaired efficiently. The most recently used of high-performance thermoplastics in aerospace applications are PEEK, PEKK, PAEK or PEI.

Bearing in mind the environment benefits of thermoplastics, TPC are considered as the best material candidates to be used for the next generation of airplanes and commit the environmental challenges regarding the End-of-Life (EoL) issues to employ the waste pre- and post-consuming scrap material and promote a circular economy.

In this study, a sustainable scrapping method of thermoplastic composite materials has been developed. Thus, an innovative mechanical scrapping process has been conceived through simulation and experimentation analyzing the properties of the scrap waste obtained. A cutting process has been developed for the delamination of the input material retaining long fibers in the resulting scrap. Different processing approaches have been evaluated aiming to obtain manageable scrap that can be subsequently used for a compression moulding process. The ultimate goal pursued with this study is to use this scrap with longer carbon fibers to manufacture high-quality thermoplastic composite products with recycled materials.

2. Composite recycling

Recently, there has been a tremendous uptick in worldwide research on reclaiming high performance fibers, particularly aerospace- grade carbon fiber from end-of-life cured thermoset composites. Fiber reclamation remains the main focus of such composite recycling efforts [6].

In the case of thermoset composites, traditional recycling techniques involve apart from the mechanical size reduction of the input material, complex processes such as chemical or thermal processes where the plastic is removed and wasted through different processes [7].

  doi:10.5075/epfl-298799_978-2-9701614-0-0

Traditional mechanical recycling involves the use of crushing, grinding, milling and/or shredding techniques. All the constituents of the primary composite are reduced in size to particles below 10 mm [7]. Therefore, the fibers that give the mechanical properties to the material are in a relatively short format. Thus, they can be used as a charge or partial reinforcement in other products, what limits its incorporation in new materials [10]. Additionally, concerning the thermoset-based composites, there are problems related to the bonding of the recyclate, and usually, they do not fit the thermosetting polymers.

The most used thermal recycling methods are pyrolysis and fluidized bed processes. Both approaches involve heat to break down the scrap composite and burn the resin matrix, thus recovering the carbon fibers. The operating temperature of a fluidized bed is chosen to be adequate to decompose the polymer, leaving clean fibers but without degrading them substantially [11]. The same issue arises In the pyrolysis process where the operating temperatures have a great effect on the fiber's characteristics and, thus, they have to be carefully adjusted in each case [12]. Pyrolysis' advantage is that it does not use chemical solvents and that all the outcomes can be somehow recovered. That is why pyrolysis is the only process used commercially, but the recycled carbon fibers must be still chopped or milled [7].

Solvolysis is a chemical treatment using a solvent to degrade the resin. The solvolysis process can recover both the clean fibers and fillers and depolymerized matrix in the form of monomers [13]. In chemical recycling, resin degradation is done using solvents (solvolysis) or water (hydrolysis). The use of the dangerous and concentrated chemicals results in environmental impact, so water or alcohol usually replace harmful chemicals [14].

In the case of thermoplastic composites, recycling has attracted considerable attention in the recent years. Several recycling solutions specific to CFrTPs have been implemented to convert this production scrap and mechanical recycling processes appear to be best alternative to efficiently recycle these composites. The main conventional mechanical recycling processes are shredding, electrodynamical fragmentation, conventional cutting (machining), laser cutting and abrasive waterjet cutting.

Regarding the shredding process, Vincent et al. [15,16] chose multiple shaft shredding technique for size reduction in their study for its ability to produce large and uniform flakes unlike other technologies, such as hammer mills or cutting mills. Two and four shaft shredders manufactured by UNTHA shredding technology Gmbh (hereinafter UNTHA) were used for this purpose. This type of machine was designed to shear the input material rather than impact it, as in hammer mills, which is achieved by having the shafts rotate at low speeds.

Practical experience of UNTHA and Nido Recycling Techniek had shown that these machines produce a small fraction of fine particles compared to single-shaft shredders or hammer mills. Here, fine particles are defined as being five to ten times smaller than the intended main output of a machine [17]. Therefore, this method allows to choose the particle size, but there is not control over the internal fiber layup of the particles.

Electrodynamical fragmentation is a process where a solid placed in an isolating liquid is separated through its natural material internal boundaries by high voltage discharges. The electrical discharge has a high energy (10 to 100 J cm1) that produces a plasma channel in the solid inducing high pressures and temperatures in the very close area. Besides those very aggressive conditions, the plasma channel in the material creates pressure waves also called

  doi:10.5075/epfl-298799_978-2-9701614-0-0

shock waves that lead to the disintegration and the cracking of all the surrounding materials, especially the weakest material constituents with the lowest mechanical properties. After several pulses, the created cracks propagate and reach the edges of the part causing the fragmentation [18].

Conventional cutting or machining can be used as an alternative to shredding where control on the fiber content in the scrap can be achieved. The basic knowledge provided by studies about simulation and orthogonal cutting of CFRP addresses that the main factors influencing the chip morphology are, namely the depth of cut (DOC) and the fiber orientation (angle θ). The latter plays the dominant role [19].

It is especially interesting the cutting mechanism observed under parallel fiber cutting conditions where interface layering separation occurs favoring the separation of the fiber layer affected by the tool [20]. Therefore, it can be said that when θ =0 the chip formation is by debonding-bending mechanism and the magnitude of the cutting force and thrust force increases slowly with the depth of cut, this is, low forces are needed to cut the material.

Other non-conventional cutting processes such as laser cutting or abrasive waterjet cutting have their drawback in the generation of tapered kerfs that depend on the depth of the cutting is being performed [21,22]. Therefore, these cutting techniques are useful for the cutting of composites of low thickness but not for delaminating the material.

In this study, a cutting process has been developed to delaminate CFrTP and get scraps containing long fibers, so that they can be used in a compression moulding process to manufacture high quality recycled parts.

3. Delamination process

A cutting process has been developed for the scrapping of CFrTP panels retaining long fibers in the scrap. This has been done using FEM based simulation and experimentation at a lab scale.

3.1 Material

The material used for the experimentation has the following specification:

- Material Ten Cate Cetex TC1320-1 PEKK AS4 D 6.35 mm
- panel thickness around 2.2 mm
- panel dimensions around 200 x 200 mm^2 (see Fig. 1)

TenCate Cetex® TC1320 is a PEKK-based thermoplastic composite based on a semi crystalline thermoplastic polymer. It has excellent resistance to chemicals and solvents excellent elevated service performance, good hot/wet strength and excellent performance in flammability properties. Its glass transition temperature Tg is 159ºC, its melting temperature Tm is 337ºC and its crystallization temperature is 265ºC. Some of its mechanical properties are shown in Table 1.

Table 1: Tencate Cetex® TC1320 PEKK on AS4D unitape with 145 FAW, 34% resin content.

Property	Condition	Test method	Result
Tensile Strength	RTD	ASTM D 3039	2,300 MPa
Tensile Modulus	RTD	ASTM D 3039	139 GPa

Tensile Strength – 90º	RTD	ASTM D 3039	87.5 MPa
Tensile Modulus – 90º	RTD	ASTM D 3039	10.5 GPa
Compression Strength	RTD	ASTM D 6641	1,400 MPa
Compression Modulus	RTD	ASTM D 6641	124 GPa

Three different layups have been produced to evaluate their performance under the developed scrapping process:

- 45 panel: 16 layer QI laminate ([0,+45,90,-45]2s)
- 0 panel: 16 layer unidirectional laminate ([0]16)
- 90 panel: 16 layer bidirectional laminate ([0,90]4s). 90 panel

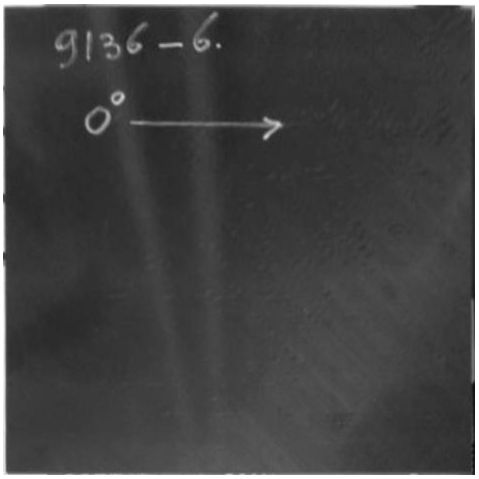

Figure 1. One of the 45 panels

3.2 Scrapping process

A cutting process has been developed to get scrap tapes containing long fibers. The aimed width of the tapes is of 12.7 mm and their length, 200 mm, this is, the same length of the panel. From the experimentation carried out, different scrap tape thicknesses have been obtained, and, therefore, different internal fiber layups.

All the material configurations were composed of 16 layers of fibers, having a panel thickness around 2.2 mm. Therefore, ideally, one fiber layer should be expected every 0.14 mm. In a first approach, the objective was to get unidirectional scrap tapes, containing just one long fiber layer, this is, 0.14 mm thick scrap tapes. However, due to panels' manufacturing accuracy, this was very difficult, and resulted in bad quality scrap tapes, not uniform and heterogenous. Taking into account that the process aims to be scalable, a different approach has been undertaken, so that it is more robust and less dependent on panel manufacturing issues.

In order to get more uniform and better-quality scrap tapes, more thick tapes have been cut, trying to get two fiber layers in each one. In this way, tapes with a layer of long fibers around 200 mm can be assured. Depending on the initial panel's layup, the second layer present in the scrap tapes can be as long as the first one (0 panels), as short as the width of the tape when the second layer is at 90º, this is 12.7 mm (90 panels) or slightly longer than the tape's width when this second layer is at 45º (45 panels) (see Fig. 2).

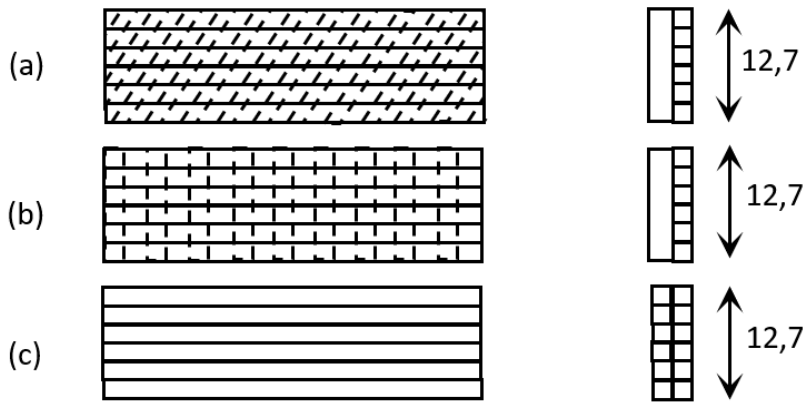

Figure 2. Fiber layup in the scrapped tapes: a) 45 panel; b) 90 panel; c) 0 panel

It has been found that this approach gives the best quality scrap tapes and has a high potential to industrially scale the process. However, there are some issues that have to be addressed. The process of delamination itself induces a plastic deformation on the input panel. In the case of non-unidirectional layups, when the fiber orientation symmetry is broken, the material tends to deform. In the case of 45 panels, the deformation increases gradually as different levels are removed from the panel. This impairs the process making impossible to process the last layers of material due to the high deformation of the workpiece that makes impossible its correct clamping. In the case of 90 panels and 0 panels, the deformation is not an issue and higher ratio of long fiber tapes can be obtained.

Figure 3. Scrap tapes for the different panel layups: (a) 45 panel; (b) 90 panel; (c) 0 panel

Regarding the tapes' geometry, in the case of 45 panels, the presence of a longitudinal fiber layer and another one at 45º results in a helical deformation of the scrap tape. This makes more

  doi:10.5075/epfl-298799_978-2-9701614-0-0

difficult their manipulation for the compression moulding process (see Fig. 3a). In the case of 90 panels, a curvature can also be observed due to the 90º fiber layer, but in this case, it does not difficult their manipulation (see Fig. 3b). Finally, when delaminating unidirectional panels (0 panels) the scrap tapes are fully planar without deformation or curvature (see Fig. 3c). This is the ideal case where only long fibers are present in the scrap and additionally they can be easily manipulated in a compression moulding process.

Concerning the recyclability, each panel type can be scrapped differently, achieving different long fiber scrapped tapes fractions. In the case of 45 panels, 45% of the initial panel can be transformed into long fiber scrap. Around 70% of the 90 panel can be scrapped into long fiber tapes. This fraction rises to 85% when scrapping 0 panels. 45 panels low fraction of tapes comes from the deformation arisen during the delamination process. The 90 panels do not have this problem but the lower scrap quality lowers the long tapes fraction.

4. Characterization

The characterization part of the different samples obtained from the scrapping method has been focused on different tests that show the different properties of these resulting scraps. With this, the main idea is to ensure the recycling process of these materials for the composition of different parts.

These scrapped samples have been compared themselves. Tensile tests have been done on samples scrapped from panels with different orientations (90 and 0 degrees).

This test procedure is based on the UNE EN ISO 527-4, because of the nature of the sample (carbon fiber reinforced materials). The main properties that have been evaluated are the modulus of elasticity, the ultimate tensile strength and the elongation at this point. Another, test has been the TGA, where the specimens are exposed to thermal degradation cycle that goes from room temperature to 900ºC in 2 steps. There is a first heating from the room temperature to 900ºC in a N2 and then a cooling step until 450ºC to expose the sample to another heating cycle up to 900ºC, but this time in air. This procedure has been done to obtain information in all the ranges and atmospheres. Finally, the occlusion content has also been characterized to clarify the different homogeneity of the fibers plus matrix in the different scrap samples.

The mechanical properties of the different plates, from which specimens were obtained by machining, and the scrapped specimen were determined. These mechanical properties are shown in Table 2.

Table 2: Tensile properties for plate specimen and scrapped specimens.

	PEKK/AS4 UD (0)16				
	Panel (machined)	Scrapped 0º “Level 2”	Scrapped 0º “Level 3	Scrapped 0º “Level 4”	Scrapped 0º “Level 7”
Property					
Modulus of elasticity (MPa)	136000	101000	89600	85400	80400

  doi:10.5075/epfl-298799_978-2-9701614-0-0 published under CC BY-NC 4.0 license

Tensile Strength (MPa)	1310	776	661	790	747
Tensile strain at tensile strength (%)	0.89	0.76	0.76	0.90	1.0
Tensile Strength at break (MPa)	1310	776	661	790	747
Tensile strain at break (%)	0.89	0.76	0.76	0.90	1.0

As shown in table 2, the different mechanical properties indicate that the samples obtained through the scrapping process at different levels show similar results, however, as the level from which the scrapped specimens have been obtained increases, a reduction in the modulus of elasticity. The tensile strength and strain point at break and maximum are equal because there is not yield at the specimens tested.

The tensile properties of two different samples were compared, the PEKK/AS4 UD (0)16 sample whose fiber had orientation at 0º and the PEKK/AS4 UD (0/90)4s sample with fiber orientation at 0 and 90º. These mechanical properties are shown in Table 3.

Table 3: Tensile properties for plate specimen 0º and 0/90º

	Panel (machined)	
	PEKK/AS4 UD (0)16	PEKK/AS4 UD (0/90)4s
Property		
Modulus of elasticity (MPa)	136000	71900
Tensile Strength (MPa)	1310	815
Tensile strain at tensile strength (%)	0.89	1.1
Tensile Strength at break (MPa)	1310	815
Tensile strain at break (%)	0.89	1.1

As shown in table 3, the sample that contains all fibers with the same orientation, coinciding with the direction of the specimens obtained for testing, has a higher resistance, as expected, than the specimens obtained from samples that have a 0/90 distribution in the orientation of the fibers.

In this mechanical characterization, the tensile properties of scrapped specimens were also evaluated in the direction of the fibers (longitudinal) and in a direction perpendicular to their orientation (transversal). These mechanical properties are shown in Table 4.

Table 4: Tensile properties for plate specimen 0º and 0/90º

	Panel (machined)

  doi:10.5075/epfl-298799_978-2-9701614-0-0

	PEKK/AS4 (L)	PEKK/AS4 (T)
Property		
Tensile Strength (MPa)	973	10.2
Tensile strain at tensile strength (%)	0.96	0.09
Tensile Strength at break (MPa)	973	10.2
Tensile strain at break (%)	0.96	0.09

The sample whose orientation of the fibers coincides with the orientation of the test piece, logically shows a higher resistance than the sample in which the reinforcement of the fibers does not contribute. Therefore, the orientation of these fibers should be well controlled when obtaining scrapped specimens that contribute to the mechanical resistance of the materials in which these scrapped samples are used.

The scrap quality was determined by evaluating the porosity (content in occlusions). The determination of the % of porosity was made by comparing the theoretical density of the samples with the real density in each of the samples evaluated. The procedure based on the ISO 7822 standard has been followed.

The results obtained do not show great differences between the different samples evaluated, all being close to 0.6%. However, comparing the values obtained at different levels of scrapped samples, it is observed that at the lower levels, the occlusion content is reduced.

The thermal degradation was determined by thermogravimetry analysis (TGA). This analysis showed that all the samples evaluated presented a behavior like the one that can be seen in the following Fig. 4.

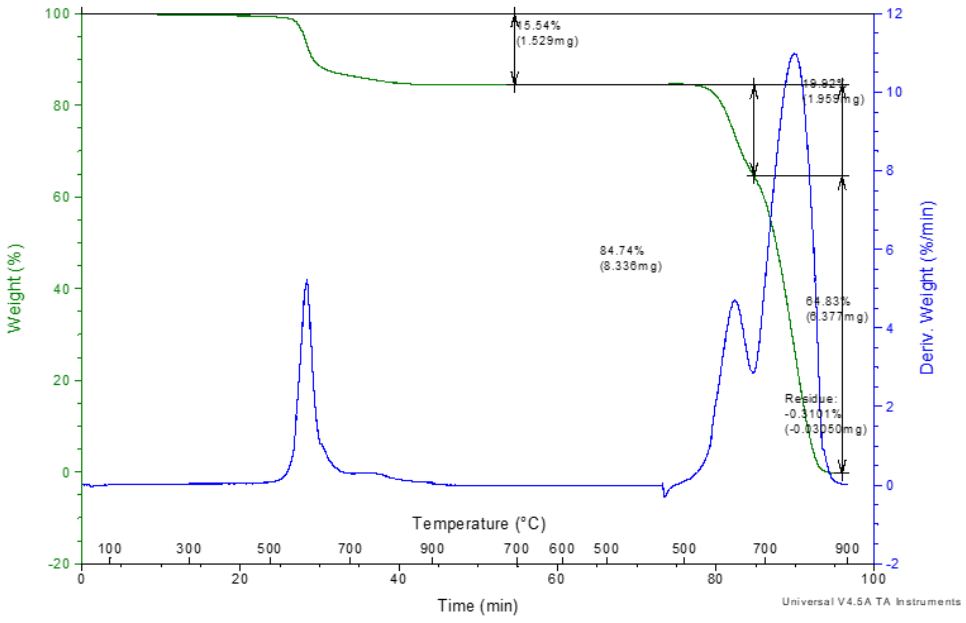

Figure 4. Thermogravimetry analysis (TGA)

As shown in Fig. 4, after the TGA scan of the different samples, the same decomposition pattern is observed in all of them: a first weight loss in a first section from room temperature to 900ºC in an inert atmosphere (N_2) and a second weight loss in the range from 450ºC to 900ºC with air. This second weight loss, after calculating the first derivative of the % weight respect to time, is made up of two components, as has been observed in all the samples evaluated.

Taking into account the composition of the samples (polymeric material + carbon fiber), and the theoretical value of the percentage by weight of both materials: approximately 34% polymer or resin + 66% carbon fiber) the different mass losses correspond to the following behavior:

- Loss 1 (in N2): Corresponds to the degradation of part of the polymeric chain of the resin (13.5-15.5%). In a nitrogen atmosphere, the entire polymeric matrix composed of polymers with double bonds or aromatic rings in its composition does not burn completely, leaving a carbonaceous residue.
- Loss 2 (in air): Corresponds to the degradation of the carbonaceous residue of the resin that has not been degraded into N2. In the presence of air, this residue degrades at a temperature below the carbon fiber degradation temperature. The sum of these two losses will correspond to the weight percentage of the resin present in the sample.
- Loss 3 (in air): Corresponds to the degradation of the carbon fiber (55-65%). This carbon fiber degrades at temperatures higher than those at which the carbonaceous residue degrades, although as can be seen in figure 3, both losses overlap (for this reason, the first derivative is calculated to determine both losses).

The inorganic residue obtained in all the samples is very low (1-0.1%). This residue corresponds to the ashes of the carbon fiber, so it can be deduced that there are no inorganic loads in the samples evaluated.

5. Conclusions

A scrapping method has been developed capable of process carbon fiber reinforced thermoplastics into scrap tapes retaining long fibers. The scrap's geometry and properties depend on the initial panel's layout. The best quality scrap is obtained from unidirectional 0 panels, where the scrap tapes have no deformation and contains only longitudinal fibers.

Delamination of just one carbon fiber layer is not possible in an industrial scale due to the manufacturing accuracy of the input panels. Therefore, scrap tapes containing 2 carbon fiber layers is the most successful strategy.

The highest fraction of scrap tapes containing long fibers is given by unidirectional 0 panels, where up to 85% of the input panel can be transformed into scrap that can be used in a subsequent compression moulding process. This fraction decreases to 70% when processing 90 panels. The lowest fraction of valuable scrap is obtained with 45 panels, where only 45% of the input panel can be transformed into long fiber scrap tapes, due to the high deformation caused by the delamination process.

  doi:10.5075/epfl-298799_978-2-9701614-0-0

Acknowledgements

This work has been done in the frame of the project SPARTA. This project has received funding from the Clean Sky 2 Joint Undertaking under the European Union's Horizon 2020 research and innovation programme under grant agreement No. 887073.

6. References

1. The Paris Agreement. Available online: https://unfccc.int/process-and-meetings/the-paris-agreement/theparis-agreement
2. EU Climate Action. Available online: https://ec.europa.eu/clima/citizens/eu_en
3. Fontaine, P., Weiss-Hortala, E., Botaro, V. et al. Impact of Atmosphere on Recovered Carbon Fibers From Poly Ether Ether Ketone (PEEK) Based Composites During Thermoconversion. Waste Biomass Valor 12, 6389–6402 (2021). https://doi.org/10.1007/s12649-021-01445-7
4. Aerospace Composites Market - Forecast (2020-2025). ID: 5231245. November 2020
5. Butenegro, J.A.; Bahrami, M.; Abenojar, J.; Martínez, M.Á. Recent Progress in Carbon Fiber Reinforced Polymers Recycling: A Review of Recycling Methods and Reuse of Carbon Fibers. Materials 2021, 14, 6401. https://doi.org/ 10.3390/ma14216401
6. Gaurav Nilakantan, Steven Nutt, Reuse and upcycling of aerospace prepreg scrap and waste, Reinforced Plastics, Volume 59, Issue 1, 2015, Pages 44-51, ISSN 0034-3617, https://doi.org/10.1016/j.repl.2014.12.070.
7. Borjan, D., Knez, Ž., & Knez, M. (2021). Recycling of carbon fiber-reinforced composites—difficulties and future perspectives. *Materials*, *14*(15), 4191.
8. Kaplan, M. D. G.: In an industry that parks old jets, Bombardier aims for fully recyclable aircraft. URL: http://www.smartplanet.com/blog/puregenius/ in-anindustry-that-parks-old-jets-bombardier-aims-for-fullyrecyclable- aircraft/5631 [as of 08.05.2014]
9. https://eur-lex.europa.eu/legal-content/EN/TXT/?uri=CELEX%3A32013D1386
10. Howarth, J., Mareddy, S. S., & Mativenga, P. T. (2014). Energy intensity and environmental analysis of mechanical recycling of carbon fibre composite. Journal of Cleaner Production, 81, 46-50.
11. Pickering, S. J., Yip, H., Kennerley, J. R., Kelly, R., & Rudd, C. D. (2000). The recycling of carbon fibre composites using a fluidised bed process. In FRC 2000–Composites for the Millennium (pp. 565-572). Woodhead Publishing.
12. Lam, K. L., Oyedun, A. O., Cheung, K. Y., Lee, K. L., & Hui, C. W. (2011). Modelling pyrolysis with dynamic heating. Chemical engineering science, 66(24), 6505-6514.
13. Yildirir, E., Onwudili, J. A., & Williams, P. T. (2014). Recovery of carbon fibres and production of high quality fuel gas from the chemical recycling of carbon fibre reinforced plastic wastes. The Journal of Supercritical Fluids, 92, 107-114.
14. Oliveux, Géraldine & Dandy, Luke & Leeke, Gary. (2014). A step-change in the recycling of composite materials. 10.13140/2.1.1402.3043.
15. G. A. Vincent, T. A. de Bruijn, S. Wijskamp, M. I. Abdul Rasheed, M. van Drongelen, and R. Akkerman, "Shredding and sieving thermoplastic composite scrap: Method development and analyses of the fibre length distributions," Composites Part B: Engineering, vol. 176, Nov. 2019, doi: 10.1016/j.compositesb.2019.10719
16. G. A. Vincent, "Recycling of thermoplastic composite laminates: the role of processing," 2019.

17. H. Li and K. Englund, “Recycling of carbon fiber-reinforced thermoplastic composite wastes from the aerospace industry,” Journal of Composite Materials, vol. 51, no. 9, pp. 1265–1273, Apr. 2017, doi: 10.1177/0021998316671796
18. M. Roux, N. Eguémann, C. Dransfeld, F. Thiébaud, and D. Perreux, “Thermoplastic carbon fibre-reinforced polymer recycling with electrodynamical fragmentation: From cradle to cradle,” Journal of Thermoplastic Composite Materials, vol. 30, no. 3, pp. 381–403, Mar. 2017, doi: 10.1177/0892705715599431
19. H. Li, X. Qin, G. He, Y. Jin, D. Sun, and M. Price, “Investigation of chip formation and fracture toughness in orthogonal cutting of UD-CFRP,” International Journal of Advanced Manufacturing Technology, vol. 82, no. 5–8, pp. 1079–1088, Feb. 2016, doi: 10.1007/s00170-015-7471-x
20. Q. An, C. Cai, X. Cai, and M. Chen, “Experimental investigation on the cutting mechanism and surface generation in orthogonal cutting of UD-CFRP laminates,” Composite Structures, vol. 230, Dec. 2019, doi: 10.1016/j.compstruct.2019.111441
21. D. Herzog, M. Schmidt-Lehr, M. Oberlander, M. Canisius, M. Radek, and C. Emmelmann, “Laser cutting of carbon fibre reinforced plastics of high thickness,” Materials & Design, vol. 92, pp. 742–749, 2016, doi: https://doi.org/10.1016/j.matdes.2015.12.056
22. I. W. Mm, A. Azmi, C. Lee, and A. Mansor, “Kerf taper and delamination damage minimization of FRP hybrid composites under abrasive water-jet machining,” International Journal of Advanced Manufacturing Technology, vol. 94, no. 5–8, pp. 1727–1744, Feb. 2018, doi: 10.1007/s00170-016-9669-y

APPROACHES ON SELF-HEALING OF AN INTERPENETRATING METAL CERAMIC COMPOSITE

Joél Schukraft[a], Carolin Pieper[a], Christoph Lohr[a], Kay A. Weidenmann[a]

a: Augsburg University, Institute of Materials Resource Management (MRM), Chair of Hybrid Composite Materials – joel.schukraft@mrm.uni-augsburg.de

Abstract: *An interpenetrating metal ceramic composite (IMCC), manufactured via gas pressure infiltration of AlSi10Mg melt into a open porous Al_2O_3-preform, was investigated upon the ability of self-healing. A specific damage is introduced into the IMCC first. Then microstructural investigations are carried out at the damaged samples and for self-healing treated samples. The nature of the interpenetrating structure is used to heat the composite above the solidus temperature of the metallic phase and provide a shape stability by the ceramic phase to melt the metal and fill the cracks formed before. The investigation is systematically compared to the results of the undamaged samples as well as the pre-damaged samples without treatment for self-healing. The microstructural results show a change in crack geometry and therefore the possibility of self-healing. Nevertheless, open questions in process control as well as parameter-optimization require further research to achieve microstructural improvement of the healed samples above the performance of the pre-damaged ones.*

Keywords: Interpenetrating metal ceramic composite (IMCC); self-healing approaches; X-ray computed tomography (CT); microstructural characterization.

1. Introduction

In nowadays engineering success regarding to reduction of greenhouse gases and environmentally compatible implementations in mobility and transportation, light-weight materials for structural application play a key role. By combining light metals and ceramics, improved mechanical properties, as well as wear resistance for a long-lasting use of the composite can be achieved and the reached limits of light weight metals can be outperformed [1]. Metal matrix composites (MMC) reinforced with ceramic particles or fibers have already shown the high potential of this material group in an industrial application like e.g. in piston rings, brakes, engine blocks, connecting rods and propeller shafts [2]. By creating an interpenetrating composite, so that all phases are topologically continuously connected [3], additional advantages can be reached, as different authors stated from the early stage of the development up to latest investigations [1, 4].

In addition to the resource efficient design of components by using superior materials, sustainability, durability, and life cycle extension are becoming increasingly important in nowadays development and research. Based on the biological model of the self-healing ability of living organisms, a new field of possibilities was opened and reached increasing interest in the last decade [5]. The general definition of self-healing, as the ability of a material to heal itself without any external intervention automatically and autonomously is often not the case for manmade materials. Therefore, a differentiation in autonomous and non-autonomous self-healing is made by Gosh et al. [6]. Especially for polymers, many approaches have already been

  doi:10.5075/epfl-298799_978-2-9701614-0-0

investigated and even autonomous self-healing approaches have shown success, making them highly interesting for industrial applications [7, 8]. To achieve healing in damaged metals, external triggers in form of thermal or electrical energy are required [9] to overcome their strong atomic bonding and the associated diffusion limitation in application environment [10].

In underaged alloys, healing of nanoscale flaws can be achieved by an increase of temperature which enables the diffusion of solute atoms into high stress areas such as cracks to form precipitates [5]. Another approach is the introduction of ceramic capsules containing a low-melting metal into the metallic matrix. In case of damage, the ceramic shell is broken and the metal contained flows into the crack upon heating to its' melting temperature [5].

The above mentioned self-healing concepts were designed and investigated to heal pure metals. Concerning composites, there are generally less ideas to incorporate self-healing due to the more complex structure. However, considering the high costs and complex manufacturing, in composites self-healing is even more beneficial than in conventional materials. Self-healing methods developed to heal composite materials are not to be confused with concepts that require the manufacturing of special composites to achieve healing. The latter include the above mentioned embedding or capsules containing a healing agent. The existing self-healing concepts designed to heal composites are limited to polymeric composites, e.g. to prevent delamination failure in CFRPs [11]. In contrast to that, no research was done with the aim to heal metal-based composites. Considering the big differences of mechanical and physical properties between MMCs and pure metals, the lack of knowledge in the field of self-healing metallic composites makes further investigations necessary.

In this study, first approaches on (self-)healing of an interpenetrating metal ceramic composite are investigated under the condition of a high temperature stable interpenetrating ceramic phase and a "low-melting", near eutectic light-weight aluminum alloy. To heal the internal damage, the influence of heating the metallic phase above the melting temperature is used as an external healing trigger with varying atmosphere, pressure and sample treatment.

The related research question is whether non-autonomous (self-)healing of the interpenetrating composite is possible with the tested approaches by melting the liquid aluminum alloy into the cracks of the sample and which parameters influence the self-healing process. The visibility of microstructural changes will be investigated in the following.

2. Materials and Methods

2.1. Material and sample preparation

To investigate the success of self-healing, an interpenetrating metal ceramic composite is used, based on a porous alumina preform with approximately 74 % open porosity. The preform is firstly evacuated up to a residual pressure of $6 \cdot 10^{-2}$ mbar. Then the metallic phase is infiltrated into the open porosity via gas pressure infiltration technique with an argon gas pressure of 60 bar. Details of the setup are described by the authors in Horny et al. [12]. 2D sections of the morphology are given in Figure 2.

Specimens were extracted from the infiltrated material with a diamond wire saw DWS 250 by Diamond WireTec GmbH&Co. KG and a hollow diamond drill. The cylindrical shaped specimens used for the self-healing approach had a mean diameter of 3.8 mm; a height of approx. 8 mm

  doi:10.5075/epfl-298799_978-2-9701614-0-0

and parallel polished end faces according to DIN 50134 [13] (see Figure 1 a). For the healing approach, a parallelepiped with dimensions of 30 x 23 x 5 mm³ was cut, surface grinded and finally drilled in the surface extension with a hollow diamond drill with a diameter of 18 mm (see Figure 1 b).

2.2. Experimental procedure

Mechanical characterization

The specimens were systematically pre-damaged via compression testing, carried out in the universal testing machine ZwickRoell Z1464 with a nominal strain rate of 0.06 1/s. The sample strain was captured with a videoXtens optical strain measurement system, also by ZwickRoell.

Microstructural characterization and evaluation

For microstructural characterization, an X-ray computed tomograph (Phoenix Nanotom M) by General Electrics was used. The software components Phoenix data sx2 acquisition and Phoenix data sx2 reconstruction were used to process the data and reconstruct a 3D image of the sample, each also by GE Sensing & Inspection Technologies GmbH. The focus-object distance was 10.5 and 24 mm and the focus-detector distance 300 and 480 mm with a resulting voxel size of 3.5 and 5 µm³ for the self-healing and healing approach, respectively. The beam source was powered with 80 kV and 180 µA. Each sample was scanned three times: In the undamaged state, right after pre-damaging and after the healing attempt.

Evaluation of the CT data was carried out with the Avizo® software by ThermoFisher Scientific. The aim was to compare the CT data of a sample in pre-damaged and healed state concerning changes in crack volume. This was achieved by following two major procedures. Avizo®-specific operations are given in italic letters in the following:

The first procedure was required to align the 3D-data in the coordinate system of the software and therefore ensure comparability of both data sets. By applying *Register Images,* one of the data sets was visually realigned with the second data set serving as reference. The module *Resample Transformed Image* generated a new data set corresponding to this alignment.

The second procedure was separately applied on each data set to obtain the volume fraction values of the crack volumes. First, an *Image Stack Processing* workflow including an *AutoThresholding* module as well as subsequent operations was applied to extract the darker grey values, which are representative for the cracks. To remove artifacts and pores from the resulting data, first *Labeling* and then *Filter by Measure Range* were applied, using the shape function *Shape_VA3d*. The value 1 of this function corresponds to a perfect sphere, whereas higher values represent a less compact object. The resulting crack volume was visualized using *VolumeRendering* and its value was calculated with the module *VolumeFraction.*

Non-autonomous (self-)healing treatment

Temperature induced self-healing was carried out in a conventional furnace by Nabertherm. A pre-damaged sample was heated at 10 K/min to a maximum temperature of 650 °C, hold for 5 min there and then cooled to room temperature with the same cooling rate.

  doi:10.5075/epfl-298799_978-2-9701614-0-0

For the pressure-assisted (self-)healing approaches, a gas pressure infiltration setup described by the authors in Horny et al. [12] was used, which enabled the variation of atmosphere, pressure and temperature. The process was modified, as given in Figure 1 c).

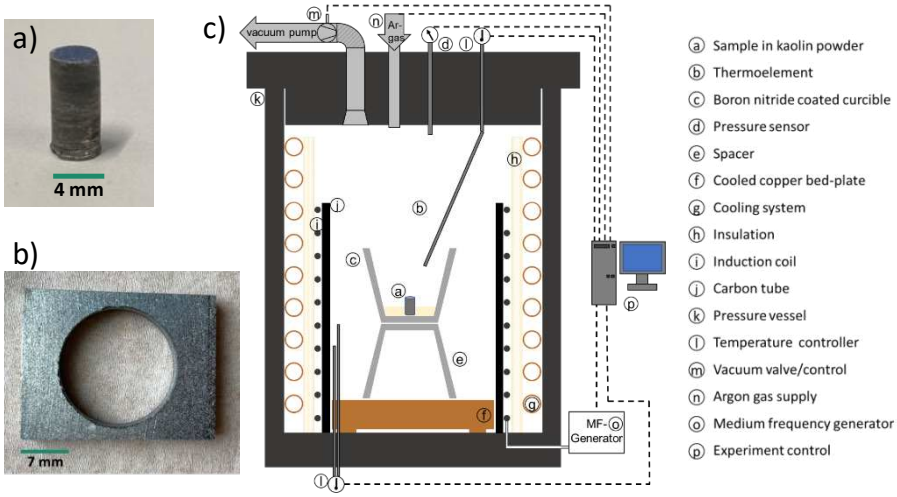

Figure 1. a) Sample geometry for self-healing approaches. b) Sample geometry for alloy supported healing. c) Gas pressure infiltration setup for pressure-assisted (self-)healing experiments.

The sample was put in a crucible with calcined kaolin powder as support material. For accurate temperature control, the thermocouple was positioned as close to the sample as possible. Like during manufacturing of the composite, vacuum of 0.06 mbar was used during heating with a heating rate of 10 K/min. For self-healing approaches under gas atmosphere, a pre-pressure of 5 bar was applied at 550 °C, before the solidus temperature of the alloy was exceeded. Heating then was continued above the liquidus temperature of the alloy, up to 700 °C. Additional gas pressure up to 60 bar was then brought onto the sample. In the end, cooling was carried out, maintaining the atmosphere condition from maximum temperature. For self-healing approaches under vacuum, no pressure was brought up to the sample and the vacuum was held for the whole process.

For the healing approach, additional alloy was put together with the sample into the empty crucible prior to applying the above-described procedure under argon atmosphere.

3. Results

3.1. Temperature induced self-healing approach

When the sample was removed from the setup, an accumulation of alloy on the surface (cf. Figure 2 b, right) could be detected, indicating that the alloy had melted and flowed out of the sample. Quantitative analysis of the corresponding CT-images using the *Image Stack Processing* Workflow revealed a 2.5-fold increase in porosity after the temperature induced self-healing. In addition, the rearrangement of porosity was observed: Some pores were already present in the microstructure before but were no longer visible at this location after the self-healing tests. An example for the pore rearrangement is marked with a blue arrow in Figure 2. The cracks remained mostly unchanged. Figure 2 shows slight changes in the crack thickness that could be found at some locations of the microstructure. The red arrow marks a widening of the crack due to self-healing, while the green arrow points on a crack part that became narrower

  doi:10.5075/epfl-298799_978-2-9701614-0-0

with self-healing. These changes were only observed for cracks at phase boundaries or in metal areas whereas cracks in the ceramic phase remained unchanged by the self-healing experiments.

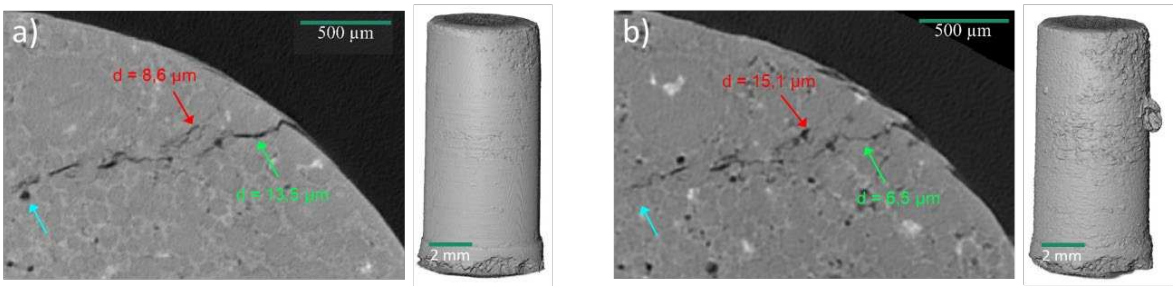

Figure 2. CT-images of a crack and the corresponding samples: a) before and b) after self-healing. The blue arrows pointing on a pore disappearing after self-healing, the red and green arrows marking crack positions that became bigger/smaller due to self-healing.

3.2. Temperature and Pressure induced self-healing approaches

To prevent the alloy from flowing out, the self-healing experiments were extended by additionally applying gas pressure on the sample during self-healing. Different experiments were carried out under vacuum (0.06 mbar), nitrogen or argon atmosphere (40 – 60 bar) as well as varying target temperatures (600 – 700 °C).

Although the self-healing parameters were varied, each sample showed similar microstructural changes analogous to the temperature induced self-healing results in Figure 2.

3.3. Temperature, pressure, and alloy-supported healing approach

After the alloy-supported healing experiments, the sample surface was completely covered in aluminum, indicating full liquefaction of the alloy. The CT-Images shown in Figure 3 reveal that the additional alloy penetrated the crack, resulting in a decrease of crack thickness. Nevertheless, some parts of the crack remained porous after healing. Figure 3 shows the 3D-volume of the crack before and after healing, clearly indicating a strong decrease in crack volume. The quantitative analysis revealed a crack volume of 2.8 vol% before healing, whereas the healed sample had a crack volume of only 0.6 vol%.

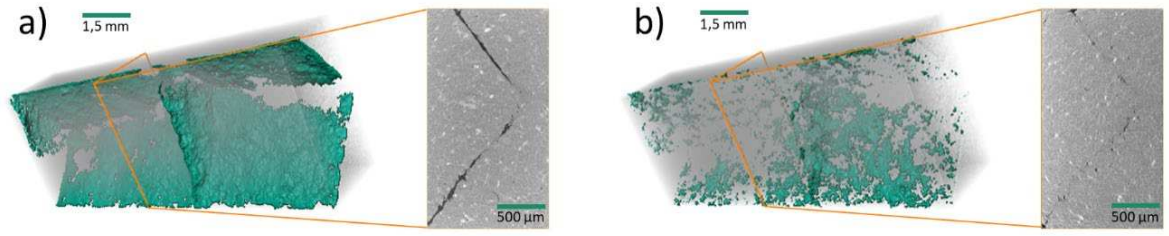

Figure 3. Crack volumes and corresponding CT-images of a) pre-damaged sample with a crack volume of 2.8 % and b) sample healed with additional alloy, showing a crack volume of 0.6 %.

4. Discussion

Firstly, the definition of (self-)healing should be discussed considering its applicability on IMCCs. The differentiation in autonomous and non-autonomous self-healing according to Gosh et al. [6] cannot be transferred to IMCCs because activation by an external trigger is always required for

  doi:10.5075/epfl-298799_978-2-9701614-0-0 published under CC BY-NC 4.0 license

the metallic phase to perform healing. Instead, a more extensive distinction can be made. According to its definition, the term self-healing includes the application of external energy, but not support by additional alloy. Keeping that in mind, the alloy-supported experiments described above can be defined as healing experiments, whereas experiments without additional alloy count to self-healing approaches.

From the observations of the experiments, it can be deduced that IMCCs have a high potential for self-healing due to their interconnected microstructure, which enables to heal cracks both in the metallic and ceramic phase. Blaiszik et al. [14] presented a general formula for the quantitative determination of the healing success, which can be applied to the IMCC:

$$\eta = \frac{f_{healed} - f_{damaged}}{f_{undamaged} - f_{damaged}} \quad (1)$$

The variable f stands for any property of the material that is changed by the healing attempt. The result η is a percentage value indicating to what extent the material property could be restored by healing. Considering the above presented results of changes in crack thickness, the healing success η for the self-healing approach is 51.8 % for the crack marked with a green arrow in Figure 2. However, as already mentioned, most cracks did not change with the self-healing approach or even became bigger. For example, the widening of the crack marked with the red arrow in Figure 2 results in a negative healing success η of –75.6 %. In contrast to that, the healing approach (see chapter 3.3.) with additional alloy resulted in evenly distributed healing with a healing success η of 78.6 % concerning crack volume. The reason for the increased porosity and little crack changes in the self-healed samples is the outflow of alloy which was prevented in the healing experiments by the additional alloy.

To explain the different observations, it is first necessary to look at the underlying physical parameters. Generally, positive capillary pressure is required for the metal melt to autonomously penetrate cracks [15]. The value of capillary pressure p directly depends on the surface tension σ_L of the metallic melt, contact angle θ between melt and matrix and the capillary radius r, which is the crack diameter in this case [16].

$$p = \frac{2\sigma_L \cdot \cos\theta}{r} \quad (2)$$

Aluminum alloys and alumina show non-wetting behavior with a contact angle θ between 90 and 180 degrees [16], resulting in a negative capillary pressure. The wetting is inhibited by the naturally existing oxide layer on the aluminum surface [17], which transforms and thus possesses even higher hardness above temperatures of 500 °C [18]. Experiments showed a decrease of contact angle down to 90 ° with decreasing oxide layer thickness, which can be achieved by high vacuum atmospheres, inhibiting the oxide layer growth [17]. Considering equation 1, the capillary pressure can also be altered by decreasing the surface tension of the metal melt, e.g. by using nitrogen atmosphere above 850 °C, resulting in the formation of AlN [16]. Nevertheless, the capillary pressure will always be negative for this material system, making an external pressure required to exceed the capillary resistance of the cracks [16].

This is confirmed by the unsuccessful temperature induced healing attempt, resulting in an outflow of alloy instead of efficient self-healing. However, in contrast to theory, the temperature and pressure induced experiments with varying atmospheres and temperatures also showed no self-healing improvements, indicating that the effect of the gas pressure was not sufficient. As a

  doi:10.5075/epfl-298799_978-2-9701614-0-0

result, the driving forces for the melt to leave the sample exceed. A scheme of all relevant forces in the (self-)healing experiments is shown in Figure 4.

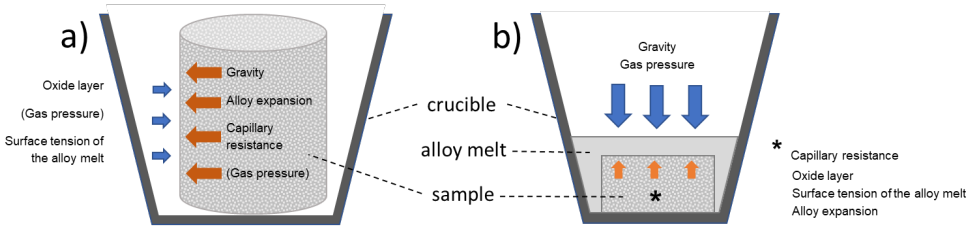

Figure 4. Schematic illustration of all relevant forces acting during the self-healing attempts a) and the healing experiment b).

During the healing experiments, the force mismatch in Figure 4 a) could be changed towards Figure 4 b) as the additional aluminum completely filled the crucible, making the gas pressure act on the upper face of the melt only. As a result, successful infiltration of cracks took place with a healing success that exceeds literature values. Srivastava & Gupta [19] carried out self-healing experiments resulting in a lower healing success of 62.8 %, even though their self-healing approach, a combination of shape-memory alloys and metal melt as healing material, usually is the most effective in the field of self-healing metal concepts. This proves that the healing approach with additional alloy is highly promising. To achieve similar results for the self-healing experiments, further parameter investigation must be carried out.

5. Summary and outlook

In this study, a systematic investigation of approaches on self-healing of an interpenetrating metal ceramic composite was carried out. The general possibility of self-healing was demonstrated, as the metallic phase could be activated by non-autonomous self-healing with thermal activation. The influence of varying the atmosphere and pressure was investigated and in a final step, the addition of aluminum alloy was tested, resulting in a healing success of 78.6 %. In this context, the concept of self-healing was discussed at IMCCs and a distinction was drawn between “healing” and possible “self-healing” concepts. Existing challenges were seen in the surface oxidation of the metallic phase, as well as in the outflow of the liquid metal during the self-healing process. For cracks with surface contact, surface oxidation counteracts the self-healing potential. The outflow of the metallic phase increases the inner porosity and potentially weakens the composites mechanical strength. A further understanding of the influence of surface tension, capillary effects, process parameters and phenomena occurring during healing is required to improve the self-healing potential of IMCCs.

Acknowledgements

The financial support of the German Research Foundation within the project WE 4273/17-1 is gratefully acknowledged. We want to thank Morgan Advanced Materials Haldenwanger GmbH for the friendly supply of complimentary preform material.

  doi:10.5075/epfl-298799_978-2-9701614-0-0 published under CC BY-NC 4.0 license

6. References

1. Mattern A, Huchler B, Staudenecker D, Oberacker R, Nagel A, Hoffmann MJ. Preparation of interpenetrating ceramic–metal composites. J. of the Eur. Cer. Soc. 2004;24:3399–408.
2. Asthana R, Kumar A, Dahotre NB. Materials Processing and Manufacturing Science. Amsterdam: Elsevier; 2006.
3. Clarke DR. Interpenetrating Phase Composites. J American Cer. Soc. 1992;75:739–58.
4. Kota N, Charan MS, Laha T, Roy S. Review on development of metal/ceramic interpenetrating phase composites and critical analysis of their properties. Ceramics International. 2022;48:1451–83.
5. Grabowski B, Tasan CC. Self-Healing Metals. In: Hager MD, van der Zwaag S, Schubert US, editors. Self-healing Materials. Cham: Springer International Publishing; 2016. p. 387–407.
6. Ghosh SK, editor. Self-healing materials: Fundamentals, design strategies, and applications. Weinheim: Wiley-VCH; 2009.
7. JE PC, Sultan MTH, Selvan CP, Irulappasamy S, Mustapha F, Basri AA, Safri SN. Manufacturing challenges in self-healing technology for polymer composites — a review. Journal of Materials Research and Technology. 2020;9:7370–9.
8. Wang S, Urban MW. Self-healing polymers. Nat Rev Mater. 2020;5:562–83.
9. Sharma S, Nandan G, Rohatgi PK, Prakash R. Recent Advances In Self-Healing Materials. Materials Today: Proceedings. 2019;18:4729–37.
10. van Dijk N, van der Zwaag S. Self-Healing Phenomena in Metals. Adv. Mater. Interfaces. 2018;5:1800226.
11. An S, Yoon SS, Lee MW. Self-Healing Structural Materials. Polymers (Basel) 2021.
12. Horny D, Schukraft J, Weidenmann KA, Schulz K. Numerical and Experimental Characterization of Elastic Properties of a Novel, Highly Homogeneous Interpenetrating Metal Ceramic Composite. Adv. Eng. Mater. 2020;22:1901556.
13. DIN Deutsches Insitut für Normung. Prüfung von metallischen Werkstoffen - Druckversuch an metallischen zellularen Werkstoffen 10.2008;ICS 77.040.10. Berlin: Beuth Verlag.
14. Blaiszik BJ, Kramer S, Olugebefola SC, Moore JS, Sottos NR, White SR. Self-Healing Polymers and Composites. Annu. Rev. Mater. Res. 2010;40:179–211.
15. Martinez Lucci J, Amano RS, Rohatgi P, Schultz B. Experiment and Computational Analysis of Self-Healing in an Aluminum Alloy. In: ASME 2008 I. Mech. Eng. Congr. and Exp.; 31.10.2008 - 06.11.2008; Boston, Massachusetts, USA: ASMEDC; 2008. p. 1759–1768.
16. Basista M, Jakubowska J, Węglewski W. Processing Induced Flaws in Aluminum-Alumina Interpenetrating Phase Composites. Adv. Eng. Mater. 2017;19:1700484.
17. Li J-G. Wetting of ceramic materials by liquid silicon, aluminium and metallic melts containing titanium and other reactive elements: A review. Cer.Intern. 1994;20:391–412.
18. Ostermann F. Korrosion. In: Ostermann F, editor. Anwendungstechnologie Aluminium. Berlin, Heidelberg: Springer Berlin Heidelberg; 2014. p. 217–270.
19. Srivastava V, Gupta M. Experimental assessment of self-healing nature in aluminum-based smart composites with NiTi wires and solder alloy as healing agents through Taguchi approach. Journal of Intelligent Material Systems and Structures. 2020;31:2101–16.

  doi:10.5075/epfl-298799_978-2-9701614-0-0

USING NEAR-INFRARED SPECTROSCOPY FOR QUALITY INSPECTION OF PREPREGS BEFORE PROCESSING

Moritz Salzmann[a*], *Michael Teuchtmann*[b], Ralf Schledjewski[a]

a: Department of Polymer Engineering, Processing of Composites, Montanuniversität Leoben, Leoben, Austria
b: i-RED Infrarot Systeme GmbH, Hafenstrasse 47-51, 4020 Linz, Austria
* moritz.salzmann@unileoben.ac.at

Abstract: *Prepregs are often discarded if the out-time after defrosting exceeds or because their shelf life has been expired. Revalidation of the quality of the prepreg is typically time-consuming and costly. On the basis of ageing measurements, the potential of near-infrared spectroscopy (NIRS), as a rapid and accurate technology to determine the degree of curing of a prepreg before or during processing. By using NIRS the discarding of prepreg could be change from a out-time or shelf life-based disposal towards quality-based one. A quality-based disposal, resulting in less waste, has ecologic as well as economic advantages towards. In the present study for an epoxy prepreg the degree of curing is determined by NIRS with high accuracy.*

Keywords: prepreg; degree of curing; near-infrared spectroscopy (NIRS);

1. Introduction

Prepregs are semi-finished products, consisting of a textile reinforcement impregnated with a matrix resin. For reactive resin matrices, there is a limited shelf life of typically 6-24 months even at low temperatures (-18 °C). When the prepreg is removed from the freezer, a limited time remains for its processing, the so-called out-time. If the prepreg cannot be processed within the out-time or if the shelf life has expired a time-consuming and costly revalidation is necessary or it must be disposed of. In both cases the degree of curing has been increased, affecting other related properties. Changes in the degree of curing are related to changes in concentration of the involved functional groups.

A technology able to monitor changes in concentration inline is near-infrared spectroscopy (NIRS). Molecular vibrations are excited by light, showing characteristic spectra. NIRS uses combination and overtone vibrations in the range of 700-2500 nm (13.000-4000 cm^{-1}). By multivariate data analysis the spectra can be assigned not only to concentrations directly but also to parameters related to changes in concentration. Possible applications of NIRS are cited for many industries, like food [1, 2], pharma [3, 4] or plastic processing industry [5, 6]. NIRS is a useful tool for inline-monitoring processes as it is fast, contactless and non-destructive. In the prepreg production NIRS has been used to inline monitor important parameters like solvent and resin content [7–12], sizing [10] , initiator content [13] and degree of pre-curing [9].

By means of a handheld NIR spectrometer, a fast verification of the state of a prepreg before and during processing would be possible. To this end, resilient regression models such as partial least square (PLS) models are required to predict the degree of curing from the spectra of the prepreg. A critical point to obtain a resilient PLS model is the quality of the reference data and

  doi:10.5075/epfl-298799_978-2-9701614-0-0

spectra used. In the present work, NIR spectra of an epoxy prepreg are measured at different "ages" and the degree of curing (reference data) is determined by differential scanning calorimetry (DSC). Different preprocessings are tested on the spectra to obtain a resilient PLS model for the prediction of the degree of curing of an epoxy prepreg.

2. Methods

2.1 Sample preparation and NIR measurements

An epoxy prepreg (Isopreg FR1179) provided by Isovolta AG (Wiener Neudorf, Austria) is aged between 0 h and 6 h at 80 °C in an oven, in steps of 30 min. After taking the sample out of the oven and cooling it down to RT, NIRS measurements are carried out using a high-quality FTNIR process spectrometer (i-RED GmbH, Linz, Austria). The spectrometer is equipped with a reflection optic (reflection measurement head/probe) consisting of an illumination optic (4 halogen spotlights) and a fiber-coupled collimation optics with a 25 mm collective lens. From each sample 10 spectra are collected, averaging 20 measurements with a gain of three.

2.2 Determination of the degree of curing

For reference, the degree of curing was determined by differential-scanning-calorimetry (DSC). The reaction enthalpy of the uncured and partially cured prepreg was determined with a DSC1 (Mettler Toledo GmbH, Schwerzenbach, Switzerland). The thermograms of the prepreg samples were recorded in the temperature range between 25 °C and 250 °C – with a heating rate of 10 K/min. Measurements were performed under nitrogen atmosphere (gas flow = 50 ml/min) in a 40 µl aluminum crucible. Three pieces of prepreg where punched out for each measurement with a punch plier (5 mm), resulting in a sample weight of 20 ± 2 mg prepreg. The instrument was calibrated using the melting enthalpy and the onset 136 temperatures of the melting of indium standards. The evaluations were done according to ISO 11357-5 (curing enthalpy) by using the Mettler Toledo DSC software (STARe, Mettler Toledo GmbH).

To obtain the resin proportion in the prepreg thermogravimetric analysis (TGA) is used. The weight loss of the prepreg was determined with a TGA 2 (Mettler Toledo GmbH, Schwerzenbach, Switzerland). Two samples were heated from 20 °C to 800 °C - with a heating rate of 20 K/min. Measurements were performed under nitrogen atmosphere (gas flow = 50 ml/min). The sample preparation was according to DSC-sample preparation. A volatile content of 34.83 ± 0.1 wt% is determined, which is used to calculate resin weight of the prepreg measured in the DSC.

2.3 Data analysis

Data analysis is done with MatLab, preprocessing as well as partial least square regression (PLS) are performed according to [14] with the MatLab-based PLS-Toolbox (Eigenvector Research Inc. Manson, United States).

From the measured wave number range, only the range between 3855 and 7244 cm^{-1} was used. The obtained energy spectra are preprocessed in five different ways, to find a good prediction PLS regression model for the degree of curing of the measured prepreg. The applied preprocessings are listed in Table 1. Standard Normal Variate (SNV) standardizes the spectra and corrects scattering effects of the sample. Mean Centering subtracts an average spectrum of all spectra from each spectrum. The origin of the spectra in the PLS becomes the center of the data,

  doi:10.5075/epfl-298799_978-2-9701614-0-0

simplifying the PLS. Smoothing can improve the PLS model quality by reducing the noise in the signal. The used filter width hereby is relevant, as a too low filter width does not remove all noise whereas a too high filter width can remove relevant information from the spectra. Derivatives (done by Savitzy Golay) remove baseline effects from the data and can improve the spectral resolution. The used filter width has here also a high impact on the result. Afterwards PLS regressions are calculated for 3-8 latent variables (LV). The chosen cross validation (CV) is contiguous blocks. Here, each test set for the sub-validation experiment is determined by selecting blocks of n/s objects in the data set, with n as the total number of objects (spectra) in the data set and s being the number of data splits. With n = 130 and s = 13, each degree of curing is once applied on a sub-validation experiment as unknown data. In total, 854 PLS models were calculated.

Table 1 : Applied preprocessings and tested LV's on the energy spectra

Preprocessings	used filter width	LV
SNV	-	3-8
SNV, Mean Center	-	3-8
SNV, Smoothing (Savitzy Golay, 0. Order), Mean Center	7-45 (in steps of 2)	3-8
SNV, 1st Derivative (1st order), Mean Center	7-45 (in steps of 2)	3-8
SNV, 2nd Derivative (2nd order), Mean Center	7-45 (in steps of 2)	3-8

The coefficient of determination (R^2), coefficient of determination of cross validation (R^2CV), root mean square error of calibration ($RMSEC$) and root mean square error of cross validation ($RMSECV$) are used to compare the quality of the PLS models.

3. Results

3.1 NIR-spectra

For different ages of the prepreg, corresponding offset-corrected absorbance spectra are shown in Figure 1. In the absorbance representation of an energy spectrum, the peaks specific to the composition of the medium are linearly proportional to the concentration. The offset was corrected between 4466 and 4454 cm^{-1}; a spectrum measured on plain aluminum was used as a background for absorbance calculation. The spectra differ mainly in two peaks. First, the broad peak around 5200 cm^{-1} which is associated with water. It is likely that the unaged sample (0 h) has some condensed water on the surface, caused by defrosting the prepreg. In all other spectra the water peak does not appear as they are stored for some time at 80 °C. The other changing peak is the epoxy peak at 4530 cm^{-1}. In general, it decreases over time, although the peak after 6 h at 80 °C appears to be larger than at shorter ageing times. That the epoxy peak after 6 h ageing appears to be larger than at shorter ageing times is a hint for a higher concentration of epoxy groups in the sample, resulting in a lower degree of curing. As it does not necessarily need to be relevant for the determination of the degree of curing by PLS regression it is not further investigated here. The other peaks show no relevant changes at the different ageing times.

  doi:10.5075/epfl-298799_978-2-9701614-0-0

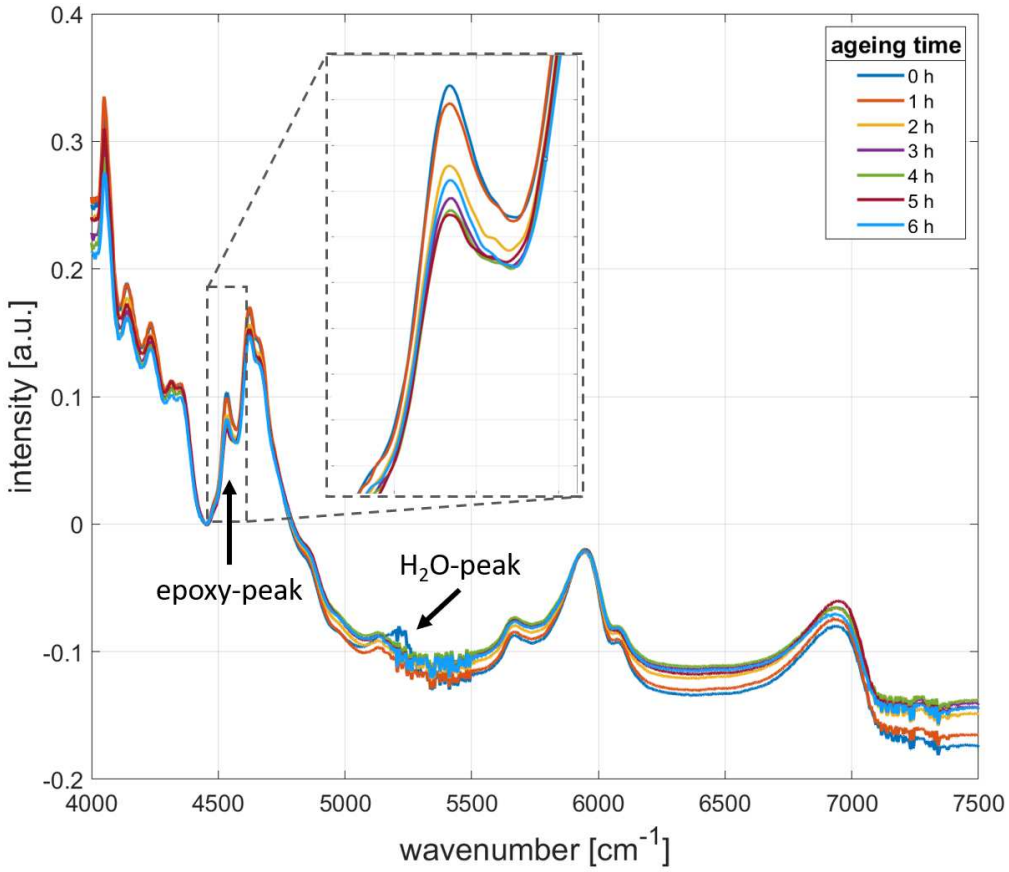

Figure 1: FTNIR-spectra of different stages of the prepreg with offset-correction. Most peaks do not show significant changes. As expected, the epoxy-peak (4530 cm^{-1}) decreases over time. Further, the unaged prepreg (0 h) shows an absorbance around 5200 cm^{-1}, which is associated with water.

3.2 Degree of curing

The degree of curing is obtained from the measured reaction enthalpy determined by DSC, using Eq. (1):

$$\alpha(t) = 1 - \frac{H_{part}}{H_{tot}} \tag{1}$$

Here, α is the degree of curing at the ageing time t, H_{part} is the remaining reaction enthalpy of an aged sample and H_{tot} denotes the reaction enthalpy of the unaged prepreg. The obtained α are shown in

Figure *2*. The sample after 0.5 h ageing shows a negative degree of cure, because the obtained $H_{part}(0.5\ h)$ was larger than H_{tot}. Together with the sample at 3 h, a second DSC scan was performed due to their large deviation from their expected degree of curing. Both scans resulted in similar degrees of curing as the first ones. Since the degree of curing obtained does not consistently increase over the course of the experiment, a linear fit is applied. Doing so, a second reference data set is obtained for the PLS-regression which is expected to provide more

consistent reference data than the originally obtained degrees of curing. Both data sets are shown in Table 2 .

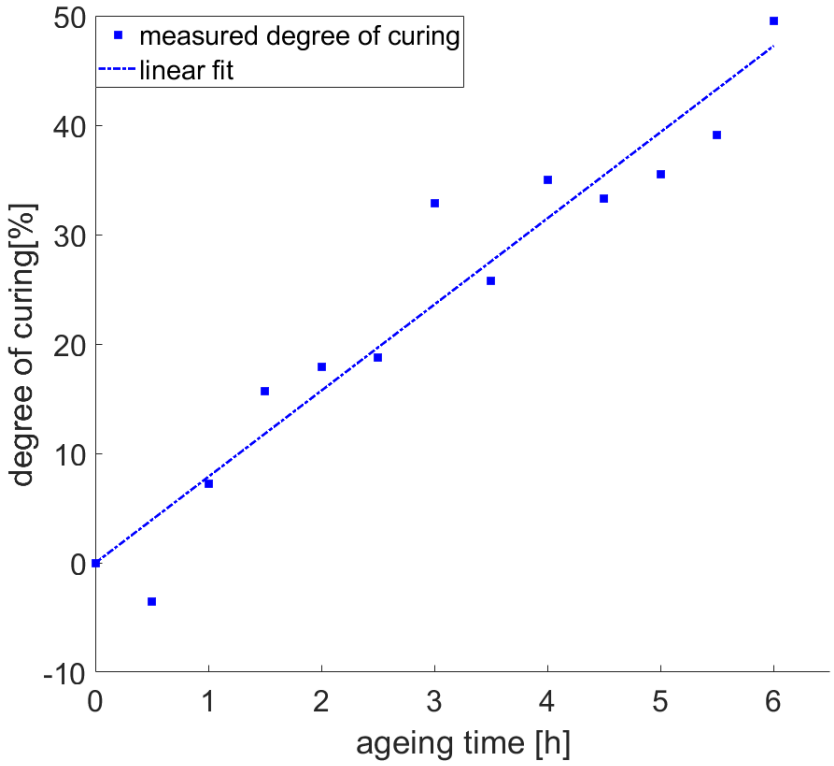

Figure 2: Degree of curing after ageing the prepreg at 80 °C.

Table 2: Measured and fitted degree of curing.

Ageing time [h]	Degree of curing [%]	
	By DSC	By fit
0	0	0
0.5	-3.5	3.9
1	7.2	7.9
1.5	15.7	11.8
2	17.9	15.7
2.5	18.8	19.7
3	32.9	23.6
3.5	25.7	27.6
4	35.0	31.6
4.5	33.3	35.4
5	35.5	39.4

  doi:10.5075/epfl-298799_978-2-9701614-0-0

5.5	39.1	43.3
6	49.5	47.3

3.3 Prediction of the degree of curing by NIR

PLS regression models to predict the degree of curing of the prepreg $\alpha_{Prepreg}$ are calculated with the measured degree of curing ($\alpha_m(t)$) as well as with the fitted degree of curing ($\alpha_{fit}(t)$) as reference data according to Table 1. The spectra corresponding to $\alpha_m(0.5)$ are excluded from the models, as a negative α is physically not possible and the spectra obviously contain another information than the reference data. The best PLS regression models found using $\alpha_m(t)$ or $\alpha_{fit}(t)$ as reference are presented in Table 3. For both reference data sets quantitative good PLS models are obtained, allowing an accurate prediction of $\alpha_{Prepreg}$.

Table 3: Best PLS-regression models found to predict $\alpha_{Prepreg}$.

PLS model	Reference	LVs/ Preprocessing	R^2	R^2CV	RSMEC	RMSECV
A	α_m	4/ SNV, Smoothing (31 fw) Mean Center	0.9803	0.9448	1.923	3.441
B	α_{fit}	4/ SNV, 2nd Deriv. (25 fw) Mean Center	0.9936	0.9796	1.179	2.113

fw: filter width

However, the PLS model B exceeds A in all parameters. Especially relevant here is the superiority in R^2CV and RMSECV, as they describe the performance of a model when it is applied to unknown data.

In Table 4 PLS models for the different preprocessing steps are shown, using α_{fit} as reference data. All applied preprocessings result, with suitable LVs and filter width, in a PLS model with at least acceptable prediction quality for $\alpha_{Prepreg}$. The obtained models show quiet similar values regarding R^2 and RMSEC, whereas significant differences show up in the more important R2CV and RMSCV values. Applying SNV (B1) on the spectra, results in a PLS model with R2CV = 0.9342 and RMSCV = 3,949. These key values are not further improved by adding Mean Center (B2) and Smoothing (B3) to the preprocessing. A significant improvement of R^2CV and RMSECV results from applying the 1st Deriv. (B4) and even more from the 2nd Deriv. (B). Both derivatives increase R^2CV, whereas RMSECV is reduced. The 2nd Deriv. even nearly halves RMSECV from 3.949 (B1) to 2.113 (B).

The improvement by applying derivatives (PLS models B4 and B) indicates the existence of baseline effects in the spectral data influencing the PLS models B1-B3, which has no correlation with the degree of curing. In addition, derivatives can separate overlaying spectral bands.

  doi:10.5075/epfl-298799_978-2-9701614-0-0

Table 4: Optimal PLS-models for preprocessing using α_{fit} as reference- data.

PLS model	Reference	LVs/ Preprocessing	R^2	R^2CV	RSMEC	RMSECV
B1	α_{fit}	6/SNV	0.9932	0.9342	1.218	3.949
B2	α_{fit}	5/SNV, Mean Center	0.9932	0.9338	1.219	3.961
B3	α_{fit}	5/ SNV, Smoothing (7 fw), Mean Center	0.9932	0.9334	1.216	3.967
B4	α_{fit}	3/ SNV, 1st Deriv. (13 fw), Mean Center	0.9928	0.9663	1.254	2.800
B	α_{fit}	4/ SNV, 2nd Deriv. (25 fw), Mean Center	0.9936	0.9796	1.179	2.113

4. Conclusion

The degree of curing of an epoxy prepreg is determined before processing by near-infrared spectroscopy (NIRS). Different preprocessing methods were tested on the spectral data. To obtain reference data for chemometric modelling, the degree of curing was determined by DSC. In addition, a fitted degree of curing based on the DSC data was tested. In total, 866 different PLS models were calculated. Both sets of reference data resulted in viable predictions models, but models based on the fitted degree of curing perform best. Accordingly, NIRS is a fast and accurate technique to determine the degree of curing of a prepreg before or during processing. Although DSC as a reference measurement method provides useful input data for modeling, preprocessing (fitting) of the reference data is recommended.

5. Acknowledgment:

Administrative support by the Österreichische Forschungsförderungsgesellschaft (FFG) is kindly acknowledged. This research was funded in the frame of the program “Produktion der Zukunft” by Bundesministerium für Klimaschutz, Umwelt, Energie, Mobilität, Innovation und Technologie (BMK) und Bundesministerium für Digitalisierung und Wirtschaftsstandort (BMDW), grant number 883906.

6. References

1. Saad AG, Jaiswal P, Jha SN. Non-destructive quality evaluation of intact tomato using VIS-NIR spectroscopy. International Journal of Advanced Research. 2014;12:632–9.
2. Grassi S, Alamprese C. Advances in NIR spectroscopy applied to process analytical technology in food industries. Current Opinion in Food Science. 2018;22:17–21. doi:10.1016/j.cofs.2017.12.008.
3. Fonteyne M, Arruabarrena J, Beer J de, Hellings M, van den Kerkhof T, Burggraeve A, et al. NIR spectroscopic method for the in-line moisture assessment during drying in a six-segmented fluid bed dryer of a continuous tablet production line: Validation of quantifying

abilities and uncertainty assessment. J Pharm Biomed Anal. 2014;100:21–7. doi:10.1016/j.jpba.2014.07.012.
4. Ojala K, Myrskyranta M, Liimatainen A, Kortejärvi H, Juppo A. Prediction of drug dissolution from Toremifene 80 mg tablets by NIR spectroscopy. Int J Pharm. 2020;577:119028. doi:10.1016/j.ijpharm.2020.119028.
5. Witschnigg A. Charakterisierung von Kunststoffen in Hinblick auf inline Qualitätskontrolle in Extrusionsprozessen mittels Nahinfrarotspektroskopie [Dissertation]. Leoben: Leoben; 2014.
6. Th. Rohe, W. Becker, A. Krey, H. Nägele, S. Kölle and N. Eisenreich. In-line monitoring of polymer extrusion processes by NIR spectroscopy. J. Near Infrared Spectrosc. 1998:325–32.
7. Jiang B, Huang YD. Quality inspection of laid fabric epoxy resins prepreg by near infrared spectroscopy. Composites Part A: Applied Science and Manufacturing. 2008;39:712–7. doi:10.1016/j.compositesa.2008.02.009.
8. Li W, Gao WJ, Chen P, Sun BL. Near-Infrared Spectroscopy and Principal Components Regression for the Quality Analysis of Glass/Epoxy Prepreg. Polymers and Polymer Composites. 2011;19:15–20. doi:10.1177/096739111101900103.
9. Li W, Huang YD, Chen P. Use of Near-Infrared Spectroscopy for On-Line Monitoring the Quality of Prepreg Cloth. Advanced Composites Letters. 2008;17:096369350801700. doi:10.1177/096369350801700201.
10. Jiang B, Huang Y. Near Infrared Spectroscopy for On-line Monitoring of Alkali- Free Cloth /Phenolic Resin Prepreg During Manufacture. IJMS. 2007;8:541–52. doi:10.3390/i8060541.
11. Bo J, Yu DH, Wei L, Li L. Non-destructive and Rapid Analysis of Resin and Volatile Contents in Carbon Fibre/Epoxy Resin Prepreg Cloth by Near-infrared Spectroscopy. Iranian Polymer Journal. 2007:19–326.
12. Li W, Huang YD, Liu L, Bo J. On-line Monitoring of Resin Content and volatile content in Carbon/Phenolic Resin Prepreg Cloth by Near-Infrared-Spectroscopy. Polymers & Polymer Composites. 2006:537–43.
13. Liu Q, Li D, Guan C. Analysis of initiator content of prepreg by near-infrared spectroscopy. Reviews in Analytical Chemistry. 2022;41:74–82. doi:10.1515/revac-2022-0035.
14. Kessler W. Multivariate Datenanalyse für die Pharma-, Bio- und Prozessanalytik: Ein Lehrbuch. 1st ed. Weinheim: WILEY-VCH; 2008.

DEVELOPMENT OF A RECIPE FOR THE PRODUCTION OF CHITOSAN/ GLYCOLIPIDS BIOCOMPOSITES FOR PLANT PROTECTION

Klaudia, Piekarska[a], Maria, Wisniewska-Wrona.*[a], Olga, Machrut-Mikolajczyk [b], Katarzyna, Struszczyk-Swita[b], Piotr, Drozdzynski [b], Hanna, Olszak-Przybys[c], Grazyna, Korbecka-Glinka [c]

a: Łukasiewicz Research Network – Lodz Institute of Technology, Sklodowskiej-Curie 19/27, 90-570 Lodz, Poland / klaudia.piekarska@lit.lukasiewicz.gov.pl

b: Institute of Molecular and Industrial Biotechnology, Faculty of Biotechnology and Food Sciences, Lodz University of Technology, Stefanowskiego 2/22, 90-537 Lodz, Poland

c: Institute of Soil Science and Plant Cultivation, Department of Plant Breeding and Biotechnology, Czartoryskich 8, 24-100 Pulawy, Poland

Abstract: *Plant protection relies mainly on the products of chemical synthesis [1]. However, the growing interest in reducing the use of pesticides stimulates research on the development of alternative plant protection agents based on natural products such as biopolymers. In the course of the conducted research, the methods of producing effective and environmentally friendly preparations for agricultural use evolved. Biocomposites based on chitosan with 5 and 15% wt. products of metabolism of endophytic bacteria – glycolipids were prepared and studied. The properties, like pH and dynamic viscosity, were parameterized and changes in structure were examined by FTIR spectroscopy. The effectiveness of biocompositions was assessed in plant tests which are a preliminary assessment of the biological activity.*

Keywords: biopolymers; biosurfactants; chitosan salts; plant growth

1. Introduction

Despite the tendency of developing countries to limit the use of plant protection products in agriculture, due to their potential harmfulness, chemical plant protection has so far dominated [1,2]. Taking into account health and ecological aspects, one should strive to follow the global trend of eliminating or significantly reducing the use of harmful plant protection products in favor of implementing modern plant protection products based on natural polymers, which is an alternative strategy with harmless substitutes and a similar mechanism of action [3,4].

Chitosan as a natural and positively charged polymer applied to the plant externally reacts with negatively charged molecules on the surface of pathogens (fungi and bacteria) and reacts with specific, chemically compatible active areas, which causes significant changes in the composition of the membrane function [5]. Properly selected chitosan also acts as an elicitor, activating defense mechanisms, which induces the resistance of the entire plant to several diseases caused by pathogens [6].

Biosurfactants, are surface active compounds produced by living organisms mainly microbes. These molecules are biodegradable and non-toxic and have also a promising role in agriculture. They take part in many microbial processes like biofilm formation or signaling, which makes them crucial in plant–microbe interactions [7]. Biosurfactants that contained sugar moieties in their structure are named glycolipids. These compounds may improve plant growth

  doi:10.5075/epfl-298799_978-2-9701614-0-0

promotion, as well as, play a role as an antimicrobial agent, so they may be used as a possible agent for the promotion of plant growth [7,8].

2. Experimental Part

2.1 Materials

As matrix chitosan, Chitoclear HQG 95 (TM3442) was purchased from Primex Company (Iceland), with a deacetylation degree (DD) of 81% and molecular weight average (Mw) 373kDa. Lactic acid was purchased from Avantor Performance Materials Poland S.A., earlier POCH S.A., (Poland). Glycolipids from the endophytic bacterial strain *Bacillus pumilus* 2A were obtained according to the method of Marchut-Mikołajczyk et al. 2018 [7]. The strain came from the resources of the Institute of Molecular and Industrial Biotechnology, Lodz University of Technology, Poland.

2.2 Chitosan lactate preparation

To achieve 1.0% chitosan lactate (CL) an appropriate amount of chitosan powder was weighed and dissolved in 0.5% lactic acid (LA). Homogenization with a tip G 45G, 4000 - 5200 rpm, for 2 – 3 hours. Then, stirred in with a low speed for 4 – 6 hours. Filtration was performed to separate possible impurities and undissolved particles on a Bushner funnel with filter cloth and compressed air connection. Two types of chitosan solutions were prepared at a concentration of 1.0 (CL1) and 0.98% (CL2) in 0.5% LA. pH for CL1 was determined to be 4.63. CL2 had to be raised to pH 6.6 by mixing with 10% KOH.

2.3 Compositions preparation

Compositions were prepared by mixing on an IKA Werke laboratory homogenizer, CL1, and CL2 with 5 and 15% by volumes of lyophilized milled biosurfactant (G). The composition of the prepared samples is summarized in Table 1.

Table 1: Sample compositions, pH and dynamic viscosity.

Sample	Concentration of chitosan lactate [%]	Concentration of glycolipid [wt. %]	pH	Dynamic viscosity [cP]
CL1	1.0	0	4.63	49.3
CL2	0.98	0	6.60	65.1
CL1/5G	1.0	5.0	4.82	53.9
CL1/15G	1.0	15.0	4.77	42.4
CL2/5G	0.98	5.0	6.30	58.0
CL2/15G	0.98	15.0	6.04	51.7

  doi:10.5075/epfl-298799_978-2-9701614-0-0

2.4 Testing methods

Determination of dynamic viscosity for chitosan lactate and polymer compositions. The dynamic viscosity [cP] was determined on a Brookfield model DV-II digital viscometer equipped with the Rheocalc V3.1-1 Program, at a temperature of 25 ± 1.0 ° C. CPE-40 cone was used for the measurement, sample volume - 0.5 ml. The temperature of the test was about 15 minutes. The measurement was performed according to the standard procedure developed in Institute. The pH parameter was determined using an electronic pH meter (Elmetron cp 315m) at 20°C. The tested samples were analyzed using the ATR technique to observe the changes in the structure under the influence of active additives. The tests were performed on the FTIR Nicolet iS50 spectrophotometer by Thermo Scientific (USA). Spectrophotometric analysis (FTIR) by ATR technique Infrared IR covers part of the spectrum of electromagnetic radiation in the range of 4000-400 cm^{-1}. The plant tests are a preliminary assessment of the biological activity of selected chitosan-based biopolymer compositions. The impact of tested biopolymer compositions on stimulation of seed germination was assessed on the bases of Phytotoxkit tests. During the procedure, the inhibition, presence, and increase in seeds germination after 72 hours of the exposure of seeds to biopolymer compositions in soil were measured. In control samples, seeds were hydrated with water.The Phytotoxkit tests (MicroBioTests Inc.) were carried out using seeds of *Sorghum saccharatum and Lepidium sativum* [7].

3. Results and Discussion

The pH values of the solutions with the addition of biosurfactant decrease along with the increase in the % content of biosurfactants. The effect is known, that addition of biosurfactant into chitosan lactate decrease. The dynamic viscosity values, despite low swirl, decrease along with the increase in the percentage of biosurfactant.

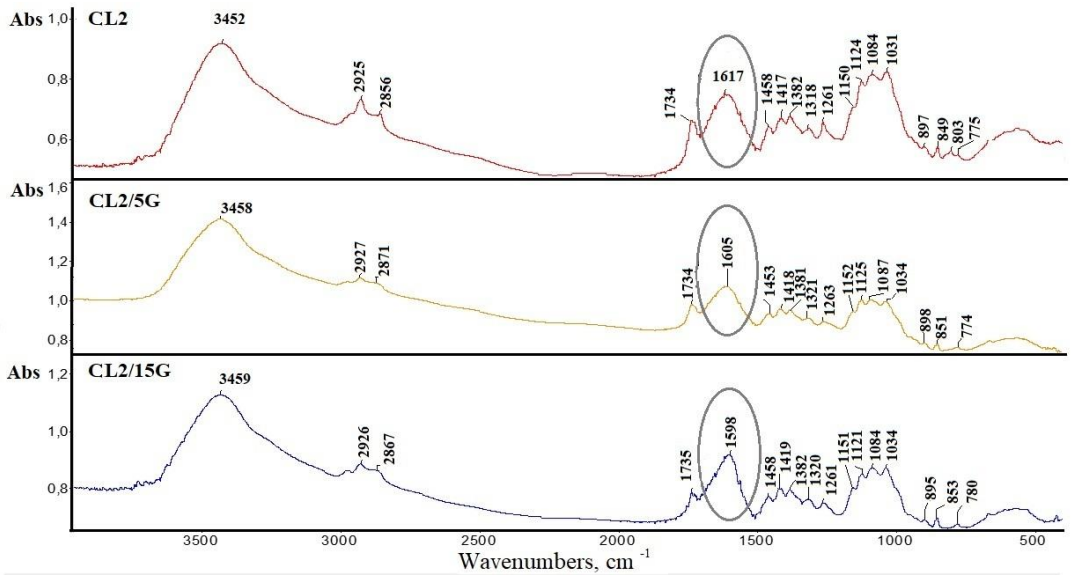

Figure 1. FTIR spectra of CL2, CL2/5G and CL2/15G.

As a result of the FTIR analysis characteristic bands for chitosan were observed for all samples. On the spectra (Fig. 1) bands around 3452 cm^{-1}, 898 cm^{-1} corresponding to O-H stretching bonds and around 2925 cm^{-1}, 2870 cm^{-1} corresponding to the symmetrical and asymmetrical

stretching vibration of C-H were observed. The bands are characteristics typical of polysaccharides and can be found in other polysaccharide spectra [9,10]. The presence of residual N-acetyl groups was confirmed by the bands at around 1617 cm^{-1} (C=O stretching of amide I) and 1320 cm^{-1} (C-N stretching of amide III). The CH_2 bending and CH_3 symmetrical deformations were confirmed by the presence of bands at around 1420 cm^{-1} and 1380 cm^{-1}. The absorption band at 1150 cm^{-1} was attributed to asymmetric stretching of the C-O-C bridge. On all spectra the bands at 1080 and 1030 cm^{-1} correspond to C-O stretching were observed. As a result of a concentration increase of biosurfactant in chitosan, a translation of the C = O bond stretching band in the N-acetyl group (amide I) was observed. For pure chitosan (CL2) band at 1617 cm^{-1} was observed, whereas after modification with biosurfactant this band was translated to wavenumber 1605 cm^{-1} for 5% (CL2/5G) and 1590 cm^{-1} for 15% (CL2/15G) of concentration. Probably, it may indicate the interaction of biosurfactant with this group.

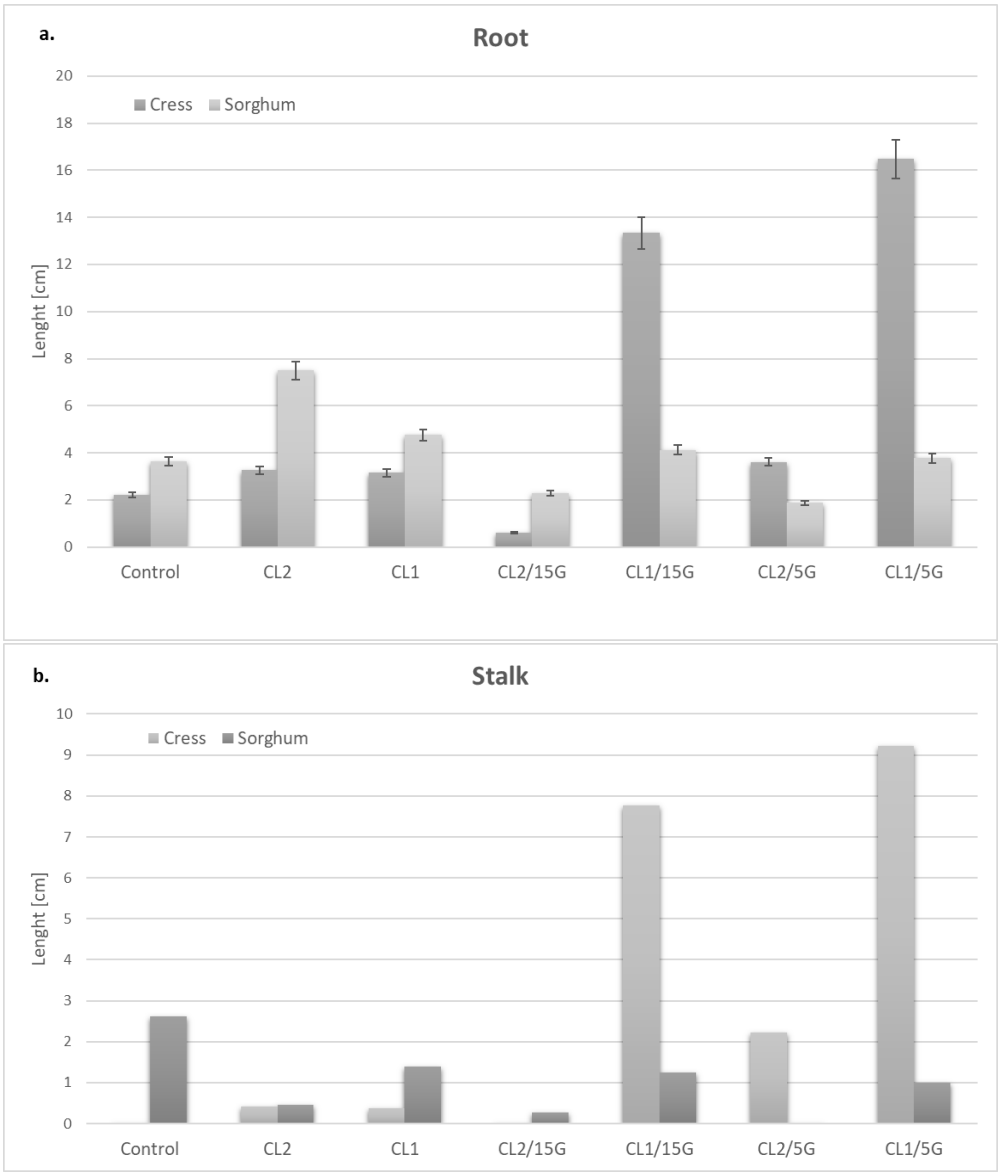

Figure 2. The effect of biopolymer composites on cress and sorghum growth :a. root lenght, b. stalk lenght.

  doi:10.5075/epfl-298799_978-2-9701614-0-0

The effect of obtained biocomposites on the seed germination and growth of *Lepidium sativum* and *Sorghum bicolor* were observed during 72 hours of plant tests. The results of our research showed that biocomposites of chitosan and glycolipids increased the growth of tested plants (both root and stalk) (Fig. 2). The most promising results were observed for cress watered with the chitosan lactate with the addition of 5% of glycolipids where the length of the stalk was 100 % higher than in samples hydrated with water and the length of the root was 80 % higher compared to the control sample.

4. Conclusions

The obtained results suggest that chitosan with glycolipids works effectively as a plant growth enhancer, and the proposed biocomposites can replace chemical fertilizers. The presence of chitosan in the biocomposites used also affects the protection of plants against pathogens. The proposed modern plant protection products based on natural polymers are non-toxic, biodegradable, and effectively accelerate the growth of the tested plants.

5. References

1 Frische T, Egerer S, Matezki S, et al. 5-Point programme for sustainable plant protection. Environ Sci Eur 30, 8, 2018.
2 Fantke P. Modelling the environmental impacts of pesticides in agriculture. In Assessing the environmental impact of agriculture. Burleigh Dodds Science Publishing. 2019.
3 Mondéjar-López M, Rubio-Moraga A, López-Jimenez AJ, Martínez JCG, Ahrazem O, Gómez-Gómez L, Niza E, Chitosan nanoparticles loaded with garlic essential oil: A new alternative to tebuconazole as seed dressing agent. Carbohydrate Polymers, 277, 118815, 2022.
4 Ghule MR, Ramteke PK, Ramteke SD, Kodre PS, Langote A, Gaikwad AV, & Jambhekar H, Impact of chitosan seed treatment of fenugreek for management of root rot disease caused by Fusarium solani under in vitro and in vivo conditions. 3 Biotech, 11(6), 1-12, 2021.
5 Palma-Guerrero J, Huang IC, Jansson HB, Salinas J, Lopez-Llorca LV, Read ND, Chitosan permeabilizes the plasma membrane and kills cells of Neurospora crassa in an Energy dependent manner. Fungal Genet. Biol. 46, 585–594, 2009.
6 Hassan O, Chang T, Chitosan for eco-friendly control of plant disease. Asian J. Plant Pathol, 11, 53-70, 2017.
7 Marchut-Mikołajczyk O, Drożdżyński P, Polewczyk A, Smułek w, Antczak T, Biosurfactant from endophytic Bacillus pumilus 2A: physicochemical characterization, production and optimization and potential for plant growth promotion. Microbial Cell Factories, 20(1), 1-11, 2021.
8 Marchut-Mikolajczyk O, Drożdżyński P, Pietrzyk D. et al. Biosurfactant production and hydrocarbon degradation activity of endophytic bacteria isolated from Chelidonium majus L. Microb Cell Fact 17, 171, 2018.
9 Silverstein RM, Webster FX, Kieml DJ, Spectrometric Identification of Organic Compounds 7th edition. John Wiley&Sons, New York, USA,2005, ISBN 0-471-39362-2.
10 Gzyra-Jagieła K, Pęczek B, Wiśniewska-Wrona M, Gutowska N, Physicochemical Properties of Chitosan and its Degradation Products. Chitin and Chitosan, 61–80, 2019.

  doi:10.5075/epfl-298799_978-2-9701614-0-0

NEW SOLUTIONS FOR THE RECYCLING OF CFRP COMPOSITES

Hannes Stadler[a], Jörn Weitzenböck[a] and Christoph Burgstaller[a]

a: Transfercenter für Kunststofftechnik GmbH, Wels, Austria
Email: hannes.stadler@tckt.at, www.tckt.at

Abstract:

In order to significantly improve the life cycle assessment of CFRP components, it would be necessary for the continuous fibers produced with high energy input to be recovered and used again in a high-quality composite material, e.g. for aerospace applications. Therefore, the aim of the present work was to recycle current production waste from fiber composite manufacturing in the aircraft industry and to use it again in a reasonable way in aviation products. An innovative semi-finished product in form of a prepreg with phenolic resin was developed from the recovered recycled fiber and subsequently used as a layer material for a sandwich structure. The rCF prepreg was processed via hot pressing and then mechanically characterized. The results are very close to the desired range and in some cases exceed the values of the reference material, a glass fiber phenolic resin prepreg used as standard.

Keywords: CFRP; recycling; prepreg

1. Introduction

Carbon fiber reinforced plastics (CFRP) are becoming increasingly important as aircraft components. The composite material, in which carbon fibers are embedded in a polymer matrix, is lighter than previously used materials, but at the same time enables high-strength and -rigid component structures. CFRP components can be manufactured by various processes, but the most important in the aerospace industry is the processing of carbon fiber textiles that are pre-impregnated with a defined amount of matrix, so-called prepregs. Due to their low specific weight, these fiber-reinforced composites have great potential for weight reduction and thus also for resource savings during the utilization phase. However, in order to be able to evaluate the resource efficiency of the use of CFRP, it is necessary to consider the entire life cycle. [1] To date, there is no economically viable, large-scale, automated recycling technology for CFRP materials worldwide, although the volume flows of waste containing CFRP are becoming increasingly larger due to their increased use in lightweight construction in the aerospace industry, the automotive sector and in wind energy. While in the 1970s the proportion of CFRP structures in an Airbus was only 5%, the Airbus A380 already has around 22% of its structure made of CFRP. For the latest aircraft generations, such as the Boeing 787 as well as the A350 X WB, already about 50% composite materials are used, which are mainly used for primary structures (airframe, wings, etc.).[2]

An advantage over other material groups with regard to the CO2 footprint only arises if the CFRP can be fully recycled. Due to the material combination and the firm bond between carbon fibers and polymer matrix as well as the thermosetting matrix, CFRP does not actually represent a material suitable for recycling. However, recycling processes are possible and due to the price of newly produced carbon fibers, also economical. The key challenge here is the separation of

  doi:10.5075/epfl-298799_978-2-9701614-0-0

fibers and matrix material. For the recycling of impregnated carbon fibers, both as cured components and uncured waste residues, pyrolytic and solvolytic recycling approaches are currently being investigated. [3] Thereby dry carbon fiber residues, prepreg materials and end-of-life components are first sorted and shredded. In the pyrolysis process, the material is heated to 400 to 1.000 °C so that the matrix material evaporates. The relatively short fibers from the pyrolysis process (approx. 1-50mm) cannot be used to produce woven fiber or non-crimp fabric mats for high-quality CFRP components. In our view, the most promising approach is the production of nonwovens from recycled carbon fibres (rCF), which are needle-bonded or sewn as required. Although these nonwovens do not exhibit comparable mechanical properties in the composite as continuous fiber-reinforced virgin material, they can nevertheless be used as reinforcement in paneling elements, e.g. in aircraft interiors.

Therefore, the aim of this work was to develop a prepreg semifinished product with a suitable matrix system, to consolidate it by hot pressing and to evaluate its potential as an impregnated top layer for interior sandwich components in aircraft. As a reference, the glass fiber prepreg previously used by an aerospace supplier was used.

2. Materials and Methods

2.1 Materials

The material used in this work was supplied by carboNXT®, a company belonging to Mitsubishi Chemical Advanced Materials. The investigated nonwoven is a wet-laid-rCF with a grammage of 30 g/m² and an average fiber length of 6-12mm. This fleece is also called carbon fiber paper and is suitable for surface lamination or the reinforcement of sandwich components. Although the arrangement of carbon fibres is important for the mechanical properties, the rCF distribution was characterized using the F-Scan system (Profactor). A strong production-related orientation of the fibers of the wet-laid nonwoven is shown as a significant peak in Figure 1 (right).

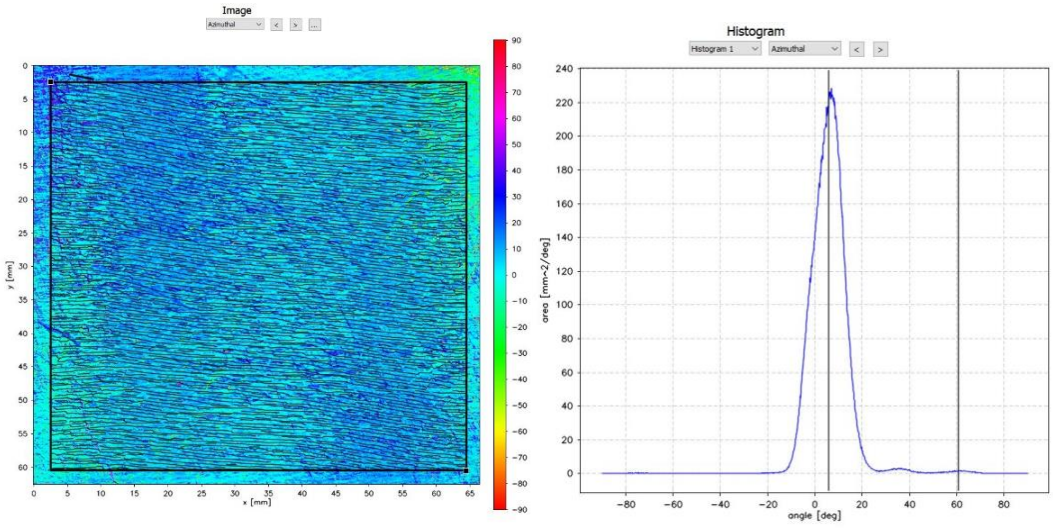

Figure 1. F-Scan of the wet-laid rCF (30g/m² left) and fibre orientation distribution (right)

The prepreg for this study was manufactured using the solvent process on a laboratory plant with a width of 300 mm. This line is a horizontal line, which offers the advantage that the tensile stresses in the manufacturing process are lower than in a line with vertical orientation. A phenolic resin (PF) certified for aerospace applications was used for impregnation. The results

of the mechanical tests were compared with a product, which is currently being used in the target application of the rCF prepreg by an aerospace supplier. This is a prepreg for processing in the heating press made of glass fiber (GF) fabric with a grammage of 105 g/m² and also a phenolic resin matrix.

2.2 Composite production

The samples in our experiments were produced in a heating/cooling press using a dipping edge tool with a size of 250x350 mm². The rCF prepreg was processed in three different constellations, as shown in Table 1. On the one hand as a solid laminate containing 50 rCF-layers and a consolidation pressure of 5 bar and on the other hand as a laminate with 90 layers and a pressure of 25 bar. For the manufacturing of the sandwich panel, a nomex core with a height of 9.4mm, a cell size of 3.2mm and a density of 29 g⁄m³ was used with 4 rCF-layers on each side. The sandwich panel was consolidated and cured at a pressure of 5 bar.

Table 1: Overview over rCF-prepreg test plates investigated in this study

ID number	layer content	Consolidation pressure	Nomex core
1	50 (rCF)	5	none
2	90 (rCF)	25	none
3	4 / 4 (rCF)	5	yes
4	18 (GF)	5	none

For curing in the press, the respective lay-up was placed in the mold and exposed to the appropriate pressure in the cold heating press. Then heating up to 135°C takes place and the temperature was maintained for 75 min and subsequently cooled down to 40°C with 1 bar and then demolded (see Figure 2). The phenolic resin used was cured, according to the processing instructions from the prepreg supplier, without venting strokes.

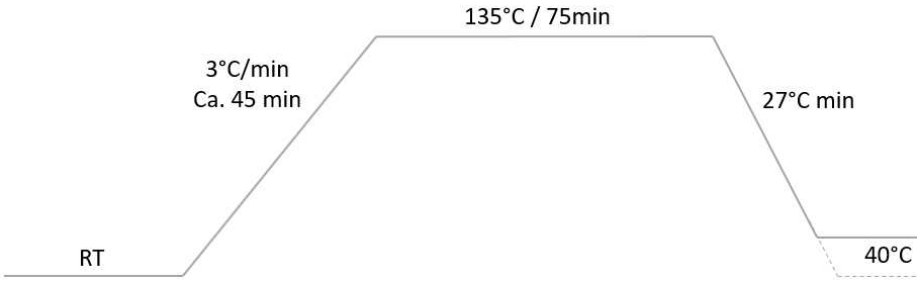

Figure 2. Curing temperature profile rCF-prepreg

The goal of producing test panels and sandwiches with this prepreg system was challenging, but it was achieved. A seen in Figure 3 the haptic and the processing of the prepreg can be rated as very positive.

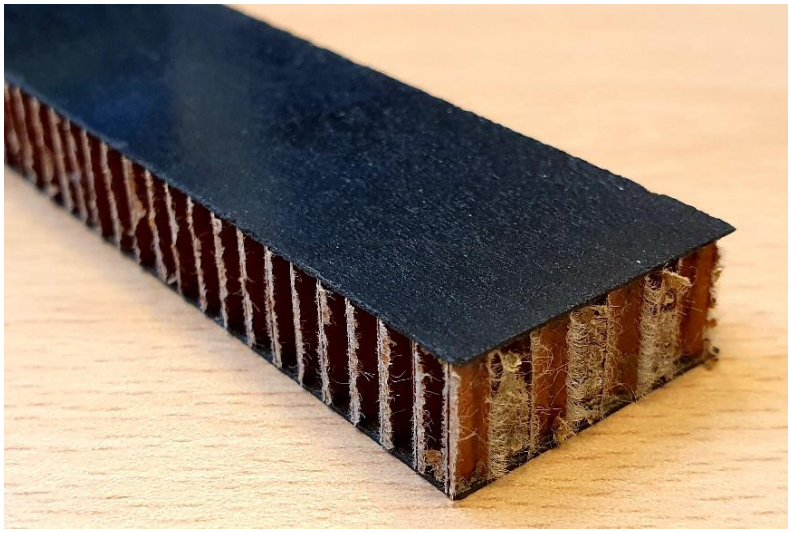

Figure 3. rCF sandwich panel

2.3 Mechanical testing and determination fibre volume fraction & porosity

Tensile test specimens were cut out of the solid laminates and the mechanical characterization of the samples was carried out on a universal testing machine Zwick/Roell type Z150 according to ISO 527-4. The dimensions of the specimen were 250x25 mm. Cap strips were used for better force application.

Furthermore, flexural test specimens for the 3-point bending test according to EN ISO 14125 were cut out of the solid rCF panels. For the 4-point bending test, the sandwich panels were used and cut to size. Testing was carried out in accordance with DIN 53293 on a 10kN Zwick/Roell flexure testing machine.

The Climbing Drum Peel Test according to standard EN 2243-3 is used to determine the bond of the top layers to the core. Test specimens were also cut to size for this and thus characterized on a universal testing machine Zwick/Roell type Z20.

The fiber volume content was determined for the rCF-PF solid laminates by chemical extraction according to DIN EN 2564. For this purpose, the fiber composite is immersed in sulfuric acid and heated, which dissolves the entire matrix and leaves the fibers behind. The acid used is washed off the fibers with distilled water. The cleaned fibers are then dried. Since matrix residues remained in the first run, this procedure was carried out twice.

3. Results and Discussion

The tensile modulus and tensile stress of the rCF solid laminate with 50 layers rCF-prepreg and the reference material made of 18 layers GF-prepreg are shown in the following figure 4. The laminate thickness was around 2 mm for both materials. The reference product achieves a tensile modulus of more than 13 GPa in both warp and weft direction and a tensile stress of more than 200 MPa. In comparison, the rCF prepreg achieves a stiffness of 18.8 MPa and a strength of 190 MPa, thus fulfilling or even partly exceeding the requirements for the reference material. Due to the relatively high porosity of over 10%, we still see significant potential for improvement and further investigations in rCF materials.

  doi:10.5075/epfl-298799_978-2-9701614-0-0

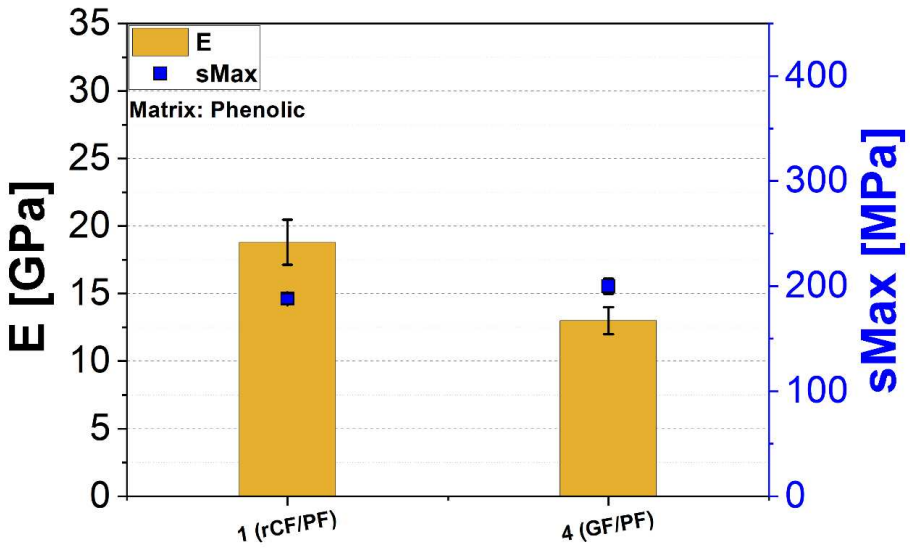

Figure 4. Tensile properties of rCF- composites (1) and GF composites (4) with phenolic matrix system

Figure 5 shows the flexural modulus and flexural strength of the solid laminate specimens with 50 (#1) and 90 layers (#2) respectively. Similar to the results of the tensile test, the rCF prepregs clearly reach the stiffness values of the reference material (#4) in the bending test. With the 50-layer composite a flexural modulus of about 21 MPa is achieved and with the 90-layer composite a very promising value of 38 MPa. Whereas the modulus for the reference material is at 14 MPa. The bending stiffness of the rCF's shows a direct proportionality in connection with the number of plies, since approximately twice the number of layers also results in twice the bending stiffness. But the large number of 90 layers also results in variations of over 11%, whereas the variation is smaller with the quantity of 50 layers. Both materials were repeatedly inter-compacted with a silicone roller during layer build-up. It was difficult to apply a vacuum to achieve better intermediate compaction due to the mold geometry. This would definitely bring further improvements.

The flexural strength increases with the number of plies but not directly proportional, like the stiffness. Nevertheless, it is sufficient to reach the reference value. The glass fiber prepreg achieves a flexural strength of over 250 MPa. The 50-layer laminate is just below the value with 230 MPa, while the 90-layer laminate, despite the greater standard deviation, always remains above the reference mark with 305 MPa.

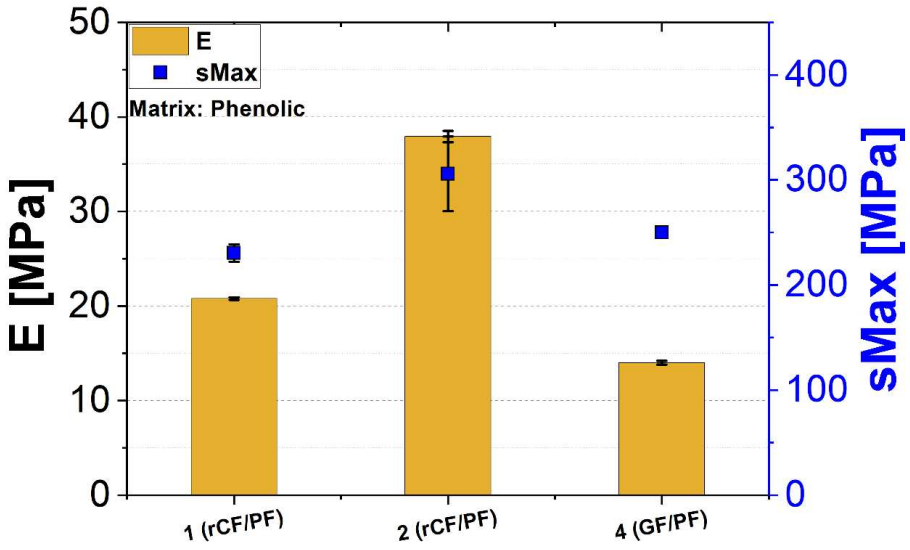

Figure 5. Flexural properties of of rCF- composites (1,2) and GF composites (4) with phenolic matrix system

Figure 6 shows the typical test setup of the sandwich 4-point bending test with the specimen clamped during the test (left) and the occurring failure mode (right). The number of top layers in the rCF sandwich panel has increased from 2 to 4 layers compared to the sandwich panel with the GF-prepregs due to the thickness requirements for these layers. Nevertheless, compared to the glass fiber fabric only 60% of the weight was used. But due to the low strength of the rCF top layers the specimens did not fail as required in the center, in the area with constant bending moment and without transverse force, but at the radii of the bending beam. In this respect, it is difficult to compare the two materials with each other and thus the determined rCF characteristic values cannot offer any conclusion on the comparison with the reference material. For future investigations, the thickness and the strength of the rCF top layers must be increased accordingly.

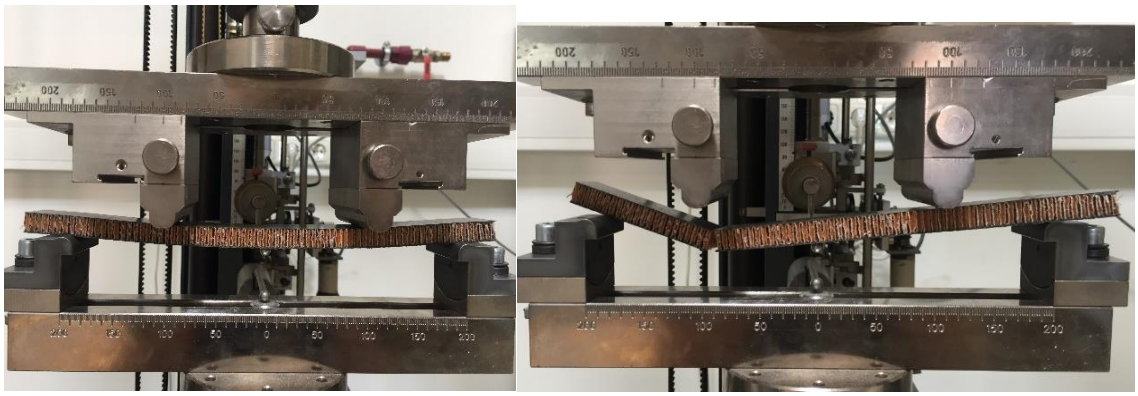

Figure 6. 4-point bending test of rCF-prepreg sandwich panel (left), failure mode (right)

The Climbing Drum Peel Test was used to determine the bond of the face sheets to the core. However, in the case of the rCF sandwich panels, the top layer breaks shortly after the measurement starts. Therefore, the adhesion could not be determined mechanically, where the reference material reached more than 32 N per 75 mm according to the EN 2243-3 standard.

For this reason, images of the cross section were taken with an optical microscope to gain an impression of the contact of the rCF prepreg to the Nomex core (see Figure 7). The interface between the top layers and the core is visually smooth and without any visible defects such as delaminations in the area of the bond. The core shows no damage caused by the pressure load during processing in the press. Porosities, on the other hand, are clearly visible.

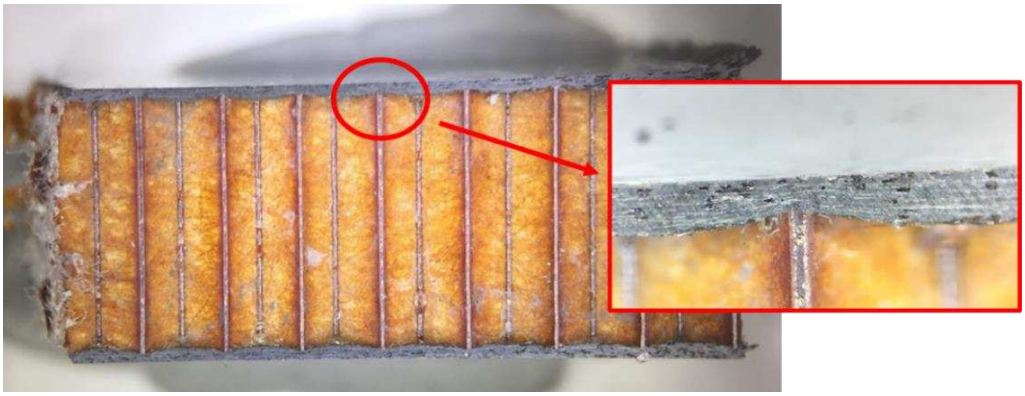

Figure 7. rCF-Sandwich cross section, Detailed view of the cut surface in the microscope

Finally, the fiber volume content of the samples from rCF solid laminates is shown in the following Figure 8. The result fits very well with the expectations, because the prepreg had a relatively high resin content of almost 80 vol%. When processed with the lower consolidation pressure of 5 bar, only a small amount of resin was squeezed out during processing and the fiber volume content for laminate 1 (#1) is consequently about 17%. The sample with 90 layers (#2) was consolidated with a higher pressure of 20 bar and results in a comparable laminate thickness. Thus, a higher fiber volume and a lower void content are obtained. As shown in equation 1 below, the ratio of the fiber volume contents reflects the number of layers.

$$\frac{50\ (layers)}{90\ (layers)} = 0{,}555;\ \frac{17{,}07\ vol\%\ (FVF)}{30{,}68\ vol\%\ (FVF)} = 0{,}556 \qquad (1)$$

As mentioned before and evident in the microscopy image, both samples have a relatively high porosity content of about 12 vol% for #1 and 7.5 vol% for #2, which certainly has a negative effect on the mechanical performance and needs to be improved.

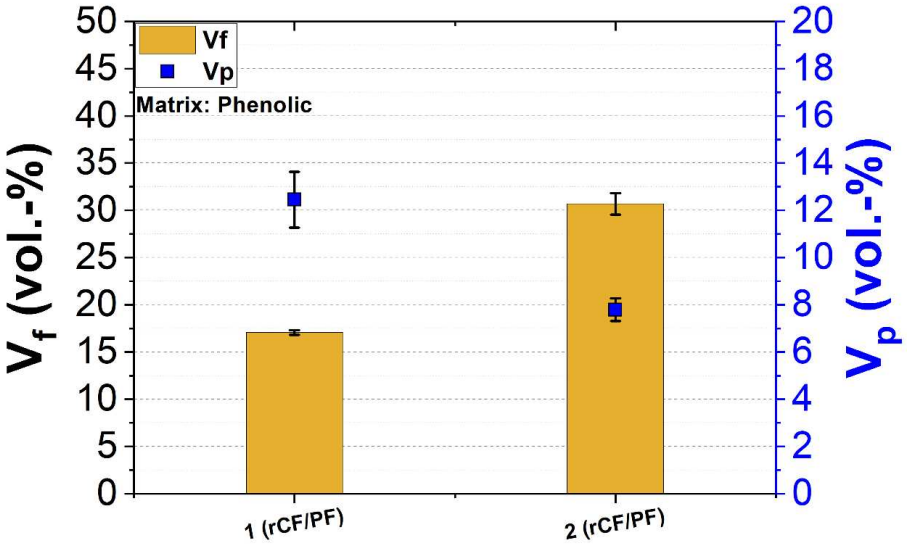

Figure 8. Fibre volume and porosity content of rCF-composites with 50 layers (left) and 90 slayers (right)

4. Conclusions

The aim of this work was to reuse recycled carbon fibers from the aerospace industry in the aerospace interior sector. The recycling of carbon fibers has been researched a lot in the last years and more and more approaches have been developed to integrate the rCF nonwovens into a series process. On the one hand, different matrix systems have been investigated and improved, both with thermoset and thermoplastic matrices. The production of a yarn from rCF was also researched, as well as different load-path appropriate reinforcement of rCF nonwovens with UD tapes. This work is part of all these projects and shows further possibilities to integrate recycled carbon fibers into series production in order to offer alternatives suitable for series production instead of uneconomical utilization in incineration. [4, 5, 6]

Within the scope of our study, a production-ready rCF phenolic prepreg was developed that could be a real alternative to conventional GF-PF prepregs. We are aware that this feasibility study does not cover all the tests necessary to approve a prepreg for aerospace applications. The results obtained from the tests carried out, tensile and bending tests of the solid laminate as well as a fiber volume content determination and a 4-point bending test of the sandwich structure, are close to the desired range and in some cases exceed the stated values of the reference material. The haptics and the processing possibilities of the rCF prepreg are really promising and offer a very good initial situation for future research projects, where the reduction of porosity and the improvement of surface layer strength should be areas of work.

Acknowledgements

The authors are grateful to the FFG – Österreichische Forschungsförderungsgesellschaft for financial support of the TAKE OFF-project “PIONEER – Prozessüberwachung und Recycling von biogenen Verbundwerkstoffen mit Funktionsintegration für Flugzeuginnenausstattungen”.

5. References

1. Achternbosch M, Bräutigam KR, Kupsch C, Reßler B, Sardemann G. Analyse der Umweltauswirkungen bei der Herstellung, dem Einsatz und der Entsorgung von CFK- bzw. Aluminiumrumpfkomponenten. Wissenschaftliche Berichte FZKA 6879 des Forschungszentrums Karlsruhe. 2003.
2. Kreibe S et al. Entwicklung ressourceneffizienter CFK-Recyclingverfahren und Prozessketten für die künftige Bereitstellung qualitativ hochwertiger rC-Halbzeuge. Final report MAI Recycling. 2015.
3. Martin C et al. Near- and supercritical solvolysis of carbon fibre reinforces polymers (CFRPs) for recycling carbon fibers as a valuable resource. J. of Supercritical Fluids 2012, 66:232-240.
4. Manis F. (2020): | Carbonfaser Recyclingwerkstoffe für industrielle Anwendungen. Fraunhofer-Institut für Gießerei-, Composite- und Verarbeitungstechnik IGCV. Final report CaRinA. 2020.
5. Tenowo GmbH. Vliesstoff auf Basis rezyklierter Carbonfasern. https://www.hoftexgroup.com/hoftexgroupag-en/news-und-media/dateien/Carbon-

Magazin-Die-Fachbroschuere-rund-um-den-Werkstoff-der-Zukunft-Edition-Winter-2016.pdf. 2016.

6. Schramm S. Nendel S. Neuartige hybride Halbzeuge auf Basis von Recycling-Carbonfasern für Anwendungen im Strukturleichtbau. Institut für Zellstoff und Papier IZP PTS-Forschungsbericht 04344/17. 2017

  doi:10.5075/epfl-298799_978-2-9701614-0-0

CONDUCTIVE SMART NANOCOMPOSITE MATERIALS FOR STRUCTURAL HEALTH MONITORING AND MOTION DETECTION

Olalla. Sanchez-Sobrado, Daniel del Rosario, Ricardo Losada and Elena. Rodriguez*
Advanced Materials, AIMEN, O Porriño, Spain.
**olalla.sanchez@aimen.es*

Abstract: *Presented work collects results from evaluation of different polymeric based composite materials for Structural Health Monitoring and Strain Detection. With the aim of show the variety of key materials in sectors like civil aviation, wind energy, automotive or railway that present this ability, specimens of very different nature have analyzed: a) thermoplastic commercial 3D printing filaments loaded with carbonic nanofillers; b) epoxy resin loaded with graphene and c) Long carbon fiber reinforced resin composite. Measurements of electrical properties of resulting materials were taken to evaluate capability to detect the presence and the size of a structural defect as well as its spatial location. On the other hand, simultaneous measurements of electrical resistivity and mechanical strain during tensile tests were performed to analyze the behavior of materials as strain detectors. All composites studied have shown a positive response (modification of electrical performance) to external mechanical stimulus: induced damage and deformations.*

Keywords: conductive nanocomposites; structural health monitoring; motion detection; carbonic nanomaterials; graphene, carbon nanotubes.

1. Introduction

Structural maintenance in several industrial sectors like civil aviation, wind energy, automotive or railway is being currently based on scheduled maintenance on-ground inspections, in which Non-Destructive Inspections (NDI) are used to detect damage within the structural materials. In this scenario, in-service Structural Health Monitoring (SHM) of nanocomposite material parts plays a key role in the assessment of their performance and structural health [1]. Conductive carbon-based materials networks like those based in carbon nanotubes (CNTs) and others have been recently utilized as in situ sensors to detect microcracking and deformations in polymer and fiber reinforced polymer composite materials by using resistivity change method [2], [3]. The low electrical percolation threshold of these conductive materials allows forming an electrically conductive network withing the composite structure. This network allows identification of the formation of microcracks due to the changes in the electrical resistance as well as the detection of mechanical deformations of the structure [4].

The resistivity change method to perform SHM is since the generation of a microcrack in the polymer matrix of a composite material breaks conducting chains in the percolating conductive material or nanofiller network producing a modification on the electrical resistivity that can be related with the formation and size of the produced crack [5]. However, the spatial localization remains difficult. To overcome this drawback, resistance maps have been proposed to locate damage position [6] together with multi-scale modelling approach for simulating crack sensing [7]. On the other hand, the use of the coupled electro-mechanical response of these materials to self-sense their strain and damage during mechanical loading has been also widely studied

  doi:10.5075/epfl-298799_978-2-9701614-0-0

[8]. Carbonic materials like CNTs (but not only) have been deeply analyzed as candidate for strain and motion sensors at the macroscale, due to the dependence of the electrical properties on mechanical deformation at the nanoscale due to piezoresistive behavior. Many publications report the use of this carbonic based polymer nanocomposite for in textile-based, wearable sensing system for real-time motion detection [9], muscle, breathing and pulse motion [10] or electronic skins [11].

In the presented work, electrical properties, and both damage and strain dependent electrical resistance characteristics of several different carbon-based/polymer composite and nanocomposite materials were investigated: (a) CNTs reinforced RTM6 Epoxy resin, (b) different carbon-based nano additives thermoplastic composite for 3D printing technologies prepreg composite: PLA/CB; ABS/CNTs; PETG/CNTs and PEKK/CNTs and (c) long carbon fiber composite laminates. To analyze the ability of the different developed materials to detect different structural defects, the evolution of the electrical resistance when the size of the produced hole is increased has been analyzed for each composite. Systematically, large, and linear enhancement is obtained, even for the smallest defects. This behavior places polymeric composites integrating carbonic materials and nanomaterials as one of the most promising solutions for SHM applications. Some preliminary tests to evaluate capacities for failure detection have been as well performed. On the other hand, in this work we show a study of the capabilities presented by reinforced polymeric composites for motion detection. Simultaneous measurements of strain and electrical resistance were taken for representative composite coupons during tensile tests. The signal-matching presented by the different materials has been discussed as a direct estimation of the capability for strain sensing and potential use for motion detection applications.

2. Experimental

- FFF 3D printing manufacturing process.

Four dog-bone-type specimens and four rectangular specimens were printed for each of the four purchased filaments, with the commercial materials described below. The printing machine used was a 3D printing: A2V4 printing machine (3nt r) and Ultimaker 2+.

- Resin coupons preparation

Epocyl is the trade name of an epoxy resin with a indetermined load of CNTs that was purchased from Nanocyl. To cure mixtures a mixture of accelerator and hardener were used: Aradur 1571 (50%)/ Accelerator 1573 (50%). The 24 parts of the mixture by 76 of the mixture of resins and we cure at 120º C for 2h. The catalyst mixture is heated slightly before hand-mix it well and is mixed with the resins just before curing.

- Prepreg layup manufacturing process

The layers of Carbon Fiber prepreg, purchased from Toray, were cut manually with (0º,90º, +45º,-45º). First, a release agent was applied on the tool surface. The stack of plies was piled up manually. After the first ply was laid, debulking was made to ensure a good adhesion of the pre-preg to the tool surface. The rest of the plies were positioned following the stacking sequence. Debulking was performed for each four plies or when wrinkles appeared during stacking. This

  doi:10.5075/epfl-298799_978-2-9701614-0-0

step was accomplished by placing a non-perforated bleeder film and breather layer under a flexible vacuum bag, and by applying 0,9 bar of vacuum. After placing all the prepreg layers, the coupon was covered by a peel ply, a layer of perforated bleeder film and a non-woven breather cloth. Before introducing the tool on the oven, a vacuum test was performed to check the bag's integrity. Afterwards, the coupon was left under vacuum following the programmed curing cycle. After curing a demoulding phase was carried out.

- Measurements of electrical properties.

Once manufactured, two silver contacts 1 cm thick and 5 cm apart are painted and the ohmic resistance is measured with crocodiles in the acquirer. Data acquisitor system Keysight DAQ970A with an integrated DAQ901A-20 channels armature multiplexer module. This system acquires simultaneously measurements of electrical resistance and mechanical strain to analyse the SHM behaviour.

- Estimation of Conductivity and resistivity

Shape Factor (F)=S/L = 2x0,5/5 (mm) F=0,002 m

Conductivity $\sigma=1/\rho=1/R*0,02$ (S/m)

- Tensile tests.

They were carried out following the ASTM D3039/D3039M standard, the speed was 1mm/min, 10 cycles of ascent and descent were carried out in displacement control, until reaching the target tensions of 50, 100, 150, 200, 250, 300, 350, 400, 450 and 500 MPa. The speed of the section from 0 to 50 MPa is carried out at 0.5 mm/min. The speed of the rest of the sections is 1 mm/min. Due to the placement of the sensors on the specimen, the transverse extensometer cannot be installed.

3. Results and discussion

3.1 3D printing comercial thermoplastic filaments with nano-carbonic additives

Six dense dumbbell-type specimens were printed for each of the four purchased filaments, commercial filaments are described in Table 1. These consisted basically in thermoplastic-based polymers of different type and characteristics: PLA, ABS, PETG and PEKK. All these thermoplastics are nowadays highly considered for applications in numerous industrial sectors like aeronautics, wind energy, automotive, health, construction, or railway. All studied materials presented electrical conductivity due to small loads of different carbonic-based nanofillers: carbon nanotubes (CNTs) and Carbon Black (CB). To evaluate their conductivity, measurements of electrical resistance were taken. Once manufactured, two silver contacts of 1 cm thick and separated by 5 cm were painted directly on the polymeric surface and the ohmic resistance is measured using crocodiles with the acquirer system. The estimated values for conductivity calculated using procedure explained in experimental section, are presented in column 4 of Table 1.

Table 1: Thermoplastic based conductive polymeric filament used to evaluate conductive, SHM and Strain detection capacities.

  doi:10.5075/epfl-298799_978-2-9701614-0-0

Coupon	Description	Supplier	Resistance (ohm)
PLA	Carbon Black (load 20%)	Protopasta	0,588E3
ESD safe ABS	Unknown load of MWCNTs	3DXSTAT	0,464E6
CNT PETG	Unknown load of CNTs	3DXSTAT	0,346E9
PEKK-ESD	Unknown load of CNTs	3DXSTAT ESD	48.5E6

With the aim of analyze the potential of 3D printing conductive filaments made structures for self-monitoring the produced damage, holes of gradually increased size were performed in the center of each sample (hole enlarged using different drill bits). All materials show gradual change (resistivity increase, conductivity decrease) with increasing defect size. Results corresponding to PLA, PTGE and ABS are shown in graphs displayed in Figure 1. All materials respond positively to the formation of a defect so they could be proposed for SHM purposes, nevertheless and despite being the least conductive, CNT-PTGE is considered the best candidate since it presents the greatest change in conductivity. The type of filler integrating the nanocomposite plays a key role in this performance. Depending on the type of filler, two behaviors are observed. A) *Linear behavior* like when carbon black is the conductive filler. In this case, the change in conductivity with the size of the defect is remains linear for the whole range of defect-sizes evaluated. B) *Percolation behavior* like in the case of the CNTs used as fillers. In the second case, two regions can be set. Up to 5mm slow fall. From 5 mm abrupt drop (optimum zone). In this region a small variation in the size of a produced defect leads to high conductivity change, the higher change the easiest to detect so hence, these types of materials (filled with CNTs) are optimum for SHM purpose for a large range of defect sizes but specially above 5mm.

Figure 1 : Evolution of conductivity change with defect size for PLA, PTEG and ABS.

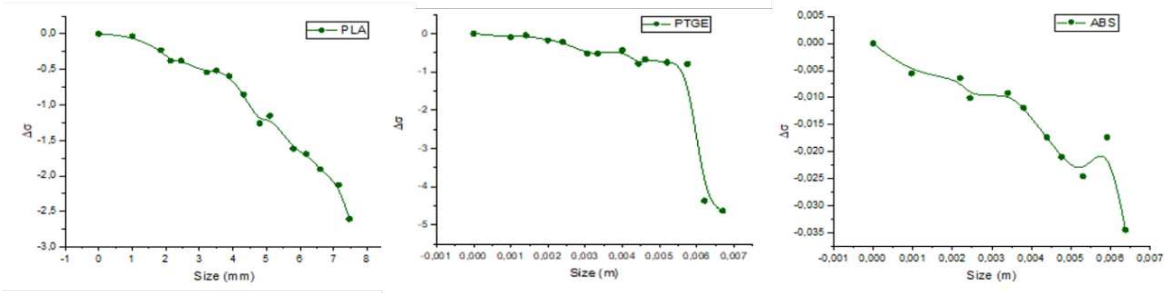

For the four polymeric filaments analyzed, simultaneous measures were taken for the variation of the strain and the variation of resistivity during a tensile test to evaluate the ability of these materials to detect mechanical deformation and evaluate their capacity for applications in body motion and strain detection. The results, shown in graphs of Figure 2 are very satisfactory: for all materials, resistivity increases during deformation, and as soon as deformation ceases and the material returns to its original state, resistivity also decreases. As expected, when polymers reach their respective break point, bot curves resistivity change and strain collapses. All polymers analyzed present have a similar value of elongation being PETG is the most "elastic", ABS is half elastic than PETG while PEKK is the one that endures more cycles as expected since

it belongs to the polymer family known as “high performance polymers” characterized by their extraordinary mechanical properties.

Figure 2. Simultaneus measurements of resistivity change (red lines) and strain (blue lines) for conductive ABS, PLA, PETG and PEKK respectively.

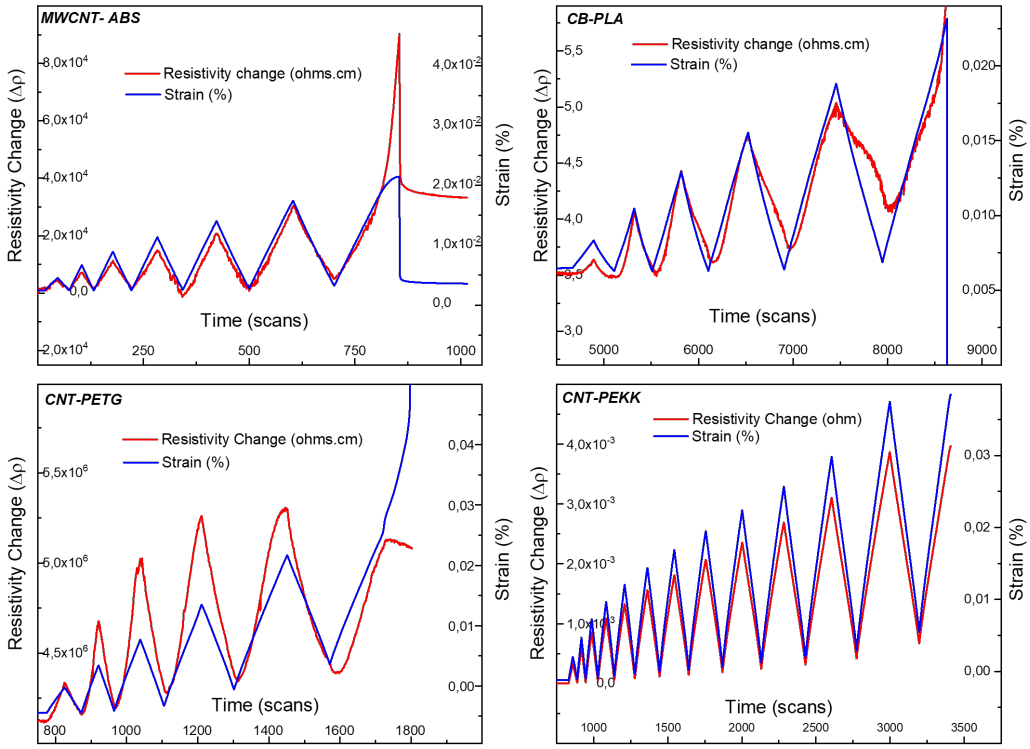

3.2 Epoxy resin with CNTs

With the aim of study the percolation curve of epoxy resin loaded with an undetermined amount of CNTs, we prepare different blends of epoxy resin RTM6 and Epocyl resin containing the CNTs load. Results corresponding to the electrical conductivity of each blend for each different blend is represented in Fig 3a. The expected plateau after reaching maximum of percolation curve is not achieved even for the blend containing a 100% of Epocyl resin. For the following experiments this was the blend selected. We prepare a batch of dog-bone test tubes for mechanical tests and a batch of rectangular (4 x 10 cm) tests to measure evolution of resistivity when the hole size increases gradually since the geometry is simpler. Results are presented in Fig 3b, the resistivity change before and after the production of the defect increases linearly with the gradual increase of size defect. For the window of hole size analyzed, a big range of resistivity is acquired which indicates that CNTs based epoxy resin is an excellent candidate for SHM, since even the smallest variation of defect size produces a clearly measured conductivity change. The reason of the good response is the effect of the breaking of the percolation chains of the CNTs dispersed in the resin. On the other hand, capability for strain detection was also evaluated by simultaneously measuring of the variation of the strain and the variation of resistivity during a tensile test. The results, shown in Fig 3c are very satisfactory: resistivity increases during deformation, and as

  doi:10.5075/epfl-298799_978-2-9701614-0-0

soon as deformation ceases and the material returns to its original state, resistivity also decreases. Results shows good capability of this material for strain and motion detection applications.

Figure 3. a) Percolation curve of Epoxy resin filled with CNT- based Epoxy resin. b) Evolution of change of the resistivity with defect size. c) Simultaneus measurements of resistivity change (red lines) and strain (blue lines) for conductive epoxy resin.

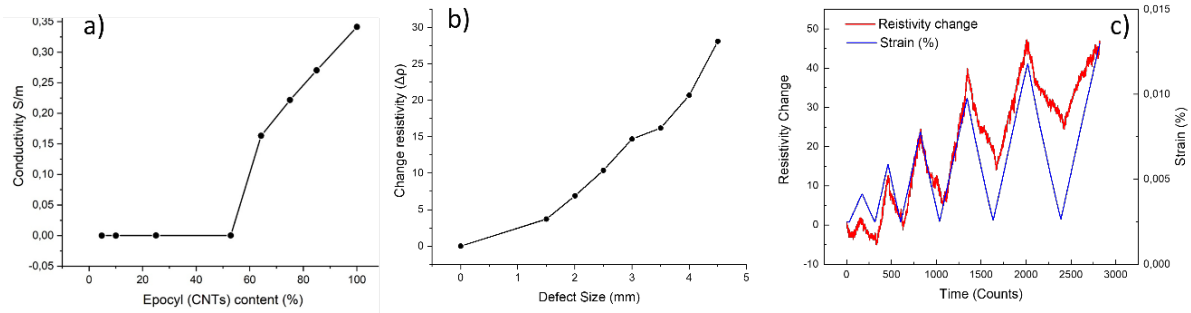

3.3 Carbon fiber reinforced polymer composite

The study of evolution of conductivity properties with the increasing size of drilled hole reveals that this material does not respond well when defect-sizes are low (below 7 mm, see Fig 4a). The reason lies in the fact that long fibers do not create percolation nets allowing conductivity changes. By expanding the range of the defect size, its influence on the conductivity measurements begins to be noticed. This means that, for defects larger than 8 mm, this material is valid for SHM by the electrical resistivity method.

We simultaneously measured the variation in resistance between two electrodes separated by a distance of 5 cm, as well as the deformation generated in the specimen during a tensile test (fig 4b). Changes in resistivity were measured using electrodes and strain using strain gauges. The electrodes consist of silver paint directly on the previously sanded surface in the center of the specimen, then the crocodiles are placed and fastened with copper tape (note, the copper tape ends up coming loose). The gauges are placed symmetrically on both sides of the specimen between the electrodes with glue.

We have started to do cycles of loading and unloading that are clearly shown in graphs displayed in fig 4b. Three different phases might be distinguished: Phase 1: The resistance measurements at the beginning follow well those of traction in phase and intensity. During this phase, at the end of the discharge cycle, the value of $\Delta R/l$ is zero. Phase 2: In phase 2, the first cracks appear and the permanent damage, therefore, at the end of the discharge cycles, $\Delta R/l$ always has a value other than zero due to the permanently open cracks (black dashed line). In this phase, the two signals (mechanical and resistive) also begin to shift. Phase 3: After the eighth cycle, the gauges stop measuring, it is assumed that there is a big damage produced in the resin until finally reach the breakage.

With the aim of evaluate failure location capacities of this material, measurements using an electrode configuration consisting of silver electrodes painted on the edges of the 20 x 20 cm

  doi:10.5075/epfl-298799_978-2-9701614-0-0

specimen (picture of Fig 4.c): 5 pairs of electrodes on the X axis and 4 pairs of electrodes on the Y axis separated by 5 cm. Two holes located at the positions indicated in the drawing of Fig4e were made using a drill, two 1.5 cm in diameter and the other 2 x 1 cm. Resistance values were measured between faced pair of electrodes, results are displayed in bars graphics of Fig 4e for pairs in X axis and Y axis. For positions where the resistivity change is reach higher values, a defect is assumed, and from values represented these graphics we can conclude that the material might self-detect the production and position of a defect of 2 x 1 cm located at X4Y4.

Figure 4. a) Evolution of resistivity change with defect-size. b) Simultaneus measurements of resistivity change (red lines) and strain (blue lines). C) Picture of the conductivity measurements set up. d) Carbon fiber based epoxy resin composite coupon prepared to evaluate failure detection capacities. e) measurements of resistivity change for different faced pairs of électrodes when holes are drilled.

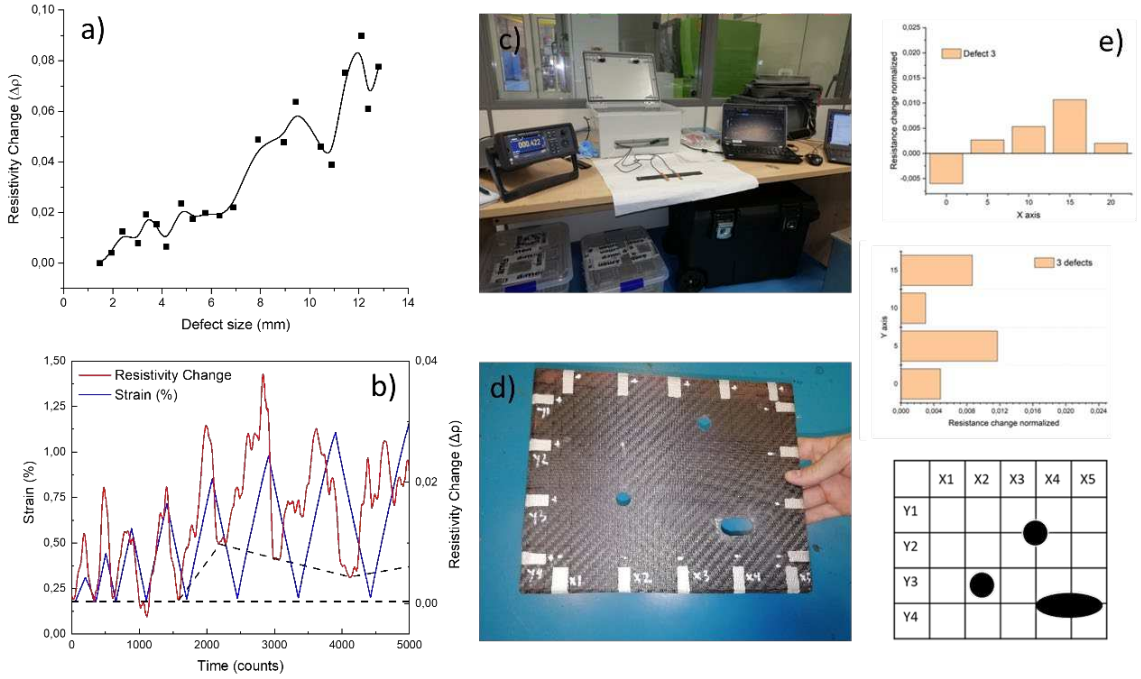

4. Conclusions

In the presented work, electrical properties, and both damage and strain dependent electrical resistance characteristics of several different carbon-based/polymer composite and nanocomposite materials were investigated: (a) CNTs reinforced RTM6 Epoxy resin, (b) different carbon-based nano additives thermoplastic composite for 3D printing technologies prepreg composite: PLA/CB; ABS/CNTs; PETG/CNTs and PEKK/CNTs and (c) long carbon fiber composite laminates.

All polymeric conductive composite and nanocomposite materials evaluated in this work present response to the formation of structural damage, being nanocomposite based in small amount of nanomaterials like CNTs the most sensitive and promised for applications in SHM.

All polymeric conductive composite and nanocomposite materials evaluated of different nature (thermoset and thermoplastic) have been proved suitable for applications in strain and motion

  doi:10.5075/epfl-298799_978-2-9701614-0-0

detection. Long carbon fiber-based composites, allow to detect the production of microcracks during tensile tests.

Long carbon fiber-based composites, allow to detect the production and the location of defects of 2 x 1 cm.

5. Acknowledgements

Works presented in this paper have been funded by the Spanish National Science and Technology Minister through the project READI (Ayudas Cervera para Centros Tecnológicos EXP - 00122598 / CER-20191020) of the Red Cervera programm.

6. References

1. K. Diamanti, et al. Structural health monitoring techniques for aircraft composites tructures. Progress in Aerospace Sciences 46 (2010) 342–352.
2. Myounggu Park, et al. Strain-dependent electrical resistance of multi-walled carbon nanotube/polymer composite films. Nanotechnology 19 (2008) 055705 (7pp). doi:10.1088/0957-4484/19/05/055705.
3. Erik T Thostenson et al. Real-time in situ sensing of damage evolution in advanced fiber composites using carbon nanotube networks. Nanotechnology 19 (2008) 215713 (6pp). doi:10.1088/0957-4484/19/21/215713.
4. Limin Gao, et al. Sensing of Damage Mechanisms in Fiber-Reinforced Composites under Cyclic Loading using Carbon Nanotubes. Adv. Funct. Mater. 2009, 19, 123–130. DOI: 10.1002/adfm.200800865.
5. Joung-Man Park et al. Inherent sensing and interfacial evaluation of carbon nanofiber and nanotube/epoxy composites using electrical resistance measurement and micromechanical technique. Composites: Part B 38 (2007) 847–861.
6. Christian Viets, et al. Damage mapping of GFRP via electrical resistance measurements using nanocomposite epoxy matrix systems. Composite part B. 2013. dx.doi.org/10.1016/j.compositesb.2013.09.049.
7. http://www.eco-compass.eu/context-2
8. Rui Zhang et al. Strain sensing behaviour of elastomeric composite films containing carbon nanotubes under cyclic loading. Composites Science and Technology 74 (2013) 1–5.
9. Katsunori Suzuki. Rapid-response, Widely Stretchable Sensor of Aligned MWCNT/Elastomer Composites for Human Motion Detection.2016. DOI: 10.1021/acssensors.6b00145.
10. Conor S Boland et al. Sensitive, High-Strain, High-Rate Bodily Motion Sensors Based on GrapheneRubber Composites. 2017. (DOI: 10.1002/adfm.201606604).
11. Hongfei Zhu. Versatile Electronic Skins for Motion Detection of Joints Enabled by Aligned Few-Walled Carbon Nanotubes in Flexible Polymer Composites.2017. DOI: 10.1002/adfm.201606604.

  doi:10.5075/epfl-298799_978-2-9701614-0-0

SUSTAINABLE POLYBUTYLENE SUCCINATE BIOPOLYMER FOR 3D PRINTING APPLICATIONS

Gerda Gaidukova[a], Sergejs Gaidukovs[b]

a: Latvian Maritime Academy, Flotes 3-7, Riga LV-1016, Latvia,
b: Institute of Polymer Materials, Faculty of Materials Science and Applied Chemistry, Riga Technical University, P. Valdena 3/7, LV-1048 Riga, Latvia,

Abstract: *The polybutylene succinate biopolymer 3D printing application has been assessed for the mean of the environmental impact and inventory analysis compared to the traditionally widely used polylactide (PLA) polymer. The waste, pollution, and energy impact were assessed for those materials. The proposed polybutylene succinate polymer filament was processed from the commercial pellets by melt blending extrusion and Fused Filament Fabrication (FFF) tests. The samples were printed using the heuristic optimization procedure for printing fabrication. The specimens were prepared by modifying printing conditions – velocity, temperature, retraction, and other processing parameters. Several shapes specimens have been tested – bars, double dog bones, and other structures. The specimens have been assessed for mechanical response in tension conditions by applying external impact factors and humidity (25%, 100%).*

Keywords: polybutylene succinate; cellulose; hemp; composites; 3D printing

1. Introduction

Additive manufacturing is three-dimensional processing, known as printing; it refers to the fabrication of objects by layer-by-layer material deposition using a printer (1). 3D printing technology was first implemented in the early 1980s (2). There are many benefits and disadvantages considered to 3D printing compared to traditional manufacturing methods (3,4). The main advantage of 3D printing is the possibility to economically build custom products in small quantities as if mass production were used.

One widely used 3D printing technology to process polymer materials and composites, is a Fused Filament Fabrication (FFF) or Fused Deposition Modeling (FDM). FFF considers extrusion of thermoplastic polymer materials previously shaped as a uniformly melted filament material onto a platform. The product structure is built up layer by layer (5–7).

Thermoplastic polymers, such as acrylonitrile butadiene styrene (ABS), polylactic acid (PLA), polyamide (PA), and polycarbonate (PC), are commonly used for FFF. Their sustainability is limited due to the fossil source (8-10). The high environmental impact of fossil polymer pollution contributes to the tremendous use of non-biodegradable polymer materials (11).

Many biodegradable polymers such as polylactic acid (PLA), poly-hydroxy-alkanoates (PHA), poly-3-hydroxybutyrate (PHB), polyhydroxy-valerate (PHV), and poly-hydroxy-hexanoate (PHH) have been obtained from renewable biomass or even biowaste resources (12-13).

  doi:10.5075/epfl-298799_978-2-9701614-0-0

This paper aims at very brief information on the first trials of ongoing research in 3D printing of biobased polymer PBS, which could be a brilliant alternative to the existing fossil polymers used in FFF 3D printing.

2. Experimental

2.1 Materials and methods

A commercial-grade PLA feedstock material PLA Janbex (with a density of 0.9 g/cm3 and a melting point of 175 °C [as determined by differential scanning calorimetry (DSC) in the first heating run], was used as a reference to compare laboratory prepared PBS (with density 0.95 and melting point 110 °C) was used in all experiments. The PLA filaments of 0.175 cm in diameter were used as received. The PBS filament of 0.175 cm was extruded by a 3DEVO laboratory extruder machine.

A FFF 3D printer was obtained from Massportal Ltd (Riga, Latvia). Printing has been performed by a developed heuristic optimization procedure for printing fabrication, as presented before (14). 30, 60, and 100% filling were chosen for the dog bone sample. Samples were printed in the so-called wet and dried state. Massportal Ltd developed a drier was used for in situ drying of the filaments before FFF processing.

The obtained PBS filaments printed dog-bone samples, and characteristic lego cube shapes are shown in Figure 1. At least ten samples were printed and tested in tension conditions using a Tinius tensile machine (5 mm/min).

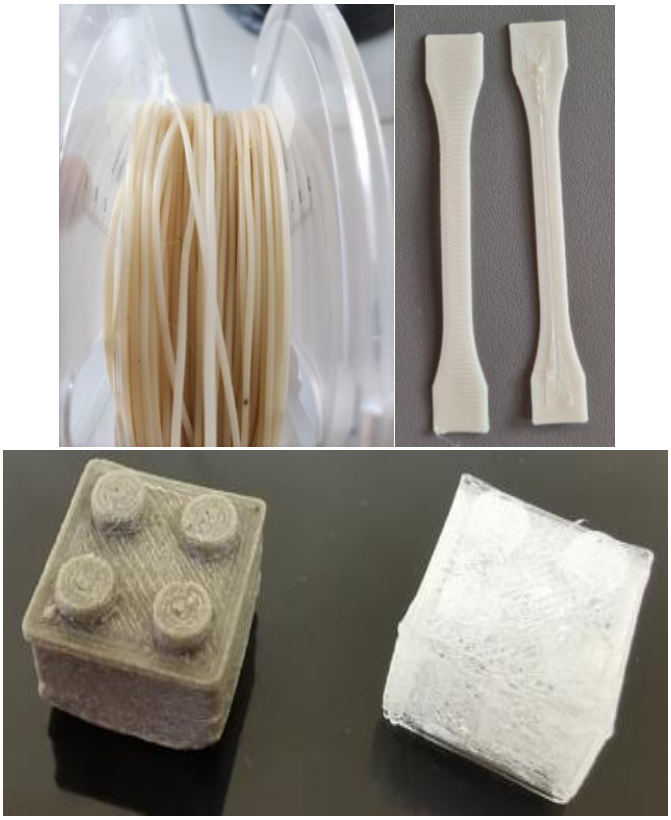

Figure 1. Prepared FFF filaments, 3D printed dog bone and lego© model cube samples

  doi:10.5075/epfl-298799_978-2-9701614-0-0

3. Discussion

The drying process conditions significantly impacts the printing of the polymer filaments, especially the quality of the prints depending on the water trace content in the polymer material. The printing started with drying the filaments with similar drying conditions by the particular convective dryer machine that the Massportal has developed. The drying curves of the obtained PBS filament and reference PLA filaments are shown in Figure 2. PBS showed a significantly higher decrease in weight than the PLA filament material.

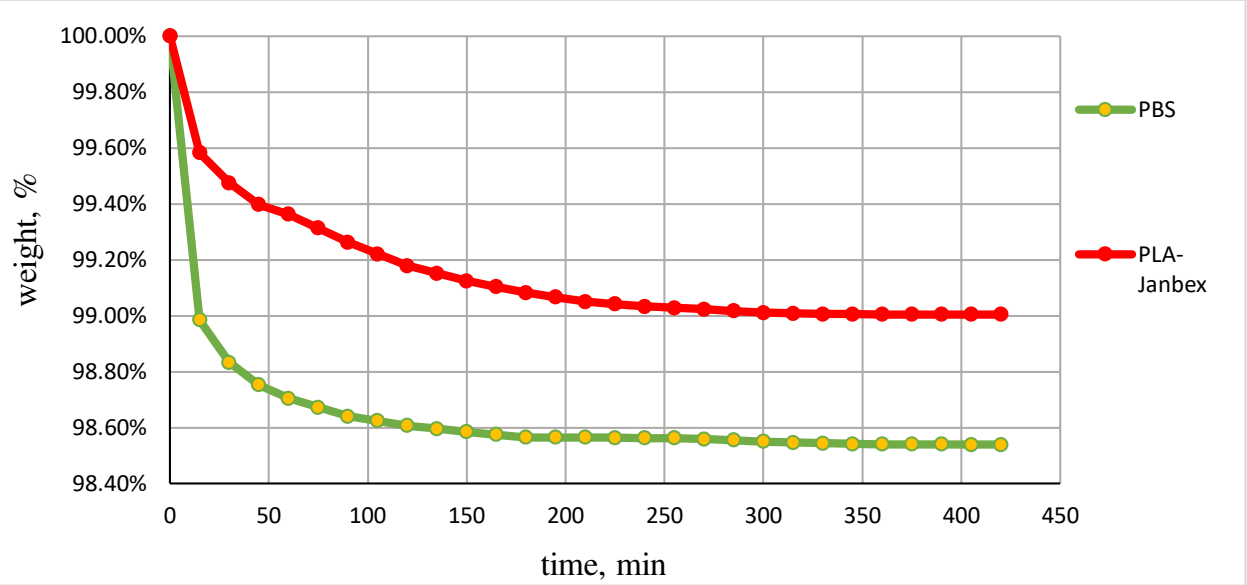

Figure 2. Drying curves for PBS and PLA filaments

The obtained tensile curves of the PLA and PBS printed samples are shown in Figure 3. It is convinced that remained water traces in the filament materials enormously decrease the mechanical performance. Both printed wet polymer materials decreased strength, while only PBS showed some deformation increase. The obtained characteristic behavior could be connected with some plasticization of the polymer material and possible degradation during the thermal printing process.

In Figure 4, the tensile curves of the dried PBS filament printed with 30, 60, and 100% infills are shown. As the infill rises from 30% to 100%, the characteristic tensile curves shift to the higher stress values. The highest strength is given for 100% infill correspondingly.

  doi:10.5075/epfl-298799_978-2-9701614-0-0

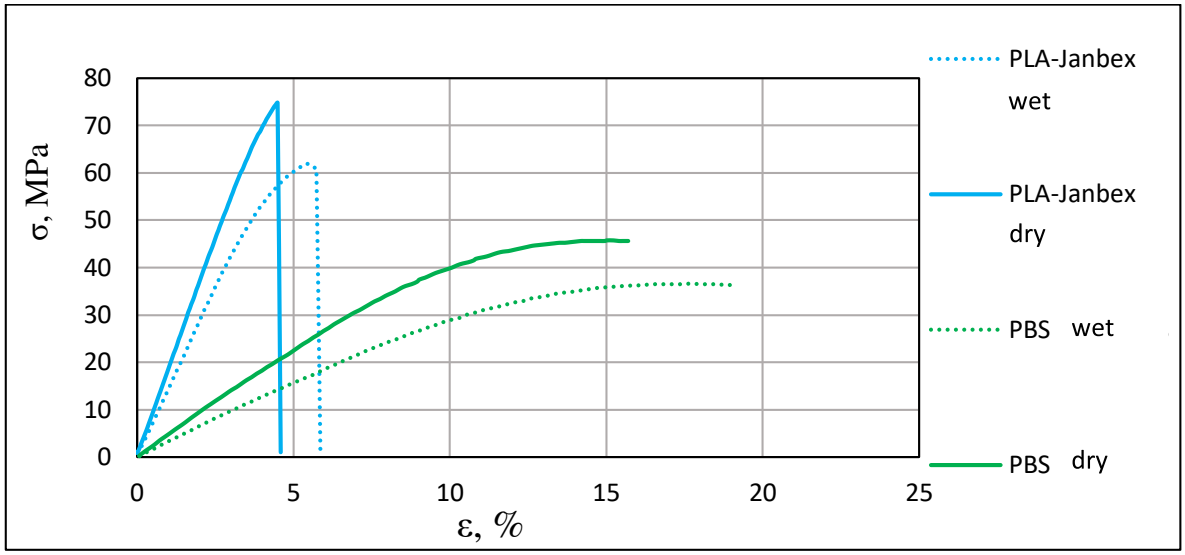

Figure 3. Tensile curves for PLA and PBS samples printed with dry and wet filaments

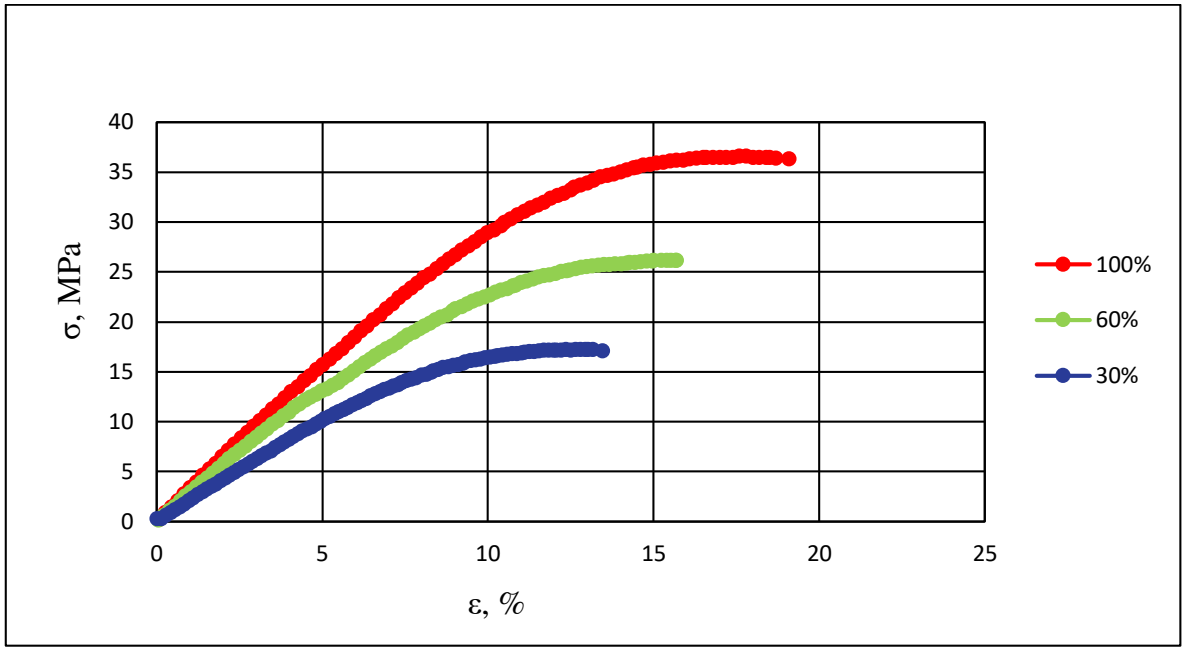

Figure 4. Tensile curves for PBS samples printed with infill 30, 60 un 100%

4. Conclusions

The present research summarizes the first tryouts and the ongoing efforts to prepare biobased PBS filaments and obtain high-quality prints. The performance of the current materials could be controlled by infill during the print. The drying quality of the polymer filament is vital to receive the highest mechanical performance of the printed parts.

5. Acknowledgments

This work has been supported by the European Regional Development Fund within the Activity 1.1.1.2 “Post-doctoral Research Aid” of the Specific Aid Objective 1.1.1 “To increase the research and innovative capacity of scientific institutions of Latvia and the ability to attract external financing, investing in human resources and infrastructure” of the Operational Programme “Growth and Employment” (No. 1.1.1.2/VIAA/3/19/478).

6. References

1. Li N, Qiao D, Zhao S, Lin Q, Zhang B, Xie F. 3D printing to innovate biopolymer materials for demanding applications: A review. Materials Today Chemistry. 2021 Jun;20:100459.
2. Zhu J, Wu P, Chao Y, Yu J, Zhu W, Liu Z, et al. Recent advances in 3D printing for catalytic applications. Chemical Engineering Journal. 2022 Apr;433:134341.
3. Berman B. 3-D printing: The new industrial revolution. Business Horizons. 2012 Mar;55(2):155–62.
4. Zhang J, Amini N, Morton DAV, Hapgood KP. 3D printing with particles as feedstock materials. Advanced Powder Technology. 2021 Sep;32(9):3324–45.
5. Kennedy ZC, Christ JF. Printing polymer blends through in situ active mixing during fused filament fabrication. Additive Manufacturing. 2020 Dec;36:101233.
6. Pei S, Wang K, Chen CB, Li J, Li Y, Zeng D, et al. Process-structure-property analysis of short carbon fiber reinforced polymer composite via fused filament fabrication. Journal of Manufacturing Processes. 2021 Apr;64:544–56.
7. Ferraris E, Zhang J, van Hooreweder B. Thermography based in-process monitoring of Fused Filament Fabrication of polymeric parts. CIRP Annals. 2019;68(1):213–6.
8. Bhagia S, Bornani K, Agrawal R, Satlewal A, Ďurkovič J, Lagaňa R, et al. Critical review of FDM 3D printing of PLA biocomposites filled with biomass resources, characterization, biodegradability, upcycling and opportunities for biorefineries. Applied Materials Today. 2021 Sep;24:101078.
9. Pei S, Wang K, Chen CB, Li J, Li Y, Zeng D, et al. Process-structure-property analysis of short carbon fiber reinforced polymer composite via fused filament fabrication. Journal of Manufacturing Processes. 2021 Apr;64:544–56.
10. Vinod A, Sanjay MR, Suchart S, Jyotishkumar P. Renewable and sustainable biobased materials: An assessment on biofibers, biofilms, biopolymers and biocomposites. Journal of Cleaner Production. 2020 Jun;258:120978.
11. Syberg K, Nielsen MB, Oturai NB, Clausen LPW, Ramos TM, Hansen SF. Circular economy and reduction of micro(nano)plastics contamination. Journal of Hazardous Materials Advances. 2022 Feb;5:100044.

  doi:10.5075/epfl-298799_978-2-9701614-0-0

12. Vinod A, Sanjay MR, Suchart S, Jyotishkumar P. Renewable and sustainable biobased materials: An assessment on biofibers, biofilms, biopolymers and biocomposites. Journal of Cleaner Production. 2020 Jun;258:120978.

13. Yaashikaa PR, Senthil Kumar P, Karishma S. Review on biopolymers and composites – Evolving material as adsorbents in removing environmental pollutants. Environmental Research. 2022 Sep;212:113114.

14. Bakradze G, Arājs E, Gaidukovs S, Thakur VK. On the Heuristic Procedure to Determine Processing Parameters in Additive Manufacturing Based on Materials Extrusion. Polymers (Basel). 2020 Dec 16;12(12):3009.

  doi:10.5075/epfl-298799_978-2-9701614-0-0

ECCM
26-30 JUNE
2022
LAUSANNE
SWITZERLAND

ECCM20 - Proceedings

ISBN: 978-2-9701614-0-0
DOI: 10.5075/epfl-298799_978-2-9701614-0-0